Experimental investigations and non-linear numerical analyses of skewed one-way prestressed concrete bridge decks

Volume 2 : Analytical Investigations

Thesis submitted in accordance with the requirements of the University of Liverpool for the degree of

Doctor in Philosophy

by

Michael D Cope

September 1987

SUMMARY

This thesis is primarily concerned with the design and analysis of composite concrete bridge decks, although some of the analytical procedures developed herein have a wider applicability. In the current study composite construction refers to precast, pretensioned concrete beams acting compositely with insitu concrete.

The work is broadly divided into two sections, experimental and analytical. For the experimental programme two 1:3.5 scale models of skewed bridge decks were designed to current standards and meticulously constructed. Comprehensive data acquisition facilities were installed and the testing programme for each model deck was based on current design loading. Detailed test results are presented and the full range structural response investigated and explained. The analytical investigation programme ran concurrently with the experimental programme and involved the development of material and structural modelling schemes and appropriate numerical modelling techniques. These were incorporated in an analytical package which involved the design and implementation of a sophisticated finite element program named SNAP.

Composite concrete bridge decks are the solutions chosen for many crossings in the UK. However, the literature survey revealed that the previous experimental research was very limited and had been conducted during the 1950's. This position is reflected in the limited and ambiguous guidance that is currently available to designers. No analytical research on composite construction could be found.

The experimental programme revealed several interesting features, such as; the inherently large factor of safety that results from current design practices; the unusual crack patterns that indicate limited breakdown of composite action; the complete breakdown of composite action along the supported edges at high load levels. The implications of the observed structural behaviour for analysts and designers are explored.

The heterosis plate bending element was selected for the finite element analyses. Sophisticated non-linear solution procedures, including the arc-length method and the BFGS quasi-Newton method, were also developed and incorporated into the SNAP program. A decisive feature in the success of the analyses described herein was the inclusion in the program of a wide range of solution procedures, which were available for selection based on the current structural behaviour. The program was endowed with limited intelligence so that it could automatically switch between solution methods as numerical difficulties were encountered during an analysis. The program was subjected to testing and verification against the results of other published investigations. The SNAP program design philosophy resulted in a simple to use, comprehensive and effective tool for the analyst. Several new analytical concepts and methods, such as; a hybrid element for analyses of composite construction; scaled space and new convergence criteria and; statistically varied material properties were developed during the present study.

Finally, conclusions are drawn from the reported investigations and recommendations for further work are given.

CONTENTS

NOMENCLATURE

General notation

$\bullet$	Denotes any variable
A	Denotes a matrix A
a	Denotes a vector a
A or a	Denotes a scalar A or a
$\Delta\bullet$	Denotes an incremental quantity
$\delta\bullet$	Denotes an iterational quantity
$\hat{\bullet}$	Denotes a local quantity defined within a section
$\bullet^n$	Generally denotes increment 'n'
$\bullet_i$	Generally denotes iteration 'i'
$\bullet_j$	Generally denotes line search trial 'j'
$\bullet_k$	Denotes element 'k' of variable $\bullet$
$\bullet_{m,n}$	Denotes the element corresponding to node m degree of freedom type 'n' in variable $\bullet$
$\lvert\bullet\rvert$	Absolute value
$\lVert\bullet\rVert$	Second Holder or Euclidean norm
$[\bullet]$	Square brackets are sometimes included around matrices or vectors to enhance clarity
$[\bullet]^T$	Transpose of vector $\bullet$

Specific quantities

α	Concrete principal angle
α_1, α_2	Concrete tension stiffening parameters 1 and 2
γ_i	Defined as $\gamma_i = r_{i-1} \cdot r_i$
γ_{xy}	Shear strain in xy
γ_{yz}	Shear strain in yz
γ_{xz}	Shear strain in xz
γ^I_{xy}	Inplane component of the shear strain in xy
γ_{f3}	BS5400 design load effects partial safety factor
γ_{fL}	BS5400 design loads partial safety factor
γ_m	BS5400 material partial safety factor

γ_T	Tangential shear strain
ϵ^*	Strains continuous over the structural domain
ϵ_{xy}	Cartesian strains
ϵ_{12}	Principal strains
$\Delta\epsilon_{12}$	Principal incremental strains
ϵ'_{12}	Principal effective strains
$\Delta\epsilon'_{12}$	Principal effective incremental strains
$\epsilon_{\overline{xy}}$	Strains resolved to either beam or steel local directions
$\epsilon_{\overline{x}}$	Strain in steel direction
ϵ_o	Strain at maximum concrete compressive stress
ϵ_u	Strain at which crushing of concrete begins
ϵ_m	Strain at which concrete stress returns to zero in the post crushing region
ϵ_{cr}	Concrete cracking strain
ϵ^o	Cartesian strain offsets
ϵ^*_{12}	Scaled principal total strains
ϵ_x	Direct strain in x
ϵ_y	Direct strain in y
ϵ^I_x	In-plane component of direct strain in x
ϵ^I_y	In-plane component of direct strain in y
θ_x	Nodal rotation around the y axis
θ_y	Nodal rotation around the x axis
θ	Angle between steel direction and the x axis
$\theta_{\overline{x}}, \theta_{\overline{y}}$	Nodal rotations transformed to either beam or steel local directions
θ_{1T}, θ_{2T}	Tangential rotations for local nodes 1 and 2
κ_x	Direct curvature in x
κ_y	Direct curvature in y
κ_{xy}	Twisting curvature in xy
λ_1 λ_2	Matrix eigenvalues

μ	Moment factor for transverse ultimate sagging resistance
μ'	Moment factor for transverse ultimate hogging resistance
ν	Poisson's ratio
ξ, η	Element local coordinates
σ^*	Stresses continuous over the structural domain
σ_{xy}	Cartesian stresses
σ_{12}	Principal stresses
$\sigma_{\overline{xy}}$	Stresses in either beam or steel local directions
σ_o	Concrete maximum compressive stress
absmax	Maximum permitted line search scale factor
B	Strain-displacement matrix
B_b, B_s	Strain-displacement matrices for bending and shear components respectively
$B^n{}_b, B^n{}_s$	Strain-displacement matrices for node 'n' for bending and shear components respectively
c	Matrix condition number
D^*	Continuous variables elasticity operator
D_{xy}	Modular matrix in Cartesian coordinates
$D^c{}_{12}$	Concrete modular matrix in principal directions
$D^s{}_{xy}$	Steel modular matrix in Cartesian directions
$D^s{}_{\overline{xy}}$	Steel modular matrix in steel directions
$D^b{}_b, D^b{}_s$	Modular matrix for beams in bending and shear respectively
$D^s{}_b$	Modular matrix for steel in bending
$\bar{D}^b{}_b, \bar{D}^b{}_s$	Bending and shear modular matrices for smeared beams in local beam directions
D_x	Modular matrix element for Cartesian x direction
D_y	Modular matrix element for Cartesian y direction
D_1	Off diagonal modular matrix element
D_{xy}	Modular matrix element for Cartesian xy direction
$Dtol_n$	Displacement convergence tolerance for dof type 'n'

$Dtol_t$	Displacement convergence tolerance for all dof types combined
$Etol_n$	Energy convergence tolerance for dof type 'n'
$Etol_t$	Energy convergence tolerance for all dof types combined
E	Young's modulus
E^c_1, E^c_2	Concrete tangent moduli in principal/crack directions
E^s	Steel tangent modulus in steel direction
f(u)	Internal force vector at displacement level u
f_t	Concrete tensile strength
$Ftol_n$	Force convergence tolerance for dof type 'n'
$Ftol_t$	Force convergence tolerance for all dof types combined
F	Non-dimensionalising factor
G^c	Concrete shear modulus
G^c_r	Residual concrete shear modulus
$G_{i,j}$	Energy dissipated by the residual forces in the direction of the iterative displacements for iteration i, line search trial j
$GO_{i,j}$	Energy dissipated by the old residual forces in the direction of the iterative displacements for iteration i, line search trial j
H_u	Interpolation functions for displacements
H_σ	Interpolation functions for stresses
H_ϵ	Interpolation functions for strains
I_d	Desired number of iterations in an increment
I^{n-1}	Number of iterations in increment n-1
I	Moment of inertia
J	Jacobian matrix
K	Stiffness matrix
$K_{k,k}$	Leading diagonal coefficient of K for dof 'K'
$K_{m,n\ m,n}$	Leading diagonal coefficient of K for dof type 'n' of node 'm'
K_1	Most recently formed stiffness matrix
K^e_b, K^e_s	Elemental stiffness matrices for bending and shear respectively

$\Delta\ell^n$	Desired incremental change in either the characteristic displacement or the 'arc-length'
L^*	Continuous variables strain operator
M^*_i	Moment of resistance per unit length of sections normal to the i'th band of reinforcement
M_1	Slab ultimate sagging moment of resistance in the longitudinal direction
M_2	Slab ultimate hogging moment of resistance in the longitudinal direction
M_3	Slab ultimate sagging moment of resistance in the transverse direction
M_4	Slab ultimate hogging moment of resistance in the transverse direction
M^P_x, M^P_y, M^P_{xy}	Moment stress resultants for the plate in x, y and xy directions respectively
M^b_n	Moment stress resultant for the beam in local directions
M_x, M_y, M_{xy}	Overall moment stress resultants for the slab in x, y and xy directions
$N_{n,x}$	Partial derivative wrt x of the serendipity interpolation function for node 'n'
p	Total applied load vector
p^*	Nominal incremental load vector
p	Total load level
Δp	Incremental load level change
δp	Iterational load level change
p^*_b	Body forces continuous over the structural domain
p^*_t	Surface tractions applied to the surface of the structural domain
p_b	Discretized body forces
p_t	Discretized surface tractions
$\bar{p}$	Scaled applied load vector
$P_{n,x}$	Partial derivative wrt x of the Lagrangian shape function for node 'n'
P^P_x, P^P_y, P^P_{xy}	In-plane force stress resultants for the plate in x, y and xy directions

P^b_n	In-plane stress resultants for the beams in local coordinates
P_x, P_y, P_{xy}	Overall in-plane force stress resultants for the slab in x, y and xy directions
r(u)	Residual force vector at displacement level u, defined as r(u) = p - f(u)
r	Residual force vector as above
$\bar{r}$	Scaled residual force vector
relmax	Maximum permitted relative change in the line search scale factor during a single trial
r_n	Force, displacement or energy ratio for dof type 'n'
r_t	Force, displacement or energy ration for all dof types combined
$\bar{r}_n$	Scaled force, displacement or energy ratio for dof type 'n'
$\bar{r}_t$	Scaled force, displacement or energy ratio for all dof types combined
s^*	Surface of the structural domain
S_n	Scaled space scaling factor for dof type 'n'
s_i	Final line search scaling factor for iteration i
$s_{i,j}$	Line search scaling factor at trial j of iteration i
Tol	Line search tolerance
T	Transformation matrix
T_n	Beam torque
u	Nodal translation in the x direction
u	Total displacement vector
$\bar{u}$	Scaled total displacement vector
Δu	Incremental displacement vector
$\Delta\bar{u}$	Scaled incremental displacement vector
δu	Either virtual displacements or iterative displacement vector
$\delta\bar{u}$	Scaled iterational displacement vector
$\delta' u$	Unconstrained iterative displacement vector, used in displacement and arc-length control methods
u^ℓ	Nominal displacement vector, defined as K^{-1} p^*

u^*	Displacements continuous over the structural domain
u_*	Unknown displacement vector at end of increment
$u_{i,o}$	Displacement vector obtained with a line search scaling factor of 0
v	Nodal translation in the y direction
w	Nodal translation in the z direction
$\bar{x},\bar{y}$	Either steel or beam local coordinates
z	Distance from section neutral axis (NA)
$\bar{z}$	Distance of section neutral axis from top of section

8. SNAP PROGRAM FINITE ELEMENT FORMULATIONS

8.1 Introduction

The text within this chapter outlines the theoretical background to the algorithms that have been incorporated into the 'SNAP' computer program. Details of the analyses of the model decks using the 'SNAP' program can be found in Chapter 9. Only brief details of standard finite element theory are given here and the interested reader is referred to standard texts[1,2,3] for a more detailed explanation.

The primary aim of structural analysis is to predict the response of a structure to a system of forces when restrained by a system of boundary conditions. The advent of the digital computer has allowed the displacement based finite element method to be a successful vehicle with which to fulfil this aim. The power of modern computing systems allows the investigator to pursue his analyses along the full range of the physical response, as far as physical failure and not numerical failure, which has been common until recently.

8.2 Analytical format

Once a structure has been defined using nodal coordinates and material properties, etc. then the mathematical model of the structure can be setup. For a finite element non-linear analysis the stiffness matrix K is not constant for all load and displacement levels and hence a single assembly of the matrix is not sufficient. The present study is concerned with the response of the structure after taking into account the effects of material degradation only. The non-linear response may be traced by sub-dividing an analysis into increments. In any one increment only a proportion of the load is applied. After the new displacement level has been achieved the stiffness matrix can be recalculated, taking

into account, to a certain extent, the non-linearity of the response, see Figure 8.9. Unless small increments are used, the analytical response will tend to drift away from the experimental response. The adoption of small increments, however, results in greatly increased cost for the analysis. This problem is generally overcome by using larger increments but incorporating iterations within increments, to redistribute the residual forces so that equilibrium can be achieved and analytical drift will be prevented.

Traditionally an analysis is subdivided into increments of load. Hence, it may be said that the iterational constraint is load since we are constrained to achieve a certain load level within an increment. In this investigation other iterational constraints have also been employed such as displacement, where a certain displacement level is achieved within an increment.

8.2.1 Standard increment/iteration format

The majority of non-linear finite element analysis programs employ a standard incremental format, whether it be incrementing load, displacement or some other variable. For example, with incremental load, the system may apply a fixed load vector to account for constant loadings such as dead load, and an incrementally increased load vector to account for live loading. During the present, study this incremental format was found to be inappropriate for the structure under investigation and, therefore, a new format was developed.

8.2.2 New stage/increment/iterational format

For the new format the analysis was subdivided into stages and these stages were further sub-divided into increments. Iterations were carried out within increments to achieve equilibrium in the normal way.

During stages a fixed vector of load or other iterational constraint were applied. To this was added a proportion of an incremental vector of load or other iterational constraint in each increment. Between stages a number of features could be changed, if required, such as material properties, load vectors and boundary conditions.

The switching of material properties allowed the analysis to model the construction sequence for this form of construction accurately. Thus, in the first stage the concrete applicable to the beams was given full properties while the insitu concrete was given weak properties. This modelled the condition where the precast beams were covered with wet insitu concrete. Extra boundary conditions were applied during this stage to prevent rigid body motions, such as a rotation of the beams, which are possible with wet insitu concrete in-fill providing the only transverse continuity.

During the second stage both precast and insitu concretes were given their full properties. The incremental load vector was switched from density loading to density correction and HA loading. The extra boundary condition that had been applied during the first stage were removed. During the third and subsequent stages only the incremental loading vector is changed to that appropriate for HB loading.

8.3 Finite element discretization

In essence, the majority of structures are three dimensional. If they are modelled as three dimensional entities for analytical purposes then the analyses are likely to be expensive and complex. However, the adoption of assumptions which are appropriate to the structure under consideration allow the analyses to be simplified. The classical example of this simplification process is in the analysis of

plates, where assumptions about the through depth normal and shear strain variations lead to a pseudo 2D modelling philosophy.

Traditionally the assumptions of Kirchoff's classical thin plate theory have been used for plate analysis. With this theory, lines which were normal to the mid-surface before deformation remain straight and normal to the mid-surface after deformation. Thus precluding the effects of transverse shear deformation. Finite elements based on Kirchoff's theory require C(1) continuity in w (i.e. $\partial w/\partial x$ and $\partial w/\partial y$ have to be continuous) since the curvatures are given by $\partial^2 w/\partial x^2$ and $\partial^2 w/\partial y^2$ and $\partial^2 \omega/\partial x \partial y$. This requirement leads to complexity in element formulations. However, thin plate theory has been favoured by engineers for its conceptual simplicity.

Recently formulations based upon Mindlin[4]/Reissner[5] plate theory have begun to supersede those based on Kirchoff's thin plate theory, since Mindlin theory only requires C(0) continuity for w and the independant rotations θ_x and θ_y across element interfaces. In addition, Mindlin elements are able to model transverse shear deformations. Mindlin deduced a two dimensional theory for flexural behaviour from the three dimensional equations through assumptions about the structural behaviour. The main assumptions are given below:-

1. Displacements are small compared with the dimensions of the structure.
2. The effects of stress normal to the mid-surface of the plate are negligible, irrespective of the type of loading.
3. Lines normal to the mid-surface before deformation remain straight but not necessarily normal to the mid-surface after deformation, see Figure 8.1.

Unfortunately standard Mindlin elements do have certain problems, such as locking and rank deficiency, and these have been the subject of extensive research. Nagtegaal[15] et al proposed the method of constraint counting as a mean of assessing an elements susceptibility to locking. Hinton[16] et al used the method of constraint counting to assess the suitability of Serendipity and Lagrangian elements for thin plate situations. It was shown that Serendipity elements may lock in thin plate situations while Lagrangian elements usually do not. Several different schemes have been proposed for the alleviation of these problems. At the moment two different approaches appear to offer solutions to these problems and they are either the application of discrete Kirchoff mode constraints[7,8,9,10,11] or reduced/selective integration[6,12,13,14].

For a fuller account, the interested reader is directed to a comprehensive discussion on the features of current plate bending elements by Rahman[17].

The 'Heterosis' element[6], which was developed by Hughes, was chosen for the present work because it is an extremely competent plate bending element which overcomes the locking and rank deficiency problems associated with standard Mindlin elements. The element is an amalgamation of the Serendipity and Lagrangian elements. It uses the Serendipity element for the transverse (z) translations and the Lagrangian element for all other degrees of freedom. It has been shown that while the 'Heterosis' element passes the patch test as a parallelogram, it does not as a general quadilateral. The element's inability to pass the patch test as a general quadilateral should not pose a problem since the meshes used for the present study will only incorporate parallelogram shaped elements.

To allow the plate element to model the section behaviour as the material degrades, a quadratic plane stress element has been amalgamated with the Heterosis plate bending element. Thus the neutral axis is free to move as the section degrades with increased curvature.

8.3.1 Heterosis finite element

The finite element used for the investigations described herein is a hybrid of the Heterosis element. Brief details of the standard element will be given first followed by the modifications that were necessary for the present study. For a more detailed description of the standard element the reader is directed to the paper by Hughes[6].

The nodal degrees of freedom are u, v, w, θ_x and θ_y. The sign convention can be seen in Figure 8.2 and the nodal degrees of freedom (dof) are defined at the reference plane.

The strains at any point are given by:-

$$\begin{bmatrix} \epsilon^I_x \\ \epsilon^I_y \\ \gamma^I_{xy} \\ \kappa_x \\ \kappa_y \\ \kappa_{xy} \\ \gamma_{xz} \\ \gamma_{yz} \end{bmatrix} = \begin{bmatrix} \frac{\partial u}{\partial x} \\ \frac{\partial v}{\partial y} \\ \frac{\partial u}{\partial y} + \frac{\partial v}{\partial x} \\ \frac{\partial \theta}{\partial x}x \\ \frac{\partial \theta}{\partial y}y \\ \frac{\partial \theta}{\partial y}x + \frac{\partial \theta}{\partial x}y \\ \frac{\partial w}{\partial x} + \theta_x \\ \frac{\partial w}{\partial y} + \theta_y \end{bmatrix} \qquad (8.1)$$

Hence the total strains at any point within the structure are given by:-

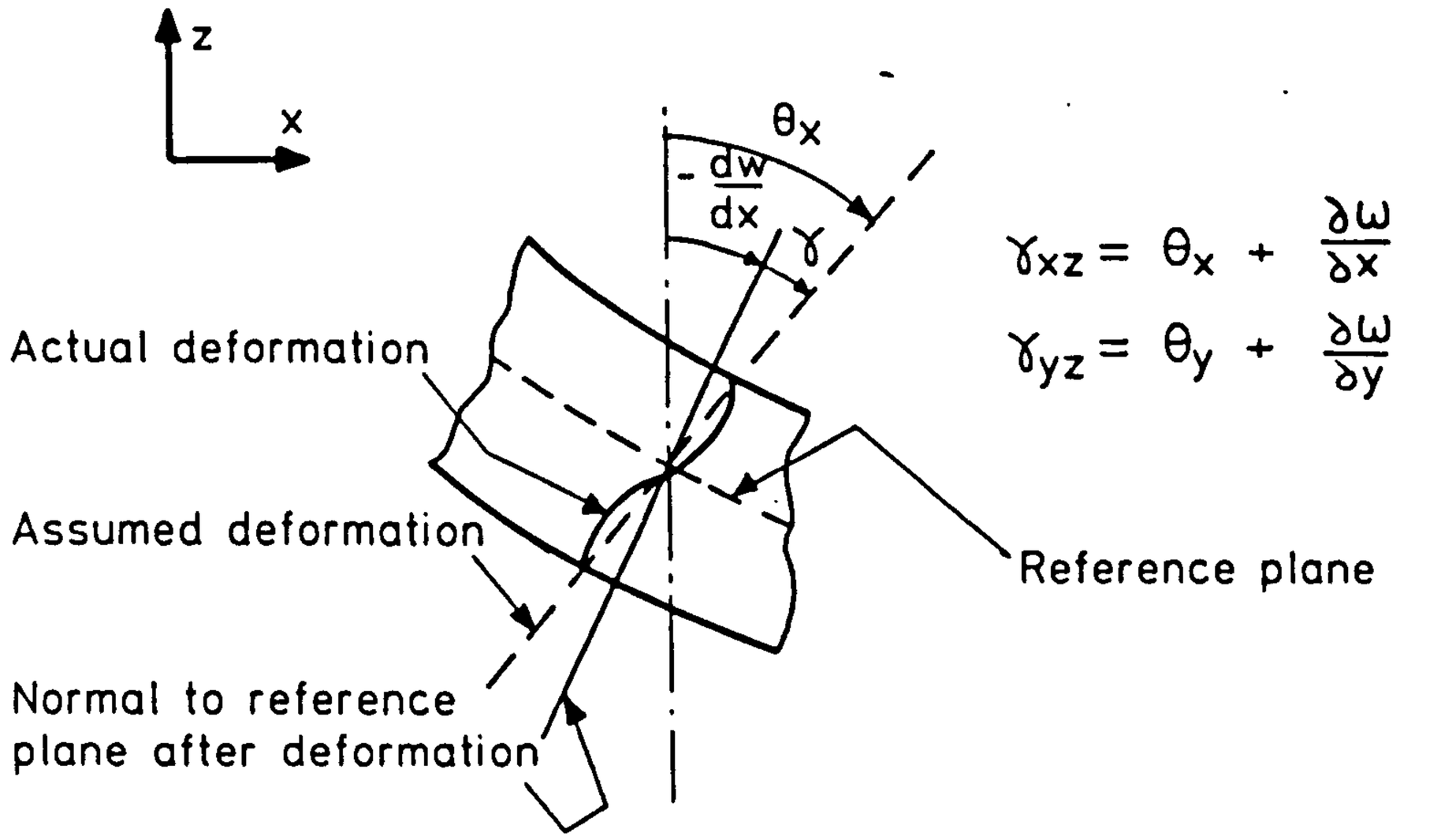

FIG. 8.1. TRANSVERSE SHEAR DEFINITION FOR MINDLIN PLATE

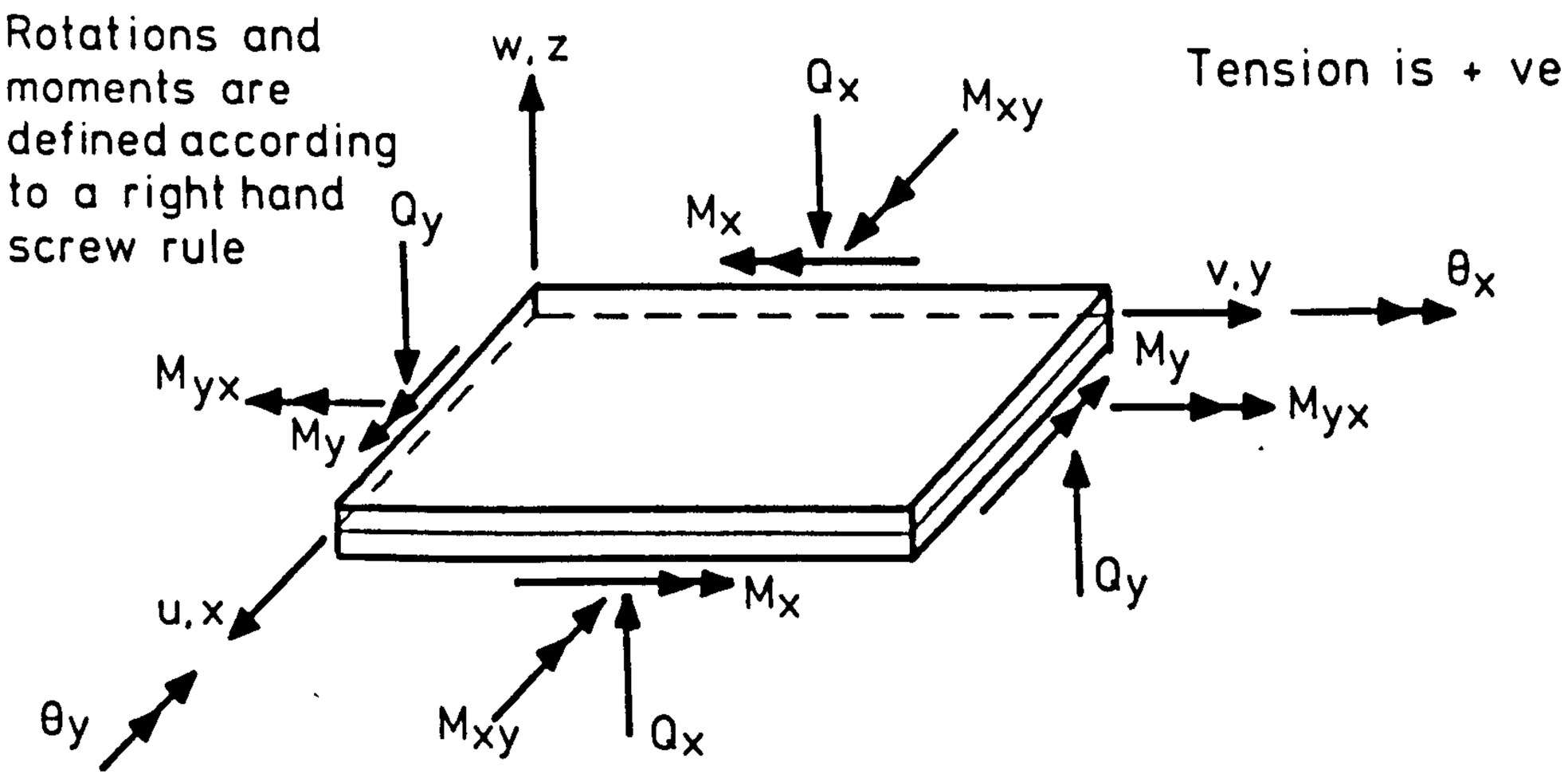

FIG. 8.2. SIGN CONVENTION FOR MINDLIN PLATE

$$\begin{bmatrix} \epsilon_x \\ \epsilon_y \\ \gamma_{xy} \\ \gamma_{xz} \\ \gamma_{yz} \end{bmatrix} - \begin{bmatrix} \epsilon^I_x + z\,\kappa_x \\ \epsilon^I_y + z\,\kappa_y \\ \gamma^I_{xy} + z\,\kappa_{xy} \\ \gamma_{xz} \\ \gamma_{yz} \end{bmatrix} \tag{8.2}$$

where z is the distance from the reference plane to the point in question.

The element is a hybrid of Serendipity and Lagrangian elements, using 8 nodes with Serendipity shape functions for the transverse displacements and 9 nodes with Lagrangian shape functions for the in-plane displacements u and v and rotations θ_x and θ_y. The element is integrated in a selective manner, using 3 x 3 for the bending energy and 2 x 2 for the transverse shear energy. The stiffness matrix for an element is given by

$$K_e = K^e_b + K^e_s \tag{8.3}$$

where

$$K^e_b = \int B^T_b\, D_b\, B_b\, dv \quad \text{bending stiffness contribution} \tag{8.4}$$

$$K^e_s = \int B^T_s\, D_s\, B_s\, dv \quad \text{shear stiffness contribution} \tag{8.5}$$

The D_b and D_s matrices contain material property information and relate the stresses to the strains. For the work described here the in-plane material properties are degraded under the control of material models, described in section 8.4, as the analyses progress. However, the transverse shear modular matrix, D_s, is assumed to remain constant throughout the analyses and is not degraded.

Numerical integration is used to evaluate the stiffness matrices given by equations 8.4 and 8.5. Gauss-Legendre integration rules are

selected for the integration over the plan area of the elements. A layered approach, involving both concrete and steel layers, was selected for the integration through depth. The use of a number of different through depth integration rules, including Newton-Cotes, Gauss, Trapezoidal etc., was investigated in the present study. Only minor differences between the predicted responses for different through depth integration schemes were noted and no difference in the required computational effort was apparent. It was found that the location of the extreme integration station was the most influential factor. If this was located away from the extreme fibre then the predicted response tended to overestimate the cracking load and underestimate the failure load.

8.3.2 Modelling of composite construction

A composite concrete bridge can be modelled as a slab of plate finite elements to which are added discrete beam elements at element boundaries. To allow this approach to be evaluated, discrete Timoshenko beam elements were incorporated into the SNAP program. Essentially a Timoshenko beam element is a one dimensional version of the two dimensional Mindlin plate element described earlier.

For structures involving relatively few beams the discrete beam approach could yield realistic results efficiently. The structures investigated for the present study incorporated numerous beams, typically 17 to 22. To obtain reasonable response predictions it was necessary to employ unrealistically fine meshes and therefore this avenue was not pursued. With discrete beams it is also difficult to model torsional stiffness and its degradation. The beams in a skew slab are subject to high torsional moments and therefore this aspect is fundamental to the response of the structure. Furthermore, the beams contained in a composite slab are encased in insitu concrete and

therefore they are subject to direct stresses orthogonal to the beam axis and in-plane shear strains. Traditional beam formulations generally treat the beam torsional stiffness as a linear quantity and ignore the orthogonal stress as being insignificant.

If, for the analysis of a skewed structure, the beam torsional stiffness is treated as a linear quantity then an artificially high failure load will generally result. The beams will generally lie at a considerable angle to the principal directions at failure, therefore, the linear torsional stiffness will preclude total failure in the actual failure directions. Even though there will be little or no shear strain in the principal failure directions, a significant shear strain will result in the beam directions after transformation. The resulting shear stress in the beam directions will, after transformation, cause a significant moment in the failure direction, which will resist failure of the section.

The integration over the volume for a beam element is generally carried out in two stages, firstly over the breadth and depth of the beam and then over the length. For the integration over the breadth and depth the section is generally divided into a number of horizontal uni-directional layers inside which the stiffness or stress is evaluated at one point as required. Knowing the distance to the neutral axis allows the section stiffness and stress resultant to be obtained as required.

When an isolated beam is subject to a torsional moment then the shear stress flows around the section approximately as shown in Figure 8.3(i). To overcome the problems described above torsional stiffness degradation could be incorporated. If one assumes that stresses orthogonal to the beam axis is insignificant, then the inclusion of

torsional stiffness integration, at the same sampling stations as direct stresses, would allow material properties to be defined in principal and not beam directions. Merely adding the integration of torsional stiffness to the existing direct stiffness evaluation at layers, is not appropriate, since the shear flow shown in Figure 8.3(ii) would be imposed.

An integration scheme similar to that shown in Figure 8.3(iii) may be more appropriate. In this scheme the section is treated as 2 dimensional and a two dimensional derivative of an integration scheme, such as Gauss-Legendre, is used. The 'z' distance for the calculation of strains from the direct and twisting curvatures, is the orthogonal distance from the axis to the integration station in question. From Figure 8.3(iii) and for integration station 3, the appropriate distances for the integration of direct bending stresses are 'a' and 'b'. For the torsional stresses the appropriate distance is 'c'. At each integration station there is a two dimensional strain system in three dimensional space and the additional effects of transverse shear have not been considered.

For the case where the precast beams are encased in hardened insitu concrete, the situation is radically different. If it is assumed that there is perfect strain compatibility at all interfaces then the portion of the slab above the bottom flanges will act as a homogeneous plate. Since a gap is left between adjacent bottom flanges during construction the detailed behaviour of the bottom flanges will be complicated. As failure of the composite deck approaches then the assumption of strain compatibility between the insitu and precast concretes may not be valid. Thus the behaviour could move towards that of a set of individual beams.

If discrete beams are used in an analysis of a composite concrete bridge deck then the best predictions are obtained with artificial values for the beam torsional stiffness. The predicted torsional stiffness of a beam in isolation can be used throughout an analysis. The underestimation of the slab torsional stiffness with this method allows better estimates of the degraded composite torsional stiffness that will occur at higher displacement levels, as failure is approached. Even with this approach, however, unrealistic failure loads can be predicted, since at very high displacement levels the small linear torsion can have a significant effect.

It has been shown above that discrete beams are not the optimum choice for the analysis of composite concrete bridge decks and therefore other avenues were investigated for the present study.

8.3.3 Modification of the Heterosis plate element for the analysis of composite concrete bridge decks

The stiffness matrix for a Heterosis plate element is formed from:-

$$K = \int B^T_b D_b B_b \, dA + \int B^T_s D_s B_s \, dA \qquad (8.6)$$

where the terms represent the bending and shear components. The integration in equation 8.6 is only carried out over the area of the element since the **B** matrices are constant through depth and the modular matrix, **D**, is the result of an integration through the depth. With smeared steel, equation 8.6 is modified to:-

$$K = \int B^T_b [D^P_b + D^S_b] B_b \, dA + \int B^T_s D^P_s B_s \, dA \qquad (8.7)$$

Implicit in equation 8.7 is the assumption of strain compatibility between the concrete and steel in the plate. For the calculation of

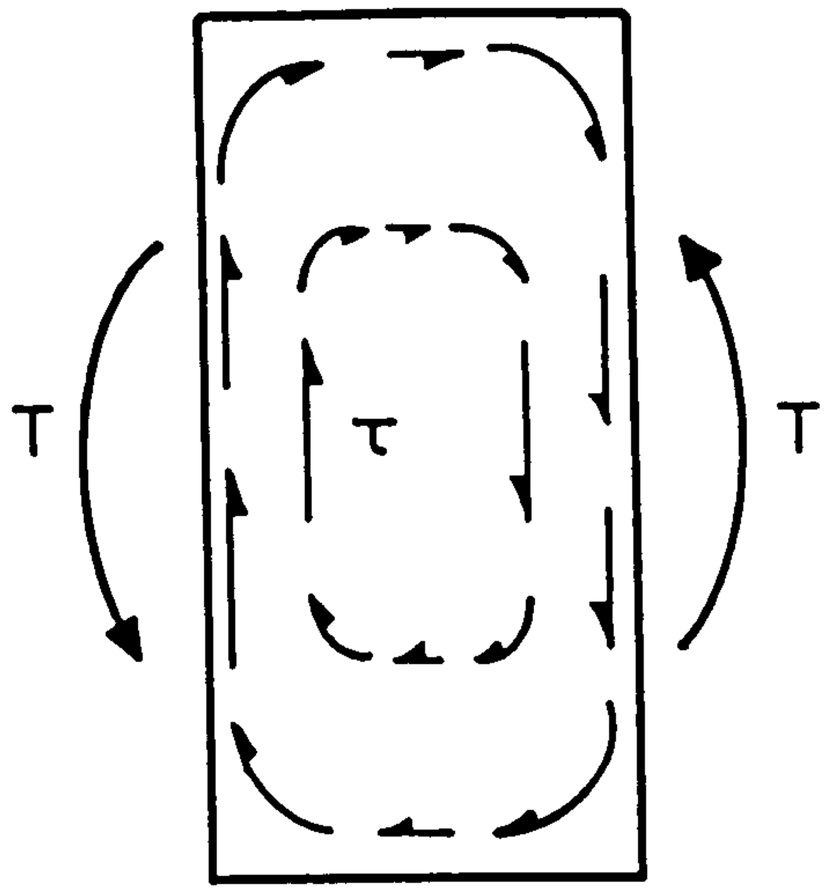

i) Approximate shear flows in a beam section subject to torsion

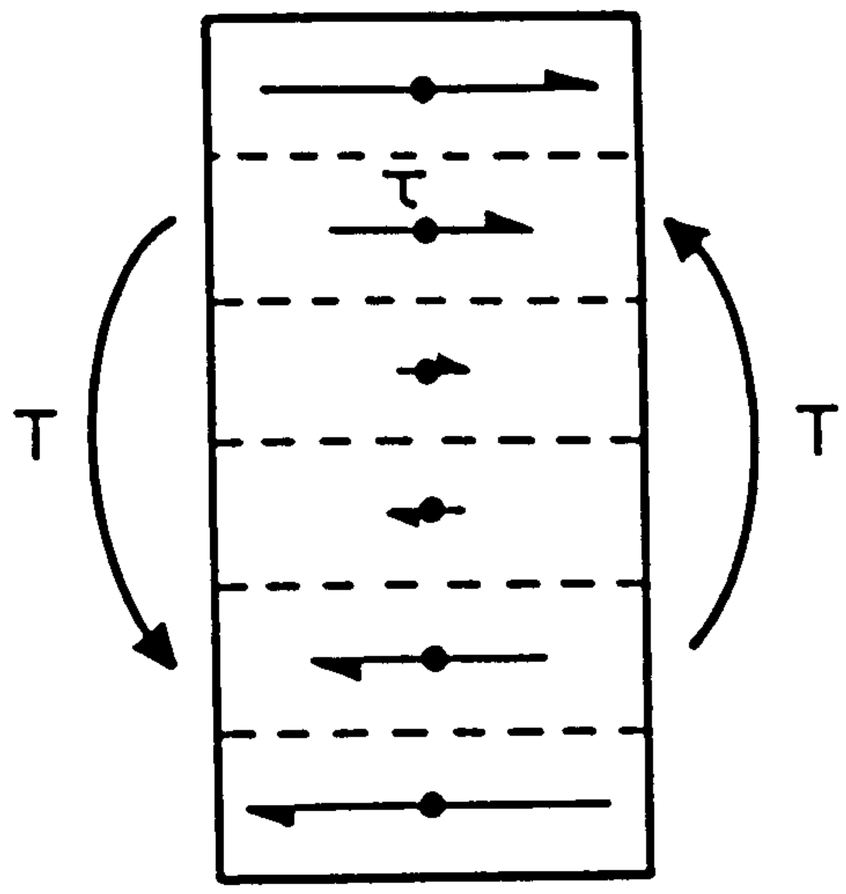

ii) Shear flows imposed by layered approach

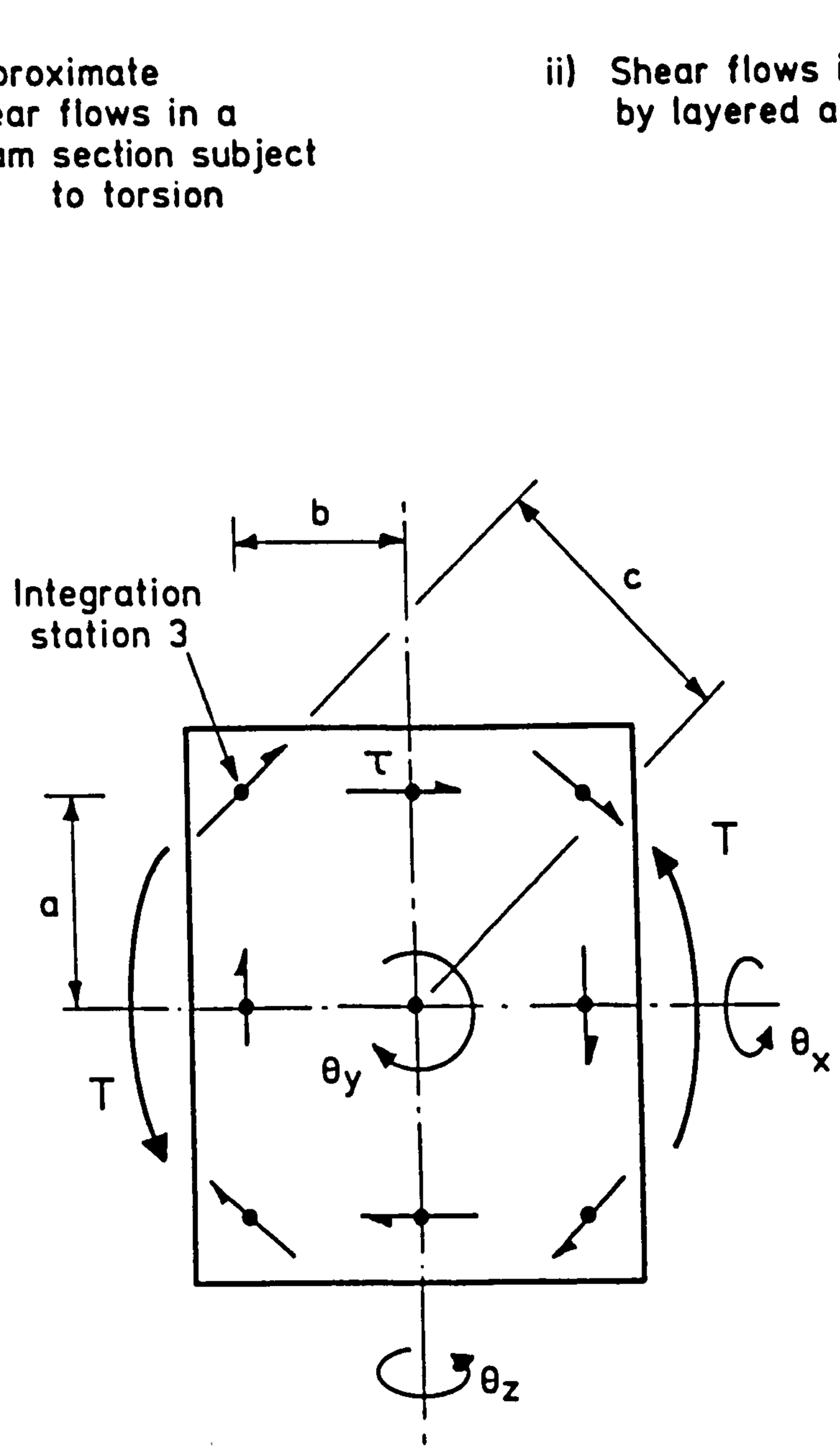

iii) Shear flows imposed by 2 dimensional integration scheme

FIG. 8.3. BEAM SHEAR FLOW MODELLING

the concrete modular matrix D^P_b the presence of the steel is generally ignored. This introduces a small error in the calculated stiffnesses.

The way in which the smeared steel was included in equation 8.6 can also be applied to the inclusion of smeared beams into equation 8.7, thus:-

$$K = \int B^T_b \, [D^P_b + D^b_b + D^s_b] \, B_b \, dA + \int B^T_s \, [D^P_s + D^b_s] \, B_s \, dA \qquad (8.8)$$

The modular matrix (D) for the calculation of a discrete beam element stiffness matrix contains stiffness terms per unit length. The smeared beam modular matrix in equation 8.8 contains stiffness terms per unit area. Thus, for a uniform spacing of beams, the smeared modular matrix is essentially equal to the discrete modular matrix divided by the orthogonal beam spacing. Again, strain compatibility between all three components, namely plate concrete, beam concrete and steel, is implicit in equation 8.8. Depending upon the assumptions that are applied, the smeared beam modular matrix can be defined in a number of ways.

8.3.3.1 Uniaxial beam approach

If it is assumed that the beams are uni-directional then the material and section properties are defined in the beam directions. Thus, the direct stiffness and transverse shear stiffness in the beam directions are specified. In addition, depending on how the beam torsional stiffness is applied, an in-plane shear stiffness may also be specified. Before the integration of equation 8.8 can be carried out the beam properties must be transformed to Cartesian directions using transformation matrix, T. Thus if $\bar{D}^b_b$ and $\bar{D}^b_s$ are the modular

matrices defined in the beam directions, then the modular matrices in Cartesian directions, $D^b{}_b$ and $D^b{}_s$, can be obtained from:-

$$D^b{}_b = T^T{}_b \, \bar{D}^b{}_b \, T_b \tag{8.9}$$

$$D^b{}_s = T^T{}_s \, \bar{D}^b{}_s \, T_s \tag{8.10}$$

$$T_b = \begin{bmatrix} \cos^2\alpha & \sin^2\alpha & \sin\alpha\cos\alpha \\ \sin^2\alpha & \cos^2\alpha & -\sin\alpha\cos\alpha \\ -2\sin\alpha\cos\alpha & 2\sin\alpha\cos\alpha & \cos^2\alpha-\sin^2\alpha \end{bmatrix}$$

$$T_s = \begin{bmatrix} \cos\alpha & \sin\alpha \\ -\sin\alpha & \cos\alpha \end{bmatrix}$$

where α is the angle between the beam direction and the x axis. Implicit in this approach is the assumption that cracks can only form orthogonal to the beam directions, since the orthogonal direct stress is undefined and therefore a transformation to principal space cannot be performed. The approach described above will be referred to as the uni-axial beam approach hereafter.

With the uni-axial beam approach a complication arises when the torsional terms are evaluated for a slender member. If the Cartesian curvature strains are transformed to the beam directions then three curvature strains result thus:-

$$\begin{bmatrix} \kappa_{\bar{x}} \\ \kappa_{\bar{y}} \\ \kappa_{\bar{x}\bar{y}} \end{bmatrix} = \begin{bmatrix} \frac{d\theta_{\bar{x}}}{d\bar{x}} \\ \frac{d\theta_{\bar{y}}}{d\bar{y}} \\ \frac{d\theta_{\bar{x}}}{d\bar{y}} + \frac{d\theta_{\bar{y}}}{d\bar{x}} \end{bmatrix} \tag{8.11}$$

where $\bar{x}$ and $\bar{y}$ are the beam local directions. Clearly, for the application of a uni-directional beam torsional stiffness, a twisting term, $\kappa_{\overline{xy}}$ equal to $d\theta_{\bar{y}}/d\bar{x}$ is required and not that shown in equation 8.11. The addition to the B matrix of an extra term equal to:-

$$\frac{d\theta_x}{dy} - \frac{d\theta_y}{dx} \tag{8.12}$$

will allow this problem to be overcome. After transformation of this term to the local beam direction, equation 8.11 becomes:-

$$\begin{bmatrix} \kappa_{\bar{x}} \\ \kappa_{\bar{y}} \\ \kappa_{\overline{xy}} \end{bmatrix} \begin{bmatrix} \dfrac{d\theta_{\bar{x}}}{d\bar{x}} \\ \dfrac{d\theta_{\bar{y}}}{d\bar{y}} \\ \dfrac{\left[\dfrac{d\theta_{\bar{x}}}{d\bar{y}} + \dfrac{d\theta_{\bar{y}}}{d\bar{x}}\right] - \left[\dfrac{d\theta_{\bar{x}}}{d\bar{y}} - \dfrac{d\theta_{\bar{y}}}{d\bar{x}}\right]}{2} \end{bmatrix} \tag{8.13}$$

Crisfield has adopted this approach with the formulation for his NFES program. Full details of this are given in Chapter 10 Section 10.1.1.2.

8.3.3.2 Biaxial beam approach

For the major part of a composite concrete slab analysis, a bi-axial stress environment will exist in the precast beams; since the insitu and precast concretes act compositely with virtually perfect strain compatibility. Except for the presence of prestress in the beams, the composite slab behaviour will be similar to a homogeneous and isotropic slab of similar dimensions. It would seem more logical, therefore, to treat the insitu and precast concretes in a similar fashion but as separate entities. With this approach the material

properties are defined in principal directions. Thus, if the tensile strength is exceeded in the principal directions, a crack will form in these directions, which could be at any angle to the beam axis. For coincident insitu and precast integration stations, the principal directions will generally differ, since the precast concrete is prestrained. This second approach will be referred to as the bi-axial beam approach hereafter.

Clearly no single approach is appropriate for all regions of the analysis, from discrete beams supporting wet insitu concrete to failure of the structure. The uni-axial approach is able to model the condition with wet insitu concrete accurately, whereas the bi-axial approach is more suited to the subsequent response as it moves towards failure. However, the bi-axial approach will not model the behaviour of the beam bottom flanges accurately, since a gap is left between adjacent flanges. As failure approaches and composite action begins to break down, neither the uni-axial or bi-axial approach will truely reflect the structural response.

Both the uni-axial and bi-axial approaches were implemented in the SNAP program. For analyses where the principal directions coincided with the beam directions, both approaches yielded similar results. For analyses where the principal directions deviated from the beam directions, significantly overstrong predictions were given by the uni-axial beam approach, whereas the bi-axial approach yielded reasonable predictions. From the earlier discussion this is the expected result.

The integration over the area in equation 8.8, together with the integration over the depth for the modular matrix, D, is carried out so that the strain energy over the volume can be equated to the energy

dissipated by the external loads. For composite construction the total strained volume is divided between plate concrete and beam material. Thus two integrations must be carried out, one over the volume of plate or insitu concrete and the second over the volume of the beam or precast concrete. Since a smeared approach has been adopted, the integrations over the area of the structure are identical for the two materials and may, therefore, be combined. The integrations over the depth, to produce the D matrices, are different, and must be carried out separately.

Finite element analyses of homogeneous and isotropic plates generally apply classical integration rules, such as Gauss-Legendre or Newton-Cotes, for the through depth integration. Due to the interlaced nature of the precast and insitu concretes in composite construction, each material is not distributed uniformly through depth. Thus the classical integration rules are not appropriate and an individually designed integration rule is required for each different structure that is analysed.

Initially, the number of integration stations through depth is selected. The analyst uses his judgement to position the stations at appropriate locations through the depth, considering the size and location of the tributory area that is associated with the station. The weight attached to each station reflects the amount of material, precast or insitu as appropriate, that is adjacent to the integration station. The weight is obtained by first calculating the volume of either the precast or insitu material that is contained within a certain through depth layer. Since the smeared approach is used the weights are then obtained by dividing the volume by the applicable area. For uniformly spaced beams, this process reduces to determining the area of the beam or insitu section, as appropriate, that is to be

attached to a particular integration station, and dividing this area by the beam spacing to obtain the weighting factor.

In addition to modelling the linear case accurately, the chosen through depth integration system should be able to model the ultimate condition, when steel is yielding and concrete is crushing, realisticaly. For the present study, the integration schemes were arranged so that stations near to the soffit enabled cracking to be modelled accurately. The stations towards the top of the section were arranged so that the concrete compression block at failure could be modelled realisticaly.

In the uni-axial beam approach, the straining of the precast material orthogonal to the beam axis is not included in the beam integration scheme. In this case it would appear appropriate to increase the insitu concrete integration weights in the orthogonal direction to reflect the total amount of strained material in that direction. However, complications arise in the calculation of a consistent integration weight for the twisting term in this case.

8.4 Material Modelling

For many years concrete has been accepted as an efficient structural material. This is clearly apparent from its extensive use throughout the world today. Until the advent of powerful computers, the detailed mathematical modelling of concrete as part of an overall structural response was not practical. This section is concerned with the detailed composition of the D matrix (also referred to as the modular matrix) and the constitutive law from which it is obtained. With a non-linear analysis, as the displacements, and hence the strains, change, then the material properties also change and the modular matrix must be updated. For the present study it is assumed that only

the in-plane material properties are non-linear and that the transverse shear properties remain linear throughout the analyses.

For concrete loaded in uni-axial compression the stress-strain curve takes the form shown in Figure 8.4. It can be seen that up to about 30% of the ultimate strength, concrete behaves in a practically linear manner. Thereafter, the concrete begins to soften and it has been suggested that the softening is caused by micro-cracks forming at the aggregate-mortar interface. As the ultimate strength is approached tensile cracks appear orthogonal to the applied compressive stress. Subsequently, the stress-strain curve begins to descend and failure of the specimen ensues. There is a tendency for higher strength concretes to be significantly more brittle, with steeper descending curves, than low strength concretes. However, the influence of the stiffness of testing machines on published data is not yet clear. Also shown in Figure 8.4 is a typical stress-strain curve for concrete in tension. It can be seen that the shape of the tension curve is similar to that in compression, however, the tensile strength is approximately 10% of that in compression.

Investigations by other researchers[36,37] have shown that biaxial stress conditions can enhance the uni-axial compressive strength of concrete by up to 25%, and reduce the uni-axial tensile strength. A typical failure envelope is given in Figure 8.5. Since many empirical bi-axial failure criteria are defined in principal stress space, it is generally necessary to implement an iterative process to apply them in the displacement based finite element method. Thus, the implementation of a bi-axial material model can be both complex and expensive in terms of computational requirements. Furthermore, there is little experimental data for the tension-compression region on which to form a consistent model.

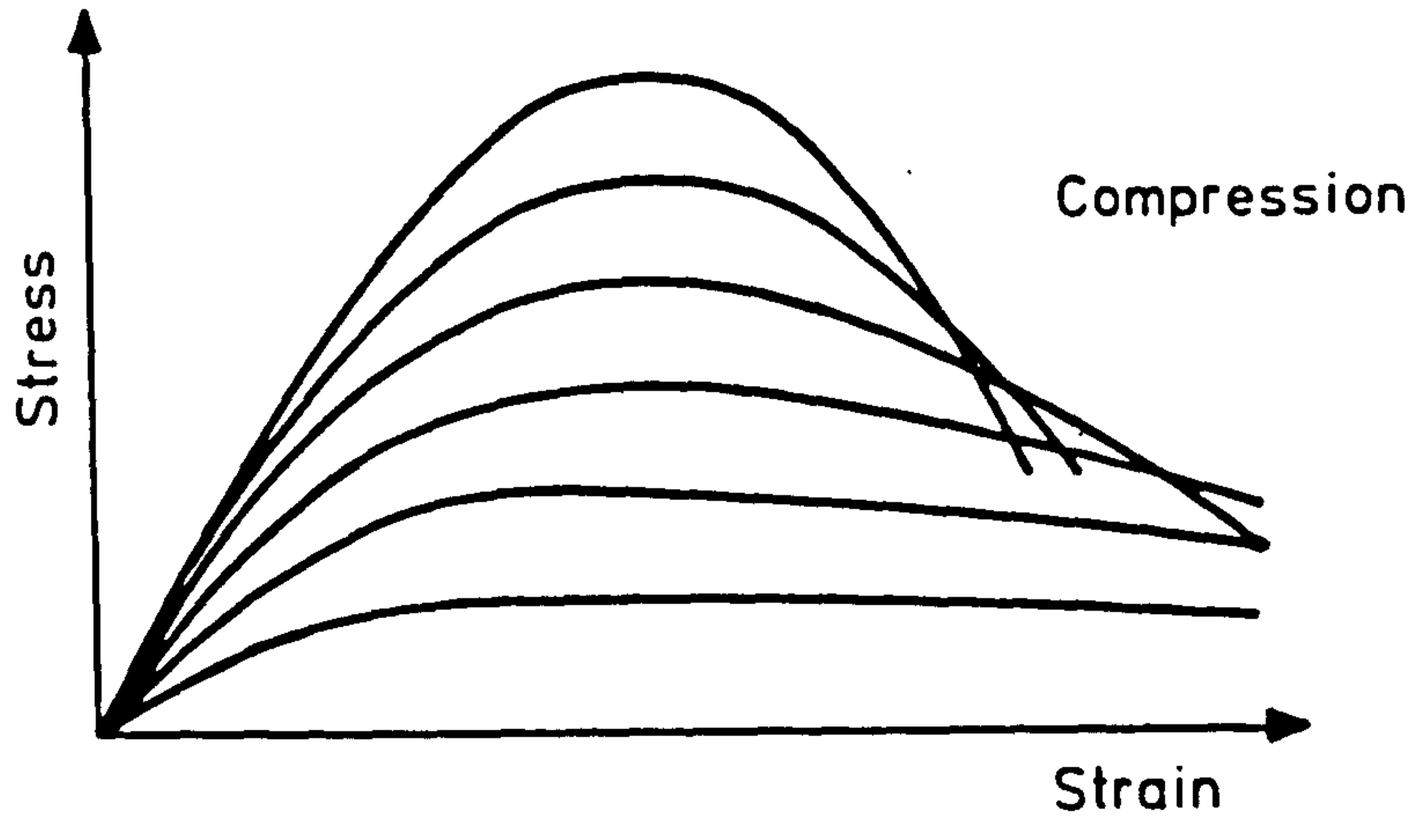

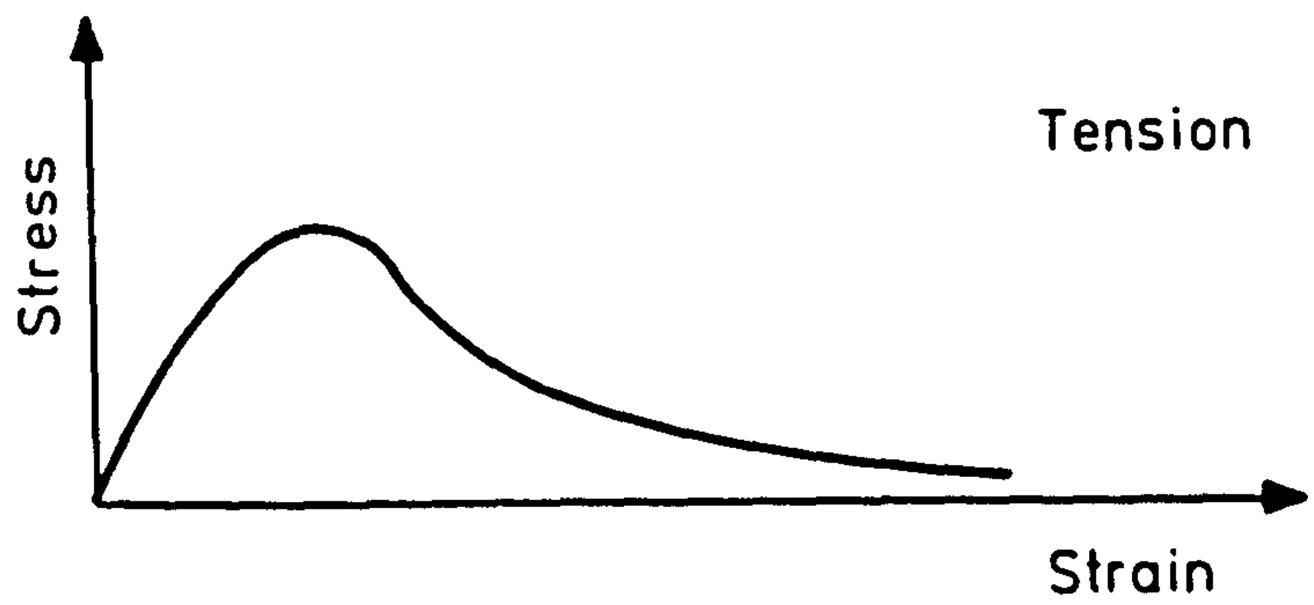

FIG. 8.4. TYPICAL UNIAXIAL STRESS-STRAIN CURVES FOR CONCRETE

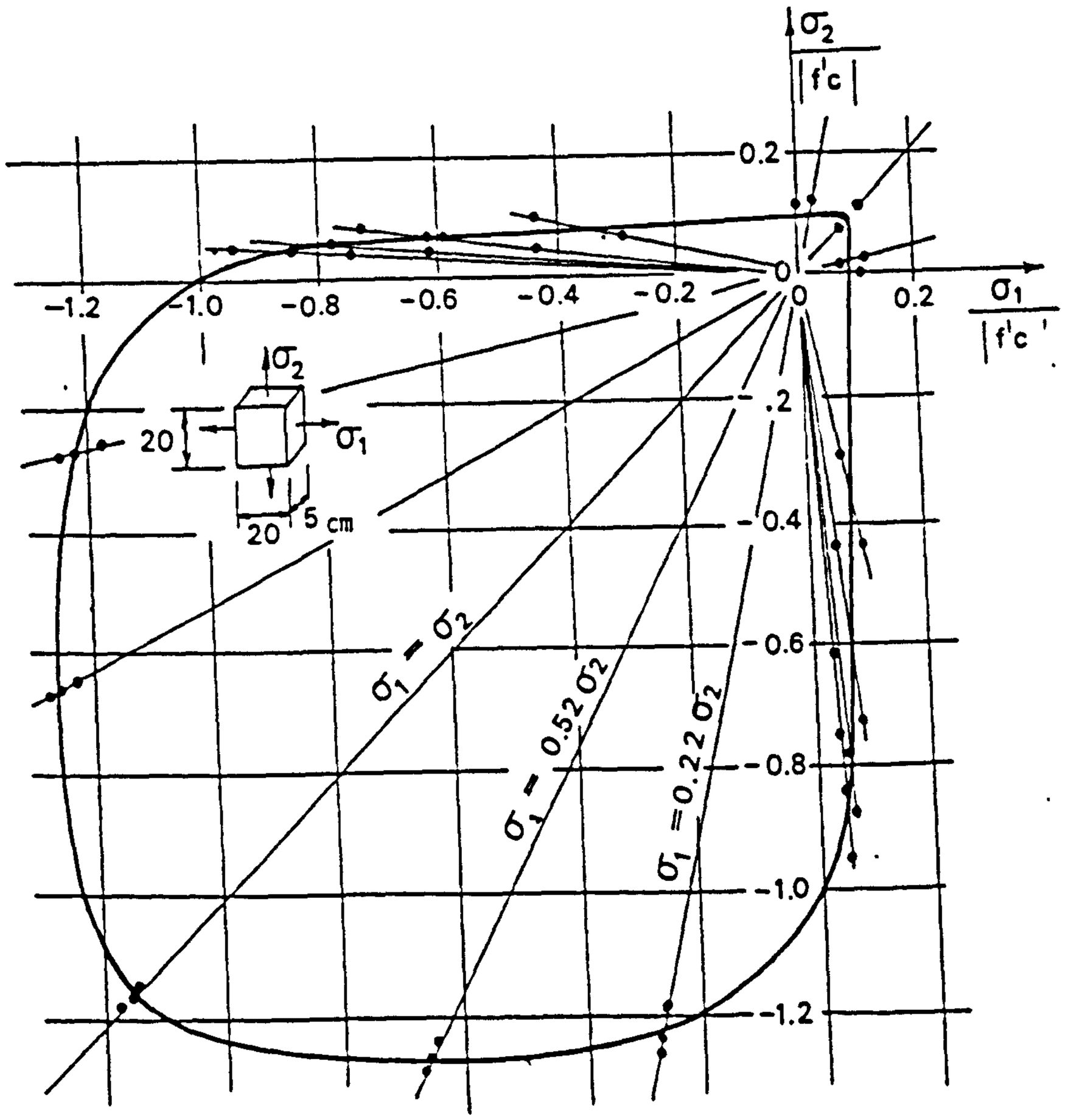

FIG. 8.5. TYPICAL BIAXIAL STRENGTH ENVELOPE FOR CONCRETE AFTER [36]

The response of reinforced/prestressed concrete is governed primarily by the cracking of concrete and subsequently by the yielding of the steel reinforcement/prestressing. Therefore, unless the structure is significantly over reinforced, minor enhancements to the concrete compressive material model will have little effect upon the structural response. Considering these points and the intrinsic variability of concrete as a material, it was decided to implement a uni-axial material model in each of the principal/crack directions. For the analysis of concrete slabs under monotonic loading it is necessary to incorporate realistic material unloading into the material model, however, a full cyclic model is not required.

Bond between steel and concrete is fundamental to the behaviour of reinforced/prestressed concrete. Bond is a combination of adhesion, friction and mechanical interlock between protruding bar ribs and the surrounding concrete. Before cracking, bond has little effect upon the structural behaviour, however, after cracking it affects several features such as; the crack spacing; crack widths; and the residual material stiffness.

If the tensile strength is exceeded anywhere in a concrete material, then a crack will form. Subsequently, all the force normal to the crack will be transmitted through any steel which crosses the crack. Either side of the crack, the bond between the steel and concrete will transfer the load to the concrete until strain compatibility is regained. Further cracks may form adjacent to the initial crack and between these cracks bond action will transfer some of the load to the concrete again. Thus, while at the crack sites there is no stress in the concrete normal to the crack, in other areas load has been transferred to the concrete.

The smeared crack approach adopted for the present study averages out the distinct phenomenon that are present in the complex concrete material. Therefore, in an average sense, the concrete is still stressed after cracking. In the limiting case, when cracking becomes intense, the average stress can tend to zero although there are test data indicating retention of bond up to and beyond steel yielding. The averaging process accounts for the post cracking falling branch of the tensile concrete stress strain curve. Assuming zero tensile strength in the concrete at yield ensures that failure correctly models yielding at cracked sections. It should be noted, however, that other investigations have indicated the presence of a post-cracking falling branch even in plain concrete specimens.

Besides normal forces, shear forces are also applied to cracks in concrete. This force is transmitted across the crack by a number of mechanisms. Since the majority of cracks in concrete are rough and angular, shear forces can be transmitted through aggregate interlock. As the crack width increases the capacity of aggregate interlock to transfer force will decrease. A second mechanism for the transfer of shear is the 'dowel action' of reinforcing and prestressing bars. Thus the bars that cross cracks act as dowels to resist shear force. The major influences upon the effectiveness of dowel action are the size and strength of the bars and the concrete cover around the bars.

The steel reinforcement and prestressing wire contained within slabs is relatively thin. Thus, a realistic steel material model need only cater for the axial properties of steel and it's shear properties can be safety ignored in the global sense.

8.4.1 Incorporation of material models into the finite element system

8.4.1.1 Concrete

The modular matrix D_{xy} links the Cartesian strains, ϵ_{xy}, to the Cartesian stresses, σ_{xy}, thus:-

$$\sigma_{xy} = D_{xy}\ \epsilon_{xy} \tag{8.14}$$

It was mentioned earlier that material models incorporated into the SNAP program treat biaxial concrete as a pseudo uniaxial material in principal strain space. The modular matrix is defined in principal strain space and thus the Cartesian strains are transformed to the principal directions using a transformation matrix T thus:-

$$\epsilon_{12} = T\ \epsilon_{xy} \tag{8.15}$$

where

$$T = \begin{bmatrix} \cos^2\alpha & \sin^2\alpha & \sin\alpha\ \cos\alpha \\ \sin^2\alpha & \cos^2\alpha & -\sin\alpha\ \cos\alpha \\ -2\ \sin\alpha\ \cos\alpha & 2\ \sin\alpha\ \cos\alpha & \cos^2\alpha\ -\sin^2\alpha \end{bmatrix} \tag{8.16}$$

Likewise the obtained principal stresses need to be transformed to Cartesian directions:-

$$\sigma_{xy} = T^T\ \sigma_{12} \tag{8.17}$$

With the modular matrix defined in principal space equation 8.14 becomes:-

$$\sigma_{xy} = T^T\ D_{12}\ T\ \epsilon_{xy} \tag{8.18}$$

and $$\sigma_{12} = D_{12}\ \epsilon_{12} \tag{8.19}$$

or in incremental format, $\Delta\sigma_{12} = D_{12}\,\Delta\epsilon_{12}$ (8.20)

where D_{12} is the principal space modular matrix. Since the non-linear material constitutive laws are solved as a set of linearised steps, the incremental approach of equation 8.20 is most appropriate for the formation of the stiffness matrix. Under plane stress assumptions, for the orthotropic case which occurs after the material becomes non-linear, equation 8.20 becomes:-

$$\begin{bmatrix}\Delta\sigma_1\\ \Delta\sigma_2\\ \Delta\tau_{12}\end{bmatrix} = \frac{1}{(1-\nu^2)}\begin{bmatrix}E^c{}_1 & \nu E^c{}_1 & 0\\ \nu E^c{}_2 & E^c{}_2 & 0\\ 0 & 0 & (1-\nu^2)G\end{bmatrix}\begin{bmatrix}\Delta\epsilon_1\\ \Delta\epsilon_2\\ \Delta\gamma_{12}\end{bmatrix} \qquad (8.21)$$

This is assuming that the value of Poisson's ratio is the same in each of the two directions[49] and that there is no linking between direct stresses and shearing strains, or vice versa, in the non-linear region. The variables $E^c{}_1$ and $E^c{}_2$ are the concrete tangent moduli in the two principal directions. It will be realised that the modular matrix is unsymmetrical and thus is not appropriate for the symmetric solvers contained in the majority of finite element programs. In the SNAP program this was overcome by setting the off diagonal terms to either $\nu[E^c{}_1\ E^c{}_2]^{1/2}$ or $\nu[E^c{}_1 + E^c{}_2]/2$. This approach is justified to some extent by test data. Carefully conducted tests by Maekawa and Okamura[49] in the compression-tension zone have indicated symmetry up to about 90% of the cylinder strength. Tests by Kupfer and Hilsdorf[36] in the compression-compression zone suggested the preservation of an approximate symmetry until the failure envelope was approached. It is not possible to employ the first form of averaging if the moduli in the two directions are of different signs and therefore the second form was used for the present study. Using equation 8.21 the tangent stiffness matrix may thus be evaluated.

For the evaluation of the residual forces in the iterative process the strains are obtained. Through the use of the material's constitutive law the stresses may be calculated from these strains. For the material models incorporated into the SNAP program, total strains are used in preference to incremental strains for this process. Since concrete is treated as a uniaxial material in each principal direction, effective strains, ϵ'_{12}, must be calculated for input into the material models such that:-

$$[\epsilon'_{12}] = [V]\,[\epsilon_{12}] \tag{8.22}$$

where

$$[V] = \begin{bmatrix} \frac{1}{1-\nu^2} & \frac{\nu}{1-\nu^2} & 0 \\ \frac{\nu}{1-\nu^2} & \frac{1}{1-\nu^2} & 0 \\ 0 & 0 & 1 \end{bmatrix} \tag{8.23}$$

It will be realised from equation 8.23, that unless Poisson's ratio is constantly updated during the iterative process, residual forces will remain when the material properties are updated at the end of the 'converged' increment. The nodal force can then be calculated from:-

$$[f] = [B]^T\,[\sigma_{xy}] \tag{8.24}$$

8.4.1.2 Steel

The modular matrix for steel, $D^{S}\overline{_{xy}}$, links the steel strains to the stresses, however, since the steel is uni-directional this matrix consists of only one element:-

$$\sigma\overline{_{xy}} = D^{S}\overline{_{xy}}\;\epsilon\overline{_{xy}}, \qquad D^{S}\overline{_{xy}} = [E^{S}] \tag{8.25}$$

where $\epsilon_{\overline{xy}}$ are the strains in the direction of the steel and $\sigma_{\overline{xy}}$ are the stresses in the direction of the steel. In Cartesian directions:-

$$\sigma_{xy} = T^T D^s_{\overline{xy}} T \epsilon_{xy} \tag{8.26}$$

Thus,

$$D^s_{xy} = T^T D^s_{\overline{xy}} T \tag{8.27}$$

where T is a transformation matrix such that:-

$$\epsilon_{\overline{xy}} = [\epsilon_{\overline{x}}] = T \epsilon_{xy} = [\cos^2\theta \quad \sin^2\theta \quad \sin\theta \cos\theta] \begin{bmatrix} \epsilon_x \\ \epsilon_y \\ \gamma_{xy} \end{bmatrix} \tag{8.28}$$

where θ is the angle between the steel direction and the x axis.

8.4.2 Concrete material models

Popovics[39] has reviewed the experimental work of many researchers and in a subsequent paper[40] he noted that stress-strain curves have significantly different characteristics according to whether the load was applied in stress or strain increments, with higher failure loads being recorded for stress increments. Obviously, the rates of stressing or straining are also of fundamental importance in a study of this kind. Gerstle et al[41] have argued that the falling part of the concrete stress-strain curve is mainly dependent upon the nature of the testing machine, and in particular the stiffness of its interface with the specimen. Generally it is argued that if there were no restraint, the concrete would fail completely at its maximum stress.

From the test data that he studied, Popovics proposed the following equation:-

$$\sigma = \left[\frac{\sigma_o}{\epsilon_o}\right] \frac{n\epsilon}{(n-1 + (\epsilon/\epsilon_o)^n)} \tag{8.29}$$

where n = 1.0 - 0.058 σ_o for normal weight concretes; σ_o is the maximum stress (N/mm^2); ϵ_o is the corresponding strain. When ϵ_o is not known Popovic suggested that it could be evaluated using $\epsilon_o = 9.368 \times 10^{-4\ 4}\sqrt{\sigma_o}$

The tangent modulus may be evaluated by differentiating equation 8.29:-

$$E = \frac{d\sigma}{d\epsilon} = \left[\frac{\sigma_o}{\epsilon_o}\right] \frac{(1 - (\epsilon/\epsilon_o)^n)\ n\ (n-1)}{(n-1 + (\epsilon/\epsilon_o)^n)^2} \qquad (8.30)$$

For strains beyond ϵ_o, because of the restraint offered by adjacent, less highly stressed material, the concrete can be assumed to behave plastically until crushing begins at the ultimate strain, ϵ_u. Tests on plain concrete specimens under eccentric loading have indicated that stress-strain curves for a flexural member are similar to those from axially loaded specimens. Other tests have indicated greater strength and ductility in the presence of a strain gradient. Blume[42] has suggested the use of an ultimate strain of 0.004. There is little experimental data on which to base the falling branch of the compressive curve, i.e. for strains greater than the ultimate strain, ϵ_u.

The uni-axial tensile stress-strain response for concrete is approximately linear until cracking. Tests have indicated that plain concrete specimens are able to resist a falling tensile force with strains that are several times the strains at the maximum stress, when the deformation is displacement controlled. The tensile strength may be determined from a number of different tests, including modulus of rupture, split cylinder and direct tension tests. While each of these

tests will generally indicate a different tensile strength, the split cylinder strength has been found to give reasonable predictions[43].

In the smeared crack approach equivalent stress-strain curves are applied at a discrete number of sampling stations. The spacing of the sampling stations give the lengths over which average deformations are considered. To obtain mesh independence, it is necessary to take this length into account when specifying the post peak tensile stress strain curve. For the present study the finite element meshes employed are essentially uniform and it was not considered necessary to vary the tensile curves according to the sampling station spacing.

8.4.2.1 COSIG2 material model

Popovic's equations (8.29 to 8.30) are employed in this model for compressive stresses up to the maximum stress, σ_o, see Figure 8.6. For strains beyond the strain corresponding to the maximum stress, ϵ_o, the stress is assumed to be constant until the ultimate strain, ϵ_u, is attained. For strains beyond ϵ_u, the stress reduces linearly to zero at the maximum strain, ϵ_m.

In tension either a two or three segment curve is employed, see Figure 8.6. The post cracking tension stiffening curve is defined by the points $\alpha_1\ \epsilon_{cr}$ and $\alpha_2\ \epsilon_{cr}$, where ϵ_{cr} is the cracking strain and α_1 and α_2 are constants. The values of α_1 and α_2 are affected by many factors, including bond, concrete cover and bar spacing. Test data on tension stiffening exhibits considerable scatter and this is due in part to the nature of the phenomenon. Test results for beams and one way spanning slabs, with different steel ratios, reported by Clark and Speirs[44], indicate that the effect of tension stiffening decreases with an increase in the steel ratio and the steel strain. The tension-stiffening curve used in the present study is based on the

data obtained by Clark and Speirs. Values for α_1 were in the range 1.25 to 4.5 and for α_2 in the range 10 and 30. Low values of α_2 can lead to nett section stiffnesses which are negative in the post-cracking region. With negative section stiffnesses severe numerical difficulties can be encountered.

For compressive unloading before the maximum stress, σ_o, is reached, the response returns down Popovic's curve. At strains greater than ϵ_o the response unloads down a line parallel to the initial modulus. In compression Poisson's ratio is kept constant at its initial value until crushing begins at ϵ_u. Subsequently Poisson's ratio is reduced linearly to zero at the maximum strain, ϵ_m, and is zero for strains greater than this. The shear modulus is kept constant until the onset of crushing at ϵ_u. For greater strains the shear modulus is reduced linearly to the residual shear modulus at the maximum strain, ϵ_m. For the present study the residual shear modulus was generally between 10% and 1% of the full shear modulus.

For tensile unloading before cracking, the response returns down the initial line. In the post cracking region the response returns down a line joining the state of maximum stress and strain reached in an analysis with the cracking strain at zero stress, see Figure 8.6. For the present study this approach gave reasonable predictions, however, in several cases the residual deflections after unloading were significantly underestimated. Until cracking Poisson's ratio is constant at the initial value. After cracking Poisson's ratio is reduced linearly to zero at a crack normal strain equal to $\alpha_2\ \epsilon_{cr}$. For greater strains than this a zero Poisson's ratio is used, see Figure 8.6. After cracking the in-plane shear modulus is linearly reduced to the residual shear modulus at a strain of $\alpha_2\ \epsilon_{cr}$. For greater strains the residual shear modulus is used. If the material unloads and the

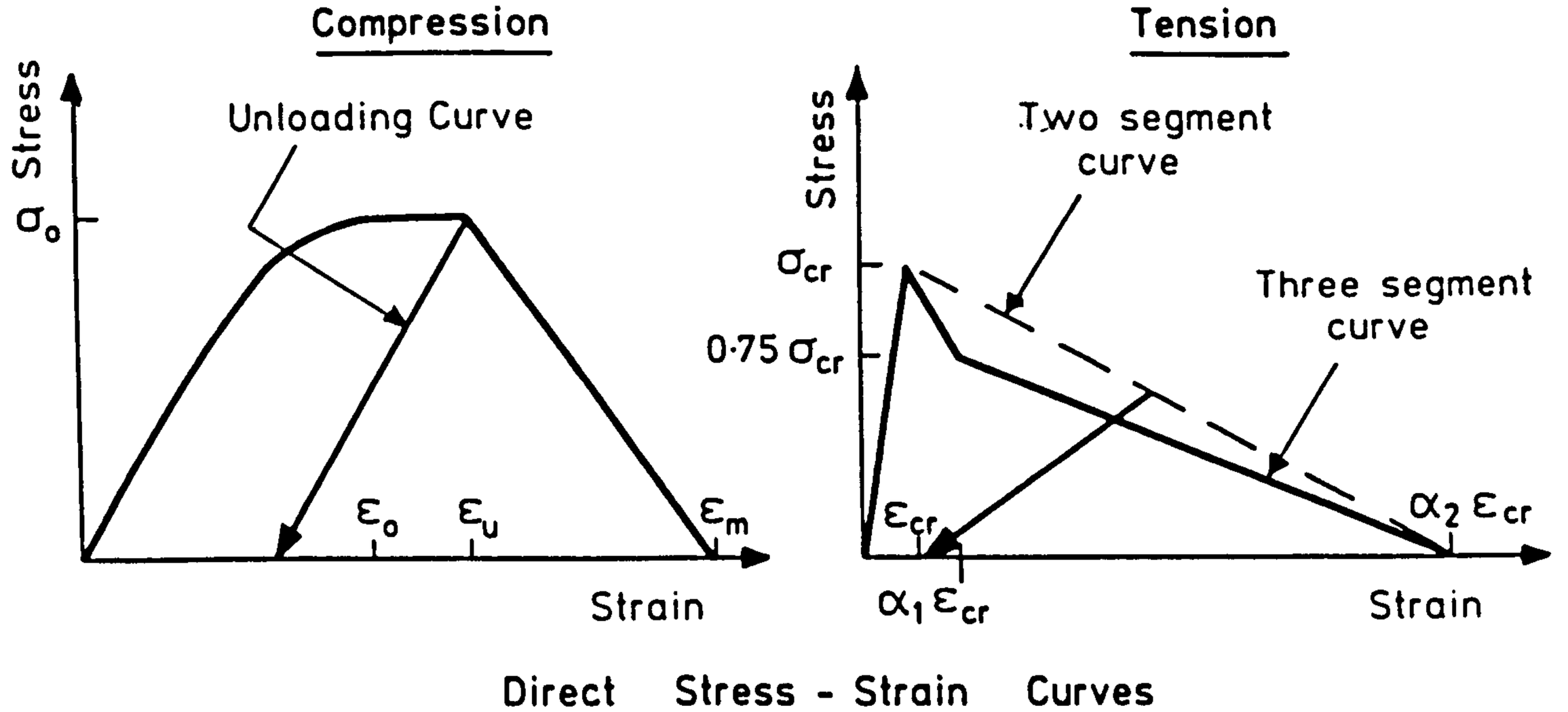

Direct Stress - Strain Curves

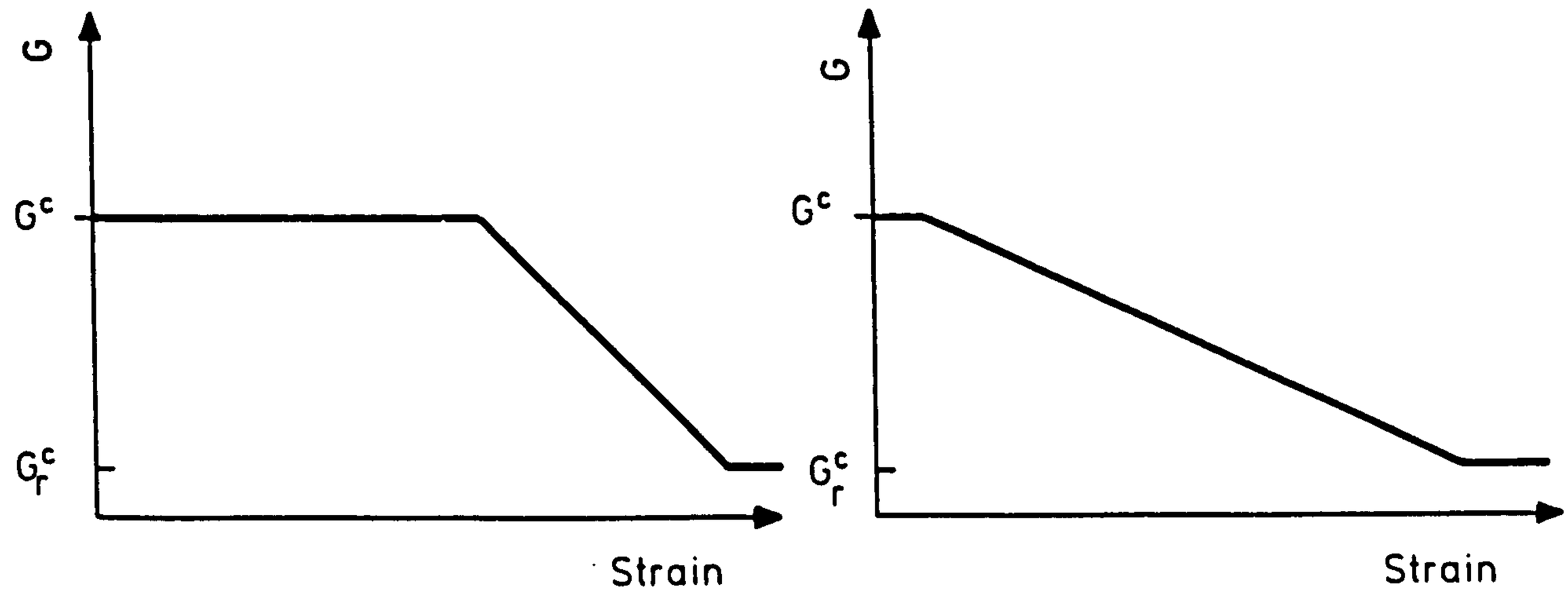

Strain Modulus Degradation Curves

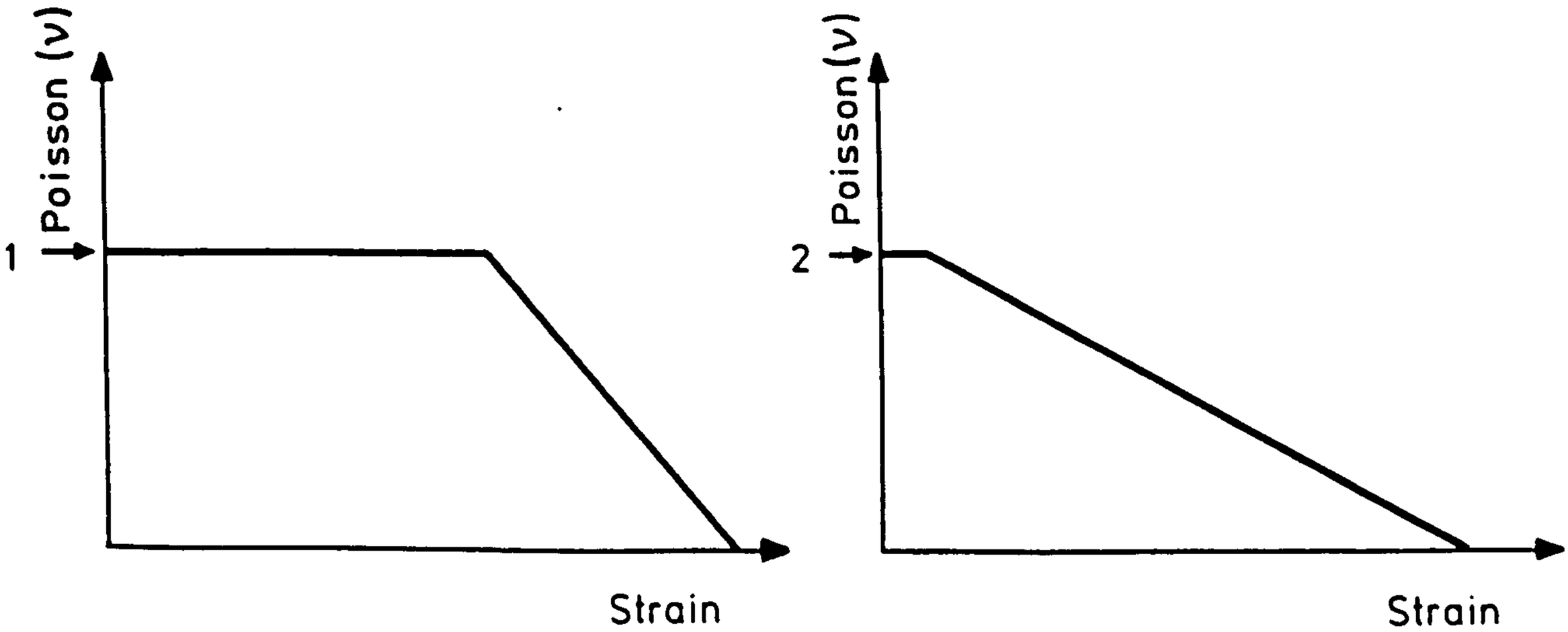

Poissons Ratio Degradation Curves

FIG. 8.6. COS1G2 MATERIAL MODEL

stress reduces, Poisson's ratio is increased linearly so that it regains its initial value when the crack is fully closed. A similar approach is used to reinstate the in-plane shear modulus as the crack closes. Stress reversal is allowed if the compression state is still elastic. Therefore cracks are allowed to close and go into compression during the redistribution process but plastic or crushed concrete is not allowed to crack. If this criteria is violated the run is aborted.

8.4.2.2 MLCMLT material model

This material model is similar to the COSIG2 model. However, in compression a linear segment is used in preference to Popovic's curve, see Figure 8.7. In the plastic and crushing regions the MLCMLT model is identical to the COSIG2 model. In the crushing region Poisson's ratio and the in-plane shear modulus are reduced in a stepped manner and not a linear manner. For strains greater than ϵ_u Poisson's ratio equal to half the initial value is used. For strains greater than the maximum strain, ϵ_m, Poisson's ratio is set to zero. The in-plane shear modulus is degraded to $(G^c + G^c_r)/2$ for strains greater than ϵ_u. For strains greater than the maximum strain, ϵ_m, the residual shear modulus, G^c_r, is used.

A similar approach is adopted in the tensile region. For strains greater than the cracking strain, ϵ_{cr}, the shear modulus is set to $(G^c + G^c_r)/2$ while Poisson's ratio is set to half its initial value. For strains greater than $\alpha_2\ \epsilon_{cr}$ the shear modulus is set to its residual value, G^c_r and Poisson's ratio is set to zero. Again stress reversal is allowed if the compression state is still elastic.

8.4.2.3 Fixed and rotating material axes

Reinforced concrete slabs are complex statically indeterminate

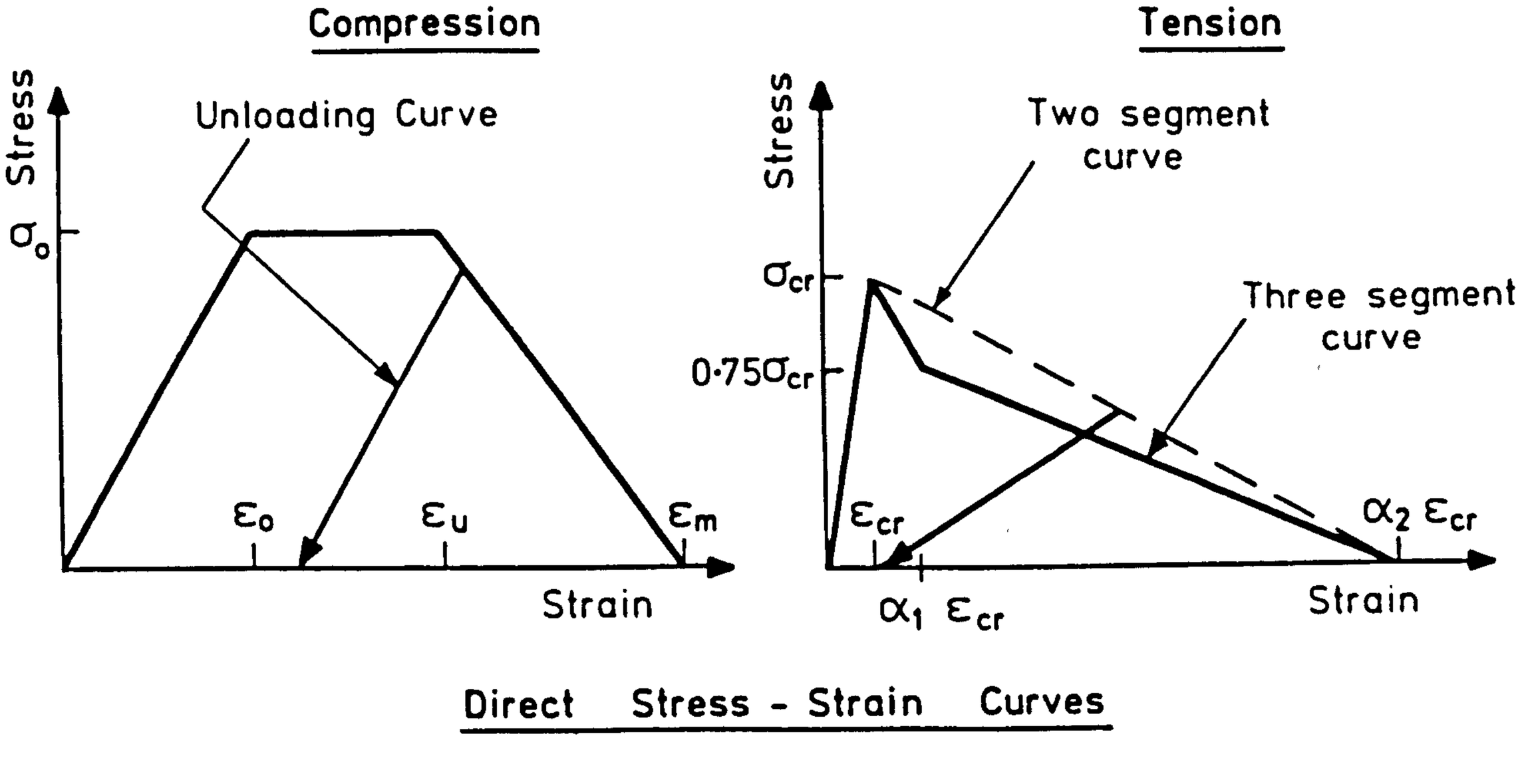

Direct Stress - Strain Curves

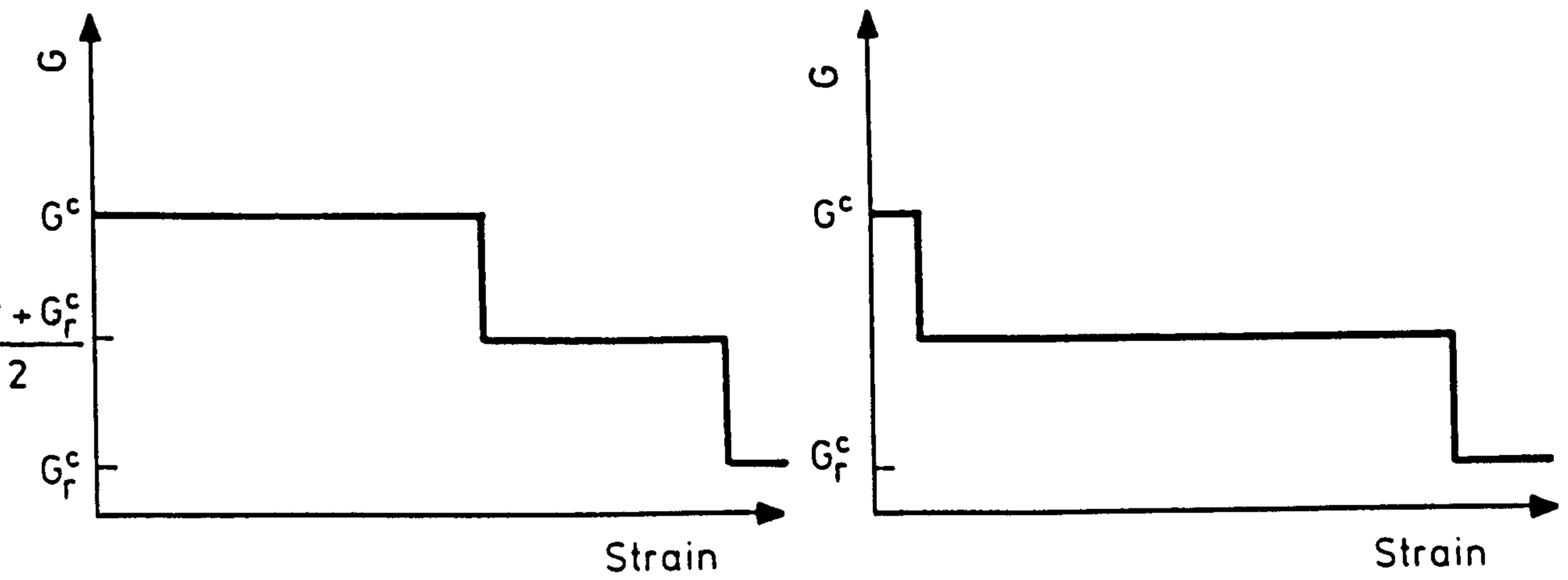

Strain Modulus Degradation Curves

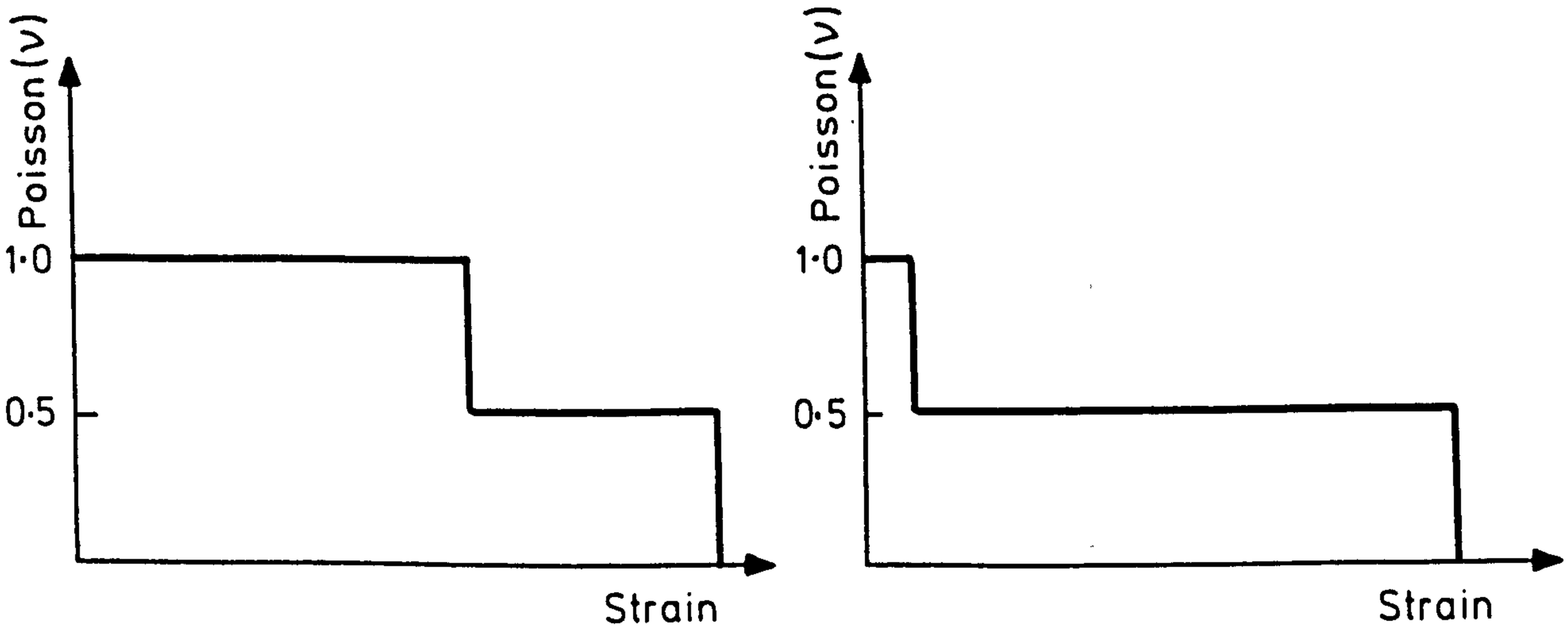

Poissons Ratio Degradation Curves

FIG. 8.7. MLCMLT MATERIAL MODEL

structures, where stress redistribution and rotation of the principal stress and strain directions occur after cracking.

If the post cracking material property axes are fixed in the direction of initial cracking, then the effective strains of equation 8.22 are calculated in the crack directions and not in principal directions. The uni-axial material models described earlier are applied to these effective strains. The Poisson's ratio and shear modulus degradation curves can be used to degrade those parameters as the strain normal to the crack increases. In the present study this approach is referred to as the fixed material property axis model (FMP). The fixed material property axis approach makes it difficult for the principal axes to rotate as the failure mode forms. This phenomenon is particularly apparent with 'real' bridge slabs where the failure loading regime can be significantly different from that which caused initial cracking. Thus the retention of a significant shear modulus in the FMP model can lead to large over strength predictions.

In answer to these problems, the Rotating Material Property axis (RMP) model was developed by Cope and Rao[45]. With this method the material property axes are allowed to follow the principal strain directions as they rotate. Thus, even in the post cracking region, the effective strains are calculated in the principal strain directions. With this approach the principal stress and strain directions are coincident and the in-plane shear modulus degredation curve is not required. With both the FMP and RMP model a second crack is only allowed to form orthogonal to the first crack. The RMP model has been shown to give reasonable predictions for a number of types of structures, including slabs[45]. This view is supported by the present study where the RMP model gave significantly better predictions than the FMP model. The

RMP model, however, does not meet with the approval of material scientists[46].

8.4.3 Steel material models

The material parameters relating to steel are generally consistent and well defined. For the present study the analytical curves were fitted to data obtained from numerous tests on specimens of the reinforcement and prestressing contained within each of the models. For the analysis of prestressed slabs, a steel material model must include facilities for limited stress cycling in addition to unloading. With the large range of steel strengths present in a prestressed concrete section, it is possible for low strength reinforcement to yield in compression as an intensly cracked section unloads. The stress cycling facilities implemented for the present study are simple and do not consider the Bauschinger effect[47].

8.4.3.1 STSIG2 steel material model

The STSIG2 model is shown diagrammatically in Figure 8.8. The stress strain curve is divided into a number of linear segments and is symmetrical in compression and tension. For the majority of analyses described herein a five segment curve was employed. It can be seen that at the maximum steel strain, the stress is reduced to zero. In some cases it was possible to specify the shape of this falling branch from test results, however, for the majority of test specimens it was not possible to obtain data for the falling branch. In this case, an approximate falling branch was specified for the analytical curves. For some of the analyses described herein, the lack of material data dictated the use of elastic-perfectly plastic curves. In regions of very low structural stiffness it was found that elastic-perfectly plastic curves led to severe numerical difficulties.

If unloading occurs then the material state returns down a line parallel to the initial modulus. If unloading continues then stress reversal is allowed to continue as far as yielding in the reverse direction. If this condition is violated the analysis is aborted.

8.4.4 Multi-stage material properties

It will be appreciated that during the analysis of a composite concrete bridge deck, some of the material parameters must change as the analysis progresses. Initially the insitu concrete is in a wet state as the load is carried by the precast beams. Subsequently, the insitu concrete hardens and the load is carried by the insitu concrete and the precast beams acting compositely.

This feature is modelled in the SNAP program by applying different material curves to the insitu concrete at different stages of the analysis. During the wet stage a material curve with initial modulus of 1.0×1.0^{-10} N/mm^2 is applied. Subsequently, for the hardened state, the material curves are switched so that the material has the measured material parameters. Equilibrium must be maintained after the material curve switching is carried out and therefore a system of strain offsets was implemented.

Total strains are used in the material models contained within the SNAP program. The strain offsets for each integration station are added to the strains caused by loading to get total strains before input into the material models. Initially the strain offsets are zero unless the material is prestrained, in which case the prestrains are contained within the strain offsets. Cracking was not expected until after the insitu concrete had hardened and this simplified the calculation of the strain offsets. The strain offsets are calculated in a generalised way so that the switch of material properties could

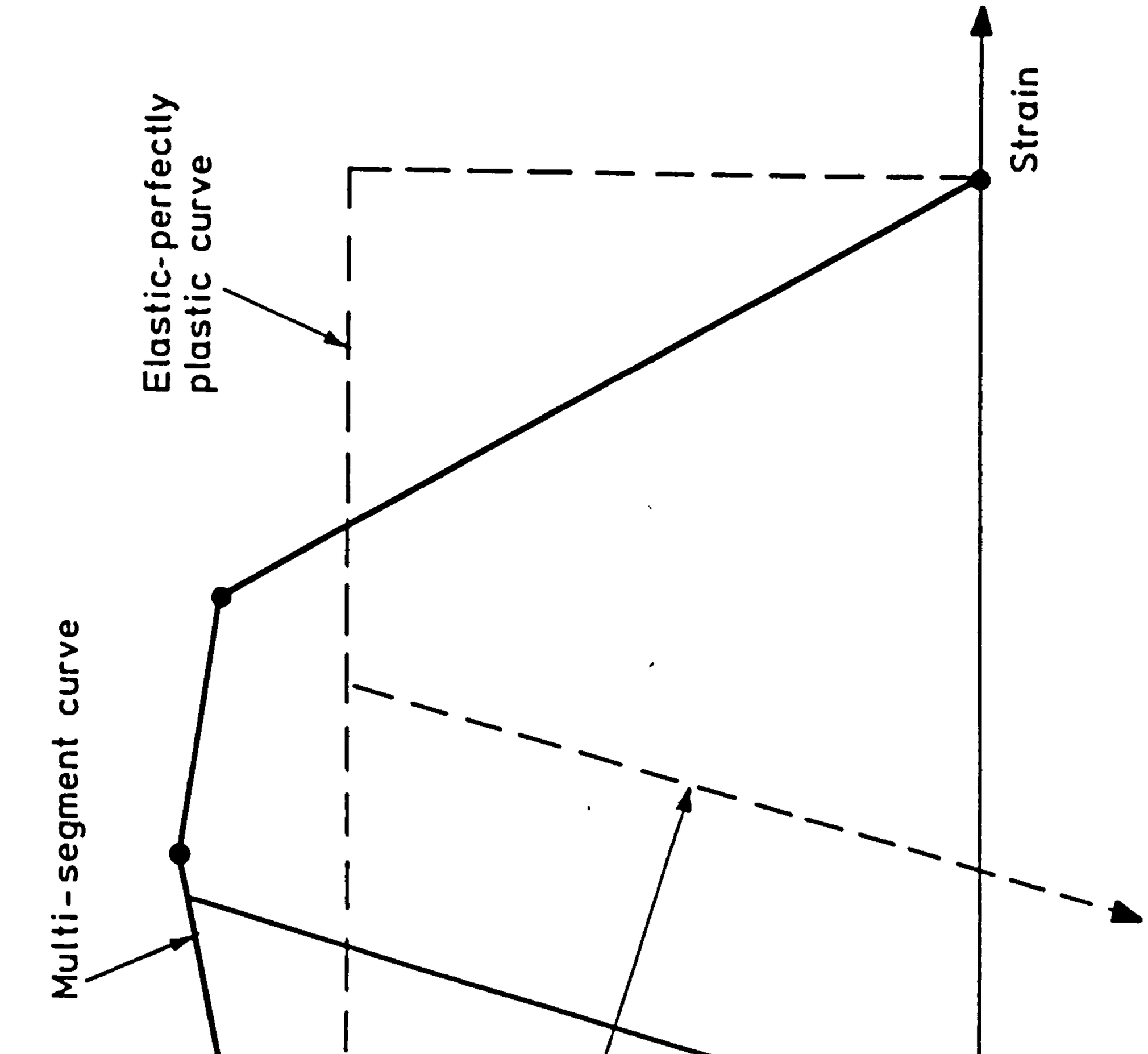

STSIG2 MATERIAL MODEL

FIG. 8.8.

be between long and short term values, as defined by the various British Standards. Thus from equation 8.22 the effective strains become:-

$$[\epsilon'] = [V]\,[T]\,[\epsilon + \epsilon^{o}] \tag{8.31}$$

The strain offsets are calculated from; the current strain level, ϵ; the old material properties, designated i; and the new material properties, designated i+1. For convenience the offsets are first calculated in principal directions and then transformed back to Cartesian directions. Thus in principal directions:-

$$\begin{bmatrix}\epsilon^{o}_{1}\\ \epsilon^{o}_{2}\end{bmatrix} = \left[\frac{E_i}{(1-\nu^{2}_{i})\,E_{i+1}}\begin{bmatrix}1-\nu_i\,\nu_{i+1} & \nu_i-\nu_{i+1}\\ \nu_i-\nu_{i+1} & 1-\nu_i\,\nu_{i+1}\end{bmatrix} - \begin{bmatrix}1 & 0\\ 0 & 1\end{bmatrix}\right]\begin{bmatrix}\epsilon_1\\ \epsilon_2\end{bmatrix} \tag{8.32}$$

where ϵ_1 and ϵ_2 are the current total principal strains and ϵ^{o}_{1} and ϵ^{o}_{2} are the strain offsets in principal directions.

8.4.5 Statistically varied material properties

Generally for nonlinear finite element analyses separate material property curves are defined for each type of material contained within a structure. These material property curves are applied in an identical manner, at each applicable integration station in the analytical structure. In the physical structure, however, the material properties vary over the structural domain. It is not practical or realistic to obtain individual insitu material property information for all the integration stations contained within the analytical structure. However, many concrete cubes and cylinders are generally cast at the same time as the structures. When these specimens are tested an indication of the mean and standard deviation

can be obtained. These values will not have a high accuracy since other factors, such as through depth material variation, have not been investigated. However, the specimen test results can form a basis from which a simple material variability model can be implemented and such a model has been incorporated into the SNAP program. Essentially the procedure assigns the same material property curve to each integration station, in addition, a material property scaling factor is also assigned. The scaling factors are generated[48] so that they have the required mean and standard deviation and are normally distributed. On entry into a material model the scaled strains are obtained from the total effective strains thus:-

$$\epsilon^*_{12} = \frac{\epsilon'_{12}}{m} \qquad (8.33)$$

where 'm' is the material property scaling factor for the integration station in question. The material model uses the scaled strains as though they were effective strains to obtain the resulting scaled stresses, σ^*_{12}. The unscaled stresses are then obtained from:-

$$\sigma_{12} = m\,\sigma^*_{12} \qquad (8.34)$$

In the present study the statistically varied material properties had a significant effect in areas of constant stress. Details of the analyses illustrating this can be seen in Chapter 9.

8.5 Solution Procedures

The solution of the linear finite element problem can be relatively straightforward, requiring only the solution of the 'n' equations that form the stiffness matrix K. For the non-linear finite element problem, more sophisticated solution strategies are required in order for the response to be traced throughout the range to failure.

Using these sophisticated solution methods to reach equilibrium in each increment is by far the most time consuming section in the majority of non-linear analyses. The judicious choice of a particular solution method can, not only significantly effect the computational time, but also whether convergence to equilibrium is ever achieved. The sudden changes in stiffness that occurs with concrete cracking and steel yielding can plague a reinforced concrete analysis with solution difficulties.

The philosophy behind the solution systems that have been implemented into the SNAP program is one of semi-automation. The analyst has overall control of which solution methods may be used, however, the program is endowed with some intelligence, so that it is able to select and implement a solution strategy which it considers appropriate given the constraints set by the analyst and its previous experience. This philosophy was devised so that the program was able to make the most effective use of the allocated computer resources, enabling the program to continue even though one particular solution method was unable to achieve convergence.

During the last few years much effort has been devoted to the development of efficient new solution algorithms which overcome some of the disadvantages of traditional methods. Some effective alternatives to the traditional Newton-Raphson and Modified Newton-Raphson methods have been suggested. Those include methods such as the BFGS Quasi-Newton algorithm which was introduced by Matthies and Strang[50] and the Arc-length methods introduced by Riks[29] and modified by Crisfield[51].

The objectives of this section are to give an outline of the traditional methods that can be used in the solution of non-linear equations, such as the Newton-Raphson method; to expand more fully on the newer methods, such as the Arc-length methods and finally to give full details where methods have been enhanced or modified. This section also outlines how the aforementioned methods may be linked together to form a successful solution strategy. This section begins with the introduction of a new concept, called scaled space, which allows the finite element equations to be scaled so that they are better conditioned in certain solution methods. The concept can also reduce the unit dependence of convergence criteria.

8.5.1 Scaled Space

In a plate bending analysis the stiffness matrix contains terms of widely different magnitudes and units. This can be seen if one compares the terms that link forces to translations with those that link moments to rotations. These problems are most apparent in the selection of convergence criteria, when attempting to compare, say residual moments, with applied direct forces. The scaled space concept attempts to convert the residual and applied forces to comparable units so that they can be compared directly. A related concept has been introduced previously by Crisfield[18]. However, in this case the scaling factors were not normalised and were only applied to convergence checking. In this context they convert a force convergence check to a form of energy convergence check and, therefore, have not found wide acceptance.

The leading diagonal elements of the stiffness matrix $K_{mn\ mn}$ link the deflection component at node 'm' degree of freedom (dof) 'n' to the corresponding force at the same location. If we now calculate scaling factors S_n such that:-

$$S_n = \left[\frac{n_n \sum_{m=1}^{n_1} K_{m1\ m1}}{n_1 \sum_{m=1}^{n_n} K_{mn\ mn}} \right]^{1/2} \quad \text{For all dof types 'n'} \qquad (8.35)$$

where n_n is the number of nodes with dof type 'n' and K is the stiffness matrix before the application of boundary conditions. The scaling factors are effectively a measure of the ratio between the average stiffness for each dof type 'n', and the average stiffness for the reference dof type, in this case type 1.

The scaling factors S_n give the ability to scale displacement or force vectors into units similar to those used for the reference dof (in this case dof type 1 was used as the reference):

$$\bar{u}_{mn} = \frac{u_{mn}}{S_n} \quad \text{for } m = 1, n_n; \text{ for } n = 1, \text{ndof} \qquad (8.36)$$

$$\bar{p}_{mn} = S_n\, p_{mn} \quad \text{for } m = 1, n_n; \text{ for } n = 1, \text{ndof}$$

where ndof is the number of dof types at any node and n_n is the number of nodes that have dof type 'n'.

It would be more consistent to calculate an individual scaling factor for each degree of freedom in the structure, thus avoiding problems with different sized elements, different dof at different nodes. However, for the sake of simplicity, at the expense of the small error involved, the calculation of a scaling factor for each type of dof, rather than each individual dof, was found to be preferable.

8.5.2 Iterative Solution Methods

The majority of incremental solution procedures are linked with iterations within increments which aim to reduce the residual force vector 'r' towards zero within the limits of the chosen convergence

criteria. An initial estimate of the incremental displacement (Δu^n) is calculated, to which is added a corrective displacement (δu^n_i) during each iteration.

The general sign convention is worthy of emphasis at this point, enboldened capital alphabetics generally represent matrices, such as the stiffness matrix K. Emboldened lower case characters, generally stand for vectors, such as u the displacement vector. Symbols preceeded by Δ represent incremental quantities while those preceeded by δ represent iterational quantities. Superscripts generally refer to increment numbers while subscripts refer to iteration numbers.

8.5.2.1 Newton-Raphson Method

The finite element equilibrium requirements amount to finding the solution to the equations

$$r\,(u^n_*) = 0 \qquad (8.37)$$

where u^n_* is the unknown solution vector at the end of increment 'n', $r\,(u^n_*)$ is defined as:-

$$r\,(u^n_*) = p^n - f(u^n_*)$$

and $r\,(u^n_*)$ = the gradient of the total potential energy or the out of balance (residual) force vector

$f\,(u^n_*)$ = the vector of internal forces at displacement level u^n_*

p^n = the vector of externally applied energy consistent nodal point loads

Assume that in the iterative solution we have evaluated u^n_{i-1} then a Taylor series expansion gives:-

$$r(u^n_*) = r(u^n_{i-1}) - \left[\frac{\partial r}{\partial u}\right]_i (u^n_* - u^n_{i-1}) \qquad (8.38)$$

where higher order terms are neglected and hence substituting equation 8.37 into 8.38 gives

$$\left[\frac{\partial r}{\partial u}\right]_i (u^n_* - u^n_{i-1}) = p^n - f(u^n_{i-1}) \qquad (8.39)$$

If we define:-

$$u^n_* - u^n_{i-1} = \delta u^n_i \qquad (8.40)$$

and recognise that:-

$$\left[\frac{\partial r}{\partial u}\right]_i = K_i \qquad (8.41)$$

then equation 8.39 can be written as

$$K_i \, \delta u^n_i = p^n - f(u^n_{i-1}) \qquad (8.42)$$

Thus the iterative displacements can be calculated from:

$$\delta u^n_i = K^{-1}_i (p^n - f(u^n_{i-1})) = K^{-1}_i \, r^n_{i-1} \qquad (8.43)$$

and hence a better approximation to the displacements u^n_* is

$$u^n_i = u^n_{i-1} + \delta u^n_i \qquad (8.44)$$

The concept of a line search will be introduced in a future section, however, it will be useful to define the concept upon which a line search is based here. In essence, a line search involves scaling the iterative displacements so that a preset criterion can be attained. In this way one hopes to accelerate the solution process. A line search algorithm modifies equation 8.44 to:-

$$u^n_i = u^n_{i-1} + s_i \, \delta u^n_i \qquad (8.45)$$

where s_i is the line search scaling factor.

8.5.2.2 Modified Newton-Raphson Method

With the Newton-Raphson method the tangential stiffness K is updated at every iteration. This procedure can be very expensive, especially in reinforced concrete analysis where concrete cracking and steel

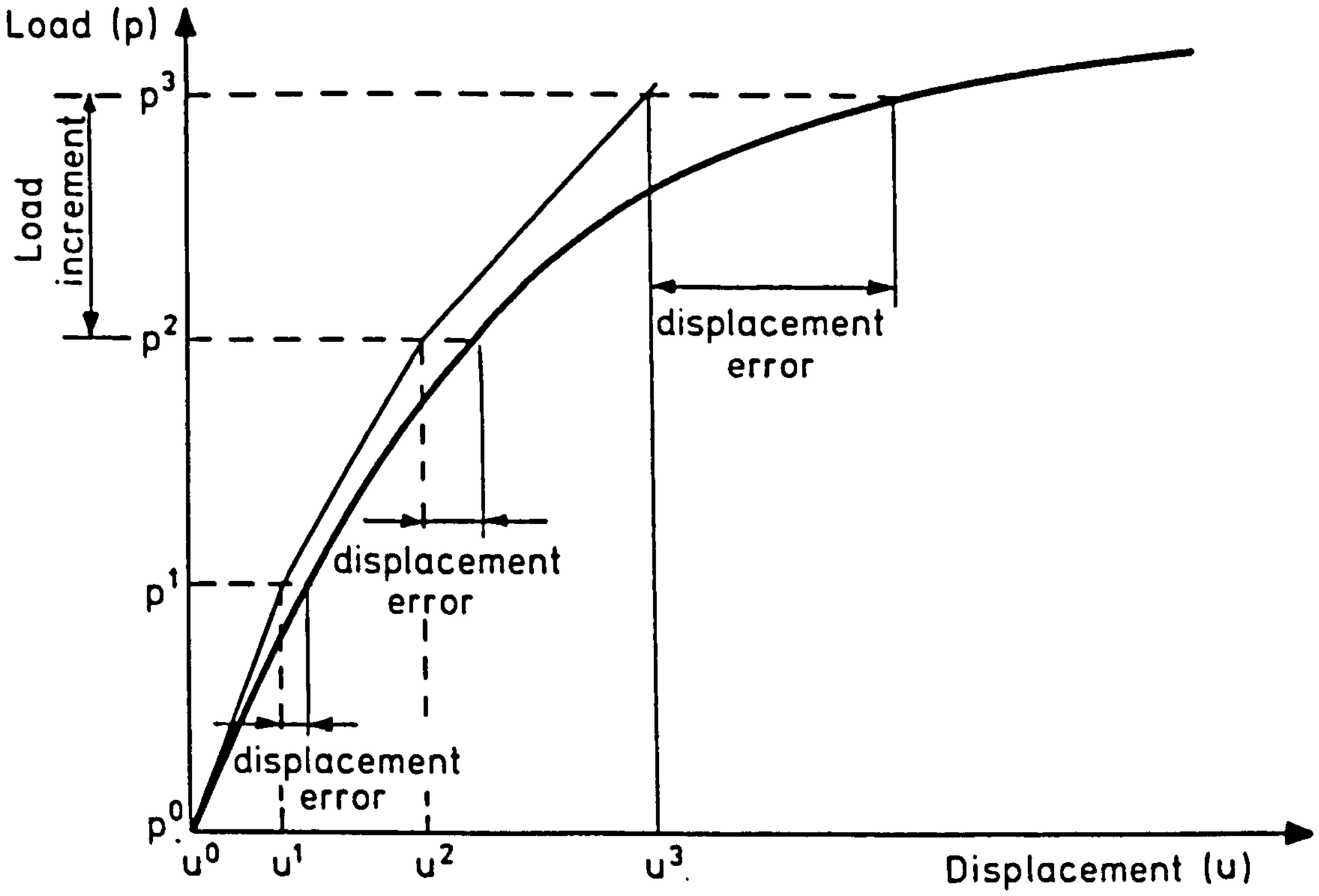

FIG. 8.9. EFFECT OF PURELY INCREMENTAL METHOD

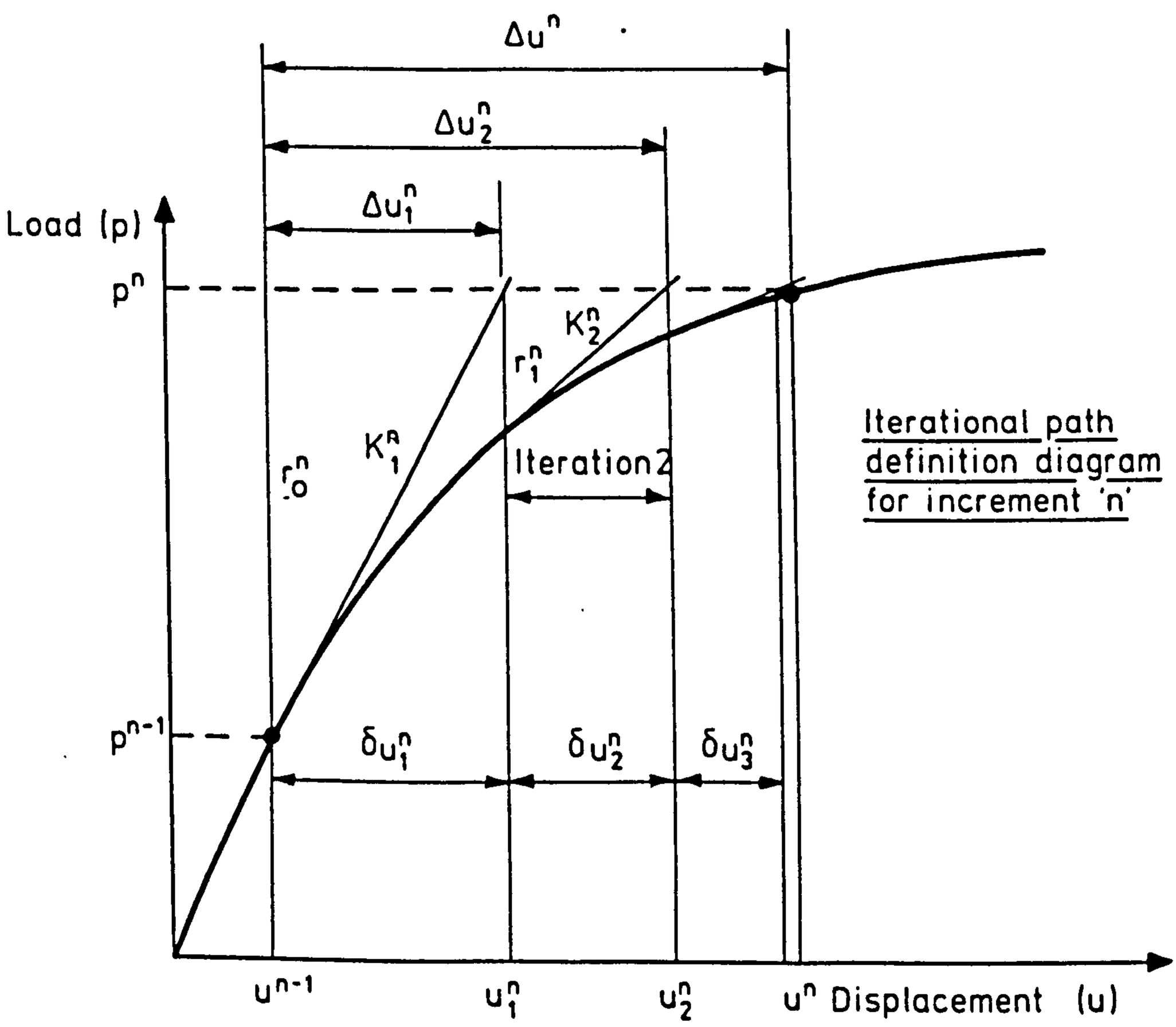

FIG. 8.10. NEWTON-RAPHSON METHOD

yielding can lead to a large number of iterations within an analysis. To overcome this disadvantage the Newton-Raphson technique can be modified so that the tangential stiffness matrix is only updated occasionally. Probably the most popular approach is the updating of the stiffness matrix once in an increment, generally at either the first or second iteration, see Figure 8.11. This modifies equation 8.43 to:-

$$\delta u^n_i = K^{-1}_1 (p^n - f(u^n_{i-1})) = K^{-1}_1 r^n_{i-1} \qquad (8.46)$$

where K^{-1}_1 refers to the most recently formed stiffness matrix. This equation is repeatedly solved with different residual force vectors, but the same stiffness matrix during subsequent iterations.

It can be seen that the modified Newton-Raphson technique could result in a reduced cost due to the fewer stiffness reformations. However, convergence is slower with the modified Newton-Raphson method, this is particularly true during large stiffness changes, such as occur with concrete cracking and steel yielding. Even though there are fewer stiffness reformationsin an increment, the residual force still has to be calculated at each iteration and since this forms a large part of the required resources, the modified Newton-Raphson method results in an increased overall cost in many cases. It can be seen that the modified Newton-Raphson technique is more suited to early increments, where little material degredation is taking place and therefore it would seem sensible to use this technique early on and switch to a more powerful technique when required.

8.5.2.3 BFGS Method

In recent years a new group of algorithms which offer advantages over the traditional Newton-Raphson and modified Newton-Raphson techniques

have emerged. These methods, which are generally known as quasi-Newton methods, were introduced by Davidon[19] in 1959 for the solution of minimization problems. The first practical implementation of these methods for the solution of the non-linear equations in finite-element analyses was made by Matthies and Strang[50] in 1979. The quasi-Newton methods are based upon the idea that instead of reforming the stiffness matrix, or leaving it unchanged, the matrix should be updated in a simple way at each iteration. The new stiffness matrix K_i should satisfy the quasi-Newton condition:-

$$K_i\ (\delta u^n_{i-1}) \;=\; r^n_{i-2} - r^n_{i-1} \;=\; \gamma_{i-1} \qquad (8.47)$$

This condition is shown diagrammatically in Figure 8.12. For the one-degree of freedom case this completely defines the matrix K_i, however, for a multi-degree of freedom case, all matrices satisfying equation 8.47 are candidates for K_i. The rank of the update is generally one or two. A requirement for the majority of finite element analyses is that the stiffness matrix should continue to the symmetric. The most successful of the update algorithms appears to be the BFGS method, which has been selected for the present study. An additional feature of the BFGS method is that the updated matrix is positive definite if the previous matrix was positive definite.

It is more convenient to store the updates rather than to apply them directly to the stiffness matrix since this reduces the computational work in many cases and also allows the updates to be discarded if necessary. If the updates are stored then it is more efficient to apply them in multiplicative, rather than additive form so that:-

$$K^{-1}_i = [(I + w_i\, v^T_i) \ldots (I + w_3\, v^T_3)\ (I + w_2\, v^T_2)]\ K^{-1}_1$$
$$[(I + v_2\, w^T_2)\ (I + v_3\, w^T_3) \ldots (I + v_i\, w^T_i)] \qquad (8.48)$$

where I is the identity matrix. The vectors v_i and w_i are defined as follows:-

$$v_i = \left[\frac{\delta u^T_{i-1}\ \gamma_{i-1}}{\delta u^T_{i-1}\ K_{i-1}\ \delta u_{i-1}}\right]^{1/2} K_{i-1}\ \delta u_{i-1} - \gamma_{i-1} \qquad (8.49)$$

$$w_i = \frac{1}{\delta u^T_{i-1}\ \gamma_{i-1}}\ \delta u_{i-1} \qquad (8.50)$$

where,

$$\gamma_{i-1} = r_{i-2} - r_{i-1}$$

Hence,

$$v_i = \left[s_{i-1}\left[\frac{\delta u^T_{i-1}\ \gamma_{i-1}}{s_{i-1}\ \delta u^T_{i-1}\ r_{i-2}}\right]^{1/2} - 1\right] r_{i-2} + r_{i-1} \qquad (8.51)$$

where s_{i-1} is the optional line search scaling factor contained in equation 8.45. The expansion is increased by one as each new update is added. The stiffness matrix inverse $K^{-1}{}_i$ is never explicitly formed. The updates are applied during the forward and back substitution process on the matrix $K^{-1}{}_1$. As the number of updates increases the overall efficiency of the algorithm decreases so it is desirable to set an upper limit upon the number of updates. Often, convergence is achieved before the limit is reached. If the limit is reached there are several options:

(i) Update the material properties and form a new tangent stiffness matrix to which new updates are applied in subsequent iterations.

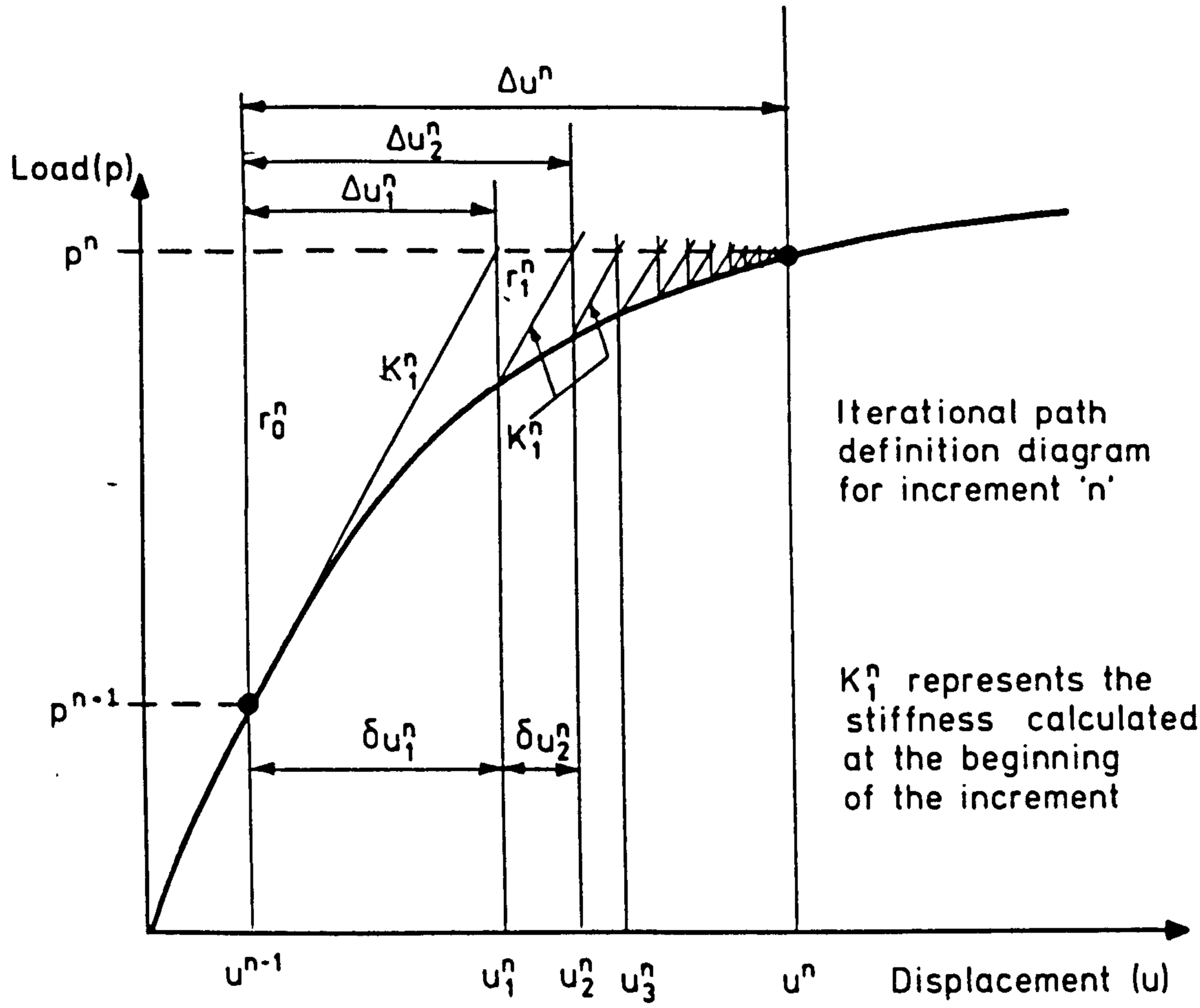

FIG. 8.11. MODIFIED NEWTON-RAPHSON METHOD

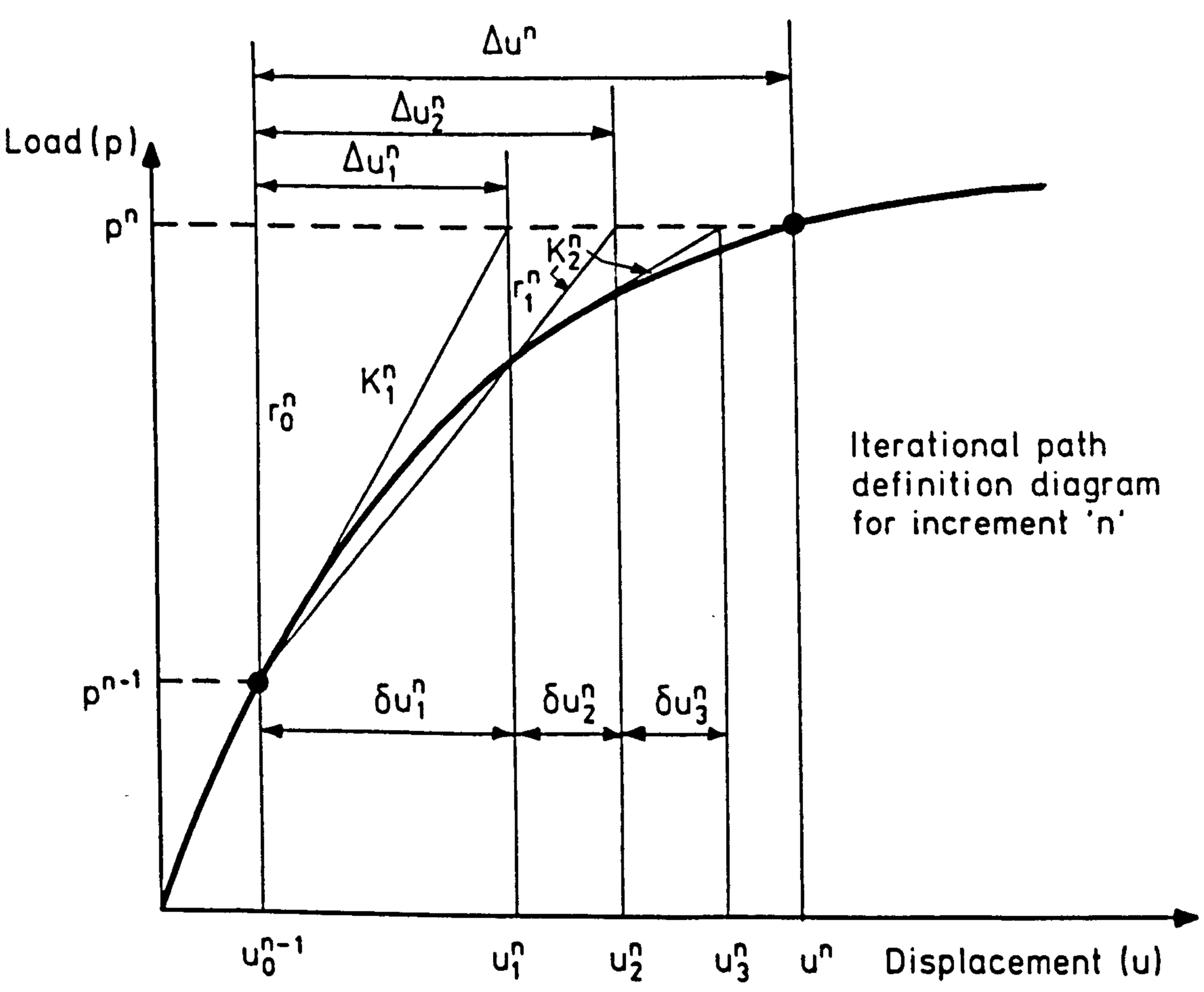

FIG. 8.12. BFGS QUASI-NEWTON METHOD

(ii) Discard the oldest set of update vectors and form a new pair for the current iteration, thus maintaining the number of updates at the maximum allowable.

(iii) Discard all the current update vectors and begin updating the old tangential stiffness matrix again from the beginning.

For the present study option (i) was chosen when the number of updates reached the maximum of twenty. Option (i) was chosen since it logically provides a more efficient algorithm. In addition this method could be used to provide a hybrid solution algorithm whereby the tangential stiffness matrix is reformed every, say 4 iterations, and BFGS updating is used for iterations between stiffness reformations.

It has been suggested in references 50 and 21 that dangerous updates, if applied, may adversely effect the numerical stability and efficiency of the BFGS algorithm. Reference 50 suggests that the condition number (c) of the update matrix, $Q = I + v\,w^T$, be calculated and checked against a preset criteria. The condition number is defined as

$$c = \left[\frac{\text{Maximum eigenvalue of matrix}}{\text{Minimum eigenvalue of matrix}}\right]^{1/2} \tag{8.52}$$

Since Q is unsymmetric than it is the eigenvalues of Q^TQ which enter into equation 8.52. The matrix Q^TQ is of rank 2 and therefore will have n-2 eigenvalues equal to 1 and two non-unit eigenvalues λ_1 and λ_2. Thus, and with reference to 20, the condition number is equal to:-

$$c = \left[\frac{\lambda_1}{\lambda_2}\right]^{1/2} = \frac{[(v^Tv)^{1/2}\,(w^Tw)^{1/2} + \{(v^Tv)(w^Tw) + 4(1 + w^Tv)\}^{1/2}]^2}{4(1 + w^Tv)} \tag{8.53}$$

In contrast, reference 21 recommends that the condition number of the matrix Q and not Q^TQ be checked. The matrix Q is of rank 1 and therefore possesses n-1 eigenvalues of unity and one equal to $1 + v^Tw$. From equations 8.49 and 8.50:-

$$\lambda_2 = 1 + v^Tw = \left[\frac{\delta u^T_{i-1}\ K_{i-1}\ \delta u_{i-1}}{\delta u^T_{i-1}\ \gamma_{i-1}}\right]^{1/2} \tag{8.54}$$

$$\therefore\ c = \left[\frac{\lambda_1}{\lambda_2}\right]^{1/2} = \left[\frac{\delta u_{i-1}\ \gamma_{i-1}}{\delta u^T_{i-1}\ K_{i-1}\ \delta u_{i-1}}\right]^{1/4} \tag{8.55}$$

It would appear that an incorrect subscript to K of i, instead of i-1, appears in the definition of $\lambda_2 = 1 + v^Tw$ in reference 50.

A number of researchers have suggested various values from 10^5 to 10^{10} as the limit for c, above which updates are considered dangerous and are not applied. Generally, for the present study if the condition number defined by equation 8.53 exceeded 10^8 than the update was avoided. Analyses were carried out with larger limits on c (10^{11} and 10^{20}). With these analyses no problems were encountered and the solution converged to the expected configuration.

8.5.2.4 Line Searches

Matthies and Strang specifically recommended that the BFGS algorithm be combined with a line search procedure. However, the BFGS algorithm may be used independently of the line search procedures, in some cases this may be preferable for maximum efficiency. Line searching is not exclusive to the BFGS algorithm and may improve the effectiveness and efficiency of many other algorithms, such as the Newton-Raphson and Modified Newton-Raphson techniques, that have been described in previous sections. Moreover the line search principle may be used with good effect even when an iterative solution method, such as BFGS, is combined with an iterative constraint method, such as displacement

control. Line searching can be particularly useful for problems involving rapid changes in structural stiffness, such as in reinforced concrete analyses when concrete cracks or steel yields.

In a problem involving 'n' degrees of freedom, given an approximation u^n_{i-1} to the solution of $r(u^n_*) = 0$ an iterative solution method, such as BFGS, may be used to obtain a direction, δu^n_i, in which to search for a better approximation. A new guess will lie along the line $u^n_i = u^n_{i-1} + s_i \delta u^n_i$ where s_i is a scalar scaling factor. Along this line it cannot be expected that an exact solution to the equation, $r(u^n_*) = 0$ will be found, however, a value of s_i can be chosen so that s_i $r(u^n_i)^T \delta u^n_i = 0$. Thus, the component of the residual force vector, $r(u^n_i)$, in the search direction, δu^n_i, is zero. This, implies equilibrium in the direction of δu^n_i and, thus, the aim is to achieve:-

$$s_i \; r(u^n_i)^T \delta u^n_i = 0 \qquad (8.56)$$

Equation 8.56 is generally solved through an iterative technique. An exact solution of equation 8.56 can be prohibitively expensive since the residual forces have to be evaluated for each new trial value of s_i. Therefore equation 8.56 is generally solved within some tolerance so that:-

$$|s_{i,j} \; r(u^n_{i,j})^T \delta u^n_i| < Tol \; |s_{i,j} \; r(u^n_{i,0})^T \delta u^n_i| \qquad (8.57)$$

$$0 < Tol < 1$$

If we also define:-

$$G_{i,j} = s_{i,j} \; r(u^n_{i,j})^T \delta u^n_i \qquad (8.58)$$

and $$GO_{i,j} = s_{i,j} \; r(u^n_{i,0})^T \delta u^n_i \qquad (8.59)$$

so that the criterion becomes:-

$$G_{i,j} < Tol\ GO_{i,j} \tag{8.60}$$

where j denotes the line search trial number. A small value for Tol, and hence a tight tolerance, will, most probably, result in fewer iterations, but the number of line search trials may increase significantly resulting in an increased solution cost. For the present investigations, a value for Tol of between 0.3 and 0.5 was chosen. This is in line with the values chosen by other researchers[50,21].

Two different line search algorithms were employed for the present investigation. The first, which is based on the Illinois algorithm, is the more stable, while the second, which is based on a secant approach, has the potential to be the most efficient.

The Illinois based algorithm is divided into two stages. The first locates a bracket on zero so that $GO_{i,j}\ G_{i,j} < 0$, that is the solution for 's' in equation 8.56 lies between $s_{i,j-1}$ and $s_{i,j}$. The second stage iterates within this bracket to locate a value of s_i which satisfies equation 8.57. This procedure is shown diagrammatically in Figure 8.13(ii), however, for full details the interested reader is directed to reference 50.

The second line search algorithm is based upon a secant approach, see Figure 8.14. As with the first method values for $GO_{i,j}$ and $G_{i,j}$ with $s_{i,j} = 1$ and $j = 1$ are calculated. Using these values and a linear prediction a value of s which will satisfy equation 8.56 is thus calculated:-

$$s_{i,2} = \frac{GO_{i,1}}{GO_{i,1} - G_{i,1}} \tag{8.61}$$

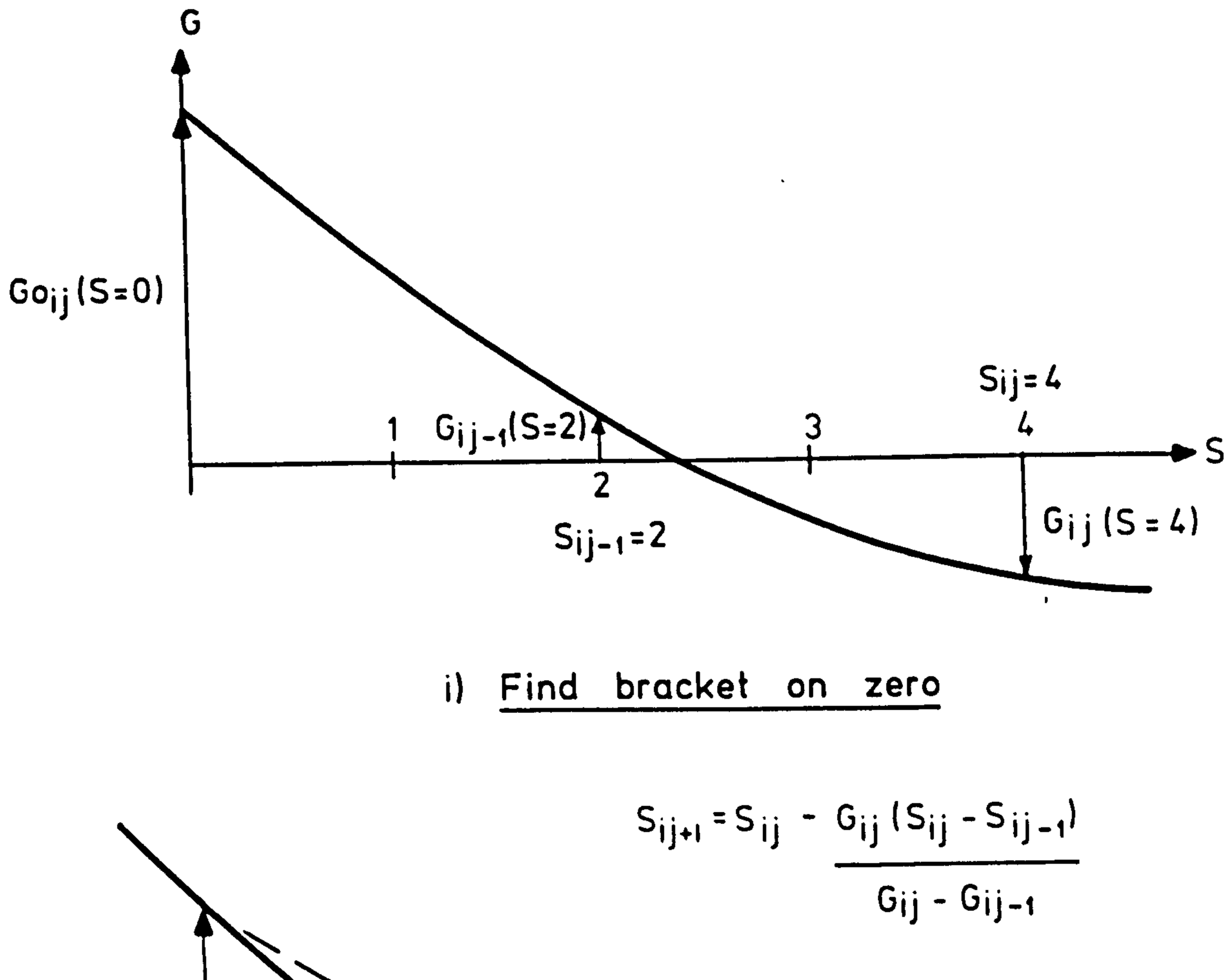

i) Find bracket on zero

$$S_{ij+1} = S_{ij} - \frac{G_{ij}\,(S_{ij} - S_{ij-1})}{G_{ij} - G_{ij-1}}$$

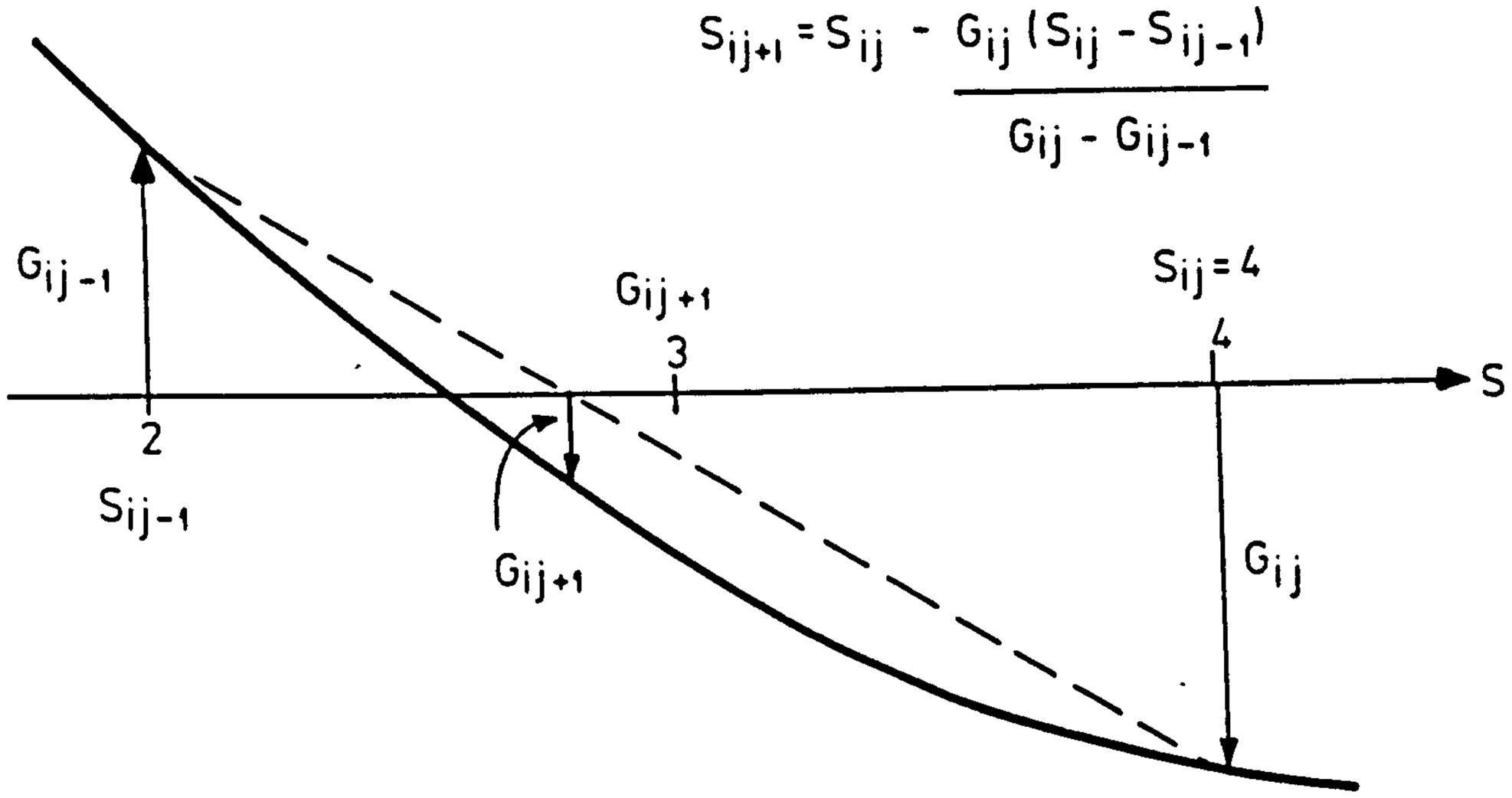

ii) Interpolate for zero

$$S_{ij+2} = S_{ij+1} - \frac{G_{ij+1}\,(S_{ij+1} - S_{ij-1})}{G_{ij+1} - 0{\cdot}5\,G_{ij-1}}$$

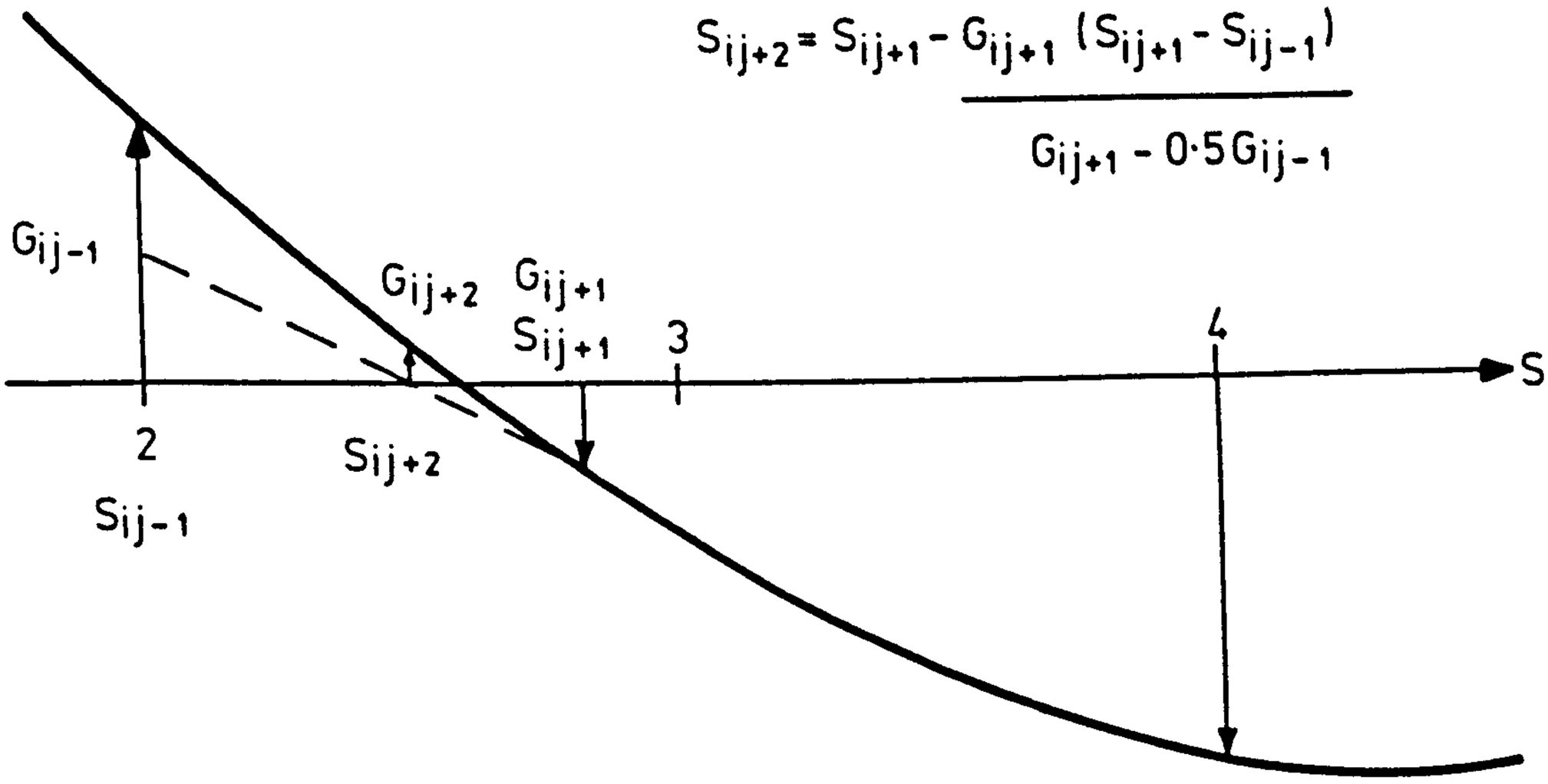

FIG. 8.13. ILLINOIS LINE SEARCH ALGORITHM

For subsequent line search trials the predictor equation becomes:-

$$s_{i,j+1} = s_{i,j-1} - \left[\frac{s_{i,j-1} - s_{i,j}}{G_{i,j-1} - G_{i,j}}\right] G_{i,j-1} \qquad (8.62)$$

It would be dangerous to accept any value that equation 8.62 produces. Therefore, in order to avoid dangerous extrapolations, relative and absolute constraints are placed upon the predicted step length and these are given below:-

$$|s_{i,j+1} - s_{i,j}| < \text{relmax} \qquad (8.63)$$

$$|s_{i,j+1}| < \text{absmax} \qquad (8.64)$$

For the present study relmax was set to 5 and absmax was set to 15. The iterative process is terminated when either of the following conditions are met:-

$$G_{i,j} < \text{Tol}\ G0_{i,j} \qquad (8.65)$$

$$|s_{i,j} - s_{i,j-1}| < \text{Tol} \left|\frac{s_{i,j} + s_{i,j-1}}{2}\right| \qquad (8.66)$$

The value for Tol is the same in both equations and, as with method 1, a value in the range 0.3 to 0.5 was chosen for the present study. The second criterion in equation 8.66 is included to prevent the algorithm expending resources obtaining unnecessarily accurate values of $s_{i,j}$.

It was mentioned earlier that method 1 is the most stable, since it essentially follows a preset path, regardless of the information about G that is being obtained. While method 2 is more efficient in many cases, severe difficulties can be encountered if G is discontinuous and in this case method 1 would probably succeed. However, method 2

is able to search in negative s space which can be an advantage in situations of sudden stiffening.

8.5.3 Iterative Constraint Methods

It was mentioned earlier that a non-linear analysis is generally split into increments with only a small section of the response being traced within a particular increment. Within an increment one wishes to attain an increase in the magnitude of a variable, whether it be load, displacement or some hybrid constraint as in the arc-length method. Thus, these methods may be termed iterative constraint methods since the solution is constrained to attain an increase in a variable during an increment.

The most frequently used iterative constraint is load control which has been dealt with in an earlier section. The present section will be concerned mainly with the other two iterative constraint methods that have been implemented in the SNAP program, namely displacement and arc-length control.

8.5.3.1 Displacement Control

For the ascending branch of a load-deflection response, load control is generally the most efficient method. As the plateau in the response is reached, see point A in Figure 8.15 then difficulty in converging under load control will be encountered. After this point either displacement or arc-length control will be required in order to achieve convergence. It was found in this investigation that displacement control was the more efficient in situations where both displacement and arc-length control were able to achieve convergence.

With displacement control an incremental increase in the displacement at a particular dof is specified for an increment and the load level

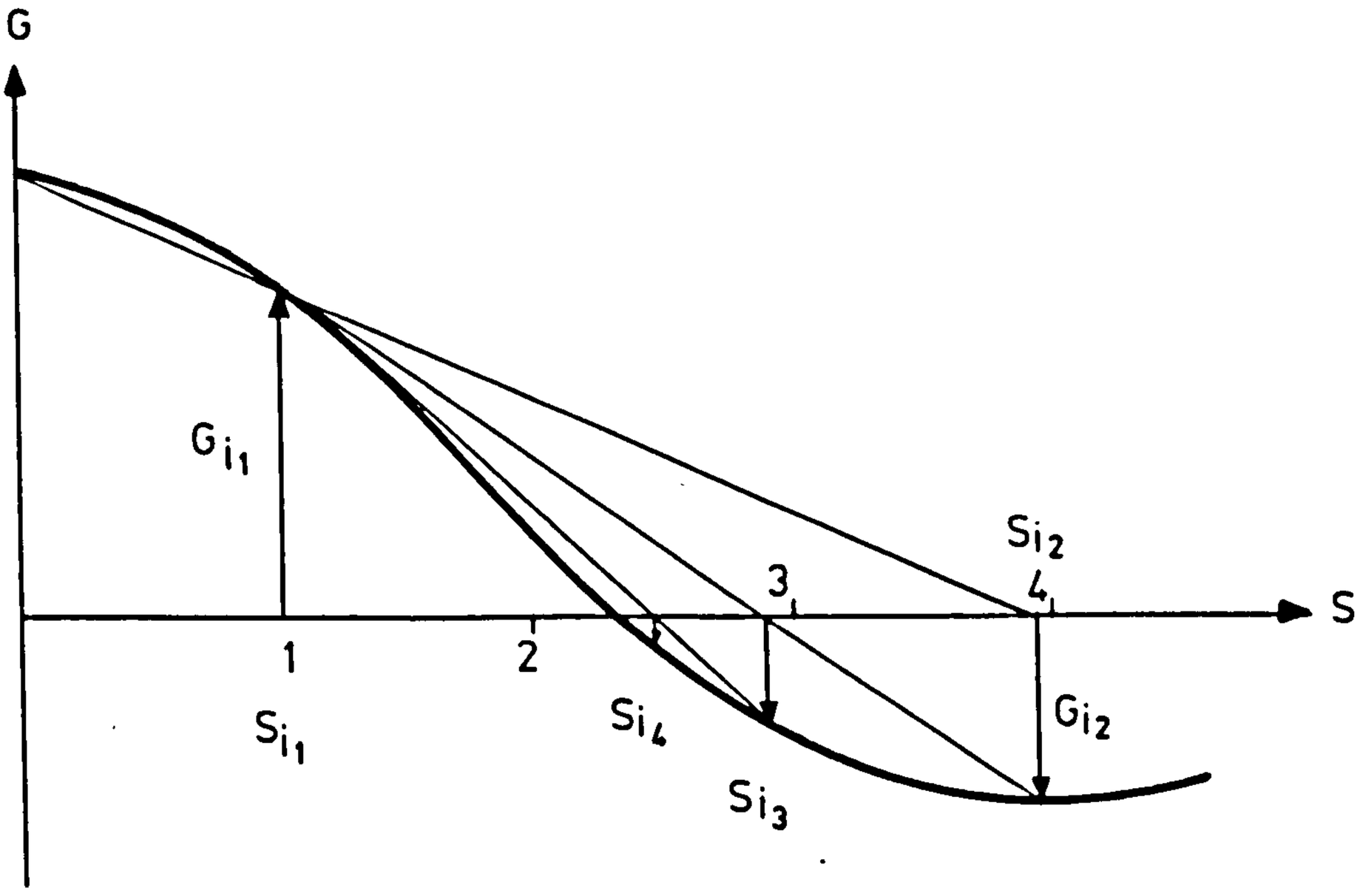

FIG. 8.14. LINE SEARCH ALGORITHM BASED ON A SECANT APPROACH

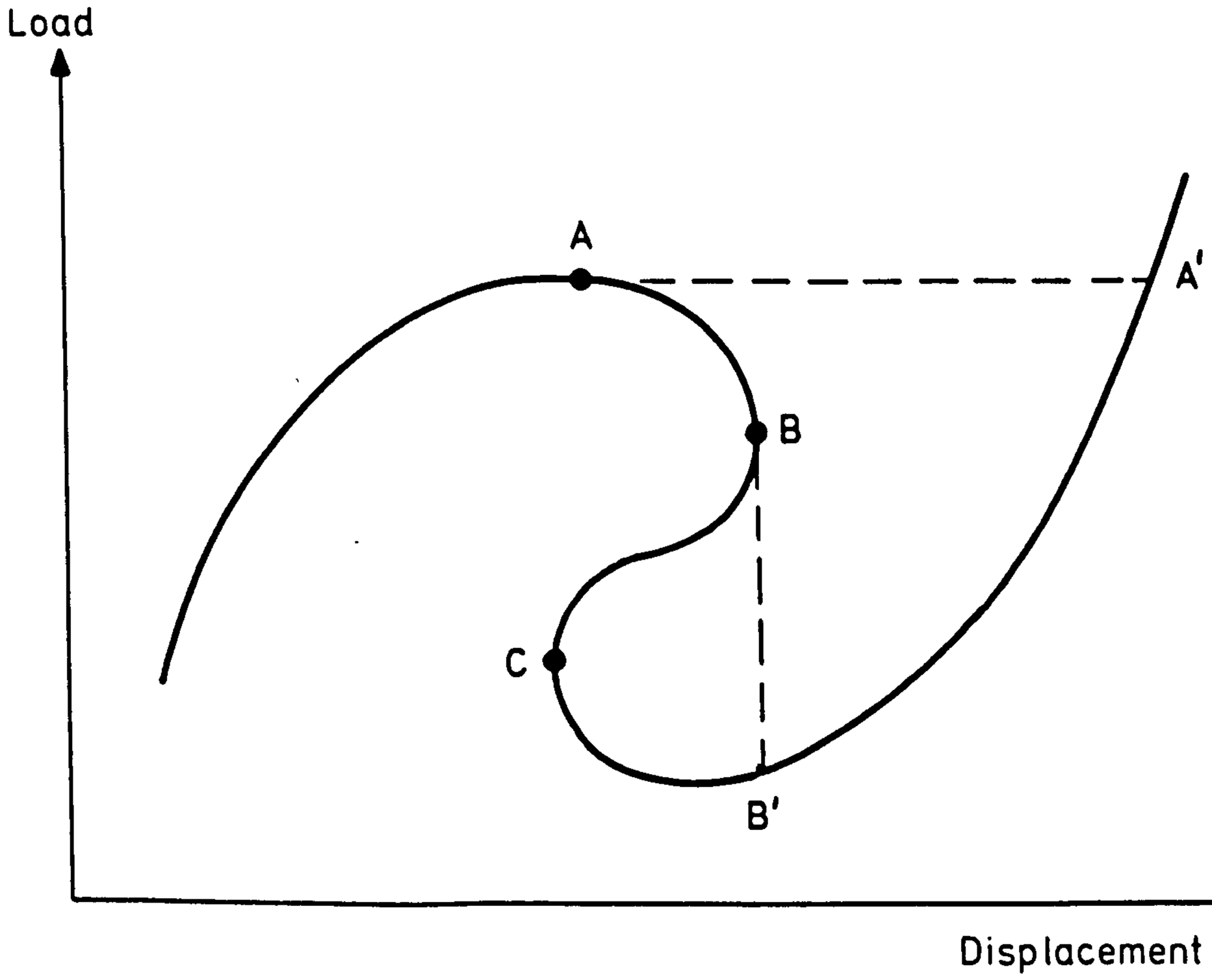

FIG. 8.15. SOME CAUSES OF SOLUTION METHOD FAILURE

is varied during the increment so that equilibrium can be achieved. Essentially two forms of displacement control are available, one involves the manipulation of the stiffness matrix, **K**, while the other is related to the arc-length method. Both methods will be presented.

Haisler, Stricklin and Key[23] have proposed a method for incrementing a characteristic displacement in an analysis past a limit point, which does not result in unsymmetric equations. The retention of symmetry increases its suitability for finite element programs, which generally incorporate symmetric equation solvers. A novel approach to the problem of pursuing an analysis past a limit point has been presented by Sharifi and Popov[24], in which they overcome the singularity at the limit point by introducing a fictitious spring into the problem.

From equation 8.43 we see that a corrective displacement, δu^n_i can be found within increment, n, at iteration, i, which gives a better approximation to:-

$$r(u^n_*) = 0 \tag{8.67}$$

where

$$u^n_* = u^n_{i-1} + \delta u^n_i \tag{8.68}$$

$$K_i \, \delta u^n_i = r(u^n_{i-1}) - p^n - f(u^n_{i-1}) \tag{8.69}$$

If we now replace the load vector, p^n with a load factor p^n_i and a nominal load vector p^* then equation 8.69 can be written as:-

$$K_i \, \delta u^n_i = p^n_i \, p^* - f(u^n_{i-1}) \tag{8.70}$$

If we also define:- $$p^n_i = p^n_{i-1} + \delta p^n_i \tag{8.71}$$

then:-

$$K_i \, \delta u^n_i = \delta p^n_i \, p^* + p^n_{i-1} \, p^* - f(u^n_{i-1}) = \delta p^n_i \, p^* + r^n_{i-1} \tag{8.72}$$

If we now denote the controlling dof as dof number k and for simplicity make this equation the last equation, then equation 8.72 can be written as:-

$$\begin{bmatrix} K_{11} & K_{1k} \\ K_{k1} & K_{kk} \end{bmatrix} \begin{bmatrix} \delta u^n_i \\ \delta u^n_{i,k} \end{bmatrix} - \delta p^n_i \begin{bmatrix} p^* \\ p^*_k \end{bmatrix} + \begin{bmatrix} r^n_{i-1} \\ r^n_{i-1,k} \end{bmatrix} \quad (8.73)$$

Partitioning we obtain:-

$$K_{11}\ \delta u^n_i + K_{1k}\ \delta u^n_{i,k} = \delta p^n_i\ p^* + r^n_{i-1} \quad (8.74)$$

$$K_{k1}\ \delta u^n_i + K_{kk}\ \delta u^n_{i,k} = \delta p^n_i\ p^*_k + r^n_{i-1,k} \quad (8.75)$$

Rearranging equations 8.74 and 8.75 we obtain:-

$$K_{11}\ \delta u^n_i = \delta p^n_i\ p^* + r^n_{i-1} - K_{1k}\ \delta u^n_{i,k} \quad (8.76)$$

$$K_{k1}\ \delta u^n_i - \delta p^n_i\ p^*_k = r^n_{i-1,k} - K_{kk}\ \delta u^n_{i,k} \quad (8.77)$$

Solving for δu^n_i in equation 8.76 we obtain

$$\delta u^n_i = K^{-1}_{11}\ [\delta p^n_i\ p^* + r^n_{i-1} - K_{1k}\ \delta u^n_{i,k}] \quad (8.78)$$

$$\delta u^n_i = a + \delta p^n_i\ b \quad (8.79)$$

where

$$a = K^{-1}_{11}\ [r^n_{i-1} - K_{1k}\ \delta u^n_{i,k}]$$

$$b = K^{-1}_{11}\ p^*$$

Substituting equation 8.79 into equation 8.77 yields:-

$$K_{k1}\ [a + \delta p^n_i\ b] - \delta p^n_i\ p^*_k = r^n_{i-1,k} - K_{kk}\ \delta u^n_{i,k} \quad (8.80)$$

$$\delta p^n_i\ [K_{k1}\ b - p^*_k] = r^n_{i-1,k} - K_{kk}\ \delta u^n_{i,k} - K_{k1}\ a \quad (8.81)$$

$$\therefore \delta p^n_i = \frac{r^n_{i-1,k} - K_{kk}\ \delta u^n_{i,k} - K_{k1}\ a}{K_{k1}\ b - p^*_k} \quad (8.82)$$

Thus at the beginning of any iteration the current displacement field u^n_{i-1} and hence the residual force vector, r^n_{i-1} are known. a and b may be evaluated and hence by equation 8.82 δp^n_i may be calculated. From equation 8.79 the iterational displacement vector δu^n_i may be obtained, and hence u^n_i may be calculated from:-

$$u^n_i = u^n_{i-1} + \delta u^n_i \tag{8.83}$$

The process is then repeated for iteration i+1. In practice the stiffness matrix would not be partitioned but boundary conditions would be applied to the k'th row and column. These boundary conditions would consist of setting all locations in the k'th row and column to zero except for the leading diagonal location which would be set to 1. In the calculation of a and b the k'th location in each right hand side vector would be set to $\delta u^n_{i,k}$ and zero respectively.

Equation 8.82 is only truely applicable to the first iteration since for subsequent iterations $\delta u^n_{i,k} = 0$, therefore, equation 7.103 simplifies to:-

$$a = K^{-1}_{11}\, r^n_{i-1} \tag{8.84}$$

$$b = K^{-1}_{11}\, p^* \tag{8.85}$$

and,

$$\delta p^n_i = \frac{r^n_{i-1,k} - K_{k1}\, a}{K_{k1}\, b - p^*_k} \tag{8.86}$$

The second form of displacement control uses equation 8.72 to calculate a new iterational displacement vector δu^n_i such that:-

$$\delta u^n_i = \delta p^n_i\, K^{-1}_i\, p^* + K^{-1}_i\, r^n_{i-1} \tag{8.87}$$

The displacement control constraint is applied through the equation:-

$$\Delta u^n_{i,k} = \Delta \ell^n \tag{8.88}$$

$$\Delta u^n_i = \Delta u_{i-1} + \delta u^n_i = \Delta u_{i-1} + \delta p^n_i \, K^{-1}_i \, p^* + K^{-1}_i \, r^n_{i-1} \tag{8.89}$$

Let

$$\delta' u^n_i = K^{-1}_i \, r^n_{i-1} \tag{8.90}$$

$$u^\ell_i = K^{-1}_i \, p^* \tag{8.91}$$

$$p^n_i = p^n_{i-1} + \delta p^n_i \tag{8.92}$$

The iterational load level change δp^n_i is calculated from:-

$$\Delta u^n_{i,k} = \Delta \ell^n = \Delta u^n_{i-1,k} + \delta' u^n_{i,k} + \delta p^n_i \, u^\ell_{i,k} \tag{8.93}$$

where k = dof to which the constraint is applied

$\Delta \ell^n$ = required incremental displacement for dof k.

so that,

$$\delta p^n_i = \frac{\Delta \ell^n - u_{i-1,k} - \delta' u^n_{i,k}}{u^\ell_{i,k}} \tag{8.94}$$

If the displacement constraint was satisfied at the previous iteration then equation 8.94 simplifies to:-

$$\delta p^n_i = \frac{-\delta' u^n_{i,k}}{u^\ell_{i,k}}$$

In effect the displacement constraint brings the iterational displacements back to the required level using the displacements, u^ℓ_i, obtained from the nominal incremental load vector, p^*.

Since the application of method 2 has no effect upon the calculation of the unconstrained iterational displacement vector, $\delta' u^n_i$, it may be implemented as a simple addition to a standard iterative algorithm.

For these reasons the second form of displacement control was incorporated into the SNAP program. The method was found to offer an efficient solution to the problem of tracing the structural response past a limit point.

Subsequent to the author's derivation and implementation of this method a paper by Batoz and Dhatt[25], which details a similar algorithm, was discovered.

8.5.3.1.1 Displacement control and iterative solution methods

The displacement control methods described above can be used in conjunction with any of the iterative solution methods, such as Newton-Raphson, which were described earlier. For the Newton-Raphson procedure the stiffness matrix K_i that was calculated at the end of the previous iteration is used in equations 8.90 and 8.91. For the modified Newton-Raphson procedure the most recently formed stiffness matrix, K_1, replaces K_i. It will be noticed that u^{ℓ}_i, need only be recomputed when the stiffness matrix is reformed. Storing the u^{ℓ}_i vector will allow it to be recalled for use in subsequent iterations.

The same principles generally apply when the BFGS method is used. The K^{-1}_i matrix represents the current stiffness matrix including all current updates. The application of displacement control does, however, complicate the calculation of new update vectors. The variable r^n_{i-2} in equation 8.51 should be replaced by $\hat{r}^n_{i-2}$ such that:-

$$\hat{r}^n_{i-2} = r^n_{i-2} + \delta p^n_{i-1}\, p^* \qquad (8.95)$$

This modification is most conveniently carried out with the application of the displacement control constraint so that in addition to updating the load level, $p^n_{i-1} = p^n_{i-2} + \delta p^n_{i-1}$, the residual force vector is also updated. Thus in equation 8.49:-

$$K_{i-1}\, \delta u^n_{i-1} = s_{i-1}\, \hat{r}^n_{i-2} \qquad (8.96)$$

8.5.3.1.2 Displacement control and line searching

First impressions may indicate that the application of line searching, in conjunction with a displacement control method, is unnecessary, since, it may be argued, the displacement level has already been constrained by the displacement control. However, it will be realised that unless the $\delta' u^n_i$ and u^ℓ_i vectors (as defined by equations 8.90 and 8.91) are parallel, the application of a line search will modify the overall displacement pattern whilst maintaining the constraint at the control dof. These two vectors will generally only be parallel at the beginning of an increment, when the incremental load is first applied. This is assuming no significant residual forces remained at the end of the previous increment. Therefore the application of a line search at this stage should be avoided. Using equation 8.87 and modifying it such that:-

$$\delta u^n_i = s_i \, \delta' u^n_i + \delta p^n_i \, u^\ell_i \qquad (8.97)$$

one can incorporate a line searching scale factor s_i. Thus the trial displacement level u_i is defined as:-

$$u_i = u_{i-1} + s_i \, \delta' u^n_i + \delta p^n_i \, u^\ell_i \qquad (8.98)$$

For a trial value of $s_i = s_{i,j}$ at the j'th line search iteration, the energy dissipated by the original residual force vector and the current residual force vector in the current search direction, $\delta u^n_{i,j}$, is defined as:-

$$GO_{i,j} = r(u_{i,0})^T \, \delta u^n_{i,j} \qquad (8.99)$$

$$G_{i,j} = r(u_{i,j})^T \, \delta u^n_{i,j} \qquad (8.100)$$

Any suitable line search algorithm, such as those described earlier, can now be used to find an approximate solution to the equation:-

$$r(u_{i,j}) = 0 \qquad (8.101)$$

within the tolerances given in section 8.5.2.4. The system proceeds with the line search algorithm selecting a trial value for $s_{i,j}$. The displacement constraint is applied to find an iterational displacement vector $\delta u_{i,j}$ and hence an iterational change in load level $\delta p_{i,j}$. Equations 8.99 and 8.100 can then be used to calculate GO and G at the current displacement level. The line search algorithm then checks whether the tolerances for the solution of equation 8.56 have been met. If not, another line search iteration begins with a new trial value, $s_{i,j+1}$.

If BFGS acceleration is also used with line searching under displacement control then the variable r^n_{i-2}, in equation 8.51 should be replaced by $\hat{r}^n_{i-2}$, since the load level has changed and the scale factor s_{i-1} is now, most probably, not equal to 1.

$$\hat{r}^n_{i-2} = r^n_{i-2} + \frac{\delta p^n_{i-1}\, p^*}{s_{i-1}} \qquad (8.102)$$

8.5.3.2 Arc-length control

For the present study it was found that displacement control was an efficient method for tracing the structural response past limit points such as point A in Figure 8.15. However, in situations where the response cuts back on itself or snaps back, as in point B of Figure 8.15, displacement control would not enable the correct load path to be followed. In places such as this it was necessary to use a method such as arc-length control. It may appear that the possibility of a snap back occurring in plate analysis is remote. However, an

injudiciously chosen displacement control point and a particular set of concrete and steel stress-strain curves may combine to cause a snap-back in the most unexpected places, see Chapter 9 Section 9.3.3.1. The arc-length method's ability to deal with problems involving snap-through and snap-back have resulted in its recent popularity[26,27,28]. Several different variants of the arc-length method are available, including the normal hyper-plane, updated normal hyper-plane and the spherical formulation. In addition all of these methods can be formulated with or without a load variable in the constraint.

Procedures for varying the load level during the iterations within an increment were advocated by Riks[29]. Essentially the applied loading is specified via a nominal load vector $\mathbf{p}^*$ and a load level, p^n, such that the total load is given by $p^n\mathbf{p}^*$ for increment n. For an 'n' dimensional problem the original Rik's method introduced a constraint equation in addition to the 'n' stiffness equations. The constraint equation takes the form:-

$$[\Delta u^n_i]^T [\Delta u^n_i] + [\Delta p^n_i]^2 [p^*]^T [p^*] = [\Delta \ell^n]^2 \quad (8.103)$$

$$\text{where, } \Delta u^n_i = \Delta u^n_{i-1} + \delta u^n_i \quad (8.104)$$

$$\delta u^n_i = \delta' u^n_i + \delta p^n_i \, p^* \quad (8.105)$$

$$\delta' u^n_i = K^{-1}_i \, r^n_{i-1} = K^{-1}_i \, (p^n_{i-1} \, p^* - f(u^n_{i-1})) \quad (8.106)$$

$$\Delta p^n_i = \Delta p^n_{i-1} + \delta p^n_i \quad (8.107)$$

where $\Delta \ell^n$ denotes the required 'arc-length' change for increment n. If equation 8.103 is added directly to the normal 'n' equilibrium equations, then both symmetry and the banded nature are destroyed. If one adopts a procedure similar to the displacement control method, described in the previous section, the desirable attributes of the

original stiffness equation such as their symmetry and banded nature can be retained.

8.5.3.2.1 Normal hyper-plane formulation

For the normal hyper-plane formulation the solution to $r(u^n_i) = 0$ is constrained lie on a hyper-plane which is orthogonal to the tangent at the beginning of the increment, see Figure 8.16. The tangent vector, t_1, can be defined as:-

$$t_1 = \begin{bmatrix} \Delta u^n_1 \\ \Delta p^n_1 \; p^* \end{bmatrix}$$

For the incremental vector at iteration i to lie on a hyper-plane which is perpendicular to this vector, then the scalar vector product of the incremental vector and t_1 must equal zero, thus:-

$$\begin{bmatrix} \Delta u^n_1 \\ \Delta p^n_1 \; p^* \end{bmatrix}^T \begin{bmatrix} \Delta u^n_i - \Delta u^n_1 \\ \Delta p^n_i \; p^* - \Delta p^n_1 \; p^* \end{bmatrix} = 0 \qquad (8.108)$$

Since the constraint which is defined by equation 8.108 is applied at the end of each iteration then equation 8.108 can be rewritten as:-

$$\begin{bmatrix} \Delta u^n_1 \\ \Delta p^n_1 \; p^* \end{bmatrix}^T \begin{bmatrix} \delta u^n_i \\ \delta p^n_i \; p^* \end{bmatrix} = 0 \qquad (8.109)$$

$$[\Delta u^n_1]^T [\delta u^n_i] + \Delta p^n_1 \; \delta p^n_i \; [p^*]^T [p^*] = 0 \qquad (8.110)$$

using $\delta u^n_i = \delta' u^n_i + \delta p^n_i \; u^\ell_i \qquad (8.111)$

We can solve for δp^n_i such that:-

$$\delta p^n_i = \frac{-[\Delta u^n_1]^T [\delta' u^n_i]}{[\Delta u^n_1]^T [u^\ell_i] + \Delta p^n_1 \; [p^*]^T [p^*]} \qquad (8.112)$$

A possible variation upon equation 8.108 ignores the load term, so equation 8.109 becomes

$$[\Delta u^n{}_1]^T \, [\delta u^n{}_i] \;=\; 0 \tag{8.113}$$

and equation 8.112 becomes:-

$$\delta p^n{}_i \;=\; \frac{-[\Delta u^n{}_1]^T \, [\delta' u^n{}_i]}{[\Delta u^n{}_1]^T \, [u^\ell{}_i]} \tag{8.114}$$

The dropping of the load terms modifies the graphical representation of the constraint to that shown in Figure 8.17. This figure depicts the 2 dof case for clarity and it can be seen that the load level does not now feature in the constraint and is in fact subservient to it.

The process is primed in the first iteration by the selection of an initial length increment, $\Delta\ell^n$, so that $\Delta p^n{}_1$ and $\Delta u^n{}_1$ can be calculated.

Any of the iterative solution methods, such as Newton-Raphson, described earlier can be used to obtain $\delta' u^n{}_i$ and $u^\ell{}_i$. The use of these methods with the normal hyperplane form of the arc-length control method is more fully described in section 8.5.3.2.4.

8.5.3.2.2 Updated normal hyperplane formulation

With the updated form of the hyperplane formulation the solution to r $(u^n{}_i) \;=\; 0$ is constrained to lie on a hyperplane which is perpendicular to the tangent in the previous iteration. Thus the t_i vector is defined as:-

$$t_i \;=\; \begin{bmatrix} \Delta u^n{}_{i-1} \\ \Delta p^n{}_{i-1} \;\; p^* \end{bmatrix} \tag{8.115}$$

For the incremental vector at iteration i to lie on the hyperplane perpendicular to this vector then:-

$$\begin{bmatrix} \Delta u^n_{i-1} \\ \Delta p_{i-1}\ p^* \end{bmatrix}^T \begin{bmatrix} \Delta u^n_i - \Delta u^n_{i-1} \\ \Delta p^n_i\ p^* - \Delta p^n_{i-1}\ p^* \end{bmatrix} = 0 \qquad (8.116)$$

And using, $\Delta u^n_i = \Delta u^n_{i-1} + \delta u^n_i$ (8.117)

gives, $\begin{bmatrix} \Delta u^n_{i-1} \\ \Delta p^n_{i-1} p^* \end{bmatrix}^T \begin{bmatrix} \delta u^n_i \\ \delta p^n_i\ p^* \end{bmatrix} = 0$ (8.118)

Figure 8.18 depicts the effect of the updated constraint graphically. It can be seen that the use of equation 8.116 results in a 'growing' tangential vector. It will be realised that, as with the normal hyperplane formulation of section 8.5.3.2.1, the load variables could be omitted from the constraint equations leaving only constraints involving displacement variables.

8.5.3.2.3 Spherical formulation

Crisfield[51] and Ramm[28] have advocated the adoption of a spherical constraint. With the spherical constraint the incremental vector is constrained to lie on a sphere whose centre is located at the structural state at the beginning of the increment, see Figure 8.19. The constraint can be specified as:-

$$[\Delta u^n_i]^T\ [\Delta u^n_i] + \Delta p^n_i\ \Delta p^n_i\ [p^*]^T\ [p^*] = [\Delta \ell^n]^2 \qquad (8.119)$$

where $\Delta \ell^n$ is the radius of the sphere and Δp^n_i and Δu^n_i are defined as:-

$$\Delta u^n_i = \Delta u^n_{i-1} + \delta u^n_i = \Delta u^n_{i-1} + \delta' u^n_i + \delta p^n_i\ u^\ell_i \qquad (8.120)$$

$$\Delta p^n_i = \Delta p^n_{i-1} + \delta p^n_i \qquad (8.121)$$

Substituting equations 8.120 and 8.121 into equation 8.119 and solving for δp^n_i yields an equation of the form:-

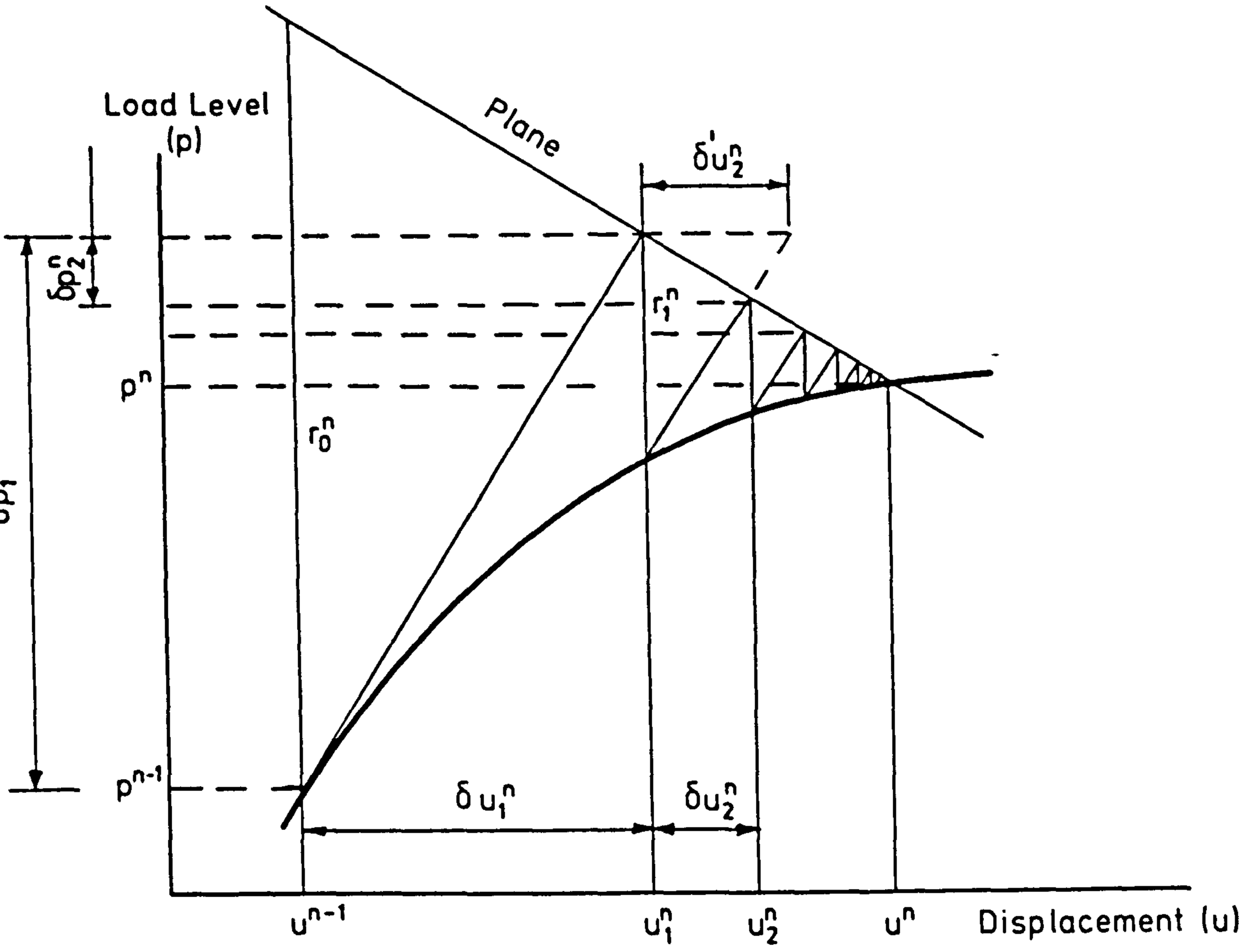

FIG. 8.16. NORMAL PLANE METHOD
(contained in load/displacement space)

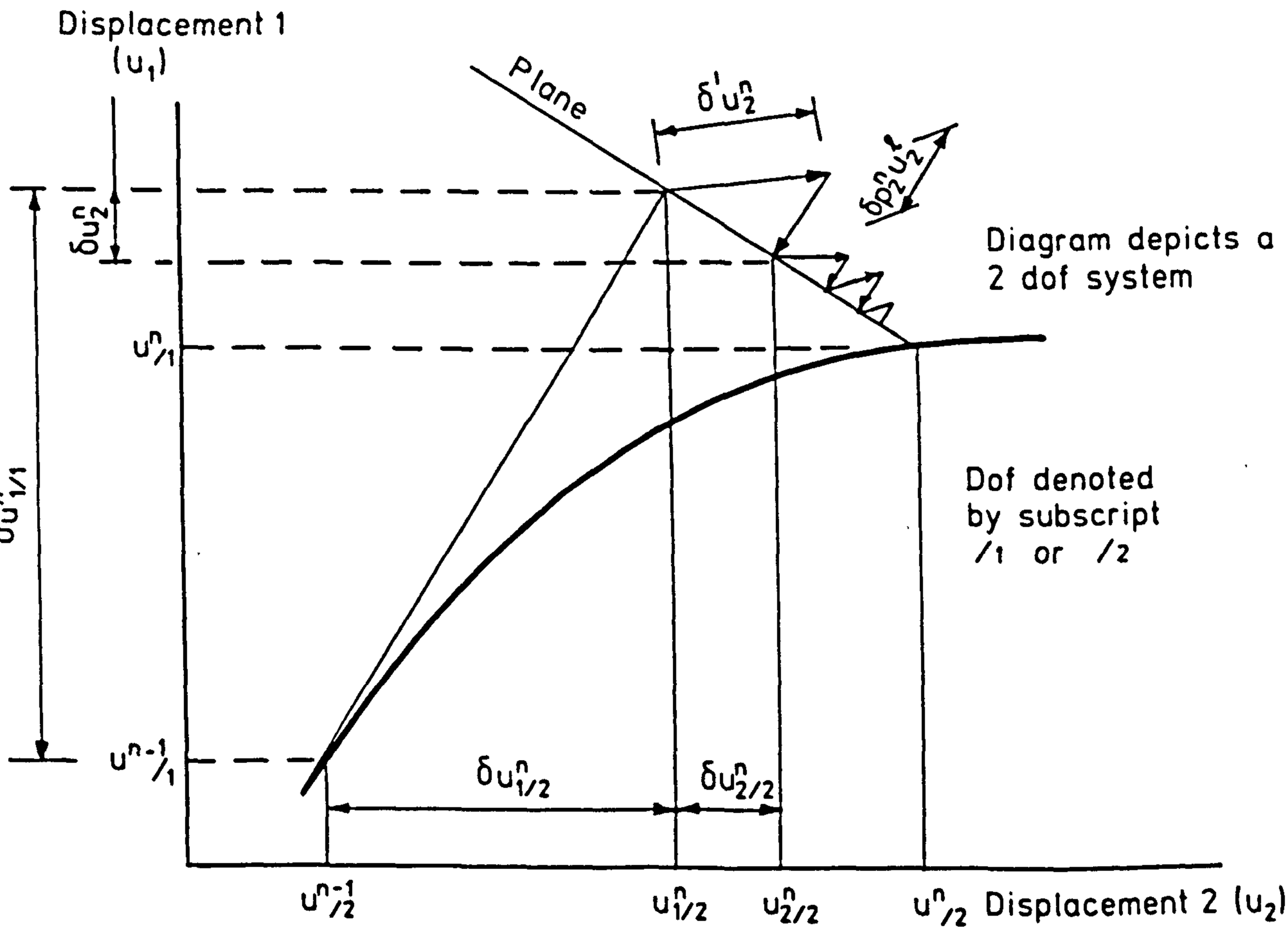

FIG. 8.17. NORMAL PLANE METHOD
(contained exclusively in displacement space)

$$A[\delta p^n_i]^2 + B[\delta p^n_i] + C = 0 \qquad (8.122)$$

where,

$$A = [u^\ell_i]^T [u^\ell_i] + [p^*]^T [p^*]$$

$$B = 2[\Delta u^n_{i-1} + \delta' u^n_i]^T [u^\ell_i] + 2\, \Delta p^n_{i-1} [p^*]^T [p^*]$$

$$C = [\Delta u^n_{i-1} + \delta' u^n_i] [\Delta u^n_{i-1} + \delta' u^n_i] + [\Delta p^n_{i-1}]^2 [p^*]^T [p^*] - [\Delta \ell^n]^2$$

This equation can be solved to yield two solutions, $[\delta p^n_i]^a$ and $[\delta p^n_i]^b$. Using these solutions two possible incremental displacement vectors for iteration i can be obtained from:-

$$[\Delta u^n_i]^a = \Delta u^n_{i-1} + \delta' u^n_i + [\delta p^n_i]^a u^\ell_i \qquad (8.123)$$

$$[\Delta u^n_i]^b = \Delta u^n_{i-1} + \delta' u^n_i + [\delta p^n_i]^b u^\ell_i \qquad (8.124)$$

In order to avoid doubling back on the original load-deflection path the 'angle' between the current incremental displacement vector Δu^n_i and the previous one, Δu^n_{i-1}, is calculated for both possibilities:-

$$\theta_a = [\Delta u^n_i]^{aT} [\Delta u^n_{i-1}],\ \theta_b = [\Delta u^n_i]^{bT} [\Delta u^n_{i-1}] \qquad (8.125)$$

The appropriate root, $[\delta p^n_i]^a$ or $[\delta p^n_i]^b$, is the one which gives a positive 'angle'. If both 'angles' are positive, which is unlikely, then the root closest to the linear solution may be chosen[51]:-

$$[\delta p^n_i]^\ell = \frac{-C}{B} \qquad (8.126)$$

Alternatively, instead of calculating 'angles' between the current incremental displacement vector and the previous one, the 'angle' between the current incremental displacement vector and the previous total displacement vector can be calculated from:-

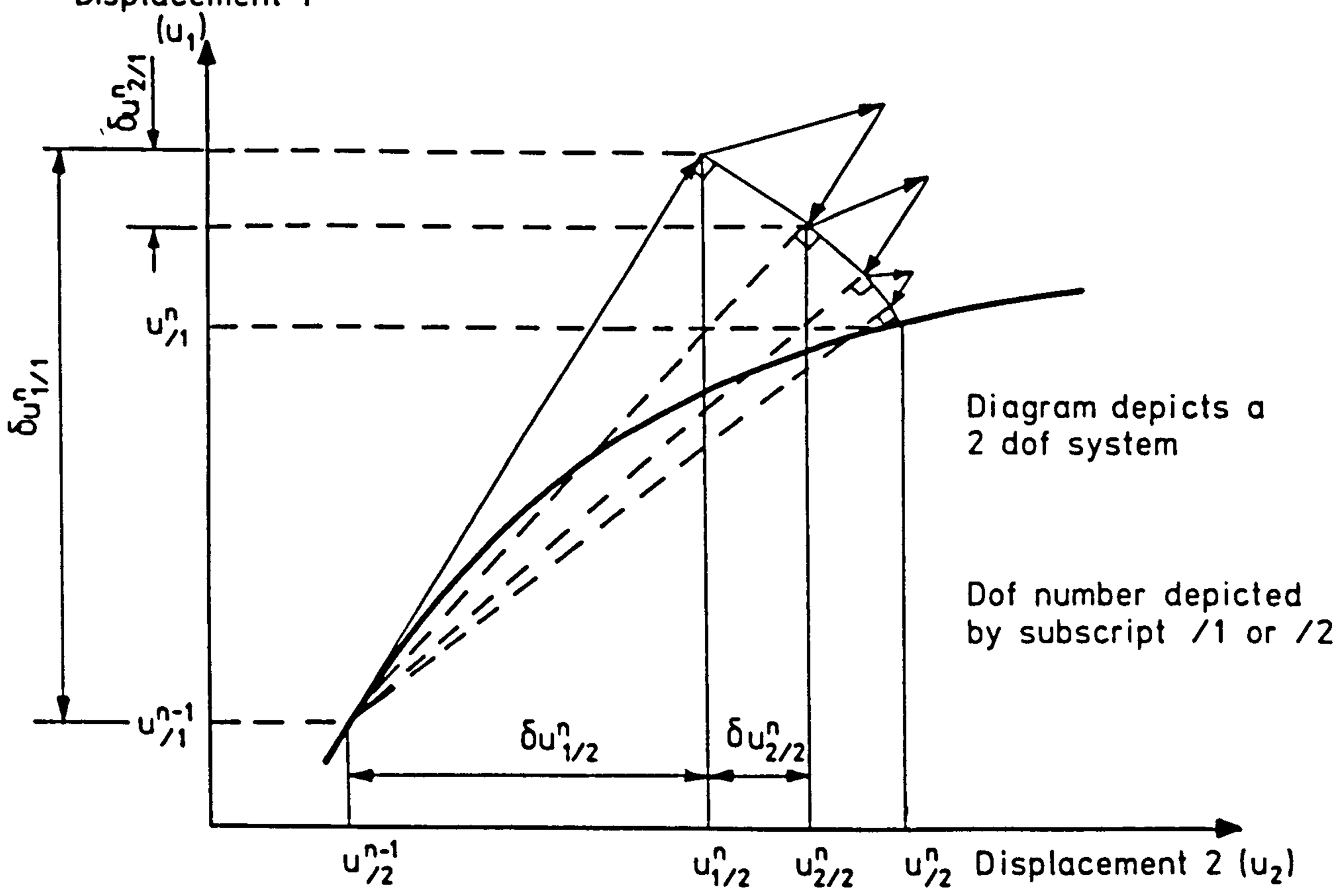

FIG. 8.18. UPDATED NORMAL PLANE METHOD
(contained exclusively in displacement space)

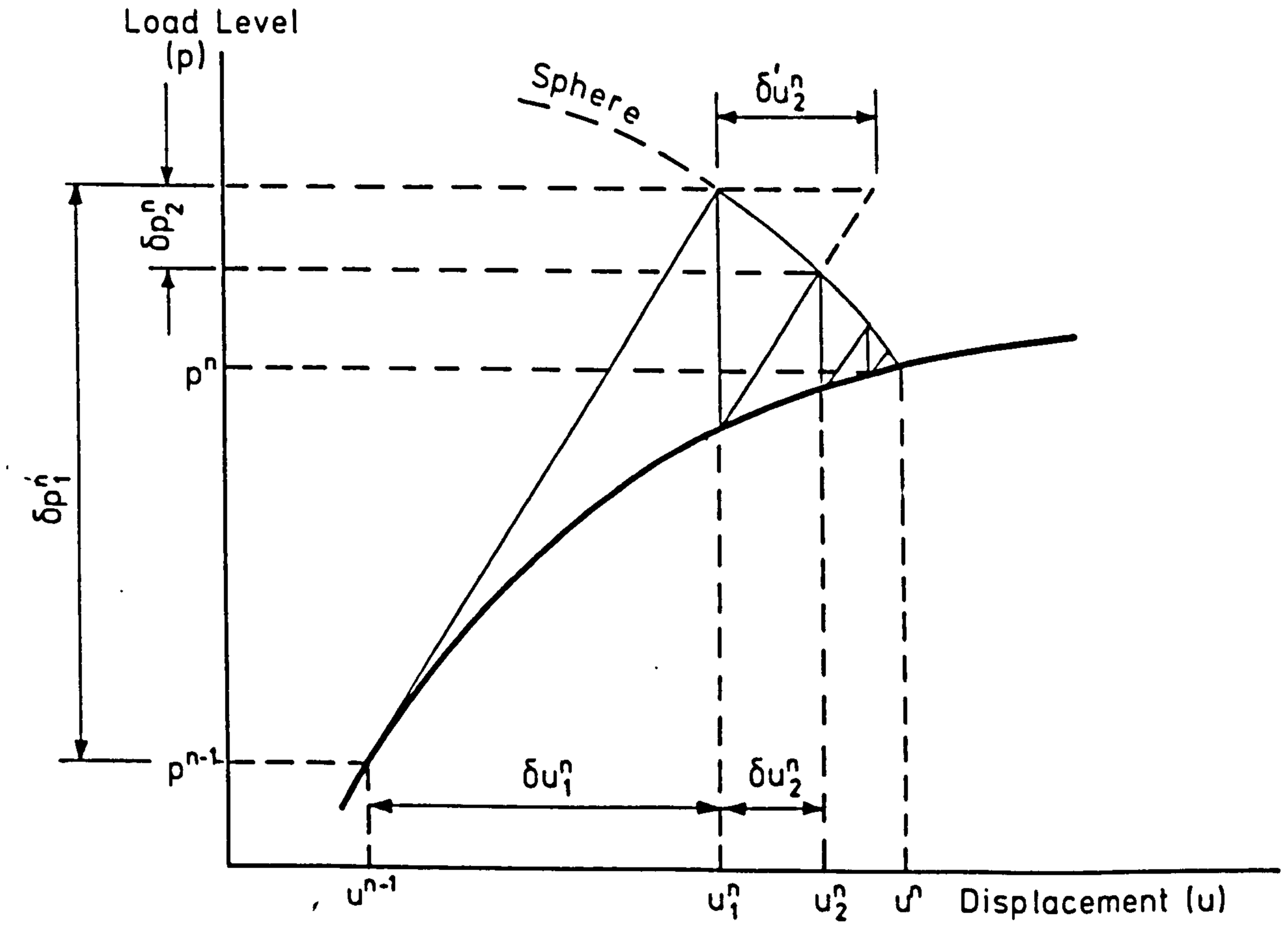

FIG. 8.19. SPHERICAL ARC-LENGTH METHOD
(contained in load/displacement space)

$$\theta_a = [\Delta u^n_i]^{aT} [u^n_{i-1}], \quad \theta_b = [\Delta u^n_i]^{bT} [u^n_{i-1}] \qquad (8.127)$$

This may prevent the analysis from slipping back on itself after a number of iterations have been carried out. Once a value of δp^n_i has been selected then the displacement vector can be updated according to:-

$$u^n_i = u^n_{i-1} + \delta u^n_i = u^n_{i-1} + \delta' u^n_i + \delta p^n_i \, u^\ell_i \qquad (8.128)$$

and the load level can be updated to $\Delta p^n_i = \Delta p^n_{i-1} + \delta p^n_i$

As with the previous forms of arc-length control it is possible to omit the load variable terms from equation 8.119, so that a constraint purely in displacement space remains, see Figure 8.20.

It is possible that equation 8.122 will not possess any real solutions, only complex ones. In the displacement space only method, this can be likened to the u^ℓ_1 vector missing the sphere as shown in Figure 8.21. In this case the only real option is to adopt the line search implementation which will be described in section 8.5.3.2.5.

8.5.3.2.4 Arc-length control with various iterative solution methods

All of the arc-length control methods described above can be linked with any of the iterative solution methods, such as Newton-Raphson, which are described in section 8.5.2. For the Newton-Raphson method the quantities contained in equation 8.120 are calculated using K_i, the stiffness matrix calculated at the end of the previous iteration. For the modified Newton-Raphson method the quantities $\delta' u^n_i$ and u^ℓ_i are calculated using the most recently formed stiffness matrix, K_1.

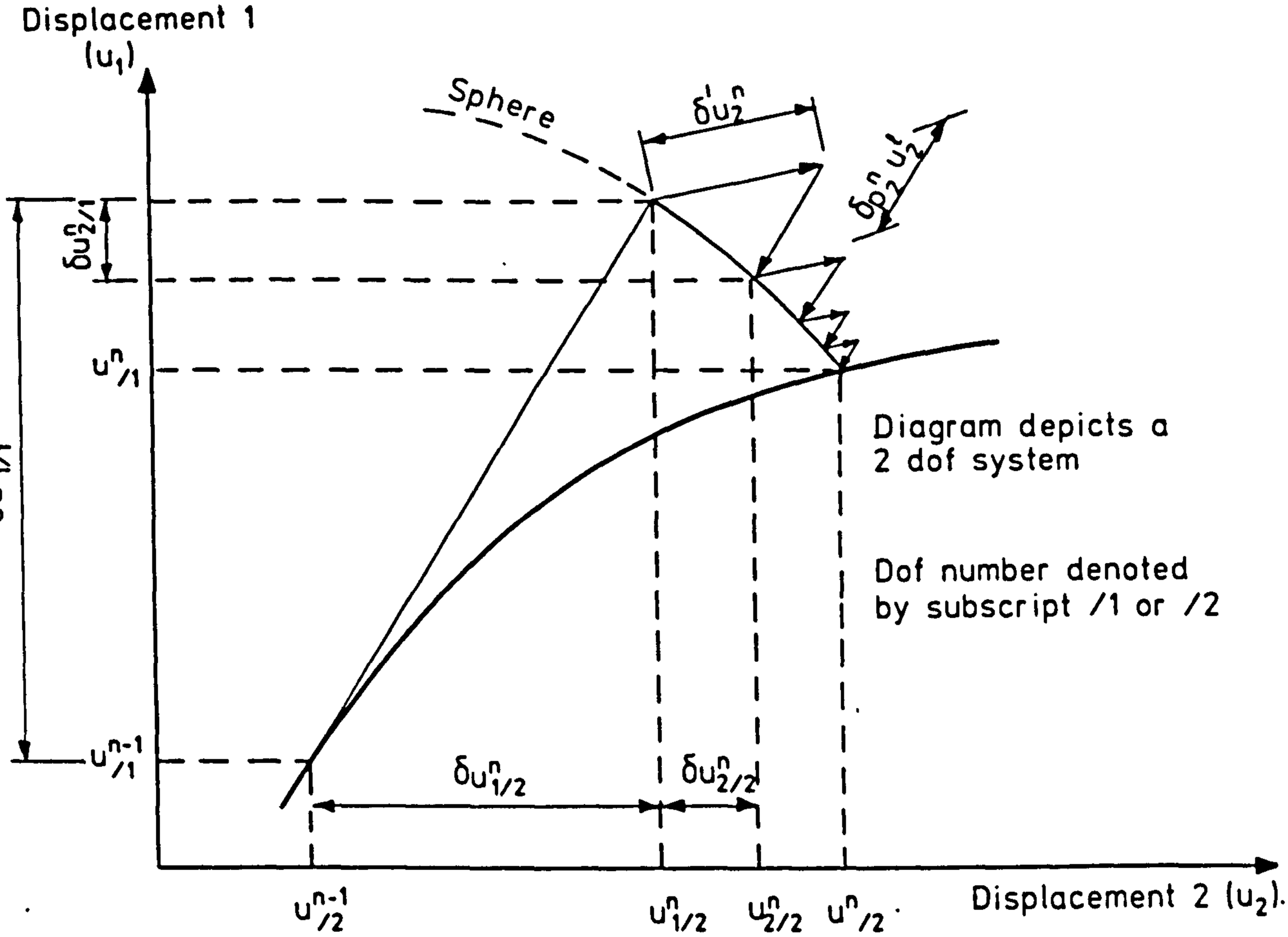

FIG. 8.20 SPHERICAL ARC-LENGTH METHOD
(contained exclusively in displacement space)

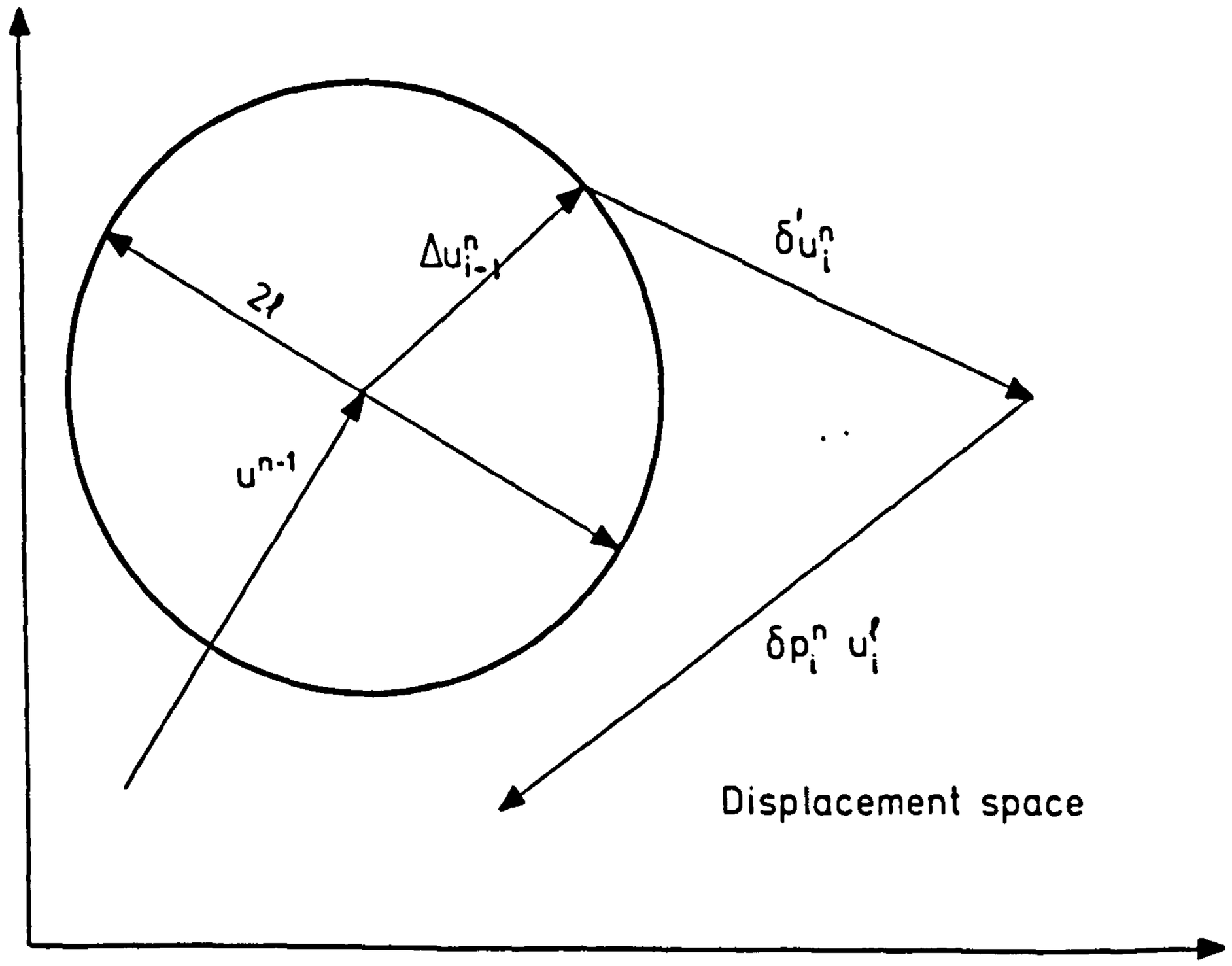

FIG. 8.21 COMPLEX SOLUTION TO SPHERICAL ARC-LENGTH CONSTRAINT

While it is necessary to recalculate $\delta' u^n_i$ for each iteration, the quantity u^ℓ_i need only be recalculated if and when the stiffness matrix is reformed.

With the BFGS method the updated stiffness matrix, K^{-1}_i, is used to obtain the quantities $\delta' u^n_i$ and u^ℓ_i. The quantity u^ℓ_i need not be recomputed unless a new update has been applied to the stiffness matrix. If the quasi-Newton condition is to be maintained with a load varying algorithm, such as the arc-length method, in equation 8.51, the quantity $r(u^n_{i-2})$ must be replaced with $\hat{r}(u_{i-2})$ such that:-

$$\hat{r}(u^n_{i-2}) = r(u^n_{i-2}) + \delta p^n_{i-1}\, p^* \qquad (8.129)$$

The variants of the arc-length control method which omit the load level variables from the constraint equations are most popular. For the present work the inclusion of the load level variables in the constraint equation was not found to offer any computational advantages. Without the load variables the arc-length methods are essentially constraints upon the incremental change in the length of the displacement vector.

8.5.3.2.5 Arc-length control and line searches

Crisfield[30] has advocated the use of line-searches with the arc-length control method. First impressions may indicate that, as with the displacement control method, the inclusion of line searches will not be advantageous. However, unless the iterational displacement vector, δu^n_i, and the notional displacement vector, u^ℓ_i, are parallel, then a different displacement pattern will result when different values of the line search scaling factor are applied. Thus, it can be advantageous to search for a value of the scale factor which gives

equilibrium in the direction of the iterational displacement vector, δu^n_i.

From the previous equations the iterative displacement change, in the search for the solution to $r(u^n_i) = 0$ when using the arc-length control method is given by:-

$$\delta u^n_i = \delta' u^n_i + \delta p^n_i \, u^\ell_i \tag{8.130}$$

and the incremental displacement at iteration i is given by:-

$$\Delta u^n_i = \Delta u^n_{i-1} + \delta u^n_i = \Delta u^n_{i-1} + \delta' u^n_i + \delta p^n_i u_i{}^\ell \tag{8.131}$$

where,

$$\delta' u^n_i = K^{-1}_i(p^n_{i-1} \, p^* - f(u^n_{i-1})) \tag{8.132}$$

p^n_{i-1} = applied load level at end of iteration i-1

δp^n_i = iterational change in load factor for iteration i

p^* = nominal incremental load vector

$f(u^n_{i-1})$ = internal forces at displacement level u^n_{i-1}

$u^\ell_i = K^{-1}_i \, p^*$

Crisfield advocates incorporating a line search step length $s_{i,j}$ where j represents line search iteration j such that:-

$$\Delta u^n_i = \Delta u^n_{i-1} + s_{i,j} \, \delta u^n_{i,j} = \Delta u^n_{i-1} + s_{i,j}(\delta' u^n_{i,j} + \delta p^n_i \, u^\ell_i) \tag{8.133}$$

However, the author prefers a relationship such that:-

$$\Delta u^n_i = \Delta u^n_{i-1} + s_{i,j} \, \delta' u^n_{i,j} + \delta p^n_{i,j} u^\ell_i \tag{8.134}$$

The benefit of equation 8.134 over equation 8.133 is that the removal of the link between $s_{i,j}$ and $\delta p^n_{i,j}$ in the constraint equation.

Therefore, in the constraint equation, $\delta p^n_{i,j}$ is now subservient to the specified value for $s_{i,j}$. This modification will somewhat simplify the subsequent algebra. If we adopt the constraint equation of 8.119 but omit the load variable terms (although this need not be the case) then $[\Delta u_i]^T\ [\Delta u_i] = [\Delta \ell^n]^2$. Substituting equation 8.134 into this equation gives an equation of the form:-

$$A[\delta p_{i,j}]^2 + B[\delta p_{i,j}] + C = 0 \qquad (8.135)$$

where

$$A = [u^\ell_i]^T\ [u^\ell_i]$$

$$B = 2\ [\Delta u^n_{i-1} + s_{i,j}\ \delta' u^n_{i,j}]^T\ [u^\ell_i]$$

$$C = [\Delta u^n_{i-1} + s_{i,j}\ \delta' u^n_{i,j}]^T\ [\Delta u^n_{i-1} + s_{i,j}\ \delta' u^n_{i,j}] - [\Delta \ell^n]^2$$

To obtain the potential energy gradients in the search direction, the scalar vector products $GO_{i,j}$ and $G_{i,j}$ need to be evaluated thus:-

$$G_{i,j} = r^T(u^n_{i,j})\ \delta u^n_{i,j} = (p^n_{i-1} + \delta p^n_{i,j}\ p^* - f(u^n_{i,j}))^T\ \delta u^n_{i,j}$$

$$GO_{i,j} = r^T(u^n_{i,o})\ \delta u^n_{i,j} = (p^n_{i-1} + \delta p^n_{i,j}\ p^* - f(u^n_{i,o}))^T\ \delta u^n_{i,j} \qquad (8.136)$$

where

$$\delta u^n_{i,j} = s_{i,j}\ \delta' u^n_{i,j} + \delta p^n_{i,j}\ u^\ell_i$$

$$u^n_{i,o} = u^n_{i-1}$$

$$u^n_{i,j} = u^n_{i-1} + \delta u^n_{i,j}$$

$$\Delta p^n_{i,j} = \Delta p^n_{i,j-1} + \delta p^n_{i,j}$$

$$\delta' u^n_{i,j} = K^{-1}_i\ (p^n_{i-1}\ p^* - f(u^n_{i,o}))$$

$$\Delta p^h_{i,o} = \Delta p^h_{i-1}$$

The criteria defined by equation 8.57 can now be applied to the potential energy gradients. If the criteria are not satisfied then any of the line search algorithms defined earlier can be used to calculate a new line search scale factor, $s_{i,j+1}$. Thus the procedure continues with equation 8.135.

Again any of the iterative solution methods, such as Newton-Raphson, may be used in conjunction with line searches when under arc-length control. A problem arises if the BFGS method is employed, when the update vectors are calculated at the start of an iteration. In the update vector calculation equation (equation 8.51) the vector r^n_{i-2} should be replaced with $\hat{r}^n_{i-2}$, where:-

$$\hat{r}^n_{i-2} = r^n_{i-2} + \frac{\delta p^n_{i-1} p^*}{s_{i-1}} \tag{8.137}$$

It will be realised that it is not possible to adopt arbitary values for the line search scaling factor since the spherical constraint equation will only yield a real solution for a limited range of scale factors. If we examine equation 8.135 then:-

$$A[\delta p^n_{i,j}]^2 + B\,[\delta p^n_{i,j}] + C = 0 \tag{8.138}$$

where

$$A = [u^\ell_i]^T\,[u^\ell_i] = e_1$$

$$B = 2[\Delta u^n_{i-1}]^T\,[u^\ell_i] + 2\,s_{i,j}[\delta' u^n_{i,j}]^T\,[u^\ell_i] = 2e_2 + 2s_{i,j}\,e_3$$

$$C = [\Delta u^n_{i-1}]^T\,[\Delta u^n_{i-1}] + 2\,s_{i,j}[\delta' u^n_{i,j}]^T\,[\Delta u^n_{i-1}] + s_{i,j}{}^2\,[\delta' u^n_{i,j}]^T\,[\delta' u^n_{i,j}] - [\Delta \ell^n]^2$$

$$= e_4 + 2\,s_{i,j}\,e_5 + s_{i,j}{}^2\,e_6 - [\Delta \ell^n]^2$$

and e_1 to e_6 define the scalar vector products. Equation 8.138 can be solved so that

$$\delta p^n_{i,j} = \frac{-B \pm [B^2 - 4\,AC]^{1/2}}{2A} \tag{8.139}$$

It will be realised that when the term under the square root becomes negative then the equation can only yield complex values. Thus, the limits on the range of scale factors that will yield real results can

be discovered by setting this term to zero. This will yield an equation of the form:

$$A\ s^2_{i,j} + B\ s_{i,j} + C = 0 \qquad (8.140)$$

where,

$$A = e_3\ e_3 - e_1\ e_6$$

$$B = 2\ e_2\ e_3 - 2\ e_1\ e_5$$

$$C = e_2\ e_2 - e_1\ e_4 + e_1\ [\Delta\ell^n]^2$$

Solving this quadratic equation may yield two real values of $s_{i,j}$. These form the limits to the real solution of the constraint equation. A line search can be carried out within these limits to locate an approximate solution to equation 8.56.

8.5.3.2.6 Arc-length control in scaled space

The displacement vectors in a finite element analysis of a plate include vector elements with different units, such as translations and rotations. Hence, it may be advantageous to scale the displacements so that they are consistent, in a unit sense, before the application of the arc-length constraint. This scaling may be effected using the scaled space concept which was described in section 8.5.1. Thus in the constraint equation:-

$$[\Delta u^n_i]^T\ [\Delta u^n_i] = [\Delta\ell^n]^2 \qquad (8.141)$$

where $\Delta u^n_i = \Delta u^n_{i-1} + \delta' u^n_i + \delta p^n_i\ u^\ell_i$ the displacement vectors Δu^n_{i-1}, $\delta' u^n_i$ and u^ℓ_i are replaced by $\Delta \bar{u}^n_{i-1}$, $\delta' \bar{u}^n_i$ and $\bar{u}^\ell_i$ respectively where:

$$\Delta \bar{u}^n_{i-1,m/n} = \Delta u^n_{i-1,m/n}\ S_n \qquad \text{for } m=1,\ n_n \text{ and } n=1,\ ndof \qquad (8.142)$$

$$\delta' \bar{u}^n_{i,m/n} = \delta' u^n_{i,m/n} S_n$$

$$\bar{u}^\ell_{i,m/n} = u^\ell_{i,m/n} S_n$$

where

n_n = number of dof of type n

m = node number

n = dof type number

ndof = number of dof types

$\Delta u_{i-1,m/n}$ = element at node m dof type n of vector Δu_{i-1}

S_n = scaling factor for dof type n (from section 8.5.1)

Thus with this application of the scaling factors, s_j, the spherical constraint is effectively converted to an ellipsoidal constraint.

8.5.3.2.7 Arc-length control family

It will be realised that the arc-length constraint methods described here are but a few members of a family of constraints which are based upon the same principles. For instance, a mask could be applied to the vectors involved in the constraint equations. Its effect would be to mask out certain dof in each vector so that the constraint is only effected against those degrees of freedom which remain. One immediately obvious option would involve a mask which caused the constraint equation to act on only one certain dof type, say the 'w' (translation) dof in a plate analysis. In the extreme case a mask could be applied which blanked out all but one dof, in such as case the arc-length constraint would, effectively, be converted to a displacement control constraint.

8.5.4 Incremental and iterational strategy

8.5.4.1 Solution control hierarchy

In the preceeding sections several powerful iterative solution methods, such as BFGS, and iterative constraint methods, such as arc-length control were described. Each of these methods have features, such as efficiency or power, which make each suitable for a particular situation in a response. Therefore, the selection of one or other method can be decisive to the success or failure of an analysis.

Restart facilities have been incorporated into the SNAP program. Thus allowing the solution method to be modified between restarts. However, these features are not the complete answer to iterational strategy selection, since one does not wish to continually stop and start the analysis merely to change iteration technique. This is particularly true when the analysis is carried out in a batch environment. For these reasons it is beneficial to endow the analysis program with some intelligence so that it is able to use past experience to select a new technique, when required. It may be wise to switch techniques not only when difficulties are encountered but also when the response becomes smooth so that more efficient and less powerful techniques will suffice. With the SNAP program the analyst has absolute power to decide which techniques the program may use. On entry the program sets up a technique hierarchy based on the analyst specified options. The analysis is then begun using the analyst specified default technique. Subsequently, if required, the program will select another of the techniques permitted by the technique hierarchy.

Crisfield[30] has introduced the concept of a desired number of iterations and this concept has been used to control the selection of solution techniques as well as automatic increment sizing. Also

specified by the analyst is the maximum number of iterations that may be used in the search for convergence with a particular solution method. Generally all increments are automatically sized in the SNAP program, except in some instances when under load control. Currently an equation suggested by Crisfield[30] is employed in the automatic increment sizing algorithm and this is given below:-

$$\Delta\ell^n = \left[\frac{I^{n-1}}{I_d}\right]^{1/2} \Delta\ell^{n-1} \qquad (8.143)$$

where

I^{n-1} - number of iterations in increment n-1

I_d - desired number of iterations.

The quoted equation specifies an increment of arc-length however it could easily specify load level or displacement level. This equation has to be primed in the first increment, generally via a manual increment size.

If during an increment the maximum number of iterations is reached without convergence then the program resets all relevant qualities to their values at the beginning of the increment. The program then seeks convergence using the next more powerful technique in the method hierarchy. If, however, very few iterations were used in the last increment, say less than half the desired number of iterations, then the program begins the current increment with the next more efficient technique in the method hierarchy. If the program exhausts the method hierarchy without achieving convergence then, if allowed by the analyst, the program will cut the automatic increment size to 0.25 of its previous value and will restart the increment with the most powerful technique available. If the program is still unable to achieve convergence then the increment cutting procedure is repeated

up to an analyst specified maximum number times. If, after this, convergence is still not achieved the analyst can specify whether the run is aborted or the next increment is begun. If during an increment the program has to switch technique then the subsequent increment is begun with the latest technique.

8.5.4.2 Stiffness matrix reformations

With the modified Newton-Raphson and BFGS techniques a fixed procedure for the reformation of the stiffness matrix at and only at the beginning of increments can be inefficient. Therefore, a system that only reforms the stiffness matrix when required is preferable. A number of different parameters can be used to indicate the need for a stiffness reformation. Two such parameters are immediately obvious, Bergan's[31] stiffness parameter and the number of iterations required to achieve convergence in the previous increment. Crisfield[30] has also suggested that a small step length in the line search procedure can indicate the need for a stiffness reformation. Bergan's current stiffness parameter may be specified as:-

$$S^n_p = \frac{\Delta p^n \, [u^\ell]^T \, [p^*]}{[\Delta u^n]^T \, [p^*]} \tag{8.144}$$

Since it is necessary to calculate the vector u^ℓ each time the stiffness matrix is reformed the vector scalar product $[u^\ell]^T \, [p^*]$ can also be recalculated. Thus, S^n_p is a measure of the current stiffness with respect to the most recent stiffness reformation.

This approach avoids complications with non-proportional loading, providing that the loading is proportional between stiffness reformations.

8.5.5 Convergence Criteria

A constant problem with the implementation of any of the iterative constraints methods described earlier is the selection of suitable criteria for the termination of the iterations. At the end of each iteration the solution is checked for compliance with the chosen convergence criteria. Checks can also be carried out to detect divergence of the solution. If the convergence criteria are too tight then increased resources will be expected to obtain unnecessary accuracy. If, on the other hand, the criteria are too slack then, amongst other things, unstable equilibrium paths may be traced.

With non-linear finite element analysis the criteria employed are usually based on either; residual forces; displacements; or energy dissipation. In the following sections the most popular criteria will be detailed and in addition a new method to improve the consistency of convergence checking will be presented.

8.5.5.1 Force convergence criterion

The basis for the force convergence criterion is the residual force at the end of an iteration. This is generally checked against the applied external loading and/or the reactions. Initially a scalar norm for each of the vectors is generally obtained. The most popular scalar norm is the second Holder[32] norm, which is usually referred to as the Euclidian norm, and is defined below:-

$$\|x\| = \left[\sum_{i=1}^{n} |x_i|^2\right]^{1/2} \qquad (8.145)$$

where x is an arbitary vector.

In a finite element analysis either total equilibrium of forces can be checked or equilibrium in a certain direction. A convergence

criterion which is frequently used to check equilibrium in a certain direction, 'n', is

$$r_n = \frac{\|r^n_{i,n}\|}{\|p^n_{i,n}\|} < Ftol_n, \text{ where Ftol is the specified tolerance.} \quad (8.146)$$

For a total equilibrium check then the equation is modified to:-

$$r_t = \frac{\|r^n_i\|}{\|p^n_i\|} < Ftol_t \quad (8.147)$$

This total equilibrium check is generally not appropriate to the majority of finite element analyses since the units of the elements contained in both the residual force and applied force vectors are generally not consistent.

Thus, in a plate analysis one may have vector elements with units of force (Newtons) and moments (Newton millimetres). Clearly the moments will swamp the direct forces. If, however, one chose moment units of Newton metres this may not be the case. The unit dependence of this check makes it generally unsuitable. The situation is further complicated in the Mindlin plate analyses undertaken here. Since the transverse shear stiffness is not degraded equilibrium in the 'w' direction is guaranteed (except possibly with BFGS type updates where numerical rounding may lead to small residual forces in the 'w' direction). Generally plates are only loaded in the 'w' direction and with the basic Mindlin formulation the consistent load vector will contain 'w' forces only. Thus equilibrium cannot be checked in any direction!

8.5.5.2 Displacement convergence criterion

For the displacement criteria the iterative displacements, δu^n_i, are used to check for convergence of the solution. A number of different forms of displacement criteria are available, however, in all cases it

is possible to carry out the checks either in individual directions, n, or totally for all dof's together. A popular criterion compares the iterative displacements in an iteration with either the iterative displacements in the first iteration or the current incremental displacements, thus for direction 'n' (i.e. dof type 'n'):-

$$r_n = \frac{\|\delta u^n{}_{i,n}\|}{s_{i,j}\|\delta u^n{}_{1,n}\|} < Dtol_n, \text{ or } r_n = \frac{\|\delta u^n{}_{i,n}\|}{s_{i,j}\|\Delta u^n{}_{i,n}\|} < Dtol_n \qquad (8.148)$$

For all dof types combined, equation 8.148 becomes:-

$$r_t = \frac{\|\delta u^n{}_i\|}{s_{i,j}\|\delta u^n{}_1\|} < Dtol_t, \text{ or, } r_t = \frac{\|\delta u^n{}_i\|}{s_{i,j}\|\Delta u^n{}_i\|} \leqslant Dtol_t \qquad (8.149)$$

The $s_{i,j}$ term in the above equations is optional and is included to reduce the possibility of a line search procedure producing artificial convergence through a small step size. However, care must be taken when line searches are used in conjunction with an iterational constraint method, such as displacement control or arc-length control.

If the total displacement, $u^n{}_i$, had been used in place of either $\delta u^n{}_1$ or $\Delta u^n{}_1$ in the above equation the criteria would effectively become slacker as the analysis progressed. Typically, final displacements in a finite analysis can be 200 times the displacements in the first increment, therefore, if the total displacements are used, the criteria is effectively 200 times slacker at the end of the analysis than at the beginning.

8.5.5.3 Energy convergence criterion

A number of researchers[33,34] have advocated the use of an energy convergence criterion in the light of the difficulties that are encountered when applying a force criterion to some finite element analyses. The energy convergence criterion was introduced to provide an indication when both displacements and forces were nearing their

equilibrium values. For this criterion, the amount of work done by the residual forces, moving through the iterative displacements, is compared against the work done in the first iteration. Generally, the energy criterion is only applied totally and not to individual degrees of freedom, thus:

$$r_t = \frac{[r^n{}_i]^T [\delta u^n{}_i]}{[r^n{}_1]^T [\delta u^n{}_1]} < Etol_t \qquad (8.150)$$

To avoid spurious satisfaction of the energy criterion Cope and Rao have suggested that for convergence the energy criterion should be satisfied in a fixed number, say 5, of consecutive iterations.

It must be noted that a line search procedure searches for an approximate solution to $r^n{}_i^T \delta u^n{}_i = 0$ which may lead to energy convergence criteria achieving an artificial convergence when line searches are also employed in the iterative solution method. The convergence could be artificial since equilibrium may only be satisfied in the iterative direction and not globally.

8.5.5.4 Scaled convergence criteria

Crisfield[18] introduced the concept of scaled displacement norms in a convergence check criterion. With this modification equation 8.148 becomes, after omitting the $s_{i,j}$ term:-

$$\bar{r}_t = \frac{\|\delta \bar{u}^n{}_i\|}{\|\Delta \bar{u}^n{}_i\|} < Dtol_t \qquad (8.151)$$

where, $\delta \bar{u}^n{}_{i,k} = \sqrt{K_{i,kk}}\ \delta u^n{}_{i,k}$ for all degrees of freedom, k

and, $\Delta \bar{u}^n{}_{i,k} = \sqrt{K_{i,kk}}\ \Delta u^n{}_{i,k}$ for all k

In effect the displacements are scaled by root of $K_{i,kk}$, which is the diagonal tangent stiffness term. The scale factors may be applied in

a similar way to the force convergence criterion of equation 8.147 resulting in the production of a scaled force convergence criterion.

It will be noted that the scaled convergence checks in this form are in effect energy convergence checks. This can be seen from the fact that terms such as $\delta u^n_{i,k}\ K_{i,kk}\ \delta u^n_{i,k}$ appear in the calculation of the displacement norms and terms such as $(r^n_{i,k}\ r^n_{i,k})/K_{i,kk}$ appear in the calculation of the force norms. Clearly these terms represent some form of work done.

The scaled convergence criteria that have been developed for the present study incorporate the scaling factors that were described in section 8.5.1. Thus the force convergence criterion takes the form:-

$$\bar{r}_t = \frac{\|\bar{r}^n_i\|}{\|\bar{p}^n_i\|} < Ftol_t \qquad (8.152)$$

where $\bar{r}^n_{i,mn} = S_n\ r^n_{i,mn}$

and $\bar{p}^n_{i,mn} = S_n\ p^n_{i,mn}$ for m=1, n_n; for n=1,ndof

The displacement criterion takes the form:-

$$\bar{r}_t = \frac{\|\delta\bar{u}^n_i\|}{\|\Delta\bar{u}^n_i\|} < Dtol_t \qquad (8.153)$$

where, $\delta\bar{u}^n_{i,mn} = \frac{\delta u^n_{i,mn}}{S_n}$

and, $\Delta\bar{u}^n_{i,mn} = \frac{\Delta u^n_{i,mn}}{S_n}$ for m=1, n_n; for n=1, ndof

where ndof is the number of dof types at any node and n_n is the number of nodes that have dof type 'n'.

Section 8.5.1 describes the derivation of these scaling factors and it was noted there that in a plate analysis, for example, the scaling factors increase the consistancy of the units, thus, allowing the applied vertical loads to be directly compared to the residual moments. Thus, it is not necessary to check convergence in individual direction since a total convergence check is all that is required.

If we carry out a units analysis for the force convergence check. Assuming that we have a two dimensional system. The first dof is a translation while the second is a rotation, as in a plate analysis. Thus:-

$$K_{11} = \text{Nmm}^{-1} \qquad K_{22} = \text{Nmm}$$

hence,

$$S_1 = \left[\frac{K_{11}}{K_{11}}\right]^{1/2} = 1$$

$$S_2 = \left[\frac{K_{11}}{K_{22}}\right]^{1/2} = \left[\frac{\text{Nmm}^{-1}}{\text{Nmm}}\right]^{1/2} = \text{mm}^{-1}$$

$$\therefore \bar{r}_1 = S_1 r_1 = 1\ \text{N} = \text{N}$$

$$\bar{r}_2 = S_2 r_2 = \text{mm}^{-1}\ \text{Nmm} = \text{N}$$

In the calculation of the norms, i.e. $\|\bar{r}^n_i\|$, terms such as $(r^n_{i,mn} K_{i,m_1} r^n_{i,mn})/K_{i,mn}$ appear. It will be noticed that, if applied, the scale factors would have no effect upon the energy convergence criterion.

Difficulty in obtaining convergence to an unscaled force convergence criterion has been mentioned by a number of researchers, notably Cope and Rao[34] and Bergan and Holland[35]. Cope and Rao found that when

monitoring indices in the non-linear analysis of reinforced concrete structures, the force norms were unlikely to converge always towards zero, even when a large number (500) of iterations were performed. Bergan and Holland commented that unbalanced forces often form equilibrium groups which do not have a significant influence on the overall structural response.

For the majority of analyses reported in this study a two tiered convergence criterion was adopted. In all cases the scaled norms were employed but the unscaled norms were also monitored and the results of this monitoring are reported in Chapter 9. The program was allowed to converge on either force or displacement. The force tolerance was generally a tight 1% while the displacement was set at an exceptionally tight 0.01% of the incremental displacements.

If difficulty in converging in an analysis was encountered then the increment was generally located in the unstable region of the response, around the plateau in the load-deflection response. As a general rule approximately 4-7 % of the computational resources for a complete analysis were expended in climbing up the response curve as far as the start of the plateau, while the rest were expended moving along the plateau and down the far side.

8.6 Ancillary details

It was intended that the SNAP program would be capable of tracing the complete analytical response to actual structural failure. Thus, if true tangent stiffness matrices are formed, as in the SNAP program, the equation solver must be capable of handling negative definite matrices in addition to the normal positive definite matrices. In addition, since solutions to a number of different right hand sides will be required, the solver must be capable of rapid solutions after

an initial decomposition has been carried out. For these reasons a Choleski L^TDL^{22} algorithm was selected and implemented.

A feature that can increase the power and controllability of a non-linear analysis is the ability to restart. For the majority of analyses carried out for the present study a restart checkpoint was carried out every 4 increments. The restart facility is also used by the iterative solution system, allowing it to repeat an increment with a different solution method but using the same initial conditions.

8.7 SNAP program implementation

In the design and coding of the SNAP program seven criteria were applied:-

1. Modularisation
2. Standardisation
3. Simplicity
4. Documentation, especially in-code documentation
5. Automation and intelligence
6. Capacity to handle large problems but highly efficient for small problems
7. Structure

The general layout of the SNAP program can be seen in Figure 8.22. The program is divided into six main modules. Each module carries out a distinct function, such as stiffness formation or input. The main controlling segment, called snap, initially calls the input module to read and assimilate the data. The input module in turn calls the gener module to generate the mesh if required. The other routines are then called as required to carry out such tasks as decomposition of the stiffness equations and the iterative solution procedure as required. Within each module, sub-modules are defined. For instance

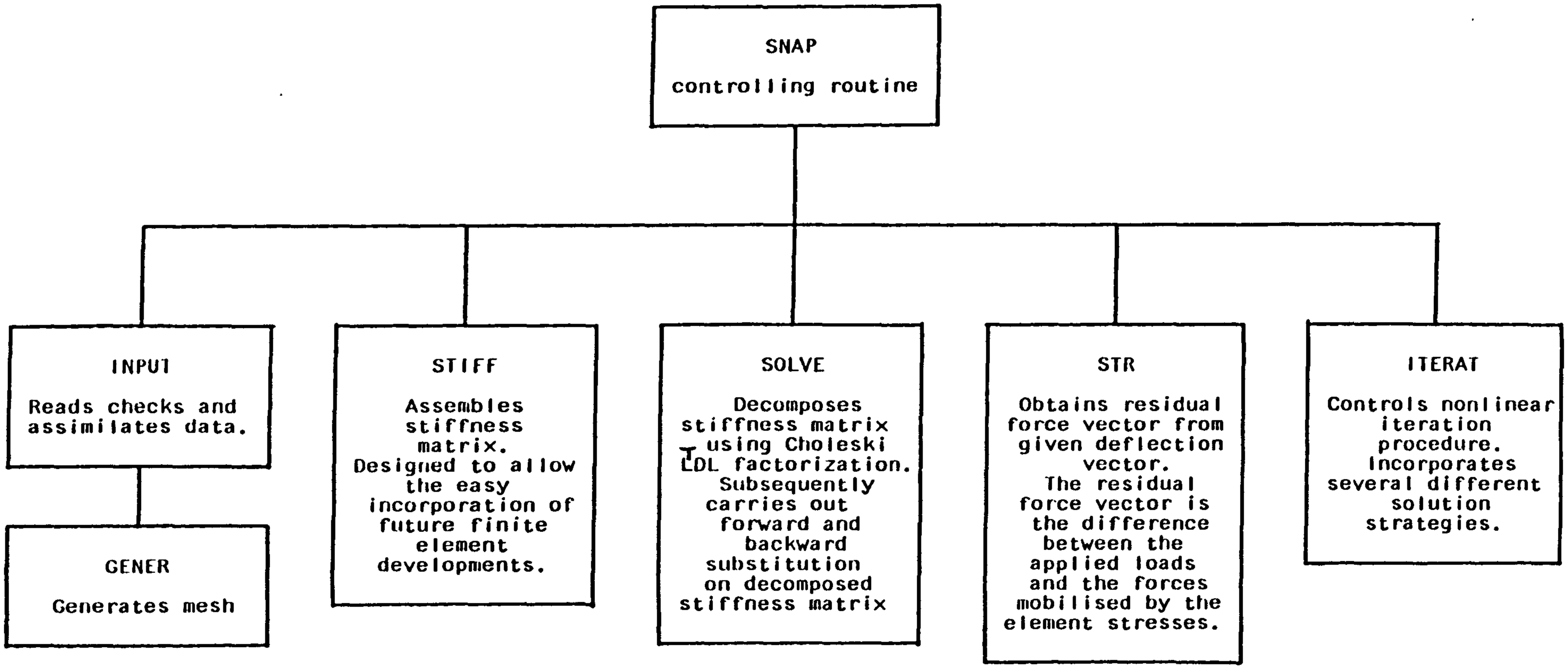

FIG. 8.22 BLOCK DIAGRAM FOR 'SNAP' (Slab Nonlinear Analysis Program) NONLINEAR FINITE ELEMENT PROGRAM.

in the iterat module there are sub-modules for displacement control, arc-length control, convergence checking etc. Therefore, it can be seen that criterion one is satisfied.

The program is written in absolutely standard Fortran 77. Standardisation extends as far as the use of individually defined arrays, in preference to the popular approach of allocating storage in one long common block, and then allowing the program to sub-divide this area for specific purposes. Flexibility is maintained in the SNAP program by the use of the PARAMETER statement. Through this the maximum size of problem can be easily and safety changed through simple changes in the PARAMETER statement. The SNAP approach avoids the complexity and resource overhead attached to the popular single storage area approach.

The SNAP program was designed to be extremely efficient at solving small problems thus allowing rapid development and checking of the program. However, realistic results can only be attained with larger problems incorporating finer meshes and thus the SNAP program was designed to handle the larger problems efficiently. Generally the smaller problems were run in an interactive environment, whereas the larger problems were despatched to remote computers running a batch environment.

8.8 References

1. CRISFIELD, M.A., "Finite Elements and Solution Procedures for Structural Analysis, Vol. 1: Linear Analysis", Pineridge Press Limited, U.K., 1986.

2. ZIENKIEWICZ, O.C., "The Finite Element Method", Third Edition, McGraw-Hill Book Company (UK) Limited, 1982.

3. BATHE, K., "Finite Element Procedures in Engineering Analysis", Prentice-Hall Inc., 1982.

4. MINDLIN, R.D., "Influence of rotary inertia and shear on flexural motions of isotropic elastic plates", J. Appl. Mech., 18, pp. 31-38, 1951.

5. REISSNER, E., "The effect of transverse shear deformation on the bending of elastic plates", J. Appl. Mech., 12, 1.69-1.77, 1945.

6. HUGHES, T.J.R., COHEN, M., "The 'Heterosis' finite element for plate bending", Comput. Struct., 9, 445-450, 1978.

7. BALDWIN, J.T., RAZZAQUE, A. and IRONS, B.M., "Shape function subroutine for an isoparametric thin plate element", Int. J. Num. Meth. Eng., 7, 431-440, 1973.

8. BATOZ, J-L. and TAHAR, M.B., "Evaluation of a new quadilateral thin plate bending element", Int. J. Num. Meth. Eng., 18, 1655-1677, 1982.

9. CRISFIELD, M.A., "A four noded thin-plate bending element using shear constraints - a modified version of Lyons' element", Comput. Meth. Appl. Mech. Eng., 38, 93-120, 1983.

10. CRISFIELD, M.A., "A quadratic Mindlin element using shear constraints", Comput. Struct., 18, 833-852, 1984.

11. IRONS, B.M., "The semi-loof shell element", in Finite Elements for Thin Shells and Curved Members (Ed. D.G. Ashwell et al) Wiley, New York, pp. 197-222, 1976.

12. ZIENKIEWICZ, O.C., TAYLOR, R.L. and TOO, J.M., "Reduced integration in the general analysis of plates and shells", Int. J. Num. Meth. Eng., 3, 275-290, 1971.

13. PUGH, E.D.L., HINTON, E. and ZIENKIEWICZ, O.C., "A study of quadilateral plate bending elements with reduced integration", Int. J. Num. Meth. Eng., 12, 1059-1079, 1978.

14. HUGHES, T.J.R., COHEN, M. and HAROUN, M., "Reduced and selective integration techniques in finite element analyses of plates", Nuclear Eng. & Design, 46, 203-222, 1978.

15. NAGTEGAAL, J.C., PARKS, D.M. and RICE, J.R., "On numerically accurate finite element solutions in the fully plastic range", Comp. Meth. Appl. Mech. Engng., 4, 153-177, 1974.

16. HINTON, E., SALONEN, E.M. and BICANIC, N., "A study of locking phenomena in isoparametric elements", Third MAFEZAP Conference, Brunel University, Uxbridge, UK, 437-447, 1978.

17. RAHMAN, H.H.A., "Computational models for the nonlinear analysis of reinforced concrete flexural slab systems", Ph.D. thesis, Dept. of Civil Engineering, University College of Swansea, 1982.

18. CRISFIELD, M.A., "A faster modified Newton-Raphson iteration", Comp. Meth. in Appl. Mech. and Engng., 20, pp. 267-278, 1979.

19. DAVIDON, W.C., "Variable metric method for minimization", Argonne Nat. Lab. Report ANL-5990, 1959.

20. BRODLIE, K.W., GOURLAY, A.R. and GREENSTADT, J., "Rank-one and Rank-two Corrections to Positive Definite Matrices Expressed in Product Form", J. Inst. Math. Appl., 11, 73-82, 1973.

21. BATHE, K.J. and CIMENTO, A.P., "Some practical procedures for the solution of non-linear finite element equations", Comp. Meth. in Appl. Meth. & Engng., 22, 59-85, 1980.

22. JENNINGS, A., "Matrix computation for engineers and scientists", John Wiley & Sons, Chichester, 1977.

23. HAISLER, W.E., STRICKLIN, J.A. and KEY, J.E., "Displacement incrementation in non-linear structural analysis by the self-correcting method", Int. J. for Num. Meth. in Engng., 11, 3-10, 1977.

24. SHARIFI, P. and POPOV, E.P., "Non-linear finite element analysis of sandwich shells of revolution", AIAA Journal, 11, 715-722, 1973.

25. BATOZ, J-L. and DHATT, G., "Incremental displacement algorithms for non-linear problems", Int. J. Num. Meth. in Engng., 14, 1262-1266, 1979.

26. CRISFIELD, M.A., "Incremental/iterative solution procedures for non-linear structural analysis", Numerical methods for non-linear problems, Edited by C. Taylor, E. Hinton and D.R.J. Owen, Pineridge Press, Swansea, 261-290, 1980.

27. CRISFIELD, M.A., "Accelerated solution techniques and concrete cracking", Comp. Meth. in Appl. Mech. and Engng., 33, 585-607, 1982.

28. RAMM, E., "Strategies for tracing non-linear response near limit points", Non-linear finite element analysis in structural mechanics, edited by W. Wunderlich, E. Stein and K.J. Bathe, Springer-Verlag, New York, 63-89, 1981.

29. RIKS, E., "An incremental approach to the solution of snapping and buckling problems", Int. J. Solids ánd Structures, 15, 524-551, 1979.

30. CRISFIELD, M.A., "An arc-length method including line searches and accelerations", Int. J. Num. Meth. Engng., 19, 1269-1289, 1983.

31. BERGAN, P.G., HOLAND, I. and SOREIDE, T.H., "Use of the current stiffness parameter in solution of nonlinear problems", in Energy Methods in Finite Element Analysis.

32. DEIF, A.S., "Advanced matrix theory for scientists and engineers", Abacus Press, Tunbridge Wells, England, pp. 21, 1982.

33. BATHE, K.J. and CIMENTO, A.P., "Some practical procedures for the solution of non-linear finite element equations", Comp. Meth. in Appl. Mech. & Engng., 22, pp. 59-85, 1980.

34. COPE, R.J. and RAO, P.V., "Non-linear finite element strategies for bridge slabs", in Advanced Mechanics of Reinforced Concrete Structures working papers, Int. Ass. Br. and Struct. Engng., Delft, pp. 275-290, 1981.

35. BERGAN, P.G. and CLOUGH, R.W., "Convergence criteria for iterative processes", AIAA Journal, 10, 1107-1108, 1972.

36. KUPFER, H.B., HILSDORF, H.K. and RUSCH, H., "Behaviour of concrete under biaxial stresses", Proc. Am. Conc. Ins., 66/8, 656-666, 1969.

37. TASUJI, M.E., SLATE, F.O. and NILSON, A.H., "Stress-strain response and fracture of concrete in biaxial loading", J. ACI., 75/7, 306-312, 1978.

38. COPE, R.J., "Non-linear analysis of reinforced concrete slabs", In Computational Modelling of Reinforced Concrete Structures, Eds E. Hinton and R. Owen, 3-43, Pineridge Press, 1986.

39. POPOVICS, S., "A review of stress-strain relationships for concrete", ACI Journal, 243-248, March 1970.

40. POPOVICS, S., "A numerical approach to the complete stress-strain curve for concrete", Cement and Concrete Research, 3/5, 583-602, 1973.

41. GERSTLE, K.H. et al, "Behaviour of concrete under multi-axial stress states", Proc. ASCE, 106 No. EM6, 1383-1403, 1980.

42. BLUME, J.A., NEWMARK, N.M. and CORNING, L.H., "Design of multistorey reinforced concrete buildings for earthquake motions", Portland Cement Assoc., Chicago, 1961.

43. COPE, R.J., "Material modelling of real, reinforced concrete slabs", Proc. Int. Conf. on Computer Aided Analyses and Design of Concrete Structures, Pineridge Press, Swansea, 85-117, 1984.

44. CLARK, L.A. and SPEIRS, D.M., "Tension stiffening in reinforced concrete beams and slabs under short term loads", Tech. Rept. 42.521, Cement and Concrete Assoc., London, 1978.

45. COPE, R.J. and RAO, P.V., "Moment redistribution in skewed slab bridges", Proc. Instn. of Civ. Engrs., 75, 419-452, 1983.

46. BAZANT, Z.P., "Discussion of session 2, structural modelling for numerical analysis", In Advanced Mechanics of Reinforced Concrete, IABSE, Final Report, Delft, 482.

47. JOHNSON, W. and MELLOR, P.B., "Engineering plasticity", John Wiley & Sons, 75-76, 1983.

48. COPE, R.J., SAWKO, F. and TICKELL, R.G., "Computer methods for civil engineers", McGraw-Hill, 226-228, 1982.

49. MAEKAWA, K. and OKAMURA, H., "The deformational behaviour and constitutive equation of concrete, using the elasto-plastic fracture model", J. of the Faculty of Engineering, Vol. XXXVII, No. 2, Uni. of Tokyo, 253-327, 1983.

50. MATTHIES, H. and STRANG, G., "The solution of non-linear finite element equations", Int. J. for Num. Meth. in Engng., 14, 1613-1626, 1979.

51. CRISFIELD, M.A., "A fast incremental/iterative solution procedure that handles snap-through", Computers & Structures, 13, 55-62, 1981.

9. 'SNAP' PROGRAM ANALYSES

9.1 Validation Analyses

9.1.1 Introduction

The primary aim of this section is to assess the accuracy and efficiency of the computational models that have been incorporated into the SNAP program. The effects upon the structural response of variations in several modelling parameters are also investigated. It is shown that if some parameters are made to reflect observed behaviour more realistically, then a more stable numerical solution results. Difficulties in obtaining the original texts of experimental tests were encountered and, therefore, it was necessary to use details that have been presented by other authors.

9.1.2 Duddeck's Slabs

The three slabs that have been tested by Duddeck et al[1] will be considered. Reference 1 was not available and therefore the details presented by Rahman[2] have been used. Comparisons with the results presented in reference 2 were particularly useful in assessing the accuracy and efficiency of the SNAP iterative solution algorithms.

The degree of reinforcement orthotropy is the only difference between each of Duddeck's slabs. In each slab the total amount of reinforcement contained within the slab is the same. The reinforcement is arranged parallel to the slab edges. The reinforcement layout details are presented in Table 9.1.

In this table the amount of reinforcement is specified as an equivalent smeared thickness in 'mm'. This is obtained by dividing the rebar area by the spacing of the bars perpendicular to the bar direction. It can be seen that isotropic reinforcement is provided in

slab S1, while in slab S2 the ratio of steel in the two directions is 1.9. For slab S3 this ratio was increased to 2.75. The general layout of the experimental slabs and their finite element idealisations can be seen in Figure 9.1. The slabs are supported on a vertical restraint at each of the four corners. A single point load is applied to the centre of each slab.

Slab mark	Smeared reinforcement thickness (mm)			
	Top layers		Bottom layers	
	x-direction	y-direction	x-direction	y-direction
S1	0.193	0.193	0.397	0.397
S2	0.252	0.133	0.520	0.273
S3	0.283	0.103	0.582	0.212

TABLE 9.1 REINFORCEMENT ARRANGEMENTS FOR DUDDECK'S SLABS

9.1.2.1 Finite Element Idealisation

Advantage was taken of symmetry, hence only a quadrant of each slab was analysed. It is not clear from reference 2 whether any in-plane restraint was present at the corner supports of each slab. It will be shown later that the experimental load-deflection response for each of the slabs exhibits an enhanced stiffness in the post-cracking to steel yielding region. It is possible that in-plane restraint at the supports could have caused this behaviour.

For the through depth integration, the suitability of both a 5 point Gaussian and a 5 point Newton-Cotes integration rule was investigated. Due to the early onset, and fast propogation of cracking in Duddeck's slabs, there was little difference in the results obtained with either

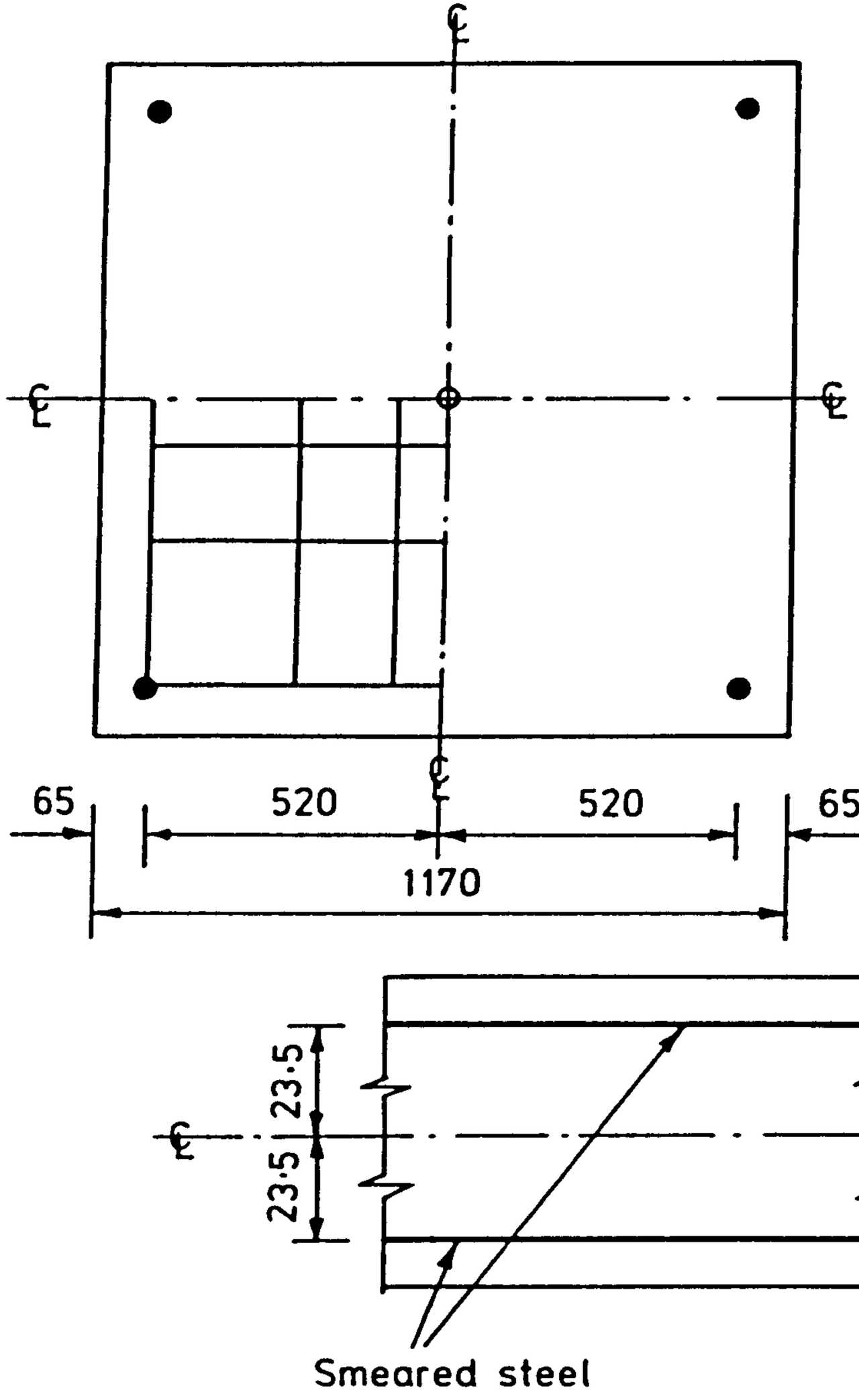

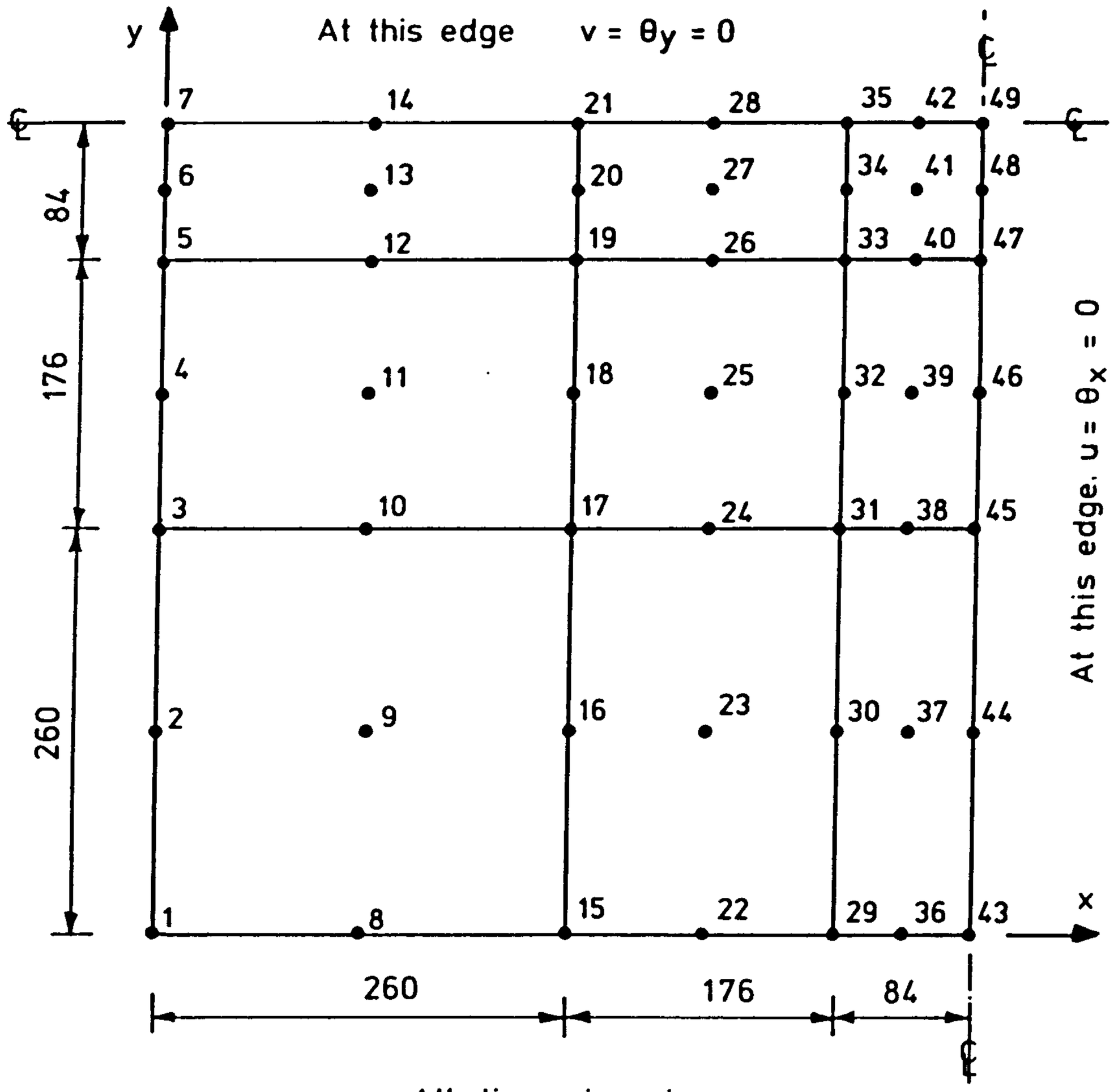

All dimensions in mm

FIG. 9. 1. FINITE ELEMENT IDEALISATION OF DUDDECK'S SLABS.

integration rule. It was decided to use the Newton-Cotes rule since this placed an integration station on each extreme fibre.

9.1.2.2 Material Models

Details of the material properties can be seen in Table 9.2. Unless otherwise stated the fixed crack direction model was employed for the analyses described here. The COSIG2 material model was used to model the concrete. After Popovic's curve, perfect plasticity was assumed until the onset of crushing at -5000 $\mu\epsilon$. For compressive strains beyond this, the compressive stress was reduced linearly to zero at an ultimate strain of -8000 $\mu\epsilon$. For concrete in tension, a two segment stress-strain curve was used with a tension stiffening factor, α_2, between 15 and 25. The lack of data on the steel material properties dictated that a simple, symmetrical, bi-linear elasto-plastic material model, with an ultimate strain of -40000 $\mu\epsilon$, was used to model the reinforcement unless otherwise stated.

Slab mark	f_c N/mm^2	f_t N/mm^2	E_c N/mm^2	f_y N/mm^2	E_s N/mm^2	Shear degredation factor
S1	43	2	16400	670	201000	0.5
S2	43	2	16400	670	201000	0.5
S3	43	2	16400	670	201000	0.5

TABLE 9.2 ASSUMED MATERIAL PROPERTIES FOR FOR DUDDECK'S SLABS (AFTER MEULLER[3])

9.1.2.3 Iterative Solution Techniques

BFGS acceleration, with line searching, was used for the iterative solution process. The structural stiffness matrix was reformed at the beginning of each increment, provided that either; the current

stiffness parameter at the end of the previous increment was below 0.7 or greater than 1.5 with respect to the most recent stiffness matrix recalculation; or the number of iterations in the previous increment had exceeded the desired number of iterations (set at 5 for these analyses). During the final increments of some of the analyses described here, the program found it necessary to switch to arc-length control in order to achieve convergence. When under arc-length control, BFGS acceleration without line searching was employed.

9.1.2.4 Convergence Criteria

An energy convergence criterion of 1% was adopted initially, this is consistent with reference 2. Several analyses were also carried out with both a 1% scaled force convergence criterion and a 1% raw force convergence criterion so that the effects of the different convergence criteria upon the structural response could be quantified. The result from these analyses have been summarised in Table 9.3 for slab S1 and in Table 9.4 for slab S2.

If one compares the results obtained with the energy convergence criterion, with those obtained using the raw force convergence criterion and with reference to Figure 9.2, then the effects of the different convergence criteria can be quantified. In the post cracking to steel yielding region the difference in the central deflection is generally limited to 0.5% and is in many cases less than 0.2%. For the post-yielding region the differences, at approximately 1% to 3% are substantially larger. A comparison between the scaled force convergence criterion central deflections and those with the raw force convergence criterion reveals little difference, even in the post yielding region.

Incr	Load (kN)	Energy convergence criterion (1%)			Scaled force convergence (1%)		Raw force convergence (1%)
		Central deflection (mm)	Scaled force norm (%)	Raw force norm (%)	Central deflection (mm)	Raw force norm (%)	Central deflection (mm)
1	5	0.522	1.18	33.64	0.522	0.38	0.522
2	10	1.10	8.18	201.8	1.10	19.00	1.10
3	15	2.06	11.19	226.4	2.05	14.83	2.05
4	20	3.69	11.22	188.8	3.69	8.94	3.69
5	25	5.82	10.46	142.2	5.85	9.76	5.85
6	30	8.29	110.3	1972.	8.26	6.55	8.26
7	35	10.6	14.42	249.	10.62	8.39	10.62
8	40	12.9	4.37	63.5	12.89	14.56	12.89
9	45	15.3	38.31	561.	15.29	11.67	15.29
10	50	17.9	0.77	11.86	17.83	11.54	17.83
11	52.5	19.3	5.50	96.53	19.31	7.20	19.31
12	55.0	20.9	6.25	118.4	20.84	16.29	20.84
13	57.5	23.9	4.72	95.6	23.67	8.17	23.67
14	60.0	32.0	3.91	54.6	31.55	16.31	31.53

TABLE 9.3 CONVERGENCE ANALYSIS FOR DUDDECK'S S1 SLAB

It can be seen from Table 9.4 that there are substantial residual forces, generally about 200%, but as large as 2000% of the applied load, remaining after energy convergence has been achieved. The residual moments constitute the major part of these residual forces, while the residual in-plane forces account for only a minor part. It must also be noted that the choice of length unit will have a major effect upon the contribution due to the residual moments, since the magnitude of the moments depend upon the selected length unit. It can also be seen that for the scaled force convergence criterion, the residual forces are generally less than 10% of the applied load.

Incr	Load (kN)	Energy convergence criterion (1%)			Scaled force convergence (1%)		Raw force convergence (1%)
		Central deflection (mm)	Scaled force norm (%)	Raw force norm (%)	Central deflection (mm)	Raw force norm (%)	Central deflection (mm)
1	5	0.524	1.39	39.31	0.524	0.82	0.524
2	10	1.12	12.33	301.6	1.12	14.61	1.12
3	15	2.33	23.42	390.7	2.34	15.68	2.34
4	20	4.66	87.87	1425.0	4.63	10.09	4.63
5	25	7.35	4.50	77.5	7.35	7.32	7.35
6	30	10.30	117.30	2098.0	10.33	12.69	10.33
7	32.5	11.80	4.81	79.9	11.78	6.57	11.78
8	35.0	13.30	44.82	676.0	13.24	7.35	13.24
9	37.5	15.40	7.87	105.5	15.30	11.70	15.31
10	40.0	18.90	33.30	534.0	19.27	8.84	19.31
11	42.5	27.20	132.20	1987.0	27.21	12.50	27.20
12	43.0	32.41	81.84	1539.0	29.92	8.50	29.54

TABLE 9.4 CONVERGENCE ANALYSIS FOR DUDDECK'S S3 SLAB

The cpu time used by each of the analyses is approximately in the ratio 3:8:13 for slab S1 and in the ratio 4:10:19 for slab S3. This investigation indicates that the adoption of an unnecessarily stringent convergence criterion, such as raw force, can dramatically increase the required computer resources. The adoption of a slack convergence criterion, such as energy, leads to substantially lower computer resource requirements. However, massive residual forces remain after 'convergence' has been achieved and also the solution drifts when the structural stiffness becomes low, typically when the steel yields. A satisfactory compromise would appear to be the scaled force convergence criterion which requires only medium computer resources, while the response agrees well with that obtained with the

raw force convergence criterion. Furthermore, the raw force convergence criteria is not suitable since it is length unit dependant.

9.1.2.5 Load-deflection Responses

Experimental and analytical load-deflection responses for each of the three slabs have been presented in Figures 9.2 to 9.5. The figures titled SNAP were obtained from the author's program while those titled PLASAN are due to Rahman[2]. Generally, for the author's plots, both the tensile strength, f_t, and the tension stiffening factor, α_2, have been varied. Rahman has only shown the effect of variations in α_2. For many of the author's analyses, the end of the response curve represents the onset of either, crushing in the top layer concrete, or rupture of the steel, in the central region of the slab.

The scheme used for the through depth integration is the most significant difference between the author's idealisation and that of Rahman. Rahman used 8 equal thickness through depth layers, with stress sampling at the mid-point of each layer, whereas the author used a five point Newton-Cotes integration rule. It is thought that this factor accounts for slight differences between the two sets of results.

The effect of variations in the tensile strength, f_t, can be seen in Figure 9.2. A relatively small change in the tensile strength from 2 N/mm^2 to 2.5 N/mm^2 has changed the early post-cracking region of the response significantly. An increase in the tension stiffening factor, α_2, from 15 to 25 has its most significant effect in the later post-cracking region, up until the onset of steel yielding. Therefore, it can be seen that, essentially, these two parameters effect different regions of the response curve. The load-deflection curve

SNAP load–central deflection responses for Duddeck's S1 slab.

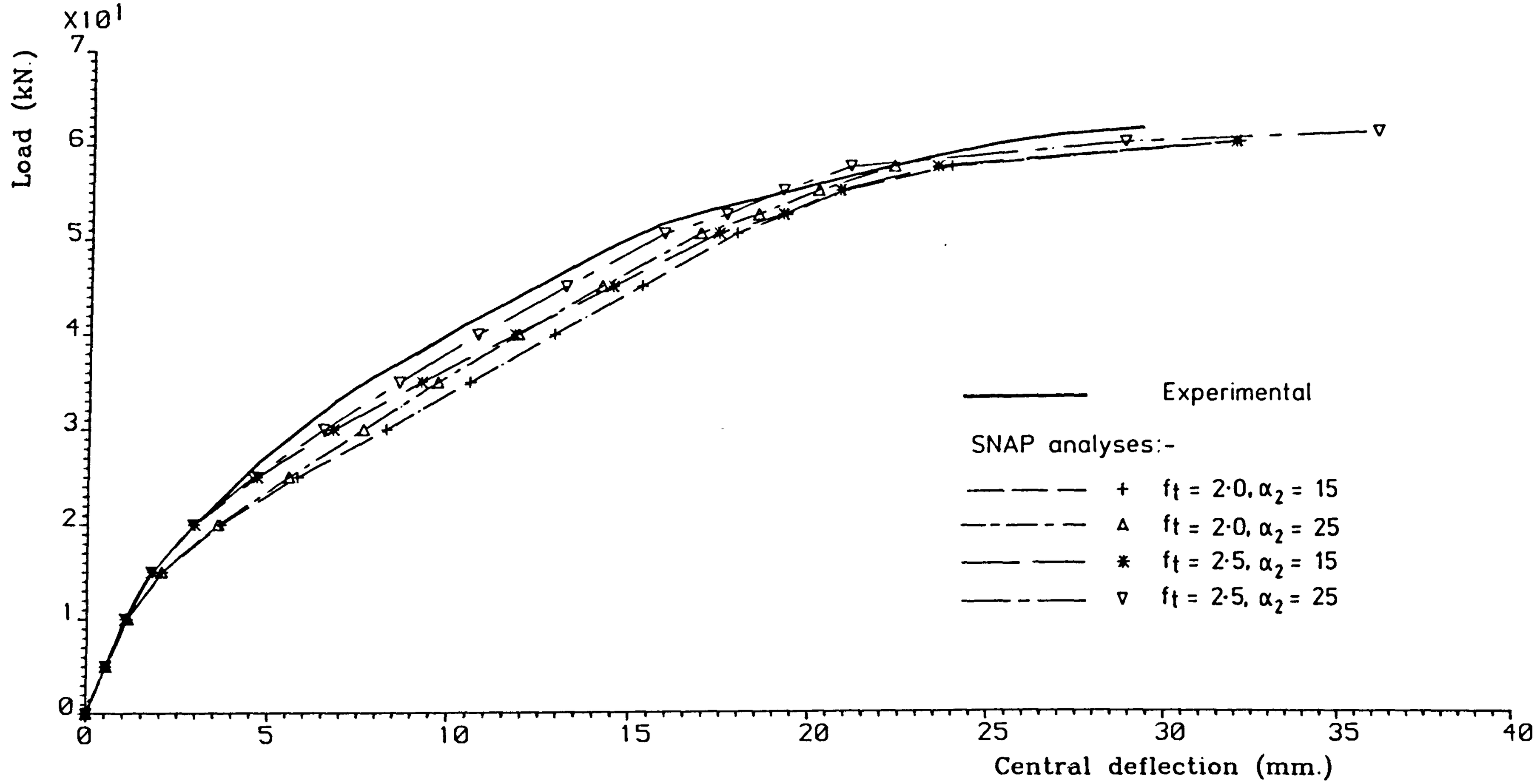

FIG. 9. 2. 'SNAP' LOAD-DEFLECTION RESPONSE COMPARISONS FOR DUDDECK'S S1 SLAB

(i) SNAP load–central deflection responses for Duddeck's S2 slab.

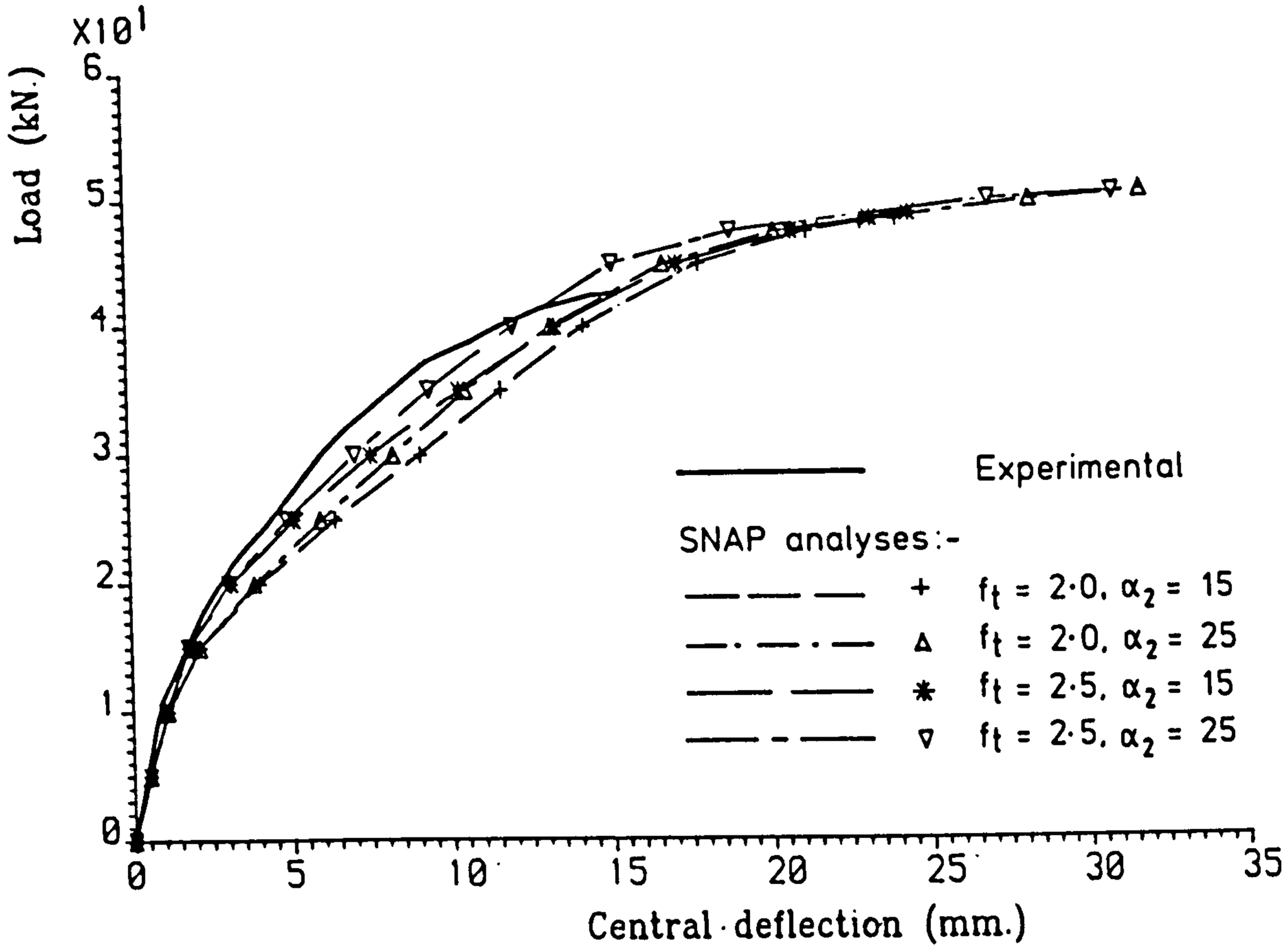

(ii) SNAP load–central deflection responses for Duddeck's S3 slab.

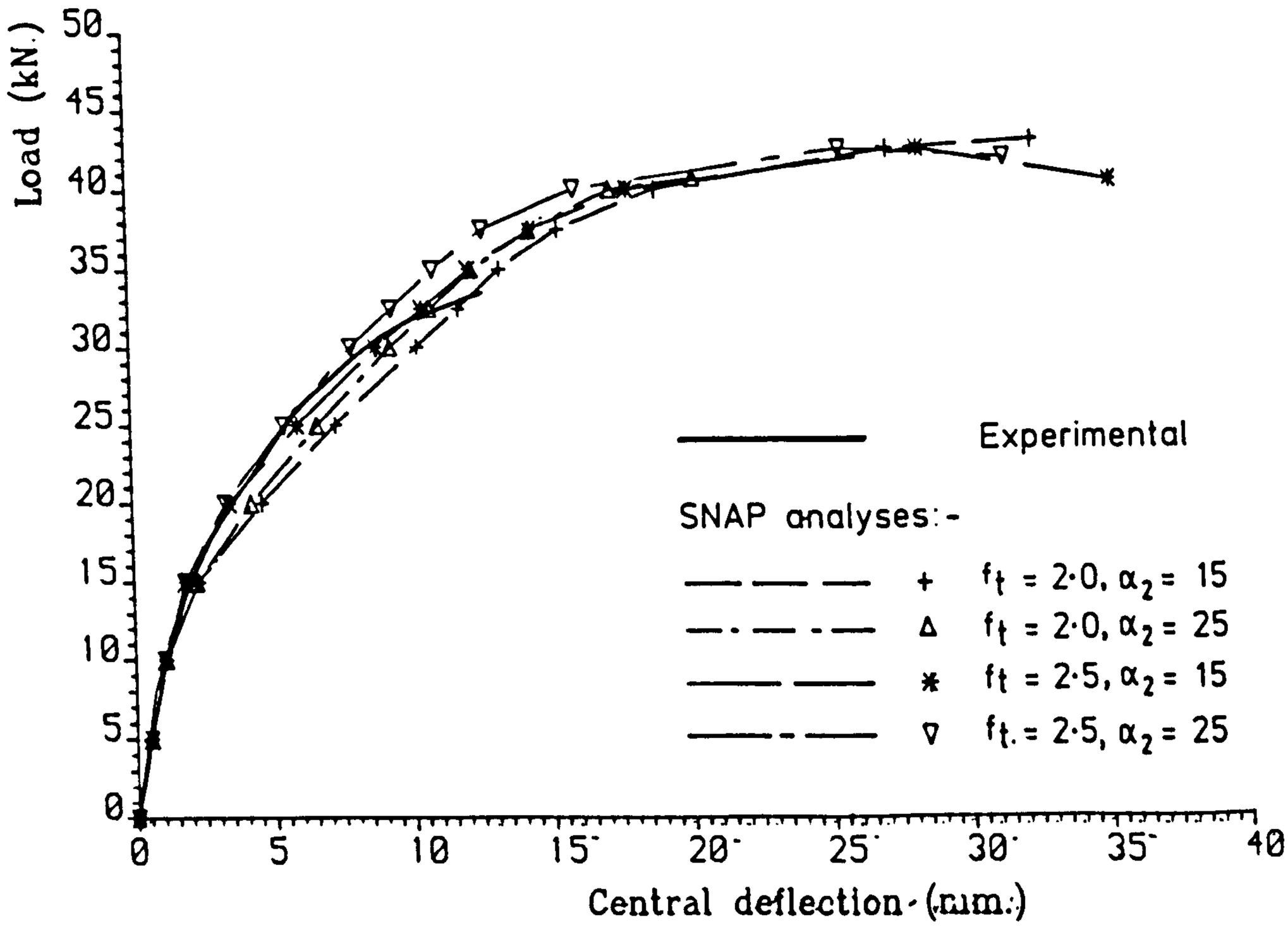

FIG. 9.3. 'SNAP' LOAD-DEFLECTION RESPONSE COMPARISONS FOR DUDDECK'S S2 AND S3 SLAB.

(i) PLASAN load–central deflection responses for Duddeck's S1 slab.

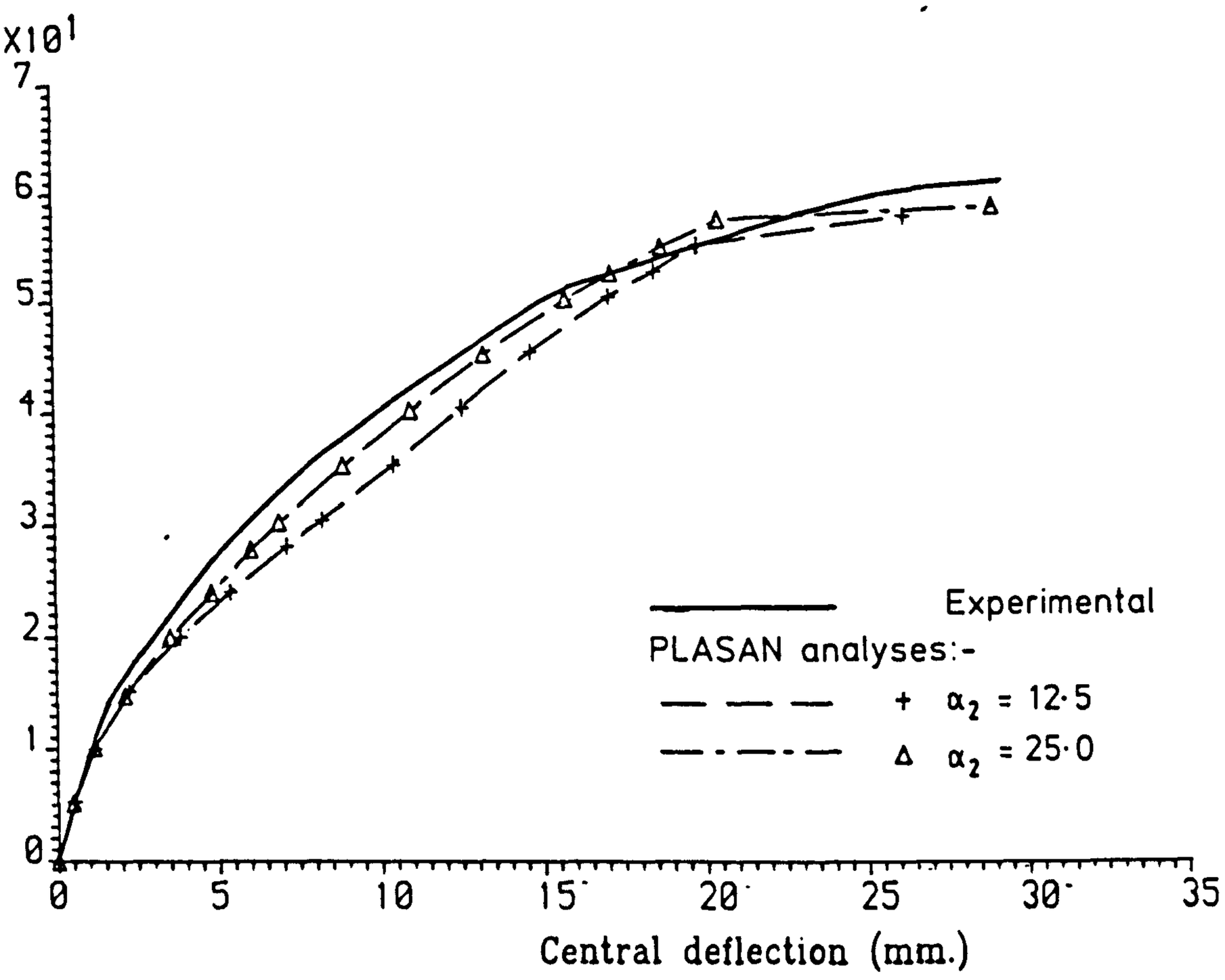

(ii) PLASAN load–central deflection responses for Duddeck's S3 slab

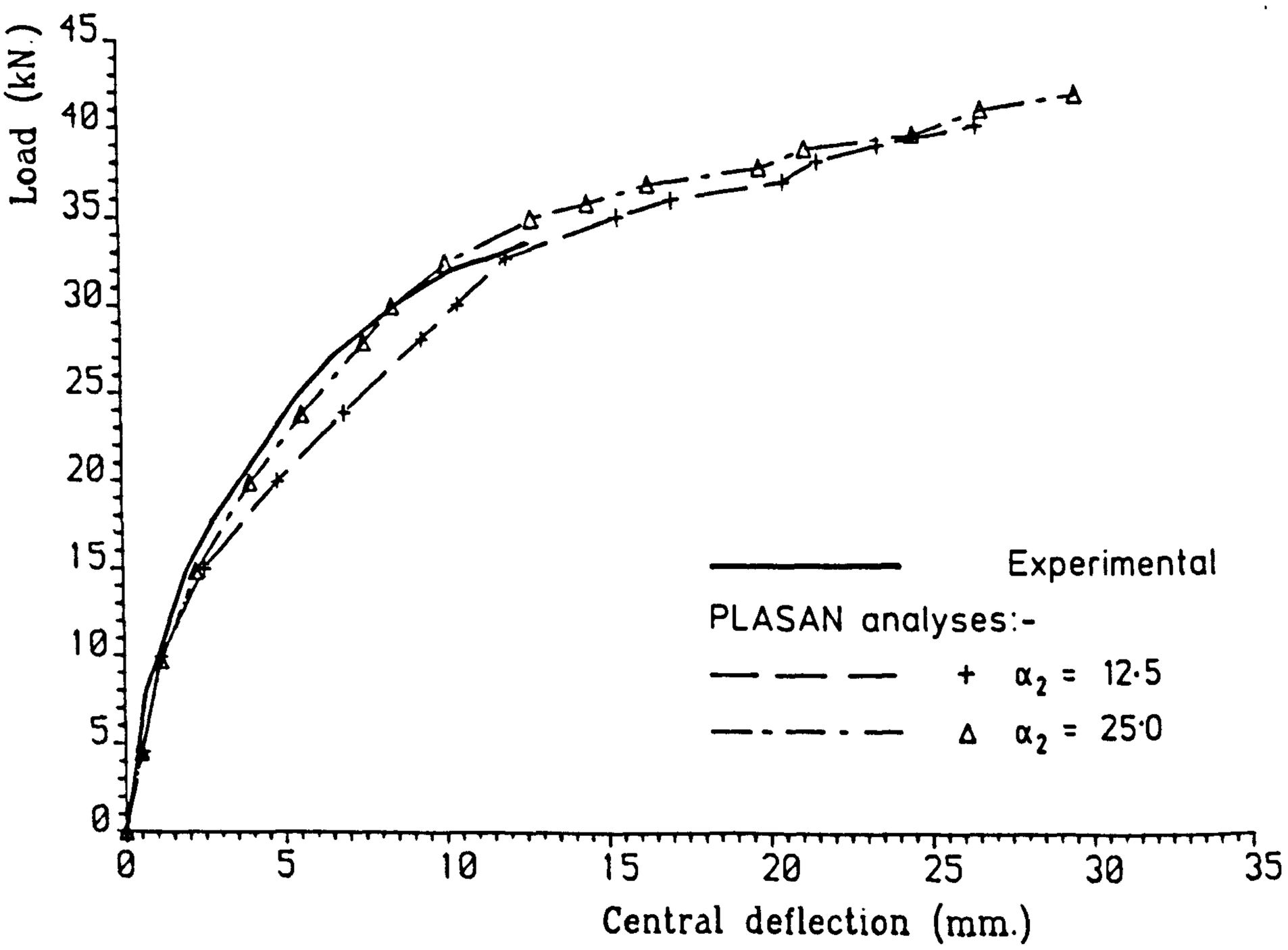

FIG. 9. 4. 'PLASAN' LOAD-DEFLECTION RESPONSE COMPARISONS FOR DUDDECK'S S1 AND S3 SLABS

that is obtained when both the tensile strength, f_t, and the tension stiffening factor, α_2, are increased has also been presented in Figure 9.2. It can be seen that this curve is in good agreement with that of the experimental, both in the post-cracking region and in the ultimate load prediction.

It must be noted that the nature of any in-plane restraint at the supports may have an effect upon the post-cracking to steel yielding/concrete crushing region.

Similar analyses for Duddeck's S2 and S3 slabs have been presented in Figure 9.3. The effects of both the tensile strength and the tension stiffening factor have again been shown to have a significant effect upon the post-cracking response. The analytical responses are again in good agreement with those obtained by Rahman with the Plasan program, see Figure 9.4.

9.1.2.6 Maximum Load Analyses

It can be seen from Figure 9.3, for slab S3, that while the general form of the analytical response curve is similar to that of the experiment, the analytical maximum load is considerably in excess of the experimental value, also see Table 9.5.

Slab mark	Experimental Maximum Load (kN)	Analytical Maximum Loads (kN)	
		PLASAN	SNAP
S1	61.66	61.0	61.0
S2	43.46	54.0	48.5
S3	34.25	45.0	43.0

TABLE 9.5 MAXIMUM LOAD COMPARISON FOR DUDDECK'S SLABS

To a lesser extent, the same is true of slab S2, see Figure 9.3 and Table 9.5. Rahman[2] attributes this phenomenon to the analytical tension stiffening effect enhancing the ultimate section strength. If this were true, as Rahman points out, one would expect different values of the tension stiffening factor, α_2, to yield different maximum loads. This view is not supported by the load deflection curves, see Figures 9.3 and 9.4, which indicate little change in the maximum load for different values of the tension stiffening factor, α_2.

Failure of a section will be preceeded by yielding of the steel and, therefore, it is interesting to examine the tension stiffening effect at the onset of steel yielding. For this structure the failure section is likely to be perpendicular to the steel. From the details presented in Table 9.2 one can calculate a steel yield strain of 3333 $\mu\epsilon$. For the concrete tensile stress to just be zero at this strain, a tension stiffening factor, α_2, of 27 is required. Thus, it is unlikely that the tension stiffening effect will have a significant effect upon the ultimate strength with $\alpha_2 < 25$.

It is interesting to note that the analysis of slab S1, with uniform reinforcement, gave a good prediction of the failure load and, therefore, slab S3 was reanalysed with uniform reinforcement equal to that originally provided in the 'y' direction. One would expect this change to produce a more flexible structure, however, a yield line analysis indicates that the structure will have a similar maximum load, provided that the section has sufficient ductility. The predicted failure load is now in good agreement with that of the experiment and, as expected, the flexibility of the structure has increased.

For these slabs the geometry and proportional loading regime would suggest that the principal strain direction will change little after the crack directions have been fixed. However, with orthotropic reinforcement, the principal strain direction will change, and hence the cracks in the lower layers, which will have formed in earlier increments, will not then lie in the current principal strain directions. Thus there will be a shear strain in the crack directions, to which the degraded shear modulus is applied. The resulting shear stress, when transformed back to Cartesian directions will yield a stress normal to the expected failure section, thus enhancing the strength of the section. Consequently, an excessive failure load results.

A scaled force convergence criteria was applied for all the analyses involved in the maximum load investigation. Generally, this was set to 1%, however, for some increments this had to be increased to 5% or even 10% in a few cases. The use of a tight scaled force convergence criterion resulted in approximately 60 increments being required for each of the full range analyses. A summary of the failure loads that were obtained from the analyses concerned with this maximum load investigation, can be seen in Table 9.6.

The original analyses carried out by the author used a degraded shear modulus equal to 0.5G, this is consistent with that used by Rahman. The total stress approach used by the author and the incremental stress approach adopted by Rahman will produce similar results, since the cracks will form in principal strain directions and thus, initially, there will be no shear stress in the crack directions.

	Analytical Maximum Load (kN)					
Crk. Mod.	Fixed	Fixed	Fixed	Fixed	Rot.	Fixed
Rein.	Orth.	Orth.	Orth.	Iso.	Orth.	Orth.
Stl. Mod.	Elasto-Plastic	Elasto-Plastic	Elasto-Plastic	Elasto-Plastic	Elasto-Plastic	Multi-Linear
Deg. Shr. Modulus	0.5G	0.1G	0.01G	0.5G	-	0.1G
Experimental Maximum Load (kN)						
34.25	43.0	38.69	35.52	35.48	35.26	38.09

TABLE 9.6 RESULTS OF MAXIMUM LOAD STUDY FOR DUDDECK'S S3 SLAB

To illustrate the phenomenon described above, slab S3 was reanalysed with degraded shear moduli equal to 0.1G and 0.01G. The resulting load-deflection responses have been included in Figure 9.5. The reduction in the maximum load, as the residual shear modulus is reduced, can clearly be seen. For the analysis using a degraded shear modulus of 0.01G there is very good agreement between the analytical failure load and that of the experiment.

An analysis was also carried out using a rotating material axis direction model. The load-deflection response for this analysis can also be seen in Figure 9.5. It can be seen that the rotating material axis model yields a response curve which is very similar to that obtained from the fixed crack model using a low residual shear modulus of 0.01G.

With the rotating material axis analysis and the fixed crack analyses with residual shear moduli of 0.1G and 0.01G, severe difficulties were encountered in achieving convergence in the region where the response curve became flat. In fact many of the 60 increments required for the complete analysis were concentrated in this region. It was suspected that the elastic-perfectly plastic steel stress-strain curve was responsible for this phenomenon. Therefore, slab S3 was reanalysed using a 4 linear segment stress-strain curve modelled on that of Torbar reinforcement. It was found that with the multi-linear steel stress-strain curve convergence was more easily achieved, while the analytical response exhibited the gradual stiffness reduction that could be seen in the experimental response.

On the basis of these results, the question arises of whether a fixed crack material model, which maintains significant residual shear modulus in the crack directions, can be justified?

9.1.2.7 Crack Patterns

Crack pattern plots for Duddeck's slabs are given in Figures 9.6 to 9.8. On these plots, concrete which has turned plastic in compression is indicated by a wavy line. Cracks are indicated by a straight line. In both cases, the length of the line is proportional to the strain normal to the line. The scale at the top of each plot indicates the constant of proportionality.

For the top layer plot of Figure 9.6 all marks indicate points that have turned plastic in compression, for some of those points the strain is small and, therefore, the wavy form of the line is not clear. It can be seen that in the central region the direction of plastic compression bisects the corner. The plastic compressive strain drops off rapidly towards the edges of the slab. The bottom

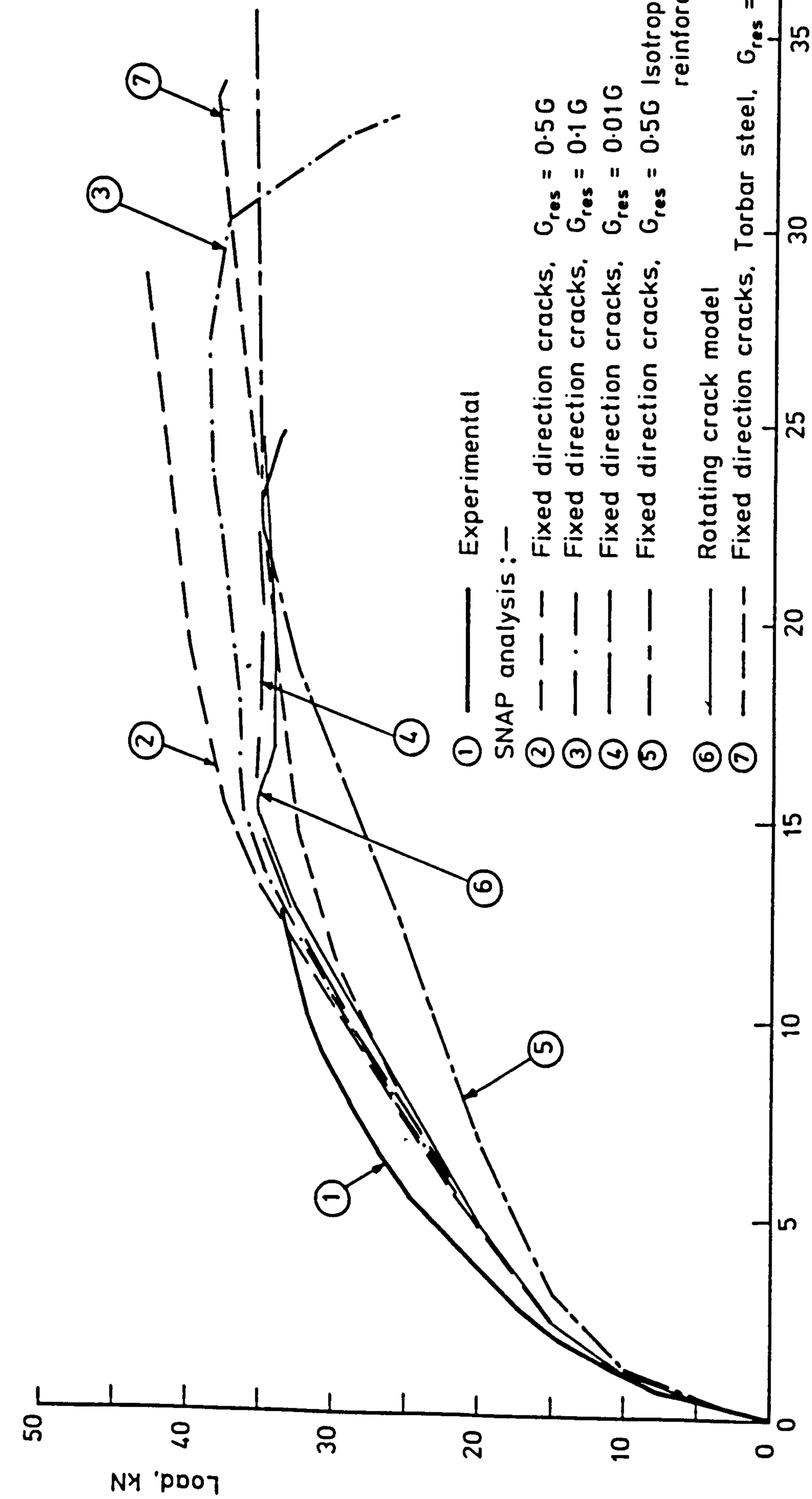
'SNAP' LOAD-DEFLECTION RESPONSE COMPARISONS FOR DUDDECK'S S3 SLAB
Load, kN
Central deflection, mm
SNAP analysis
① Experimental
② Fixed direction cracks, G_{res} = 0·5G
③ Fixed direction cracks, G_{res} = 0·1G
④ Fixed direction cracks, G_{res} = 0·01G
⑤ Fixed direction cracks, G_{res} = 0·5G Isotropic reinforcement
⑥ Rotating crack model
⑦ Fixed direction cracks, Torbar steel, G_{res} = 0·1G

FIG. 9. 5.

layer plots clearly show intense cracking in the central region of the slab. This cracking continues along both centre lines towards the edges of the slab, indicating the formation of yield lines in these regions.

The analytical crack patterns for Duddeck's S3 slab are shown in Figures 9.7 and 9.8. The top surface and soffit surface plots clearly indicate the formation of a yield line parallel to the weakest section.

On the crack pattern plots only 'visible' cracks have been plotted. For this structure the minimum visible cracking strain was calculated from a specified average crack spacing of 100 mm and minimum visible crack width of 0.05 mm. This results in a minimum visible cracking strain of 500 $\mu\epsilon$. It must be noted that this calculation is approximate and does not take factors such as tension stiffening into account.

9.2 Longitudinal and Transverse Section Analyses

9.2.1 Introduction

To obtain detailed moment curvature information of the precast inverted T beam with in-situ fill form of construction, several simply supported beam sections had been constructed and tested. Each of these beam sections modelled either a longitudinal or transverse slice of the model decks and consisted of both prestressed precast beams and insitu concrete (see Appendices 5.1, 5.2 and 7.1).

Full advantage was taken of the restart facilities that are available in the SNAP program so that the iteration strategy could be modified in the light of new developments as each analysis progressed. Initially load-control with BFGS acceleration was employed for the

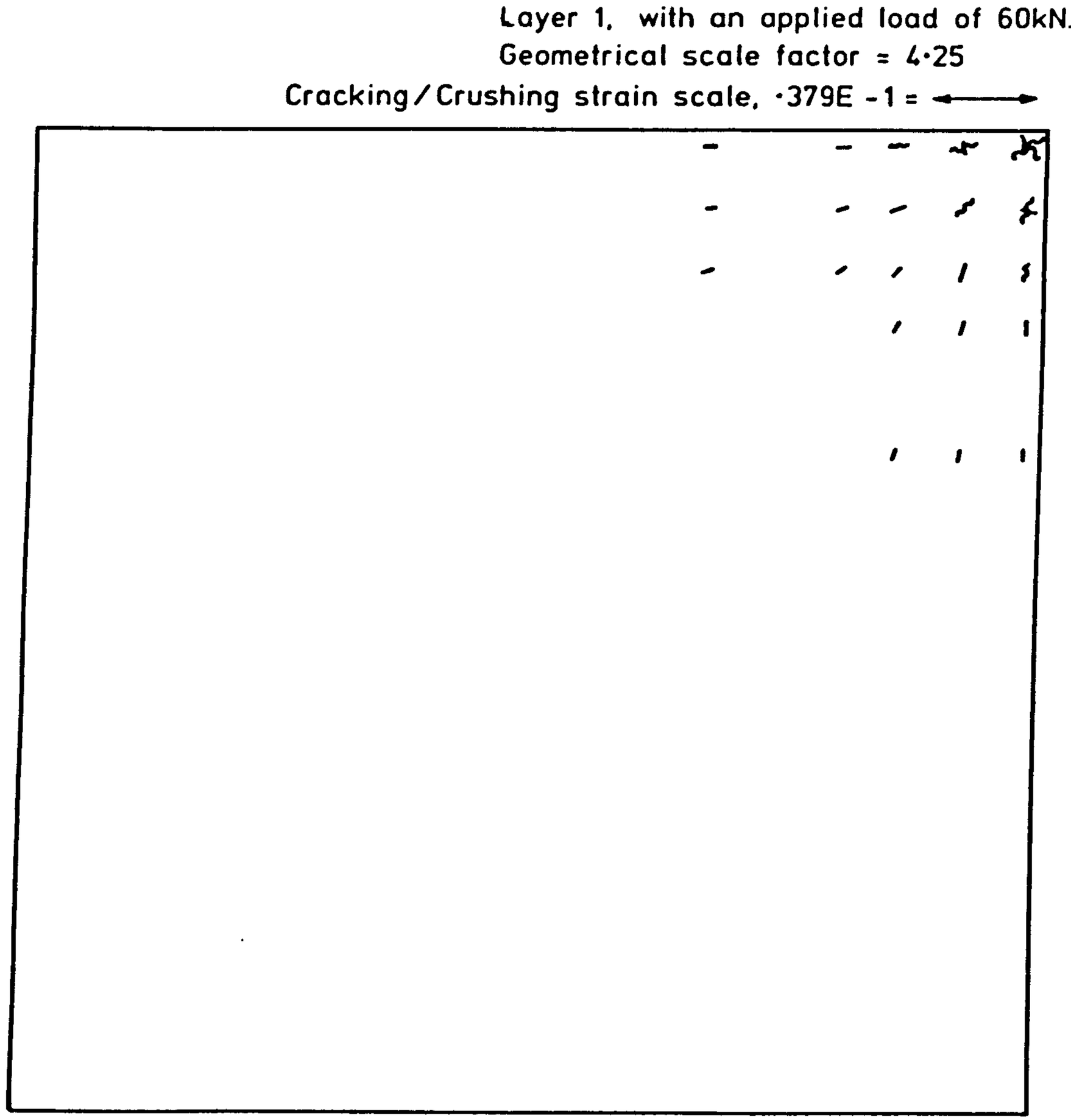

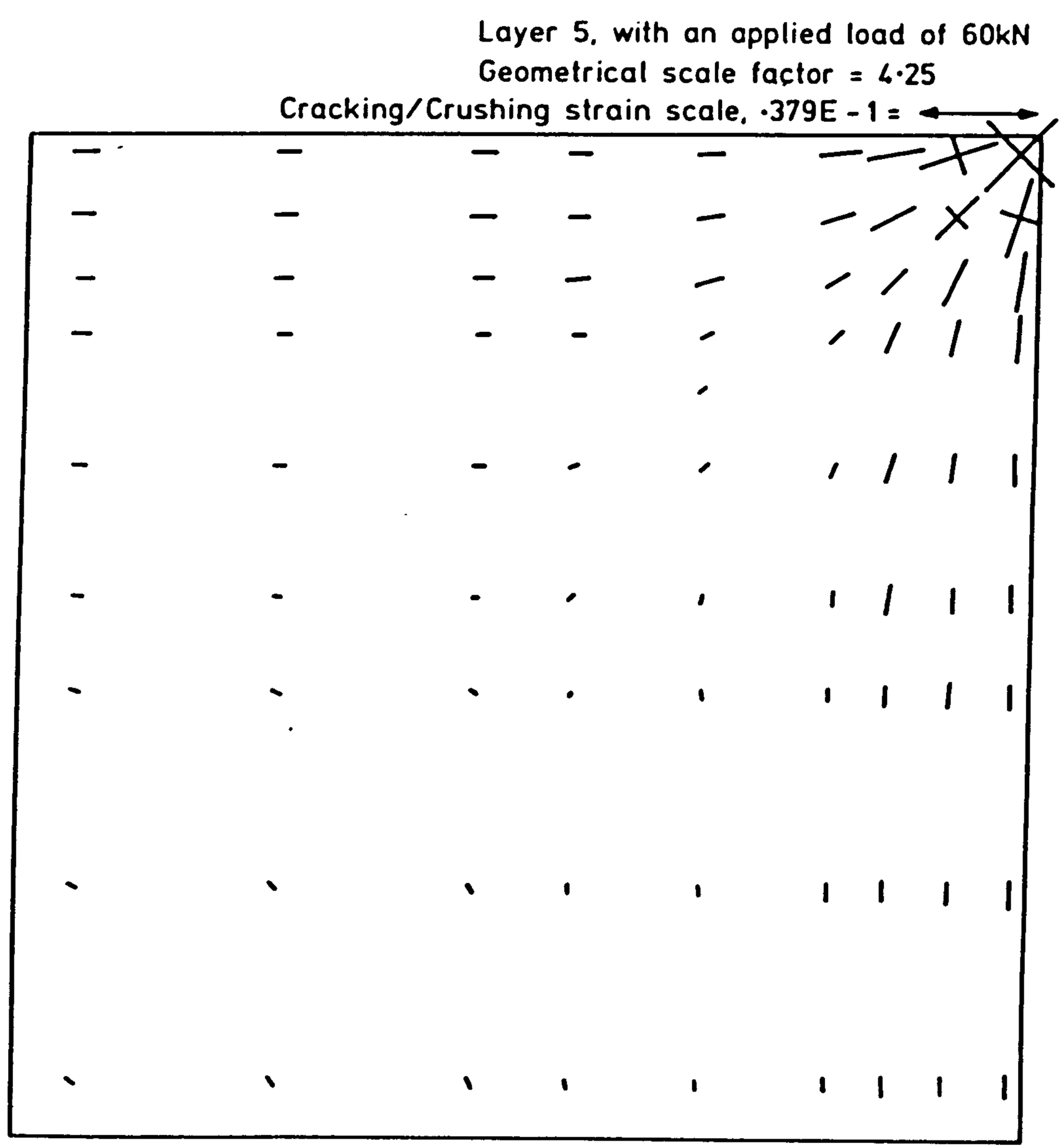

FIG. 9. 6. CRACKING/CRUSHING PLOTS FOR THE TOP AND SOFFIT LAYERS OF DUDDECK'S S1 SLAB AT A LOAD OF 60kN.

analyses. As the structural stiffness reduced and convergence under load control became difficult, or impossible, then either displacement or arc length control, with BFGS, was employed. In situations where there was a rapid change in structural stiffness, such as crushing of the concrete or rupture of the steel, then a Newton-Raphson procedure was used in preference to BFGS. While under load-control the increments were sized manually, however, while under either displacement or arc-length control, the automatic increment sizing algorithms in the SNAP program were utilised. In situations where great difficulty in converging was encountered the increment was automatically repeated with the automatic increment size cut to 0.25 of its previous value. Detailed descriptions of the iteration procedures that are incorporated into the SNAP program have been given in Chapter 8 Section 8.5.

Dual convergence criteria were employed for these analyses. Convergence was achieved when either a 1% scaled force criterion or a 0.01% scaled displacement criterion was satisfied. In reality the majority of increments converged on the force criterion, with few converging on the very tight displacement criterion. However, when the structural stiffnesses approached zero then convergence to the above force tolerances became impossible and, therefore, the scaled force convergence criterion was slackened to 5%, so that convergence on force could be achieved.

Two algorithms for the modelling of the precast beams were formulated, which treated the beams as either 1 dimensional or 2 dimensional entities. In the analyses, both formulations are used and the resulting responses are compared. A full description of the two modelling philosophies has been presented in Chapter 8 Section 8.3. Algorithms were developed for the application of statistically varied

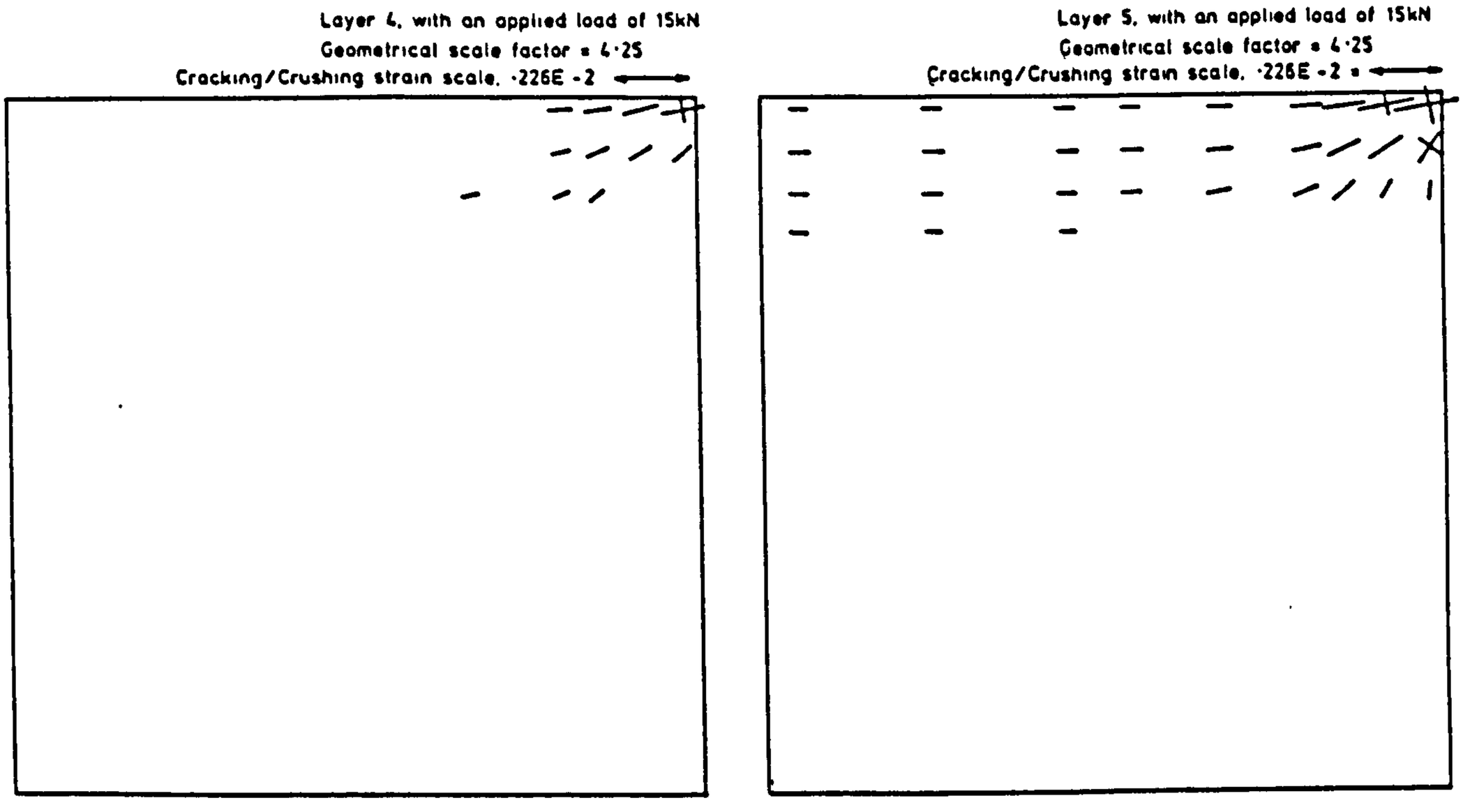

FIG. 9. 7. CRACKING/CRUSHING PLOTS FOR THE BOTTOM TWO LAYERS OF DUDDECK'S S3 SLAB AT A LOAD OF 15KN

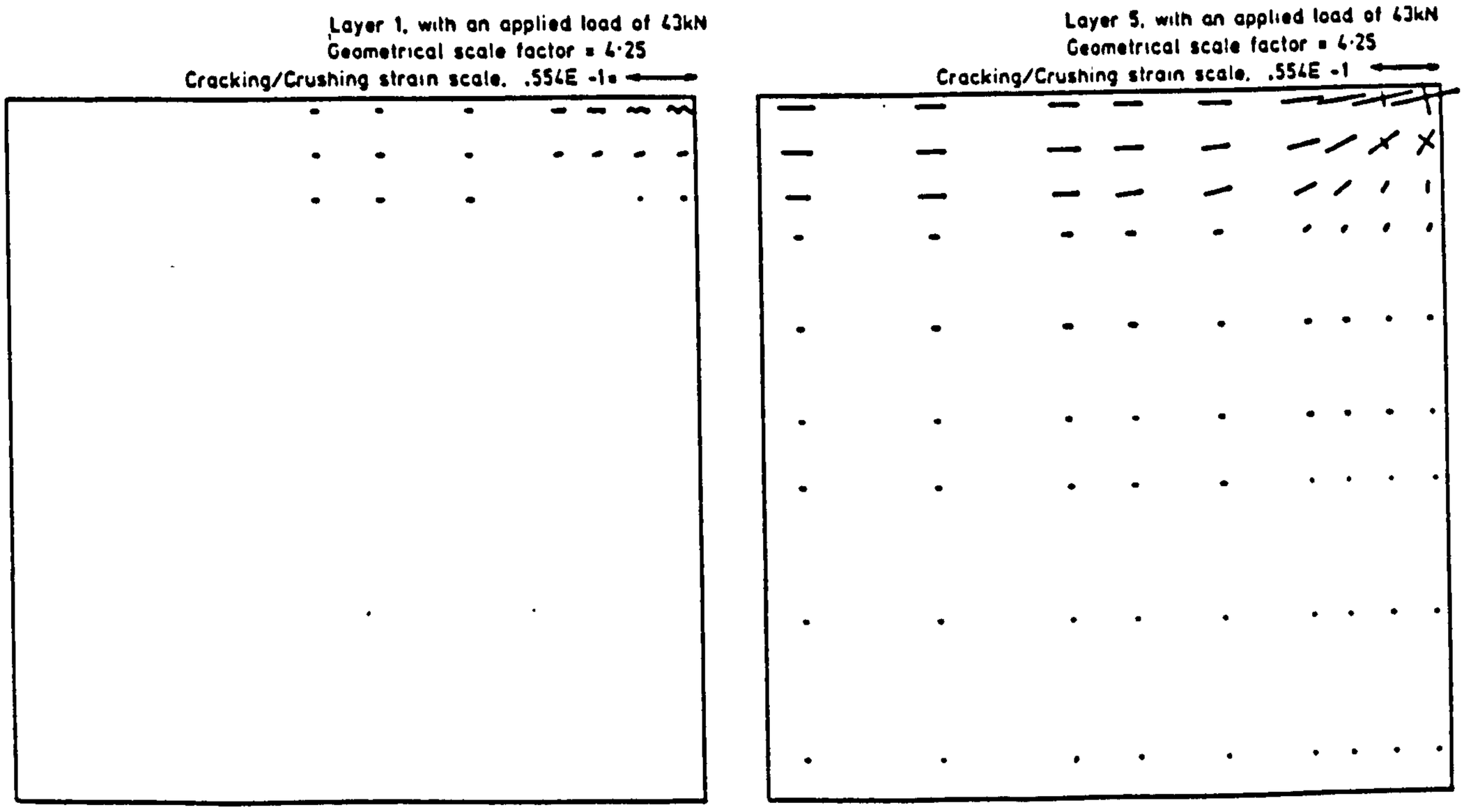

FIG. 9. 8. CRACKING/CRUSHING PLOTS FOR THE TOP AND SOFFIT LAYERS OF DUDDECK'S S3 SLAB AT A LOAD OF 43kN.

material properties in an analysis. In the following sections the effects of this feature on the response are assessed. A full description of this feature has been presented in Chapter 8 Section 8.4.4.

9.2.2 Model 1 Longitudinal Section

9.2.2.1 Finite Element Idealisation

Details of the structural configuration and finite element mesh can be seen in Figure 9.9. Advantage could not be taken of symmetry since the structure is no longer symmetrical after statistically varied material properties have been applied. The boundary conditions consisted of fixed vertical restraint at each of the four corner nodes. Besides analysing the structure with the test loading, it was also analysed with inverted applied loading, to investigate the analytical response to applied hogging moments. The through depth integration was achieved with 5 integration stations in the precast concrete and 5 stations in the insitu concrete. Details of the through depth integration scheme are contained in Tables 9.7 and 9.8 and Figures 9.10 and 9.11.

Integration station	Distance from insitu centre line (mm)	Weight (mm)	
		X' direction	Y' direction
1	68.5	10.9	10.7
2	34.25	35.1	48.7
3	0.0	13.2	18.3
4	-34.25	35.2	48.7
5	-68.50	6.31	10.7

Note: The directions X' and Y' refer to beam local coordinate space

TABLE 9.7 INSITU INTEGRATION DISTANCES AND WEIGHTS FOR MODEL 1 NON-LINEAR ANALYSES

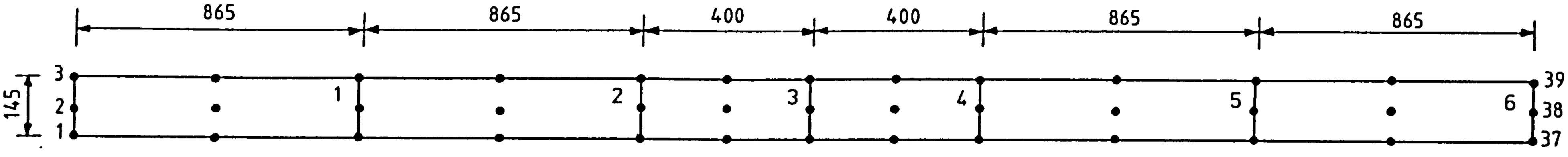

w = 0
at 1 & 3

Finite element mesh used for Model 1 longitudinal sections

w = 0
at 37 & 39

Self-weight UDL
$= 4{\cdot}09 \times 10^{-3}\ N/mm^2$

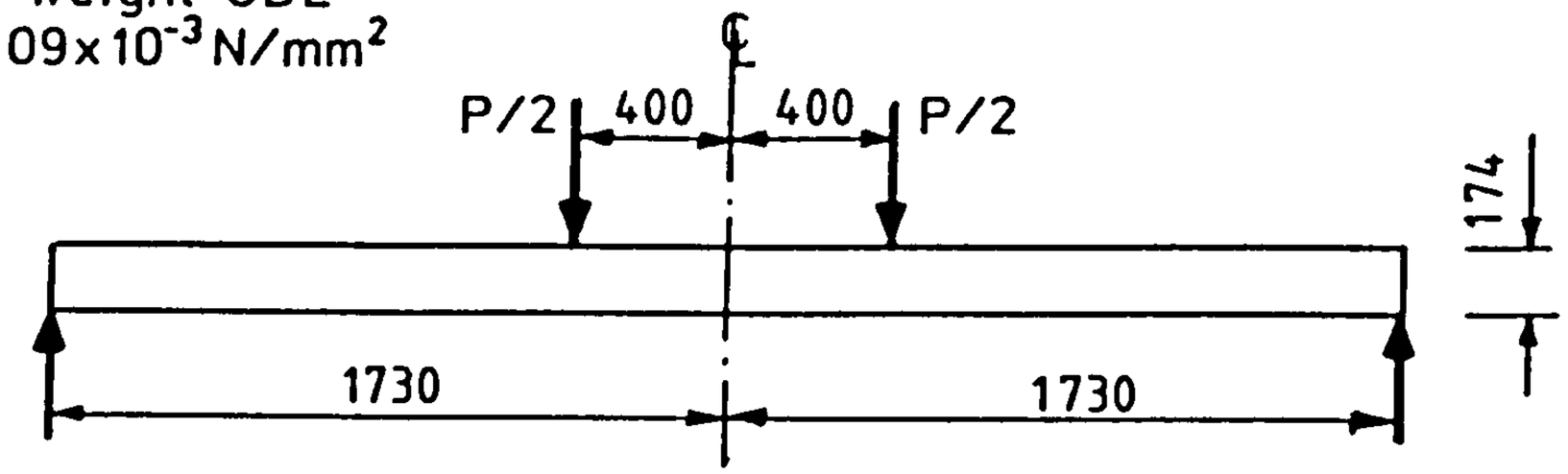

Analysed with test loading

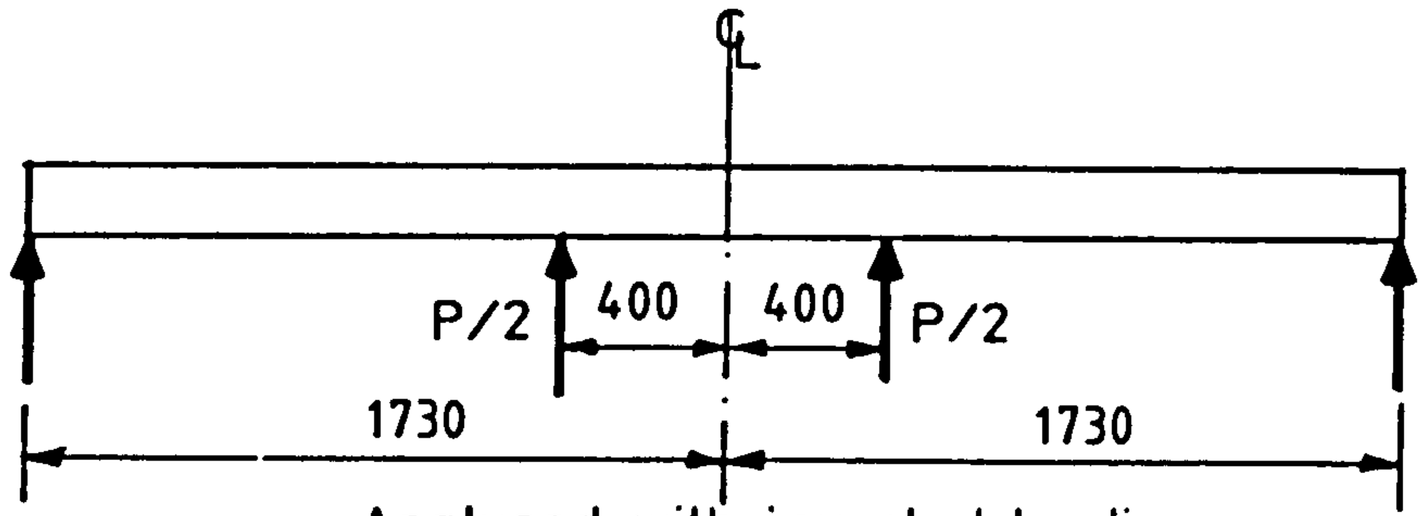

Analysed with inverted loading

ALL DIMENSIONS
IN mm

FIG. 9.9. FINITE ELEMENT IDEALISATION OF MODEL 1 LONGITUDINAL SECTION

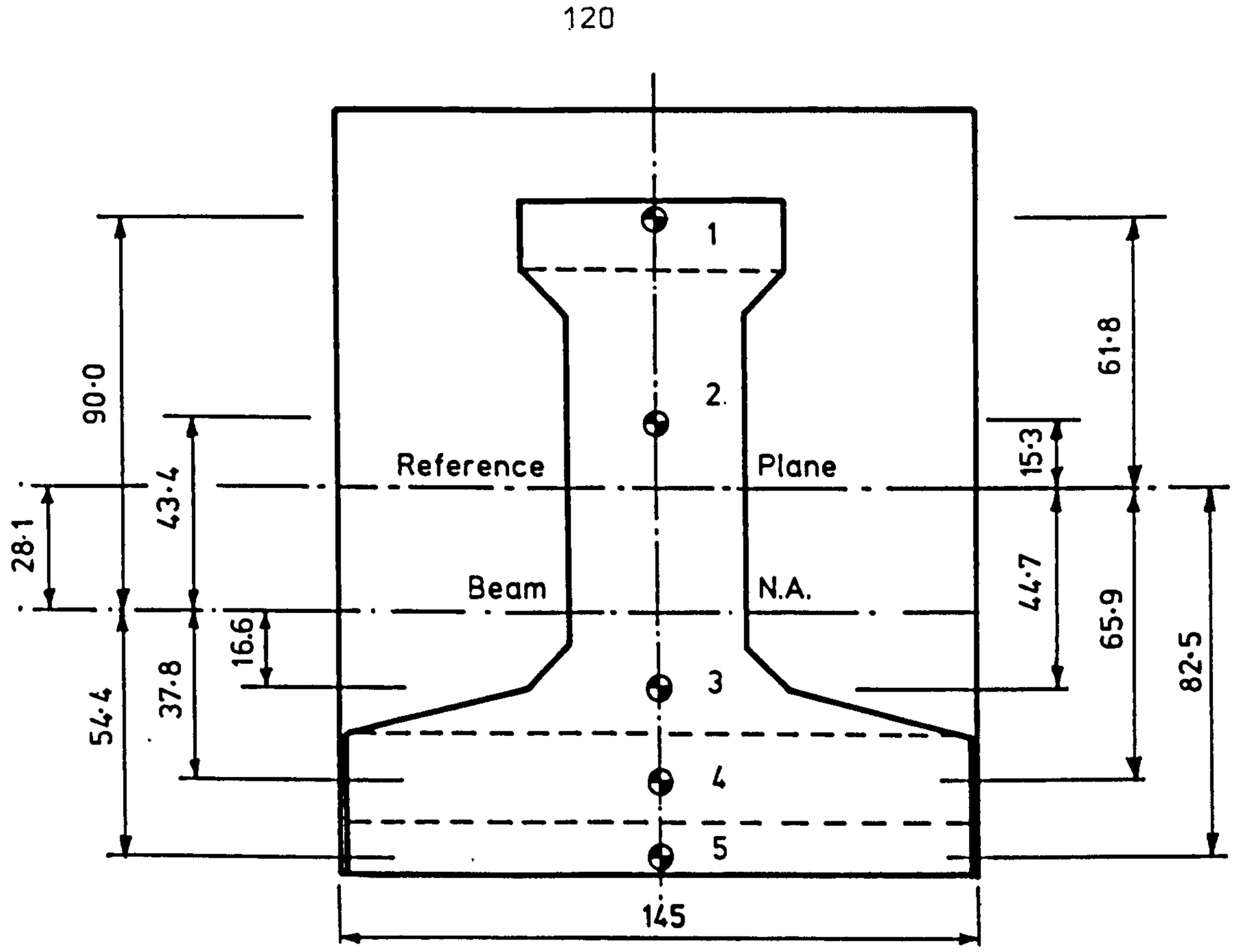

FIG. 9.10. THE BEAM INTEGRATION STATIONS FOR MODEL 1 NON-LINEAR ANALYSIS.

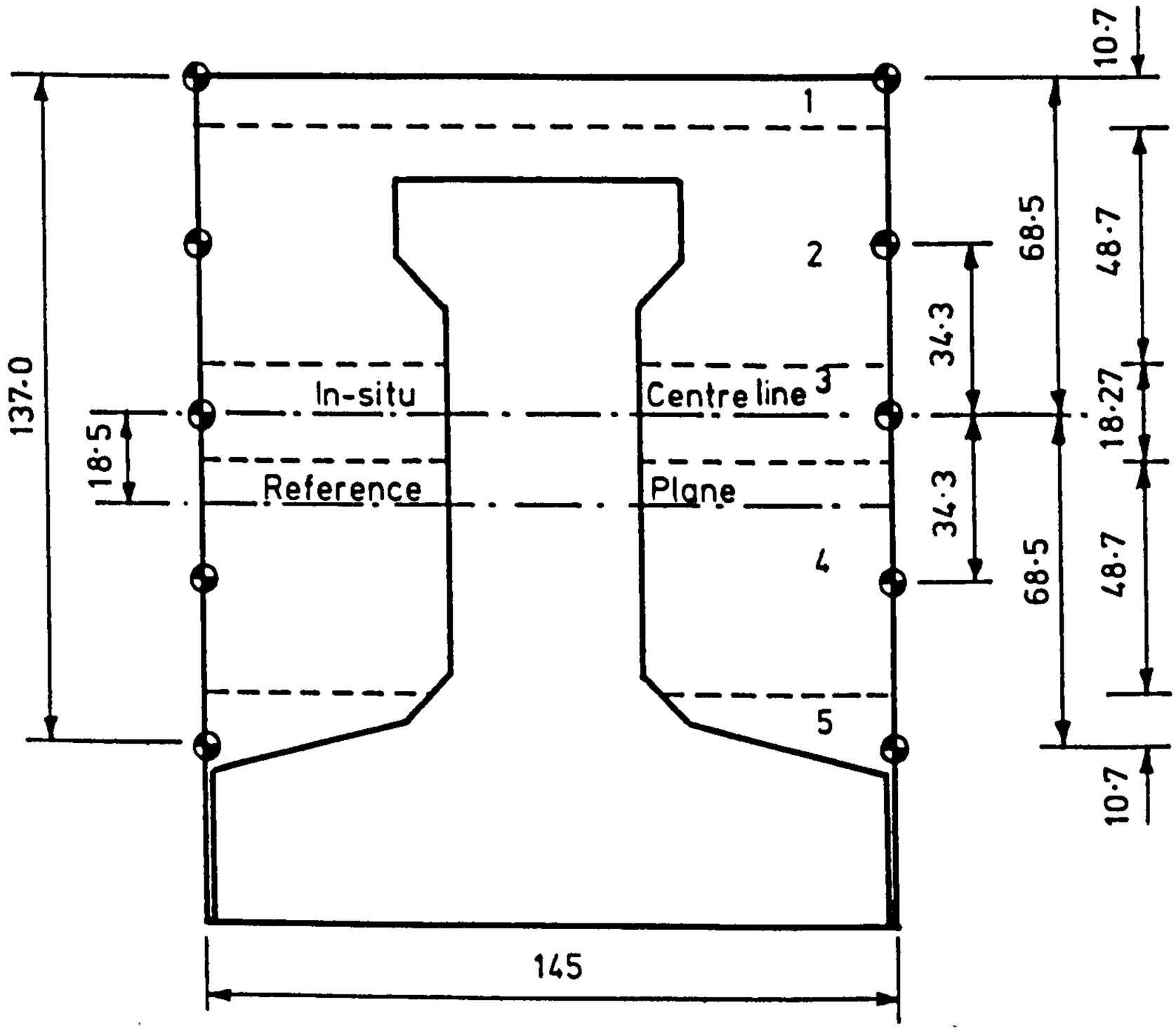

FIG. 9.11. THE IN-SITU INTEGRATION STATIONS FOR MODEL 1 NON-LINEAR ANALYSIS.

Integration station	Distance from beam NA (mm)	Weight (mm)
1	89.97	6.63
2	43.44	22.2
3	-16.64	11.6
4	-37.81	19.6
5	-54.42	11.7

TABLE 9.8 BEAM INTEGRATION DISTANCES AND WEIGHTS FOR MODEL 1 NON-LINEAR ANALYSES

The COSIG2 material model was employed for the concrete. Details of the material curves applicable to the precast and insitu concretes can be seen in Figure 9.12. From this figure it can be seen that, in the tension zone, a tri-linear curve was utilised. The material modelling curves used for the steel prestressing and reinforcement are identical to those utilised for the SNAP analyses of model deck 1, described in Section 9.3, and, therefore, details are not given here.

9.2.2.2 Load-Deflection Response with normal loading

Figure 9.13 compares the experimental load-deflection response with those obtained from the SNAP program. It can be seen that the best agreement with the experiment is obtained from the analysis using a prestress loss of 20% and a concrete tensile strength of 3.56 N/mm^2, which are the values obtained from actual tests.

In order to illustrate the sensitivity of the response to variations in these two important parameters, further analyses were carried out. It can be seen from Figure 9.13 that the adoption of a zero concrete tensile strength has only a small effect upon the response, whereas

the adoption of high prestress losses has a far larger effect. This occurs because the compressive prestress in the beam soffit is many times larger than the concrete tensile strength. It will be noticed that only a small proportion of the section strength remains to be attained after initial cracking occurs. As expected all the SNAP analyses with the different modelling parameters converge on the same ultimate strength since, essentially, only the steel strength and the lever arm affect this factor. The analytical ultimate strength is approximately 4% below the experimental value. Much of this difference can be accounted form in the necessarily coarse through depth integration scheme, which was unable to model the ultimate condition exactly. The scheme could not be expected to model all section states, up to and beyond the ultimate condition, exactly and, therefore, the scheme used for these analyses was the best compromise. The residual ultimate strength difference is most probably due to material property variations and constructional inaccuracies. From Figure 9.13 it can be seen that the final segment of the experimental curve drops below the analytical curves and this can most probably be accounted for by breakdown of bond in the experimental test.

Full range analytical responses for this section have been presented in Figure 9.14(i), together with the experimental response. If we examine the uniform property curve first, the onset of cracking is not discernible, whereas the onset of steel yielding, at point A is. The steel continues to yield as the response progresses along the top plateau. Also, in this region, at a displacement of approximately 120 mm, the top layer of the insitu concrete is crushing and has begun descending down the final linear portion of the stress strain curve. When the response reaches point B, the lower prestressing steel begins to move along the falling branch of the steel stress-strain curve towards complete rupture. Other points in the structure begin to

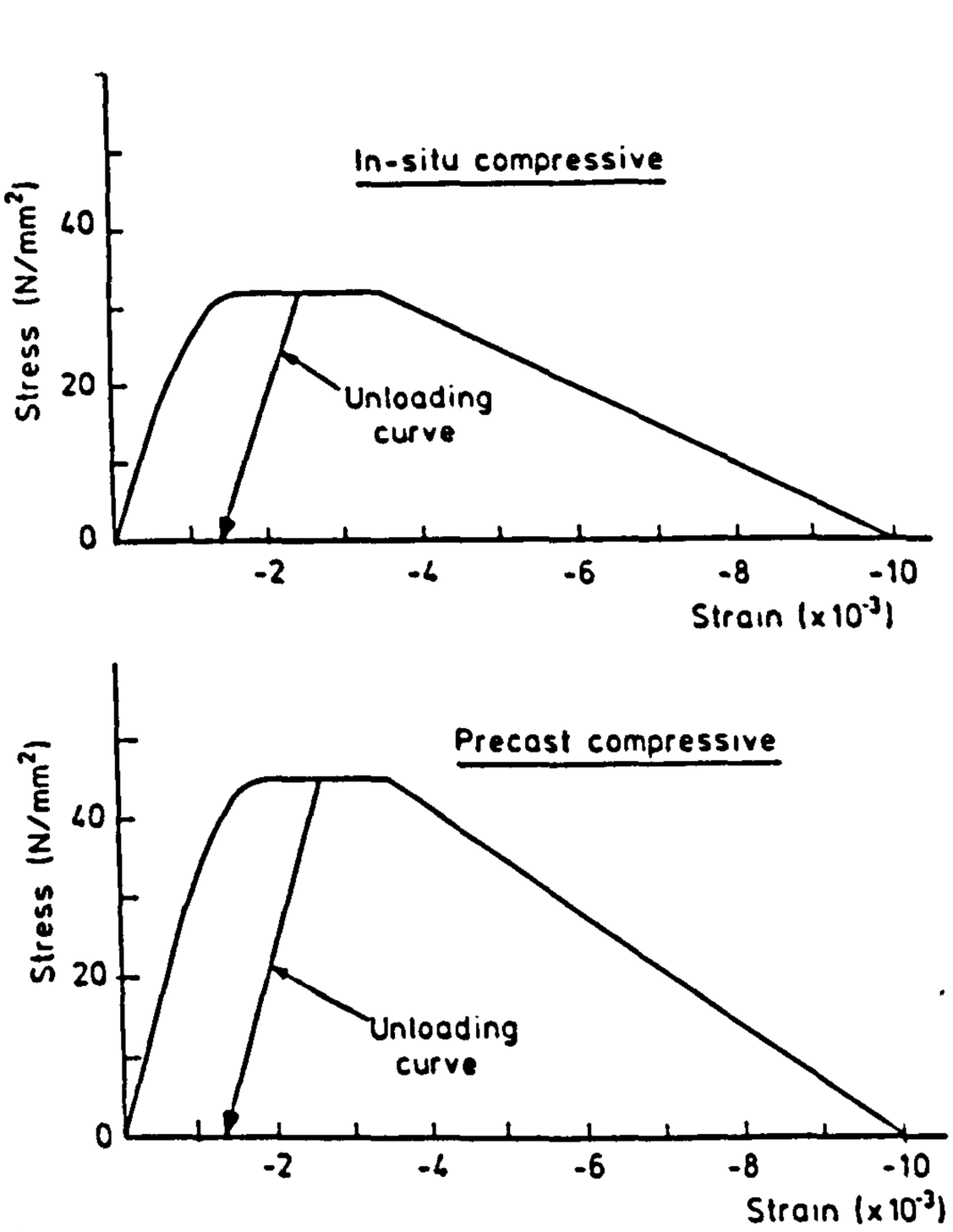

FIG. 9. 12. CONCRETE MATERIAL CURVES FOR MODEL 1 LONGITUDINAL AND TRANSVERSE SECTIONS

Comparison of load-deflection responses for model 1 longitudinal section.

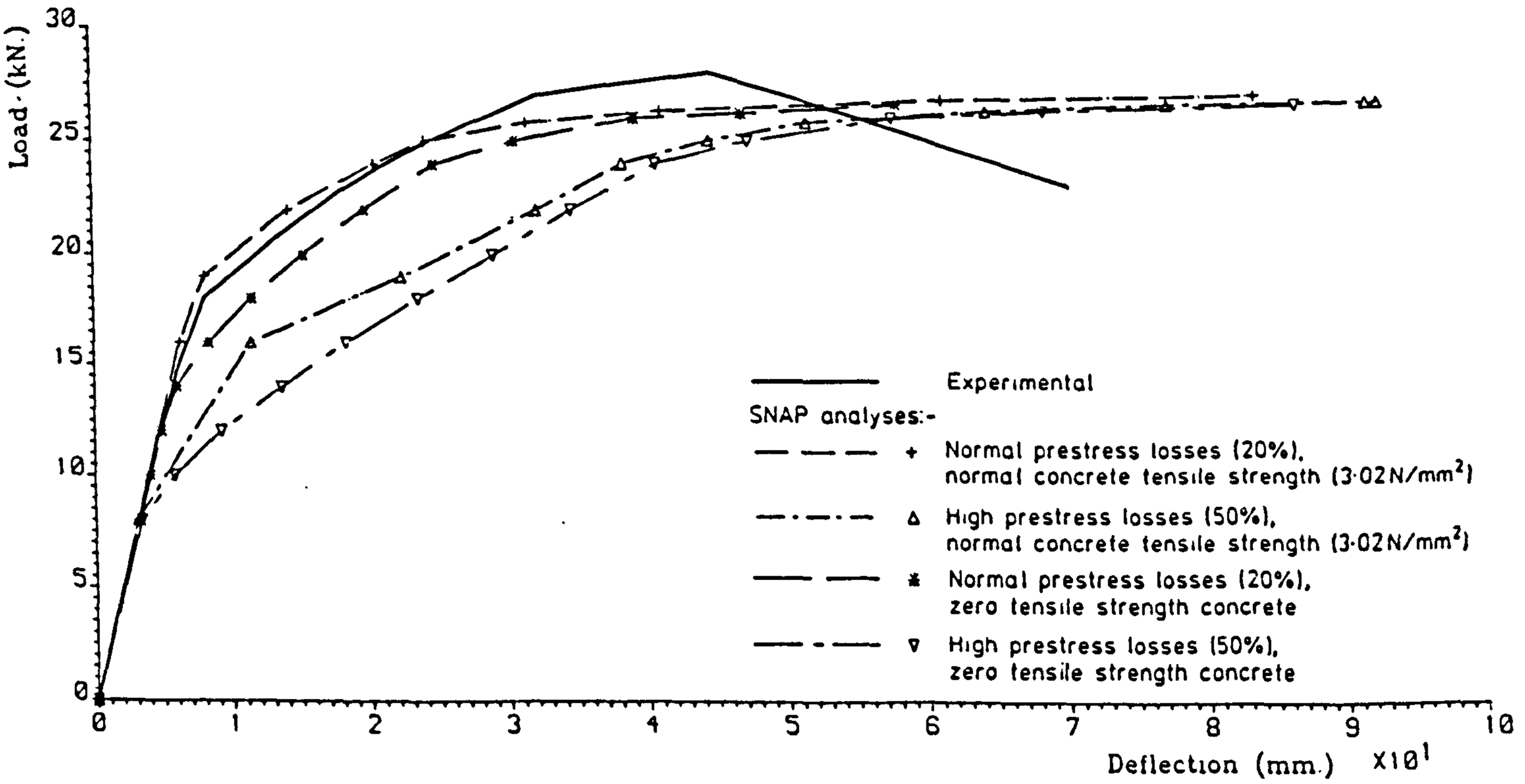

FIG. 9 13. LOAD-DEFLECTION RESPONSES FOR 'SNAP' ANALYSES OF MODEL 1 LONGITUDINAL SECTION

unload which results in the closing of cracks and steel unloading. There is some strain localisation in the near constant moment zone. However, the presence and location of this localisation appears to result, primarily, from the type of iteration procedure and the path it takes to achieve convergence. The lower prestressing steel has ruptured at point C on the curve.

The concrete statistical property descripters used for the second response curve shown in Figure 9.14(i) were derived from the data presented in Chapter 5 Section 5.1.1. Thus, the insitu concrete was assigned a standard error of 0.05 and the precast concrete 0.12. Extensive material test data for the steel materials was not available. However, the available test data, in conjunction with manufacturers published material data, was used to obtain a standard error of 0.02 for all steel materials.

Until point D on the response curve was reached the statistically varied properties had little effect upon the structural behaviour. At point D the top layer of insitu concrete at one set of integration stations in the near constant moment zone began to crush. Simultaneously, other sets of integration stations in the near constant moment zone began to unload. Thus, the strain field began to localise. This localisation was primarily due to the statistically varied properties resulting in a limited range of section strengths and not upon the iteration procedure or convergence path. Past point D the localisation effect increases until at point E the lower prestressing steel at the failing section begins to rupture. At point F the lower prestressing steel at the failing section has ruptured completely and the residual section strength is dependent upon the remaining prestressing and reinforcing steel in the section.

The rupture of the steel, in the statistically varied analysis, at a significantly lower displacement level can be explained if the effects of strain localisation are looked at in detail. After the onset of localisation at point D, the sections away from the failing section were effectively rigid, if not unloading, for extra increments of displacement. Therefore, the increments of displacement past point D were accommodated completely by increases in strain at the failing section. Thus causing the rupture of the lower prestressing steel at a lower displacement level. Three points should be noted, firstly, if advantage had been taken of symmetry, then a significantly different response would have been obtained. Secondly, the maximum load attained was virtually unaffected by the adoption of the statistically varied properties. Finally, if the falling branches of the steel stress-strain curves were made steeper then it is possible that a 'snap back' situation could occur.

9.2.2.3 Load-Deflection Response with inverted loading

In Figure 9.14(ii) the analytical response of the longitudinal section to inverted loading is shown. This response curve was obtained with uniform material properties throughout the structure. It can be seen that the strength of the section in hogging is only approximately 40% of that in sagging. Furthermore, it will be noticed that the section has limited ductility in hogging, with the maximum load being reached at a displacement of only 40 mm.

Generally the load-deflection response follows a typical pattern until point B is reached. However, there is a 'bump' at point A and this is most probably caused by the propagation of cracking to areas outside the near constant moment zone. The drop in load adjacent to point A resulted in the program switching from load control to displacement control so that convergence could be achieved. Under both load

control and displacement control a 1% scaled force convergence criterion was applied. Between points B and C, both types of top reinforcement ruptured causing a sudden decrease in applied load. Both the beam top reinforcement and the reinforcement located above the beams in the insitu concrete are nominally 'mild steel'. A gradual reduction in applied load occurs between points C and D. This reduction is the result of both the concrete and prestressing steel progressing further along their appropriate stress-strain curves. Between points D and E, concrete crushing occurs in the bottom layer of the precast beam, reducing the lever arm and hence causing the load to drop off further. It was not considered necessary to continue the analysis beyond point E.

9.2.3 Model 1 Transverse Section

9.2.3.1 Finite Element Idealisation

The transverse section incorporated 20 precast beam segments, each 440 mm long and positioned transversely across the span (see Appendix 5.2). In the model bridge deck the lower transverse steel is oriented at 65° to the beam axes. In the transverse section it was, through necessity, located at 90°. It was felt that this minor change would not have a significant effect upon the behaviour.

The structural configuration, finite element mesh and loading regime for the SNAP analysis can be seen in Figure 9.15. The effects of three different through depth integration schemes were investigated. The three schemes were (i) the section treated as a homogeneous and isotropic reinforced concrete section, thus the presence of the beams was ignored; (ii) the beams were assumed to be 1 dimensional entities and the appropriate integration scheme from the previous section was

(i) Comparison of load-deflection responses for model 1 longitudinal section.

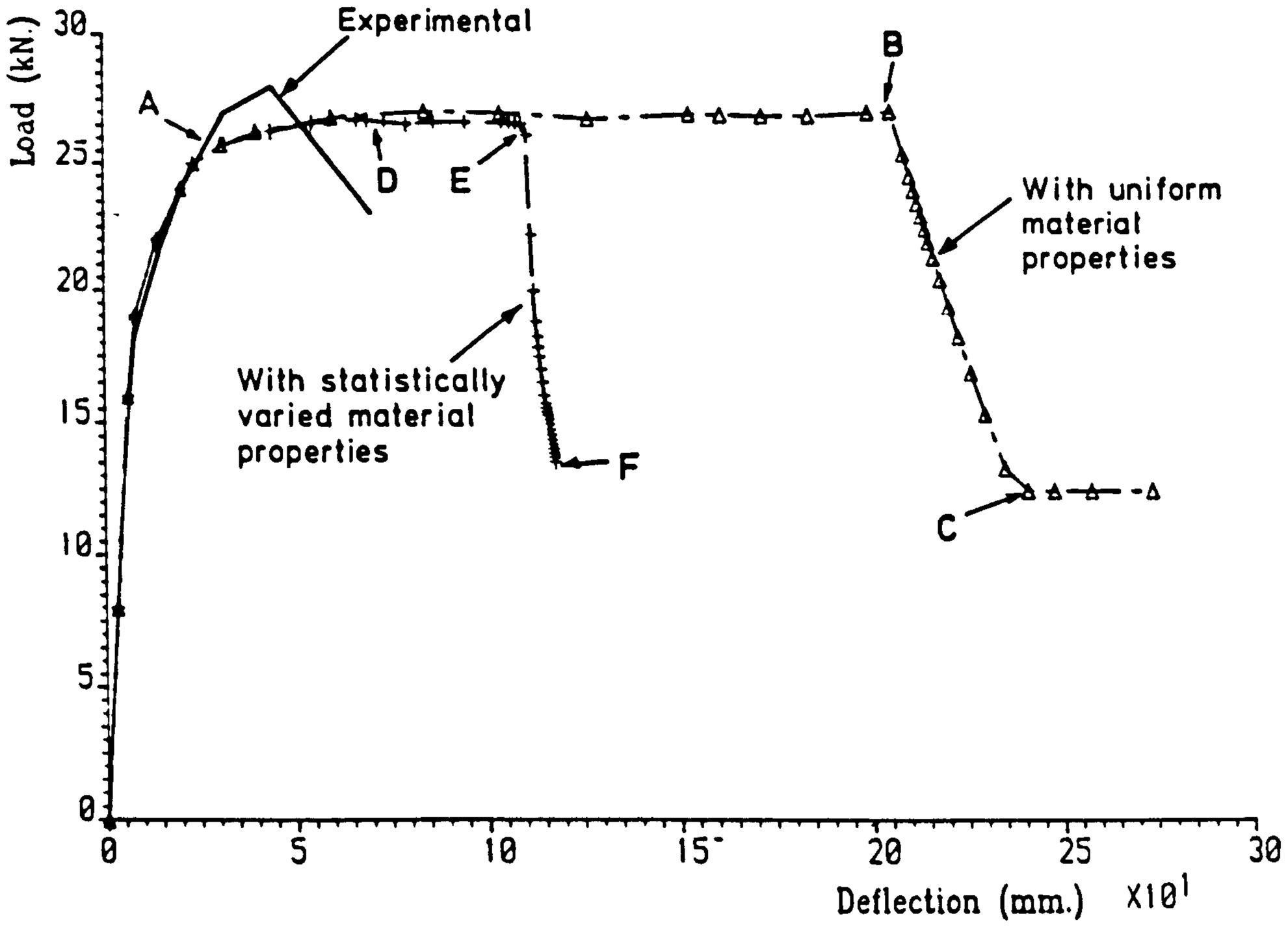

(ii) Analytical response of model 1 longitudinal section to inverted loading

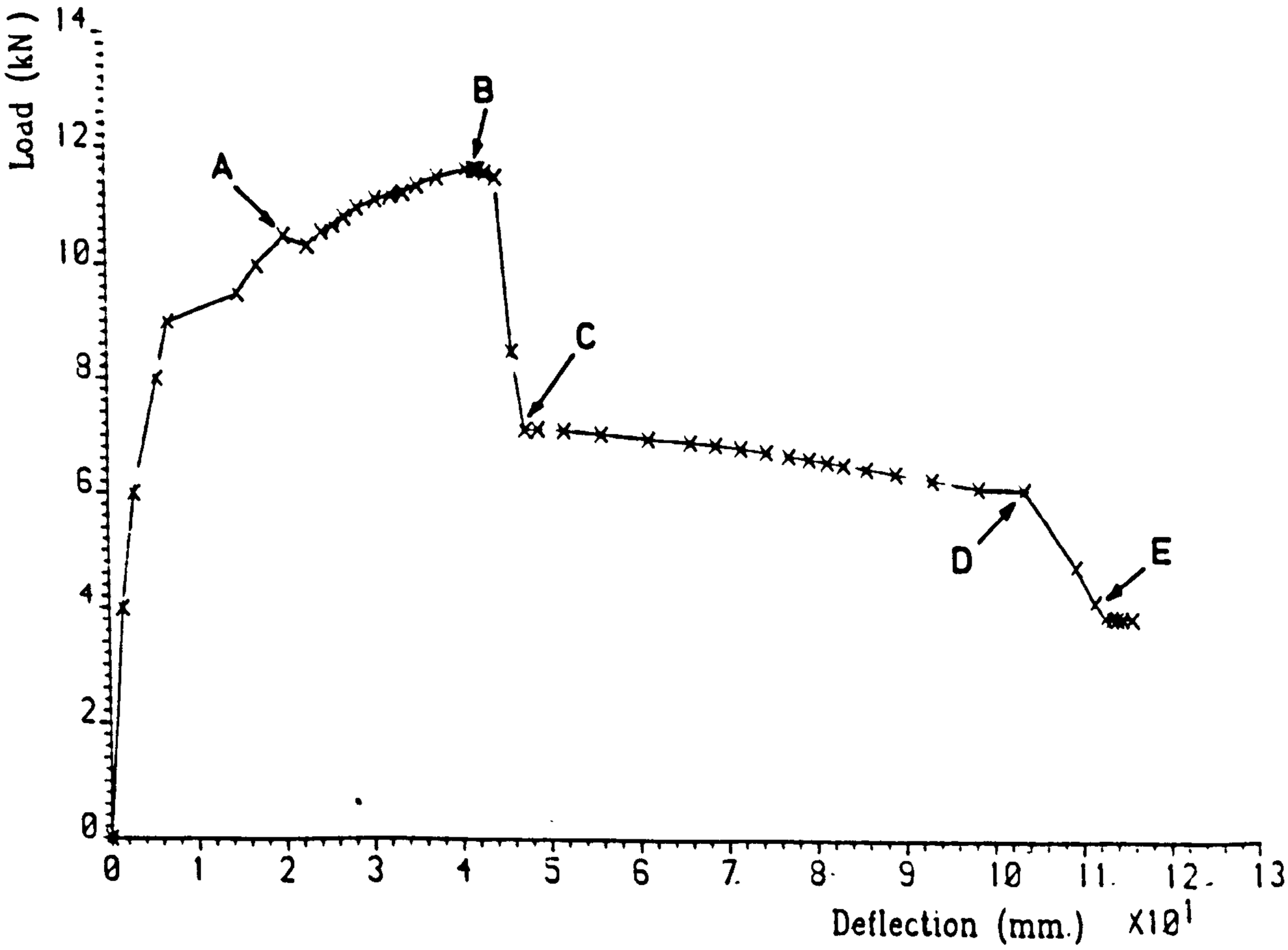

FIG. 9.14. FULL RANGE LOAD-DEFLECTION RESPONSES FOR 'SNAP' ANALYSES OF MODEL 1 LONGITUDINAL SECTION.

selected; (iii) the beams were treated as 2 dimensional entities and again the appropriate integration scheme from the previous section was selected.

Identical material properties and curves were used for the transverse section as were used for the longitudinal section analyses in the previous section.

9.2.3.2 Load-Deflection Response

The effects upon the load-deflection response of two material parameters, f_t - the tensile strength and α_2 - the tension stiffening parameter, were investigated and the resulting responses can be seen in Figure 9.16. The best agreement with the experimental curve is obtained with a tensile strength, f_t, equal to 75% of the values obtained from tests and a tension stiffening factor of 25. The interface between the precast and insitu concretes could be responsible for the reduced effective tensile strength. The load-deflection response follows the classical reinforced concrete load-deflection response with the onset of cracking at point A. The cracks propagate as the response proceeds towards point B. At point B the lower transverse steel begins to yield leading to a plateau in the response after this point. The load-deflection responses that result from different tensile strengths and the tension stiffening factors are also shown in Figure 9.16. It should be noted that the strain levels which define the tension stiffening curve are dependent upon both the tensile strength and the tension stiffening factor. Therefore, variations in either of these factors will result in a different tension stiffening curve, see Chapter 8 Section 8.4.

Figure 9.17(i) shows the responses that result from the use of different approaches for modelling the precast beams. They are:-

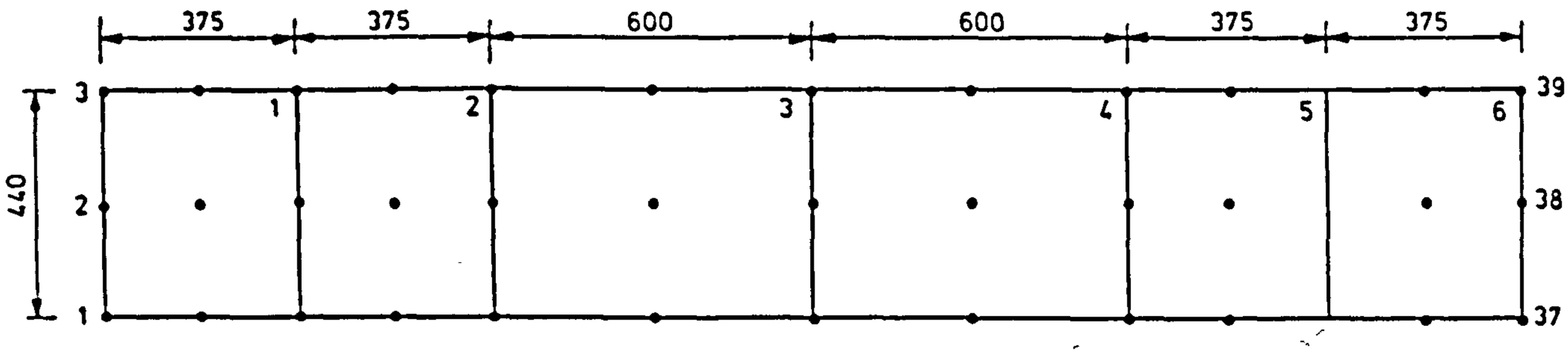

w = 0
at 1 & 3

Finite element mesh used for Model 1 transverse sections

w = 0
at 37 & 39

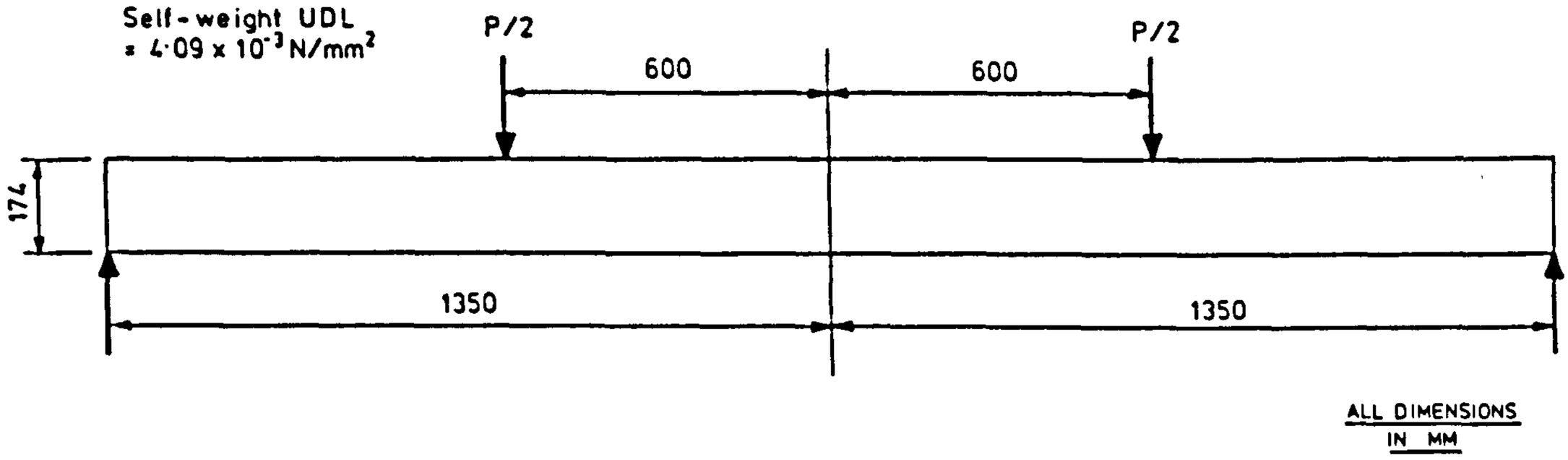

ALL DIMENSIONS
IN MM

FIG. 9. 15. FINITE ELEMENT IDEALISATION OF MODEL 1 TRANSVERSE SECTION

Comparison of load–deflection responses for model 1 transverse section.

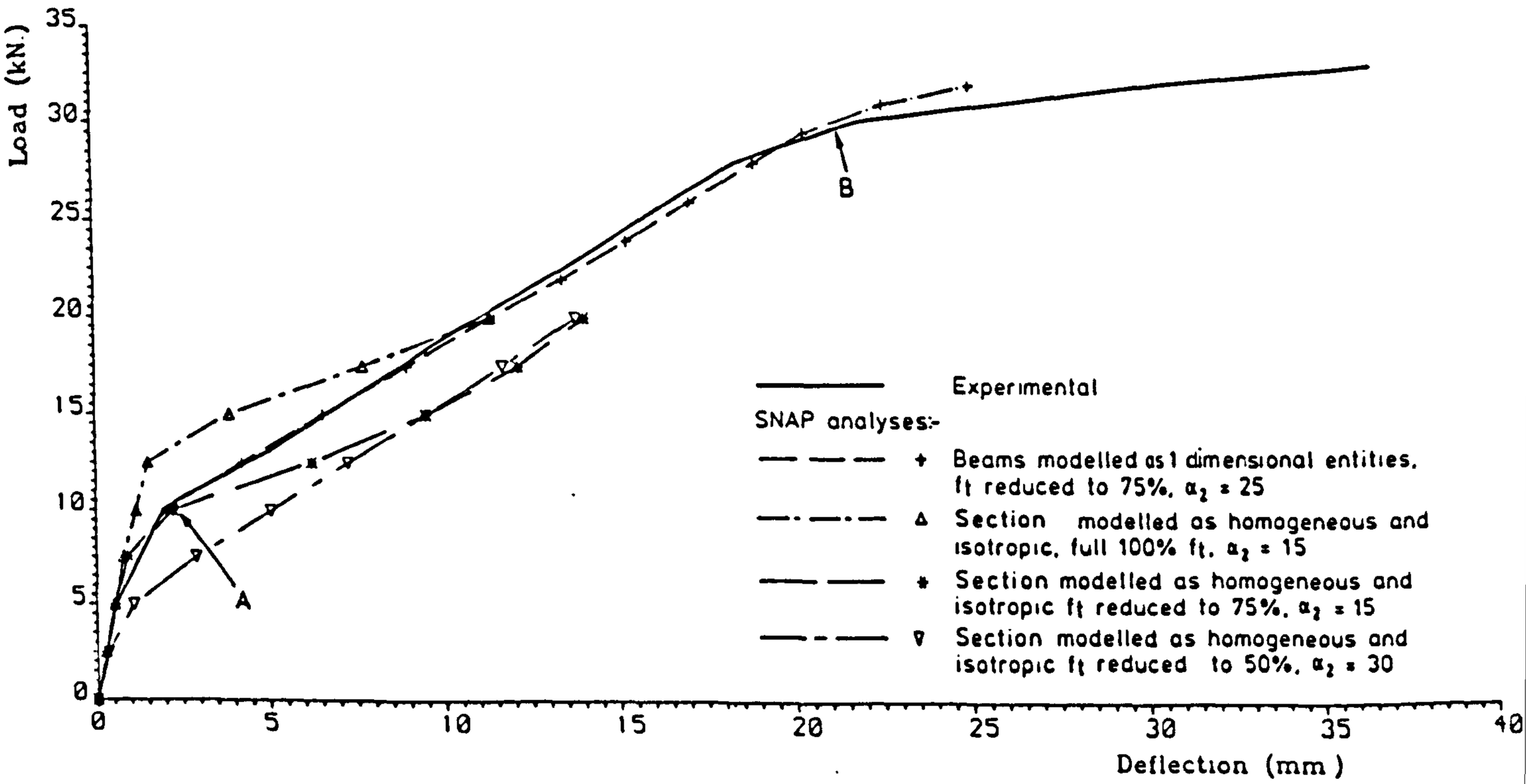

FIG. 9 16. LOAD-DEFLECTION RESPONSES FOR 'SNAP' ANALYSES OF MODEL 1 TRANSVERSE SECTION

1. Section treated as homogeneous and isotropic, ie the presence of the beams is ignored and the section is treated as reinforced concrete.
2. The beams are treated as 1 dimensional entities.
3. The beams are treated as 2 dimensional entities.

Modelling philosophies 1 and 2 result in almost identical responses. This is to be expected since the same through depth integration scheme is used in the transverse direction. The difference between the two modelling philosophies lies in the integration scheme used in the longitudinal direction, that is in the beam direction. Modelling philosophy 3 results in very similar response to that of the other two philosophies up until yielding of the steel. In the post-yielding region modelling philosophy 3 results in a lower failure load. With modelling philosophy 3, ten through depth integration stations, 5 in beams and 5 in the insitu concrete, are used in the transverse direction. In the other two philosophies, only 5 through depth integration stations are used in the transverse direction. In the post-yielding region, the response if governed mainly by the steel behaviour and the lever arm. The size of the lever arm is affected by the form of the concrete compression block. With the 10 through depth integration stations of modelling philosophy 3, the compression block extends further down the section, thus reducing the effective lever arm.

Figure 9.17(ii) illustrates the full range analytical response of the transverse section. For this analysis the precast beams were modelled as 2 dimensional entities. At point A on the response curve, the top layer of the insitu concrete is beginning to crush. The compressive load is then transferred to the top integration station in the beams,

(i) Comparison of load-deflection responses for model 1 transverse section.

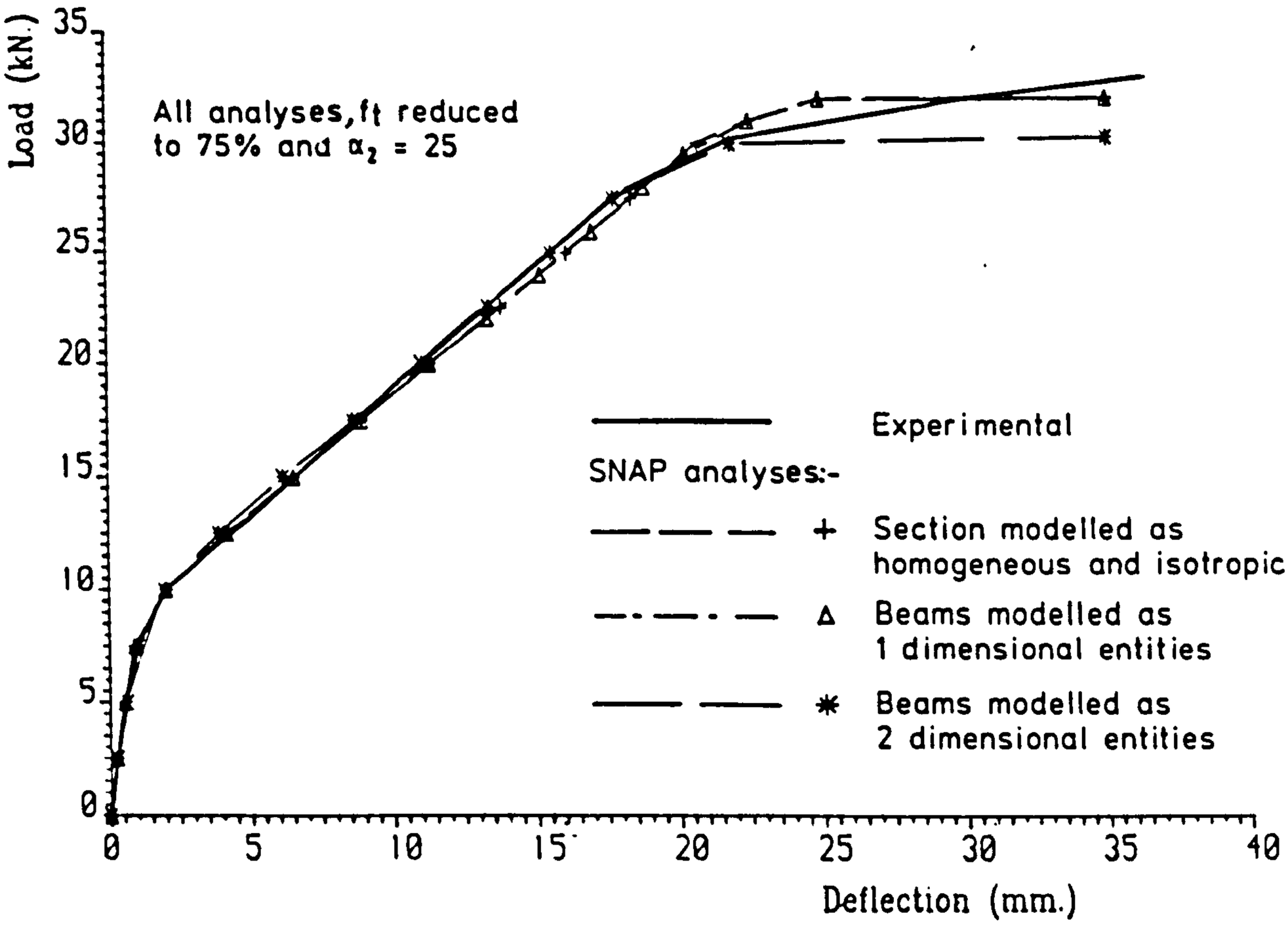

(ii) Comparison of load-deflection responses for model 1 transverse section.

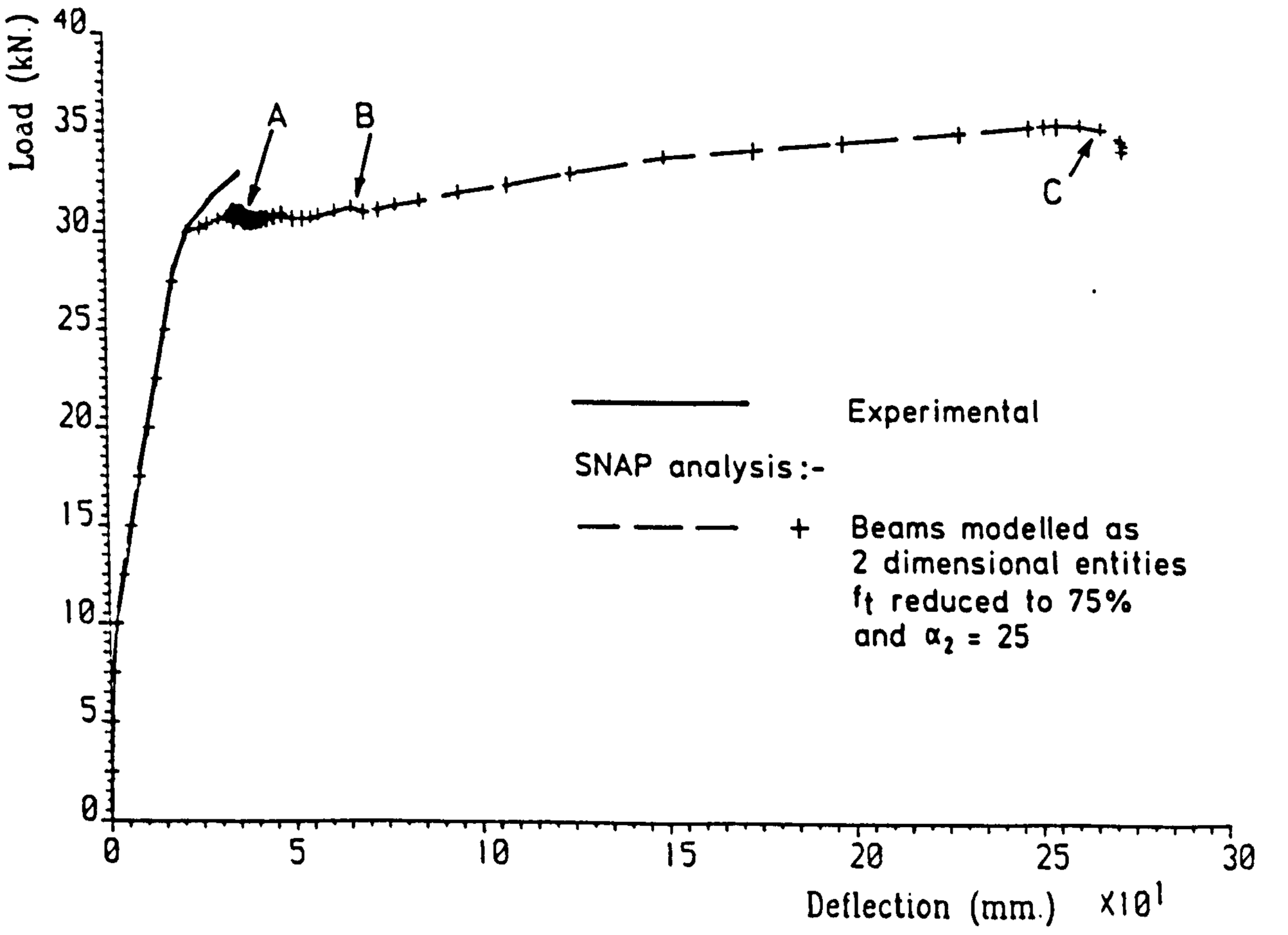

FIG. 9. 17. LOAD-DEFLECTION RESPONSES FOR 'SNAP' ANALYSES OF MODEL 1 TRANSVERSE SECTION

which is just below the failing station. Simultaneously, the steel materials are progressing along their appropriate stress-strain curves. These factors caused the analysis program severe difficulties at this point and numerous small increments were required to obtain converged solutions. By point B, the analysis has again become relatively stable, with the majority of the material property changes being concentrated around the lower reinforcing steel. At point C, rupture of the lower reinforcing steel begins and complete failure of the section ensues.

9.2.4 Model 2 Longitudinal Section

9.2.4.1 Finite Element Idealisation

Details of the structural configuration, finite element mesh and the loading arrangement can be seen in Figure 9.18. Advantage could not be made of symmetry, since it was intended to carry out analyses with statistically varied material properties. Fixed vertical restraints were applied at each of the four corner nodes.

A through depth integration scheme, similar to that of model 1, was formulated for model 2. Again, 5 integration stations were used for both the beam and the insitu concretes. Full details of the Model 2 through depth integration scheme can be seen in Tables 9.9 and 9.10 and Figures 9.19 and 9.20.

Details of the model 2 longitudinal section concrete material curves can be seen in Figure 9.21. Details of the material curves used for the steel prestressing and reinforcement can be found in Section 9.3, on the SNAP analyses of model deck 2.

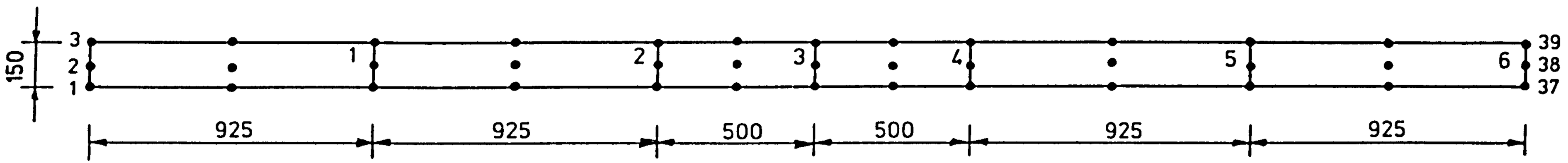

w = 0
at 1 & 3

Finite element mesh used for Model 2 longitudinal sections

w = 0
at 37 & 39

Self-weight UDL
$= 5{\cdot}98 \times 10^{-3} N/mm^2$

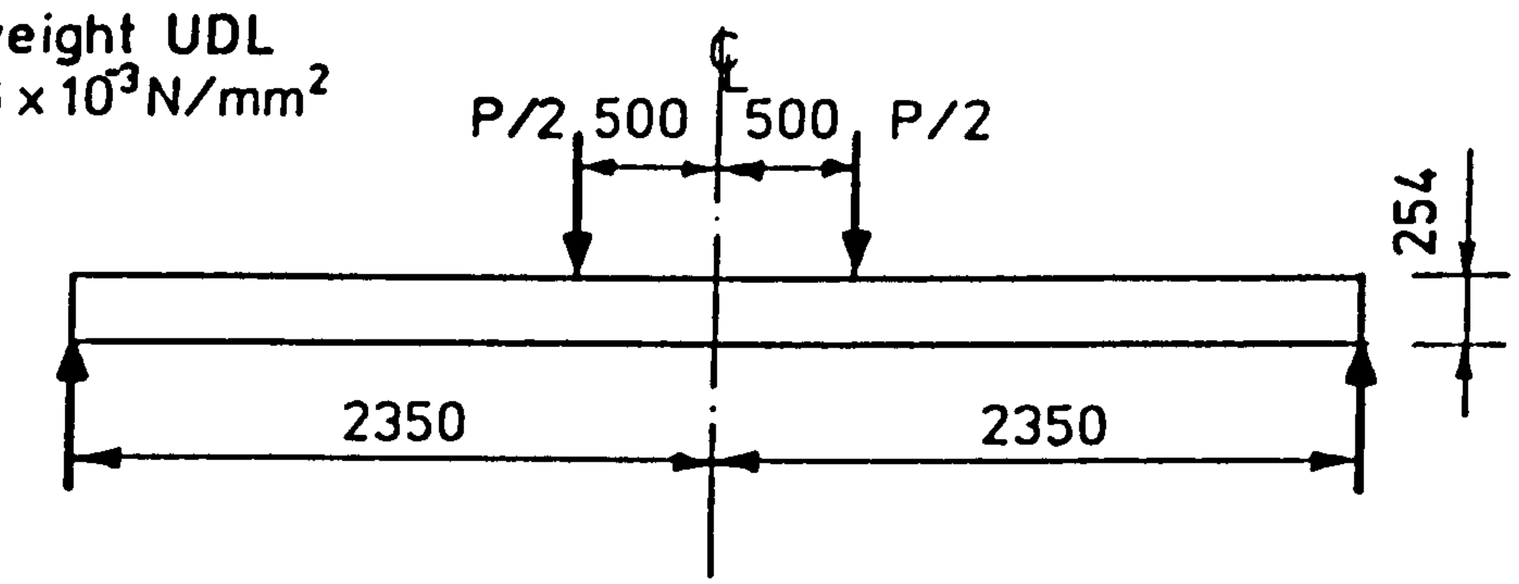

Analysed test loading

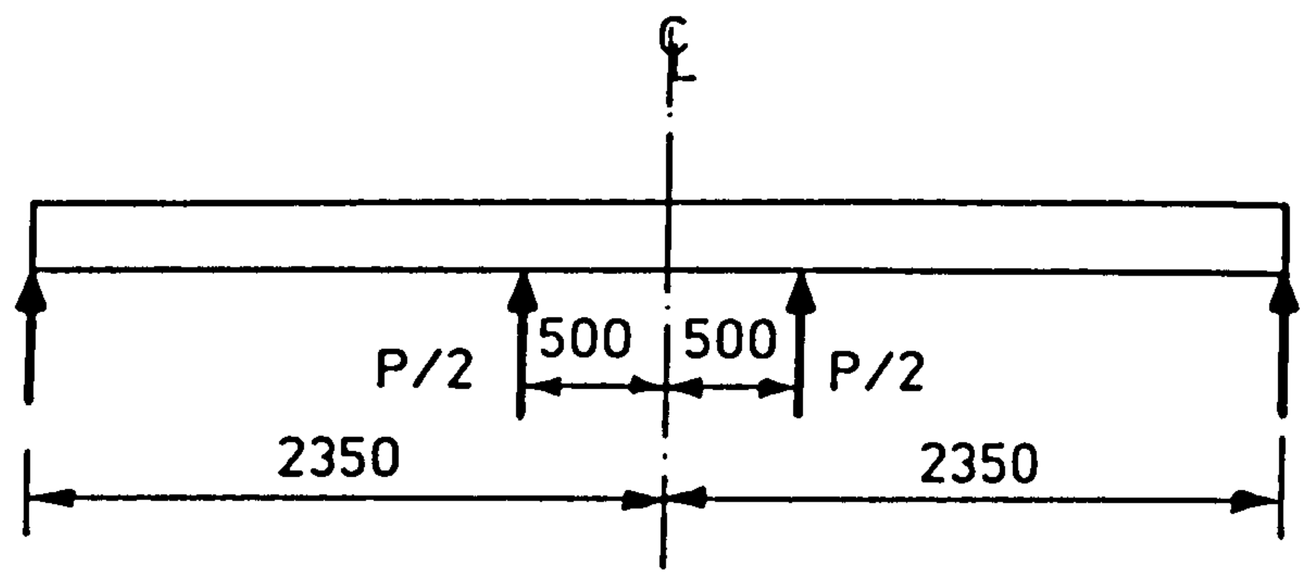

Analysed with inverted loading

ALL DIMENSIONS
IN mm

FIG. 9. 18. FINITE ELEMENT IDEALISATION OF MODEL 2 LONGITUDINAL SECTION

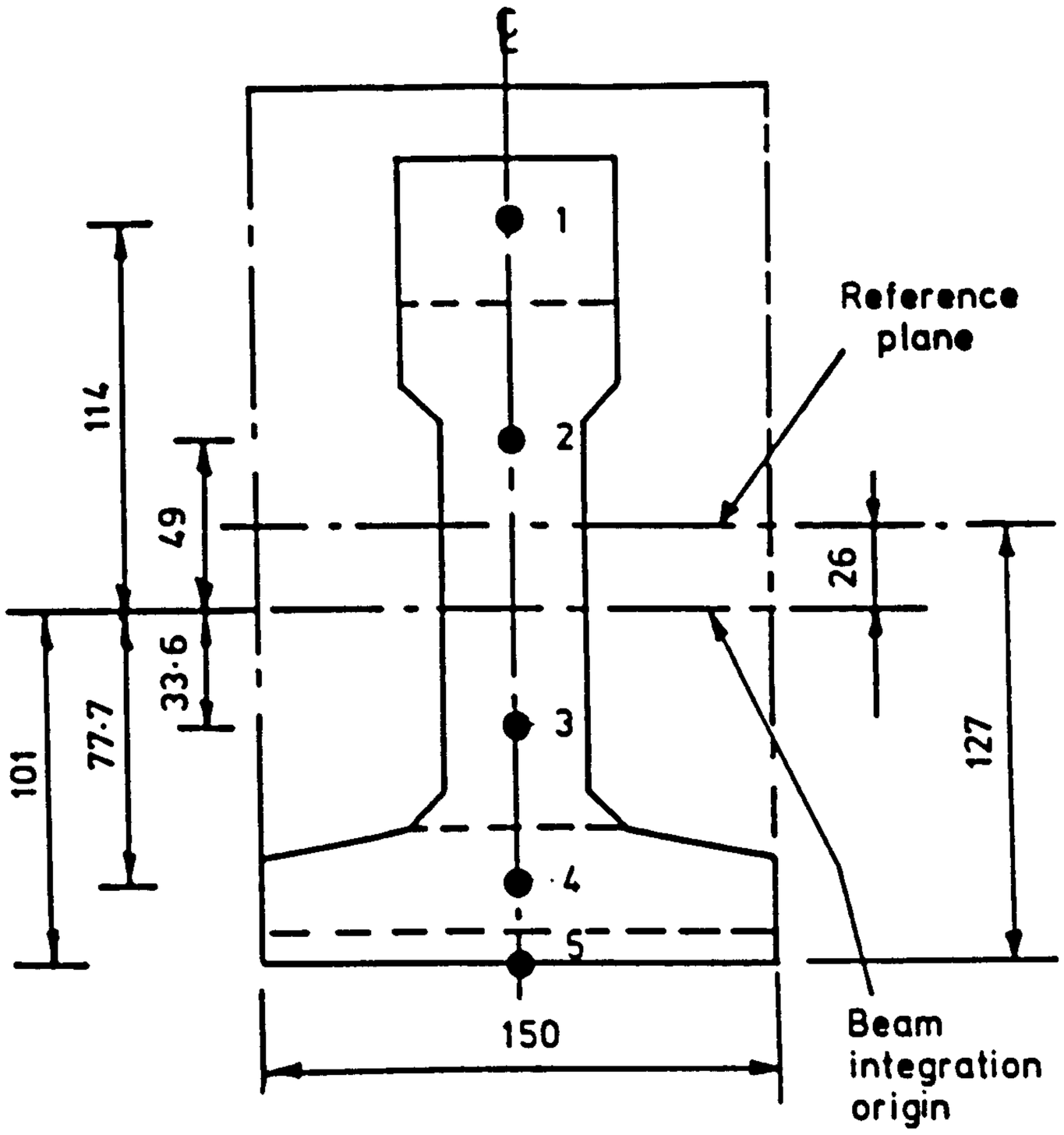

FIG. 9. 19 BEAM INTEGRATION STATIONS FOR MODEL 2 NON-LINEAR ANALYSES

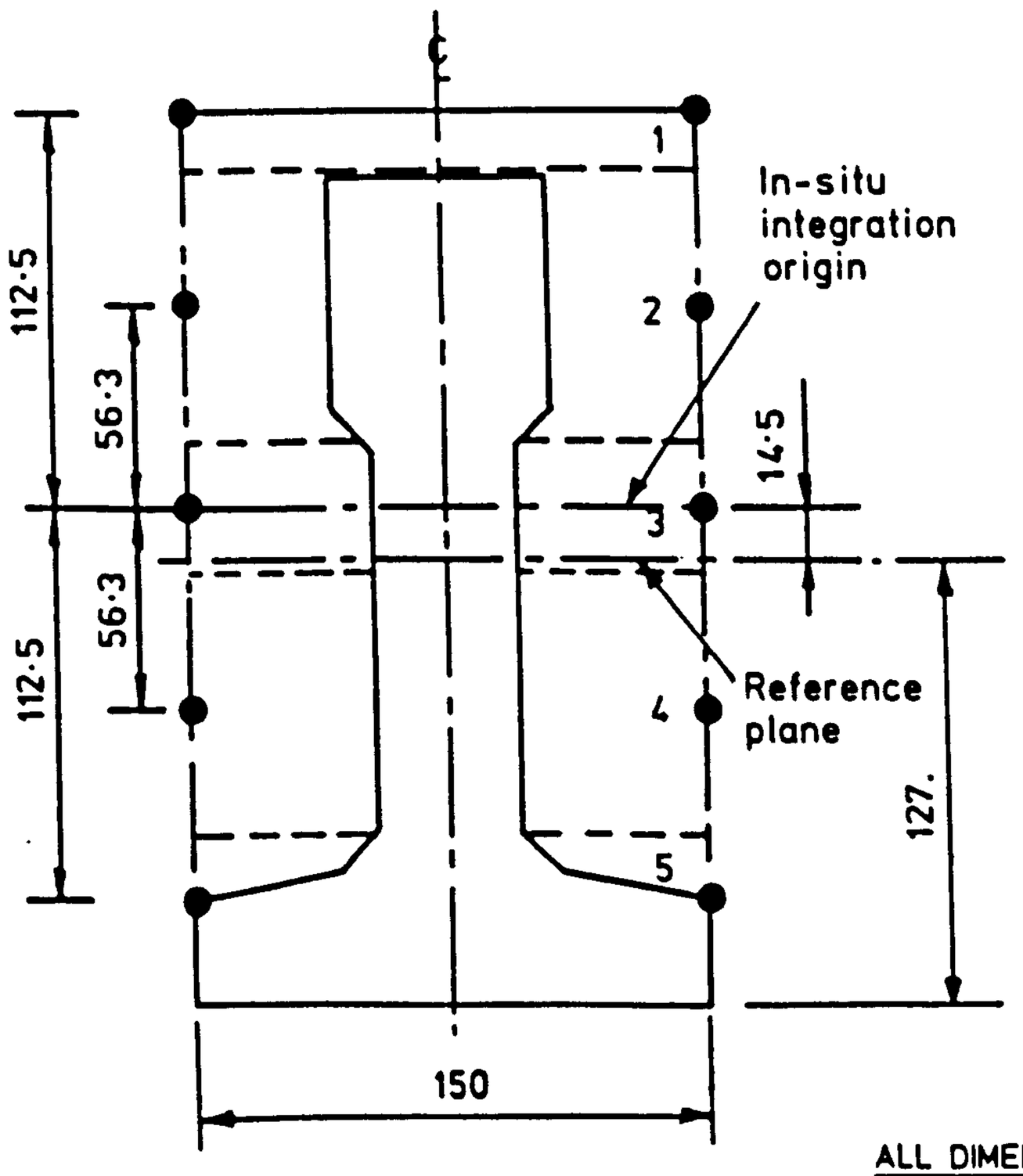

ALL DIMENSIONS IN MM

FIG. 9. 20. IN-SITU INTEGRATION STATIONS FOR MODEL 2 NON-LINEAR ANALYSES

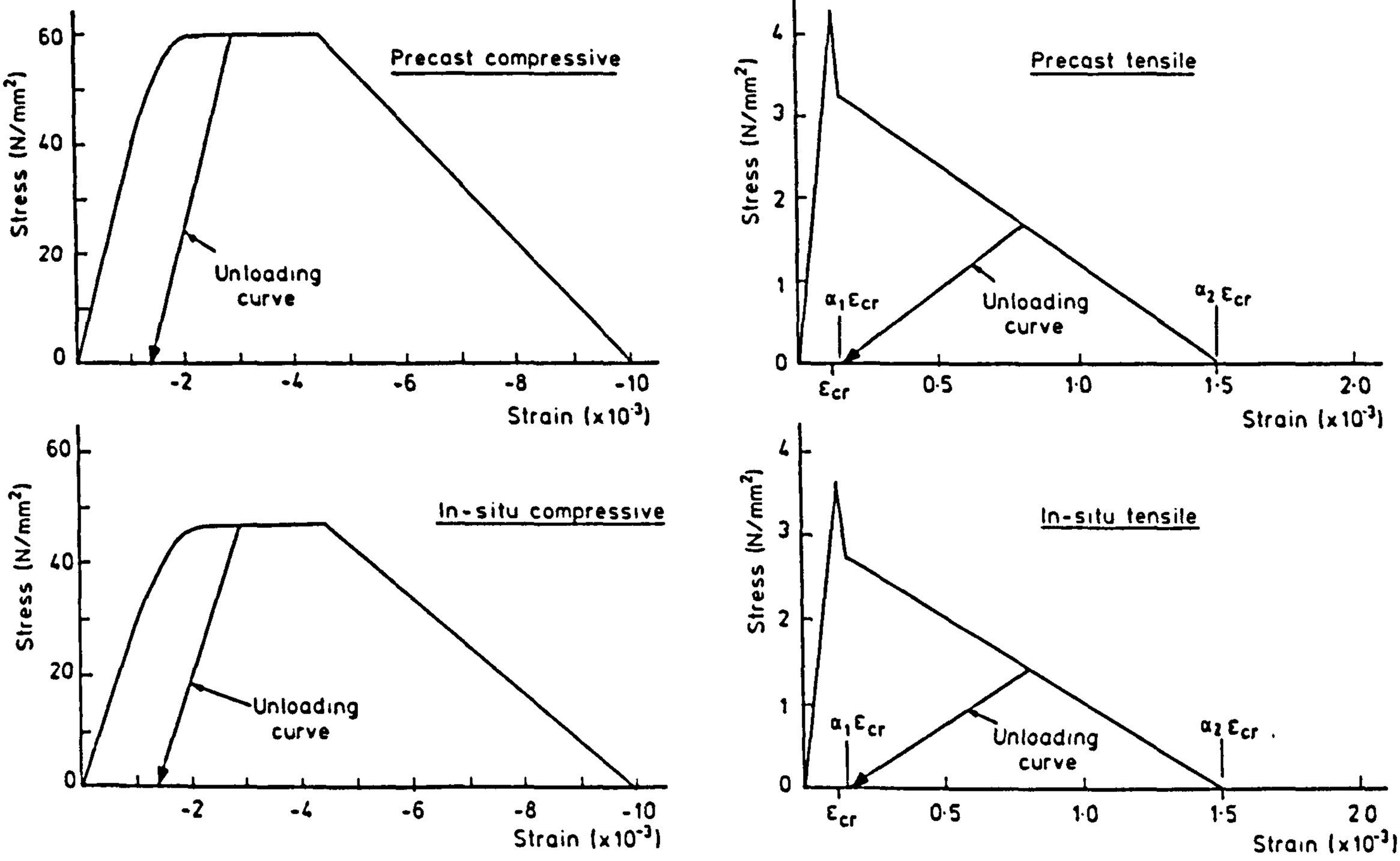

FIG. 9. 21. CONCRETE MATERIAL CURVES FOR MODEL 2 LONGITUDINAL SECTION

Comparison of load-deflection responses for model 2 longitudinal section.

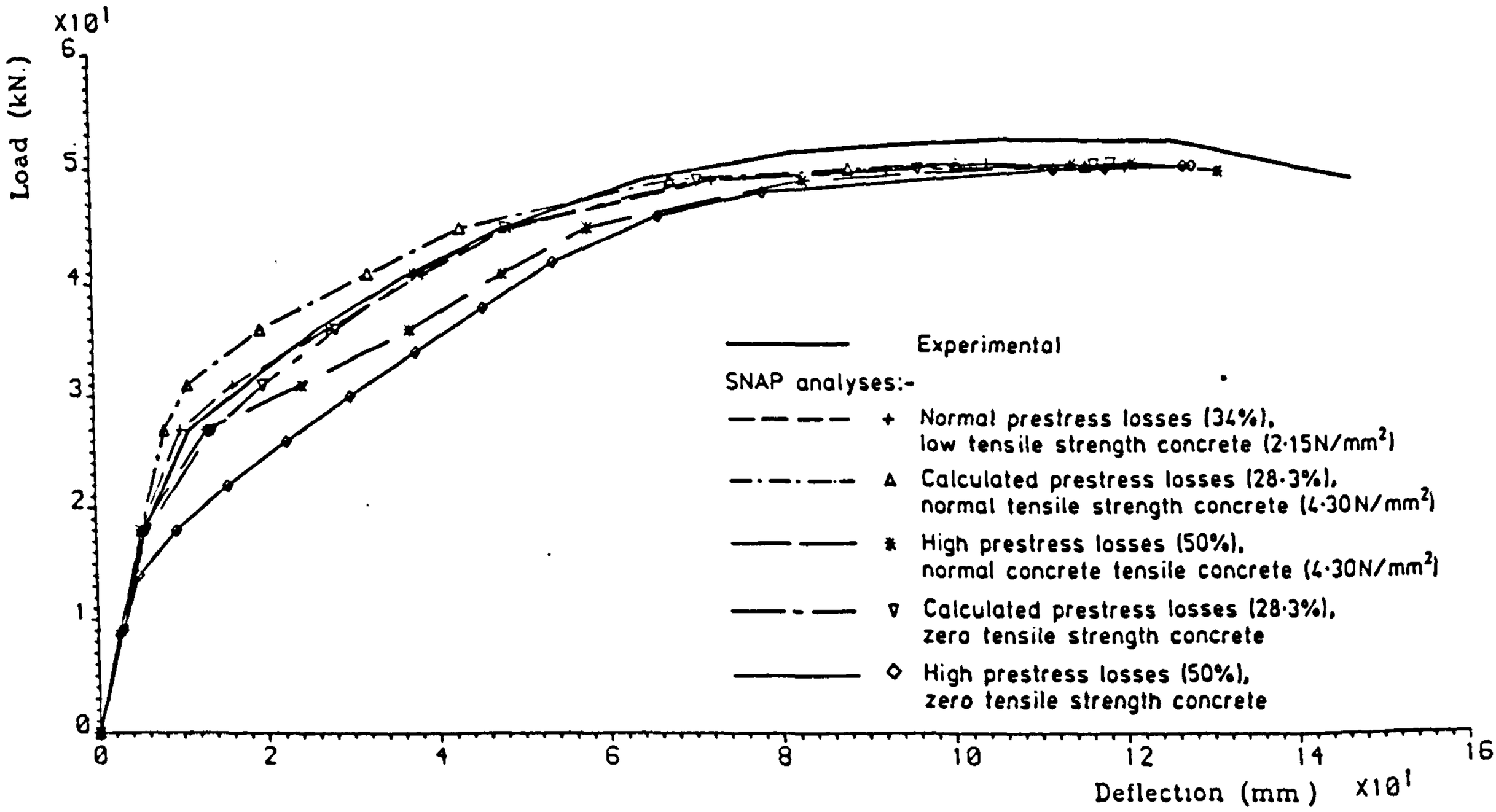

FIG. 9. 22. LOAD-DEFLECTION RESPONSES FOR 'SNAP' ANALYSES OF MODEL 2 LONGITUDINAL SECTION

Integration station	Distance from insitu centre line (mm)	Weight (mm)	
		X' direction	Y' direction
1	112.5	17.51	17.51
2	56.25	49.10	79.99
3	0.0	22.01	30.02
4	-56.25	58.66	79.99
5	-112.5	10.28	17.51

Note: The directions X' and Y' refer to beam local coordinate space

TABLE 9.9 INSITU INTEGRATION DISTANCES AND WEIGHTS FOR MODEL 2 NON-LINEAR ANALYSES

Integration station	Distance from beam NA (mm)	Weight (mm)
1	114.2	18.06
2	49.0	27.77
3	-33.6	17.20
4	-77.7	24.72
5	-101.0	9.47

TABLE 9.10 BEAM INTEGRATION DISTANCES AND WEIGHTS FOR MODEL 2 NON-LINEAR ANALYSES

9.2.4.2 Load-Deflection Response with normal loading

Figure 9.22 illustrates the load-deflection responses that resulted from the normal loading analyses. It was found that good agreement with the experimental response was achieved with a concrete tensile strength equal to half that obtained from specimen tests. No reliable data on the actual experimental prestress in model 2 was available, for the reasons given in Chapter 7. Hence, it is not possible to say

how the analytical prestress loss of 34% compares with that of the experiment. The prestress loss was calculated to be approximately 28% and it can be seen that this agrees well with the analytical loss of 34%.

Figure 9.23(i) illustrates the full range response that was obtained with both uniform material properties and also statistically varied material properties. In the uniform material property analysis, the onset of cracking was at a load of approximately 25kN and the onset of steel yielding was at a load of 45 kN. Steel yielding is well progressed at point A, when the top layer of insitu concrete begins to crush. As the concrete crushes, there is a resulting drop off in the applied load. At point B rupture of the lower prestressing steel begins and at point C the rupture of the steel is complete. After point C, the residual section strength is dependent upon the remaining steel which is higher up the section.

The third curve in Figure 9.23(i) gives the statistically varied material property response. It can be seen that this curve is in good agreement with the uniform material property curve until point D is reached. At point D, major strain localisation begins and this is quickly followed by crushing of the top layer of insitu concrete at the weakest section. At point E on the response curve, the bottom prestressing steel is beginning of proceed down the falling branch of the steel stress-strain curve, leading to rupture of the steel.

9.2.4.3 Load-Deflection Response with inverted loading

The analytical response of the model 2 longitudinal section to inverted loading is shown in Figure 9.23(ii). This response curve was obtained with uniform material properties throughout the structure. It can be seen that the section strength in hogging is only about 40% of

that in sagging. In contrast to model 1, the model 2 section exhibits a high degree of ductility in hogging. This can be accounted for by the presence of 'Torbar' high yield reinforcement in the top of the section rather than the low ductility 'mild steel' that was present in model 1.

9.3 Model deck analyses

9.3.1 Introduction

This section will deal with the analyses of the model decks that were carried out using the SNAP program. The experimental data collected during the model tests will be used for comparison with the analytical results. Deflection profiles, reaction linearity and reaction profiles have been selected for detailed comparison. These three parameters were chosen for their fundamental importance to the structural behaviour.

Detailed descriptions of the formulations and algorithms that have been incorporated into the SNAP program have been given in Chapter 8. In this section the effect of selecting or varying different parameters and algorithms will be explored. The SNAP analytical models deviate only slightly from the physical models described in Volume 1. In the physical models the UDL loading was not applied within a distance equal to one overall depth from each support line. In the analytical models the UDL loading continues as far as the support line. This was necessary since it was not possible, with the SNAP program, to apply a UDL loading to part of an element. This should not have a significant effect since this extra loading should only result in a small near uniform increase in the reactions. For model 2 a uniform mesh spacing was employed. Therefore there is a slight difference in the width of the physical and analytical footpaths. This was compensated for by adjusting the UDL load

(i) Comparison of load-deflection responses for model 2 longitudinal section.

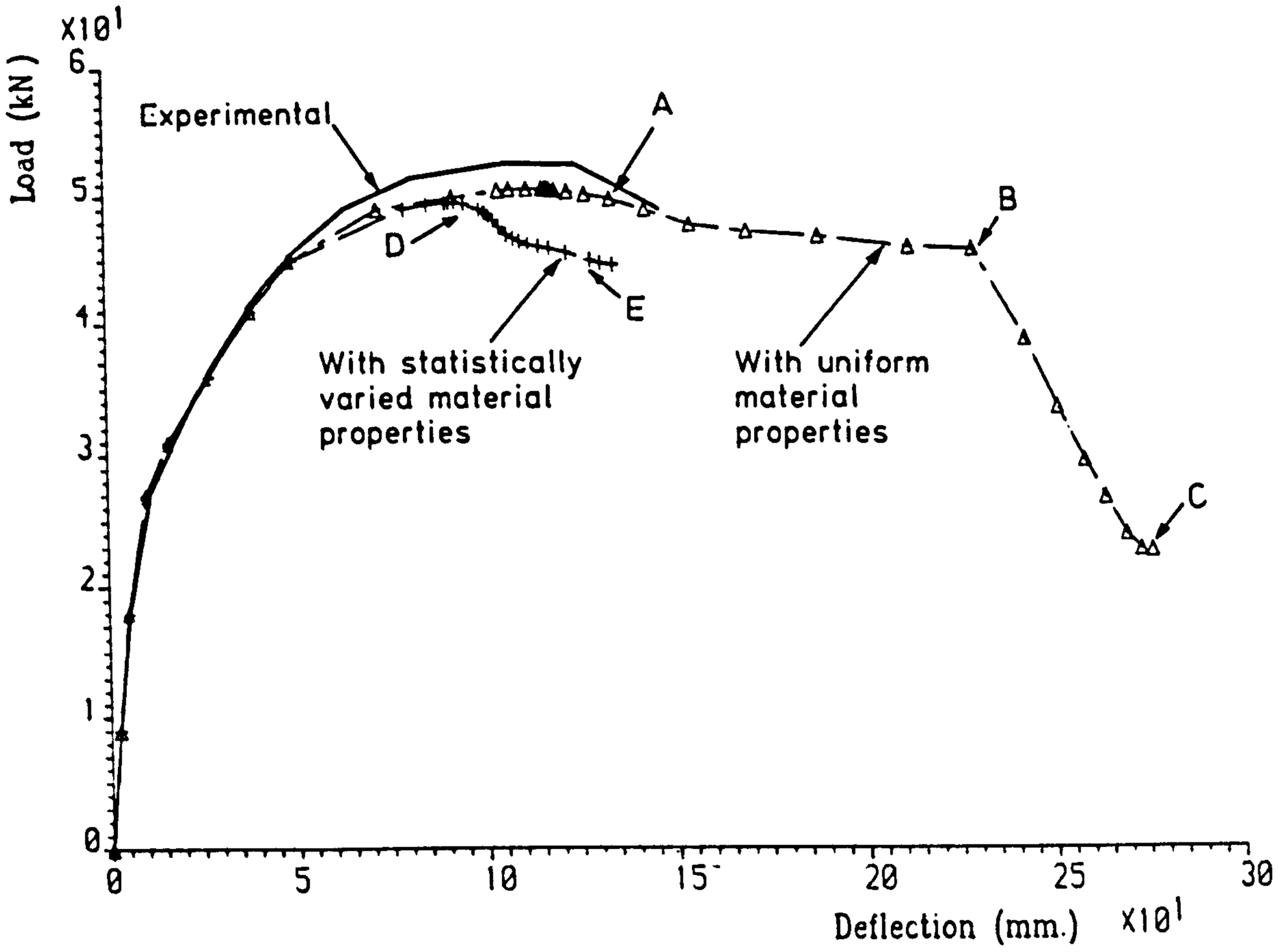

(ii) Response of model 2 longitudinal section to inverted loading.

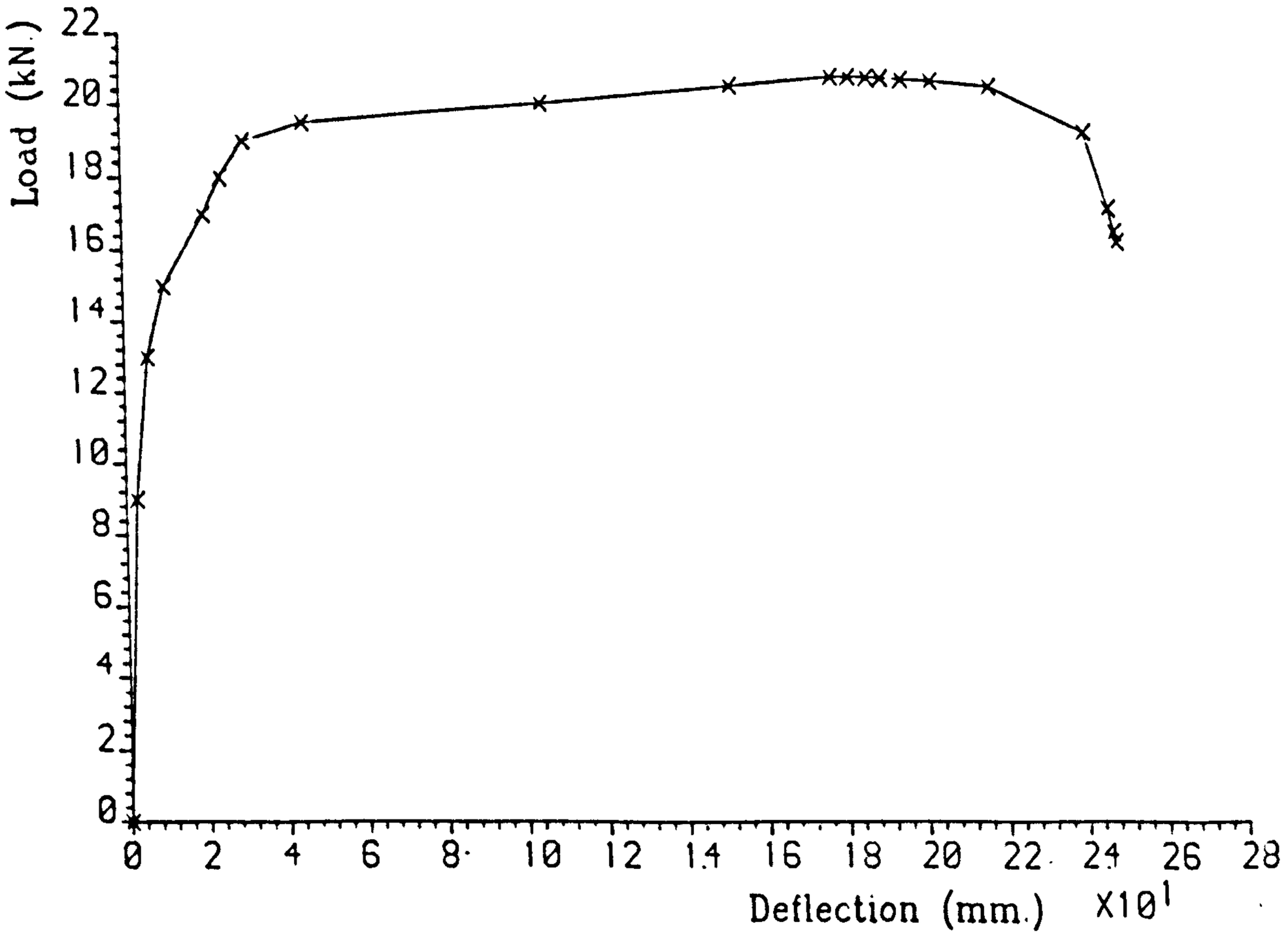

FIG. 9.23. FULL RANGE LOAD-DEFLECTION RESPONSES FOR 'SNAP' ANALYSES OF MODEL 2 LONGITUDINAL SECTION

intensities so that the same load was applied. Diagrams showing the layout of each analytical model can be seen in Figure 9.24 for model 1 and in Figure 9.25 for model 2.

The majority of these analyses were run on local and remote IBM machines using double precision (64 bit) arithmetic. Typically, a single full range analyses would require between 120 and 200 increments. A restart was generally carried out every 8 increments and thus each analysis required between 15 and 25 individual runs.

9.3.2 Finite element idealisation

9.3.2.1 Finite element meshes

The preliminary runs for each of the models was carried out using a 3 x 3 mesh of Heterosis elements. For all the detailed analysis an 8 x 6 mesh was used and a plot of this mesh can be seen in Figure 9.26 for model 1 and Figure 9.27 for model 2. It can be seen that each analytical model was divided uniformly into 8 elements along the length and 6 across the width. Details of the selected through depth integration scheme for model 1 can be seen in Table 9.7 and 9.8 and Figures 9.10 and 9.11. Details relevant to model 2 can be seen in Tables 9.9 and 9.10 and Figures 9.19 and 9.20.

Initially the effect of adopting either the bi-axial or uni-axial beam approach, as described in Chapter 8 Section 8.3.3, was investigated. It was discovered that the uni-axial approach resulted in considerably increased stiffness and failure loads far in excess of the experimental values. This was particularly true of the analyses of model 2. These features were a direct result of the way in which beam cracking and torsional stiffness were modelled. As described earlier, the high torsional strength that remained in the beams as the experimental failure load was approached, greatly enhanced the section

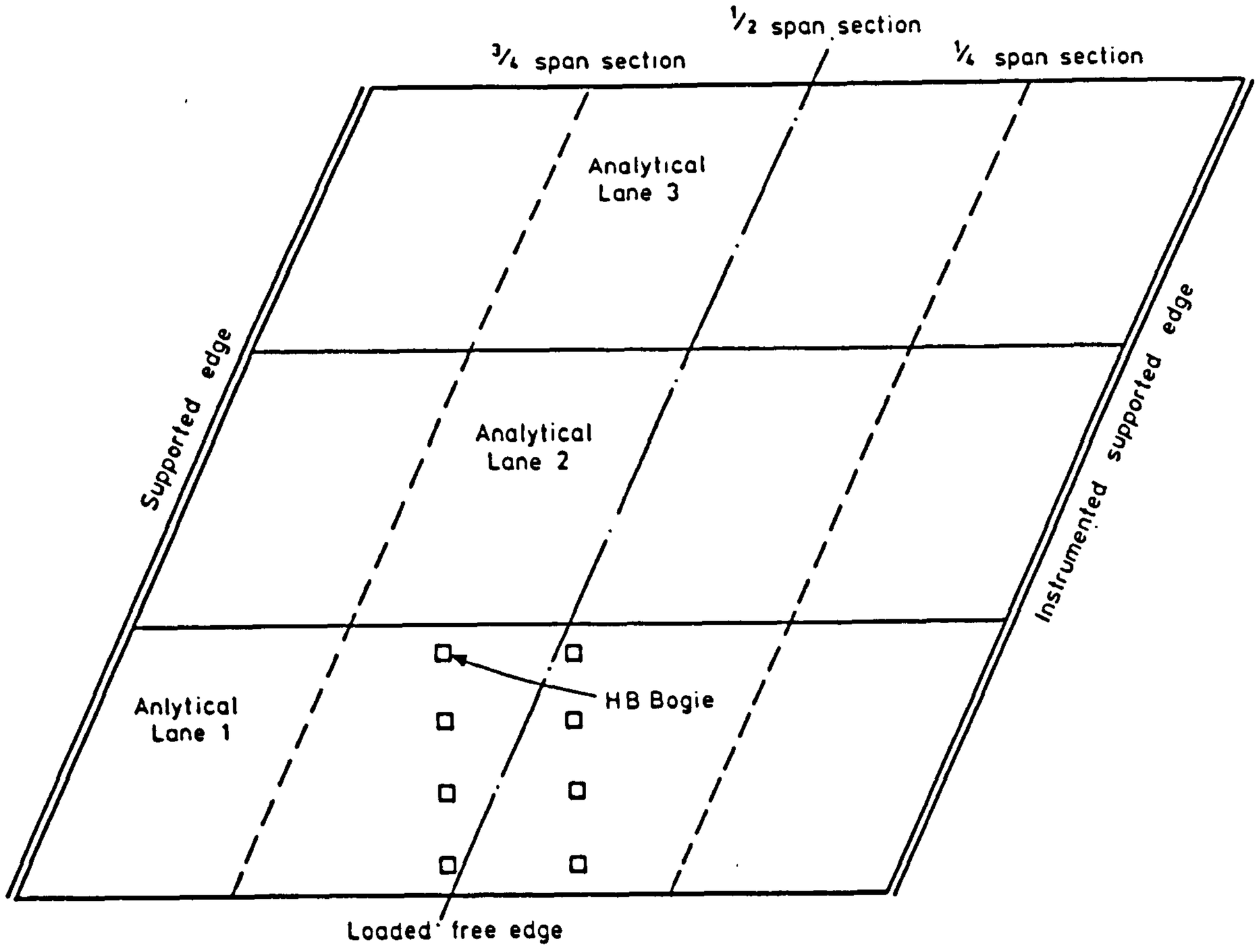

FIG. 9. 24 LAYOUT OF MODEL 1 FOR THE SNAP PROGRAM ANALYSES

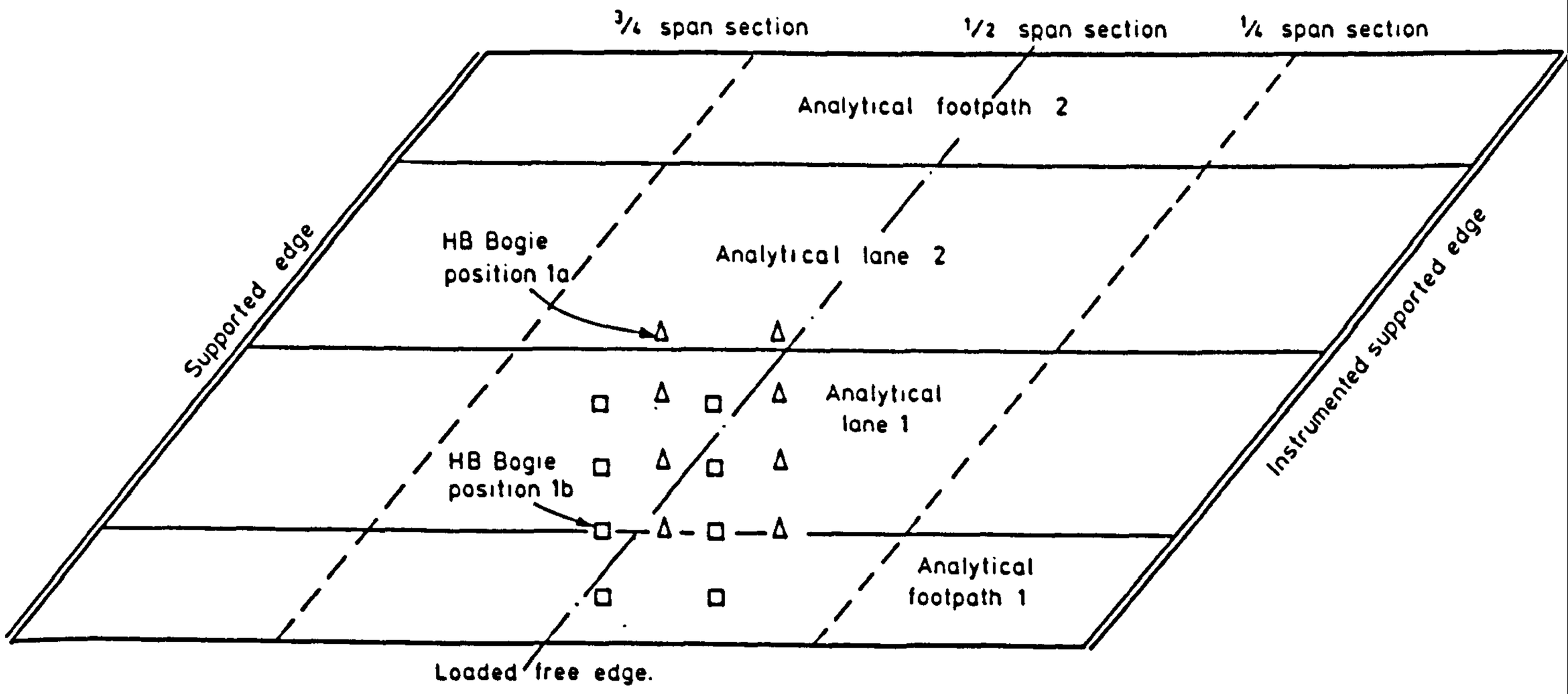

FIG. 9.25. LAYOUT OF MODEL 2 FOR THE SNAP PROGRAM ANALYSES

strength in the failure direction. This results in excessive failure loads. None of these problems were apparent with the bi-axial beam approach which allowed the beams to crack in the principal directions.

For the SNAP analyses the boundary conditions essentially consisted of x and y restraints at node 1 and a y restraint at node 209 to prevent rigid body movements with w restraints along each support line. For the majority of the analyses described herein, elastic 'w' restraints were applied along each support line. The many supports present in a composite deck may be considered to form a line support. Therefore, for the present study, the effects of the two approaches, discrete supports or line supports were investigated. For the discrete support approach, the total support line stiffness was calculated for the physical structure. This total line stiffness was allocated uniformly amongst all of the analytical supports. For the line support approach a stiffness per unit length was calculated by dividing the total support line stiffness by the support line length. The stiffnesses were allocated to each of the nodes using a procedure similar to that employed for the allocation of energy consistent nodal loads, when a line load is applied along the edge of an element. For the Heterosis element this resulted in $^1/_6$ of the element edge stiffness (that is the stiffness per unit length multiplied by the element edge length) being allocated to each of the corner nodes and $^2/_3$ of the stiffness being allocated to the midside node.

An important feature which became apparent during the SNAP analyses of the model decks was the 'lift off' of the acute corner supports. In reality physical supports are discontinuous since they can only withstand compressive and not tensile load in the majority of instances. Therefore, logically the analytical supports should be able to model this feature. It is not practical to control this

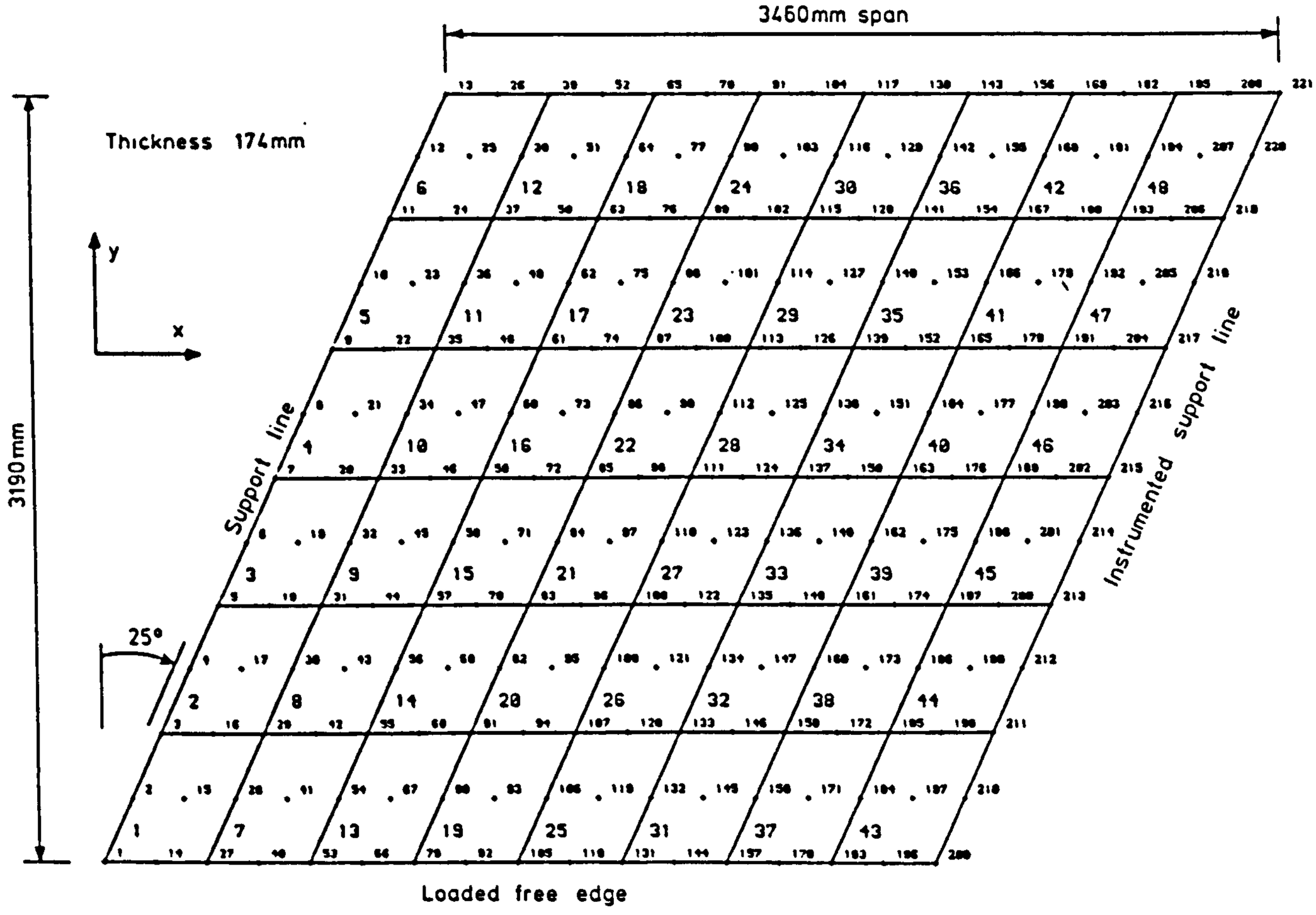

FIG. 9. 26. SNAP FINITE ELEMENT MESH USED FOR THE ANALYSES OF MODEL 1

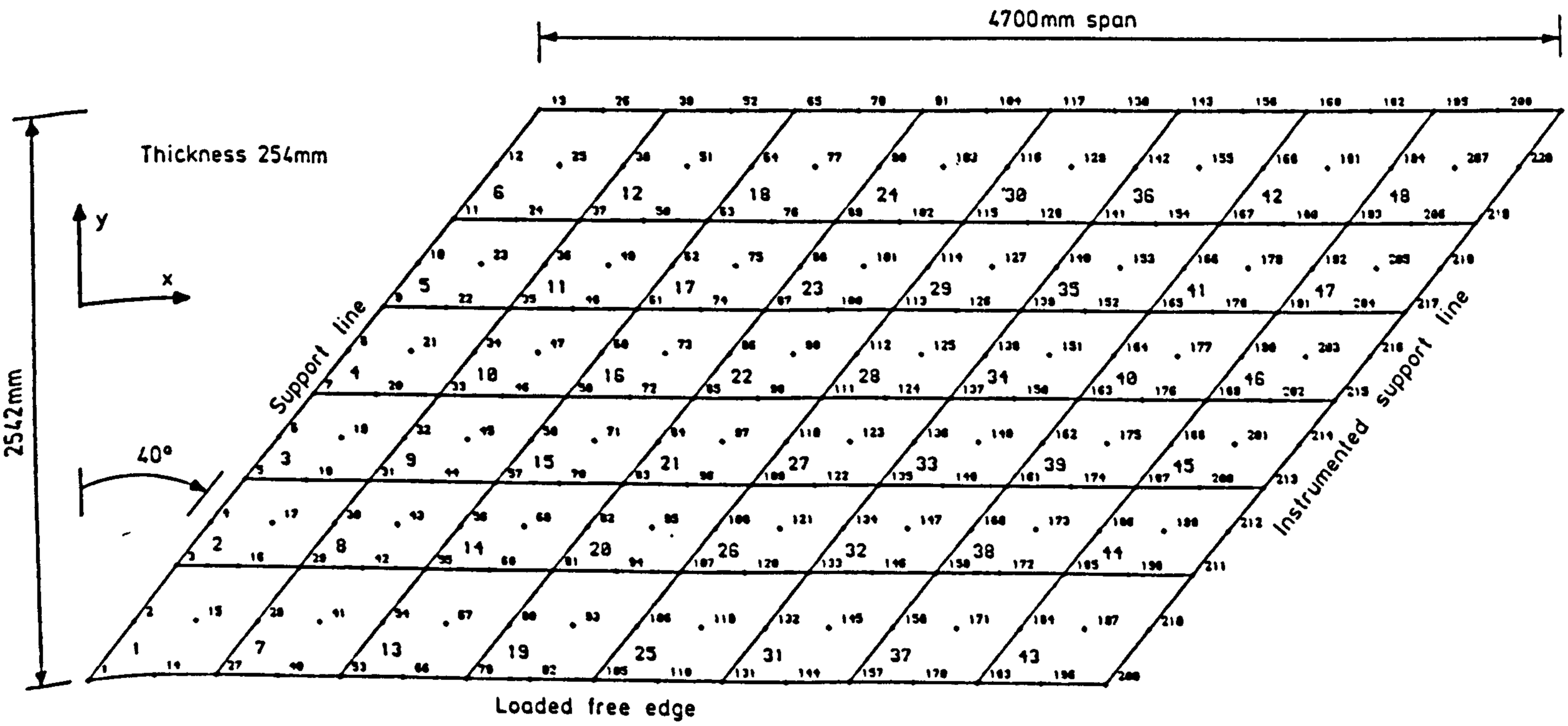

FIG. 9. 27. SNAP PROGRAM FINITE ELEMENT MESH USED FOR THE ANALYSES OF MODEL 2

aspect manually and therefore the analysis program should be capable of monitoring the support loads and removing a support if a tensile load is indicated.

9.3.2.2 Material modelling

The COSIG2 material model was chosen to model the concrete in the slab analyses. Details of the material property curves can be seen in Figure 9.28 and 9.29 for model 1 and Figures 9.30 and 9.31 for model 2. These curves were derived from material tests carried out at the time of the model tests.

Several analyses were carried out to compare the fixed crack model with the rotating crack model. It will be shown later that the use of the fixed crack model resulted in highly unrealistic structural behaviour and, therefore, all of the subsequent analyses utilised the rotating crack model. The effects of variations in several important material parameters such as tensile strength, Young's modulus and prestress will be investigated in subsequent sections. In addition, the effect of adopting statistically varied material properties will be explored. To allow the effect of material non-linearity in the analyses to be assessed and also to investigate the effects of the differences in boundary conditions in the physical and analytical structures, linear finite element analyses were also conducted. The SNAP program was used for the linear finite element analyses. The linear data was identical to the non-linear data except that material damage was suppressed at all integration stations. The effects of employing both 2 and 3 segment curves for concrete in tension were also explored. For either curve the second tension stiffening parameter, α_2, was generally set to 15, see Figure 9.28 for model 1 and Figure 9.30 for model 2. During concrete crushing, perfect plasticity was assumed until a strain of -0.0035 was attained in the

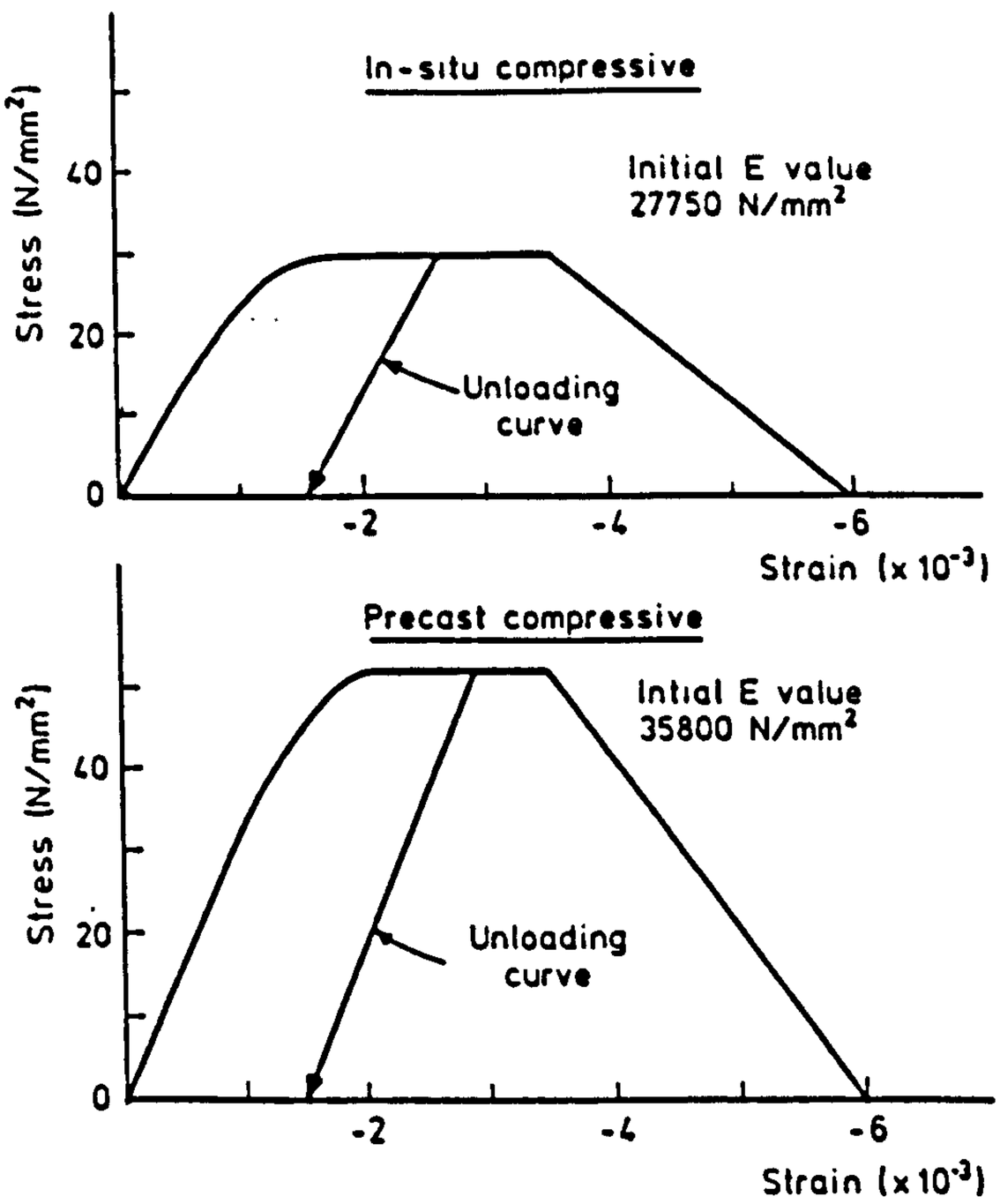

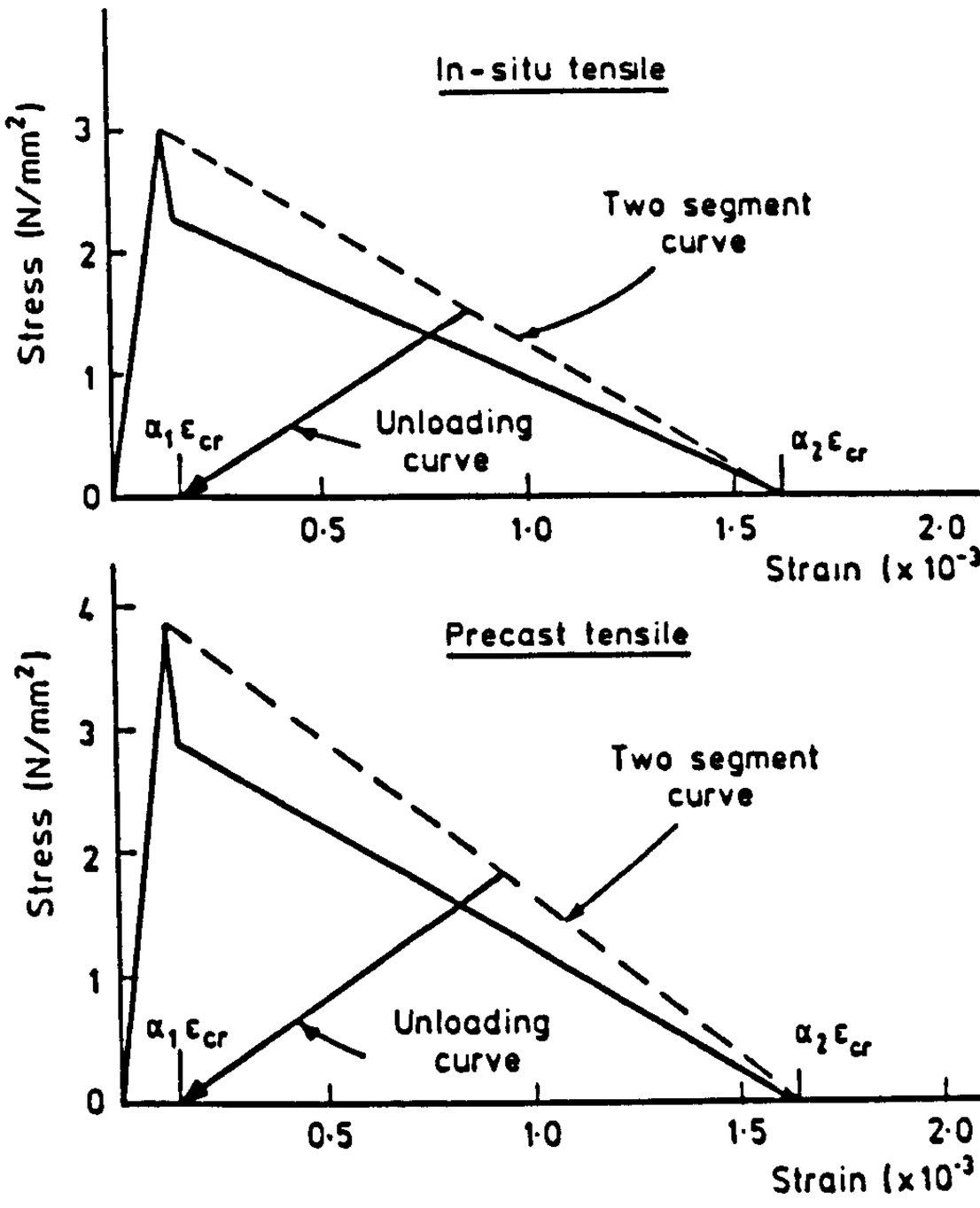

FIG. 9. 28. CONCRETE MATERIAL CURVES FOR MODEL DECK 1

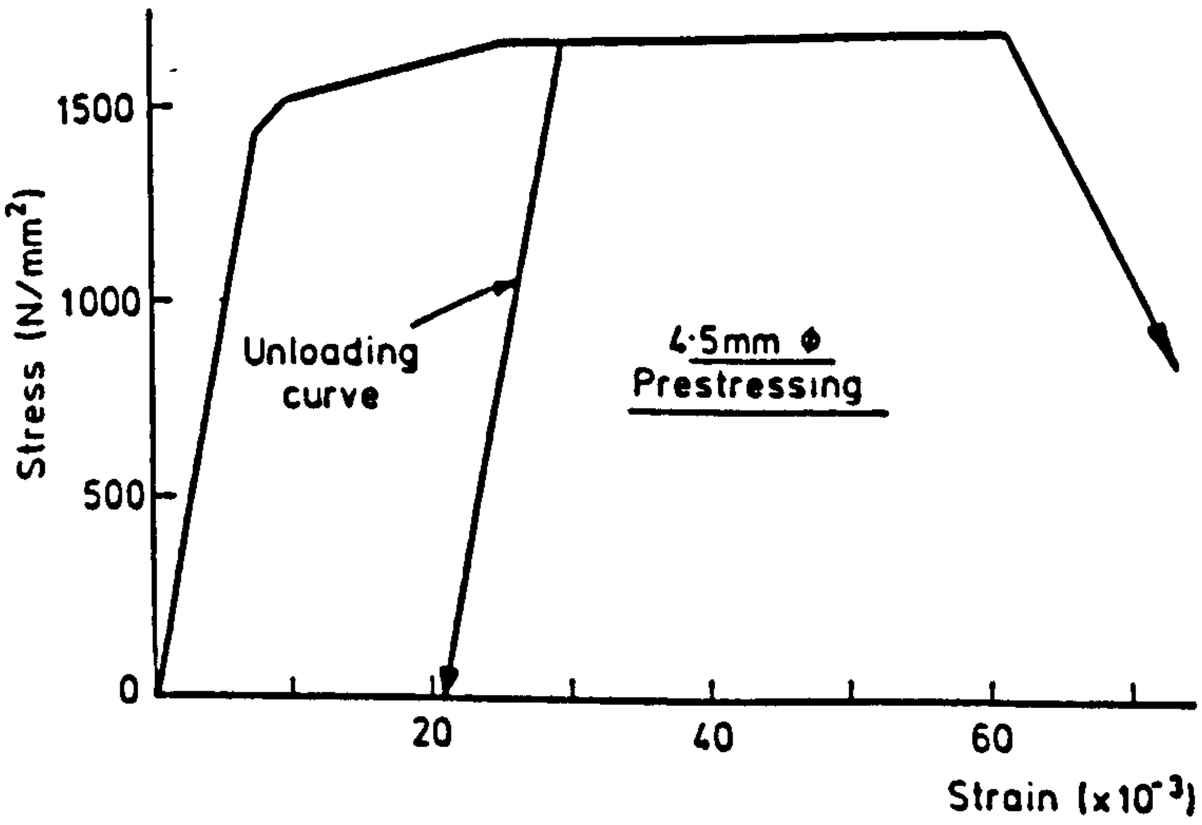

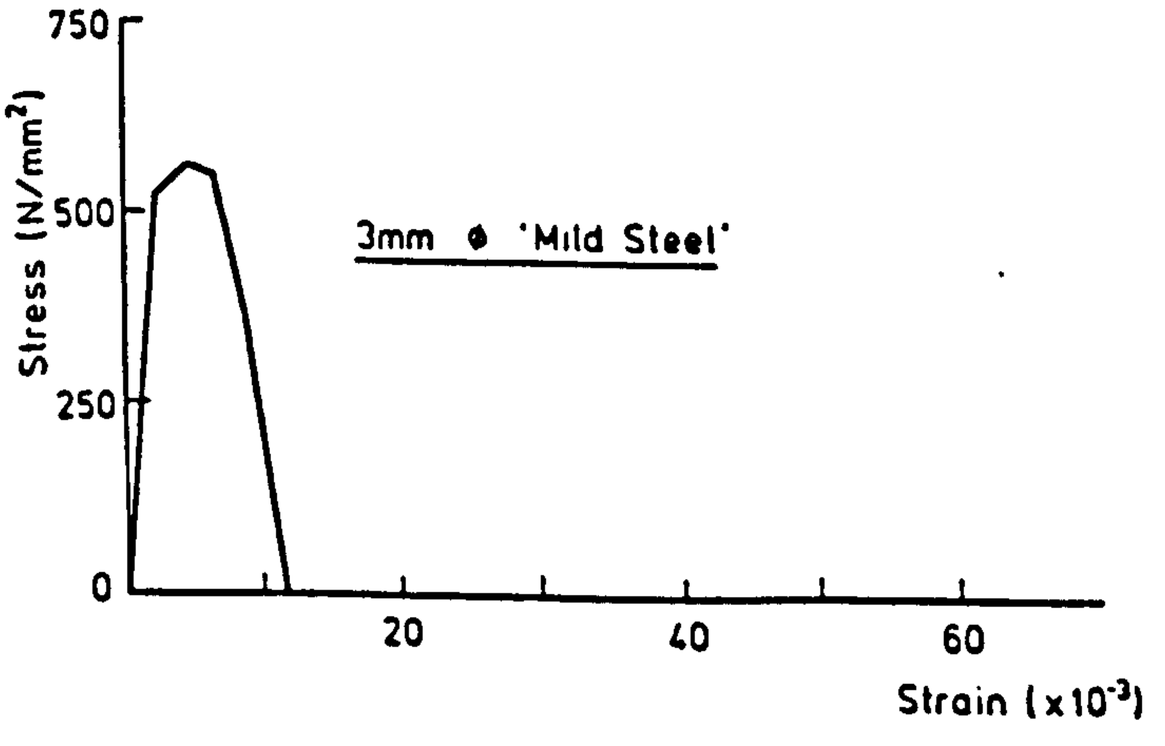

FIG. 9. 29. STEEL MATERIAL CURVES FOR MODEL DECK 1

model 1 concretes and a strain of -0.0045 was attained in the model 2 concretes. After this, the stress reduced linearly to zero at a strain of -0.006 for the model 1 concretes and -0.007 for the model 2 concretes. The increased ductility for the model 2 concretes was based on the increased ductility that was evident from the material tests on the model 2 concretes, see Figure 7.5 of Chapter 7.

9.3.2.3 Iterative solution strategy

All the SNAP model slab analyses were begun under load control with manually sized increments. The model 1 analyses were divided into three stages, the first stage modelled the precast beams with wet insitu concrete. The second stage modelled the application of dead load and HA loading to the hardened composite slab. During the third stage the HB bogie load was applied and incrementally increased to induce failure. The model 2 analyses were divided into 4 stages, the first two being identical to those of model 1. For the third stage the analytical HB bogie was placed in position 1a, see Figure 9.25, and incrementally increased to a load level equal to 4.0 x the ULS 45 unit HB bogies. The HB bogie load was then incrementally decreased and removed. For the fourth stage the HB bogie was placed in position 1b and incrementally increased to induce failure. This follows the analytical procedure which is described more fully in Chapter 8. The layout diagram for the model 2 analyses which can be seen in Figure 9.25 depicts HB bogie position 1b.

While under load control BFGS acceleration with line searching was employed. When convergence under load control became impossible then the SNAP program switched to displacement control with BFGS acceleration and line searching. At times of large stiffness change, such as when crushing of concrete or yielding of the steel occurred then it was necessary to employ the Newton-Raphson technique with line

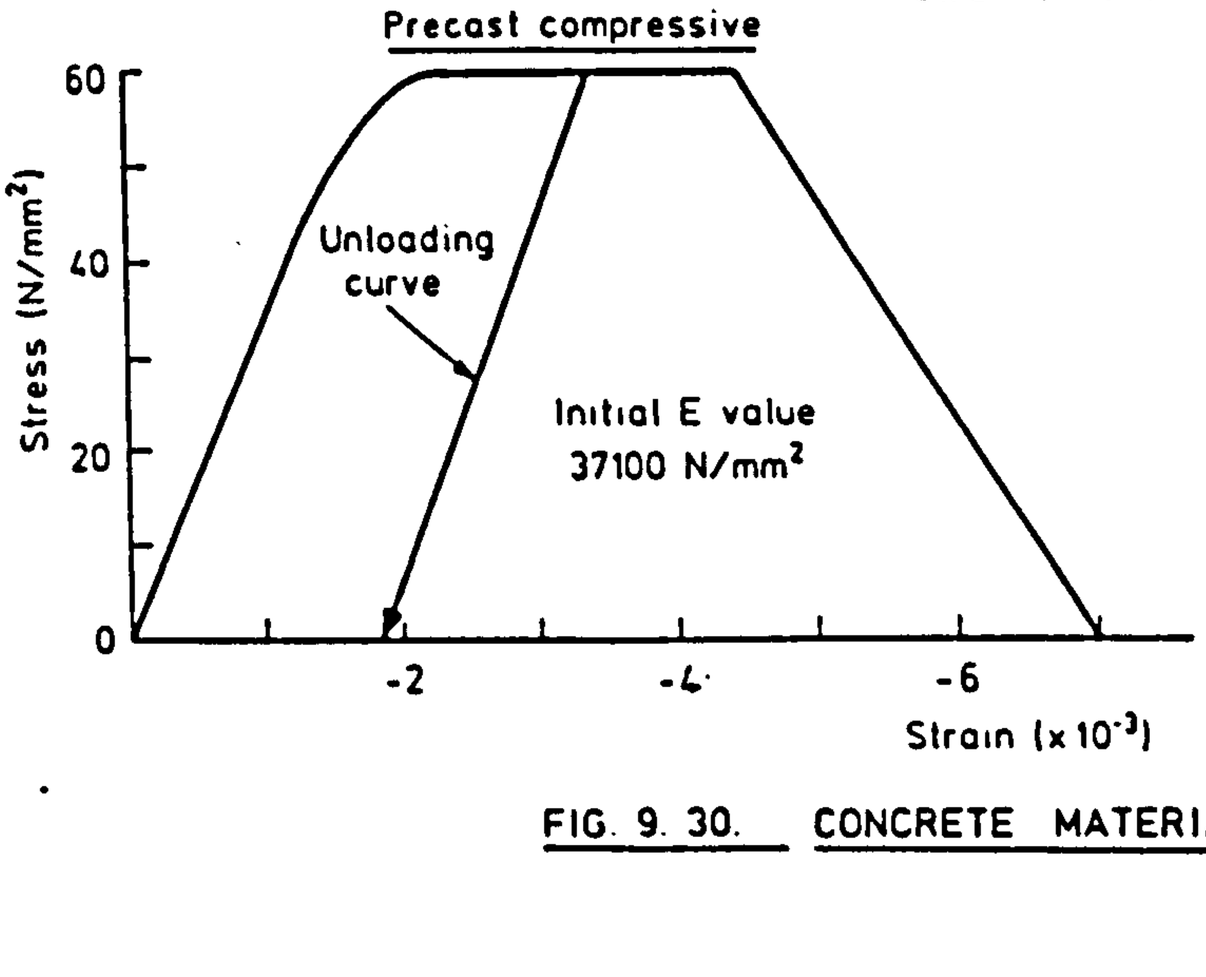

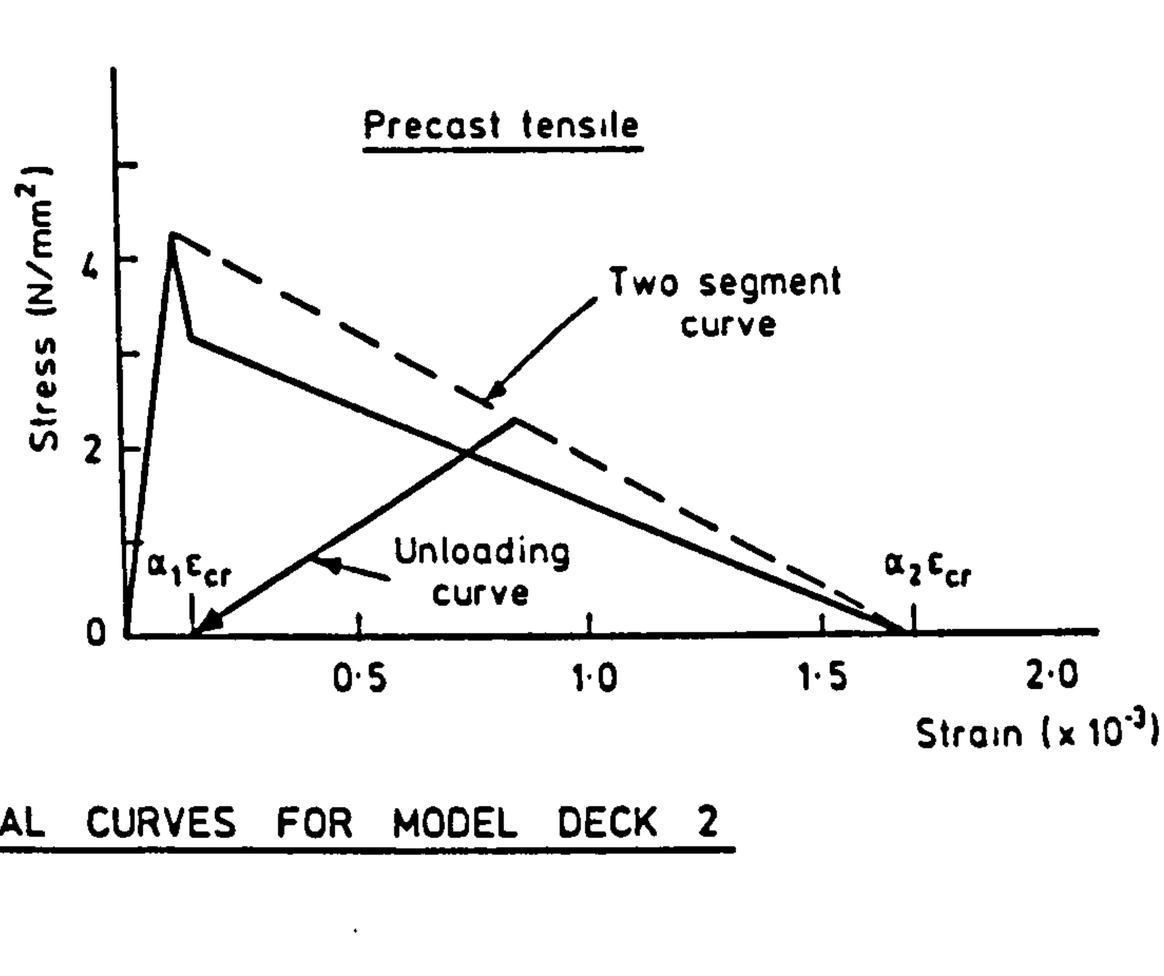

FIG. 9. 30. CONCRETE MATERIAL CURVES FOR MODEL DECK 2

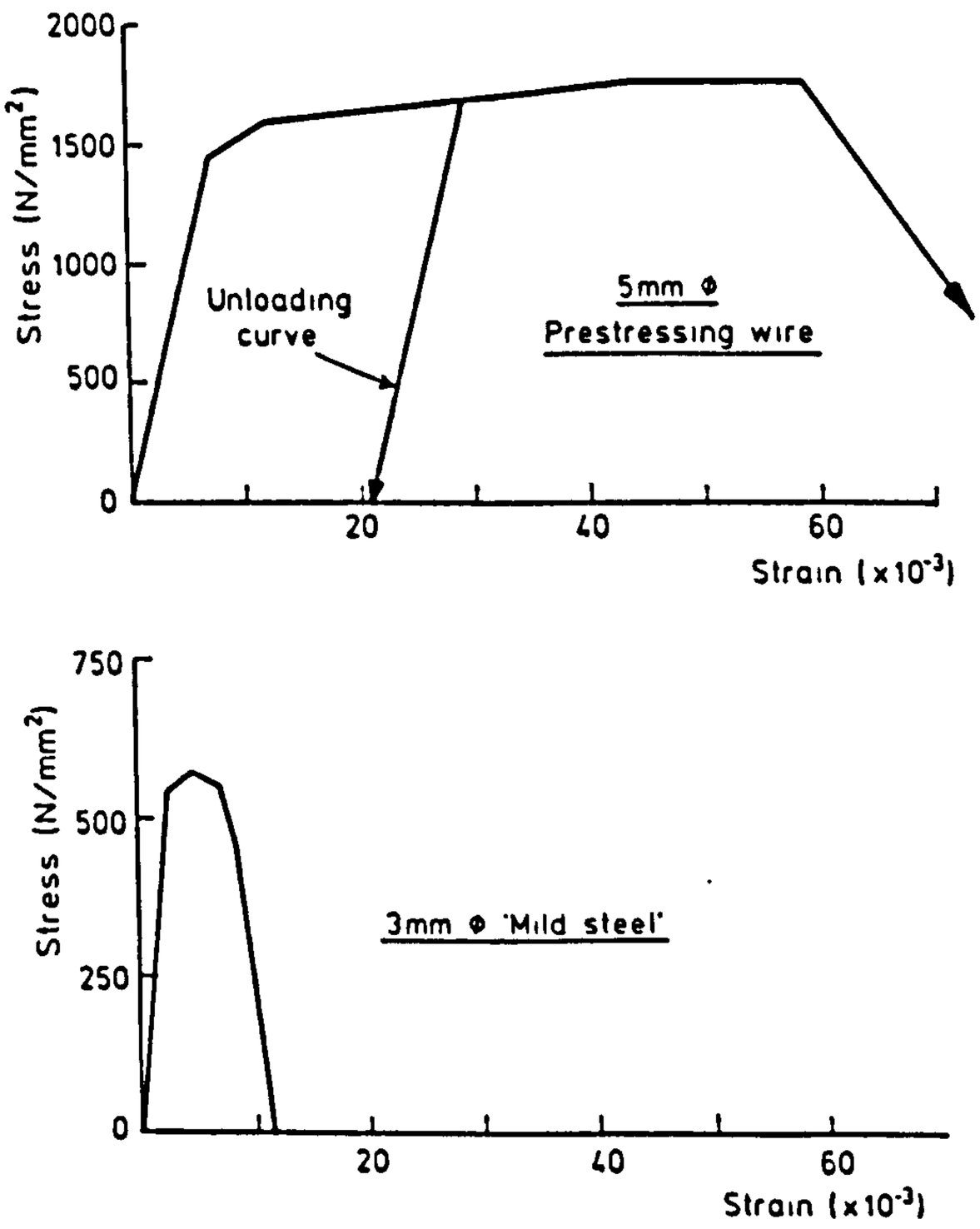

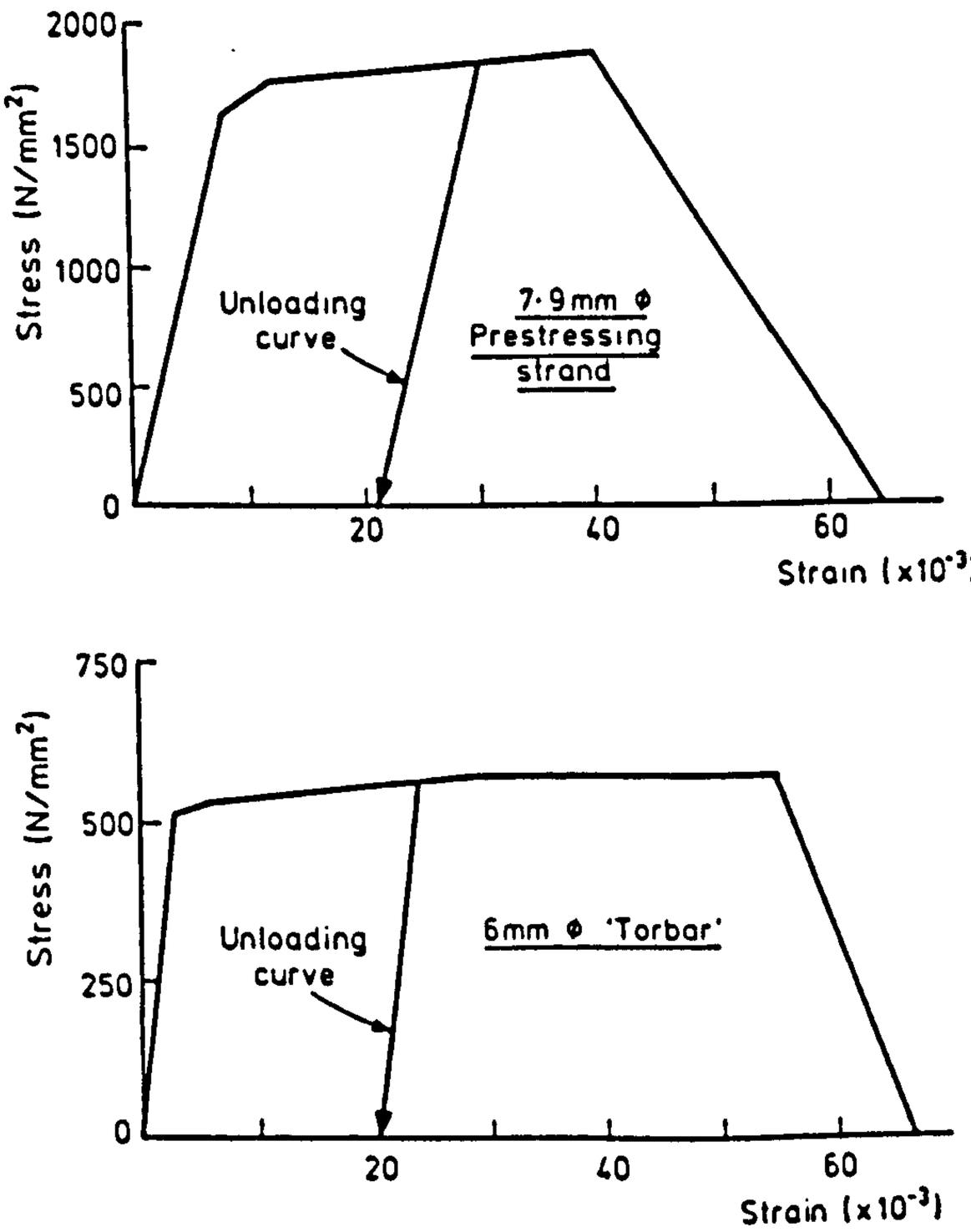

FIG. 9 31 STEEL MATERIAL CURVES FOR MODEL DECK 2

searching while under displacement control. In some instances arc-length control was employed although displacement control was found to be more efficient for the majority of situations. Under load control the increments were sized manually. While under displacement or arc-length control the increments were sized automatically. If convergence could not be achieved with the initial increment size, then the increment was repeated with the increment size cut. For the increment sizing algorithms the desired number of increments was generally set at between 8 and 12 depending upon the stability of the response at a particular section.

In some instances it was impossible to achieve convergence in an increment even with increment cutting. On these occasions engineering judgement was used to decide if the increment should be accepted and the analysis allowed to continue or whether the section should be repeated using a different approach. The out of balance force and the displacement norms were inspected. If these indicated that iterational procedure had significantly reduced the residual forces but a small residual force group (say up to 10% of the applied forces) still persisted then the increment was accepted and the next increment begun and monitored. If the subsequent increments did not achieve convergence then the whole section was repeated.

Line searches were generally carried out at all times. A definitive study of the advantages and effects of including line searches in the iterational solution strategy was not carried out. However, the analyses described herein indicated that line searches offered significantly improved solution convergence. A line search convergence factor in the range 0.3 to 0.5 was chosen.

The structural stiffness matrix was generally reformed at the beginning of each increment, except for the initial increments when the response was essentially linear.

9.3.2.4 Convergence criteria

A dual convergence criterion was selected for the SNAP analyses of the model bridge decks. Convergence was achieved when either a 1% scaled force criterion or a 0.01% scaled displacement criterion was satisfied. The majority of increments converged on the tight force tolerance with few converging on the exceptionally tight displacement criterion. When the structural stiffness approached zero and convergence on the 1% force tolerance became impossible then the scaled force tolerance was slackened to 5% to allow convergence on forces to be achieved.

The difficulty in converging in areas of very low structural stiffness was investigated. These investigations indicated that the limitations of the static analysis that had been employed were partly responsible for the difficulty in converging. The adoption of a pseudo dynamic analysis would most probably yield more stable solutions in areas of low structural stiffness. A technique similar to Dynamic Relaxation may be appropriate. The dynamic structure need not be given accurate mass or damping parameters, in fact the mass may even be omitted. The adoption of damping terms would help to stabilize the uncontrolled oscillations that can occur with a static analysis in areas of low structural stiffness.

9.3.3 Load deflection responses

The load-deflection responses for each analysis are given in Figures 9.32 and 9.33 for model 1 and Figures 9.34 to 9.36 for model 2. In addition to the response of the loaded free edge at mid-span, the

response at two other points is also given. For model 1 these are the lane 1 to lane 2 boundary and the unloaded free edge at mid-span. For model 2 these are mid-width and the unloaded free edge at mid-span.

9.3.3.1 Model 1

The model 1 load-deflection responses obtained with a 9 element mesh can be seen in Figure 9.32. An obvious feature of these curves is the 'bump' that occurs in the analytical curves as the response begins to flatten. The cause of these bumps was investigated and while it was not possible to form a definitive explanation, the studies indicated that the propagation of cracking to areas outside the central zone was a major factor. The crack propagation hypothesis is supported by the response obtained with a 2 segment curve for concrete in tension. The 2 segment curve has shifted the bump and increased its size. For the 2 segment analyses, the other parameters were as for the standard data analyses.

From Figure 9.32 it can be seen that all of the analyses are in very good agreement with the experimental response up to a load factor of 1. On the ordinate of these plots is shown the load factor in terms of the number of ULS 45 unit HB bogies. Each unit of ULS 45 unit HB bogie is equal to 45 units of one HB bogie, as defined by BS5400 Pt 2 (1978) with a partial safety factor, γ_{fL}, of 1.30. The agreement indicates that parameters other than material degradation are correct.

Significant structural cracking begins at a load factor of 1.5. The effect of large prestress losses can be seen in this section. Curve 2 depicts the response with a prestress loss of 50% and it can be seen that this results in an excessively flexible structure. The 'bumps' in the analytical responses occur at a displacement level of approximately 20 to 40 mm in the loaded free edge response. By this

Comparison of load-deflection responses for model deck 1.

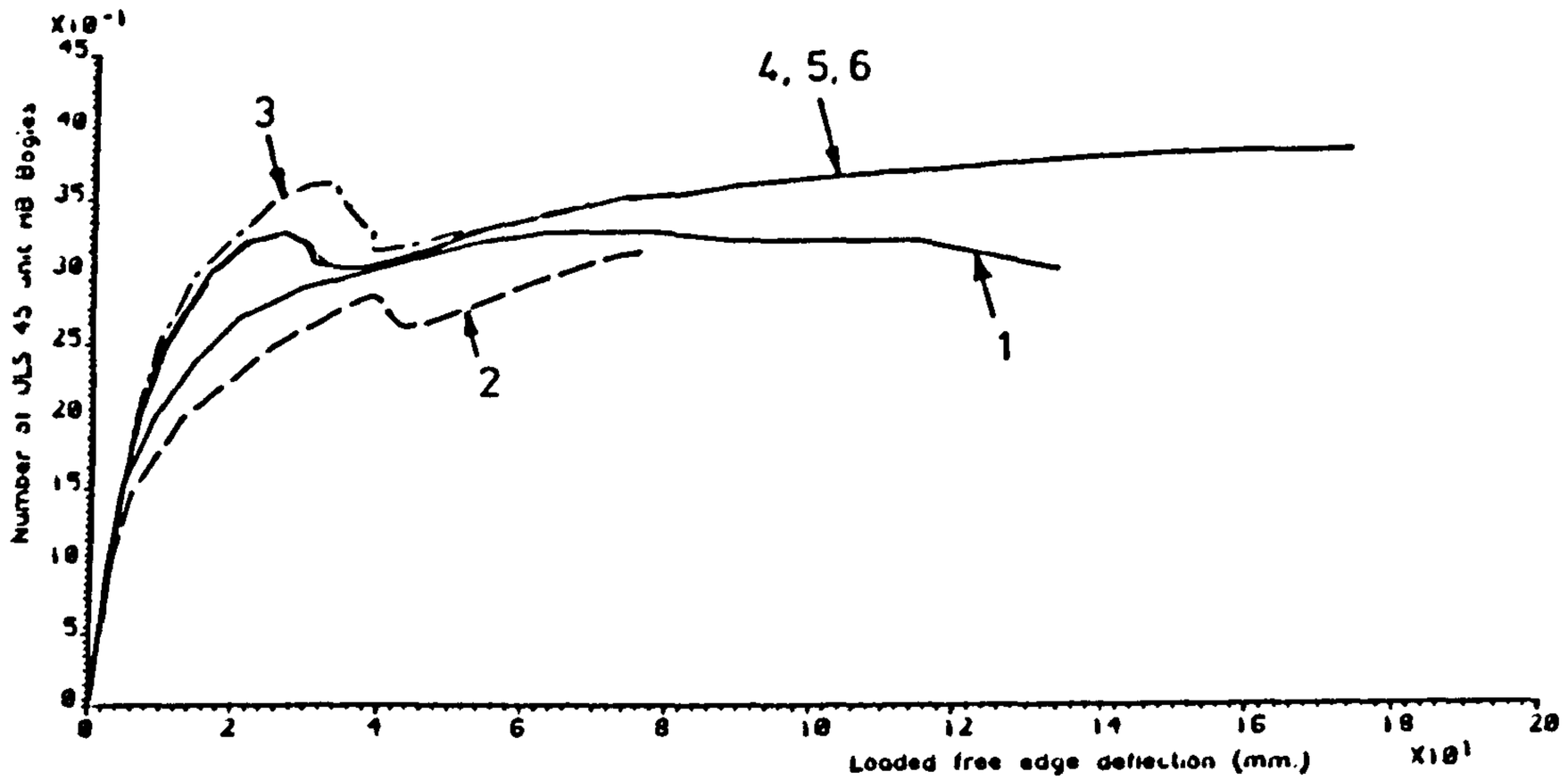

Comparison of load-deflection responses for model deck 1.

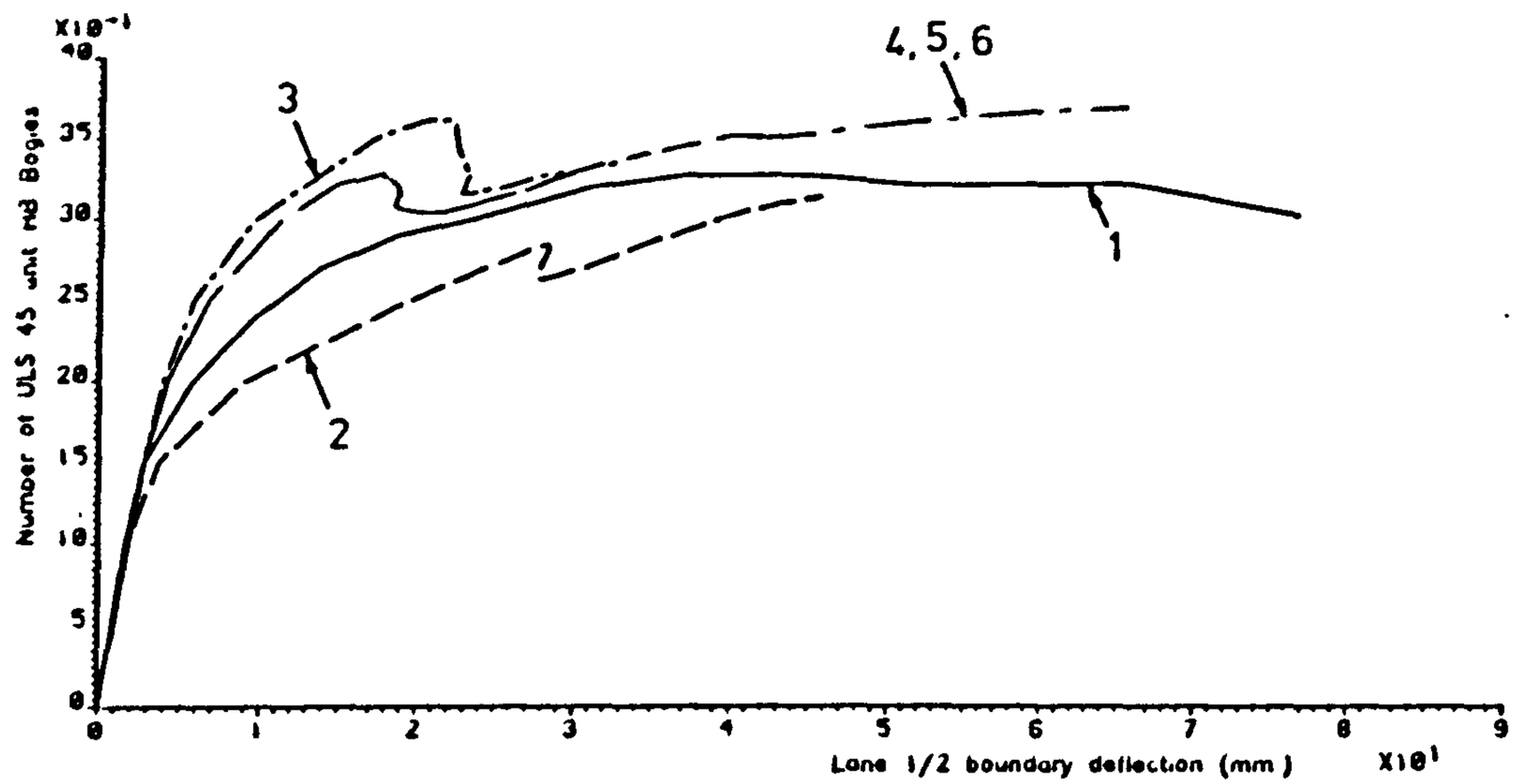

Comparison of load-deflection responses for model deck 1

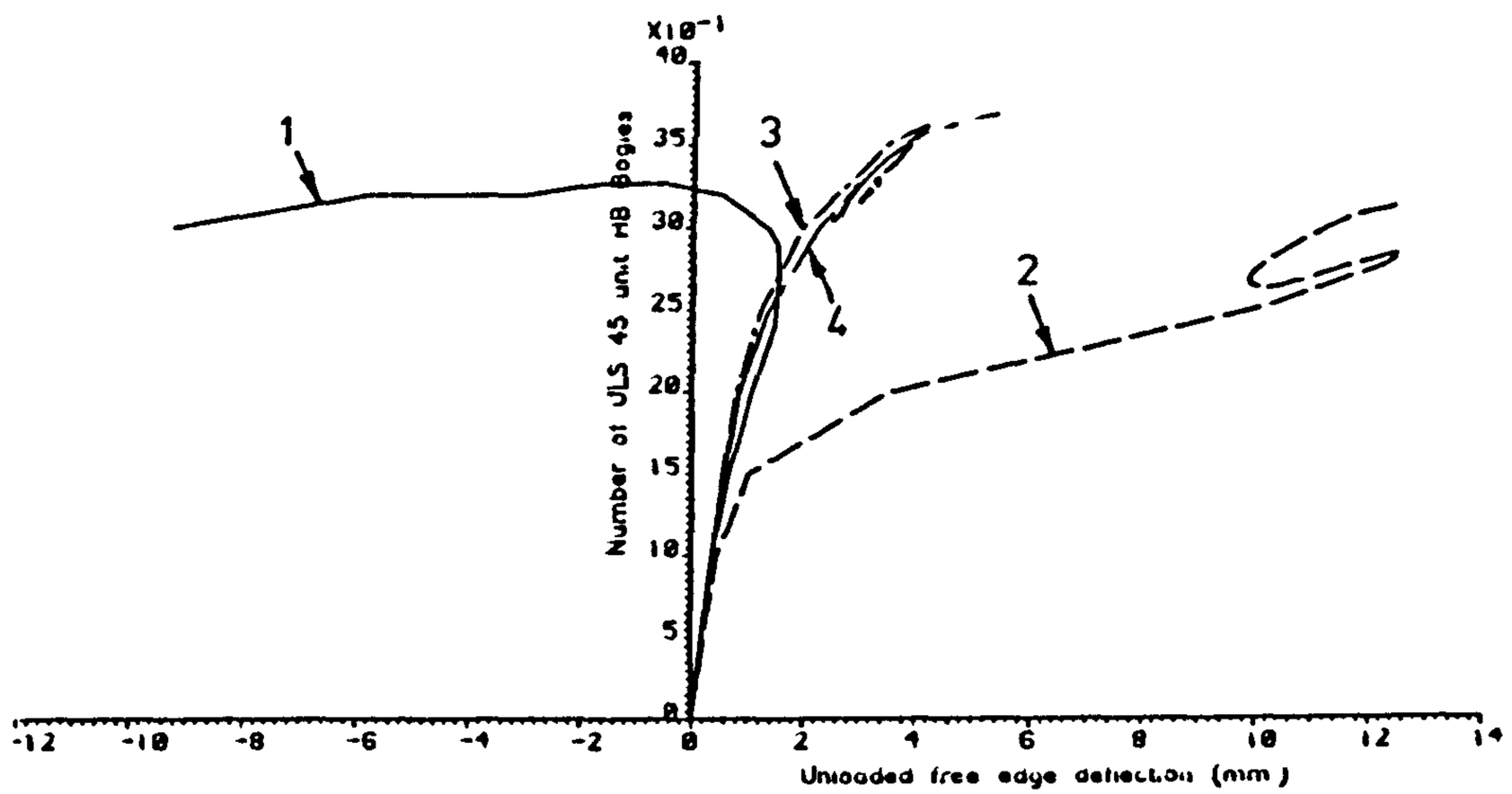

KEY:

1 ——— Experimental response

2 – – – – – 50% prestress losses

3 —·—·—·— 2 segment stress-strain curve for concrete in tension

4 — — — Large in-plane shear degradation

5 ——·—— Non-unloading material models (elastic)

6 ——— Standard data (20% prestress losses)

FIG 9. 32. SNAP PROGRAM LOAD-DEFLECTION RESPONSES FOR MODEL 1, OBTAINED WITH A 9 ELEMENT MESH.

stage the program has switched to displacement control. The 'snapping back' that could be seen in the response at the lane 1/lane 2 boundary with the 50% prestress loss analysis, serves to illustrate the problems that could be encountered with an injudiciously chosen controlling degree of freedom when under displacement control. For all the analyses described here the controlling degree of freedom was placed on the free edge adjacent to the HB bogie. If, however, the controlling degree of freedom had been placed on the lane 1/lane 2 boundary, severe difficulties could have been encountered.

In the post bump region the analytical responses follow the experimental response closely. However, for all responses except the unloaded free edge response, the analytical response begins to drift away from the experimental response at higher displacement levels. There is very poor agreement for the unloaded free edge response during the later stages of the analyses. It will be seen that in the experiment, the unloaded free edge began to lift up during the later stages of the test. The analytical responses predict a continuing slow increase in sagging deflection and there is no indication of the 'kick back' that is present in the experimental response. Again the large prestress losses have a large effect upon the response curve.

Figure 9.33 depicts the responses obtained with a finer 48 element mesh. It will be noticed that the adoption of a finer mesh has resulted in a smaller 'bump' which supports the crack propagation hypothesis for the formation of the 'bump'. Again the initial part of the analytical curves is in good agreement with the experimental data. Significant cracking begins at a load factor of approximately 2. Cracking is followed by steel yielding as the response moves along the plateau. There is little difference between the responses up to a displacement level of 120 mm. After this the standard data analysis

Comparison of load–deflection responses for model deck 1

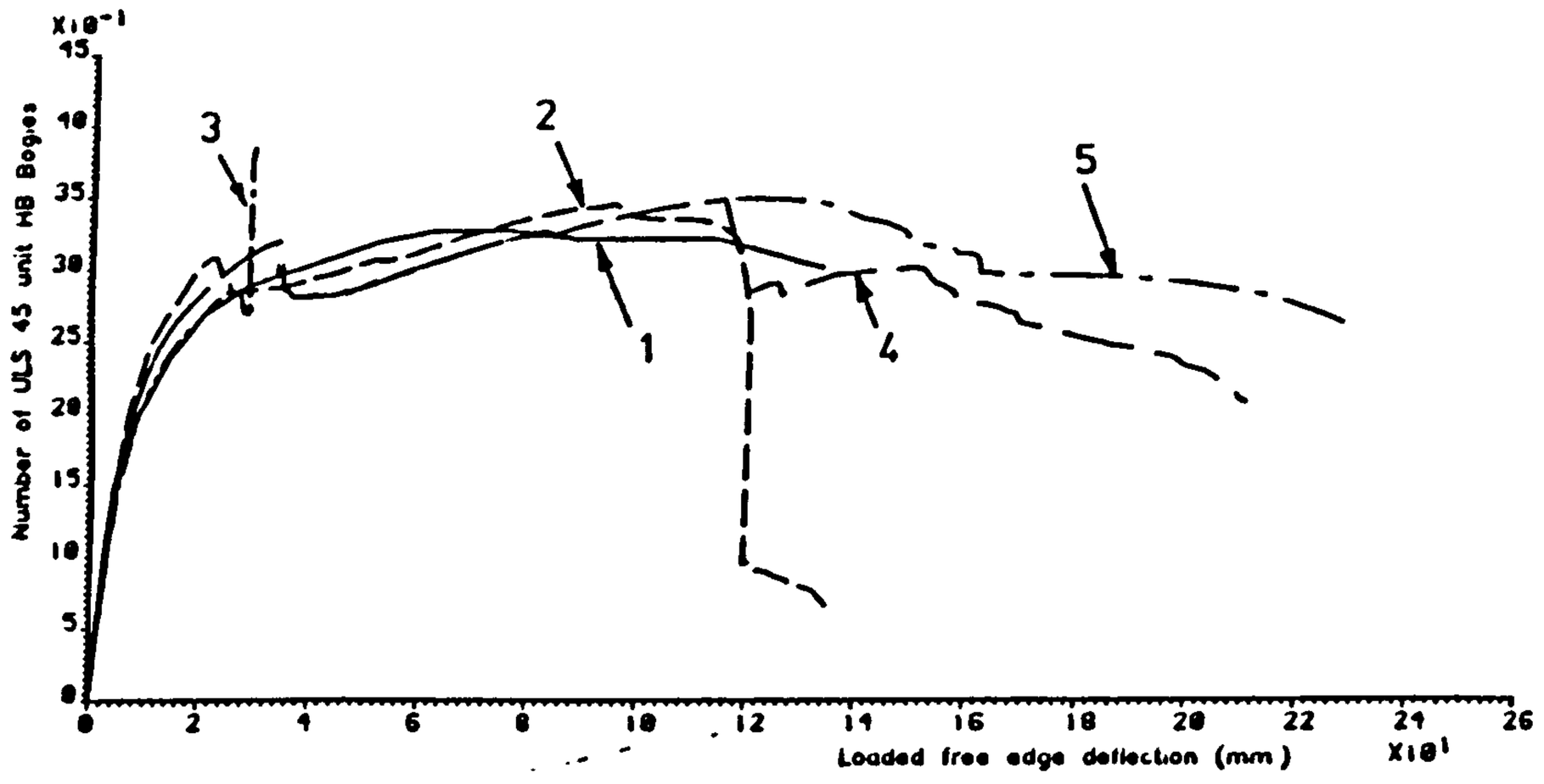

Comparison of load–deflection responses for model deck 1.

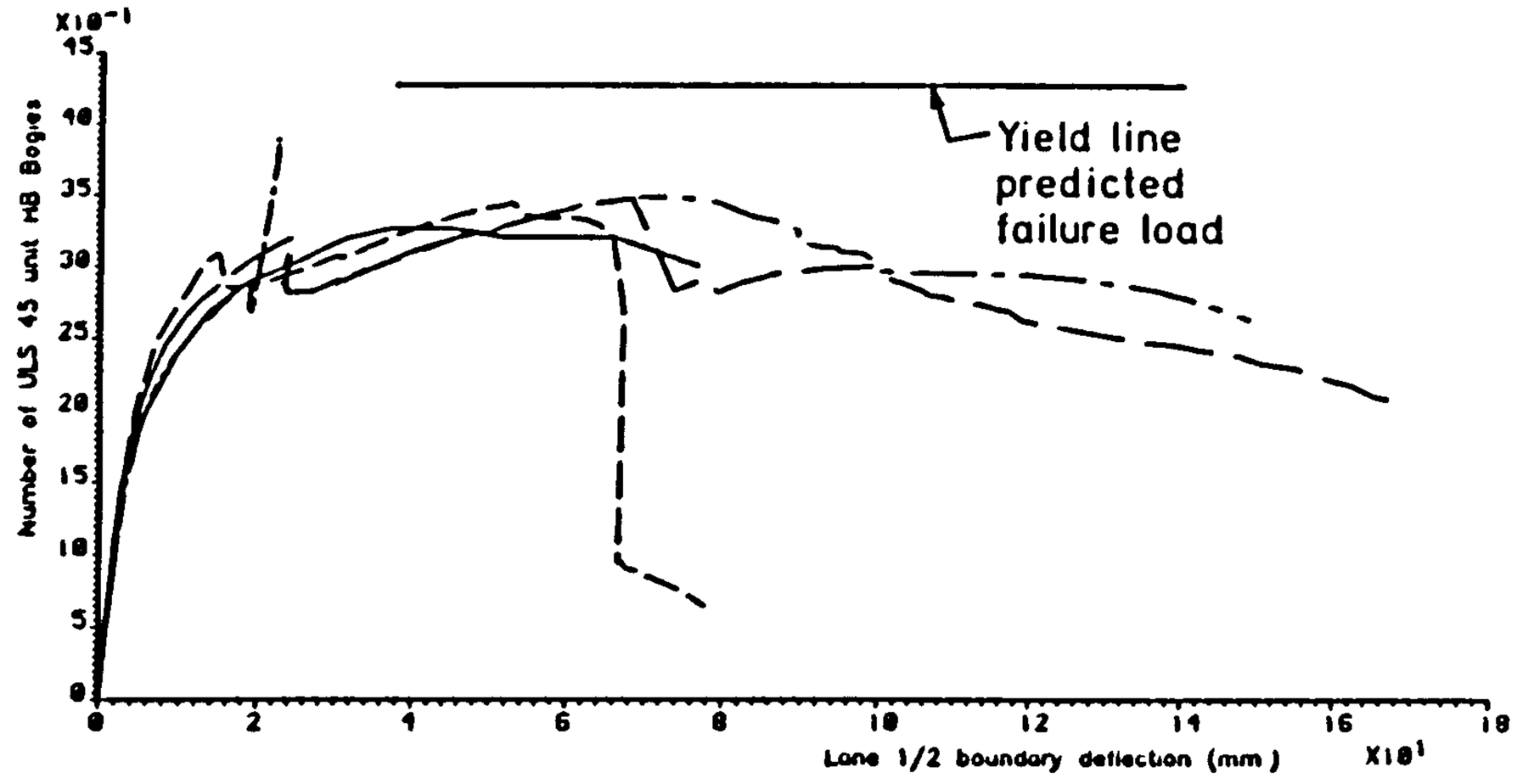

Comparison of load–deflection responses for model deck 1.

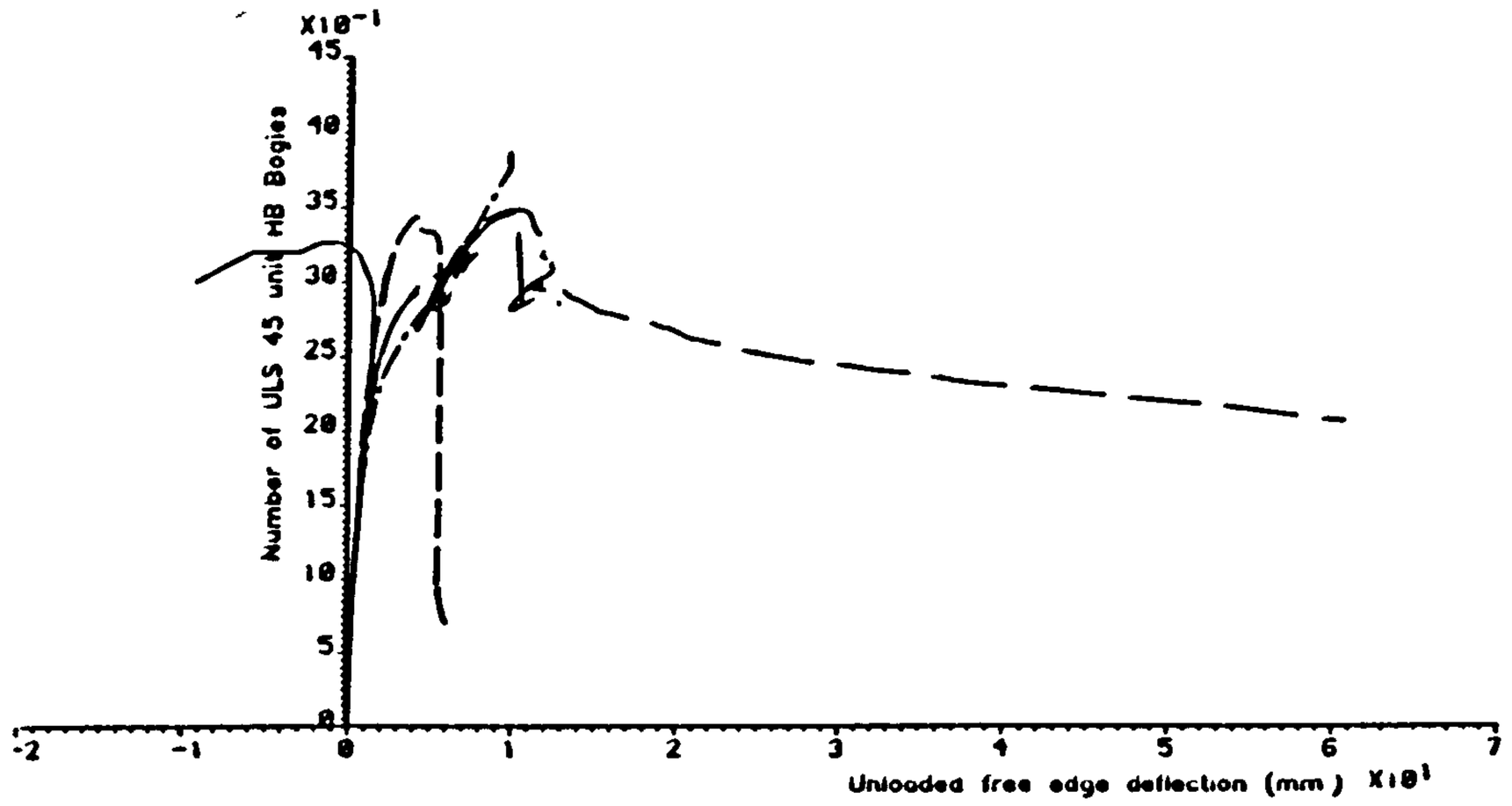

KEY:

1 ——— Experimental

2. – – – – – Standard data (20% prestress losses)

3. –·–·–·–·– 35% prestress losses

4. — — — 35% prestress losses and 2 segment curve for concrete in tension.

5. ——·—— 35% prestress losses, 2 segment curve for concrete in tension and statistically varied properties.

FIG. 9.33. SNAP PROGRAM LOAD-DEFLECTION RESPONSES FOR MODEL 1, OBTAINED WITH A 48 ELEMENT MESH.

suddenly drops off, as the prestressing steel ruptures and concrete crushes. Curve 4 in Figure 9.33 exhibits a limited drop off at the same level. The increased prestress losses and the adoption of a 2 segment curve for concrete in tension has allowed the analytical model to redistribute the load, resulting in a limited load drop off. The adoption of statistically varied properties for the analysis depicted by curve 5 in Figure 9.33 has resulted in a gradual load reduction and not the sudden drop off that was evident with the previous two curves. At the high displacement levels which occur at the end of the analyses shown in Figure 9.33, the small displacement theory on which the SNAP program is based may not be appropriate and an alternative formulation should be considered.

It will be noticed from Figure 9.33 that analysis 3, with 35% prestress losses but a 3 segment concrete tension curve, was terminated at an early stage. Just before termination the load level climbed dramatically as the analysis appeared to adopt an alternative solution path. The rapid load rise was spread over a number of increments and in these increments convergence was achieved.

As with the 9 element analyses described earlier, the 48 element analyses fail to predict the unloaded free edge response with any degree of accuracy. The unloaded free edge response does, however, provide an insight into the behaviour of analysis 4. It can be seen that the recovery that follows the limited load drop off in the loaded free edge response of this analysis, corresponds to a large deflection increase at the unloaded free edge.

9.3.3.2 Model 2

In Figure 9.34 load deflection responses for model 2, which were obtained with a 9 element mesh, are shown. This figure illustrates

Loaded free edge load–deflection response comparison.

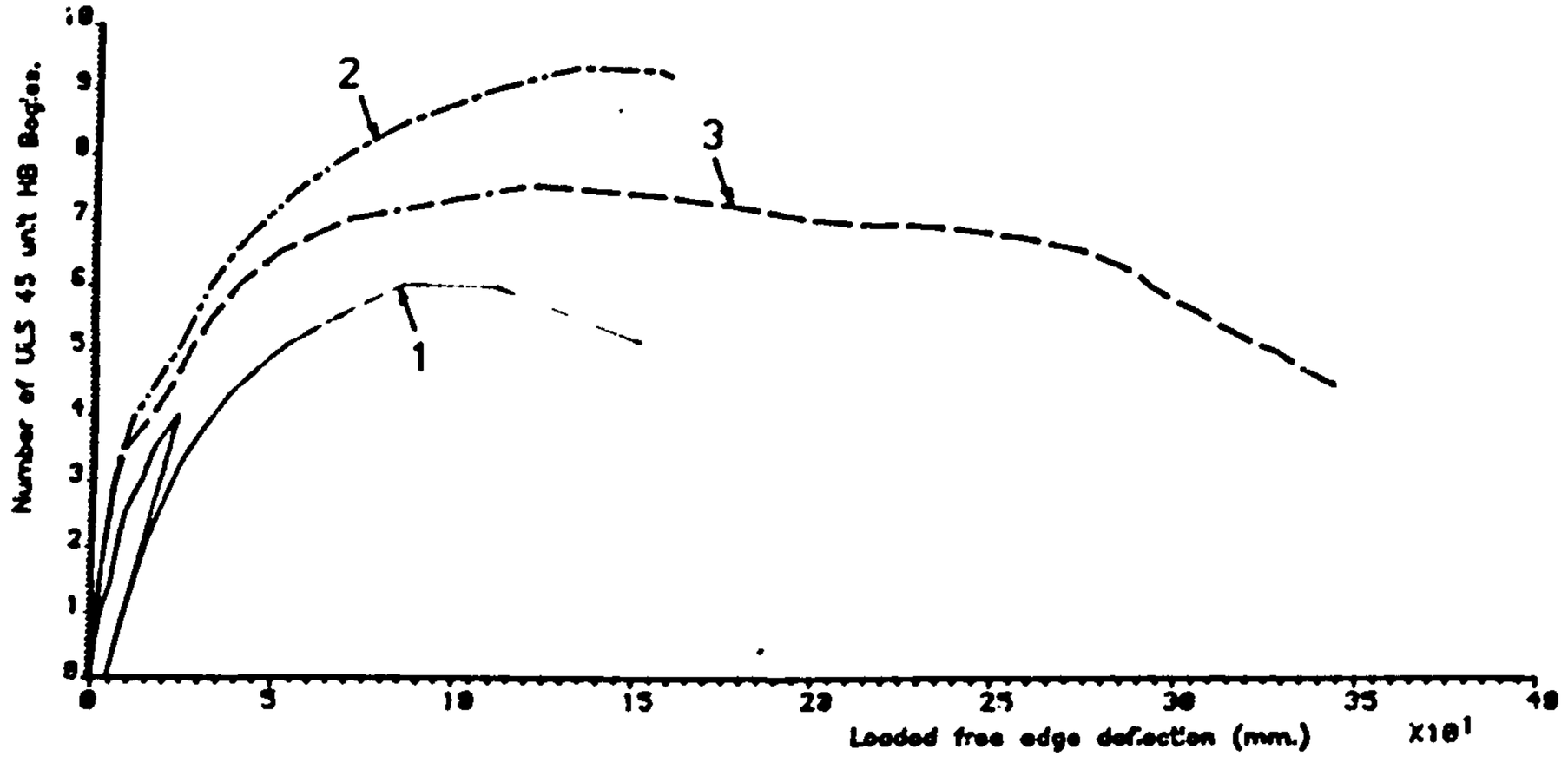

Mid–width centre line load–deflection response comparison.

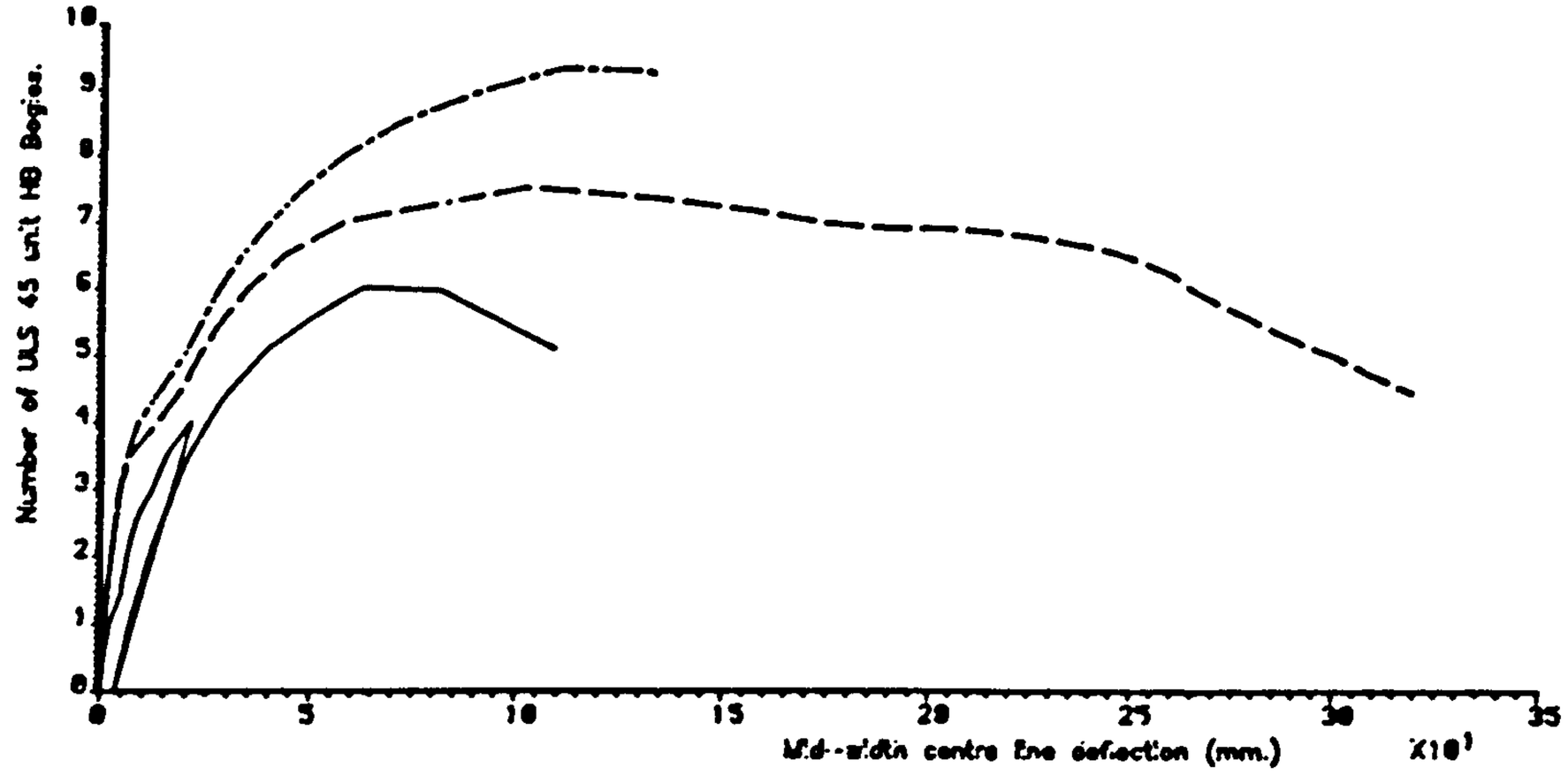

Unloaded free edge load–deflection response comparison.

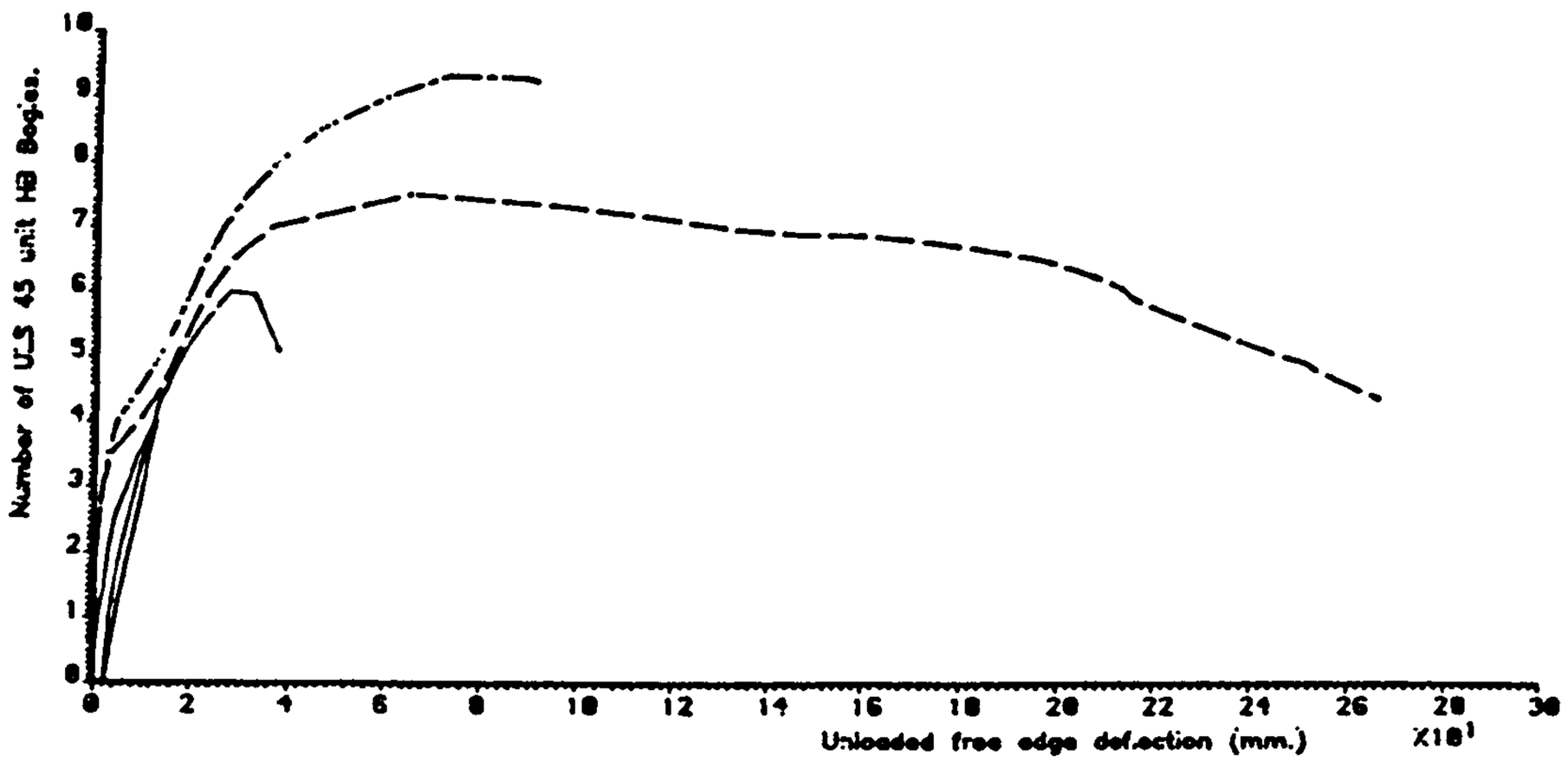

KEY:

1 ———— Experimental

2 –·—·—·— Fixed crack direction material model

3 – – – – – Rotating crack direction material model

FIG. 9.34. SNAP PROGRAM LOAD-DEFLECTION RESPONSES FOR MODEL 2, OBTAINED WITH A 9 ELEMENT MESH

the differences that result from the adoption of the fixed and rotating crack material models. With the standard data the rotating crack model does not accurately predict the experimental response. Whilst the fixed crack model results in a very large over strength prediction.

A possible reason for the inability of the rotating crack analysis to predict the experimental response can be deduced from Figure 9.34. It can be seen that the final loaded free edge analytical displacement is approximately 2.33 times the experimental value. The unloaded free edge displacement ratio is approximately 7.5. Thus it would appear that the analytical models were either too stiff in torsion, thus preventing rotation of the mid span section, or too stiff in transverse bending.

Figure 9.35 depicts the analytical load deflection responses obtained with a finer 48 element mesh. As with the 9 element mesh responses of Figure 9.34, the initial response, up to a load level of approximately 2, is not accurately predicted. This suggests that either; the analytical Young's modulus was in error; or the analytical concrete tensile strength was too high; or the prestress losses were too low. The response obtained with the standard data (curve 2 of Figure 9.35) over predicts the model strength by about 15% however the displacement level at which failure of the slab occurs is accurately predicted.

In the analysis, as in the experiment, the structure was first loaded and unloaded with the HB bogie in position 1a (see Figure 9.25). The response for this first loading can be seen in Figure 9.35. When compared with the experimental response, it will be noticed that all the analyses predict only small residual deflections after unloading in position 1a. This indicates that the 'locked in' strains predicted

Comparison of load–deflection responses for model deck 2.

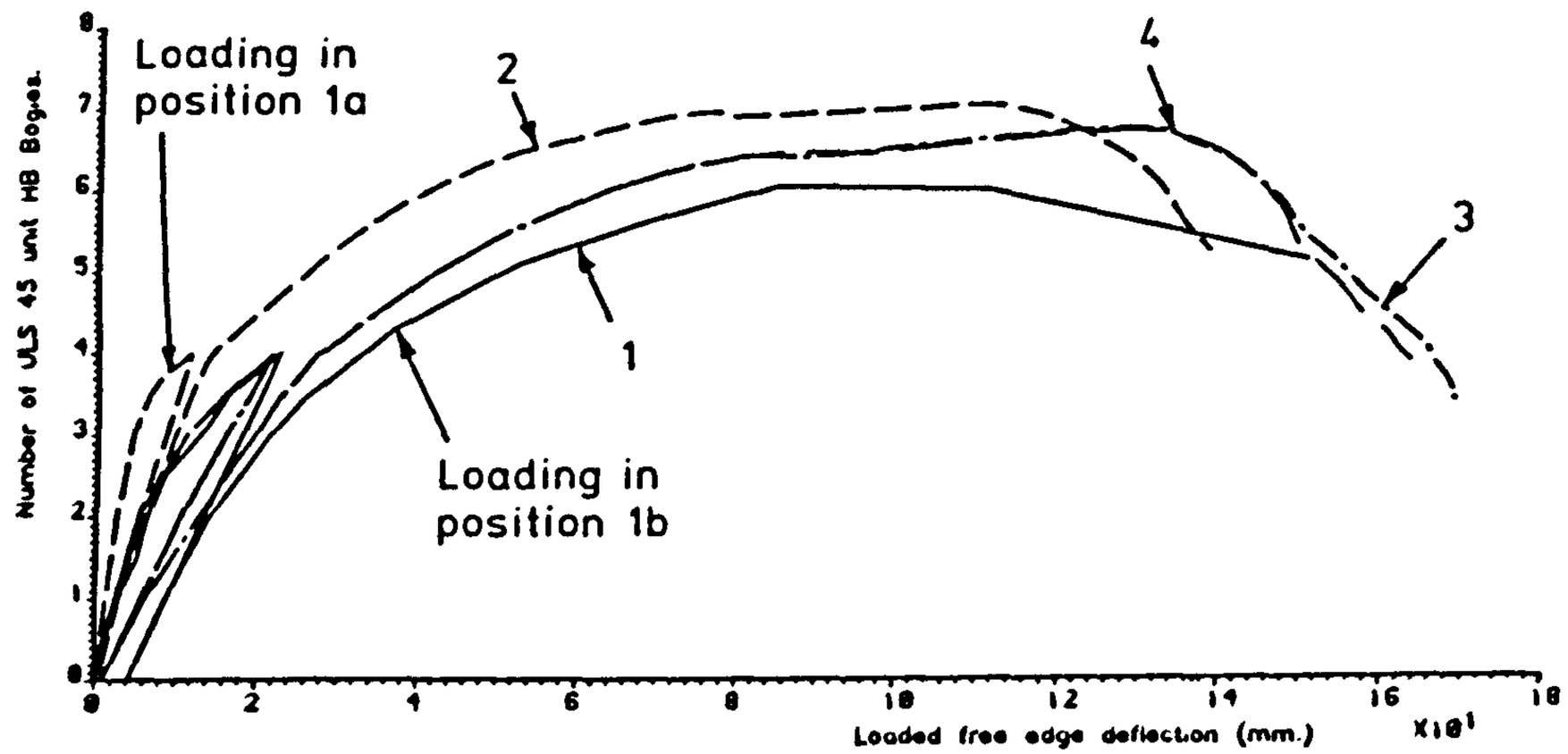

Comparison of load–deflection responses for model deck 2.

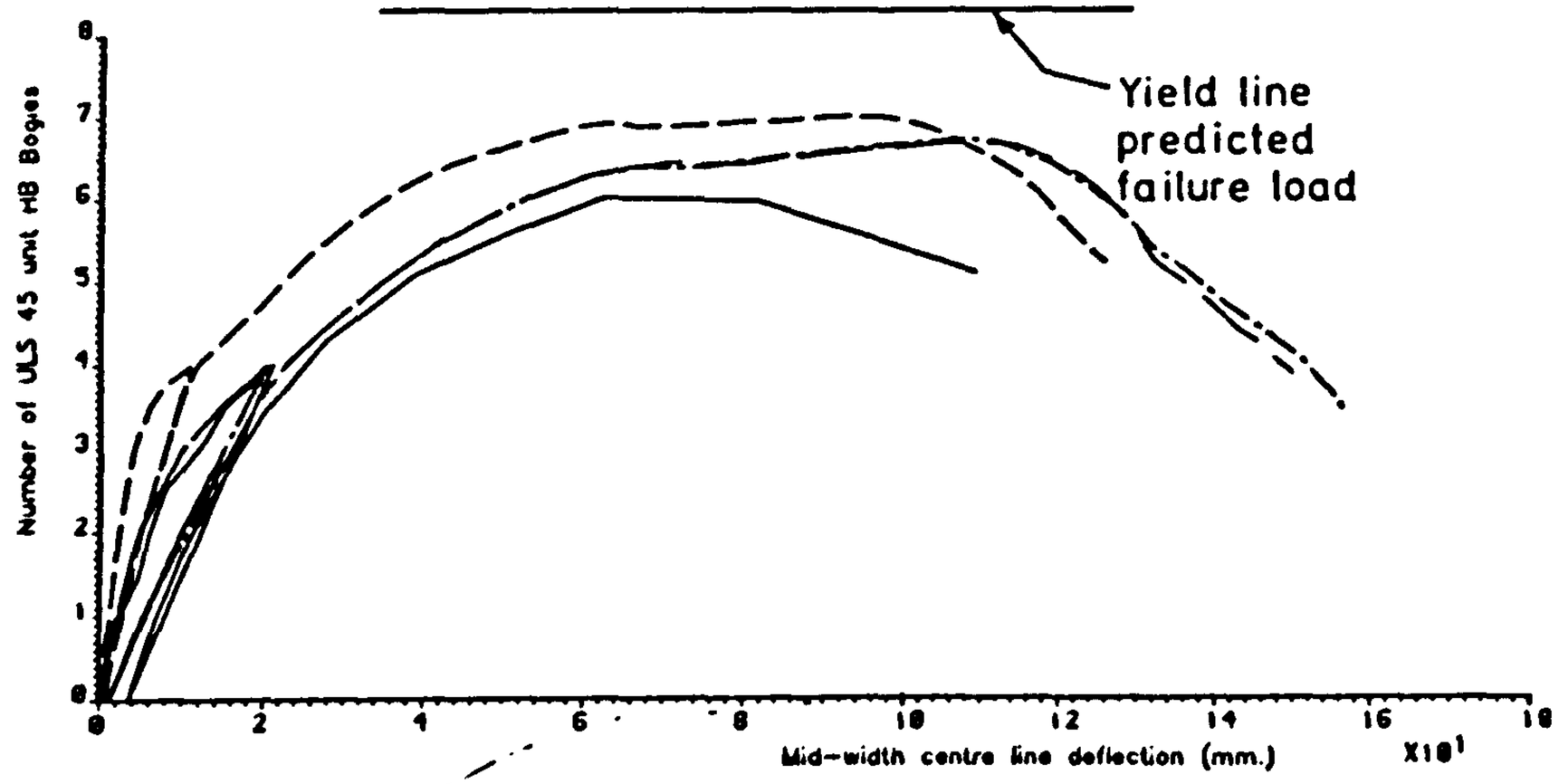

Comparison of load–deflection responses for model deck 2.

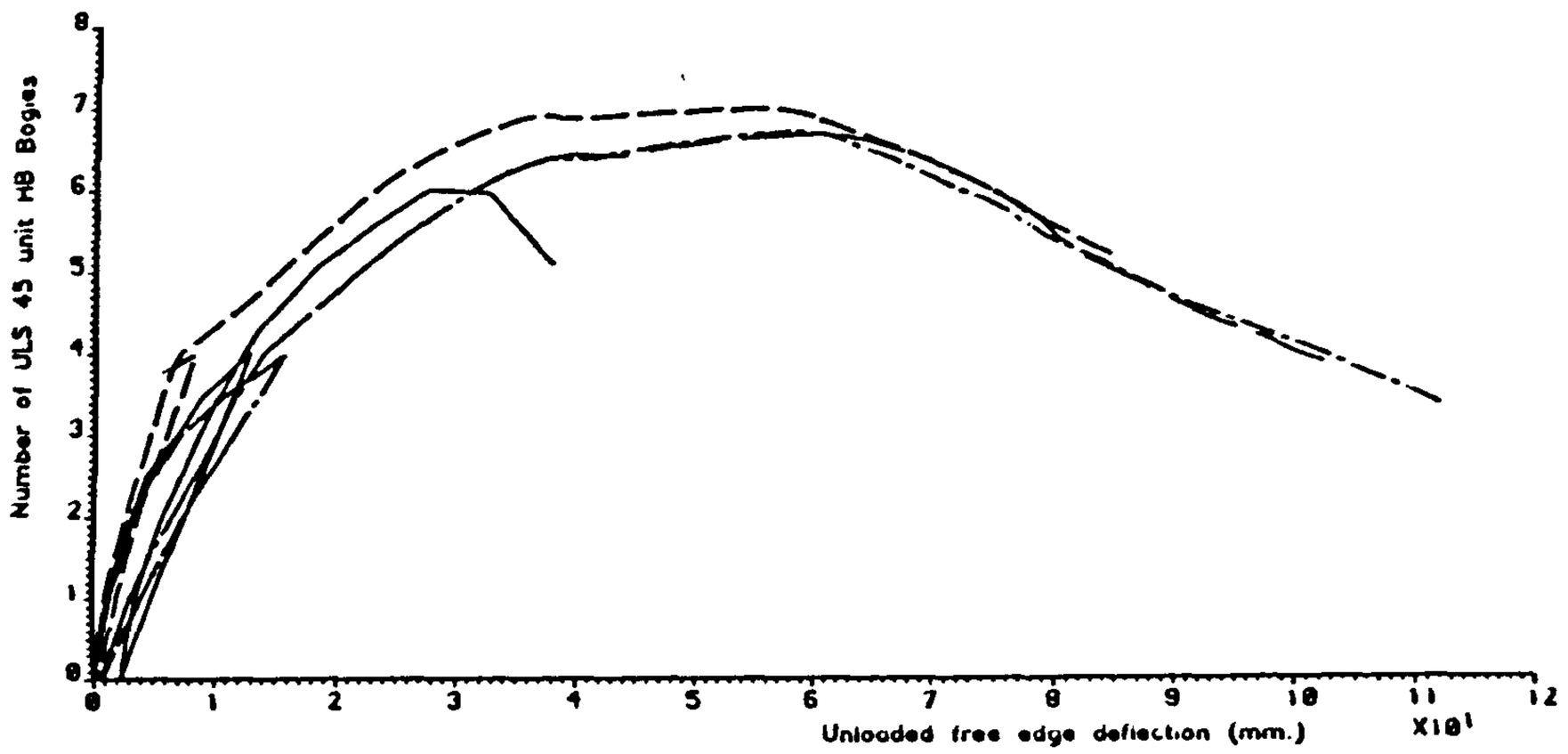

KEY:

1 ——— Experimental

2 – – – – – Standard data (34% prestress losses)

3 ·—·—·—· 40% prestress losses, E reduced by 50% and f_t reduced by 50%

4 — — — 40% prestress losses, E and f_t reduced by 50% and statistically varied material properties

FIG. 9.35. SNAP PROGRAM LOAD-DEFLECTION RESPONSES FOR MODEL 2, OBTAINED WITH A 48 ELEMENT MESH.

by the material curves of Figure 9.30 are far less than experimental values. The residual deflections may be more realistically predicted if the strain at which the tensile unloading curve returns to zero stress was increased by a factor of 4 or 5.

To discover the effects of variations in several modelling parameters, further analyses were carried out. Curve 3 of Figure 9.35 depicts the response obtained with the concrete tensile strength and Young's modulus reduced by 50% and with the prestress losses increased from the calculated 34% to 40%. This analysis produced a smooth response which is in better agreement with the experiment, however, the predicted failure load is 10% too high. Again the displacement level at which failure occurs is accurately predicted.

The adoption of statistically varied material properties had little effect upon the predicted response until the post peak region of the response curve was reached. However, the statistically varied material properties resulted in a more stable solution path which required less computational effort. The falling branches in the responses are the result of both steel rupturing and concrete crushing.

It will be noticed, from Figure 9.35, that even though the displacement level at failure is accurately predicted for the loaded free edge, the corresponding level for the unloaded free edge is considerably in excess of the experimental value. This again suggests that the analytical model was unable to model either the torsional flexibility, or the transverse moment flexibility of the physical model. These factors most probably account for the over strength predictions of between 10% and 15%. The gaps between adjacent beam flanges, that were present in the experimental models, are not modelled

Loaded free edge load–deflection response comparison.

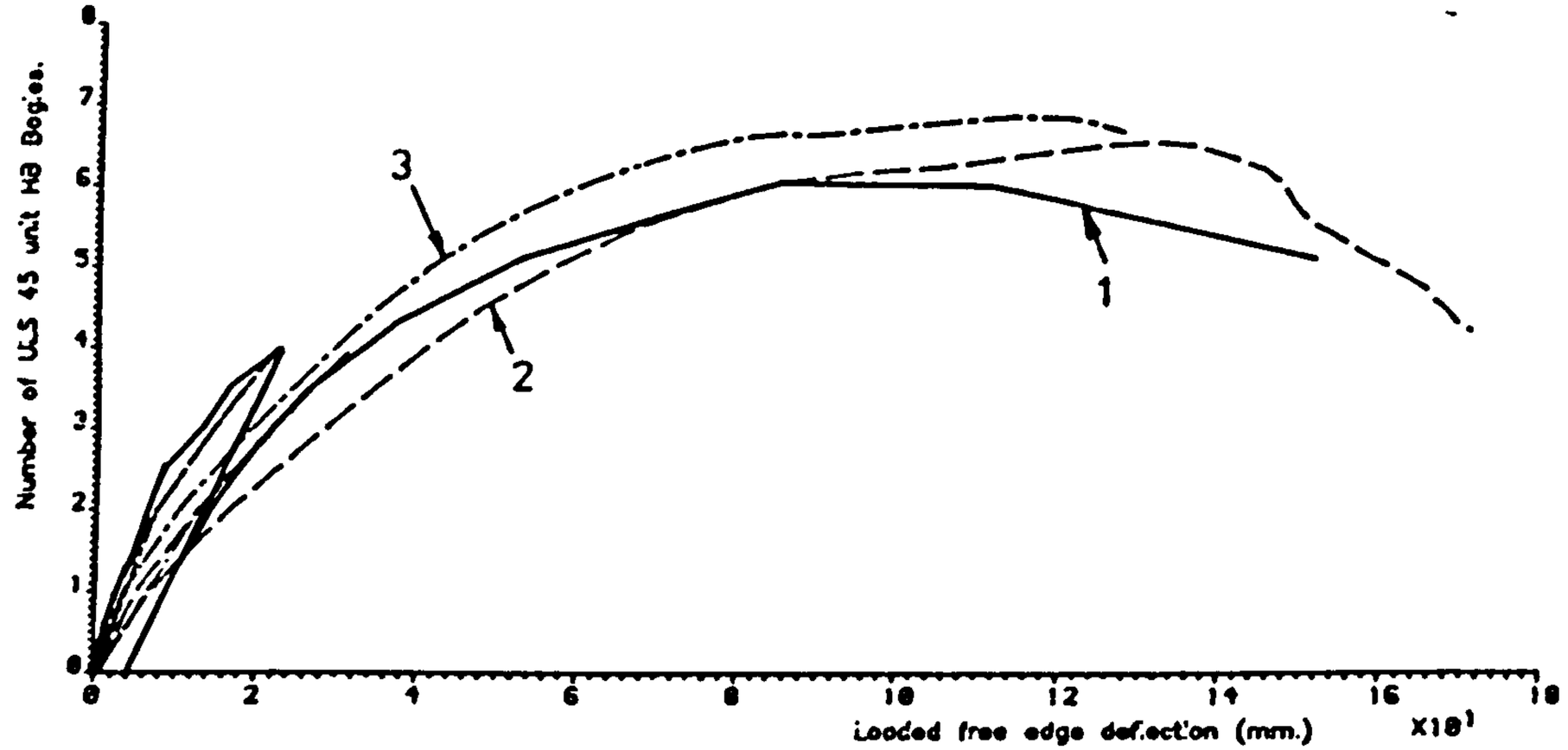

Mid–width centre line load–deflection response comparison.

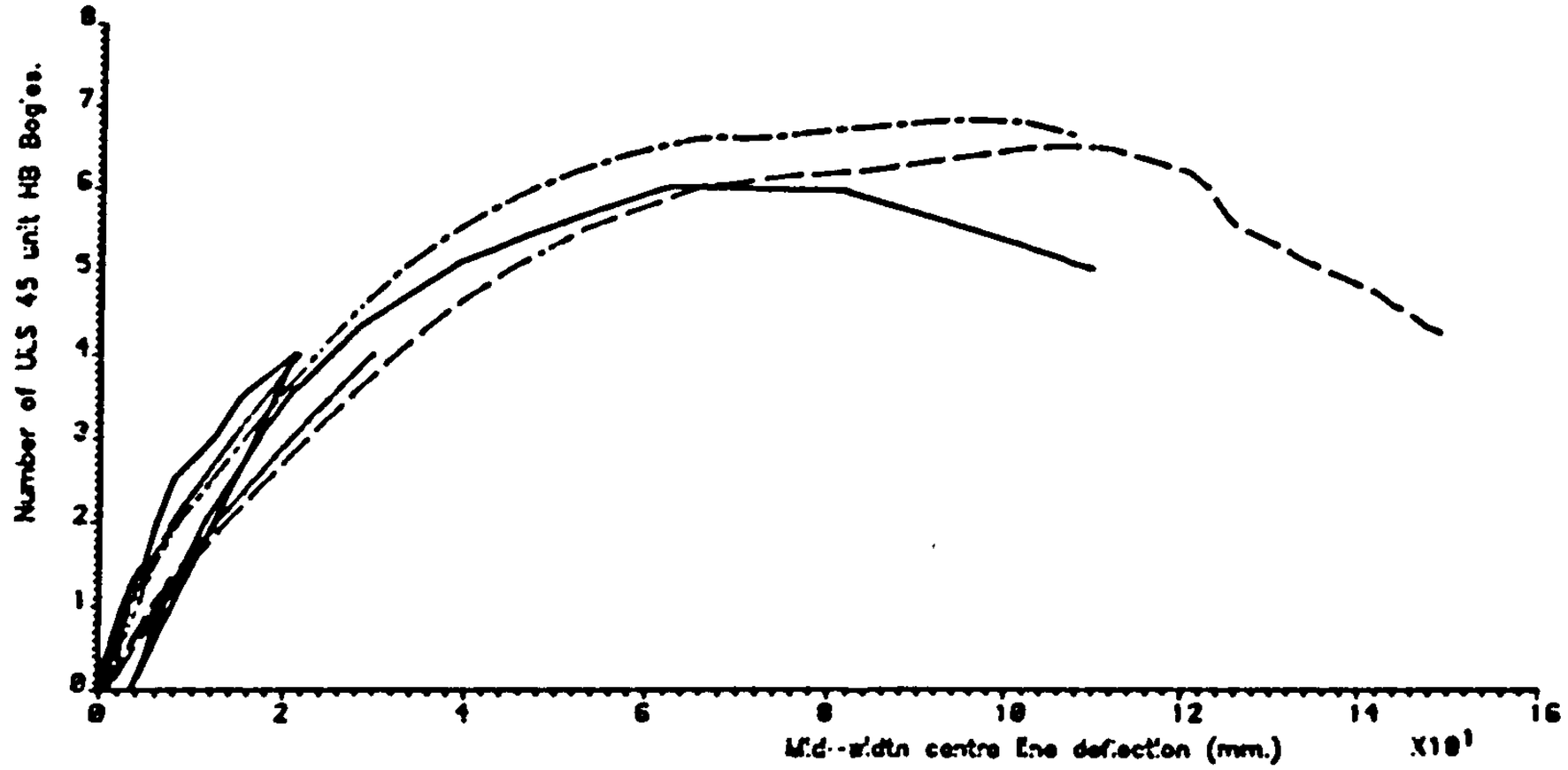

Unloaded free edge load–deflection response comparison.

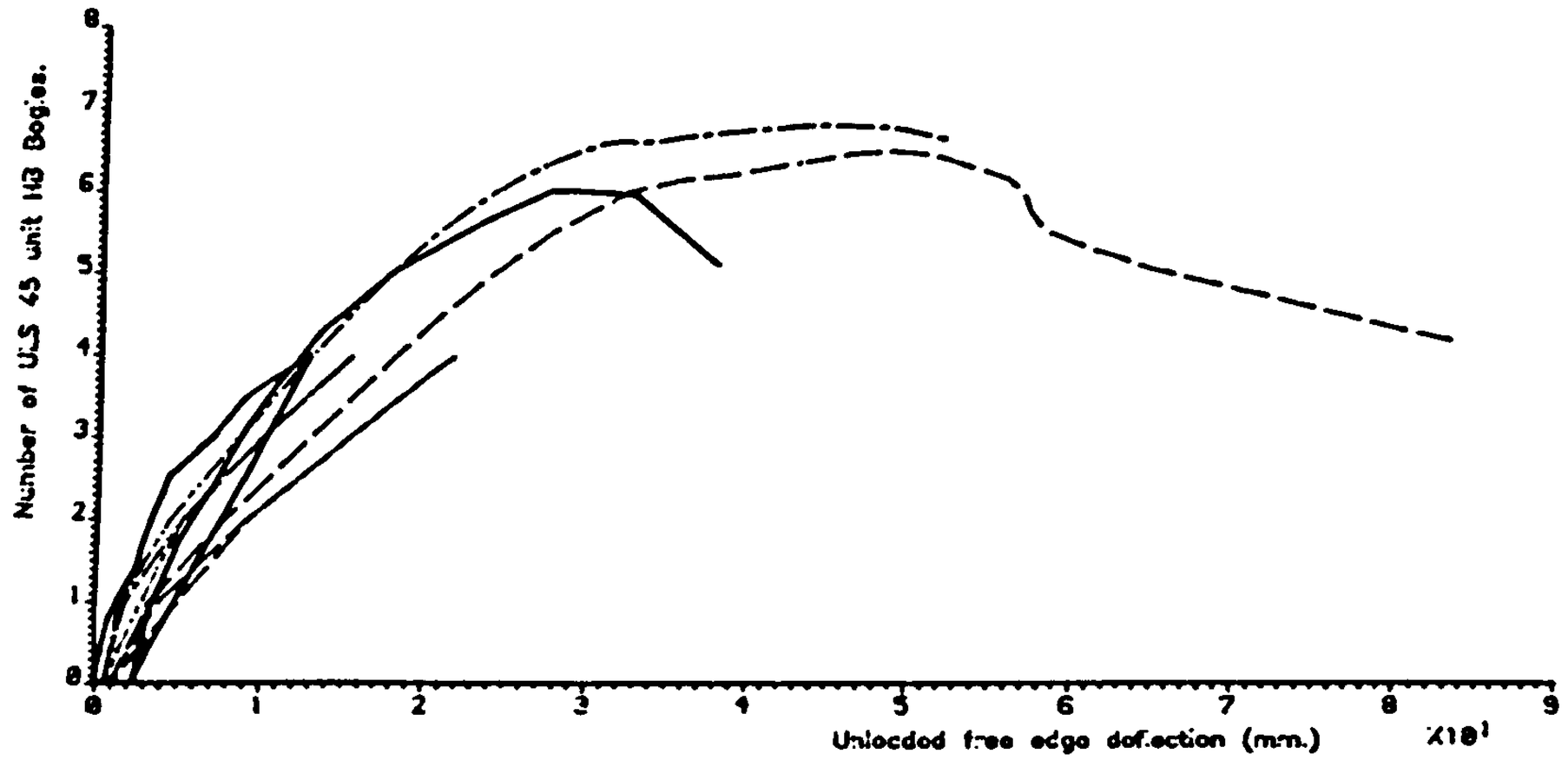

KEY:

1 ———— Experimental

2 – – – – – 40% prestress losses, E reduced by 50% and zero concrete tensile strength.

3 —·—·—· 34% prestress losses and zero concrete tensile strength

FIG. 9.36. SNAP PROGRAM LOAD-DEFLECTION RESPONSES FOR MODEL 2, OBTAINED WITH A 48 ELEMENT MESH

satisfactorily in the biaxial beam approach and in fact the gaps are assumed to be filled with concrete. The approach requires refining so that the gaps are correctly modelled. This will increase the transverse flexibility, which may result in reduced failure loads for the model 2 analyses.

Two further responses are shown in Figure 9.36 with these analyses the concrete tensile strength has been set to zero. The first analytical curve relates to an analysis with increased prestress losses and a reduced E value in addition to zero tensile strength concrete. It can be seen that this combination produces a structure which is too flexible. The ultimate strength in the analysis is approximately 8% above the experimental value.

The second analytical curve that is shown in Figure 9.36 relates to an analysis that used the standard data except that the concrete tensile strength was set to zero. It will be seen that this analysis predicts a structural flexibility which is similar to that of the experiment. However, the ultimate strength is still 10% above that of the experiment. It is interesting to note that the analytical unloaded free edge displacement is closer to that of the experiment. This suggests that this analysis is modelling the transverse behaviour of the experimental model more accurately.

It may be noticed from Figure 9.36 that the locked in deflections, after unloading in position 1a are almost non-existent. This results from the zero tensile strength concrete curve that has been adopted for these analyses. With this curve the stress returns to zero at a zero strain when unloading after cracking.

For each model three particular structural states have been selected at which comparisons will be conducted. The first of these states is located on the ascending portion of the load-deflection curve at approximately 80% of the maximum load. The second state is situated approximately half way along the plateau in the response curve, generally this is close to the experimental maximum load. The third structural state is situated at the end of each of the model tests. The first comparison level is specified in terms of load while it is necessary to specify the other two states in terms of the displacement of the loaded free edge at mid-span. Each structural state for comparison corresponds to a distinct level as defined in Appendices 5.3 and 7.2 on the presentation of the experimental results.

9.3.4 Deflection profiles

Deflection profiles from the SNAP analyses of the models are shown in Figures 9.37 to 9.39 for model 1 and Figures 9.40 to 9.42 for model 2. For each load/displacement level at which deflection profiles are given, profiles for sections at $^3/_4$, $^1/_2$ and $^1/_4$ span are included. To allow an objective assessment to be made, all the deflection profile comparions for a particular model have been plotted to the same scale.

9.3.4.1 Model 1 deflection profiles

The first deflection profile comparison that is given is at a load factor of 2.7 x ULS 45 unit HB bogies, which is equivalent to level 16 of Appendix 5.3. From the load-deflection responses of Figure 9.33 it can be seen that at a load level of 2.7 the structural response is still climbing steeply. There is extensive cracking but the steel is only beginning to yield. This profile comparison has been defined at a certain load level and therefore, as expected, there is an error in the magnitude of the predicted deflections. From the $^1/_2$ span profile comparison, the analytical response can be seen to be too rigid. It

is difficult to assess the analytical profiles at $^3/_4$ and $^1/_4$ span. They do, however, appear to be in reasonable agreement with the experiment.

Figure 9.38 depicts the deflection profiles at a displacement level of 79 mm which is equivalent to level 21 of Appendix 5.3. It can be seen that there is outstanding agreement between the experimental and analytical $^1/_2$ span section profiles. The major deviation occurs at the unloaded free edge where the analytical profile overestimates the transverse hogging curvature. There is little difference between the profiles from each of the different analyses. However, the standard data analysis tends to underestimate the deflections in the unloaded half of the slab. The restricted number of experimental readings for the $^3/_4$ and $^1/_4$ span sections makes it difficult to assess curvature agreement although reasonable agreement is indicated. The analytical profiles are generally similar except that reduced deflections in the unloaded half of the slab are predicted by the standard data analysis.

The final model 1 deflection profiles are presented in Figure 9.39 and these relate to a displacement level of 137 mm which corresponds to level 25 as defined by Appendix 5.3. These experimental readings were taken just before the model test was terminated. It can be seen that the experimental and analytical $^1/_2$ span profiles are generally in good agreement. The major differences occur at the unloaded free edge where the experimental profile 'kicks' up but the analytical profile remains horizontal. Only minor differences will be noticed between each of the analytical profiles. At $^3/_4$ and $^1/_4$ span the magnitude of the displacements are under estimated in the analytical predictions by approximately 30%. At the end of the experimental test a number of displacement transducers had reached the limit of their adjustment and were, therefore, removed. This accounts for the single data point

3/4 span section deflection profile.

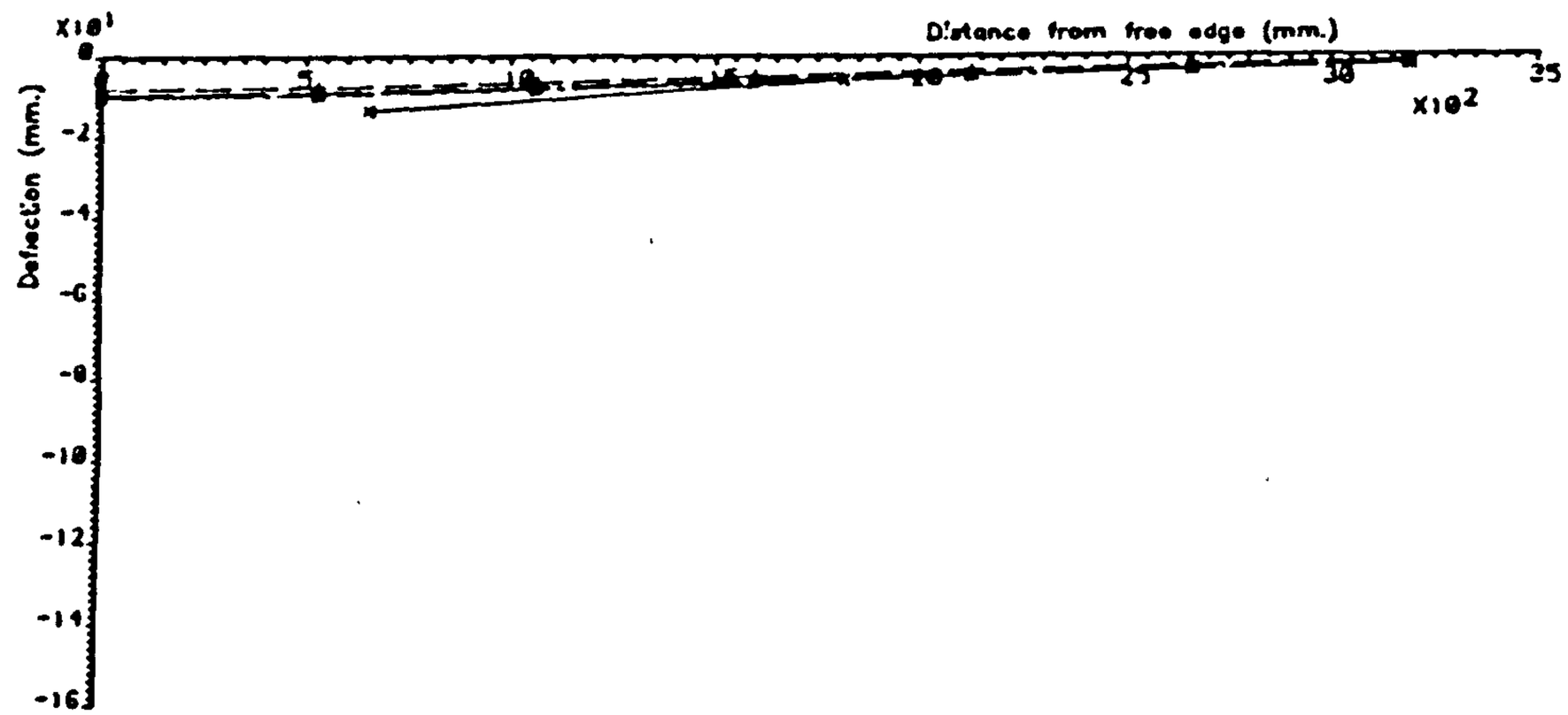

1/2 span section deflection profile.

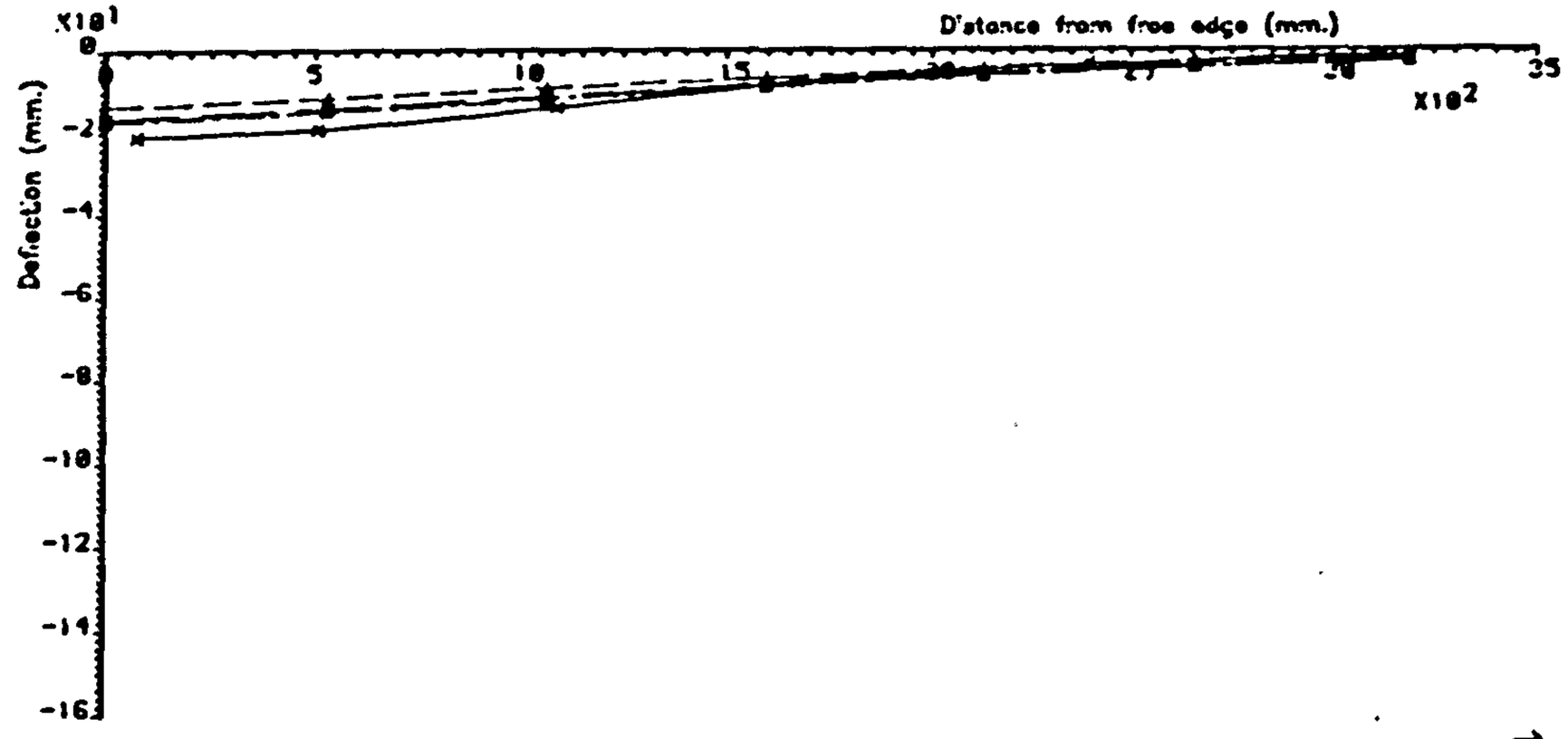

1/4 span section deflection profile.

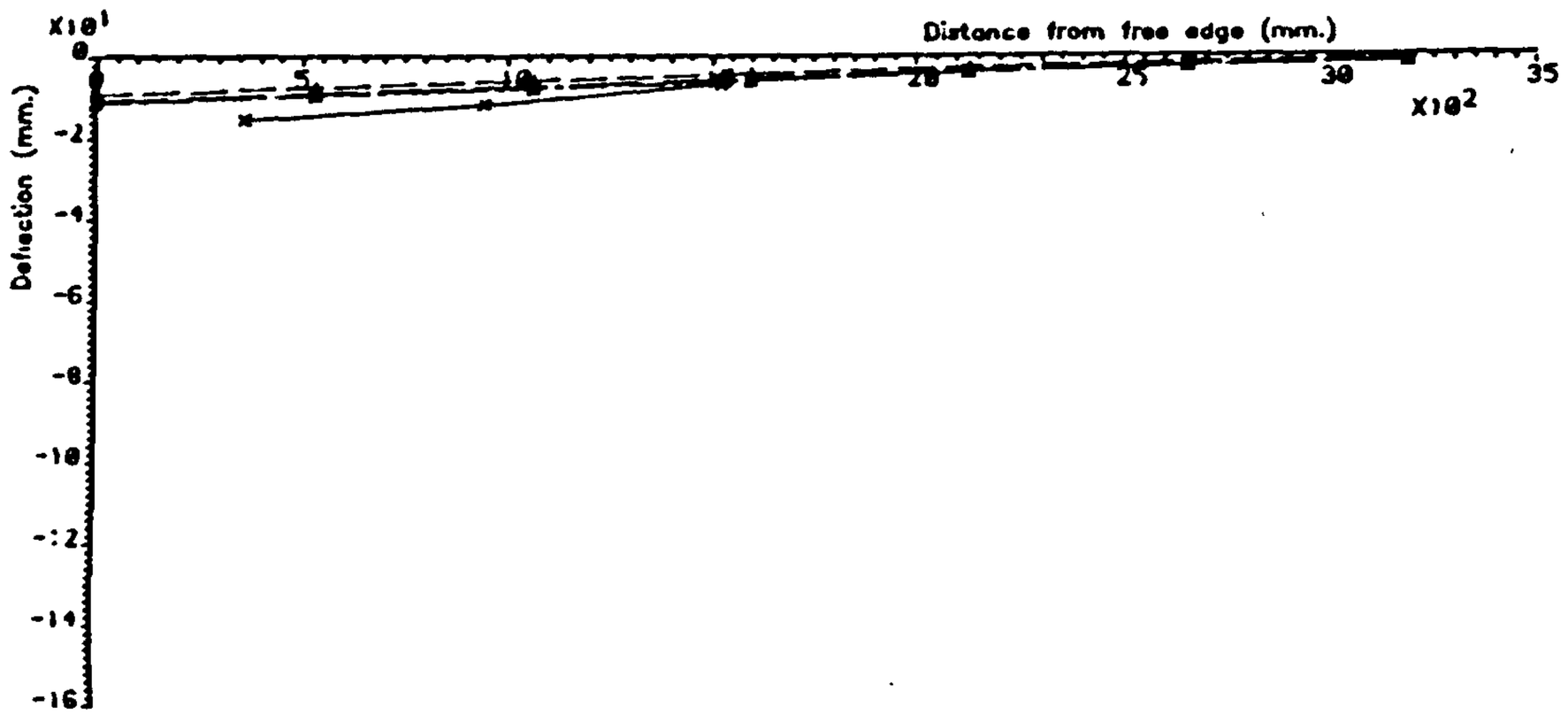

KEY:

1 ——— Experimental

2 — — — — — Standard data (20% prestress losses)

3 — . — . — . 35% prestress losses and a 2 segment curve for concrete in tension

4 — — — 35% prestress losses, 2 segment curve for concrete in tension and statistically varied material properties

FIG. 9. 37. DEFLECTION PROFILE COMPARISONS FOR MODEL 1 AT LEVEL 16 WITH AN APPLIED LOAD LEVEL OF 2.7.

that appears on the $^1/_4$ span profile comparison of this figure. From the $^3/_4$ span profile it is not possible to assess the curvature agreement between the experimental and analtyical profiles.

The poor agreement between the profiles for the unloaded free edge segment may be a direct consequence of the boundary condition arrangement in the analyses. Towards the end of the analyses tensile reaction forces were predicted for a number of supports, generally 3 or 4, at the acute corner end of instrumented support line. Tensile reaction forces were not possible in the actual tests. These analytical tensile reaction forces most probably held the unloaded free edge of the analytical model down, resulting in the differences between the profiles for that region.

9.3.4.2 Model 2 deflection profiles

Deflection profile comparisons for model 2 can be seen in Figures 9.40 to 9.42. The first comparison that is presented is at a load factor of 5.1 x 45 unit ULS HB bogie which corresponds to level 21 of Appendix 7.2. It can be seen that for all but the standard data analyses, the displacement magnitudes are predicted with reasonable accuracy for all sections. However, even at this stage the experimental profile is exhibiting far greater flexibility than those of the analyses.

The second deflection profile comparison, which is shown in Figure 9.41, depicts the situation at a displacement level of 90 mm. This corresponds to level 23 of Appendix 7.2. It can be seen that overall agreement is good with indistinguishable differences for the $^3/_4$ span comparison. From the $^1/_2$ span comparison, it can be seen that all the analytical profiles are grouped together except for curve 5, which corresponds to the analysis with zero tensile strength. Curve 5 gives

3/4 span section deflection profile.

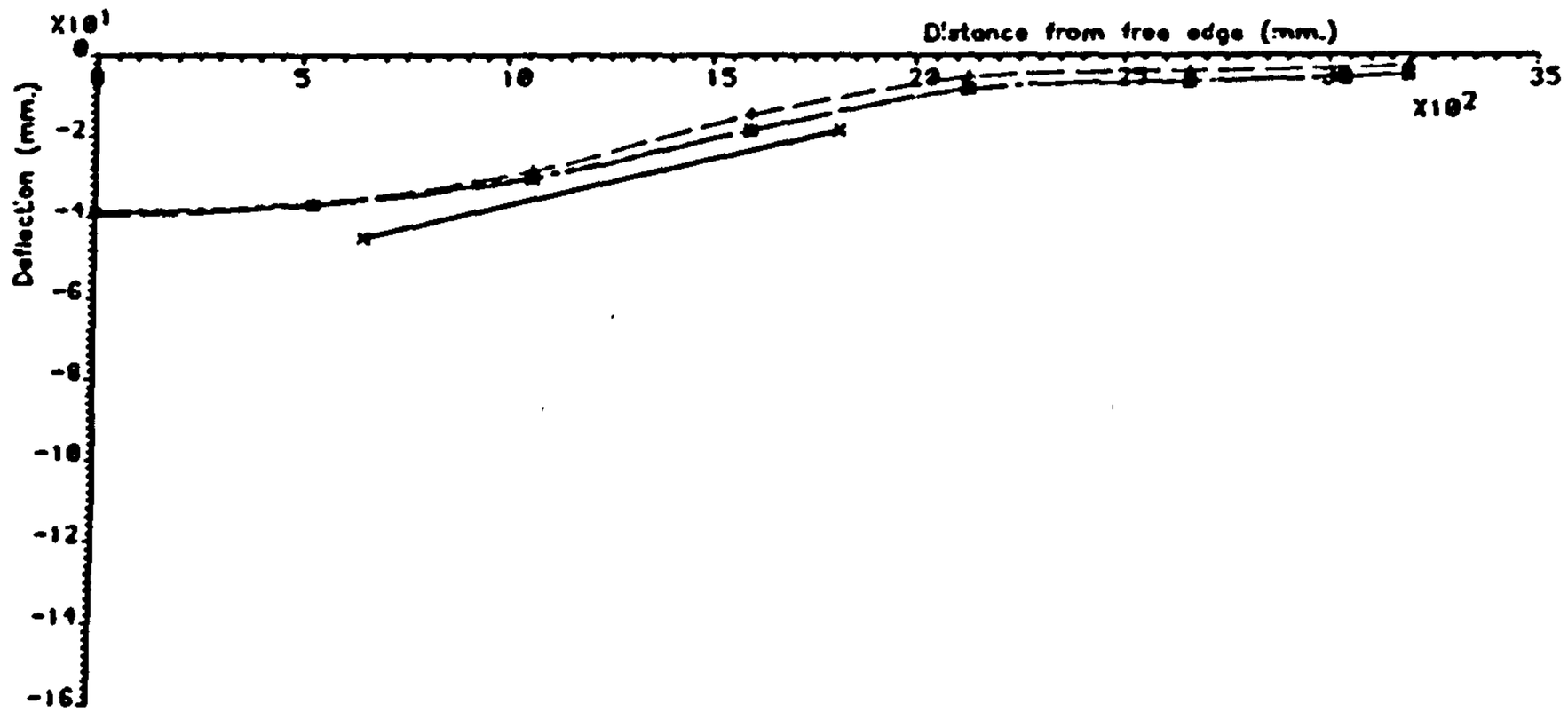

1/2 span section deflection profile.

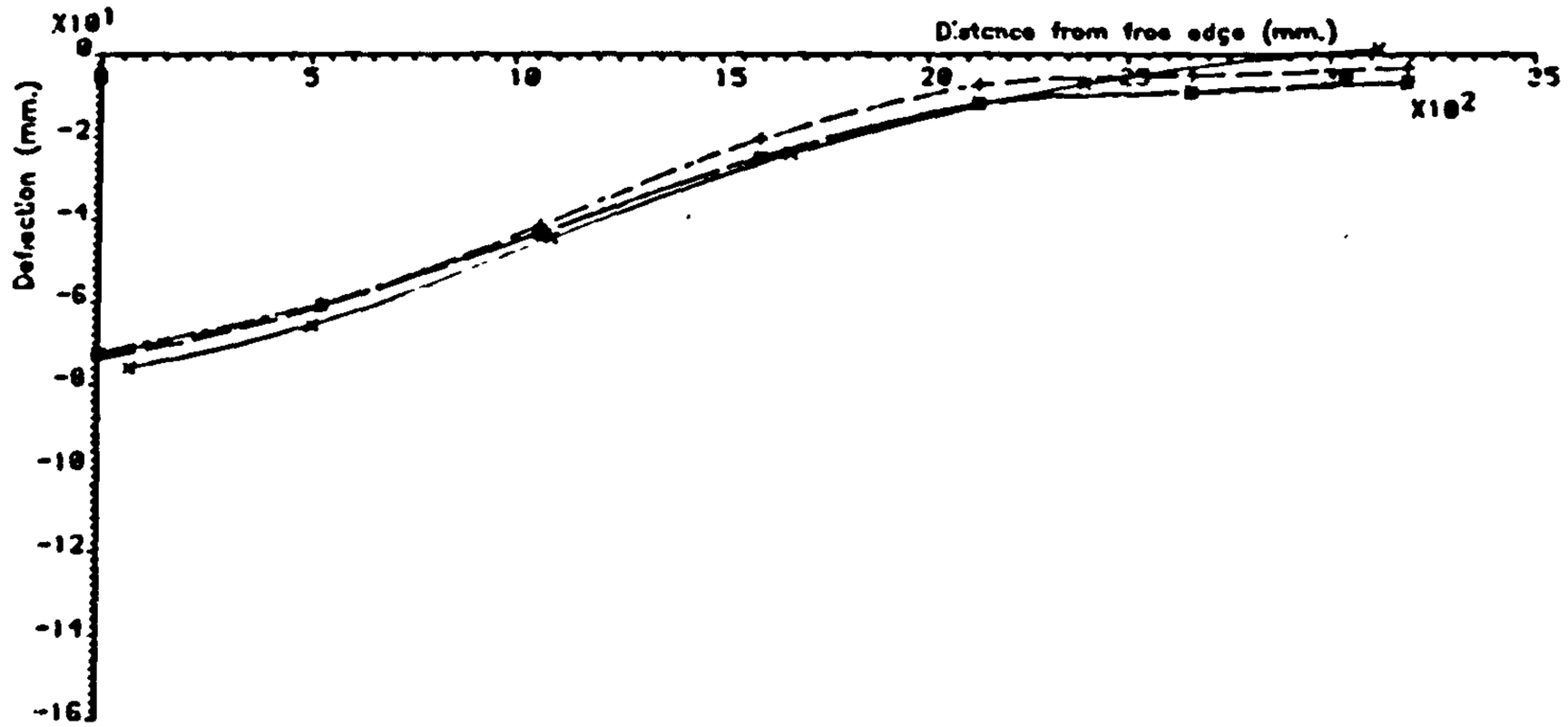

1/4 span section deflection profile.

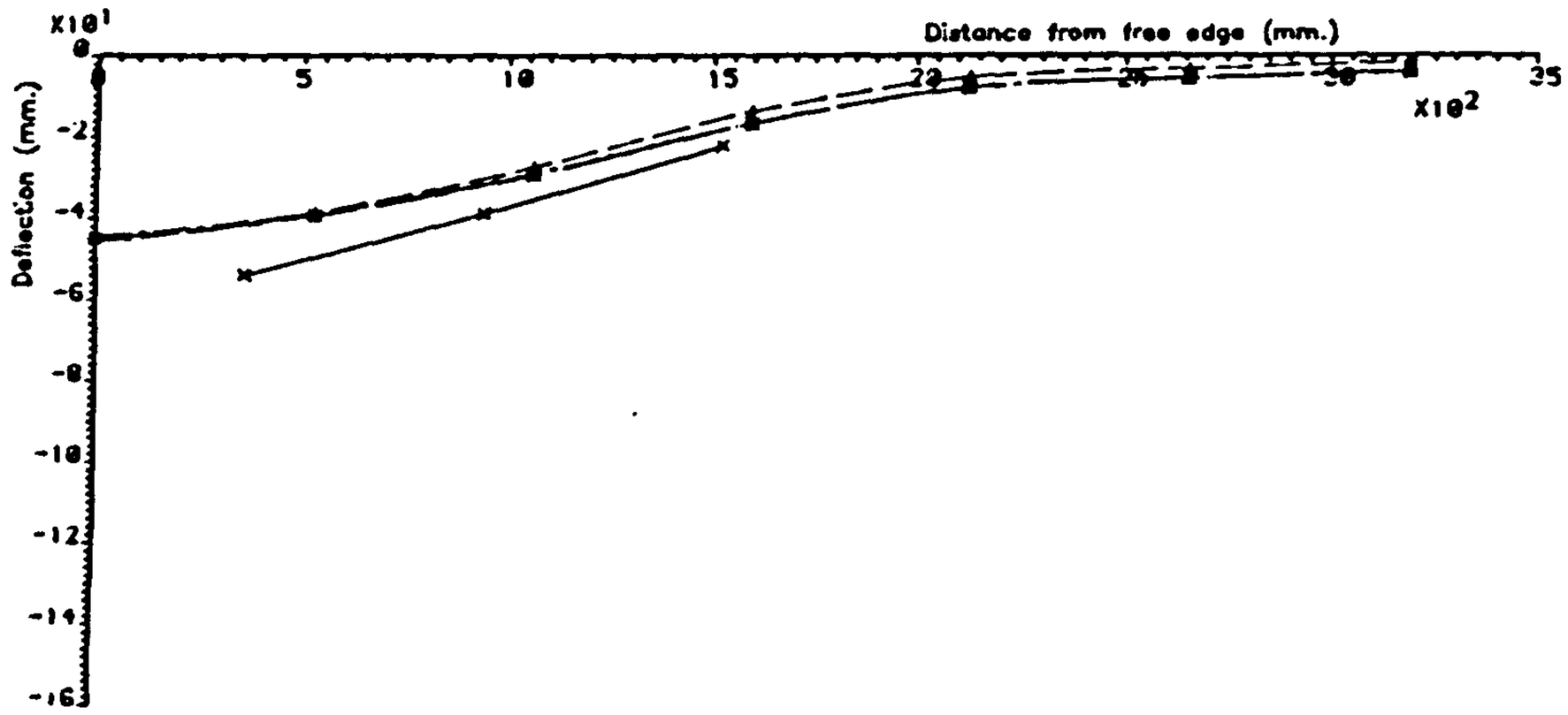

KEY:

1 ——————— Experimental

2 — — — — — Standard data (20% prestress losses)

3 —·—·— 35% prestress losses and a 2 segment curve for concrete in tension

4 — — — 35% prestress losses, a 2 segment curve for concrete in tension and statistically varied material properties

FIG. 9.38. DEFLECTION PROFILE COMPARISONS FOR MODEL 1 AT LEVEL 21 WITH A LOADED FREE EDGE DISPLACEMENT LEVEL OF 79mm

the best agreement, however the experimental profile exhibits greater flexibility and transverse curvatures.

Figure 9.42 compares the profiles at a displacement level of 156 mm which corresponds to level 25 as defined in Appendix 7.2. It can be seen that there is a large difference between the $^1/_2$ span experimental and analytical profiles. It is obvious that the analyses have not predicted the transverse flexibility that was present in the model. This feature could account for the analytical overstrength predictions. The differences can also be seen in the $^1/_4$ span comparison.

As with model 1 several acute corner supports were seen to lift off in the model 2 test. In the analyses, tensile reactions forces were predicted in this region, however there is nothing to indicate that this feature had a significant effect on either the experimental or analytical profiles for model 2.

9.3.5 Reaction profiles

Reaction profile comparisons can be seen in Figures 9.43 to 9.46 for model 1 and Figure 9.47 to 9.50 for model 2. It is not a straightforward procedure to compare experimental and analytical reaction profiles when the number and location of supports differ. To allow a direct comparison all data needs to be processed. For the present study the data was reduced to produce equivalent forces per unit width. For the experimental data this involved dividing each reaction reading by the beam spacing. For the discrete analtyical boundary conditions, each reaction was divided by a uniform proportion of the support line width except for the end supports which were divided by half this value. For the line support consistent boundary conditions, the reactions were divided by a proportion of the

3/4 span section deflection profile.

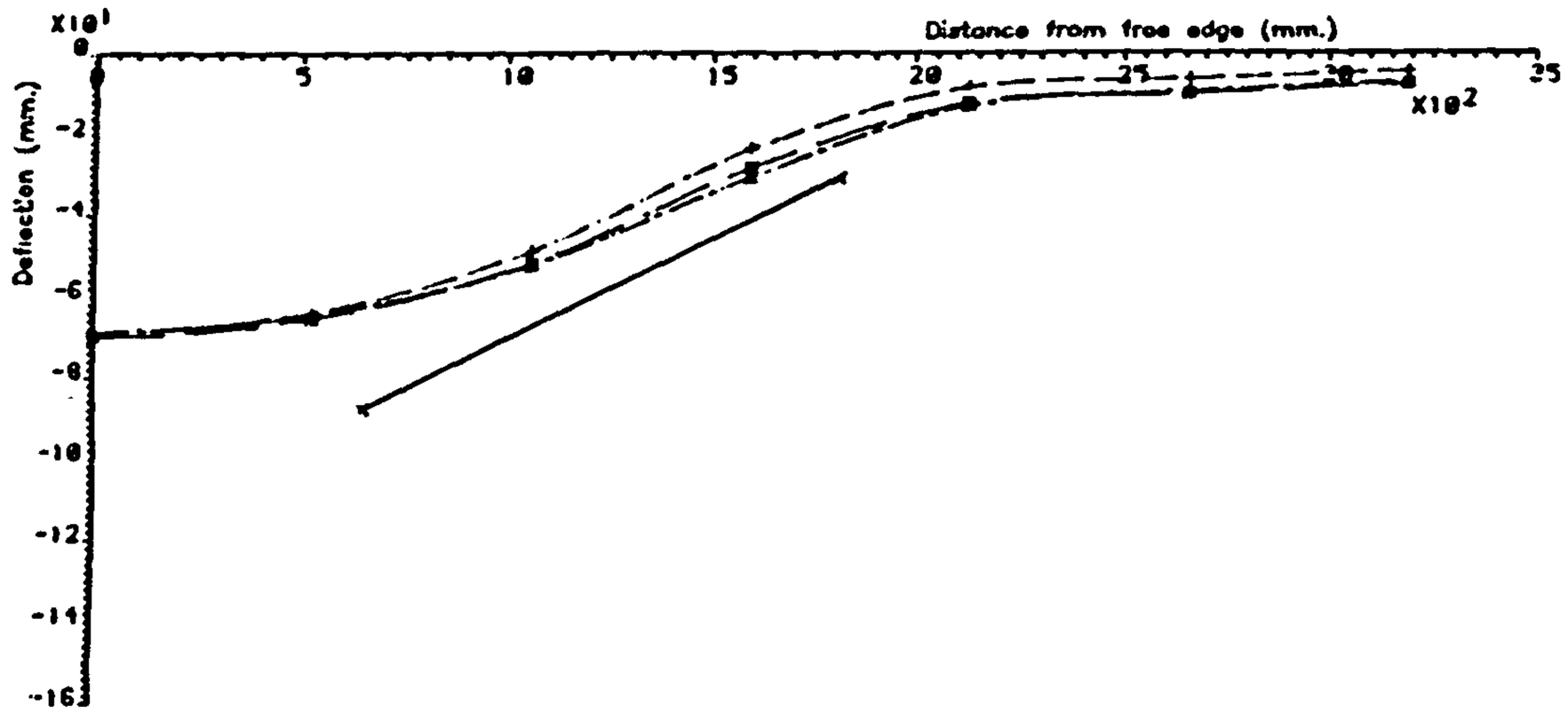

1/2 span section deflection profile.

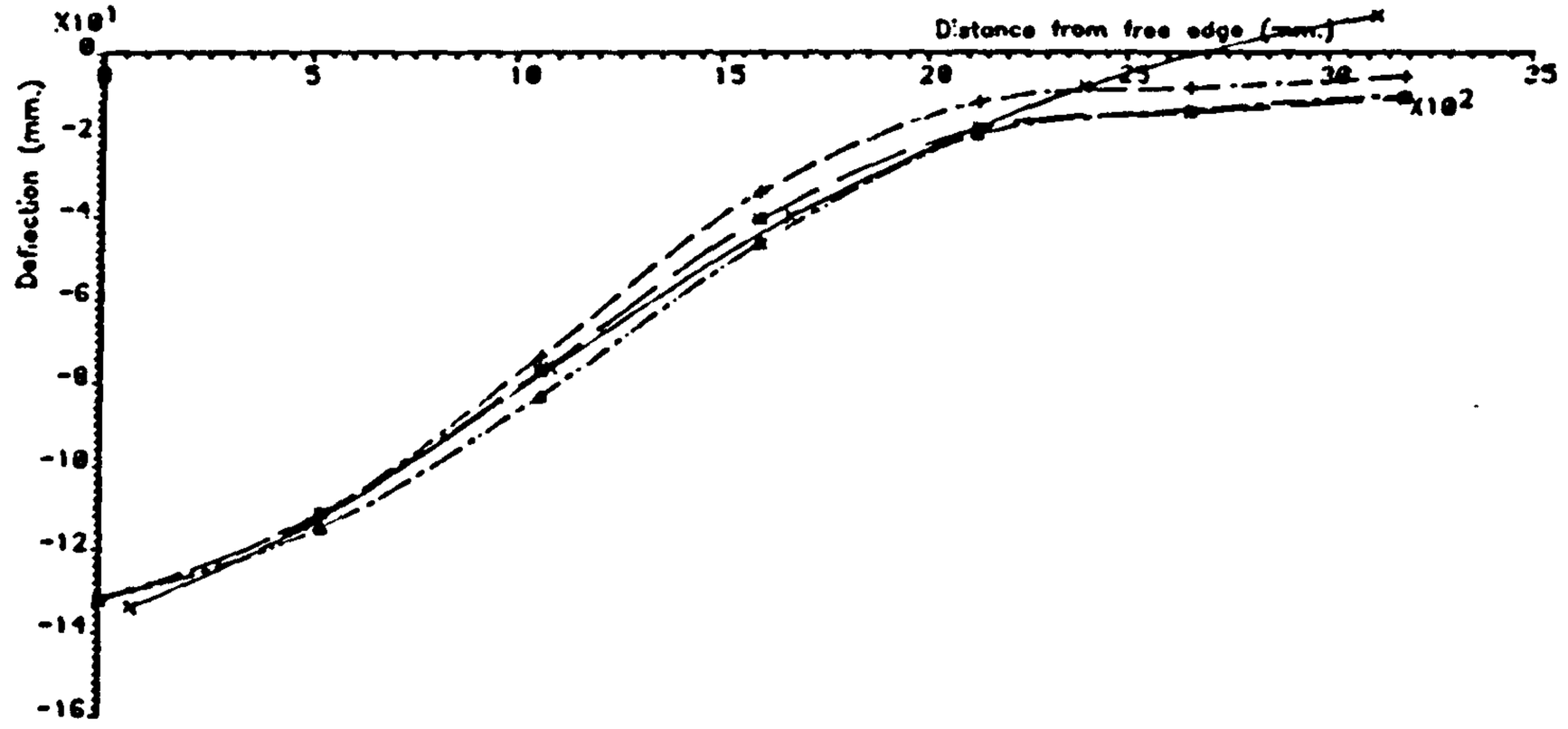

1/4 span section deflection profile.

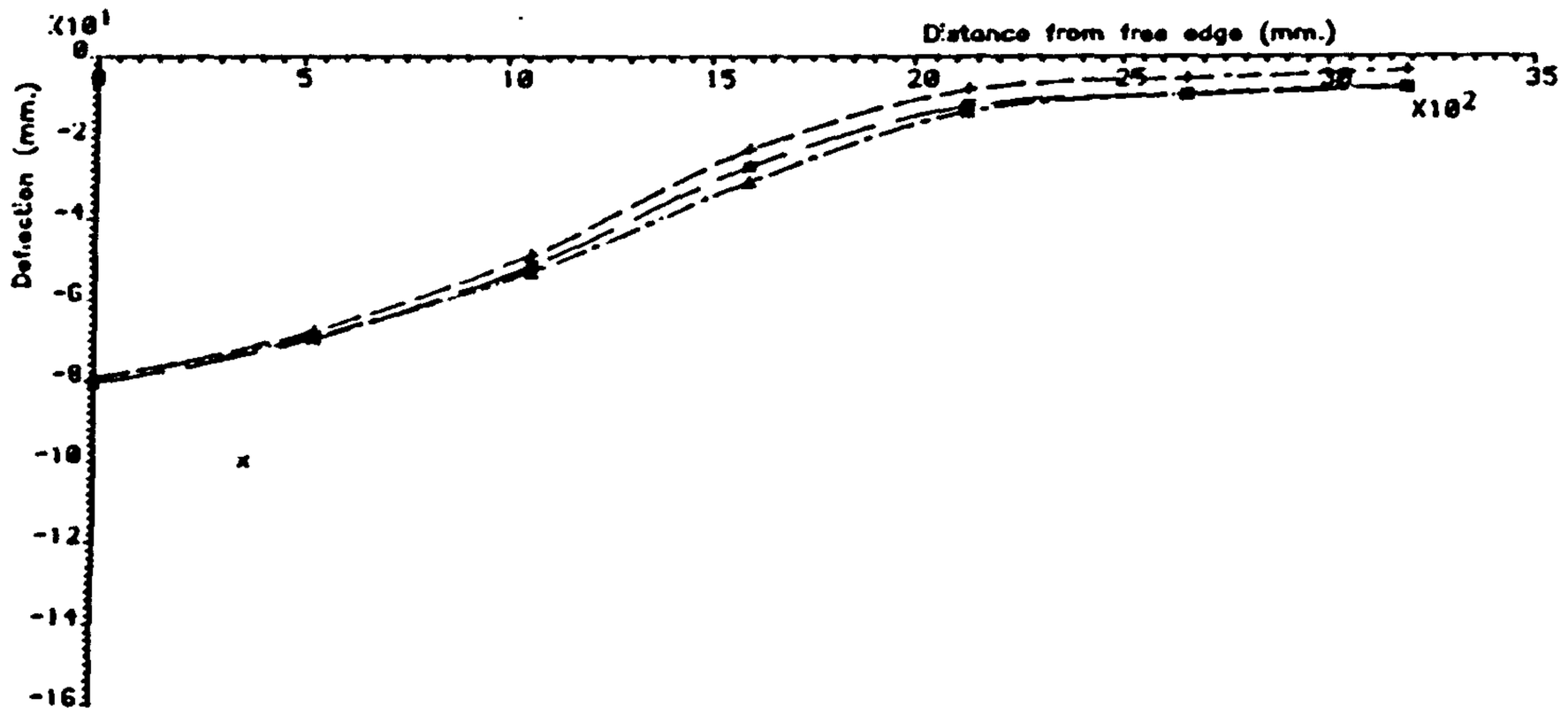

KEY:

1 ——————— Experimental

2 — — — — — Standard data (20% prestress losses)

3 —·—·— 35% prestress losses and a 2 segment curve for concrete in tension

4 —— —— —— 35% prestress losses, a 2 segment curve for concrete in tension and statistically varied material properties

FIG. 9.39. DEFLECTION PROFILE COMPARISONS FOR MODEL 1 AT LEVEL 25 WITH A LOADED FREE EDGE DISPLACEMENT LEVEL OF 137mm

3/4 span section deflection profile.

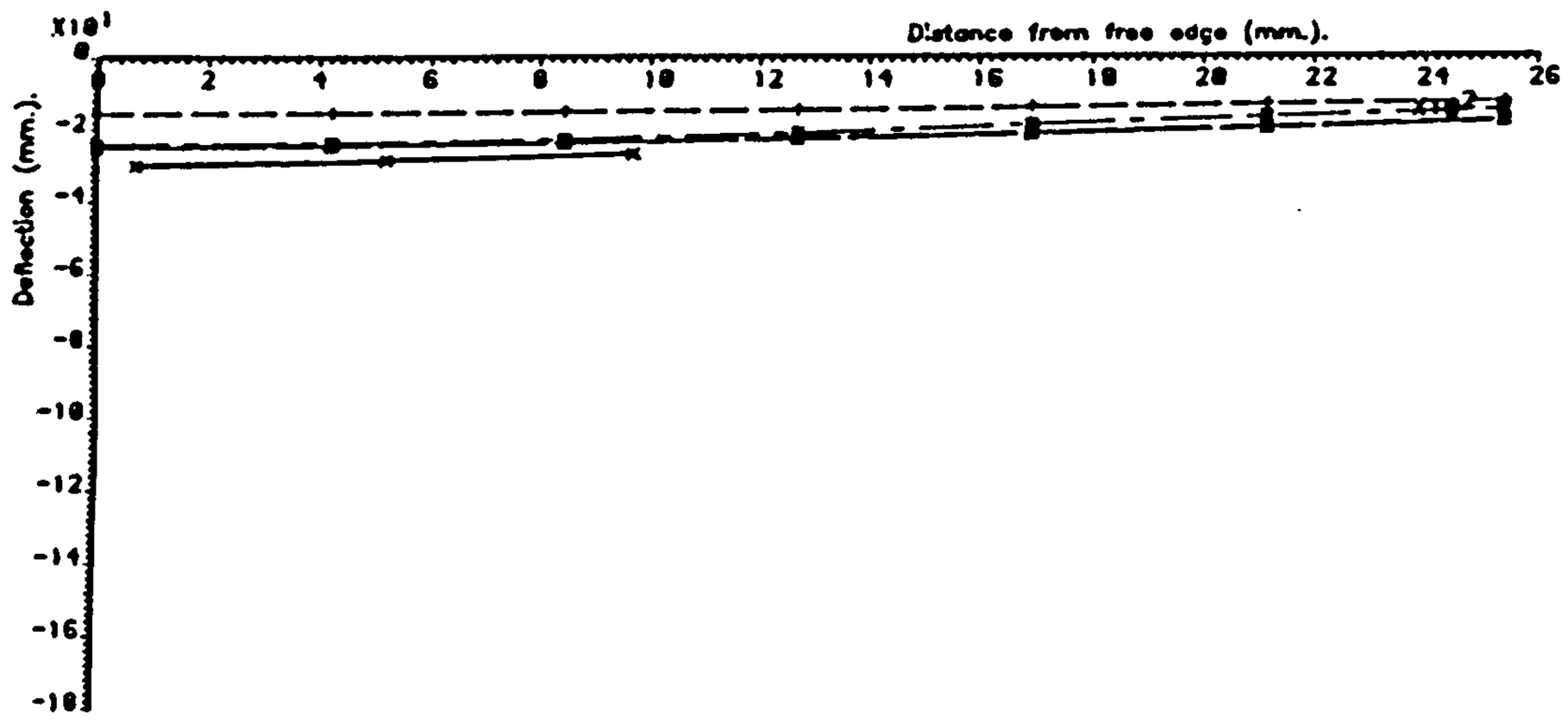

1/2 span section deflection profile.

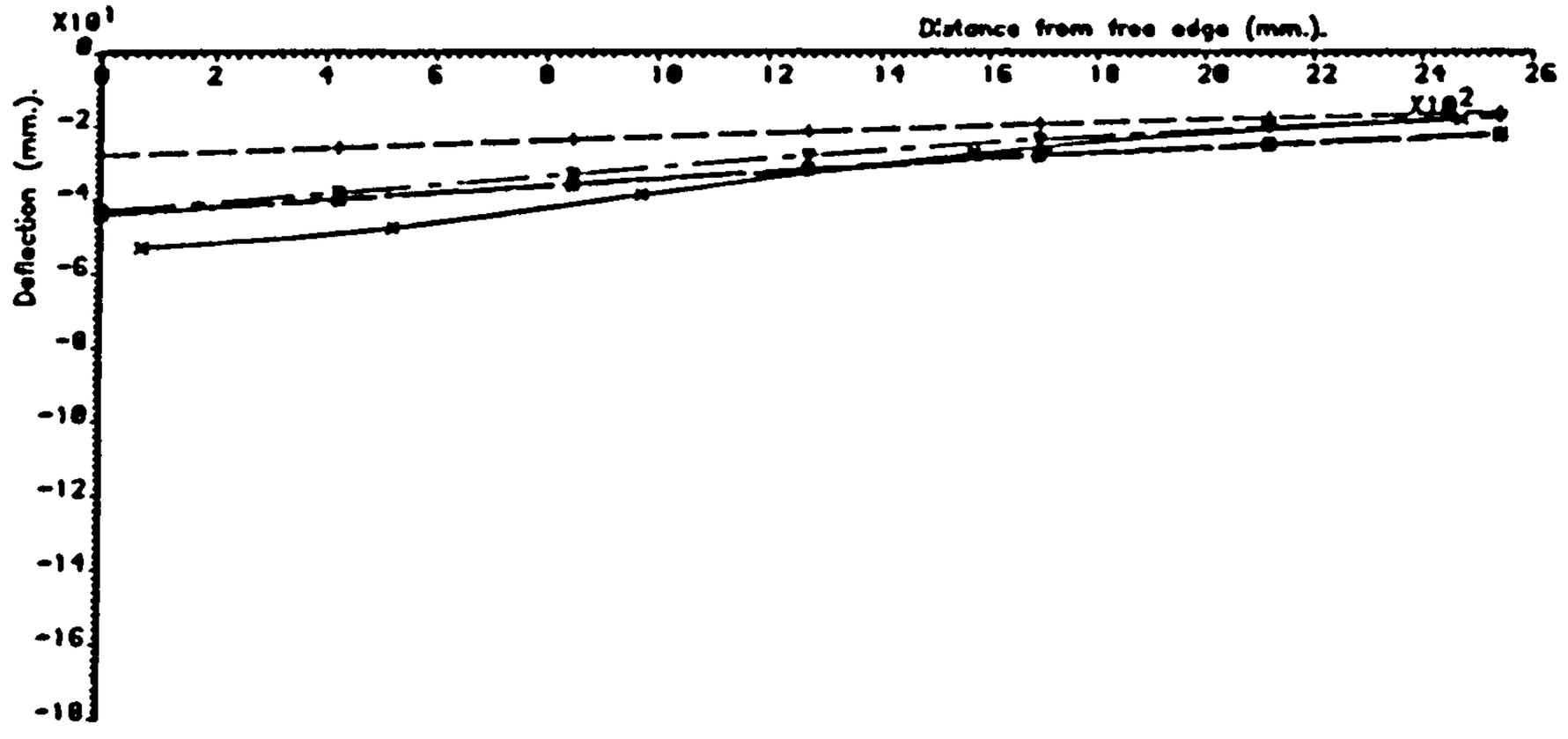

1/4 span section deflection profile.

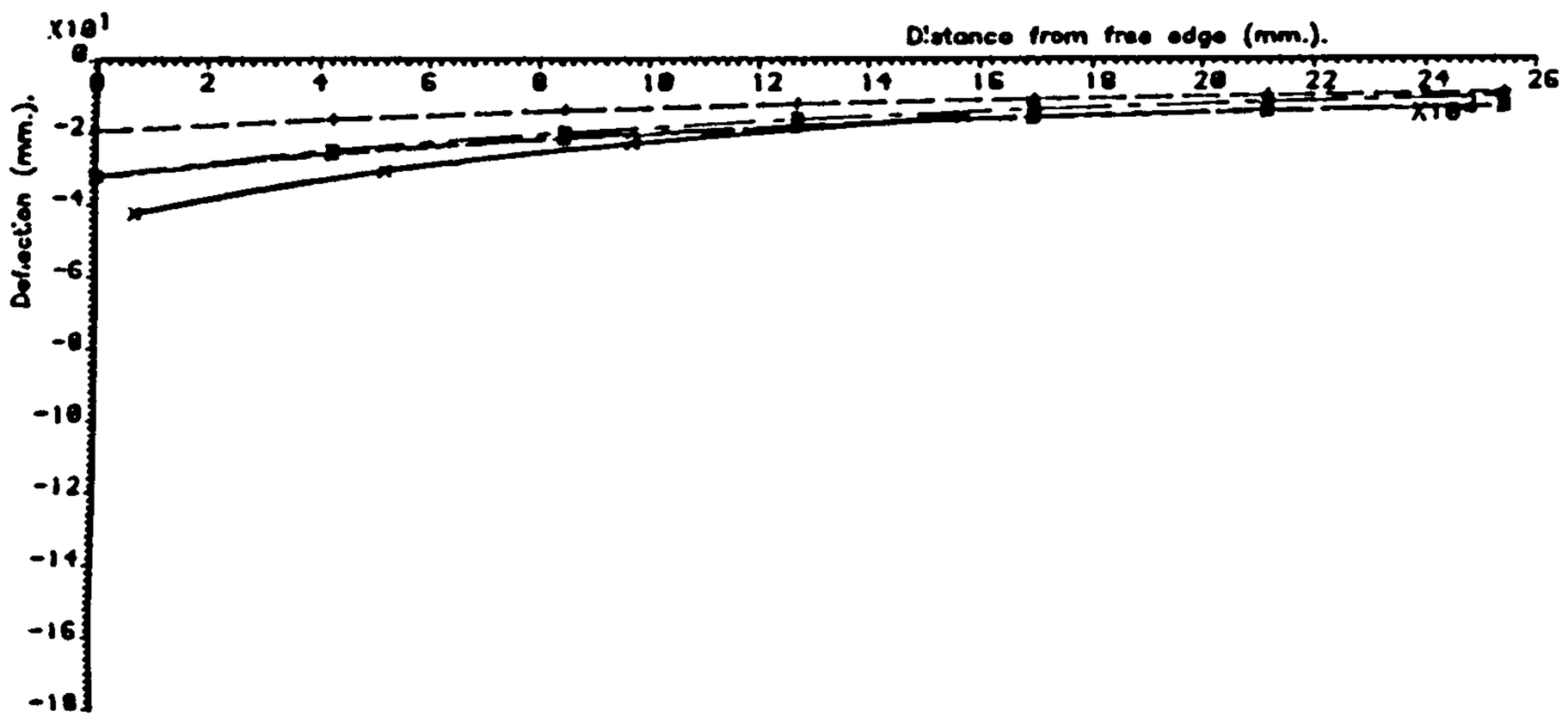

KEY:

1 ——————— Experimental

2 — — — — — Standard data (34% prestress losses)

3 —·—·—·— 40% prestress losses, E reduced by 50% and f_t reduced by 50%

4 —— —— —— 40% prestress losses, E and f_t reduced by 50% and statistically varied material properties

5 ·——·——· 34% prestress losses and zero tensile strength concrete

FIG. 9.40. DEFLECTION PROFILE COMPARISONS FOR MODEL 2 AT LEVEL 21 WITH AN APPLIED LOAD LEVEL OF 5.1.

3/4 span section deflection profile.

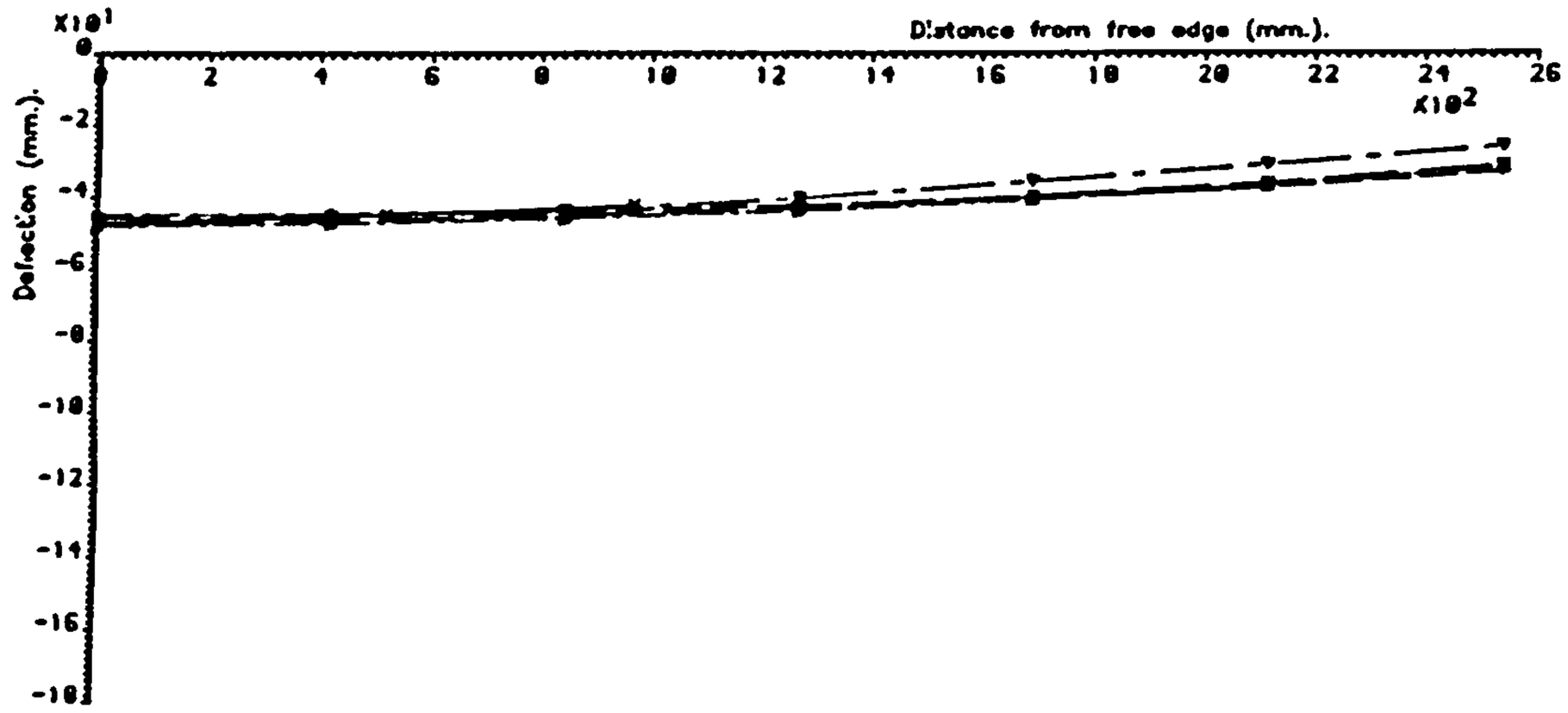

1/2 span section deflection profile.

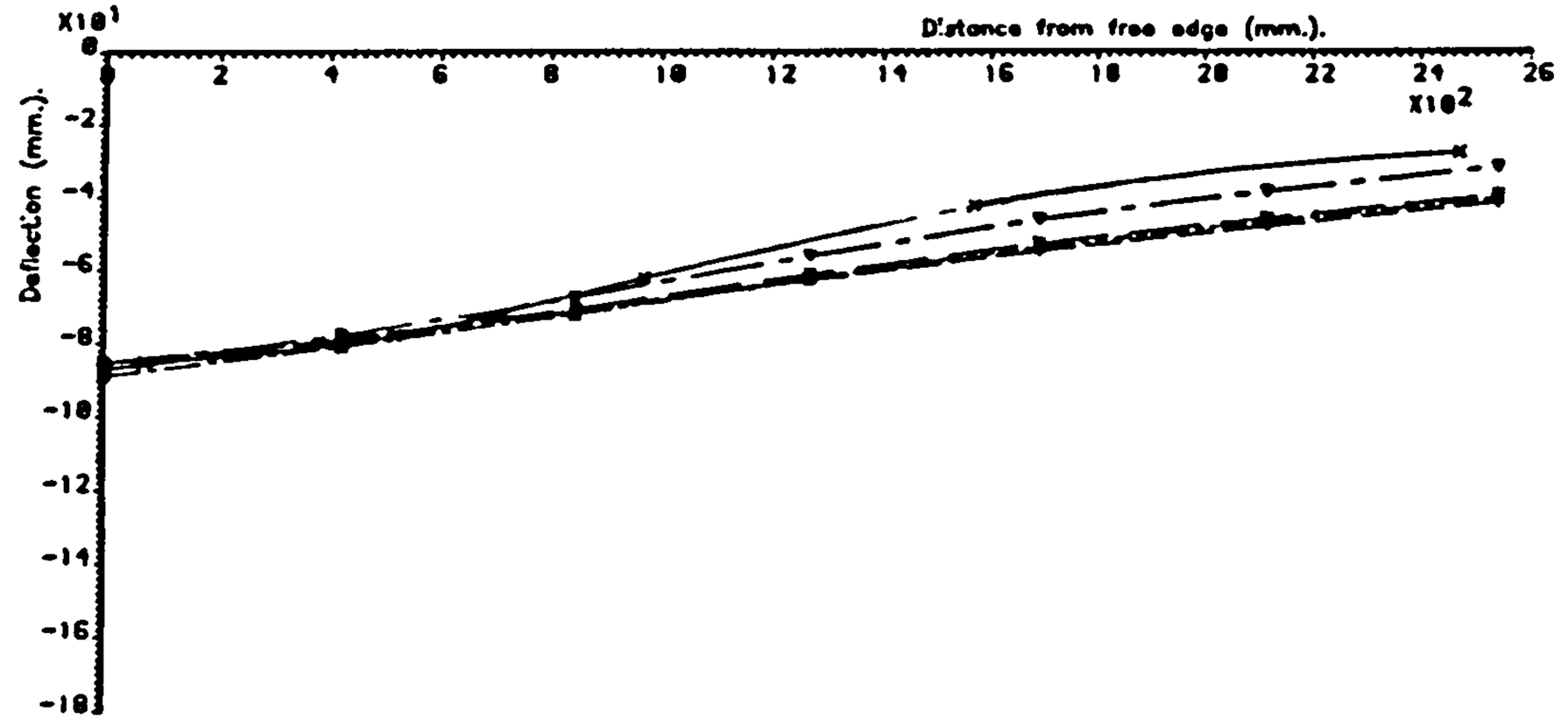

1/4 span section deflection profile.

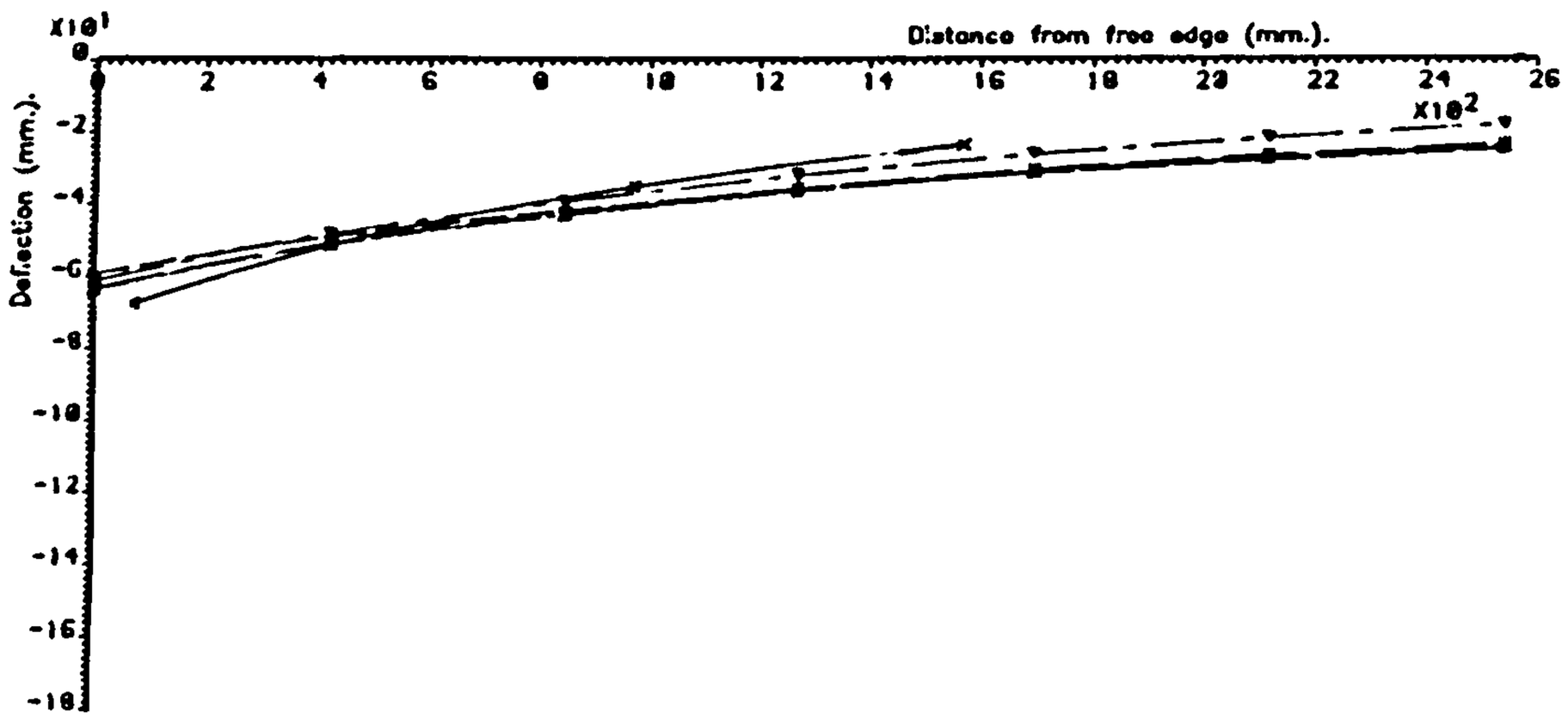

KEY:

1 ——— Experimental

2 – – – – – Standard data (34% prestress losses)

3 —·—·—·— 40% prestress losses, E reduced by 50% and f_t reduced by 50%

4 —— —— —— 40% prestress losses, E and f_t reduced by 50% and statistically varied material properties

5 ——·—— 34% prestress losses and zero tensile strength concrete

FIG 9. 41. DEFLECTION PROFILE COMPARISONS FOR MODEL 2 AT LEVEL 23 WITH A LOADED FREE EDGE DISPLACEMENT LEVEL OF 90mm

3/4 span section deflection profile.

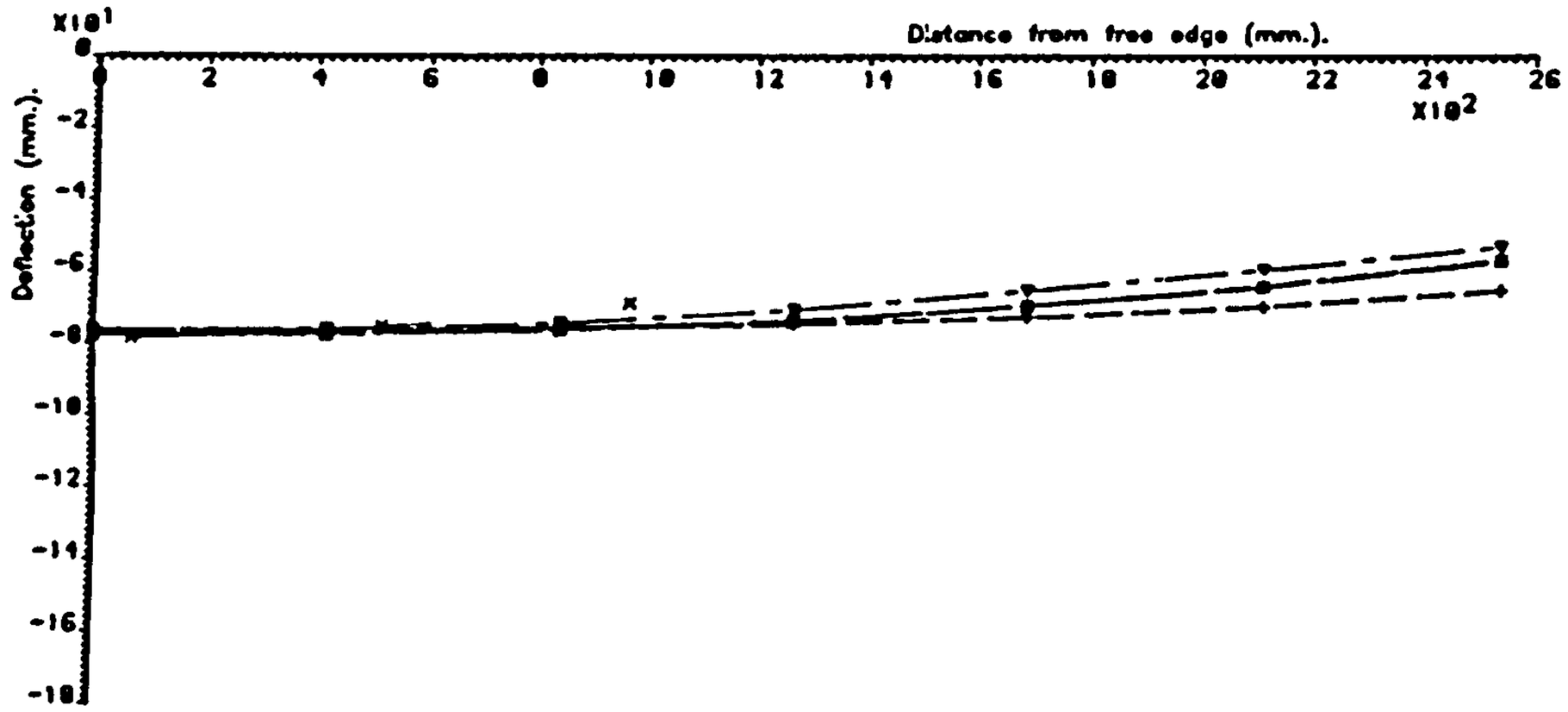

1/2 span section deflection profile.

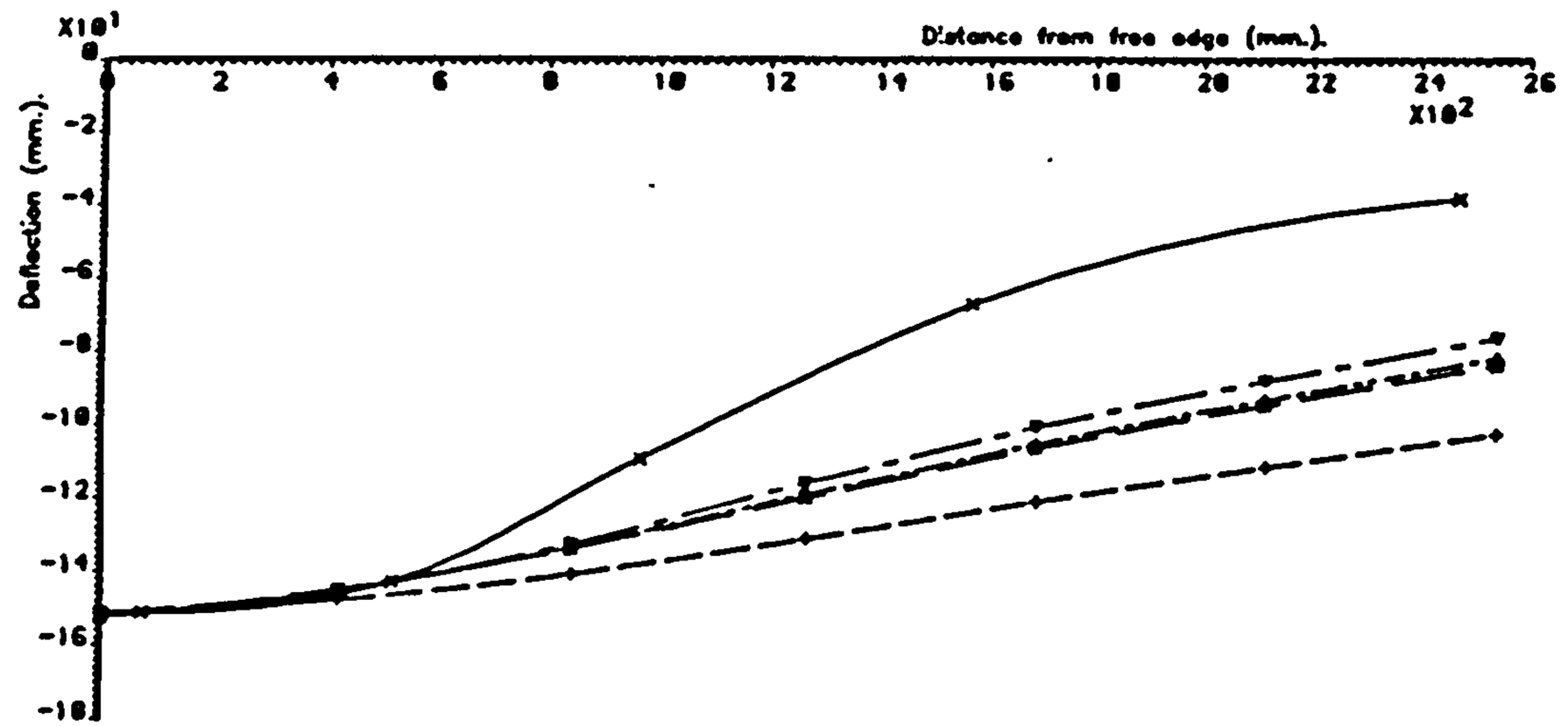

1/4 span section deflection profile.

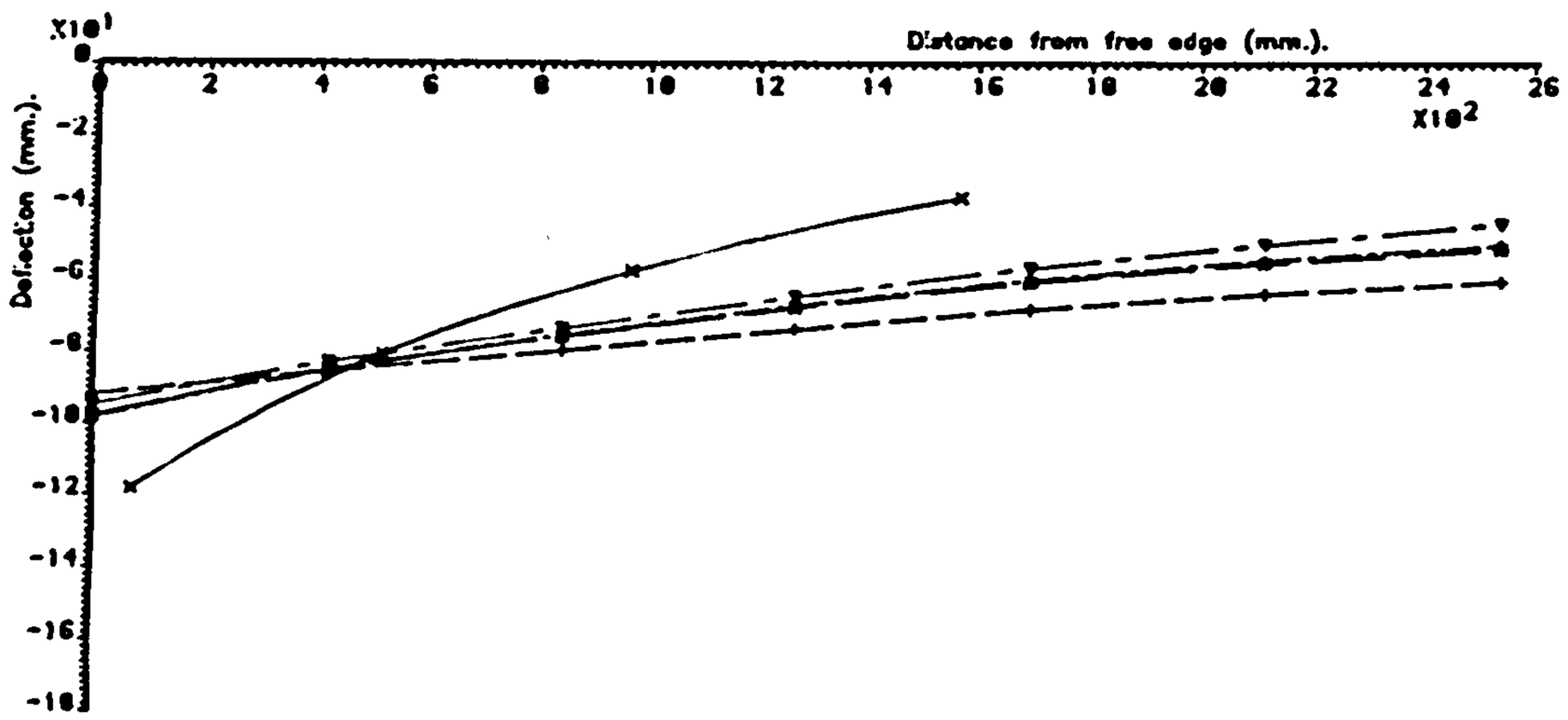

KEY:

1 ——— Experimental

2 – – – – – Standard data (34% prestress losses)

3 —·—·—·— 40% prestress losses, E and f_t reduced by 50%

4 — — — 40% prestress losses E and f_t reduced by 50% and statistically varied material properties

5 —·—·— 34% prestress losses and zero tensile strength concrete

FIG. 9.42. DEFLECTION PROFILE COMPARISONS FOR MODEL 2 AT LEVEL 25 WITH A LOADED FREE EDGE DISPLACEMENT LEVEL OF 156mm

support line width. The proportions were based on the ratio of an individual support stiffness to the total support line stiffness.

To allow an objective assessment of the effects of non-linearity on the reaction profile, a linear finite element prediction is included on each plot. The profiles for each of the different non-linear analyses were generally in close agreement and, therefore, only a single characteristic non-linear finite element curve is included on each of the plots. To allow a direct comparison between levels, all the plots for a particular model are shown to the same scale. All distances are given in terms of the width of the slab perpendicular to the loaded free edge. On some plots of the experimental reaction profiles, tensile reactions are indicated. No tensile reactions were permitted in the model tests and the tensile reactions shown on the plots are a result of the datum that was chosen for plotting the results. The datum for all reaction plots is the structure immediately before the application of the HB bogie.

9.3.5.1 Model 1 reaction profiles

From the comparison at level 16 for the discrete approach, which is shown in Figure 9.43, it can be seen that linear analysis predicts a larger obtuse corner force per unit width than the non-linear analysis. Thus, even at this stage, significant reaction non-linearity is apparent in the analyses. It appears that the non-linear analysis is beginning to shed load when compared to the linear analysis. The profile resulting from the adoption of consistent boundary conditions can be seen in Figure 9.45 for the same level. It can be seen that while the obtuse corner force per unit width is in good agreement, the non-linear analysis does not predict the rapid reduction in the force per unit width that occurs adjacent to the obtuse corner.

Support reaction profile comparison for level 16, with 2.70xULS HB.

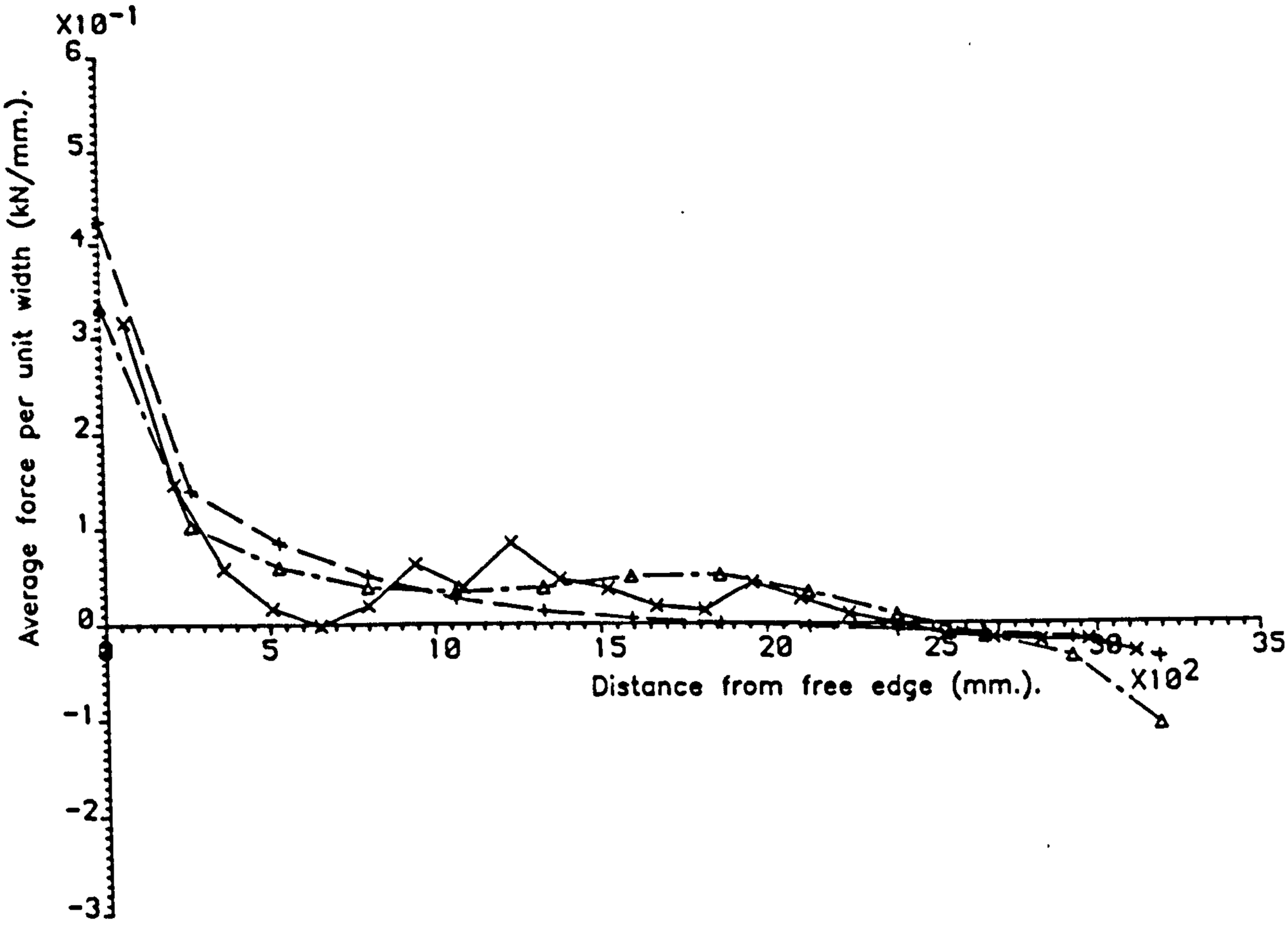

Support reaction profile comparison for level 21, at 79mm. deflection.

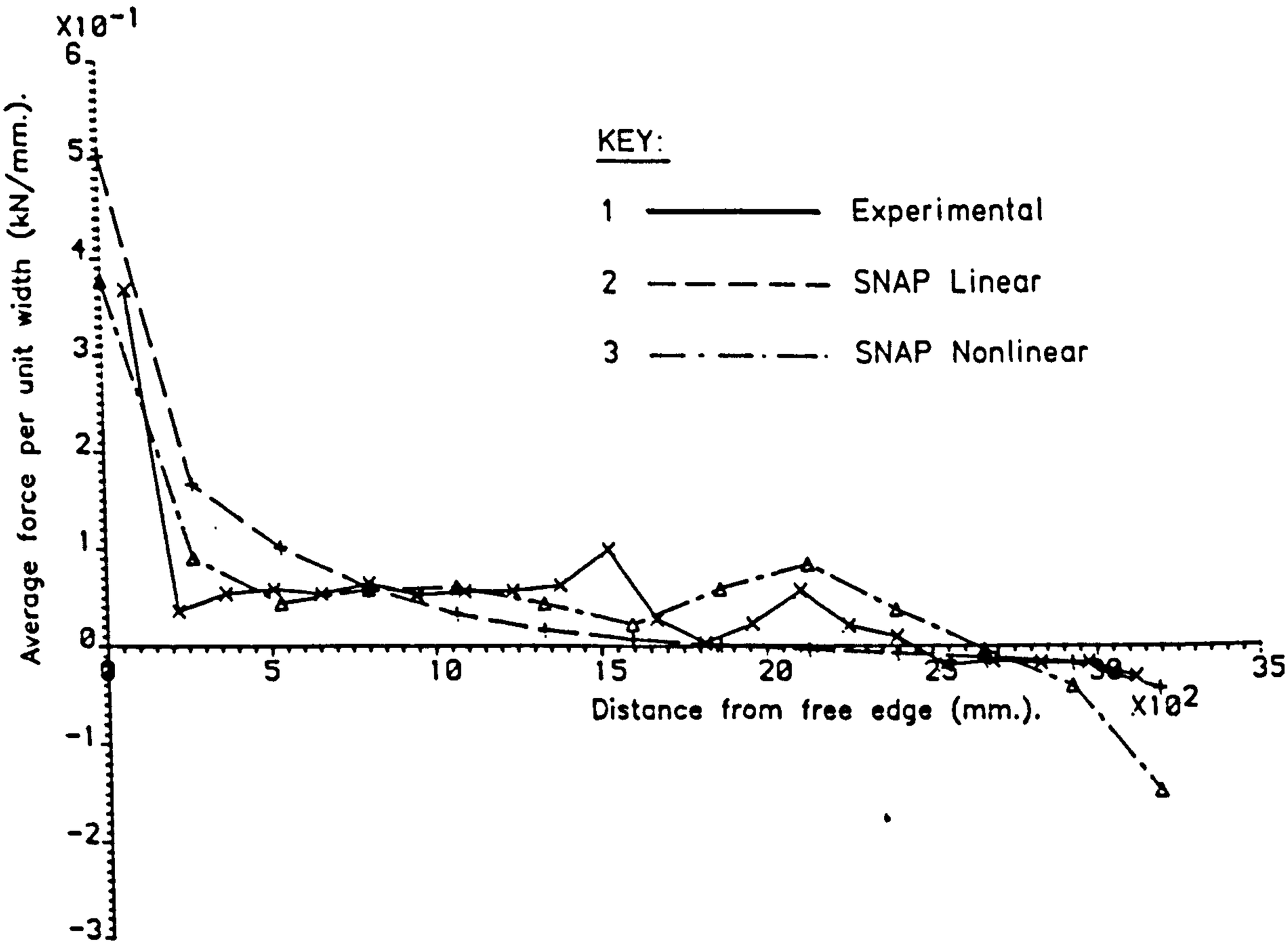

FIG. 9.43. REACTION PROFILE COMPARISONS FOR MODEL 1 USING 'DISCRETE' BOUNDARY CONDITIONS

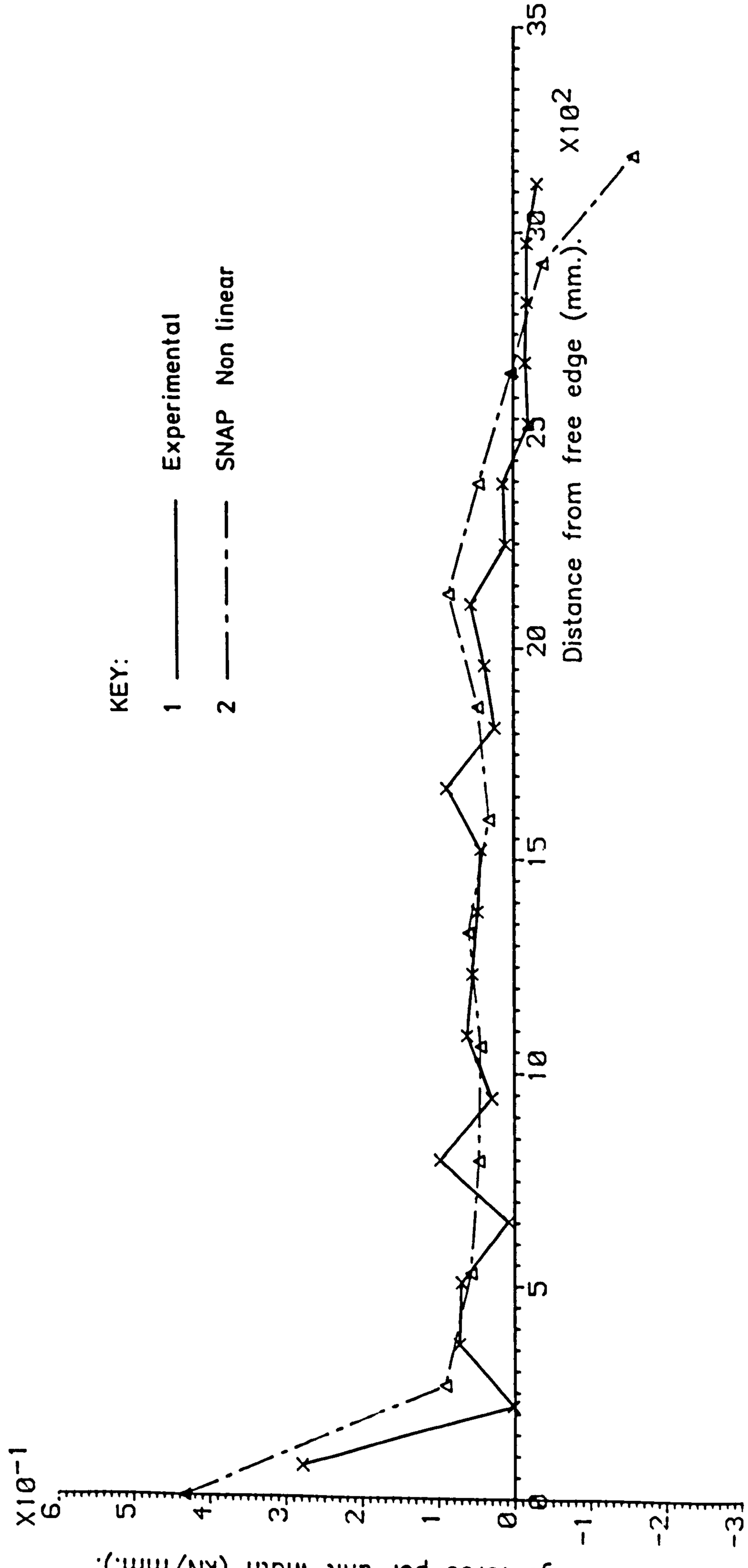

FIG. 9.44. REACTION PROFILE COMPARISON FOR MODEL 1 AT LEVEL 25, WITH A LOADED FREE EDGE DISPLACEMENT LEVEL OF 137mm, USING 'DISCRETE' BOUNDARY CONDITIONS

Support reaction profile comparison for level 16, with 2.70xULS HB.

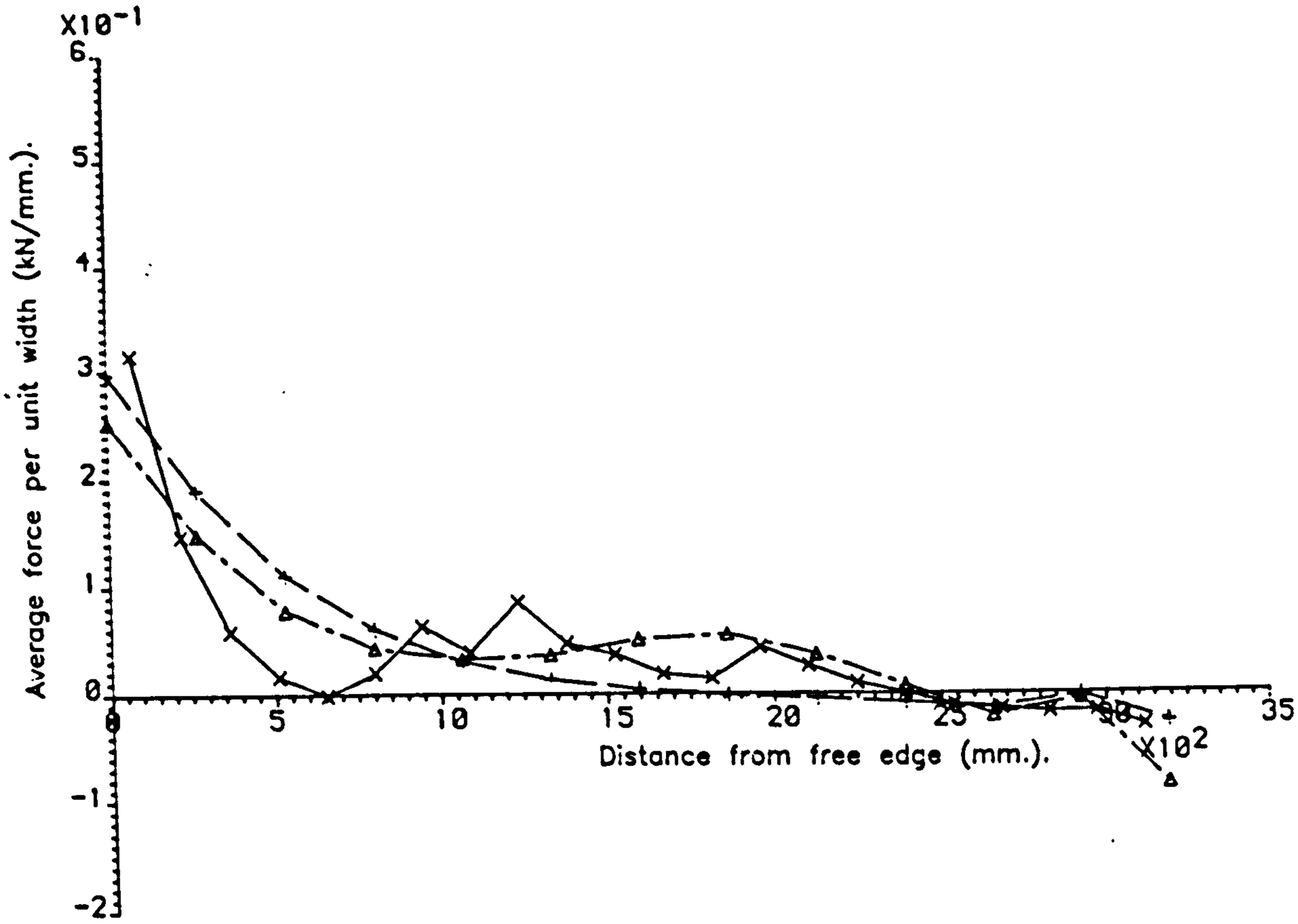

Support reaction profile comparison for level 21, at 79mm. deflection.

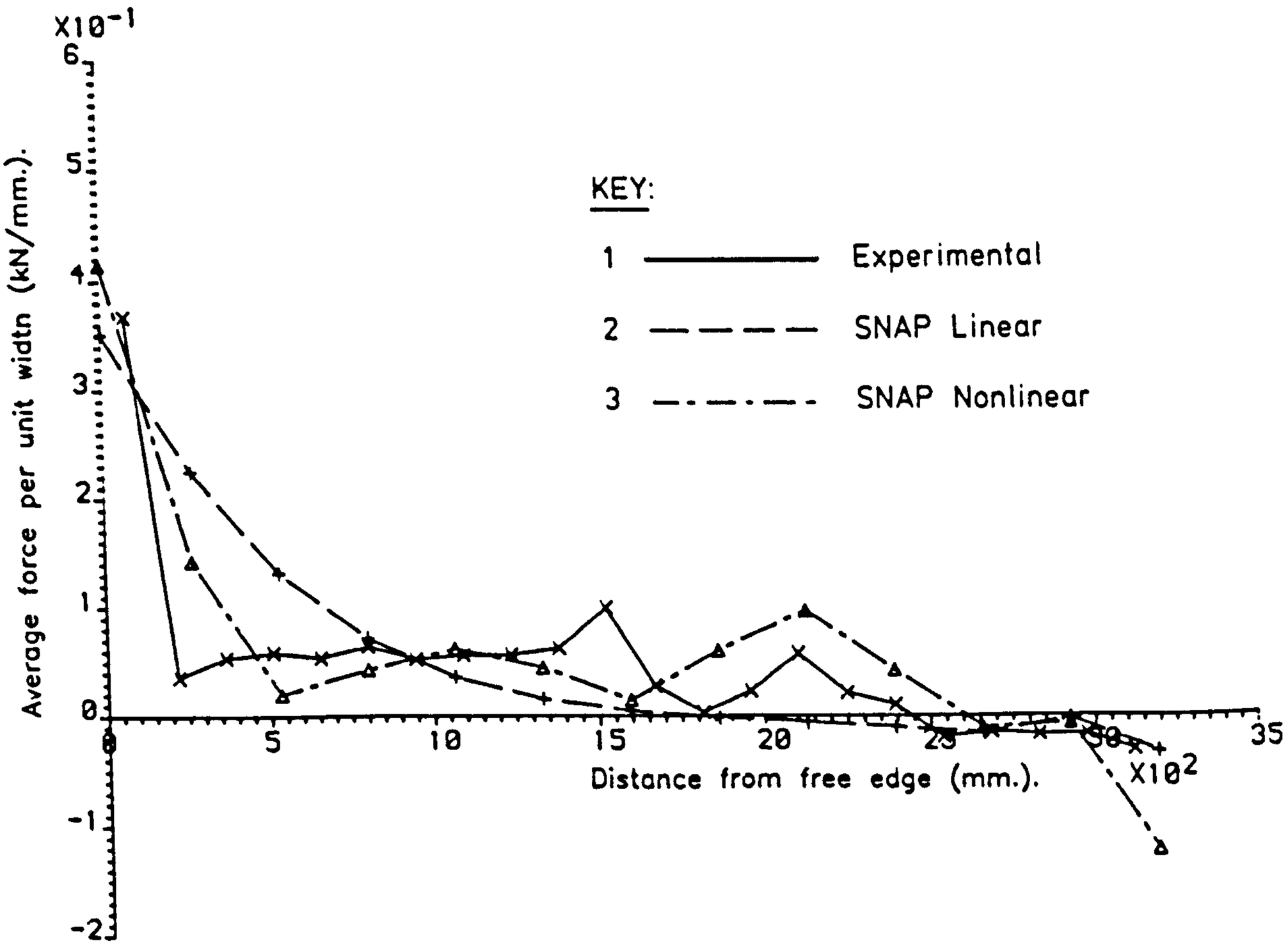

FIG. 9.45. REACTION PROFILE COMPARISONS FOR MODEL 1 USING 'CONSISTENT' BOUNDARY CONDITIONS

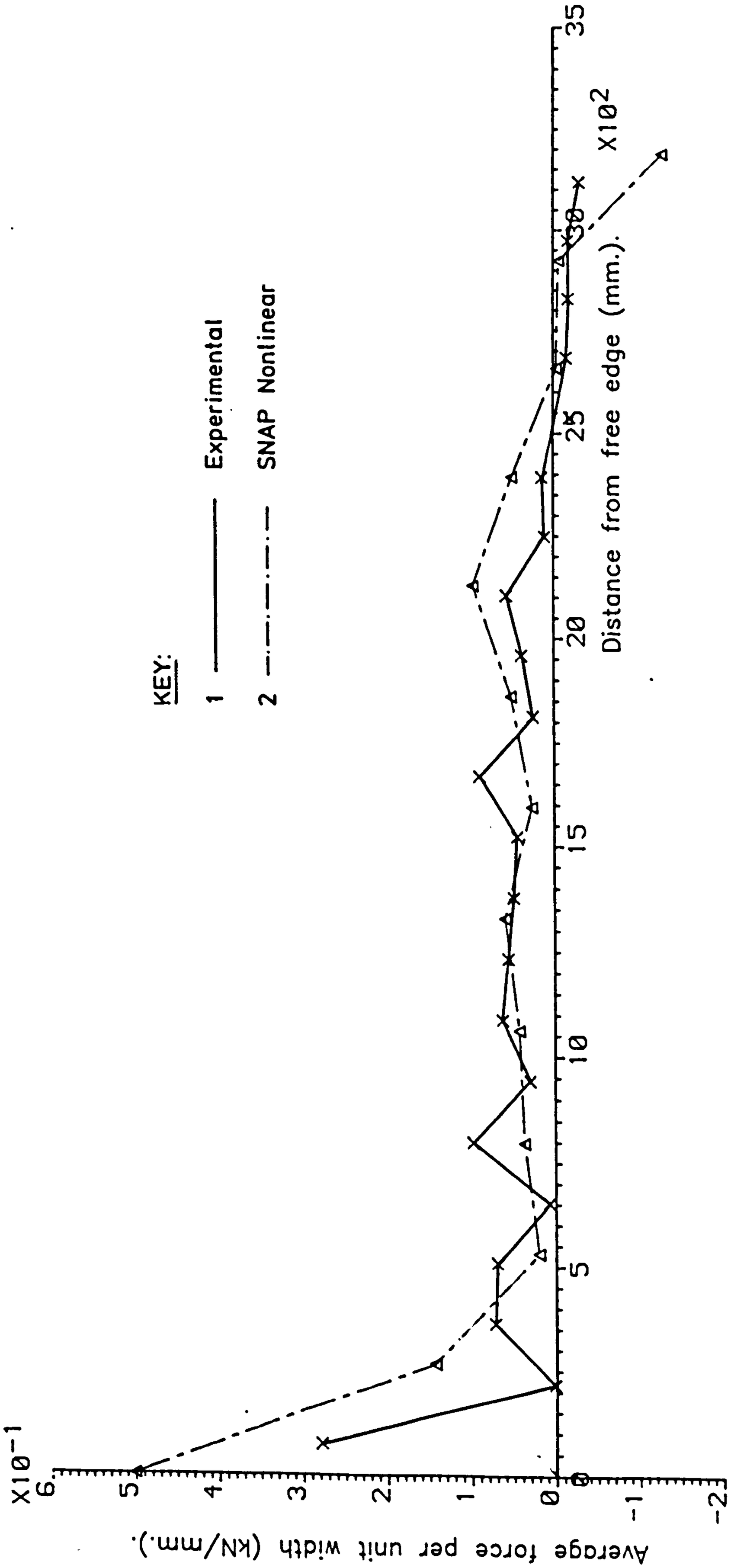

FIG. 9.46. REACTION PROFILE COMPARISON FOR MODEL 1 AT LEVEL 25 WITH A LOADED FREE EDGE

DISPLACEMENT LEVEL OF 137mm. USING 'CONSISTENT' BOUNDARY CONDITIONS

At level 21, which can be seen in Figure 9.43, for the discrete boundary condition approach, the non-linear profile is becoming erratic, suggesting significant non-linearity near the supports. The analysis predicts the large load attracted by the obtuse corner support in the experimental profile. The linear analysis significantly over estimates the peak force per unit width that occurs at the obtuse corner. It will be noticed that significant tensile reaction forces are predicted for the acute corner end of the support line. The reaction profile obtained with the consistent boundary condition approach for level 21 can be seen in Figure 9.45. It will be noticed that the non-linear profile is becoming erratic suggesting the onset of significant non-linearity. The non-linear analysis profile exhibits rapid load drop off adjacent to the obtuse corner whereas the linear analysis predicts a smooth reduction in load away from the obtuse corner. The accurate modelling of the profile shape, and not just the peak value, is important since it is unlikely that average shear stresses would be calculated from a single reaction load. The average forces per unit length can be converted to equivalent shear stresses by dividing by the slab depth. Thus at level 21 the peak force per unit width is approximately equal to 0.4 kN/mm. This corresponds to an equivalent shear stress of 2.29 N/mm^2 in model 1.

Reaction profile comparisons for level 25 are given in Figures 9.44 and 9.46. This level corresponds to the final state of the model before the test was terminated. At this level the applied load had reduced and thus no linear predictions are included in Figures 9.44 and 9.46. It will be noticed that at this level, the consistent boundary conditions, shown in Figure 9.46, are predicting larger peak forces per unit width than the discrete boundary condition analysis of

Figure 9.44. Away from the obtuse corner, the non-linear analysis predicts the reaction load with reasonable accuracy, however, the experimental profile is somewhat oscillatory. Again large tensile reactions in the acute corner are predicted by each analysis.

9.3.5.2 Model 2 reaction profiles

The first set of comparisons that are presented relate to level 21 as defined in Appendix 7.2. While the analytical discrete boundary condition profiles of Figure 9.47 show little non-linear influence, the consistent boundary condition profiles of Figure 9.49 indicate large non-linear effects. For either analysis, the $^2/_3$ of the support line which is remote from the obtuse corner, carries very little load.

The next comparison is carried out at level 23 and is shown in Figures 9.47 and 9.49. At this level both the discrete and consistent non-linear analyses significantly over estimate the peak force per unit width in the obtuse corner. At this level the peak experimental value is approximately 0.9 kN/mm. This corresponds to a shear stress in model 2 of approximately 3.5 N/mm^2, although this is perpendicular to the free edge. If transformed to a direction parallel to the support line, this is equivalent to 2.7 N/mm^2. An interesting feature of the comparisons at this level is the increased load on the third experimental support from the left. It may be recalled that during the later stages of the test on model 2, the end two beams in the obtuse corner were seen to separate from the rest of the model. This would result in load being transferred to the third support in from the obtuse corner. As with model 1, significant tensile reaction forces are predicted in the acute corner.

The final reaction profile comparisons for model 2 are shown in Figure 9.48 and 9.50. Again only the non-linear response is shown since this

Support reaction profile comparison for level 21, with 5.10xULS HB.

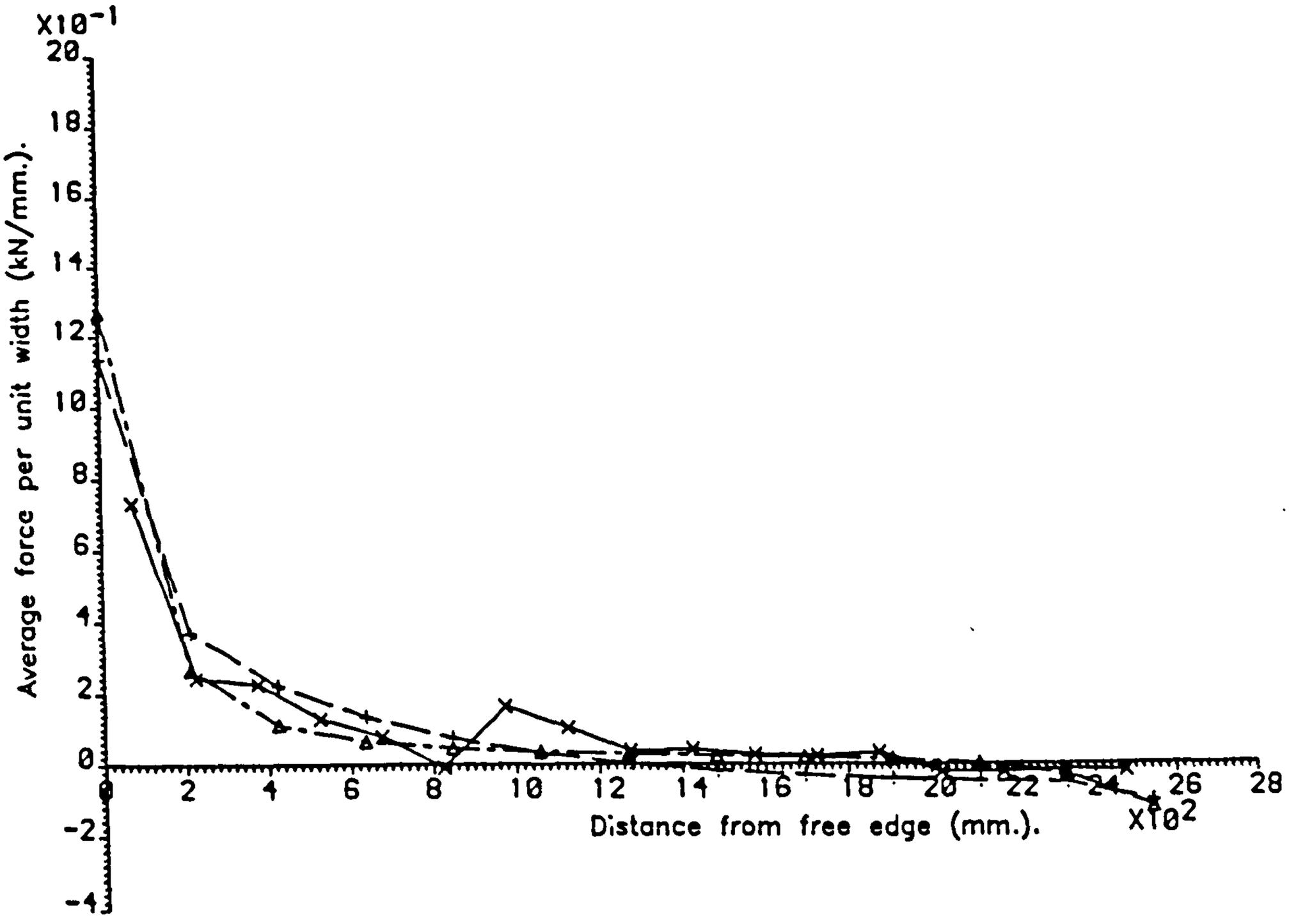

Support reaction profile comparison for level 23, at 90mm. deflection.

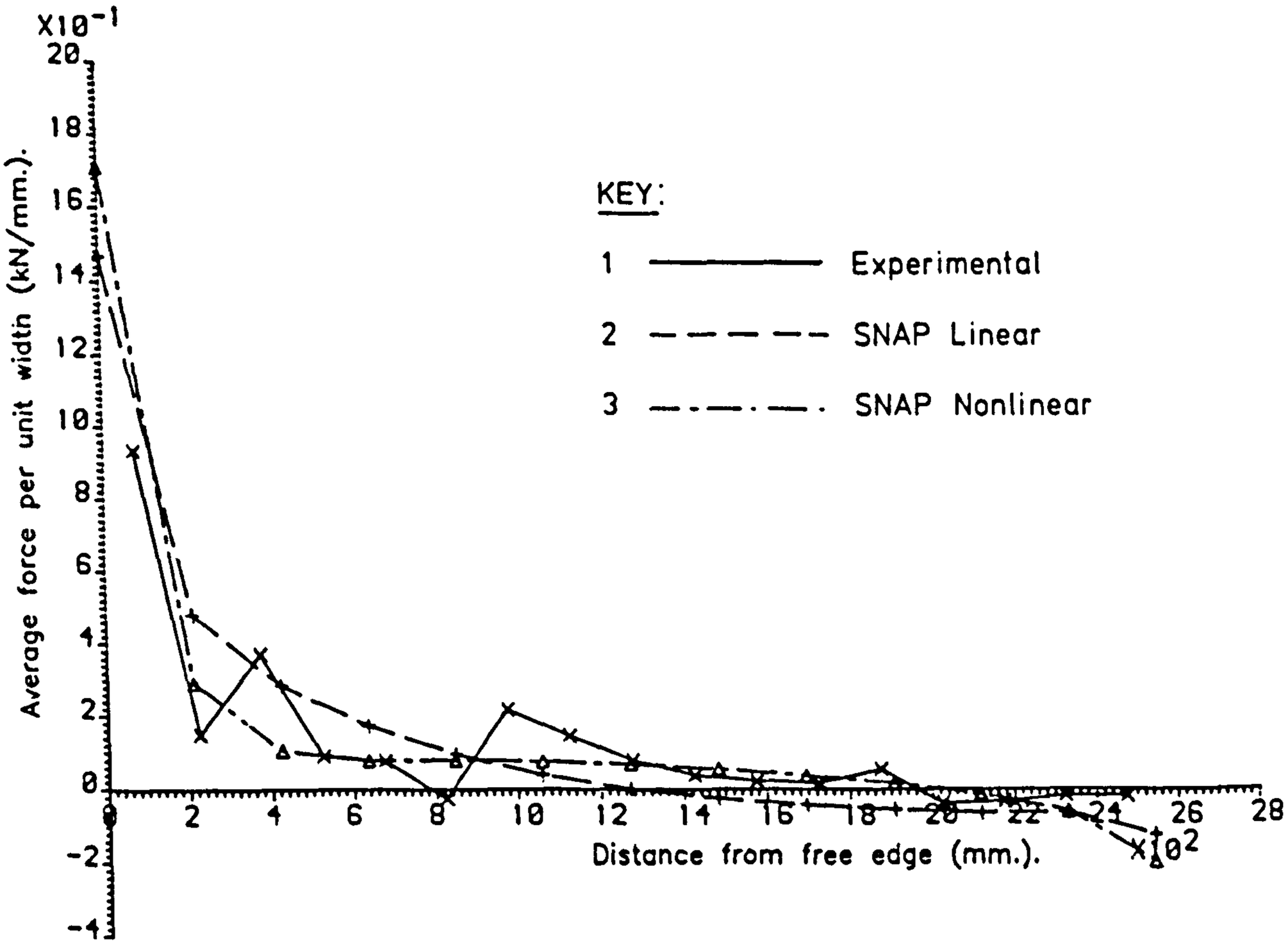

FIG. 9.47. REACTION PROFILE COMPARISONS FOR MODEL 2 USING 'DISCRETE' BOUNDARY CONDITIONS

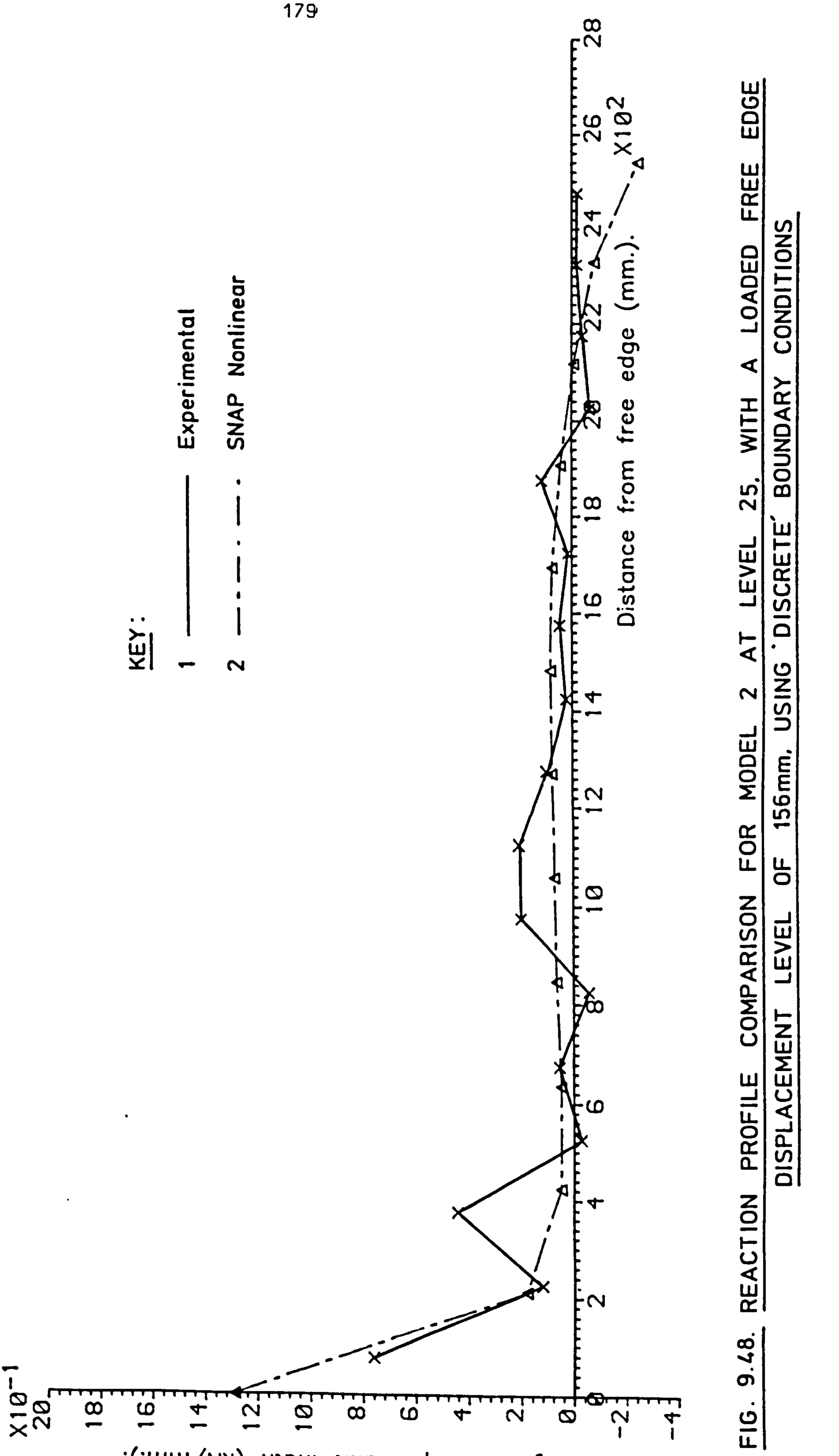

FIG. 9.48. REACTION PROFILE COMPARISON FOR MODEL 2 AT LEVEL 25, WITH A LOADED FREE EDGE
DISPLACEMENT LEVEL OF 156mm. USING 'DISCRETE' BOUNDARY CONDITIONS

Support reaction profile comparison for level 21, with 5.10xULS HB.

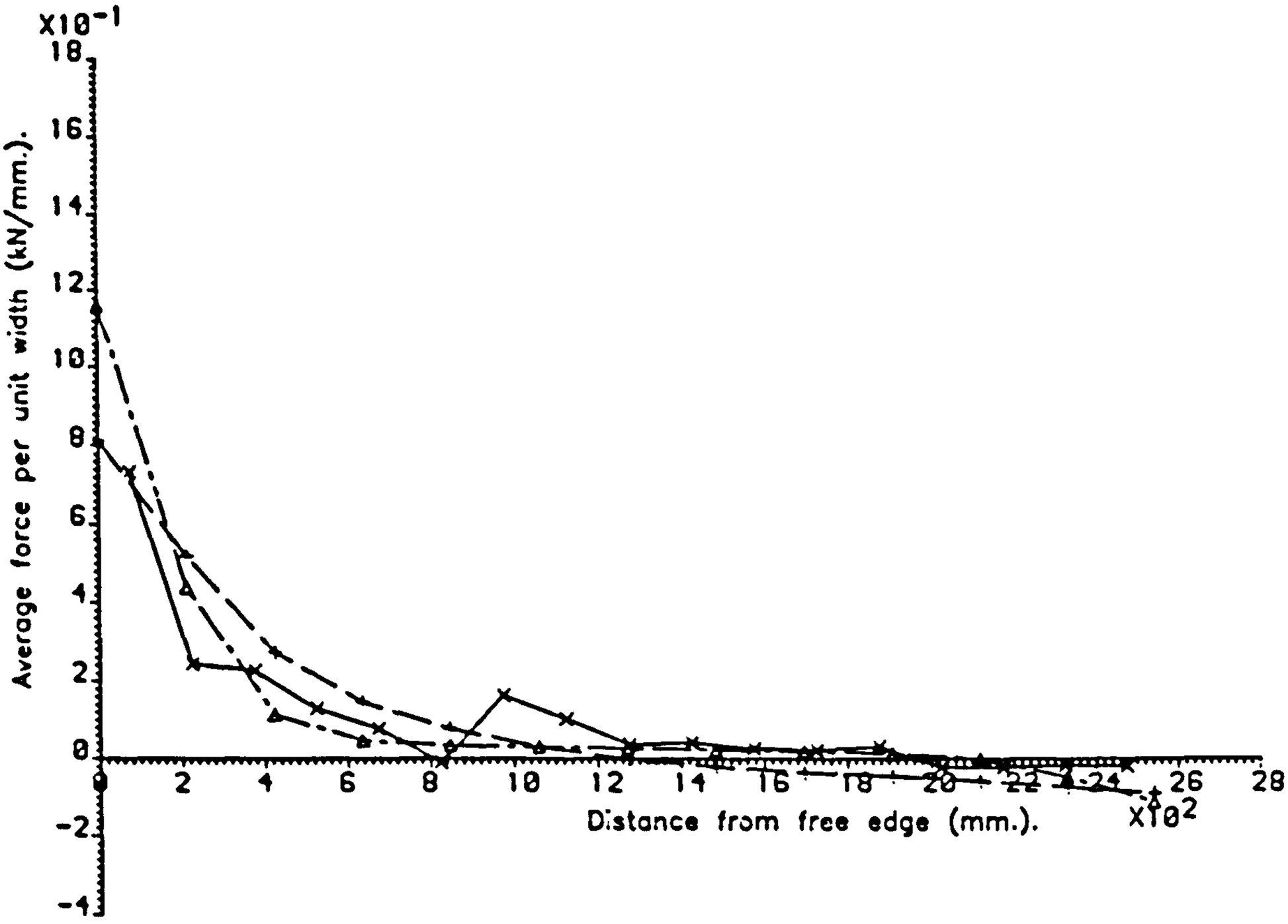

Support reaction profile comparison for level 23, at 90mm. deflection.

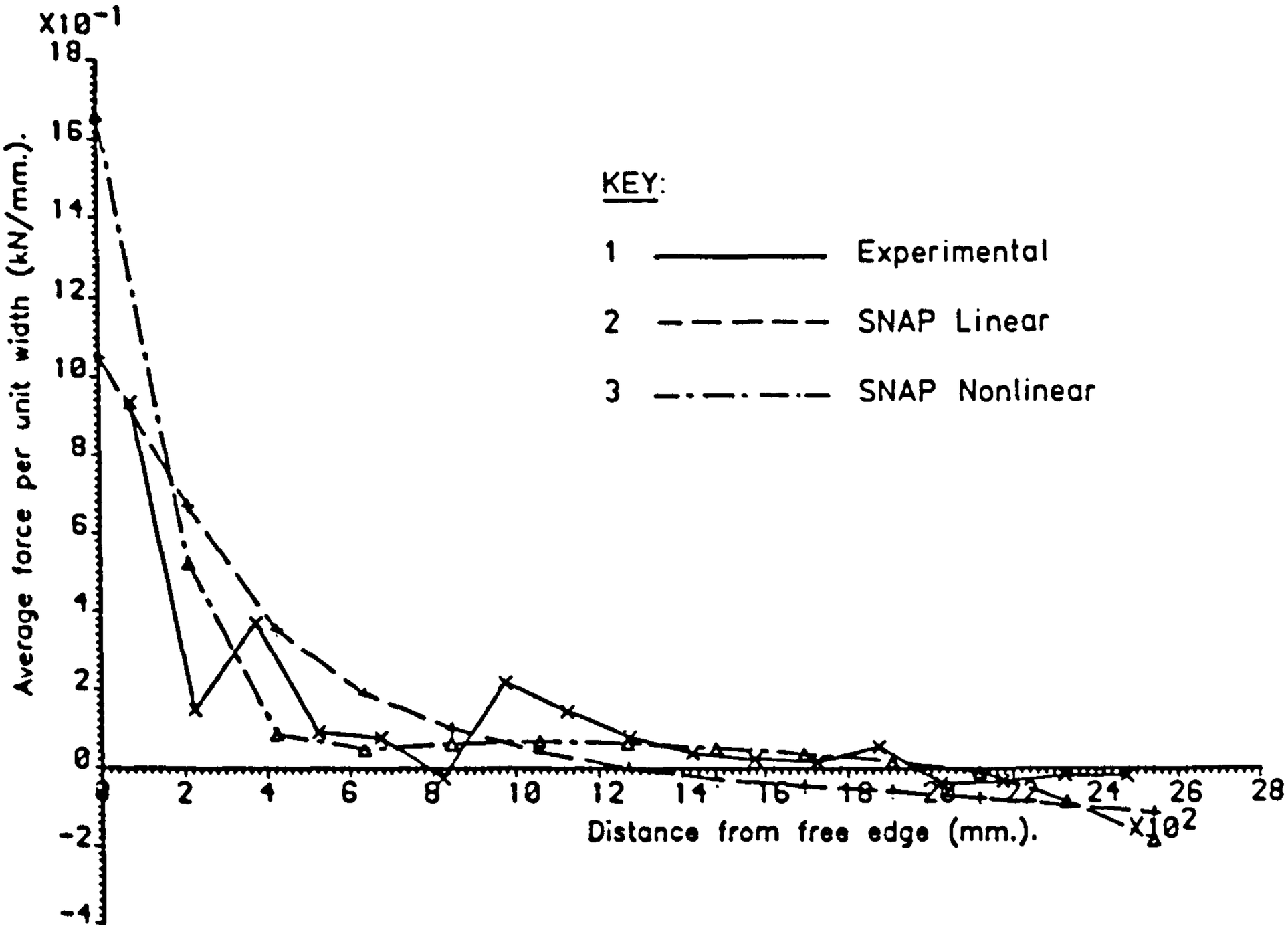

FIG. 9.49. REACTION PROFILE COMPARISON FOR MODEL 2, USING 'CONSISTENT' BOUNDARY CONDITIONS

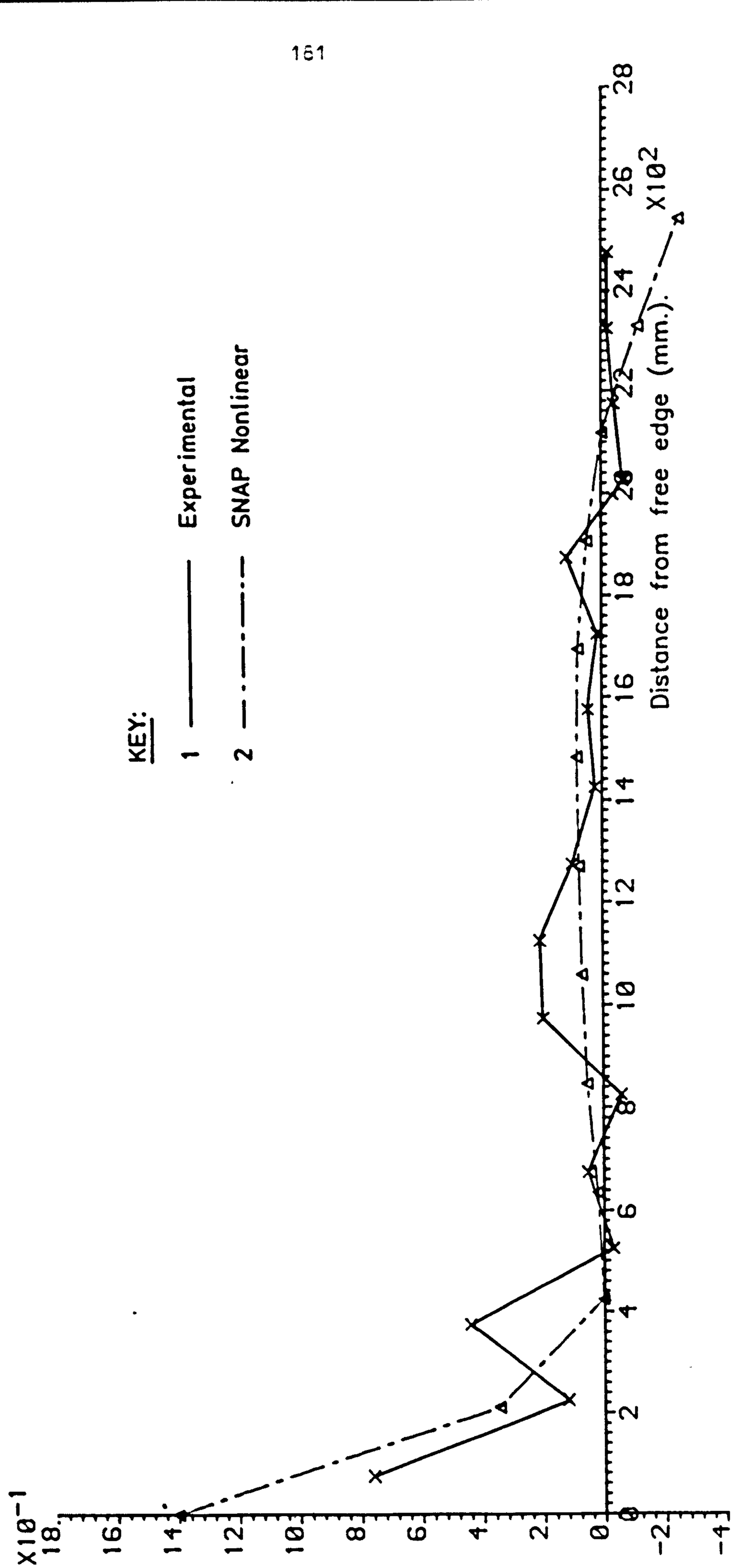

FIG. 9.50 REACTION PROFILE COMPARISON FOR MODEL 2 AT LEVEL 25, WITH A LOADED FREE EDGE
DISPLACEMENT LEVEL OF 156mm, USING 'CONSISTENT' BOUNDARY CONDITIONS

comparison is carried out in the post-peak region of the load-deflection curve. By this stage the third support from the left has attracted a large proportion of the load away from the obtuse corner reaction. This possibly explains the large differences between the experimental and analytical predictions for the obtuse corner region.

9.3.6 Reaction linearity

Reaction linearity comparisons have been presented in Figure 9.51 to 9.54. The comparison is complex since the number and location of supports is different for the experiment and the analysis. For the plots shown, the reaction loads have been converted into forces per unit width so that a comparison can be made. A method similar to that described in the previous section, on the reaction profiles, was used to produce the values of force per unit width. Plots are produced for the five analytical supports nearest the obtuse corner. For each of these supports the closest experimental support is used for comparison.

Figures 9.51 and 9.53 present the variation in the force per unit length with respect to the HB load factor. This is a common way to present reaction non-linearity plots. This method is satisfactory until the plateau and falling branches of the load-deflection response are reached, whereupon the plots can become confusing. The detail in this area is clarified in Figures 9.52 and 9.54 where the force per unit width is plotted against a compound load-displacement level. The compound load-displacement level is obtained from $c = 1.069d + 11.52p$ for model 1 and $c = 1.069d + 6.20p$ for model 2, where d is the displacement level and p is the load level.

Support 22 comparison.

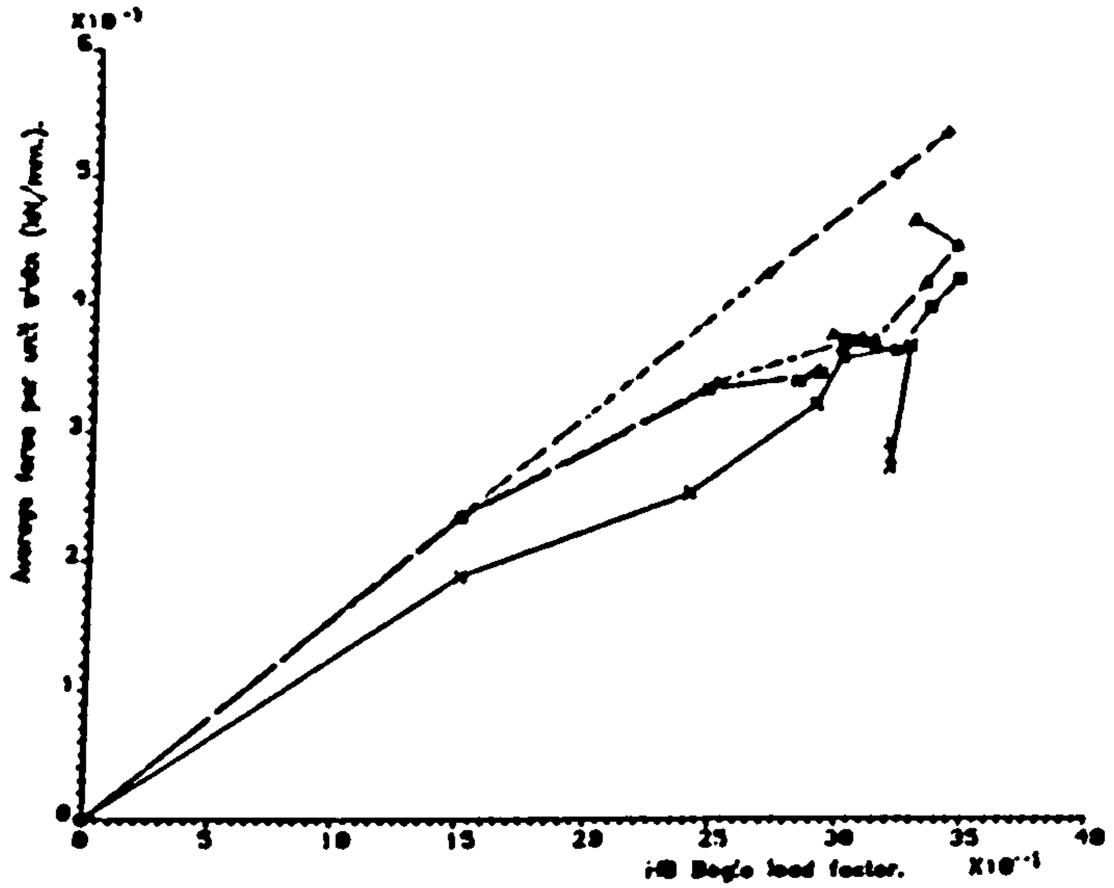

Support 21 comparison.

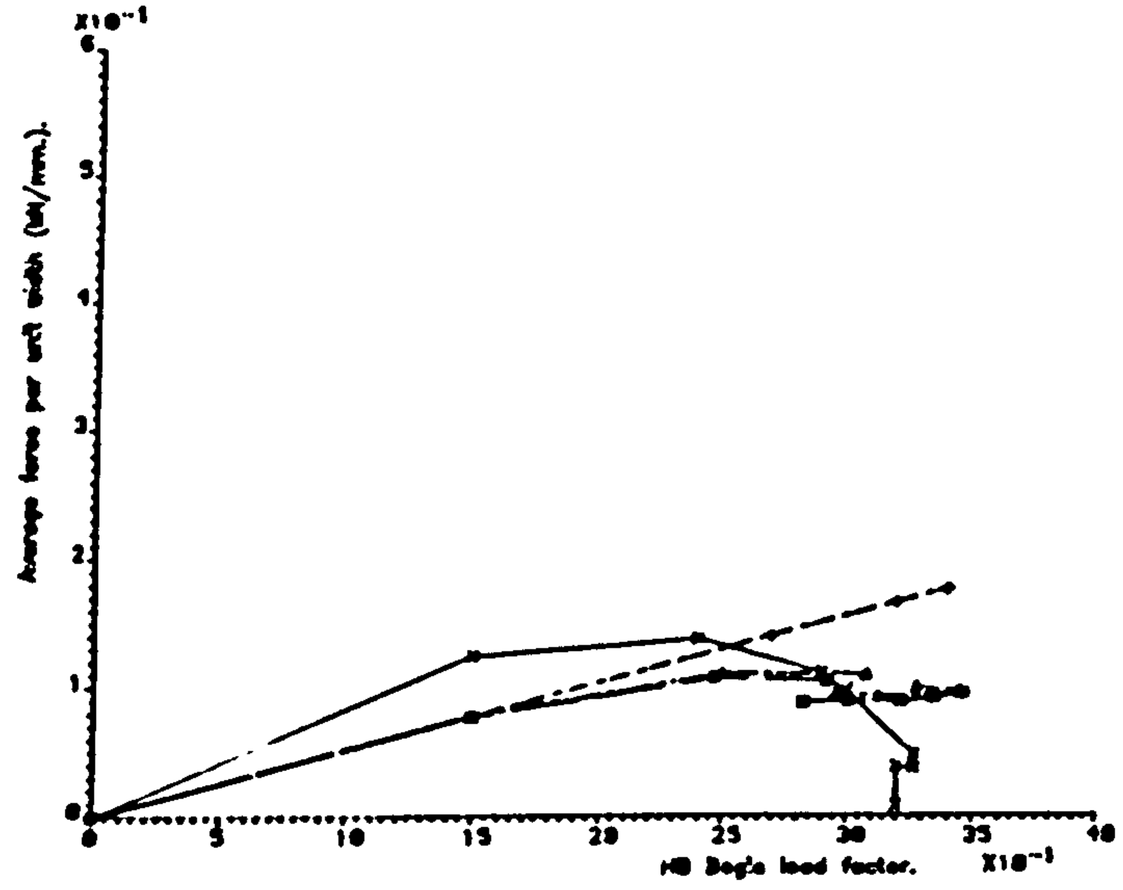

Support 19 comparison.

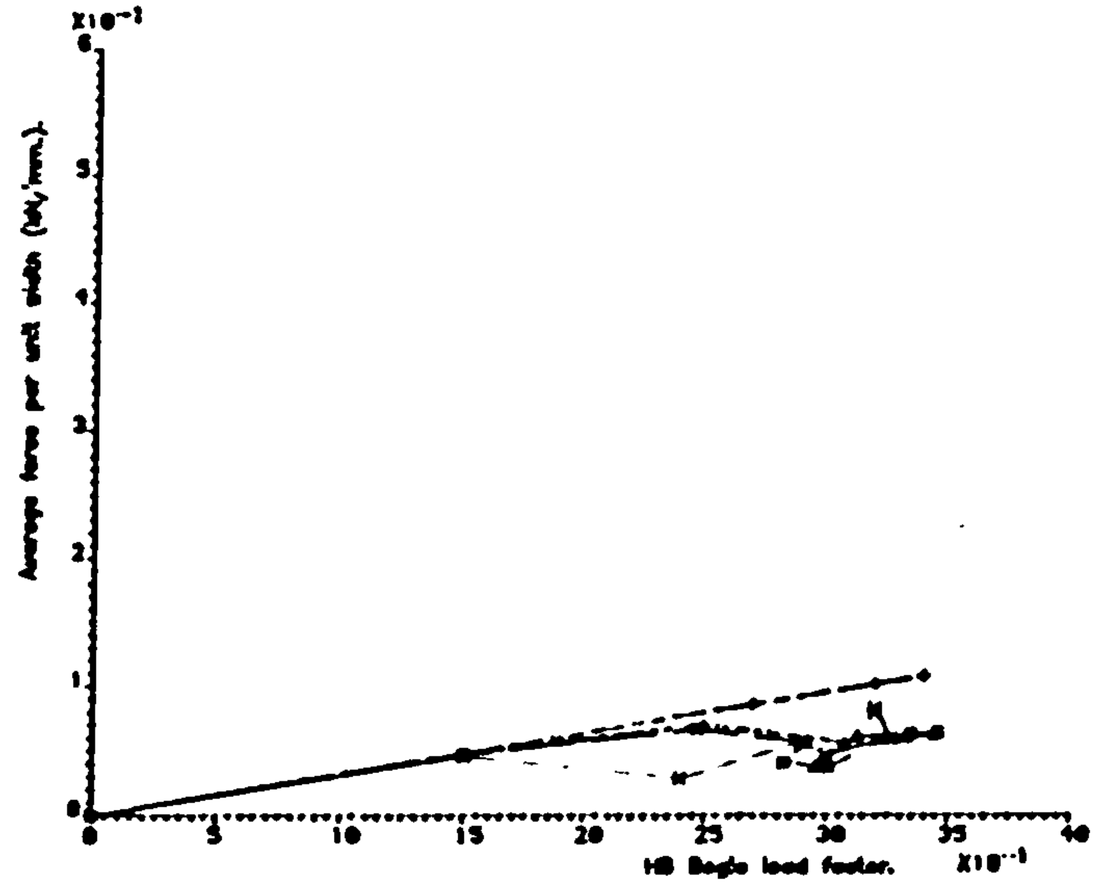

Support 17 comparison.

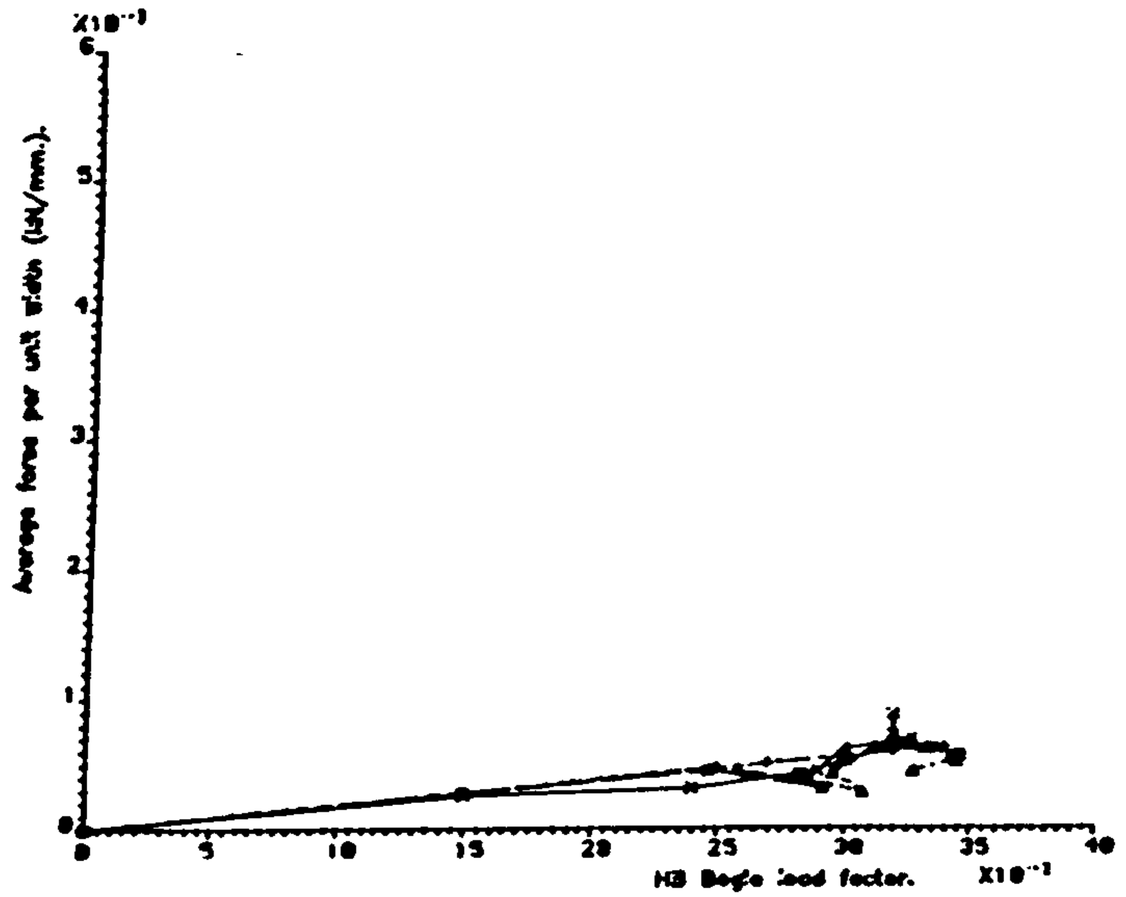

Support 15 comparison.

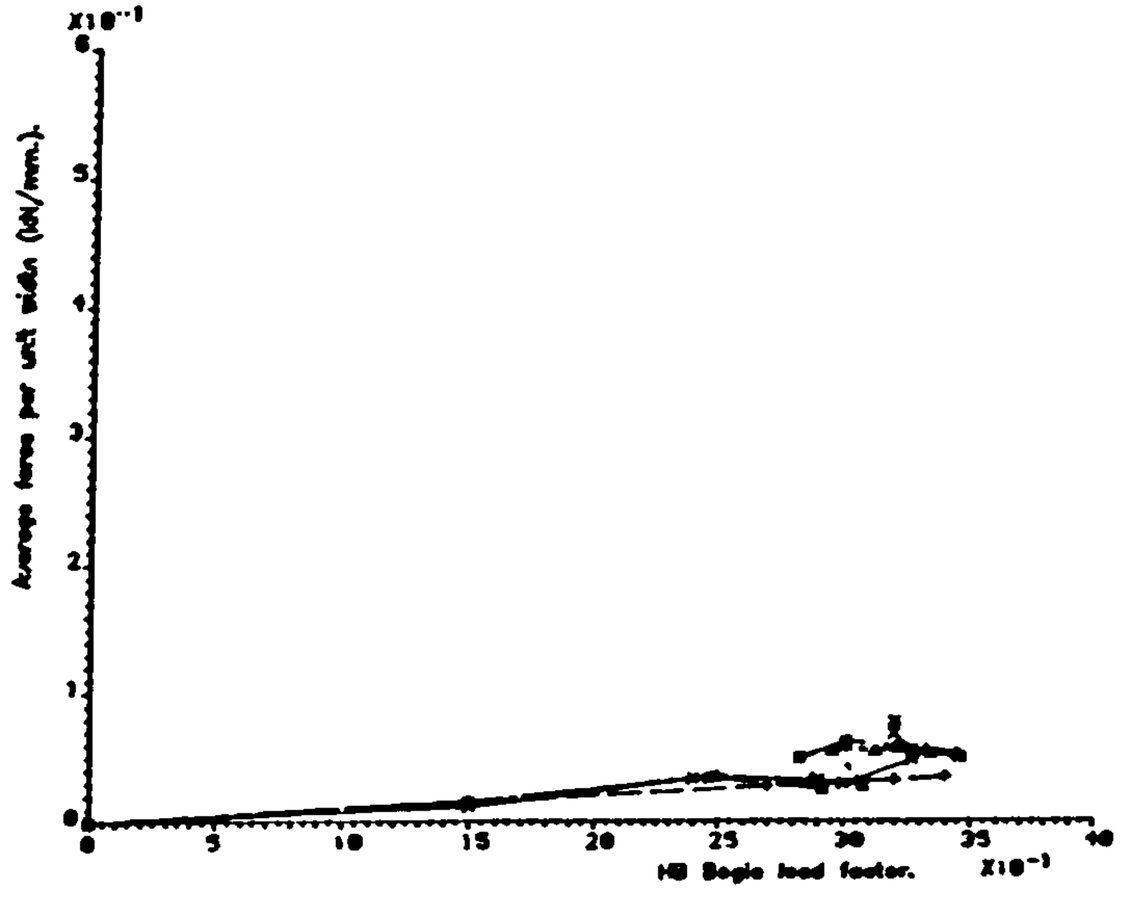

KEY:

1 ——————— Experimental

2 — — — — — SNAP linear

3 — · — · — — SNAP nonlinear with standard data (20% prestress losses)

4 —— —— —— SNAP nonlinear with 35% prestress losses and 2 segment concrete tensile curve

FIG. 9.51. REACTION NON-LINEARITY FOR MODEL 1

The reaction comparisons for model 1 are shown in Figure 9.51 and 9.52. It would appear that there is reasonably good agreement between the analysis and experiment until high displacement levels are reached. At these levels the experimental reaction load in the obtuse corner drops of suddenly while the analytical support continues to attract load. There is little difference between the traces for the two non-linear analyses.

Figures 9.53 and 9.54 depict the behaviour of model 2. It is immediately obvious that there is a large error in the predictions for the obtuse corner support, number 17. No reason for this large discrepancy is apparent, although the slightly different locations for the experimental and analytical supports may be a factor. There is good agreement for support 16, however, the analysis predicts shedding of load for support 15 while the experimental results indicate attraction of load. This deviation could be a result of the separation of the end two beams that was seen to occur in the test. Low forces occur in the final two supports in the comparison and, therefore, it is difficult to assess the accuracy of the analytical predictions.

9.3.7 Crack patterns

A simple way in which the behaviour of a complex three dimensional structure, such as a slab, may be assessed, is by monitoring the material state changes across the structural domain. With concrete this is most effectively achieved through the plotting of crack patterns. In addition, the surface analytical crack patterns may be compared to the experimental crack patterns that were recorded at the time of the model tests.

Support 22 comparison.

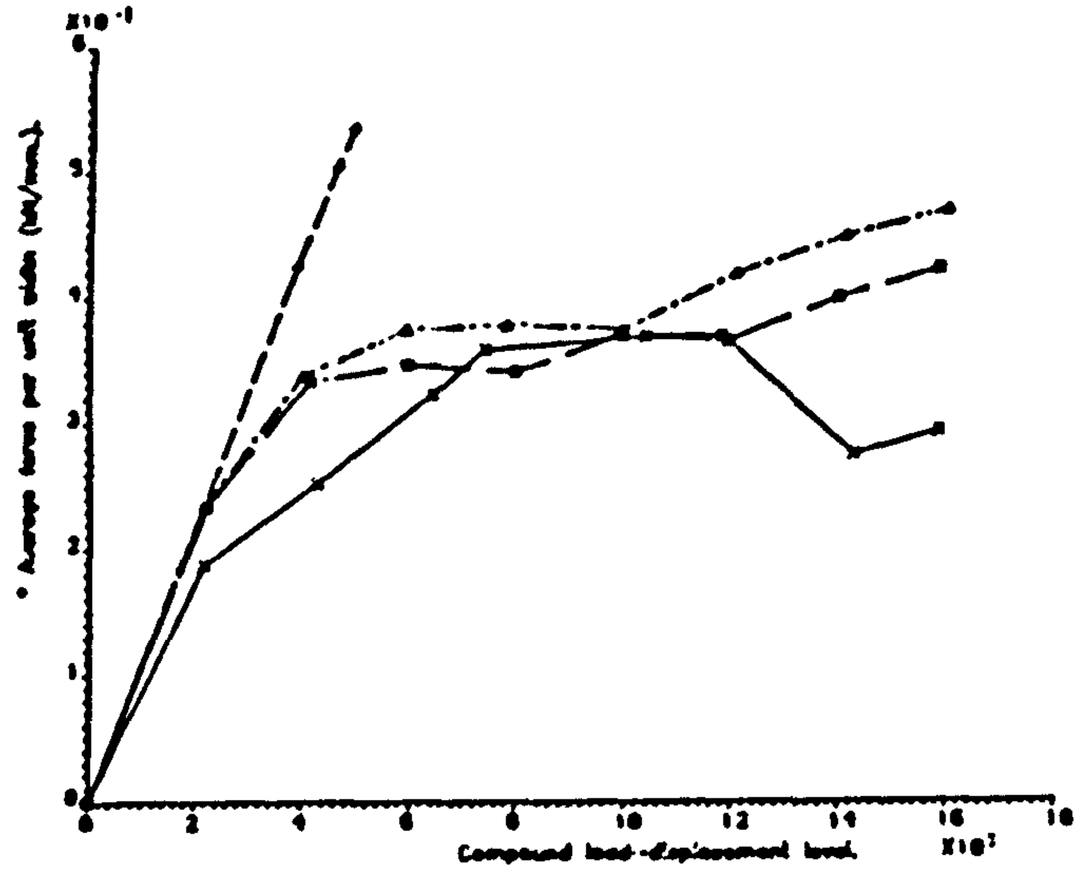

Support 21 comparison.

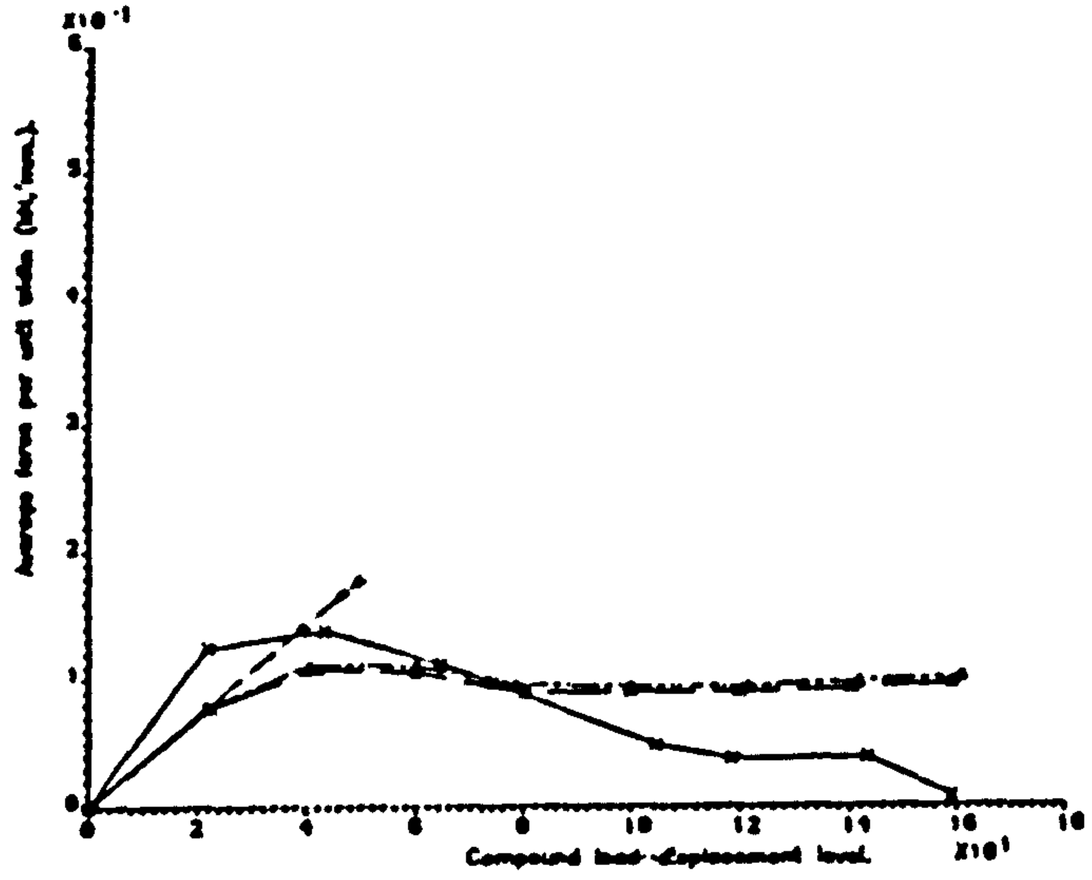

Support 19 comparison.

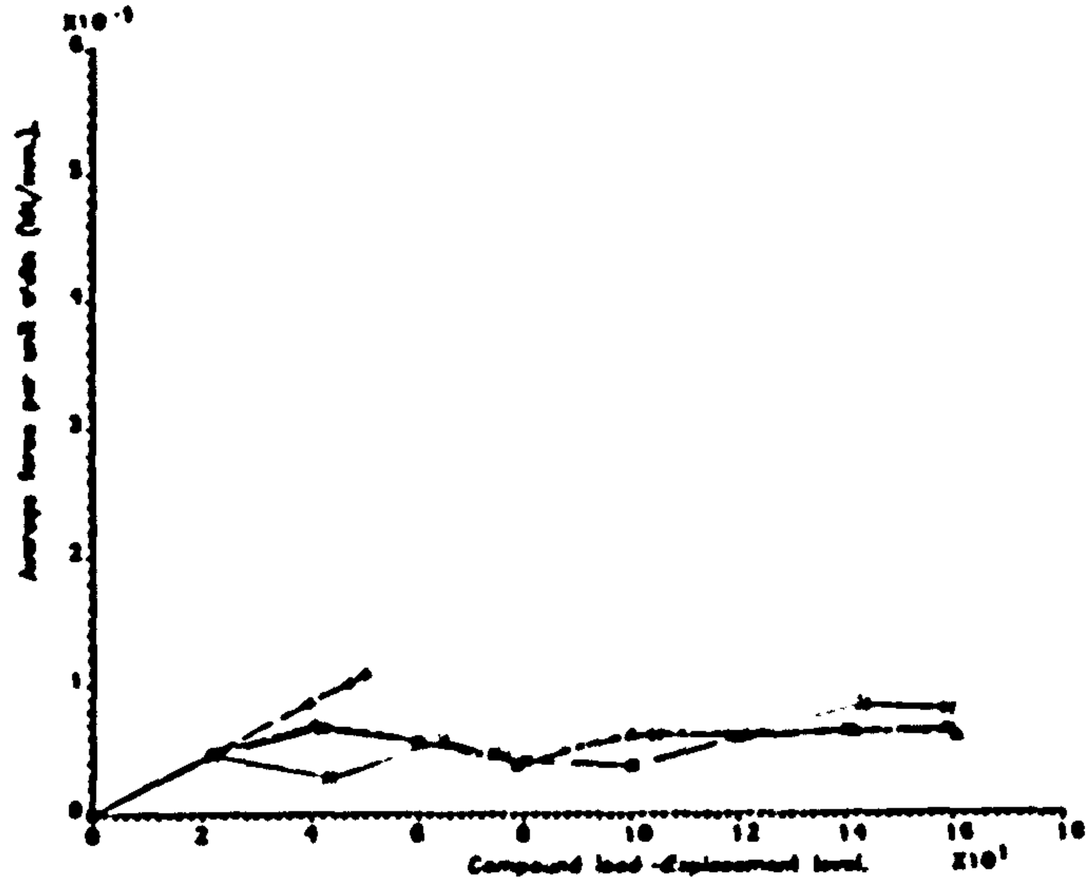

Support 17 comparison.

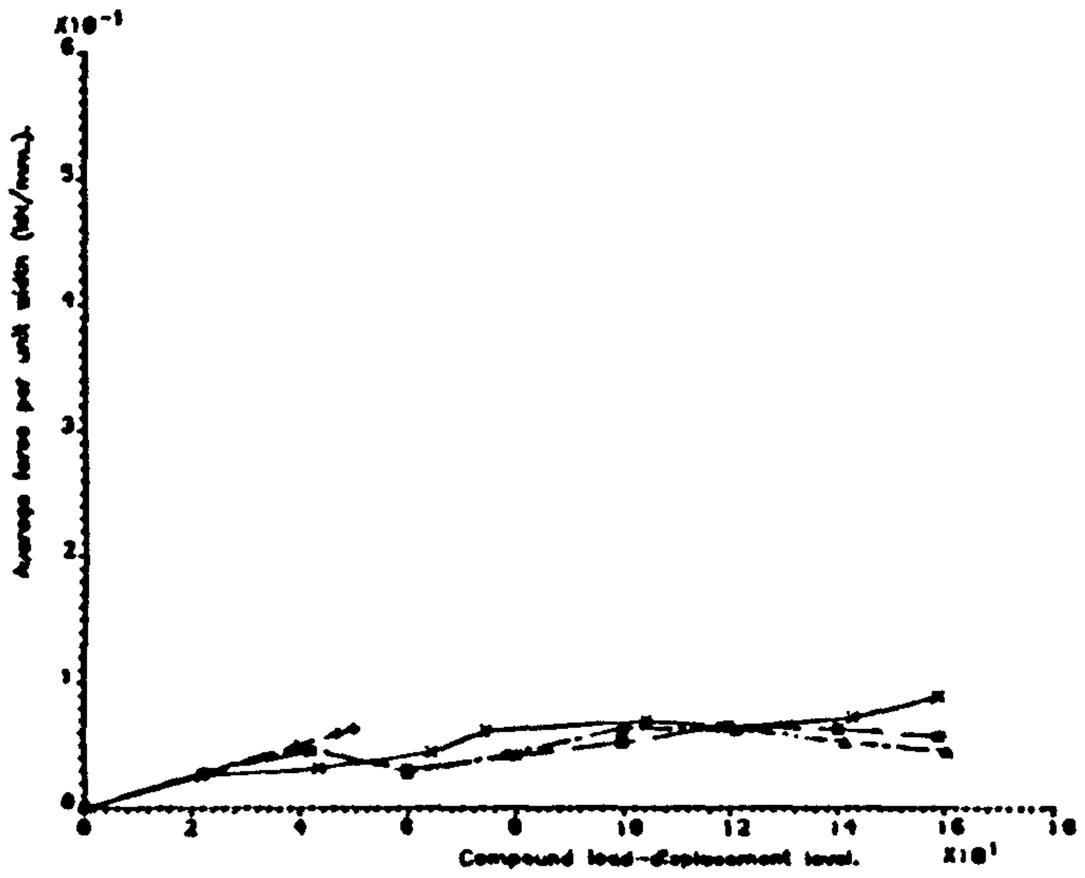

Support 15 comparison.

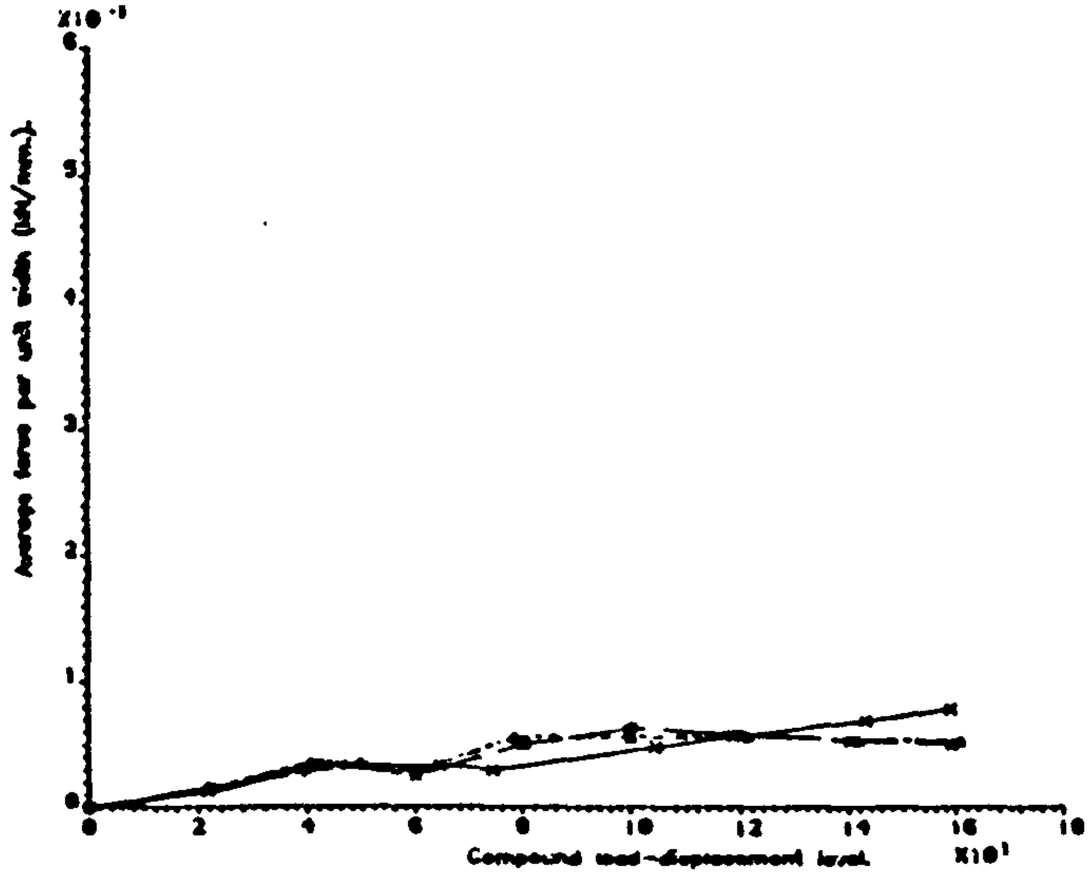

KEY

1 ——— Experimental

2 — — — — SNAP linear

3 —·—·—·— SNAP nonlinear with standard data (20% prestress losses)

4 — — — SNAP nonlinear with 35% prestress losses and a 2 segment concrete tensile curve

FIG. 9. 52. REACTION NON-LINEARITY FOR MODEL 1

For the crack pattern plots of Figures 9.55 to 9.82 only 'visible' cracks have been plotted. The strain at which a crack becomes visible is calculated from a specified crack spacing and visible crack width. Given the crack strain, ϵ_c, at a particular location the plotted crack length was calculated from:-

$$\ell_{cr} = 0.0 \qquad 0 < \epsilon_c < \epsilon_{vis}$$

$$\ell_{cr} = \left[(1 - r) + \frac{\epsilon_c}{\epsilon_{max}} r\right] \ell_{max} \qquad \epsilon_{vis} < \epsilon_c < \epsilon_{max}$$

where,

r - A ratio which was varied to enhance the clarity of the plots, set to 0.75

ϵ_{max} - Maximum strain for a particular set of plots

ℓ_{max} - Maximum permitted length of plotted crack for the particular mesh

ℓ_{cr} - Plotted crack length

ϵ_{vis} - Strain at which cracks become visible

If a crack is closing then this is indicated by the use of a dashed line for the plotted crack. Areas of crushing are indicated by wavy lines which are drawn perpendicular to the compressive strain. Again the length of the wavy line indicates the magnitude of the crushing strain, in a similar way to the length of the plotted cracks.

For each model a typical non-linear analysis has been selected. For each selected analysis a set of crack patterns have been plotted for the three different structural states used in the deflection profile and reaction profile comparisons of the previous sections.

Support 17 comparison.

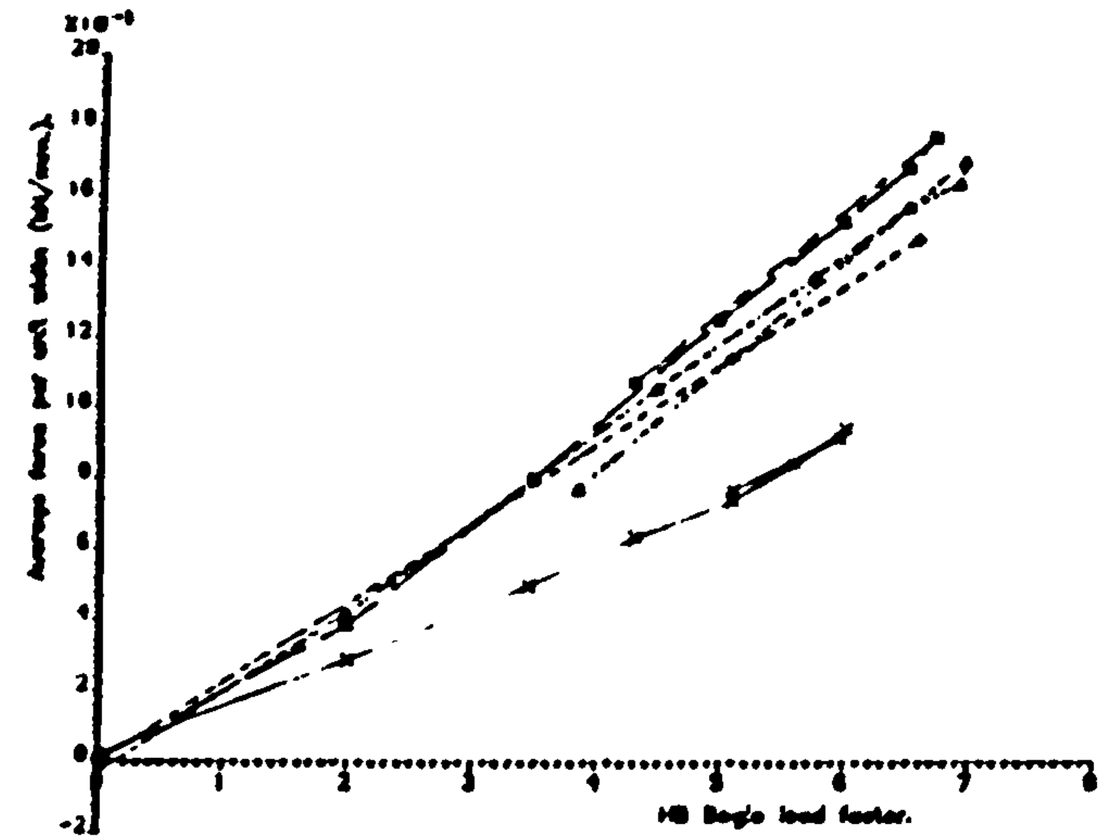

Support 16 comparison.

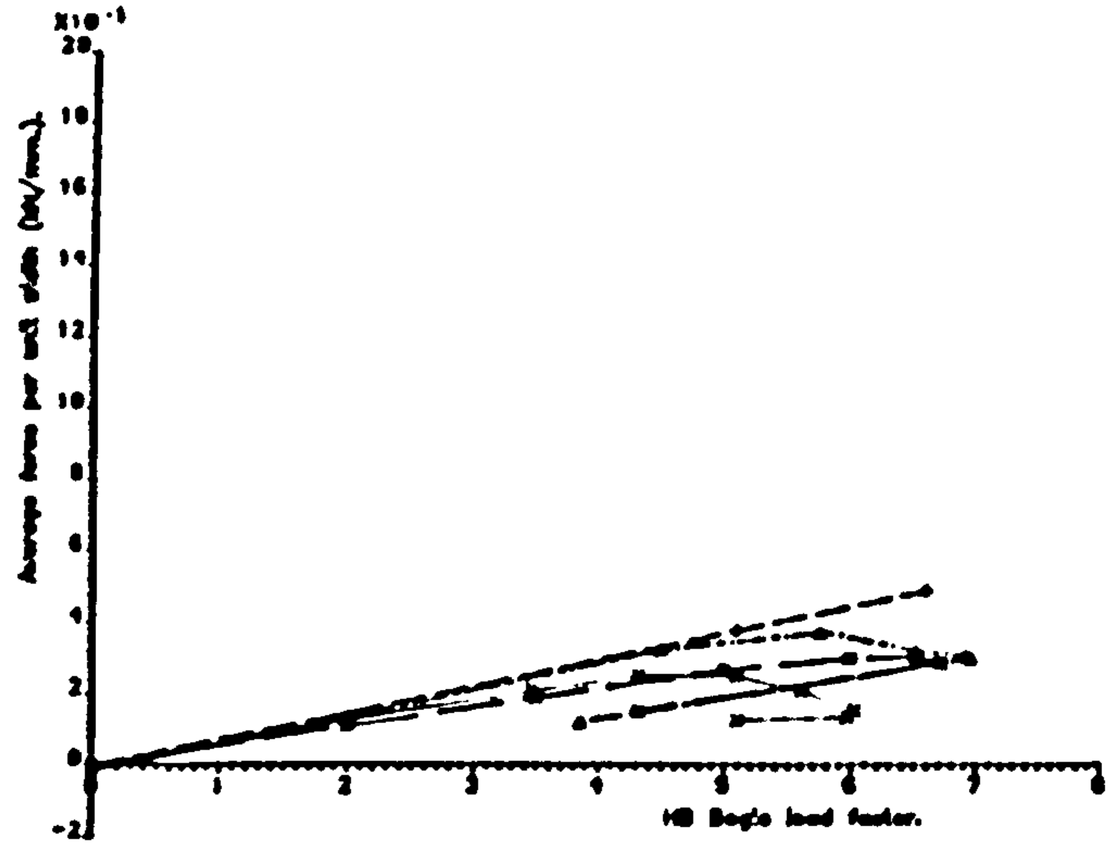

Support 15 comparison.

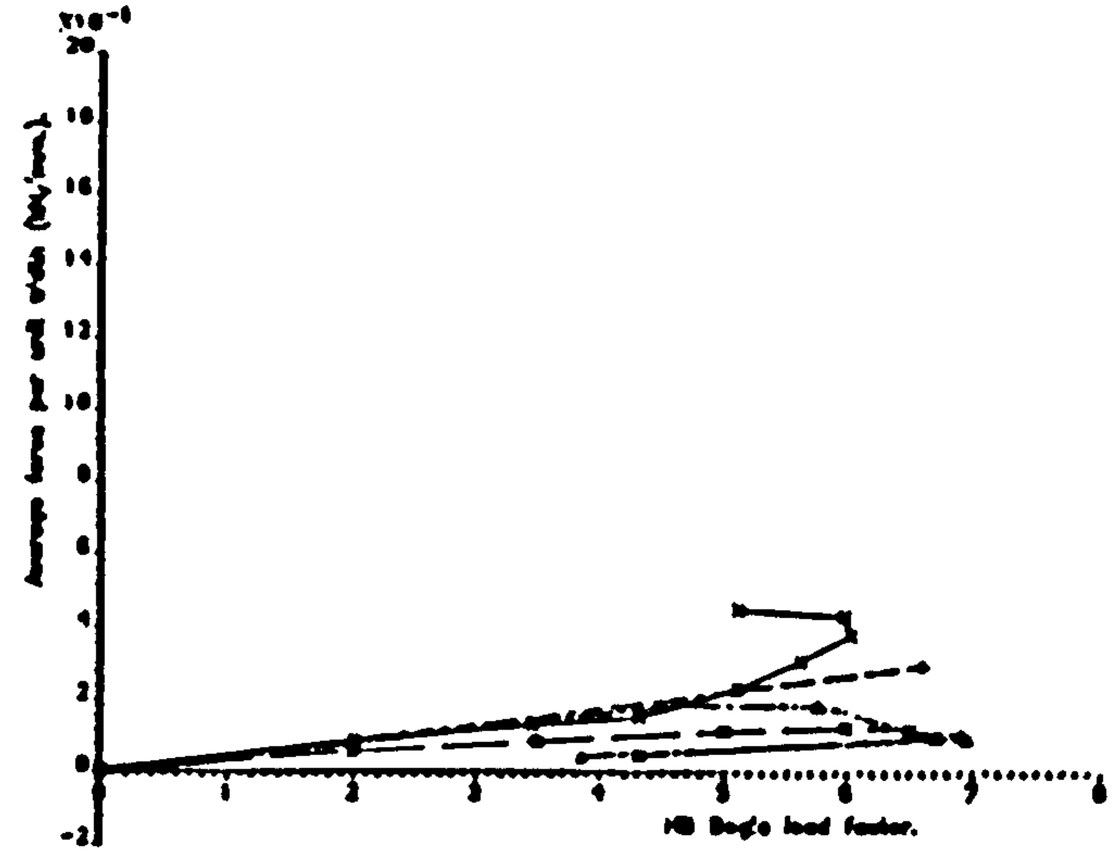

Support 13 comparison.

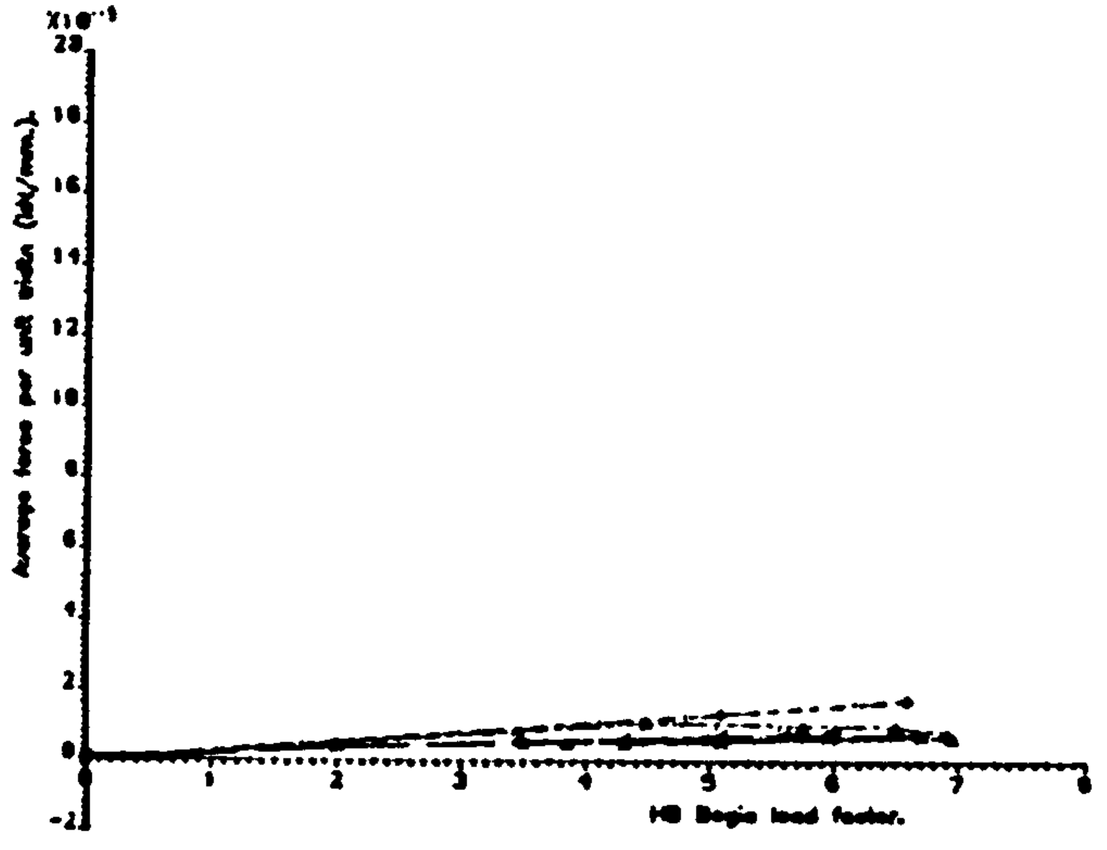

Support 12 comparison.

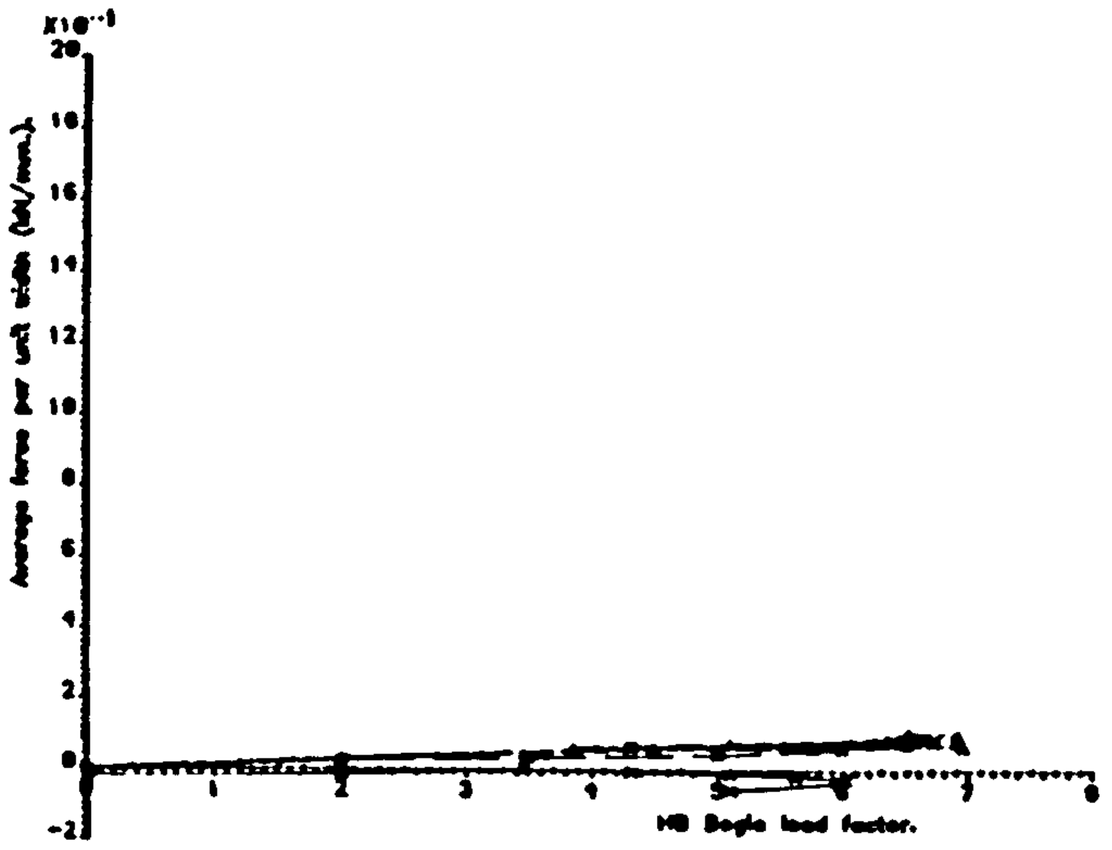

KEY:

1 ——— Experimental

2 — — — — — SNAP linear

3 — · — · — · — SNAP nonlinear with standard data (34% prestress losses)

4 — — — — SNAP nonlinear with 34% prestress losses and zero tensile strength concrete

FIG. 9.53. REACTION NON-LINEARITY FOR MODEL 2

9.3.7.1 Model 1 crack patterns

The analysis chosen for presentation in the model 1 crack pattern plots corresponds to curve 5 in the load-deflection plots of Figure 9.33. This analysis featured increased prestress losses from 20% to 35%, a 2 segment curve for concrete in tension and statistically varied material properties. This analysis gave good agreement with the experimental load-deflection response.

The first level presented is at an applied load of 2.7 x ULS 45 unit HB bogies. This level corresponds to level 16 of Appendix 5.3. Figures 9.55 to 9.57 depict the crack patterns for each of the five through depth layers in the insitu concrete. Figures 9.58 to 9.60 illustrate the crack patterns in the precast concrete. For the insitu top layer no cracking or crushing is indicated, see Figure 9.55. From Figure 9.56 it can be seen that the first cracks are indicated in layer 3 of the insitu concrete. These cracks appear to be forming a line between the HB bogie and the unloaded acute corner. For the insitu bottom layer increased cracking and even some closing cracks, which are indicated by dashed lines, are evident. From the titling on these plots it can be seen that the cracks are plotted with respect to a maximum strain of 4880 $\mu\epsilon$. The through depth location of each of the insitu and precast layers can be obtained from Figure 9.11, which defines the through depth integration scheme.

The precast concrete cracking plots which are shown in Figure 9.58 to 9.60 are similar to those of the insitu concrete. Considering the presence of prestress in the precast concrete, this similarity may seem surprising. One of the reasons for this similarity can be illustrated by looking at the initial prestrain in the precast beams. In Chapter 10 Section 10.2.6 it is deduced that the residual prestress in the precast concrete at the time of model 1 testing was

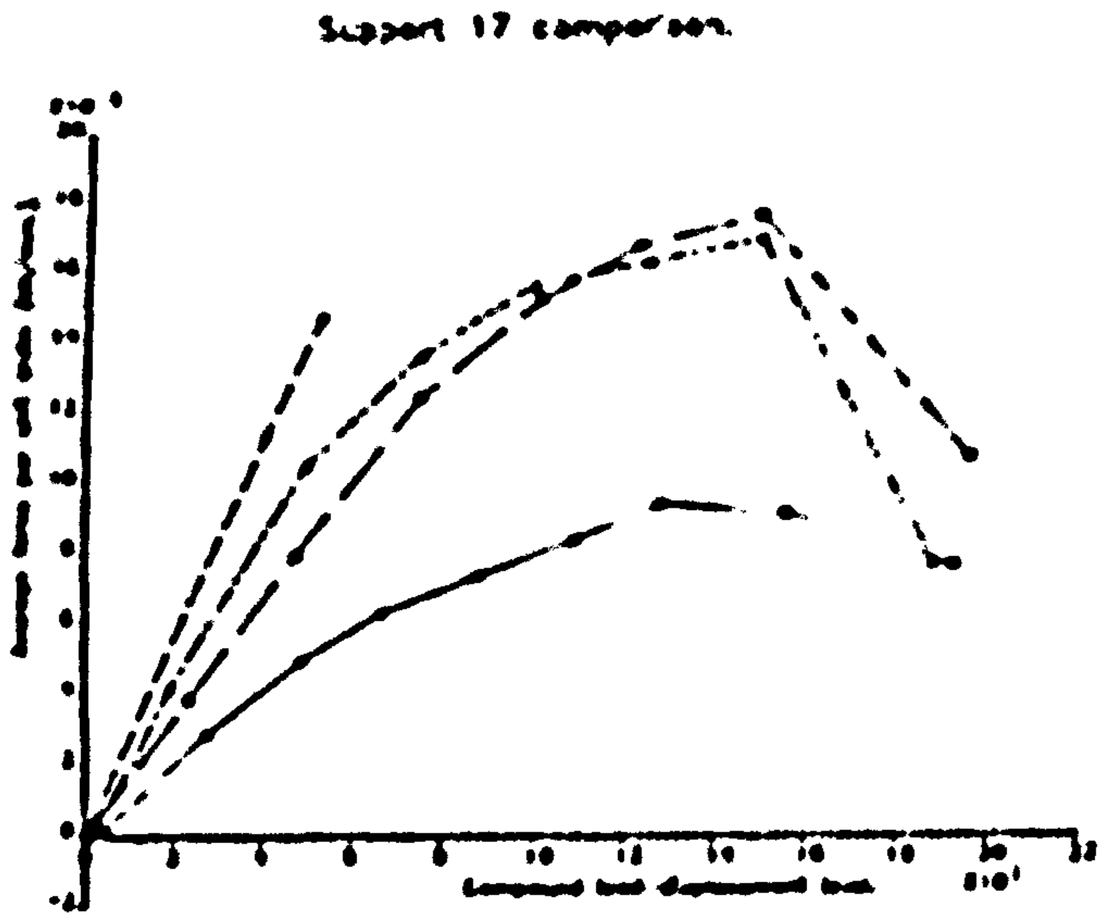

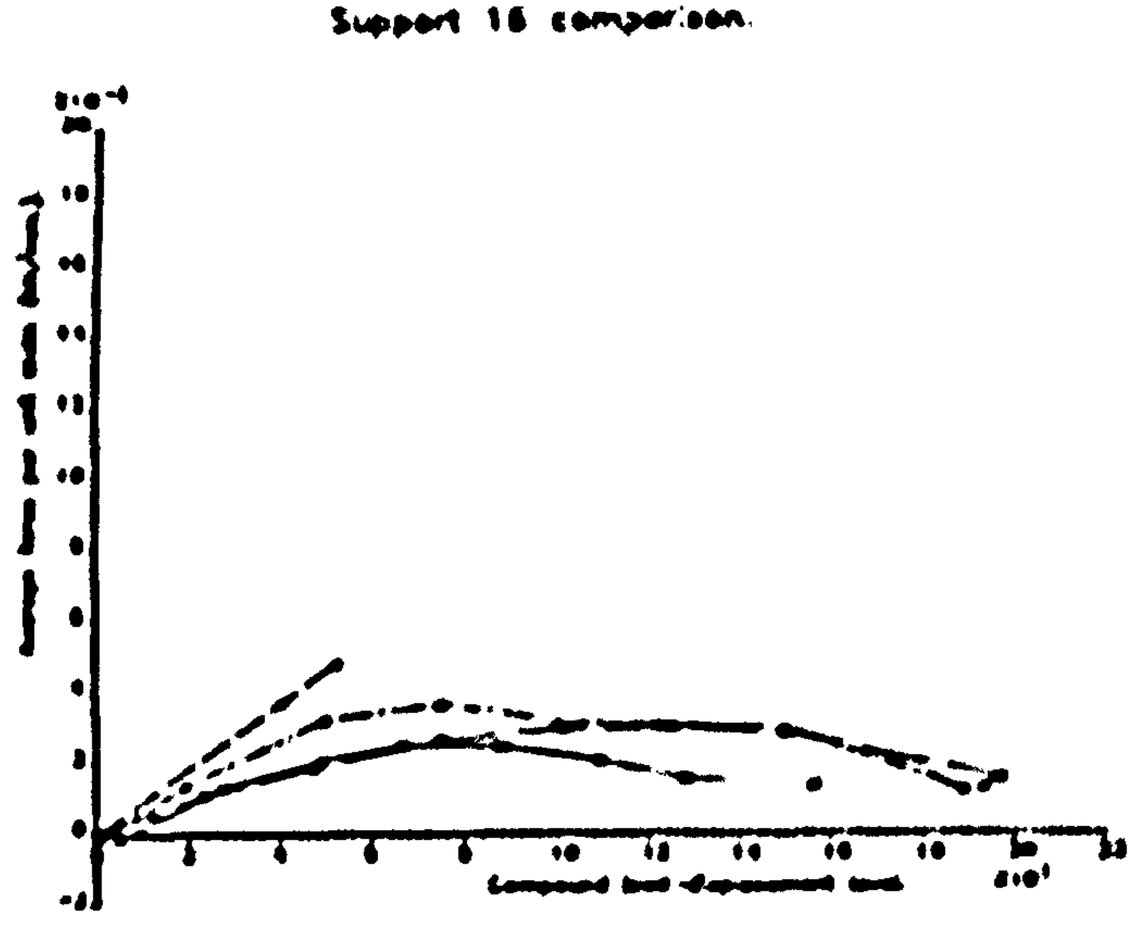

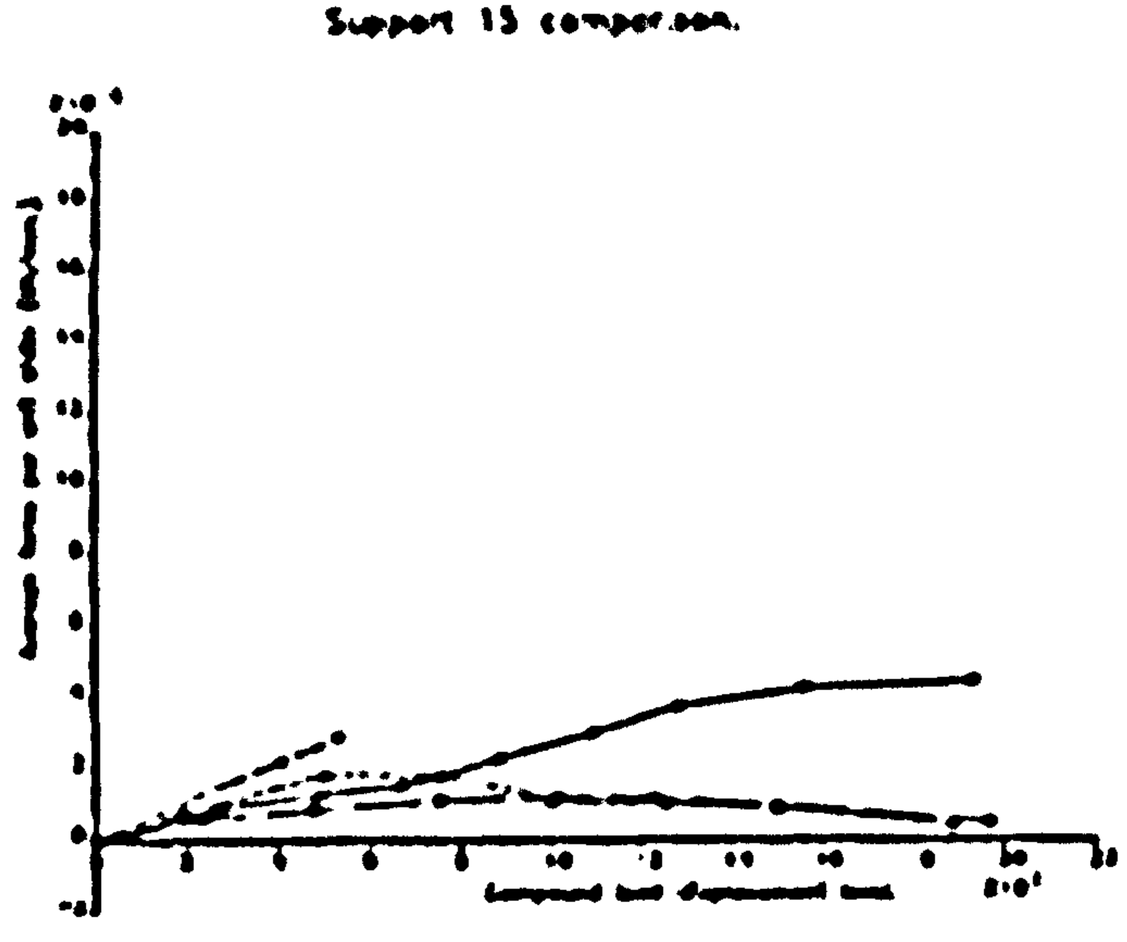

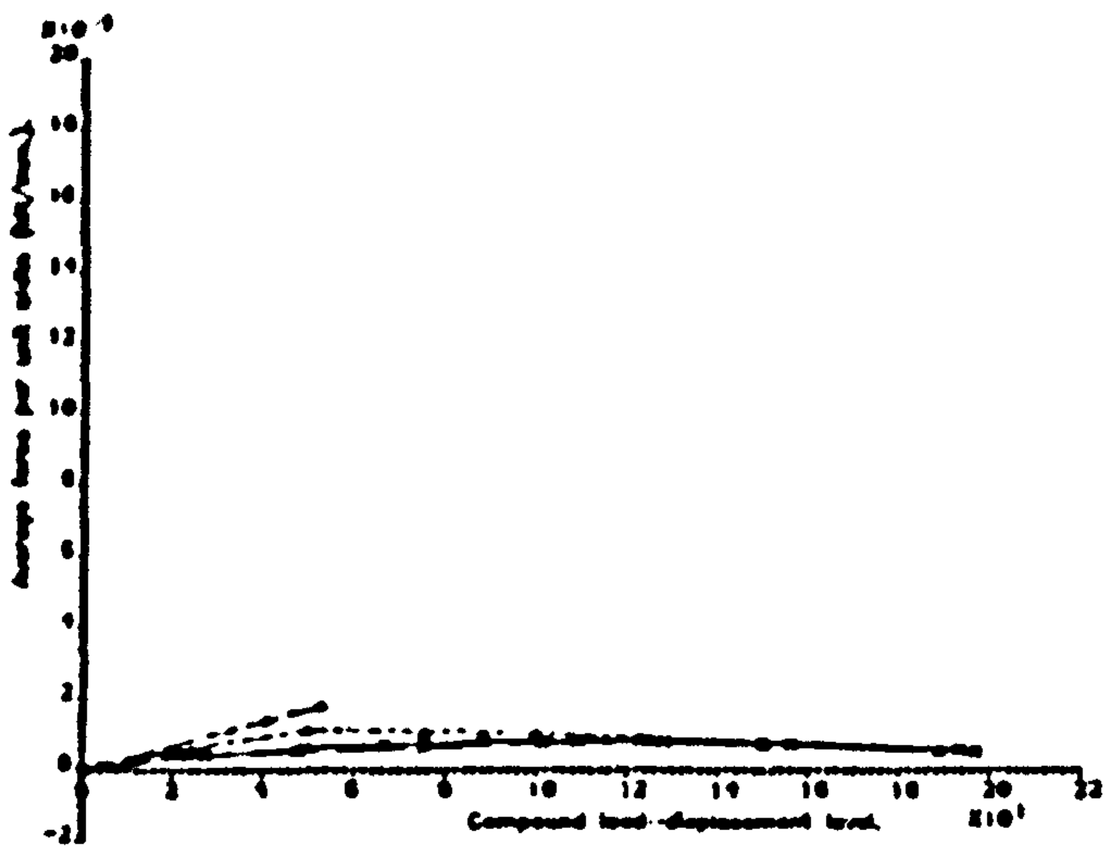

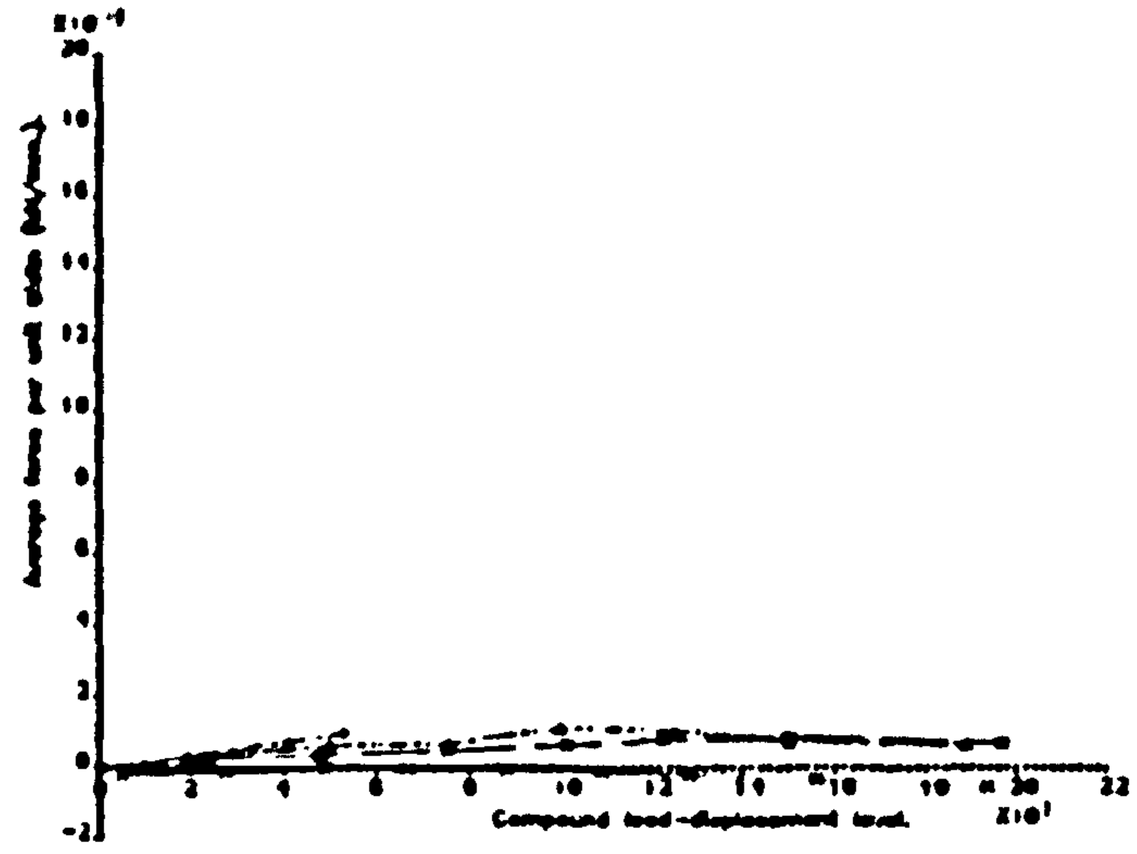

KEY:

1 ——————— Experimental

2 — — — — — SNAP linear

3 —·—·—·— SNAP nonlinear with standard data (34% prestress losses)

4 — — — — SNAP nonlinear with 34% prestress losses and zero tensile strength concrete

FIG. 9.54. REACTION NON-LINEARITY FOR MODEL 2.

approximately 10.42 N/mm^2. Assuming a Young's modulus of 35800 N/mm^2 for the precast concrete this equates to a prestrain of 291 $\mu\epsilon$. Cracking strains of approximately 4500 $\mu\epsilon$ are indicated in Figure 9.60. This relatively large magnitude is thought to be the cause of the similarity between the principal strain directions.

The second set of crack pattern plots relate to a displacement level of 79 mm and correspond to level 21 of Appendix 5.3. The top surface crack pattern plot of Figure 9.61 agrees well with the experimental crack pattern that can be seen in Figure 5.9 Chapter 5. It can be seen that an area of crushing is developing in the vicinity of the HB Bogie. The analytical soffit crack pattern plot of Figure 9.62 agrees reasonably well with the experimental plot of Figure 5.8 of Chapter 5, except that the analytical cracking is more intense. It is interesting to note in this figure that the cracks on the unloaded side of the slab are closing. This suggests that a yield line at mid-span was trying to form, but was superceded by an alternative pattern such as a Y shaped mode.

The final crack pattern plots for model 1 relate to a displacement level of 137 mm and correspond to level 25 of Appendix 5.3. From the top surface plot it can be seen that the area of concrete crushing has become very extensive and concrete compressive strains of up to 30000 $\mu\epsilon$ are indicated for the area adjacent to the HB Bogie. The cracking pattern on the top surface is largely the same as the previous level. Cracking through the depth is very intense with many doubly cracked points indicated. From the soffit crack pattern plot of Figure 9.68, it can be seen that the largest cracking strains are concentrated near to the HB Bogie. Closing cracks are indicated both along the loaded free edge and towards the unloaded free edge.

SNAP analysis of model deck 1, 48 element mesh.

Date : 11/ 8/87 at 1:50: 7 Concrete cracking & crushing pattern plots.

Plot for in-situ concrete top layer.

Geometrical Scale Factor = 30.99

Stage : 3/ 8 Strain Scale, .488E -2 = ⟷

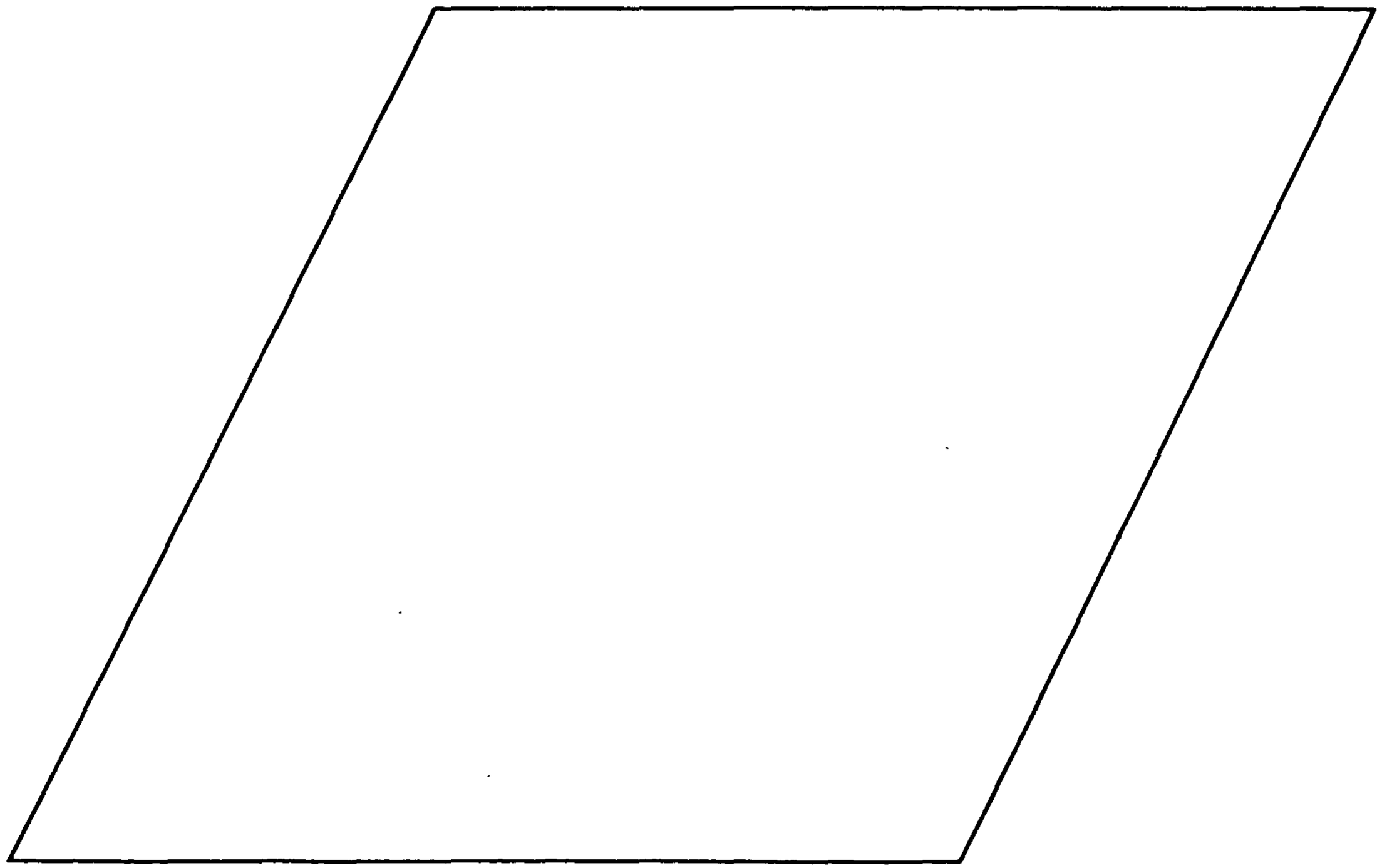

FIG 9. 55. CRACKING/CRUSHING PATTERN PLOT FOR MODEL 1 AT LEVEL 16, WITH AN APPLIED LOAD LEVEL OF 2·7

SNAP analysis of model deck 1, 48 element mesh.

Date : 11/ 8/87 at 1:50: 7 Concrete cracking & crushing pattern plots.

Plot for in-situ concrete layer 2.
Geometrical Scale Factor = 66.25
Stage : 3/ 8 Strain Scale, .488E -2 = —

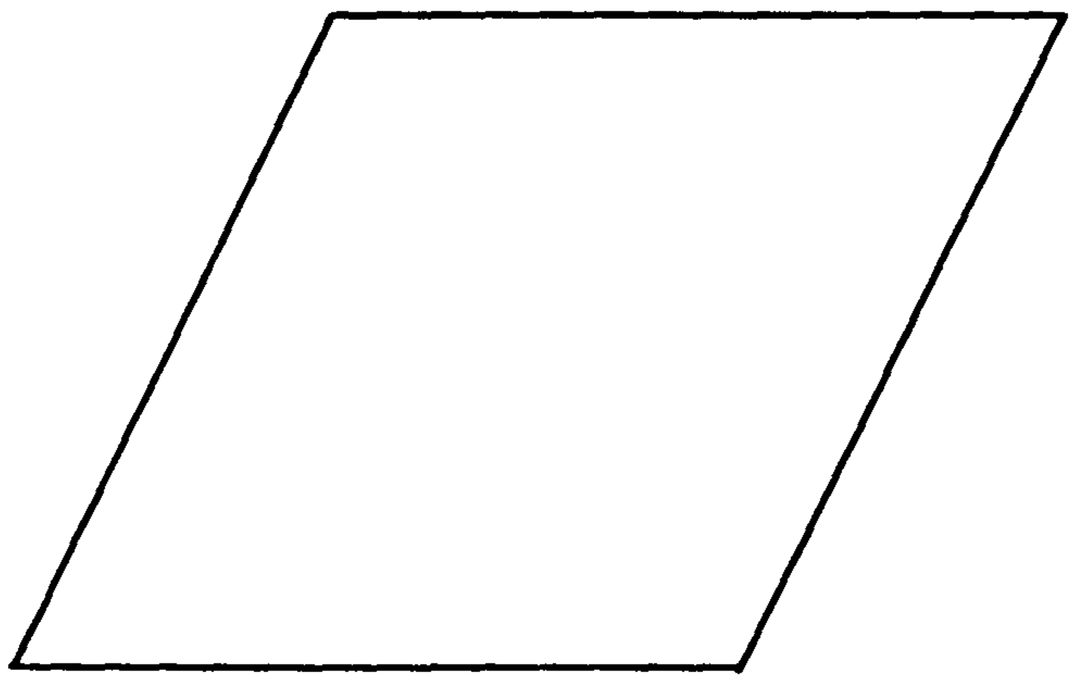

Plot for in-situ concrete layer 3.
Geometrical Scale Factor = 66.25
Stage : 3/ 8 Strain Scale, .488E -2 = —

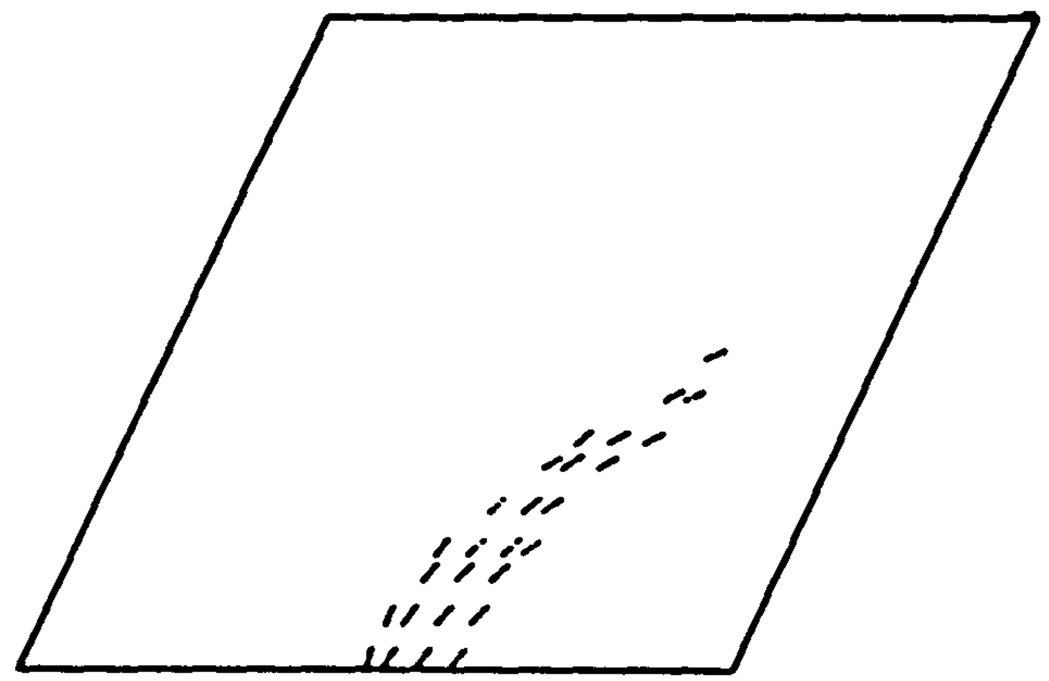

Plot for in-situ concrete layer 4.
Geometrical Scale Factor = 66.25
Stage : 3/ 8 Strain Scale, .498E -2 = —

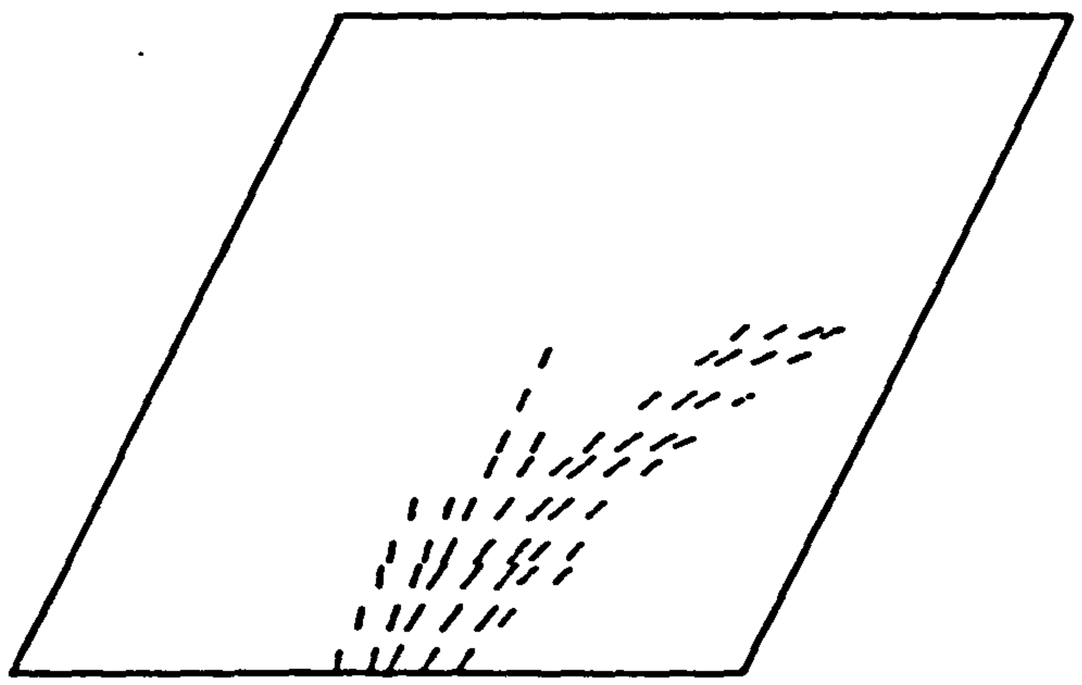

FIG. 9. 56. CRACKING/CRUSHING PATTERN PLOTS FOR MODEL 1 AT LEVEL 16, WITH AN APPLIED LOAD LEVEL OF 2·7

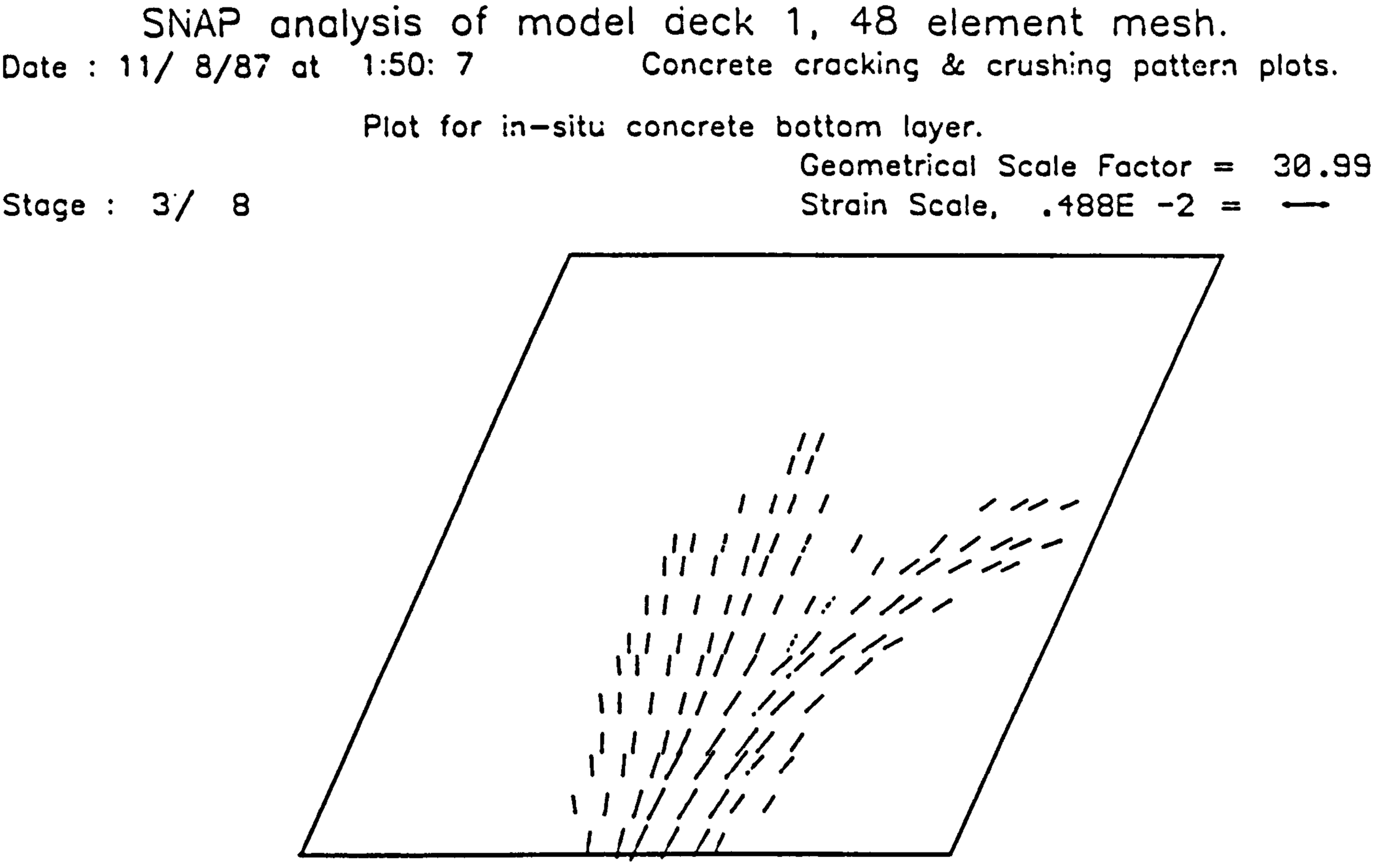

FIG. 9. 57. CRACKING/CRUSHING PATTERN PLOT FOR MODEL 1 AT LEVEL 16, WITH AN APPLIED LOAD LEVEL OF 2·7

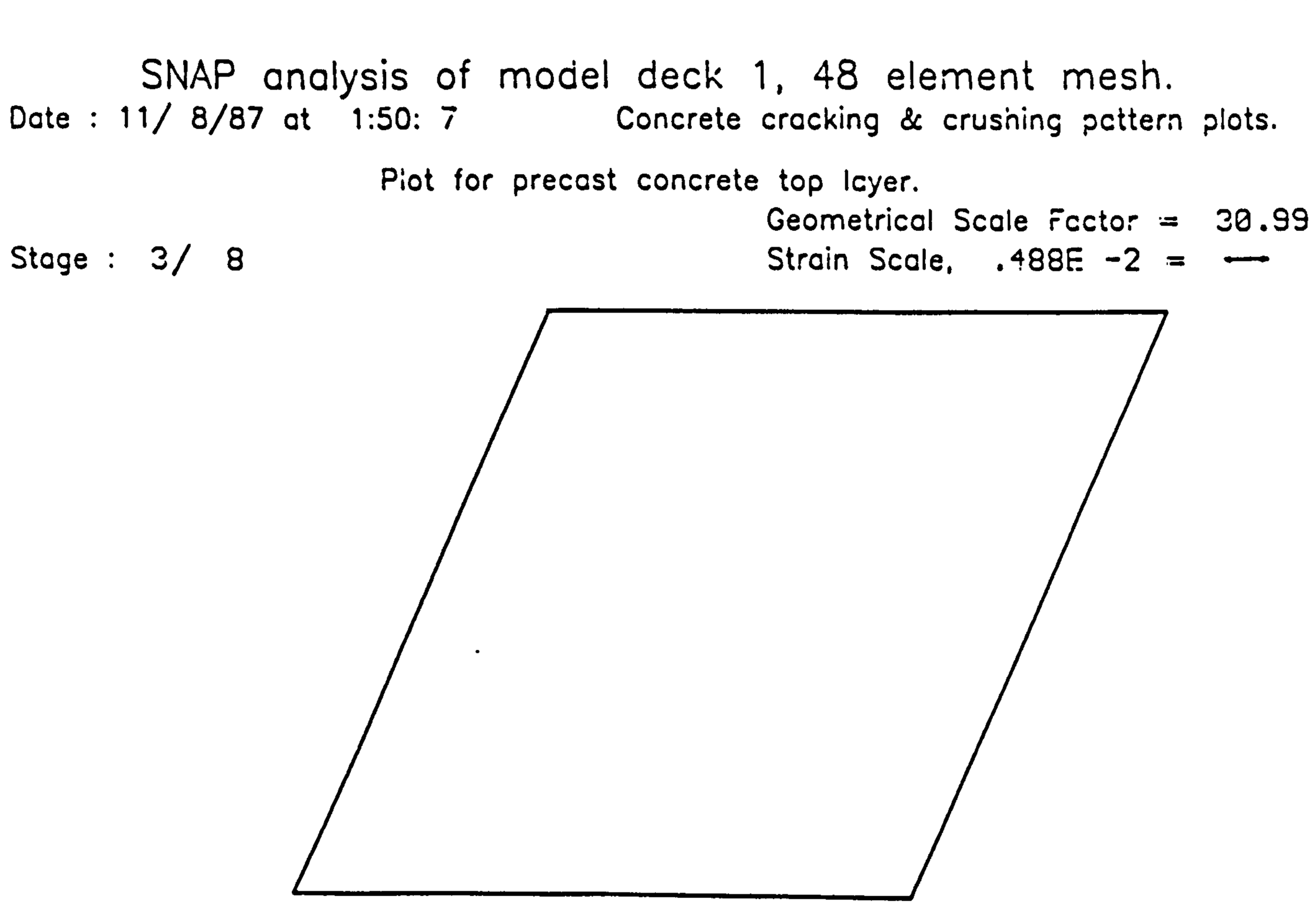

FIG. 9. 58. CRACKING/CRUSHING PATTERN PLOT FOR MODEL 1 AT LEVEL 16, WITH AN APPLIED LOAD LEVEL OF 2·7

SNAP analysis of model deck 1, 48 element mesh.

Date : 11/ 8/87 at 1:50: 7 Concrete cracking & crushing pattern plots.

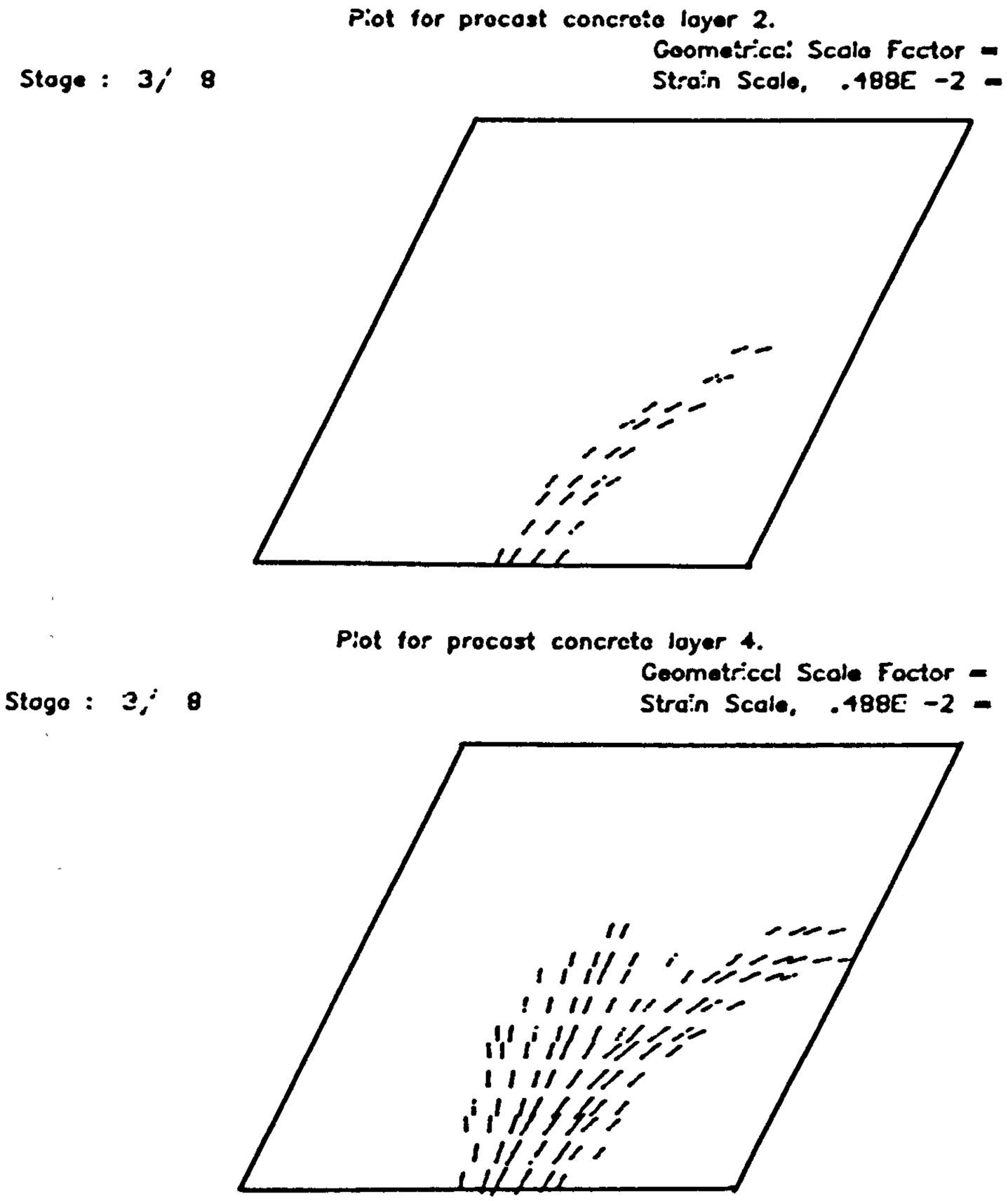

FIG. 9. 59. CRACKING/CRUSHING PATTERN PLOTS FOR MODEL 1 AT LEVEL 16, WITH AN APPLIED LOAD LEVEL OF 2·7

SNAP anclysis of model deck 1, 48 element mesh.
Date : 11/ 8/87 at 1:50: 7 Concrete cracking & crushing pattern plots.

Plot for precast concrete bottom layer.
Geometrical Scale Factor = 30.99
Stage : 3/ 8 Strain Scale, .488E -2 = ⟶

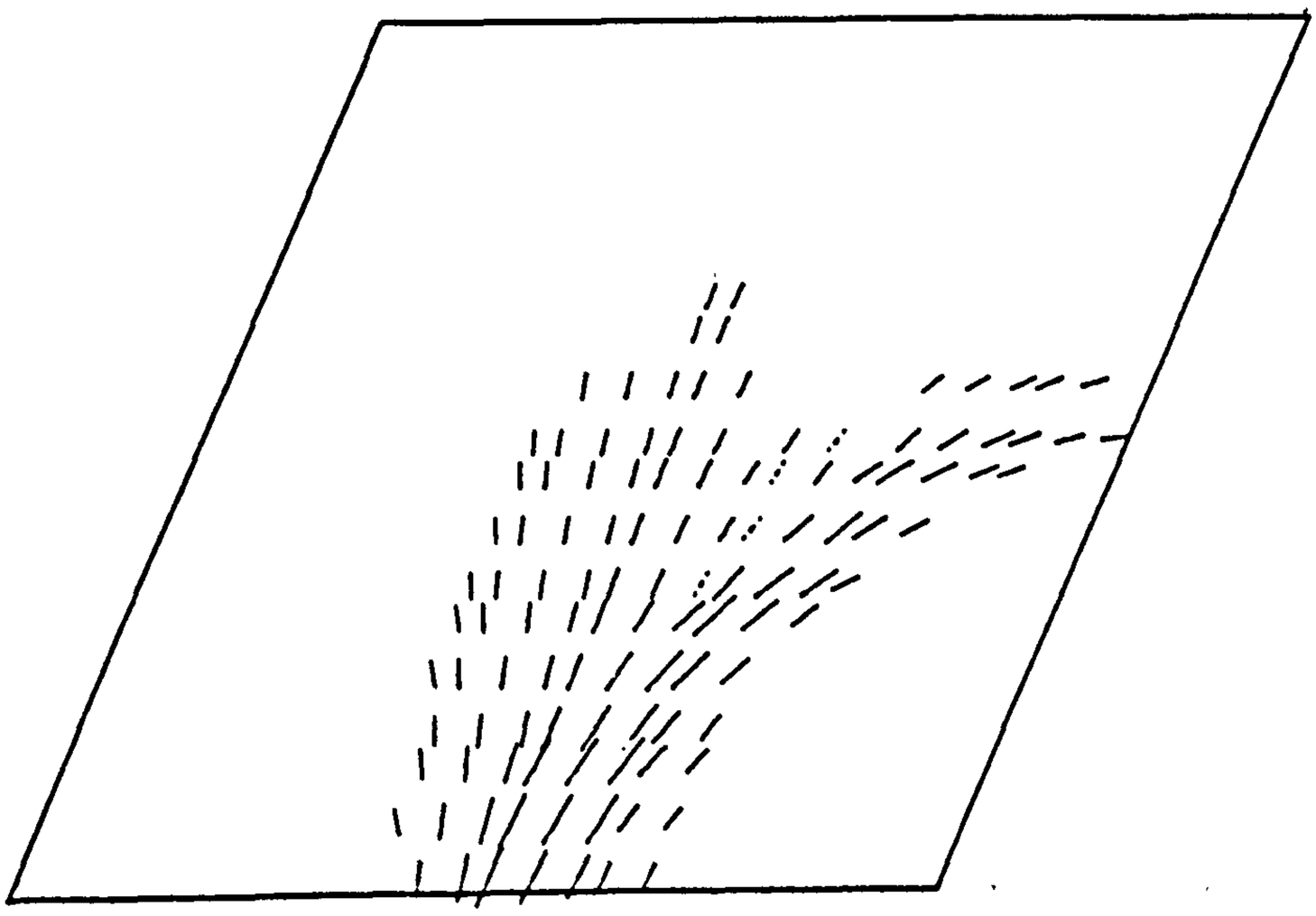

FIG 9. 60. CRACKING/CRUSHING PATTERN PLOT FOR MODEL 1 AT LEVEL 16, WITH AN APPLIED LOAD LEVEL OF 2·7

SNAP analysis of model deck 1, 48 element mesh.
Date : 11/ 8/87 at 1:53: 7 Concrete cracking & crushing pattern plots.

Plot for in-situ concrete top layer.
Geometrical Scale Factor = 30.99
Stage : 3/ 64 Strain Scale, .430E -1 = ⟶

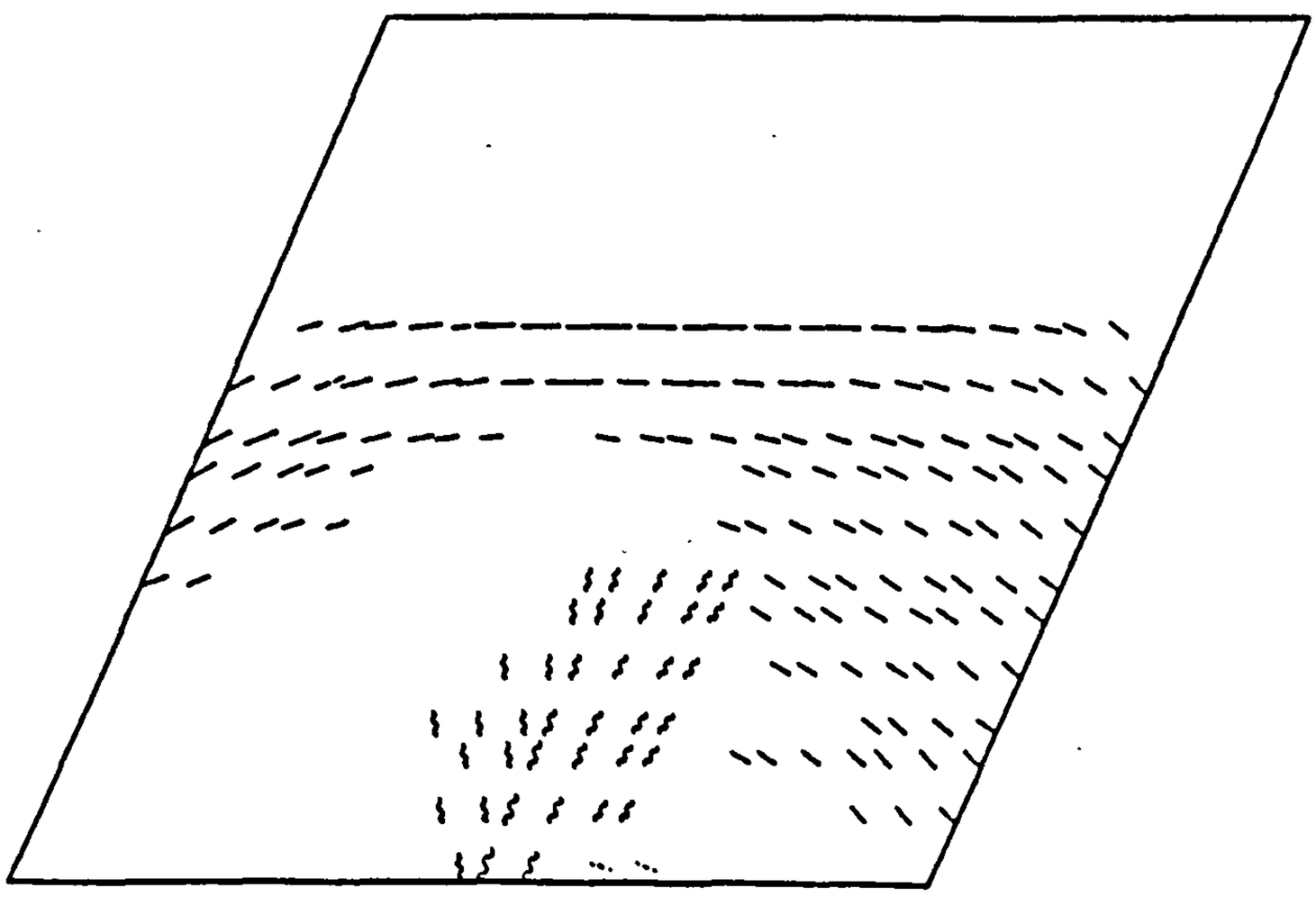

FIG. 9 61. CRACKING/CRUSHING PATTERN PLOTS FOR MODEL 1 AT LEVEL 21, WITH A LOADED FREE EDGE DISPLACEMENT LEVEL OF 79mm

9.3.7.2 Model 2 crack patterns

The analysis chosen for presentation of the model 2 crack pattern plots corresponds to curve 2 in Figure 9.35. The first level is specified in terms of a load of 5.1 x ULS 45 unit HB Bogies and the plots pertaining to level 21 can be seen in Figures 9.69 to 9.74. From the insitu top layer plot of Figure 9.69, limited cracking is indicated for the area adjacent to the loaded obtuse corner. Further down the depth, it is shown that the main cracks are concentrated at mid-span and are orientated approximately parallel to the supports. The precast concrete plots of Figures 9.72 to 9.74 are similar to those in the insitu concrete. One or two isolated closing cracks are indicated on the soffit crack pattern plot of Figure 9.74.

Top surface and soffit crack patterns are presented in Figures 9.75 and 9.76 for level 23, which is defined at a displacement level of 90 mm. By this stage the top surface crack pattern has become very extensive covering half the slab area. When compared with the experimental crack plot of Figure 7.8 of Chapter 7, it will be seen that there is good agreement for the crack located towards the instrumented support line, see Figure 9.75. While cracks are shown on the experimental plot for the far side of the slab, surprisingly, no cracks are indicated in the analytical plot. On the analytical plot, crushing is developing along a band across the slab at mid-span. The analytical soffit crack pattern plot of Figure 9.76 indicates extensive cracking over most of the slab except for the loaded acute corner. Comparison of this plot with the experimental crack pattern plot of Figure 7.9 of Chapter 7 reveals good agreement for the crack orientations. In Figure 9.76 a group of cracks close to the HB Bogie are shown to be closing.

SNAP analysis of model deck 1, 48 element mesh.
Date : 11/ 8/87 at 1:53: 7 Concrete cracking & crushing pattern plots.

Plot for precast concrete bottom layer.

Geometrical Scale Factor = 30.99
Stage : 3/ 64 Strain Scale, .430E -1 = ⟵

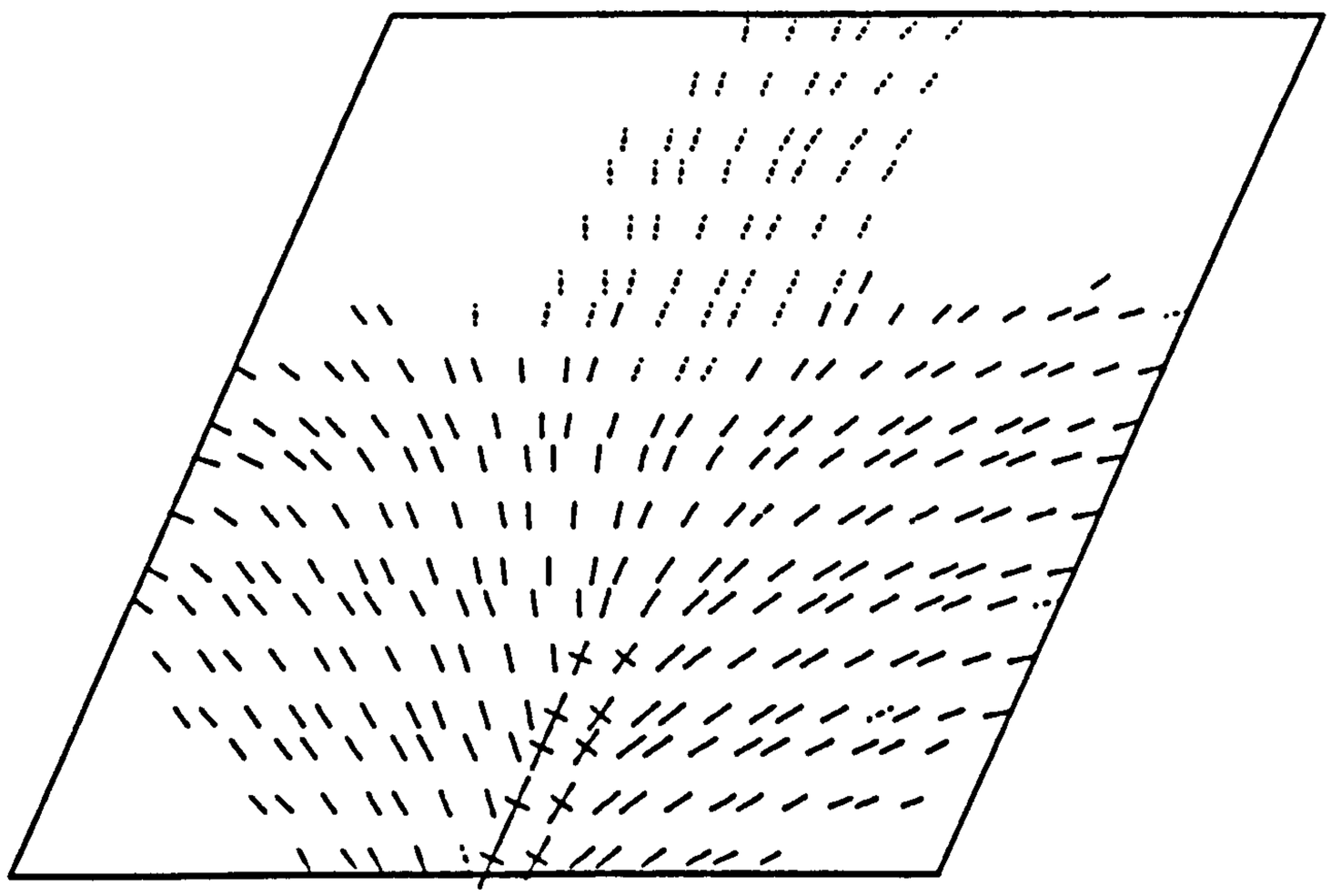

FIG. 9 62. CRACKING/CRUSHING PATTERN PLOTS FOR MODEL 1 AT LEVEL 21, WITH A LOADED FREE EDGE DISPLACEMENT LEVEL OF 79mm

SNAP analysis of model deck 1, 48 element mesh.
Date : 11/ 8/87 at 1:57:22 Concrete cracking & crushing pattern plots.

Plot for in-situ concrete top layer.

Geometrical Scale Factor = 30.99
Stage : 3/ 96 Strain Scale, .941E -1 = ⟵

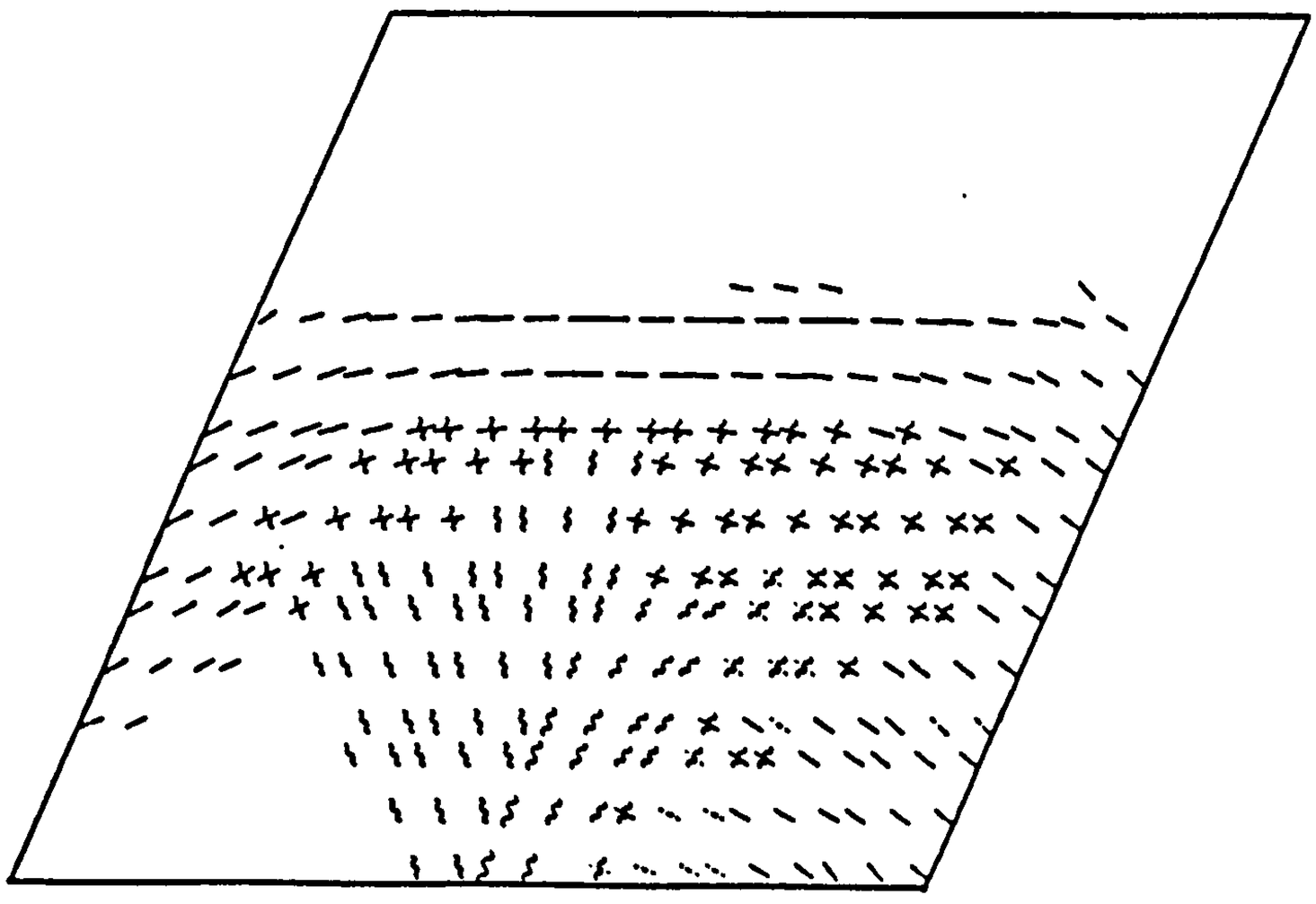

FIG 9.63. CRACKING/CRUSHING PATTERN PLOTS FOR MODEL 1 AT LEVEL 25, WITH A LOADED FREE EDGE DISPLACEMENT LEVEL OF 137mm

SNAP analysis of model deck 1, 48 element mesh.

Date : 11/ 8/87 at 1:57:22 Concrete cracking & crushing pattern plots.

Plot for in-situ concrete layer 2.
Geometrical Scale Factor = 66.25
Strain Scale, .941E -1 = —
Stage : 3/ 96

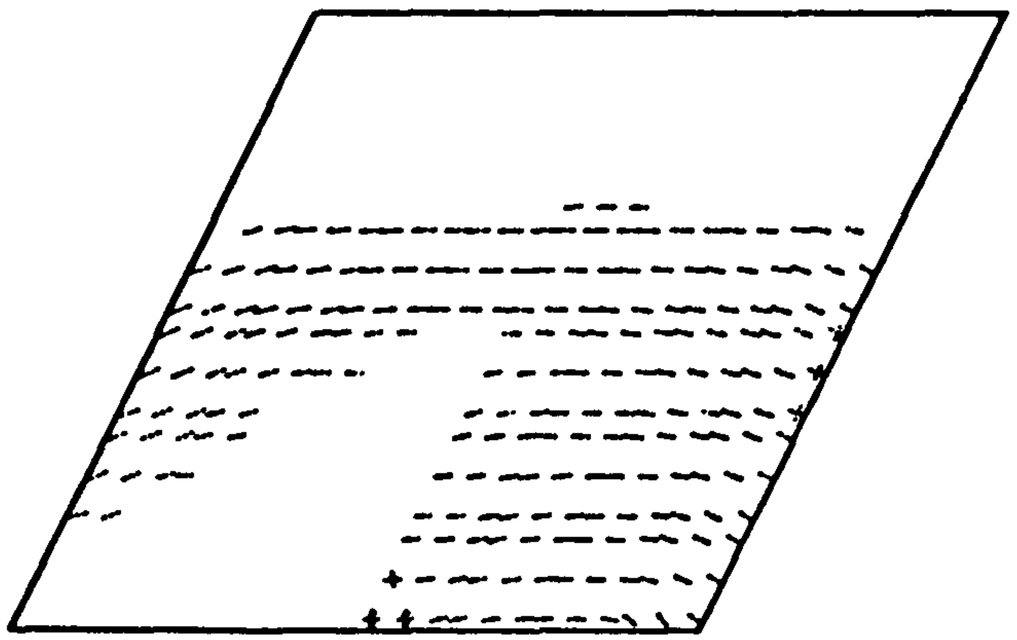

Plot for in-situ concrete layer 3.
Geometrical Scale Factor = 66.25
Strain Scale, .941E -1 = —
Stage : 3/ 96

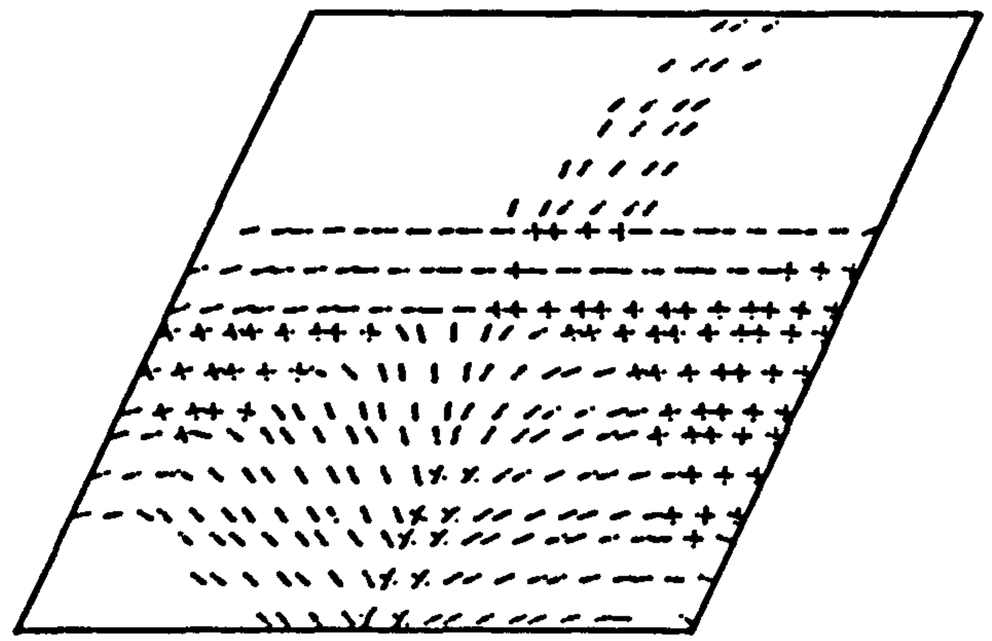

Plot for in-situ concrete layer 4.
Geometrical Scale Factor = 66.25
Strain Scale, .941E -1 = —
Stage : 3/ 96

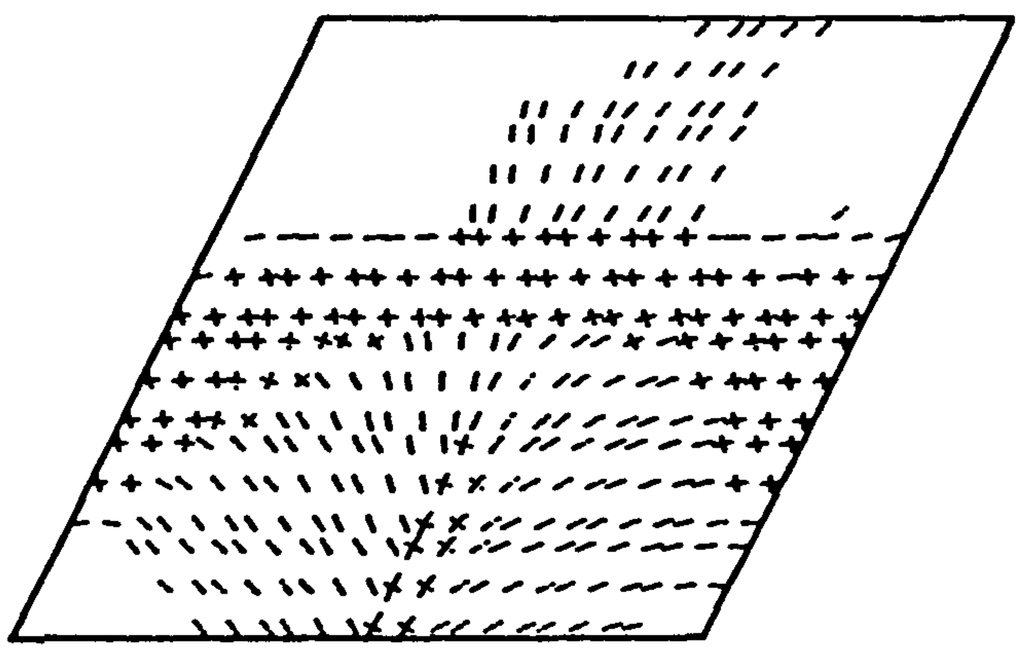

FIG. 9. 64. CRACKING/CRUSHING PATTERN PLOTS FOR MODEL 1 AT LEVEL 25, WITH A LOADED FREE EDGE DISPLACEMENT LEVEL OF 137mm

SNAP analysis of model deck 1, 48 element mesh.
Date : 11/ 8/87 at 1:57:22 Concrete cracking & crushing pattern plots.

Plot for in-situ concrete bottom layer.

Geometrical Scale Factor = 30.99
Stage : 3/ 96 Strain Scale, .941E -1 = ⟶

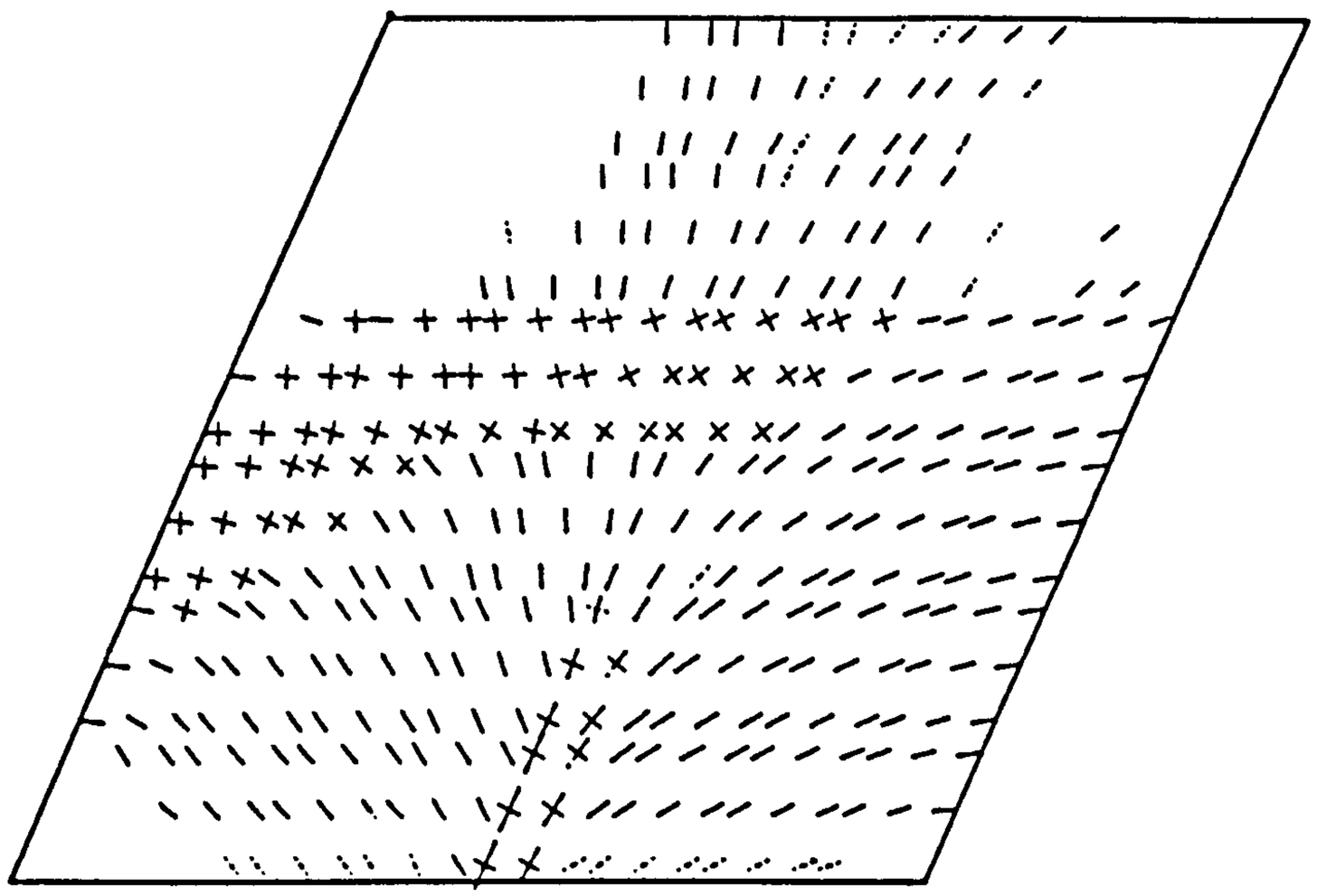

FIG 9. 65. CRACKING/CRUSHING PATTERN PLOTS FOR MODEL 1 AT LEVEL 25, WITH A LOADED FREE EDGE DISPLACEMENT LEVEL OF 137mm

SNAP analysis of model deck 1, 48 element mesh.
Date : 11/ 8/87 at 1:57:22 Concrete cracking & crushing pattern plots.

Plot for precast concrete top layer.

Geometrical Scale Factor = 30.99
Stage : 3/ 96 Strain Scale, .941E -1 = ⟶

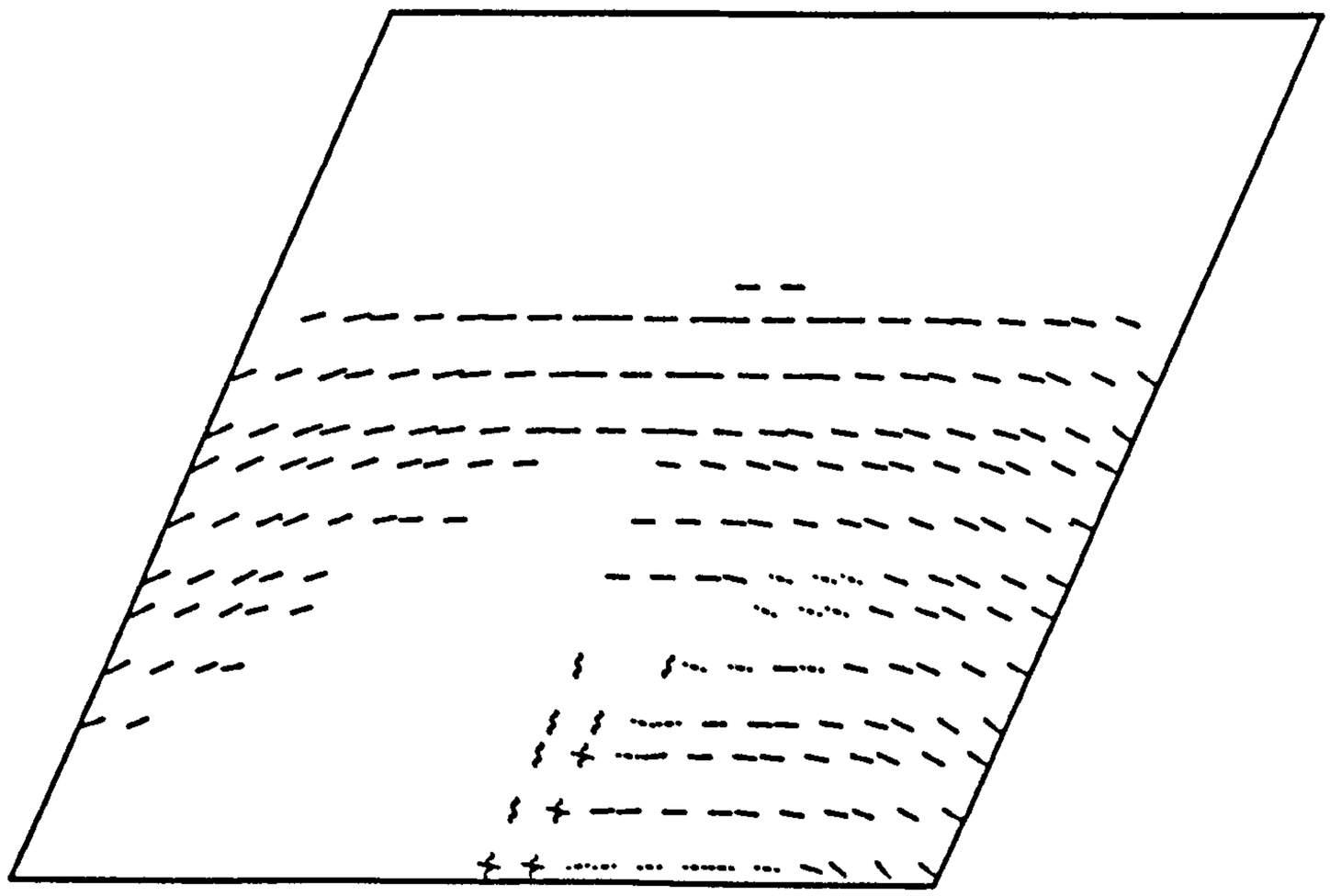

FIG 9 66. CRACKING/CRUSHING PATTERN PLOTS FOR MODEL 1 AT LEVEL 25, WITH A LOADED FREE EDGE DISPLACEMENT LEVEL OF 137mm

SNAP analysis of model deck 1, 48 element mesh.

Date : 11/ 8/87 at 1:57:22 Concrete cracking & crushing pattern plots.

Plot for precast concrete layer 2.
Geometrical Scale Factor = 66.25
Strain Scale, .941E -1 = ——
Stage : 3/ 96

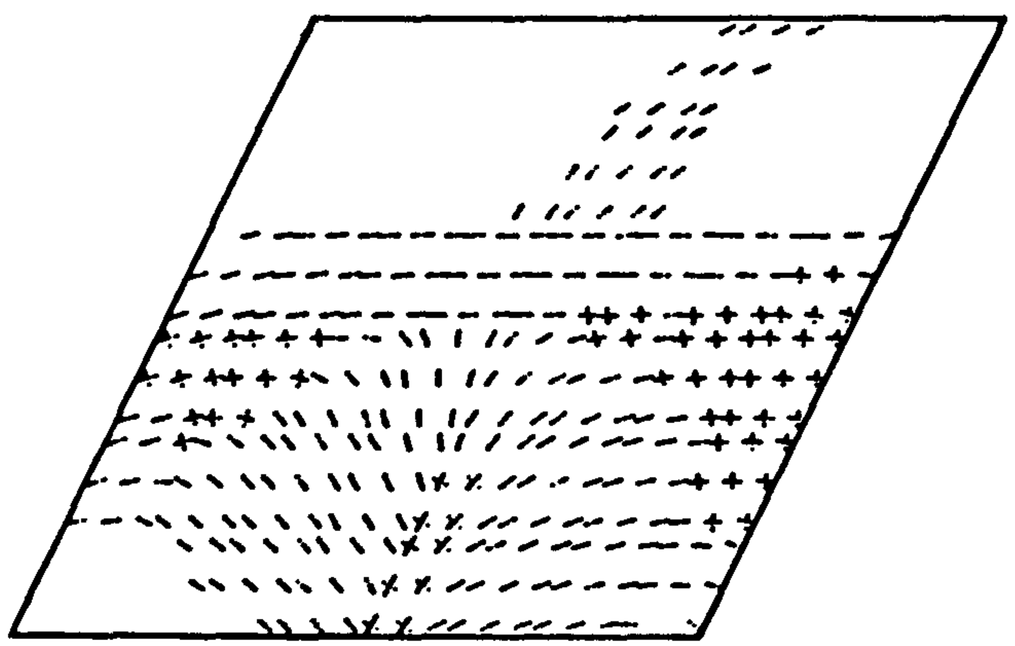

Plot for precast concrete layer 3.
Geometrical Scale Factor = 66.25
Strain Scale, .941E -1 = ——
Stage : 3/ 96

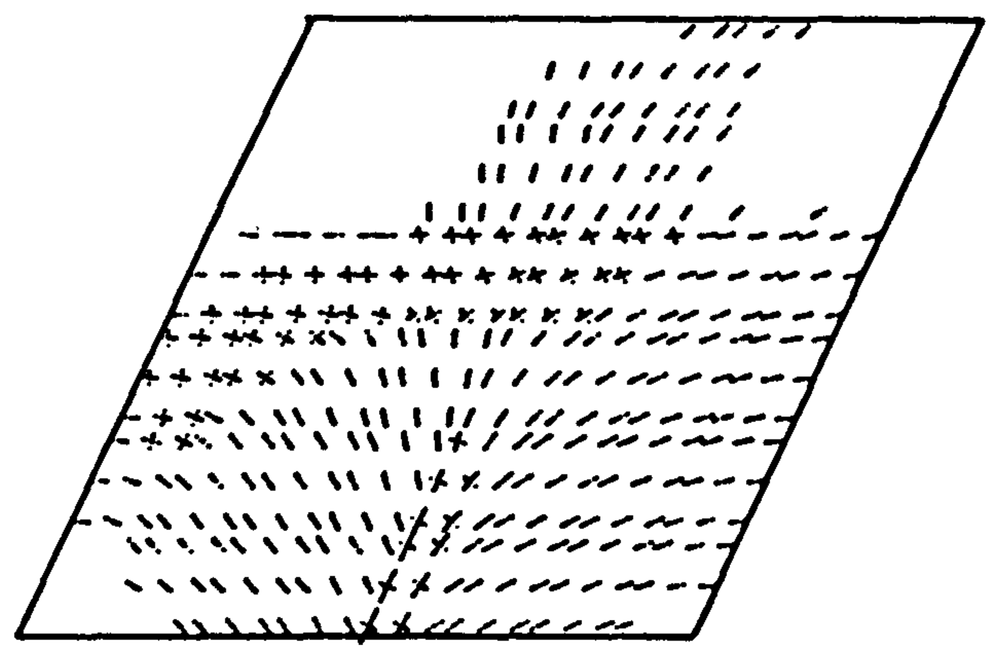

Plot for precast concrete layer 4.
Geometrical Scale Factor = 66.25
Strain Scale, .941E -1 = ——
Stage : 3/ 96

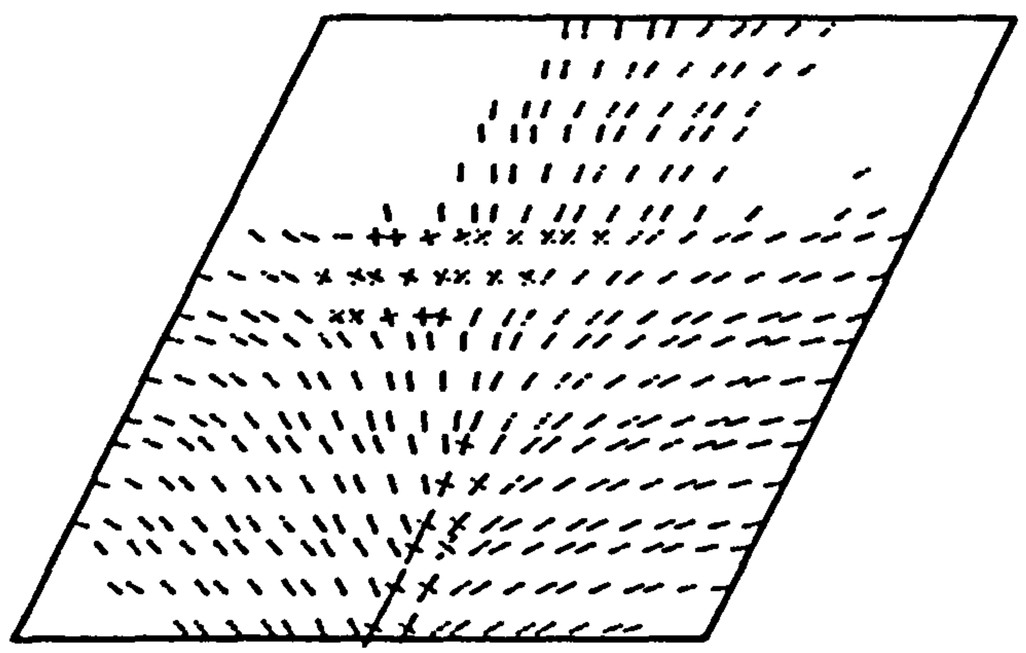

FIG. 9. 67. CRACKING/CRUSHING PATTERN PLOTS FOR MODEL 1 AT LEVEL 25, WITH A LOADED FREE EDGE DISPLACEMENT LEVEL OF 137mm

The final set of crack pattern plots for model 2 are shown in Figures 9.77 to 9.82. These figures depict the situation with a displacement of 156 mm and this corresponds to level 25 of Appendix 7.2. By this stage some of the prestressing tendons have ruptured, resulting in a reduction of the applied load. This load reduction has caused the strains to localise and the majority of cracks have begun to close. From the top surface crack pattern to Figure 9.77 it can be seen that almost all of the cracks are closing. The area of crushing now covers the complete model width. Looking through the depth it can be seen that the only active material is located in a narrow band at midspan, which stretches across the full width of the slab. From the soffit crack pattern it is clear that the slab is failing through the formation of a yield line at midspan. This was predicted by the yield line analyses of Appendix 9.1 but was not apparent in the actual test.

PAGE NUMBERING AS ORIGINAL

SNAP analysis of model deck 1, 48 element mesh.
Date : 11/ 8/87 at 1:57:22 Concrete cracking & crushing pattern plots.

Plot for precast concrete bottom layer.
Geometrical Scale Factor = 30.99
Stage : 3/ 96 Strain Scale, .941E -1 = ⟶

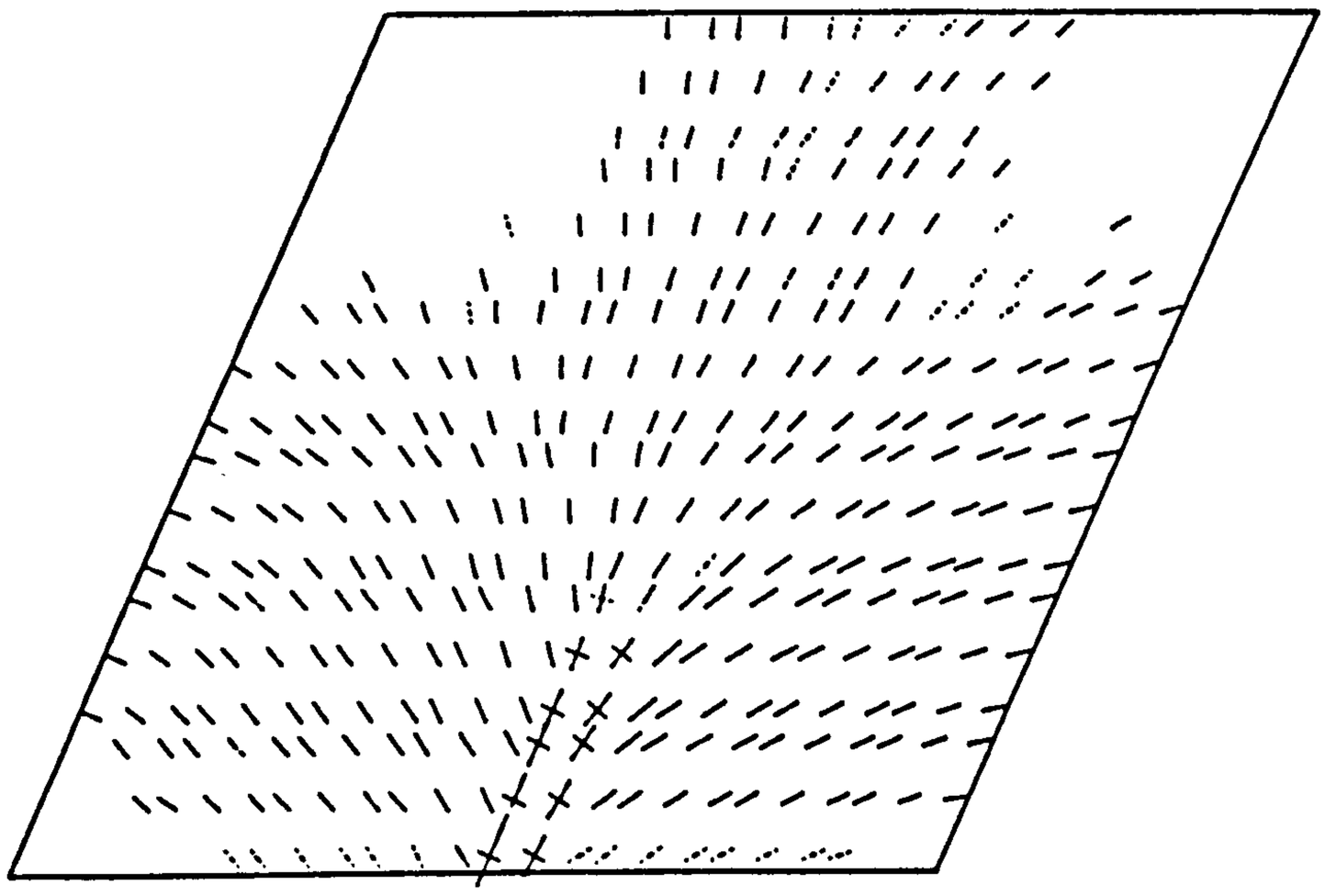

FIG. 9. 68. CRACKING/CRUSHING PATTERN PLOTS FOR MODEL 1 AT LEVEL 25, WITH A LOADED FREE EDGE DISPLACEMENT LEVEL OF 137mm

SNAP analysis of model deck 2, 48 element mesh.
Date : 11/ 8/87 at 23: 4:11 Concrete cracking & crushing pattern plots.

Plot for in-situ concrete top layer.
Geometrical Scale Factor = 26.23
Stage : 4/ 27 Strain Scale, .629E -2 = ⟶

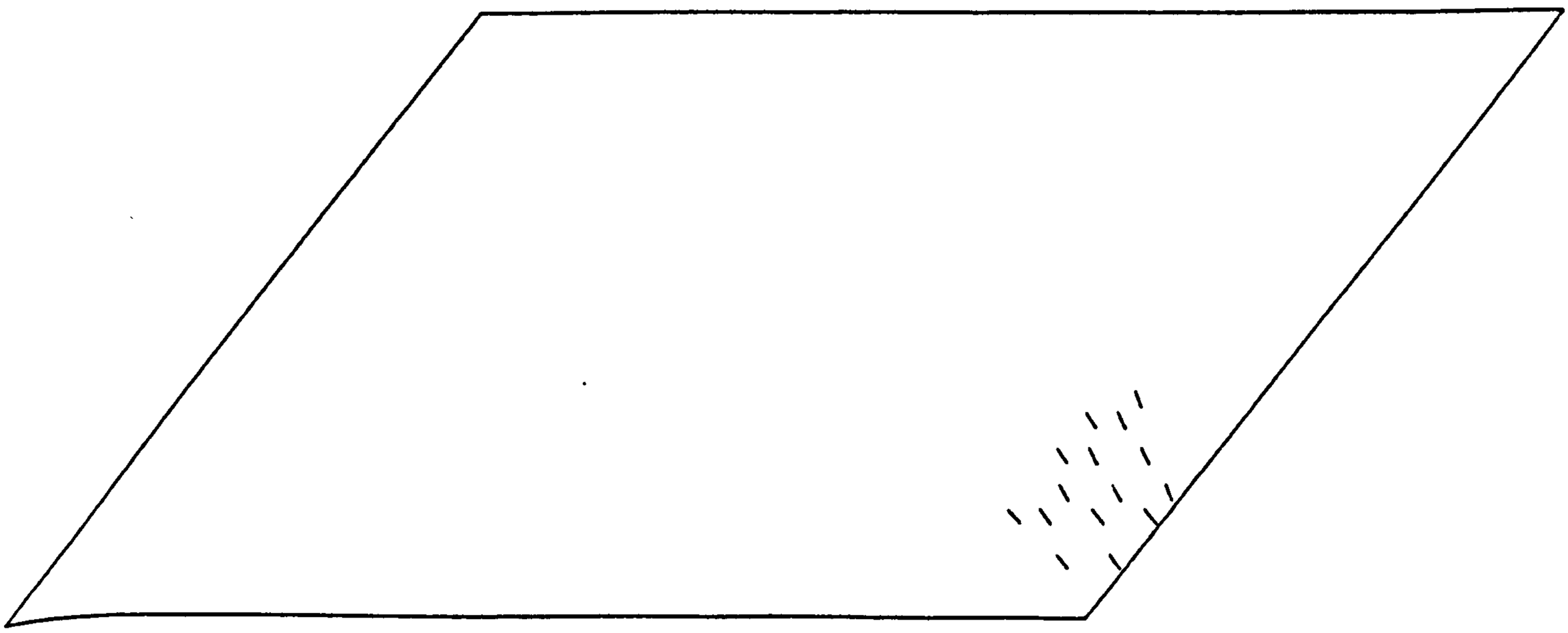

FIG. 9. 69. CRACKING/CRUSHING PATTERN PLOTS FOR MODEL 2 AT LEVEL 21, WITH AN APPLIED LOAD LEVEL OF 5.1

SNAP analysis of model deck 2, 48 element mesh.

Date : 11/ 8/87 at 23: 4:11 Concrete cracking & crushing pattern plots.

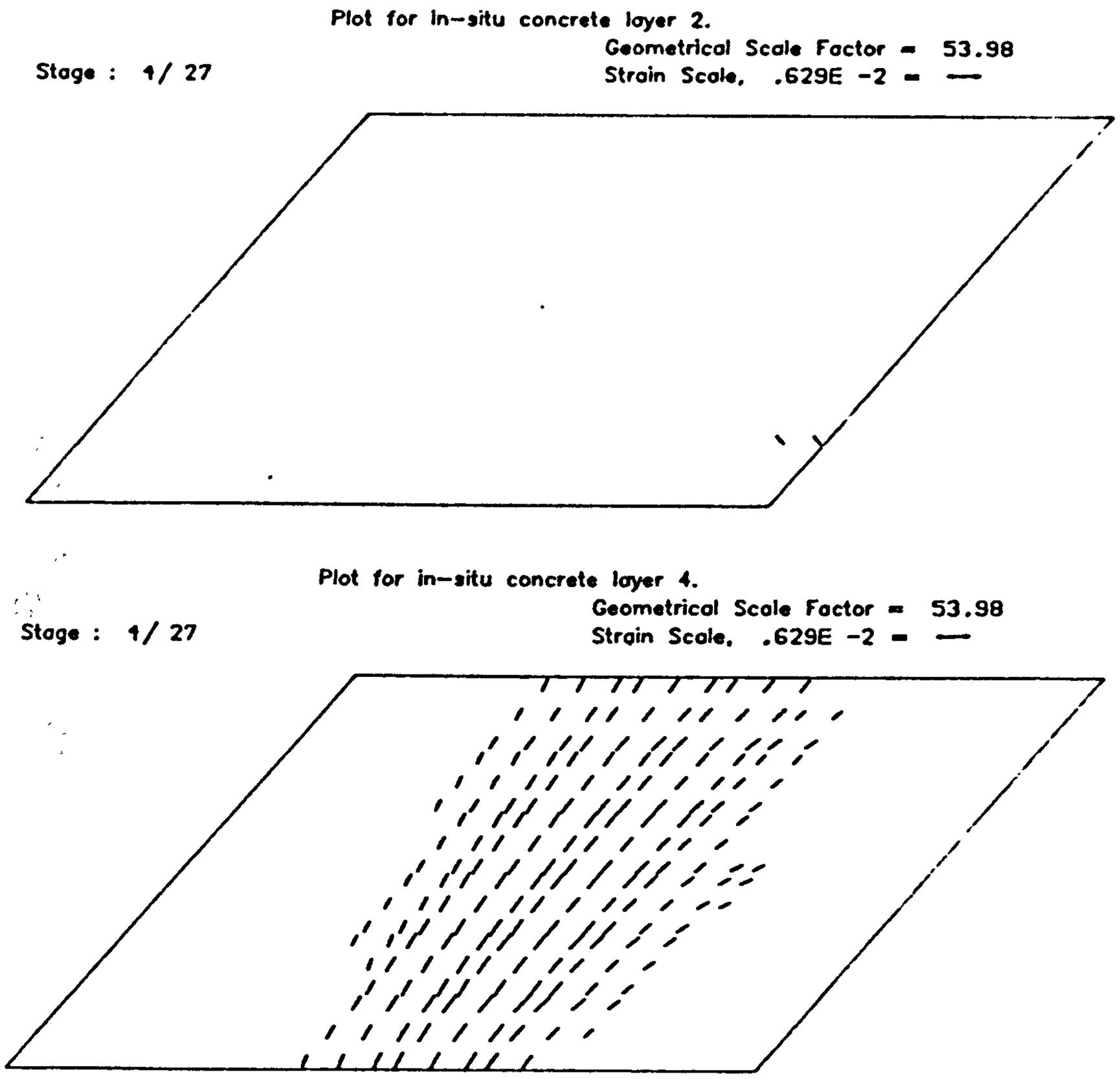

FIG. 9. 70. CRACKING/CRUSHING PATTERN PLOTS FOR MODEL 2 AT LEVEL 21, WITH AN APPLIED LOAD LEVEL OF 5·1

SNAP analysis of model deck 2, 48 element mesh.
Date : 11/ 8/87 at 23: 4:11 Concrete cracking & crushing pattern plots.

Plot for in-situ concrete bottom layer.
Geometrical Scale Factor = 26.23
Stage : 4/ 27 Strain Scale, .629E-2 = ⟶

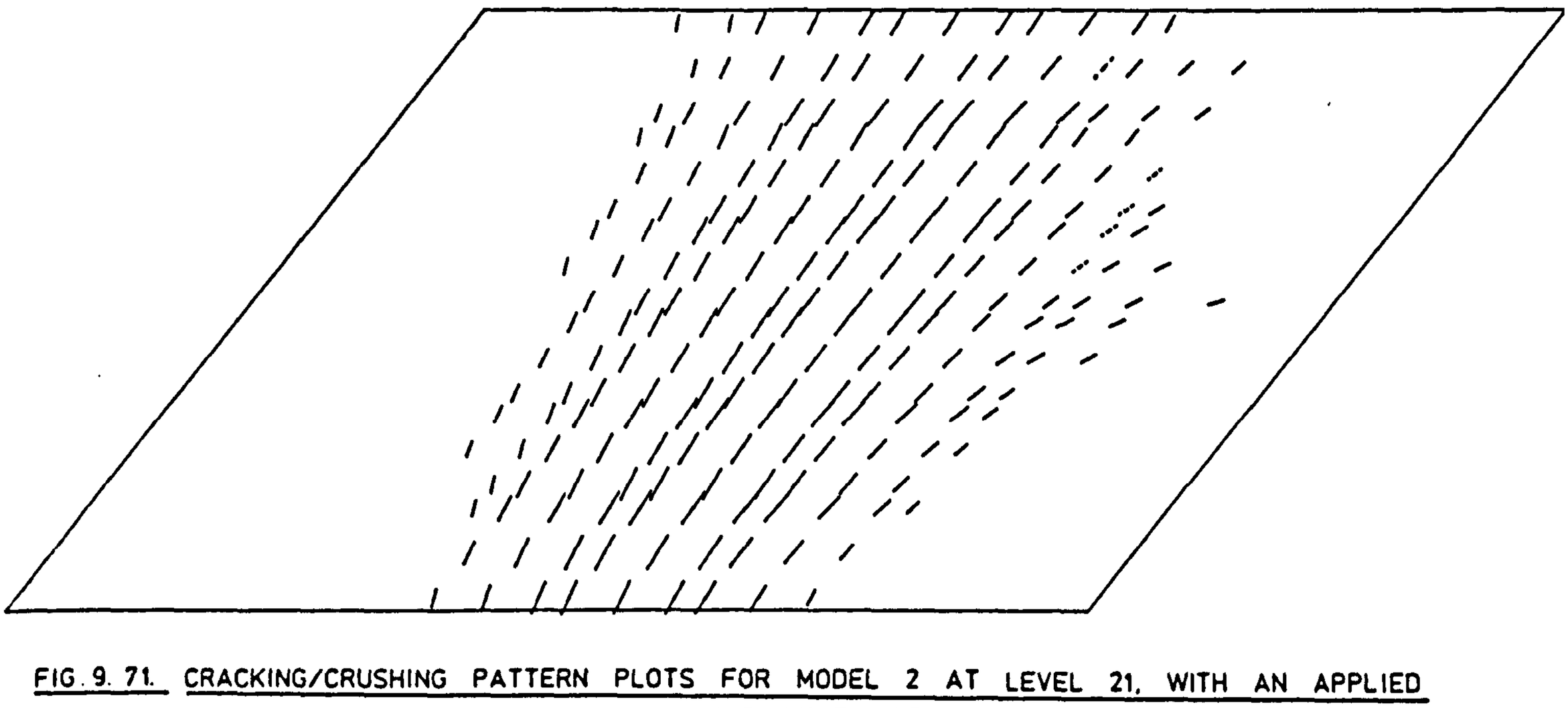

FIG. 9. 71. CRACKING/CRUSHING PATTERN PLOTS FOR MODEL 2 AT LEVEL 21, WITH AN APPLIED LOAD LEVEL OF 5·1

SNAP analysis of model deck 2, 48 element mesh.
Date : 11/ 8/87 at 23: 4:11 Concrete cracking & crushing pattern plots.

Plot for precast concrete top layer.
Geometrical Scale Factor = 26.23
Stage : 4/ 27 Strain Scale, .629E -2 = ⟶

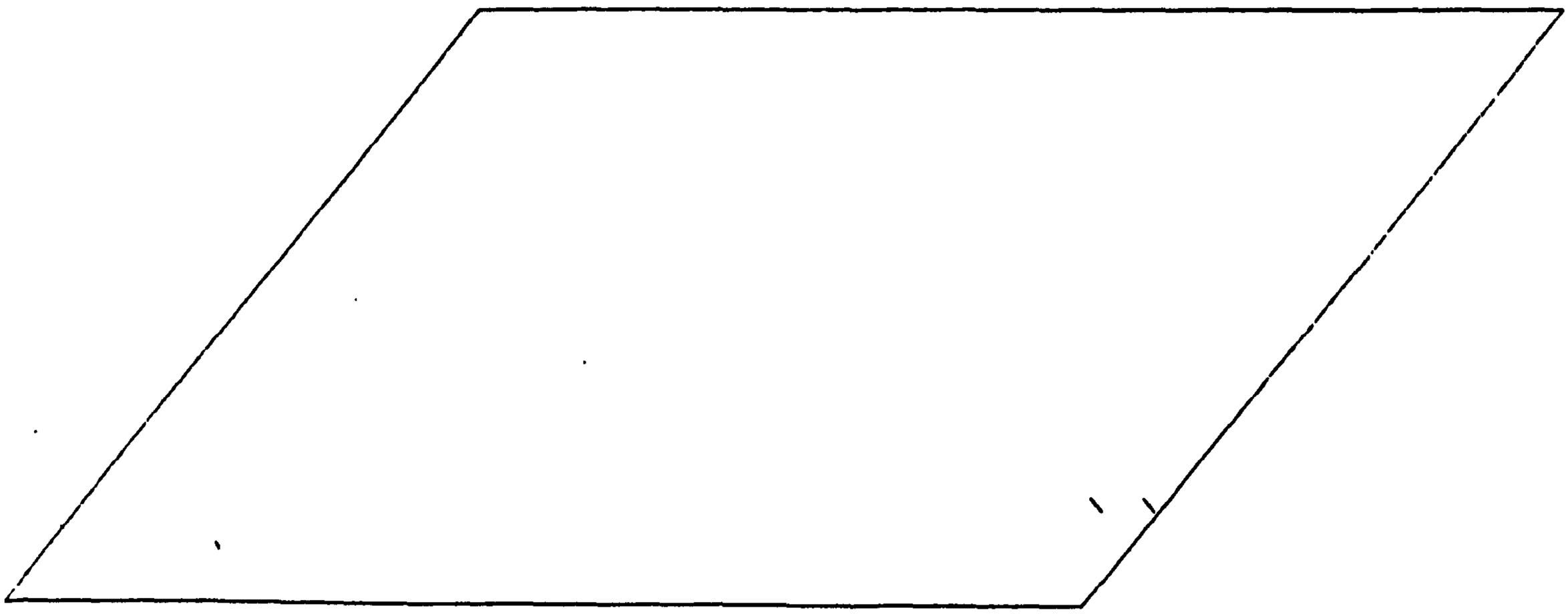

FIG. 9. 72. CRACKING/CRUSHING PATTERN PLOTS FOR MODEL 2 AT LEVEL 21, WITH AN APPLIED LOAD LEVEL OF 5·1

SNAP analysis of model deck 2, 48 element mesh.

Date : 11/ 8/87 at 23: 4:11 Concrete cracking & crushing pattern plots.

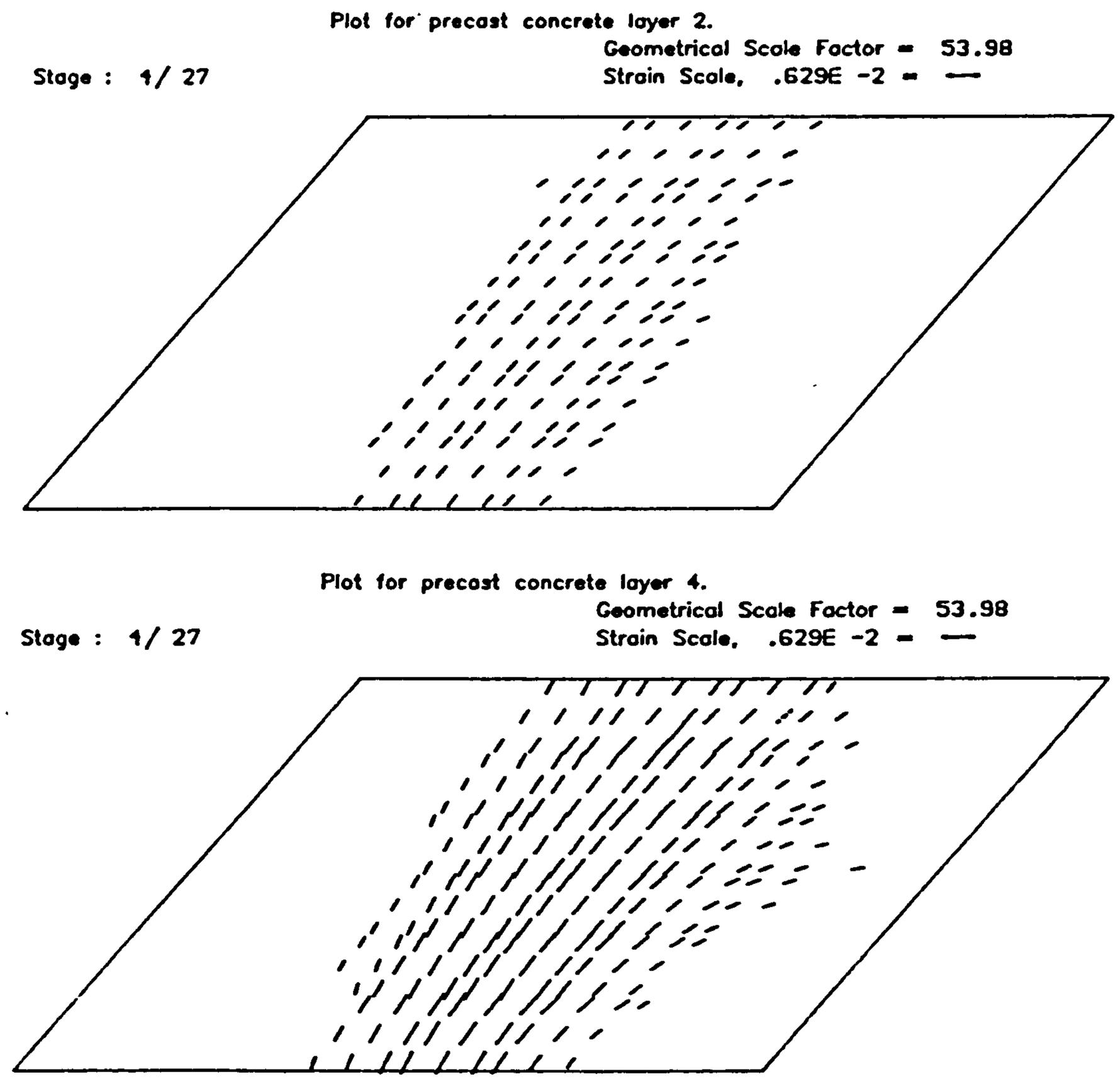

FIG. 9. 73. CRACKING/CRUSHING PATTERN PLOTS FOR MODEL 2 AT LEVEL 21, WITH AN APPLIED LOAD LEVEL OF 5·1

SNAP analysis of model deck 2, 48 element mesh.
Date : 11/ 8/87 at 23: 4:11 Concrete cracking & crushing pattern plots.

Plot for precast concrete bottom layer.
Geometrical Scale Factor = 26.23
Stage : 4/ 27 Strain Scale, .629E -2 = ⟶

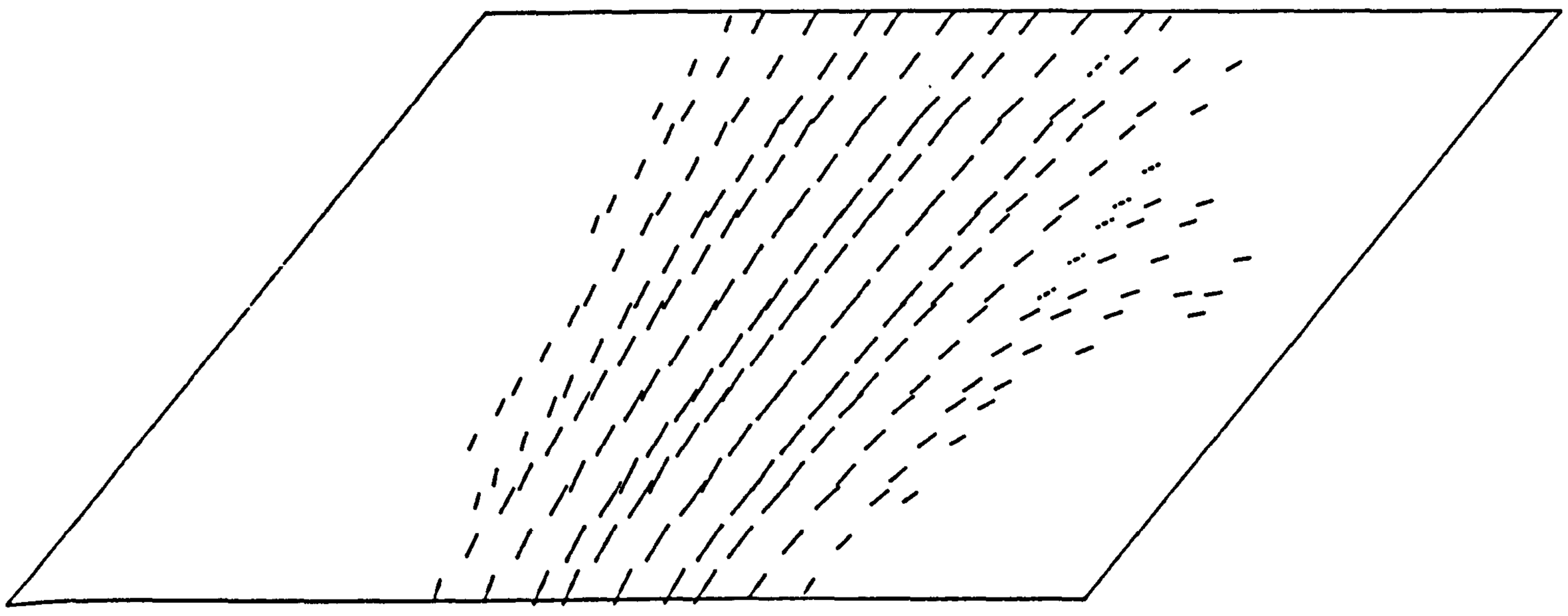

FIG. 9. 74. CRACKING/CRUSHING PATTERN PLOTS FOR MODEL 2 AT LEVEL 21, WITH AN APPLIED LOAD LEVEL OF 5·1

SNAP analysis of model deck 2, 48 element mesh.
Date : 7/ 8/87 at 9:34:58 Concrete cracking & crushing pattern plots.

Plot for in-situ concrete top layer.
Geometrical Scale Factor = 26.23
Stage : 4/106 Strain Scale, .326E -1 = ⟶

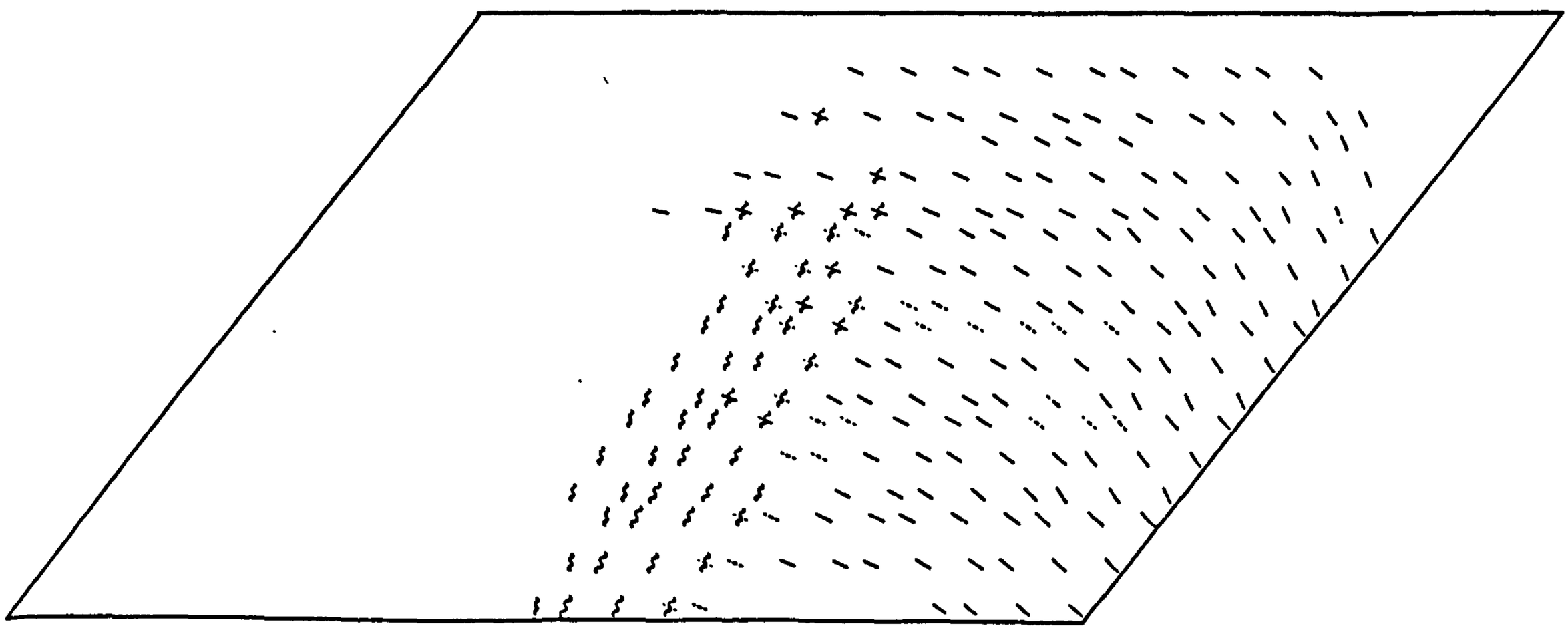

FIG 9. 75. CRACKING/CRUSHING PATTERN PLOTS FOR MODEL 2 AT LEVEL 23, WITH A LOADED FREE EDGE DISPLACEMENT LEVEL OF 90mm

PAGE NUMBERING AS ORIGINAL

SNAP analysis of model deck 2, 48 element mesh.
Date : 7/ 8/87 at 9:34:58 Concrete cracking & crushing pattern plots.

Plot for precast concrete bottom layer.
Geometrical Scale Factor = 26.23
Stage : 4/106 Strain Scale, .326E -1 = —

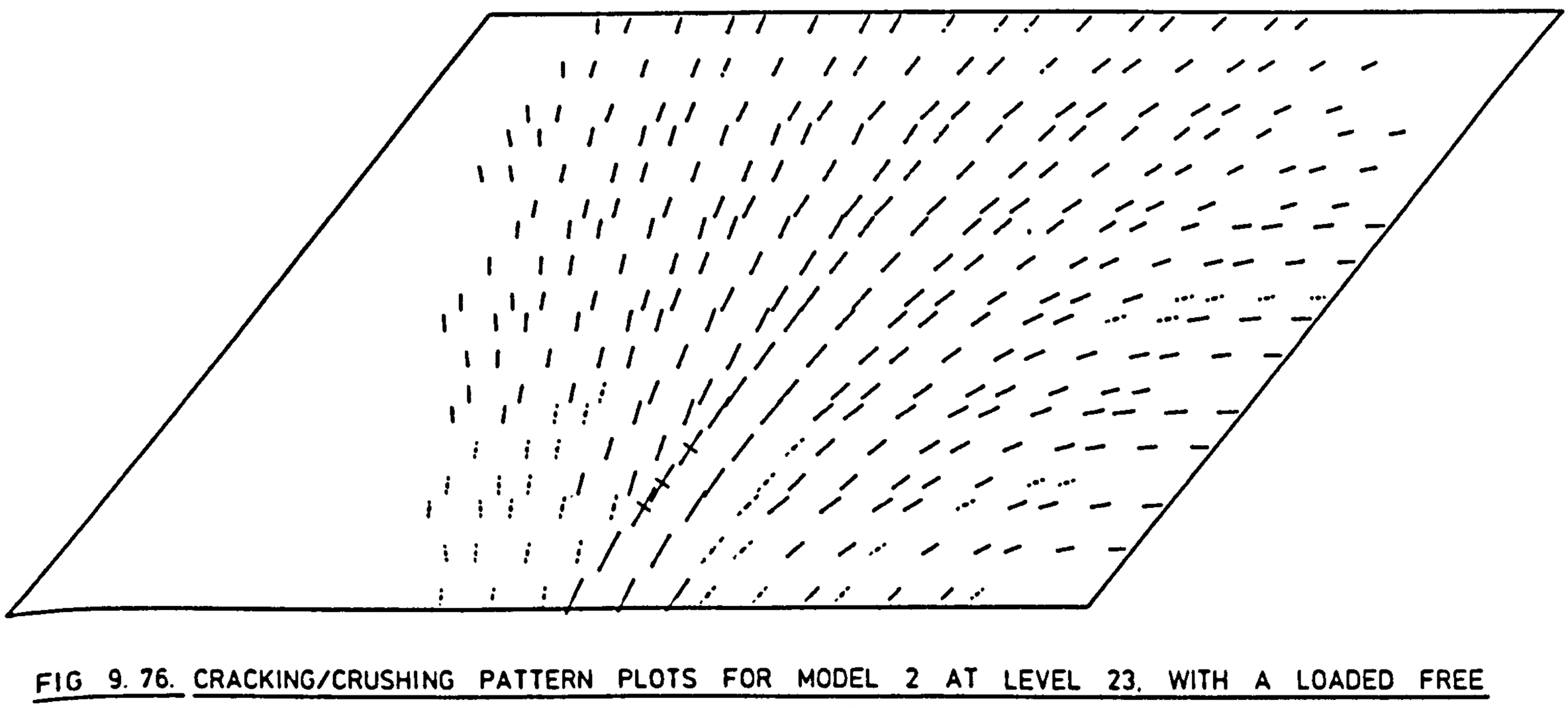

FIG 9.76. CRACKING/CRUSHING PATTERN PLOTS FOR MODEL 2 AT LEVEL 23, WITH A LOADED FREE EDGE DISPLACEMENT LEVEL OF 90mm

SNAP analysis of model deck 2, 48 element mesh.
Date : 11/ 8/87 at 1:44:56 Concrete cracking & crushing pattern plots.

Plot for in-situ concrete top layer.
Geometrical Scale Factor = 26.23
Stage : 4/158 Strain Scale, .143E 0 = —

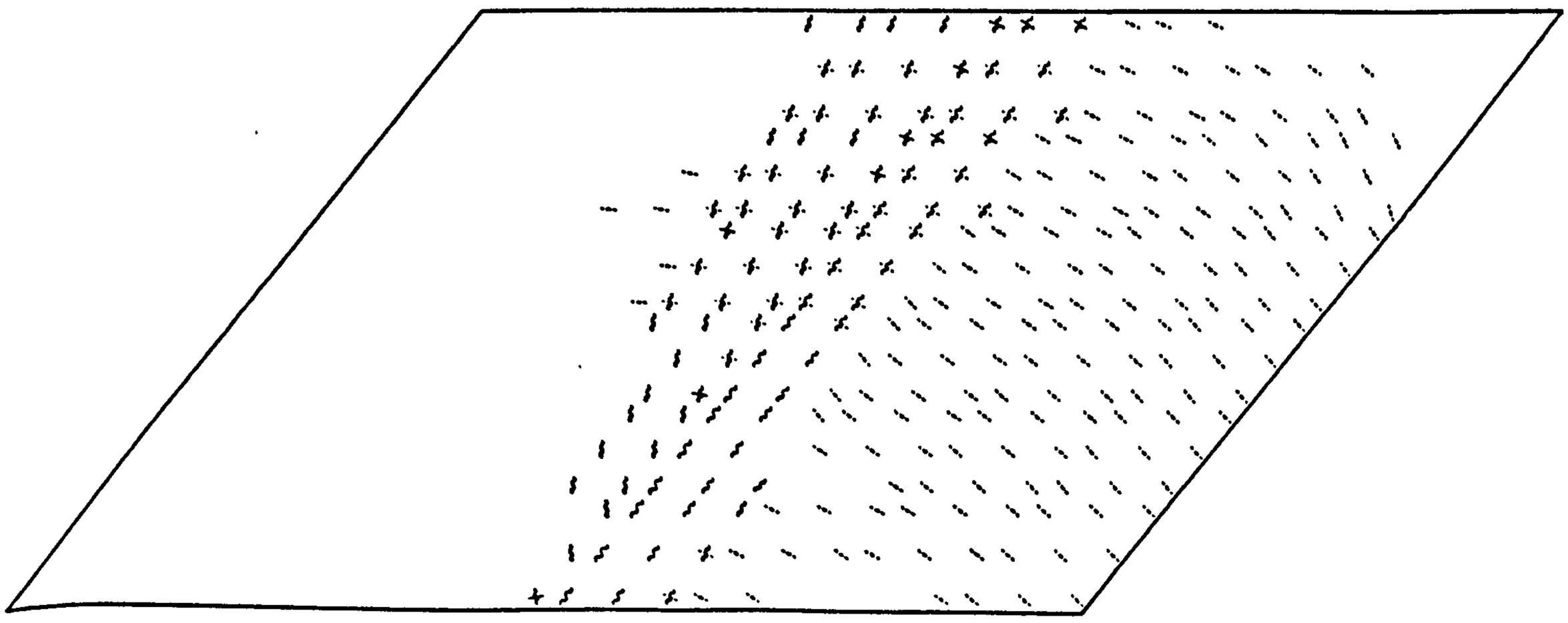

FIG 9.77. CRACKING/CRUSHING PATTERN PLOTS FOR MODEL 2 AT LEVEL 25, WITH A LOADED FREE EDGE DISPLACEMENT LEVEL OF 156mm

SNAP analysis of model deck 2, 48 element mesh.

Date : 11/ 8/87 at 1:44:56 Concrete cracking & crushing pattern plots.

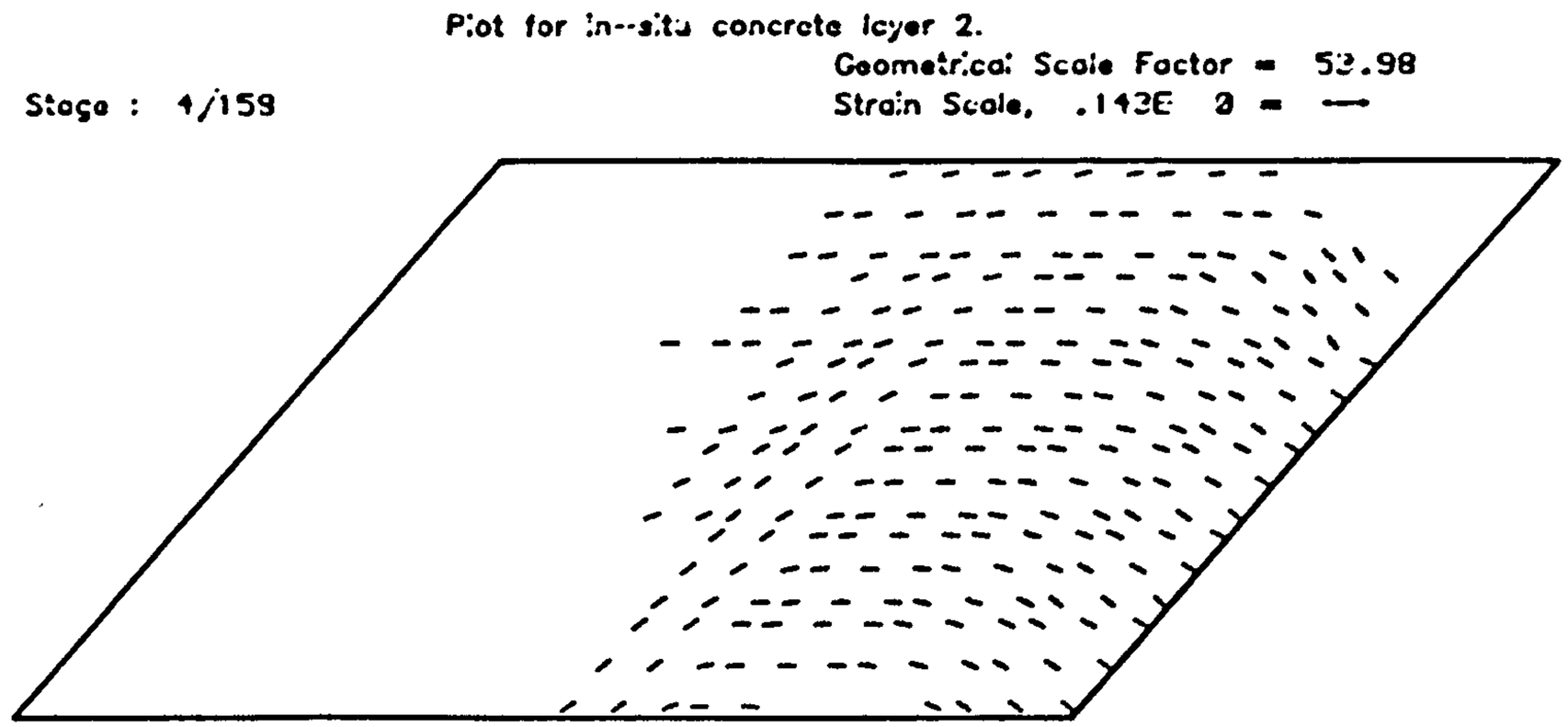

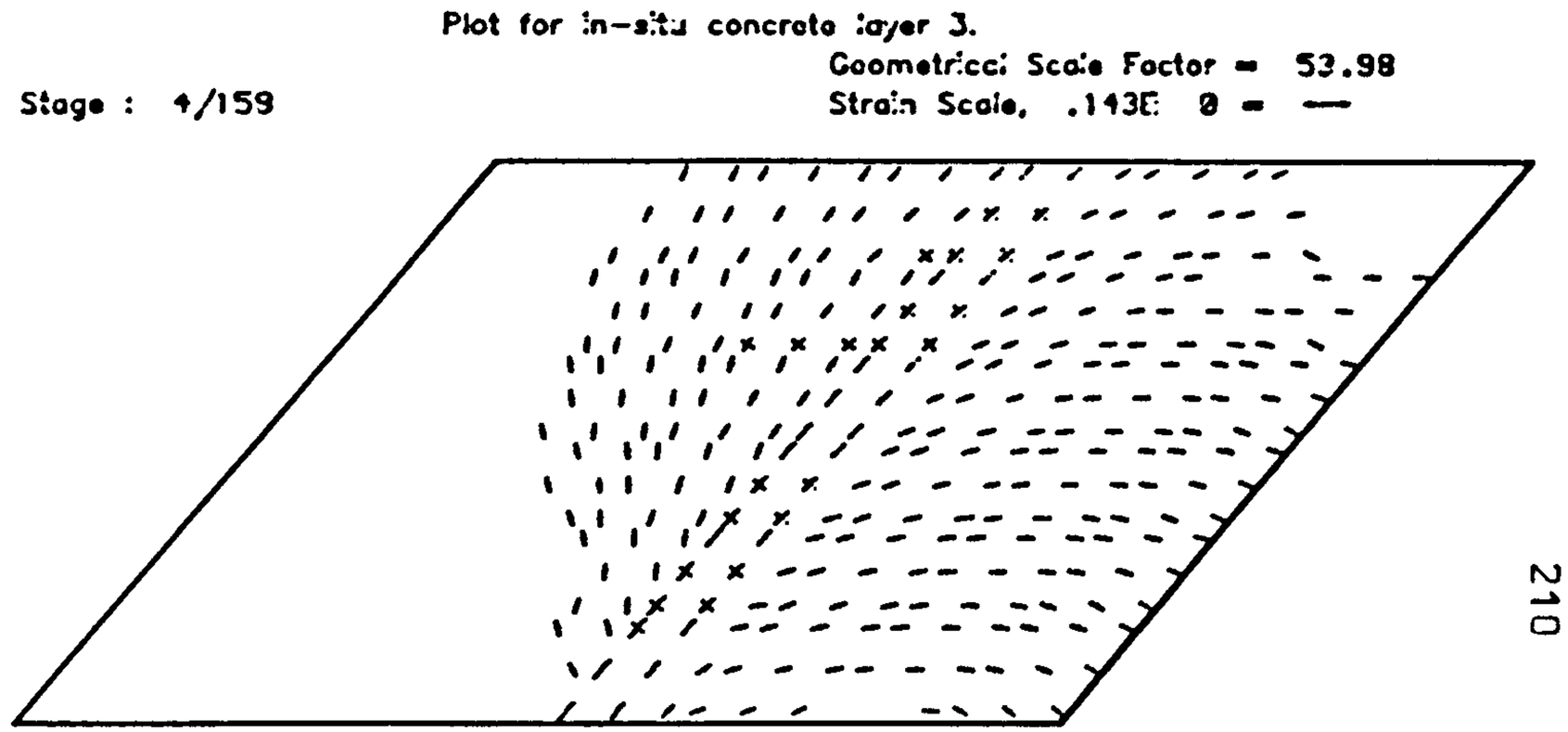

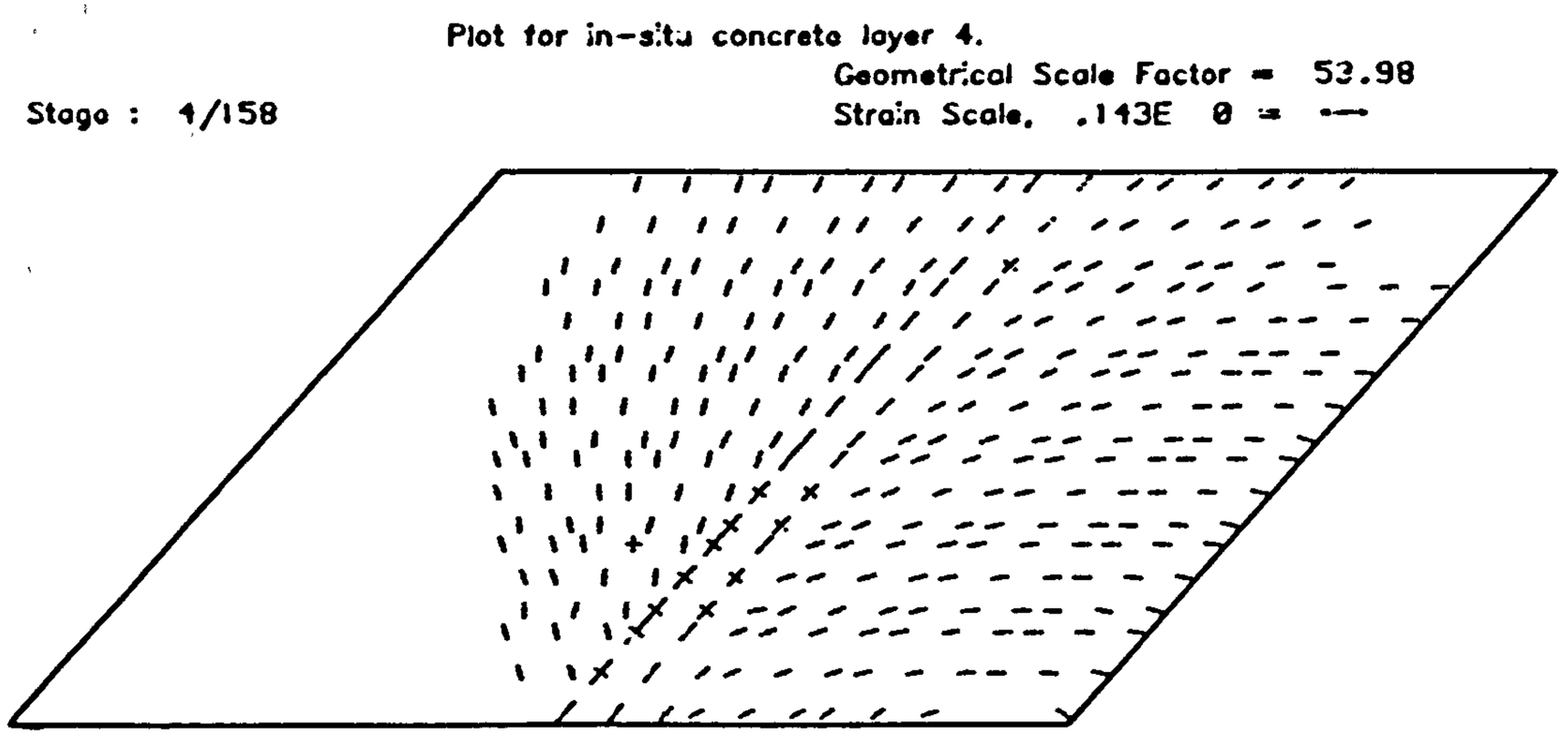

FIG. 9. 78. CRACKING/CRUSHING PATTERN PLOTS FOR MODEL 2 AT LEVEL 25, WITH A LOADED FREE EDGE DISPLACEMENT LEVEL OF 156mm

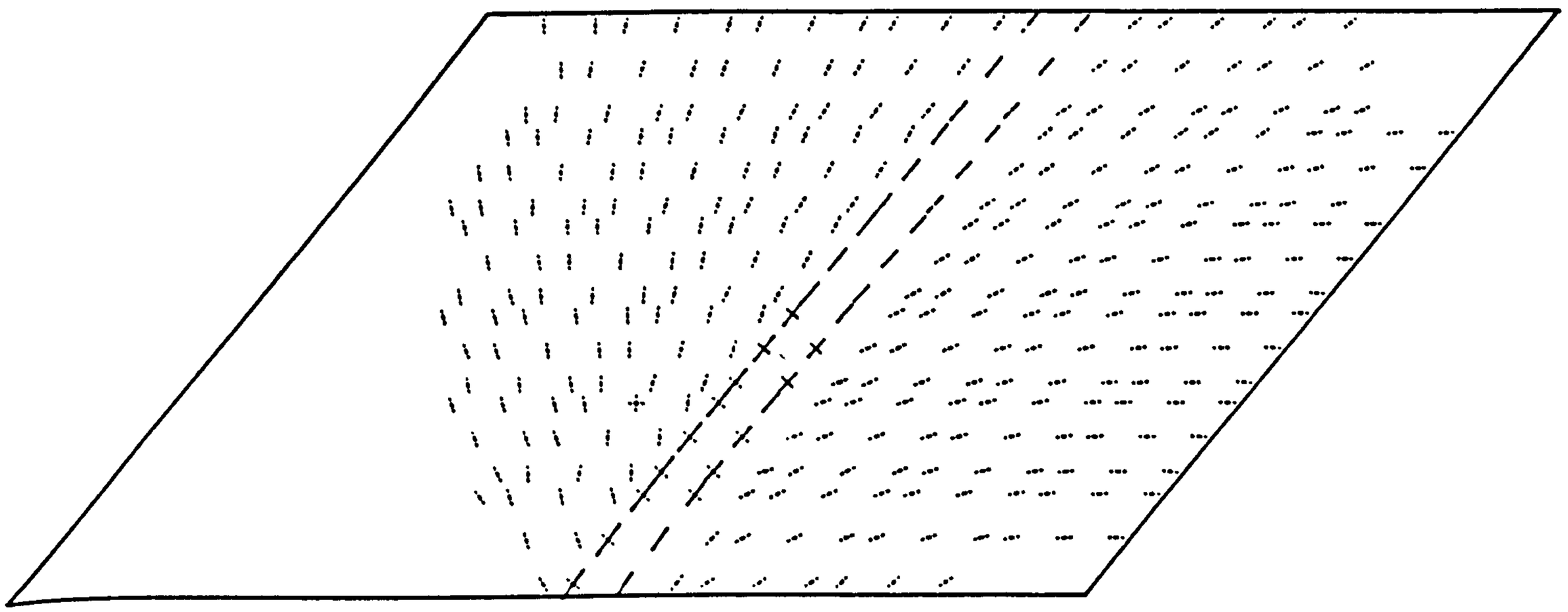

FIG. 9. 79. CRACKING/CRUSHING PATTERN PLOTS FOR MODEL 2 AT LEVEL 25, WITH A LOADED FREE EDGE DISPLACEMENT LEVEL OF 156mm

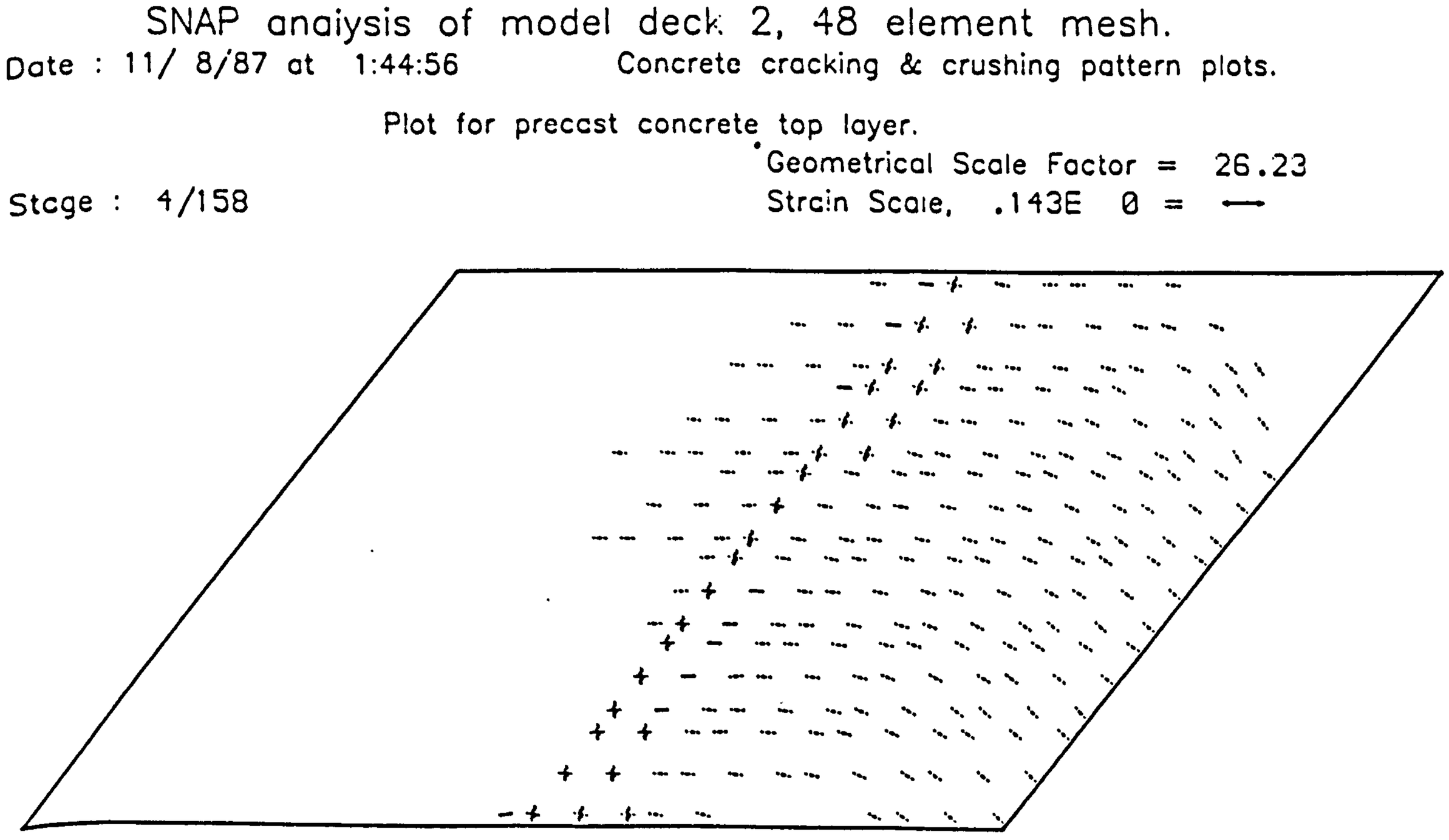

FIG 9. 80. CRACKING/CRUSHING PATTERN PLOTS FOR MODEL 2 AT LEVEL 25, WITH A LOADED FREE EDGE DISPLACEMENT LEVEL OF 156mm

SNAP analysis of model deck 2, 48 element mesh.

Date : 11/ 8/87 at 1:44:56 Concrete cracking & crushing pattern plots.

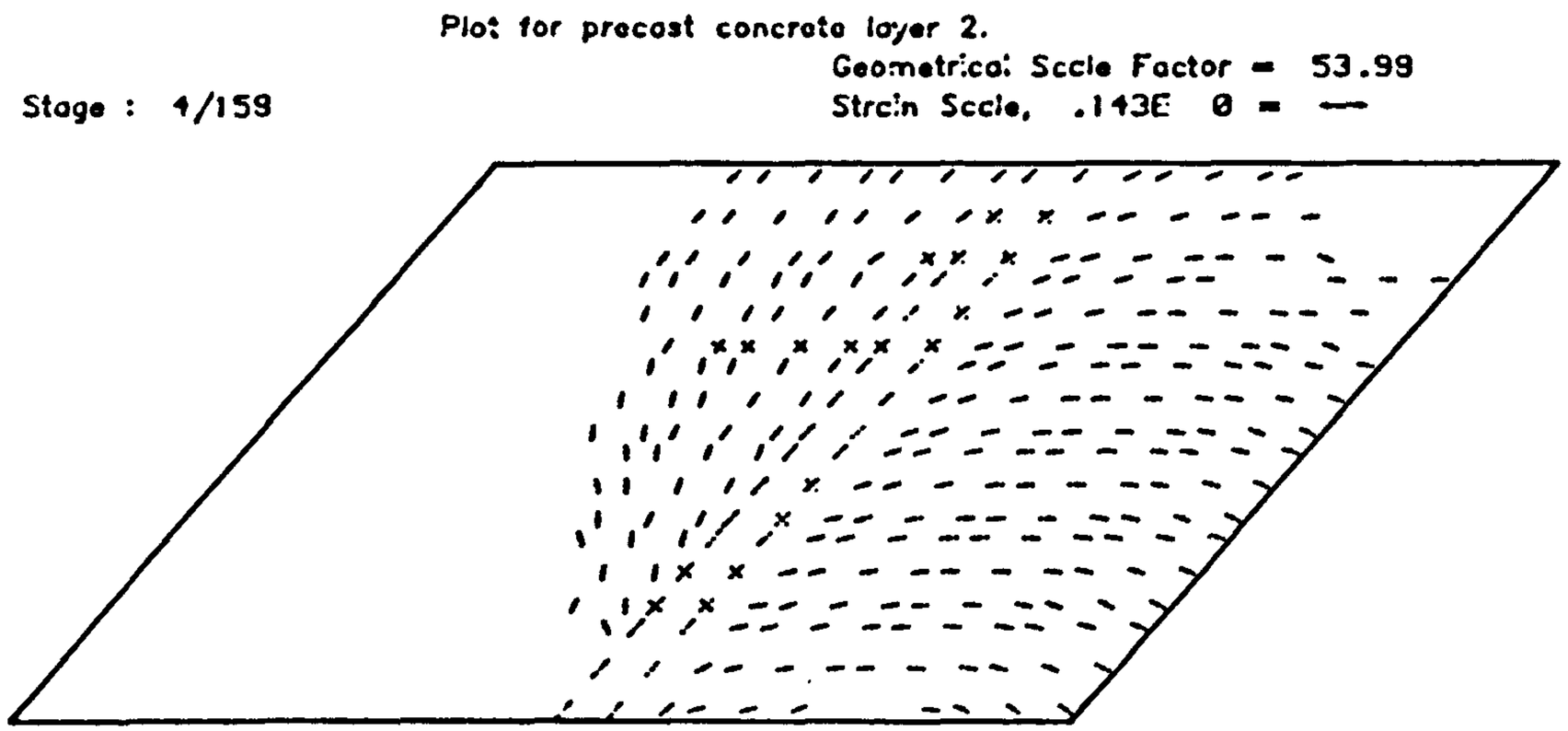

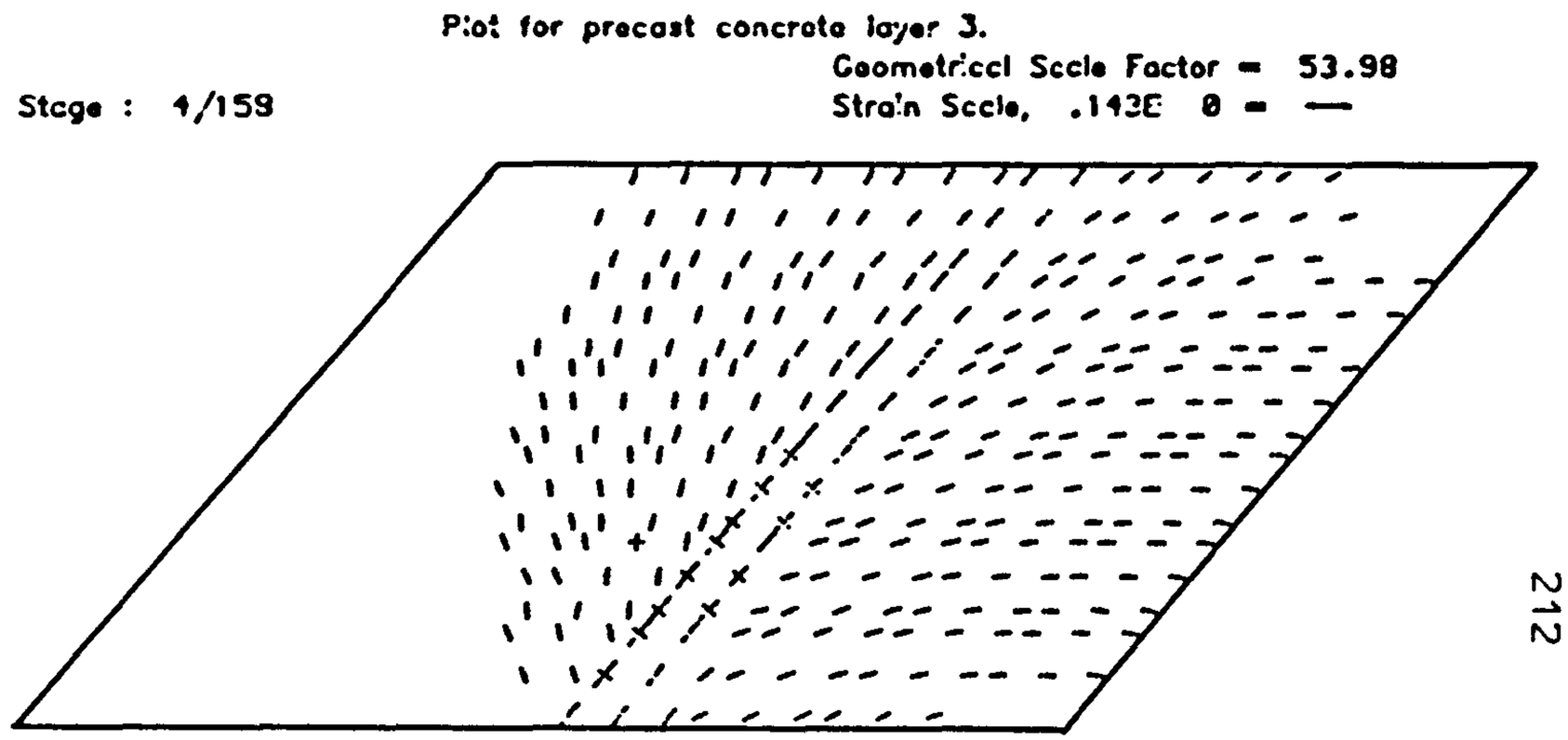

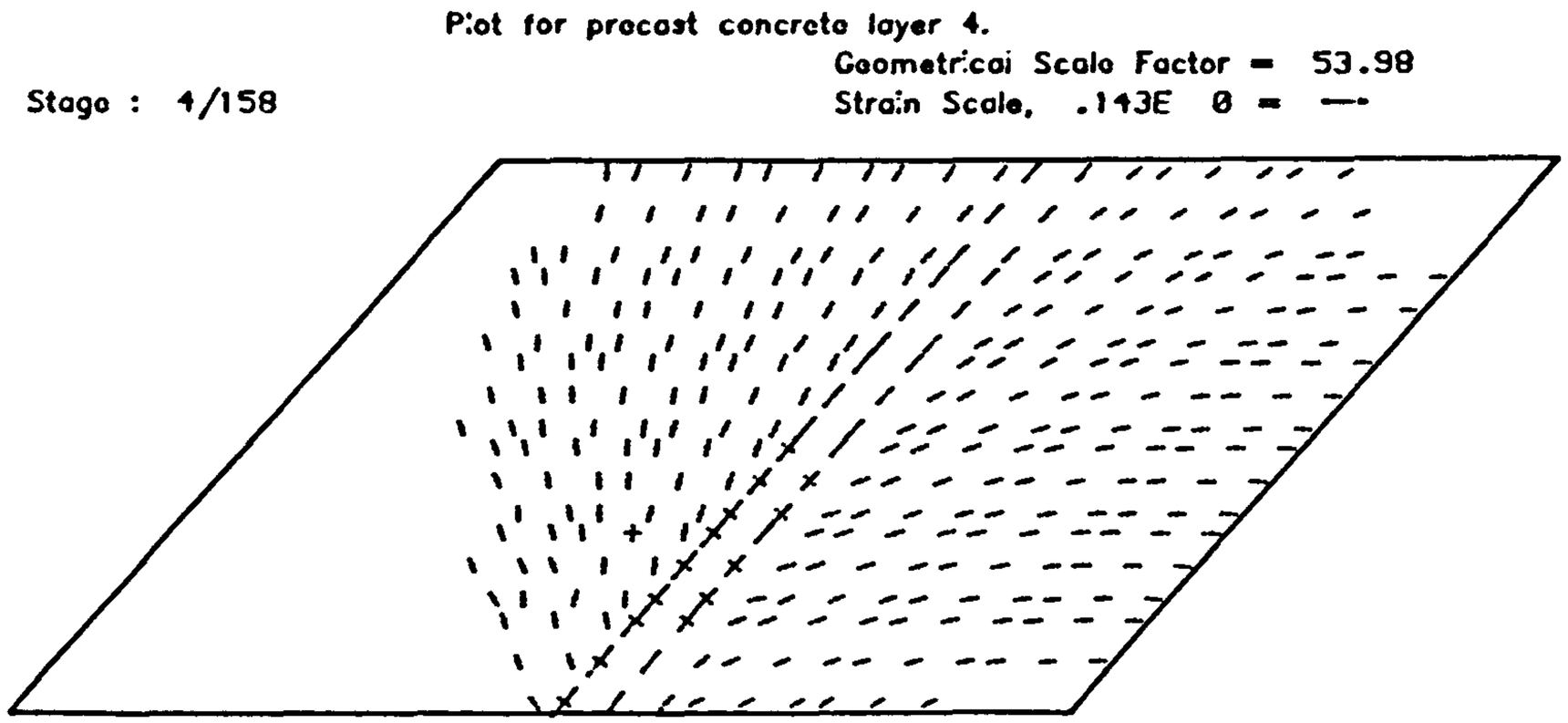

FIG. 9. 81. CRACKING/CRUSHING PATTERN PLOTS FOR MODEL 2 AT LEVEL 25, WITH A LOADED FREE EDGE DISPLACEMENT LEVEL OF 156mm

SNAP analysis of model deck 2, 48 element mesh.

Date : 11/ 8/87 at 1:44:56 Concrete cracking & crushing pattern plots.

Plot for precast concrete bottom layer.

Geometrical Scale Factor = 26.23

Stage : 4/158 Strain Scale, .143E 0 = ⟶

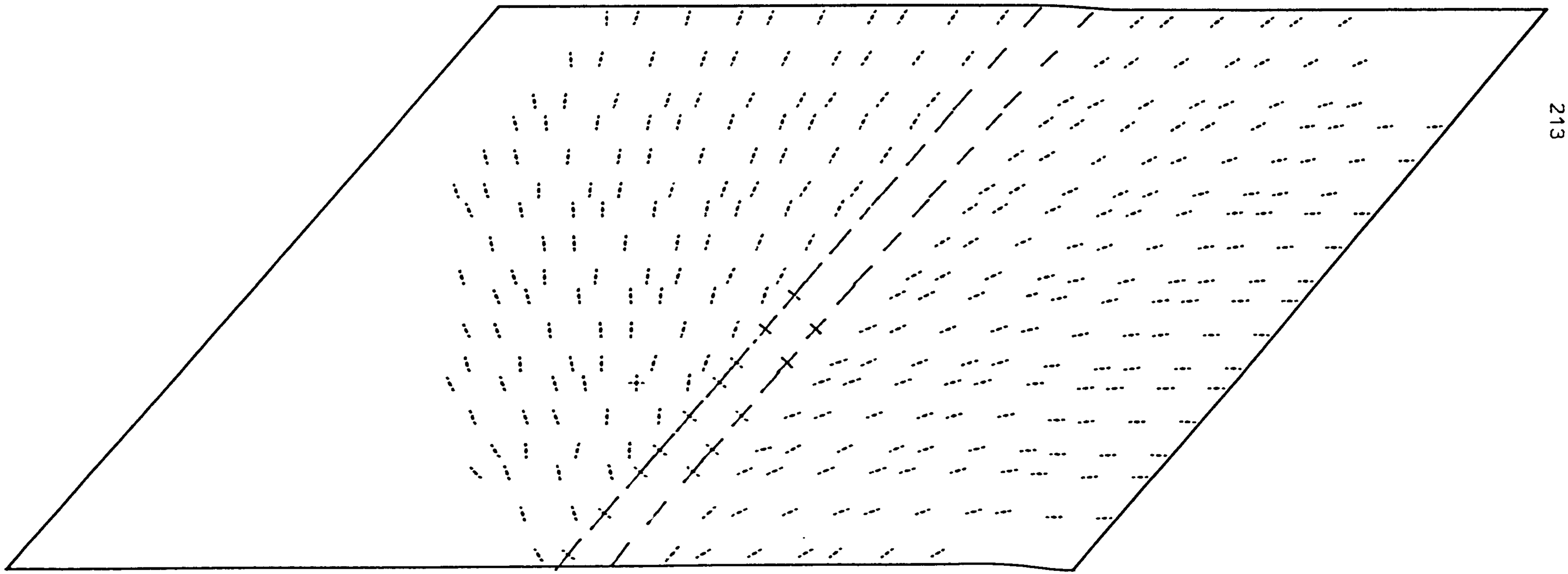

FIG. 9. 82. CRACKING/CRUSHING PATTERN PLOTS FOR MODEL 2 AT LEVEL 25, WITH A LOADED FREE EDGE DISPLACEMENT LEVEL OF 156mm

9.4 References

1. Duddeck, H., Griebenow, G., and Schaper, G., "Material and Time Dependent Nonlinear Behaviour of Cracked Reinforced Concrete Slabs", Nonlinear Behaviour of Reinforced Concrete Spatial Structures, Volume 1, Preliminary Report IASS Symposium held in Darmstadt, Eds G. Mehlhorn, H. Ruhle and W. Zerna, Werner-Verlag Dusseldorf, pp. 101-113, July 1978.

2. Rahman, H.H.A., "Computational Models for the Nonlinear Analysis of Reinforced Concrete Flexural Slab Systems", Ph.D. Thesis, University College of Swansea, May 1982.

3. Mueller, G., "Numerical Problems in Nonlinear Analysis of Reinforced Concrete", Report No UC SESM, 77-5, Department of Civil Engineering, University of California, September 1977.

10. 'NFES' PROGRAM ANALYSES

Analyses of model 1 were carried out using a finite element analysis program that has been developed by Dr M.A. Crisfield of the Transport and Road Research Laboratory, Crowthorne. The program, called NFES (Non-linear Finite Element System) is a general purpose system encompassing 3-D elements as well as plates and shells. There are three plate bending elements available in the system to which one of the material models may be assigned. With the NFES program a full range analysis of a program is carried out as a set of discrete runs. Each run restarts from the end of a previous run, in a similar way to the SNAP program.

The construction sequence was modelled through an option in the NFES program which allowed the swapping of material incremental stress-strain curves between runs. In essence the first run was used to apply prestress and deck self-weight to the beams, while the second run was used to apply the UDL live loading to the complete composite structure. The runs from the third onwards were used to apply the HB bogie loading in an incremental manner to the complete structure to cause collapse. For the first run the in-situ concrete was given a low 'E' value of 10.0 N/mm^2 (compared with a full 'E' of 30 000 N/mm^2), thus for the first run the in-situ concrete effectively did not exist and was thus unstressed. An incremental approach to the stress-strain relationships allowed a smooth transition to the second stage when the in-situ concrete was given its full properties.

10.1 Finite element modelling

10.1.1 Element

The element selected for the analysis of model 1 was developed by Crisfield[1] and is known as a Discrete-Kirchhoff element although a more exact title may be 'A Four-Noded Thin Plate Bending Element Using Shear Constraints'.

This element uses various constraints on the shear deformation in order to reduce the number of elemental dof while also avoiding element locking and zero energy modes which often occur with contemporary Mindlin plate bending elements. The basis for the formulation is a 9 noded quadilateral element with initially 3 dof (w, θ_x and θ_y) at each node. The result of applying the constraints is that some of the dof are removed, namely w, θ_x and θ_y at all mid-side nodes as well as the 9th node. Thus 12 of the original 27 dof remain and one would expect 15 constraints. In essence the formulation uses three types of constraint, namely:-

1. The transverse shear strains tangential to an element edge are constrained to zero at Gauss points located at ± 1/3 √3 along that edge (8 constraints)
2. The rotation normal to an element edge is constrained to vary linearly along that edge (4 constraints)
3. The transverse shear strains tangential to each of the element centre-lines are constrained to zero at Gauss points located at ±1/3 √3 along each centre-line (4 constraints)

It will be noticed that 16 constraints are listed above thus an ambiguity arises over Δw_9 (constraint 3), see Figure 10.1, the Δw dof at the 9th node. This problem is overcome by noting that Δw_9 does not

node type	remaining dof	constrained dof
o	ω_j θ_x, θ_y	—
X	—	$\Delta\omega$, $\Delta\theta_x, \Delta\theta_y$
□	—	$\Delta\theta_x$, $\Delta\theta_y$

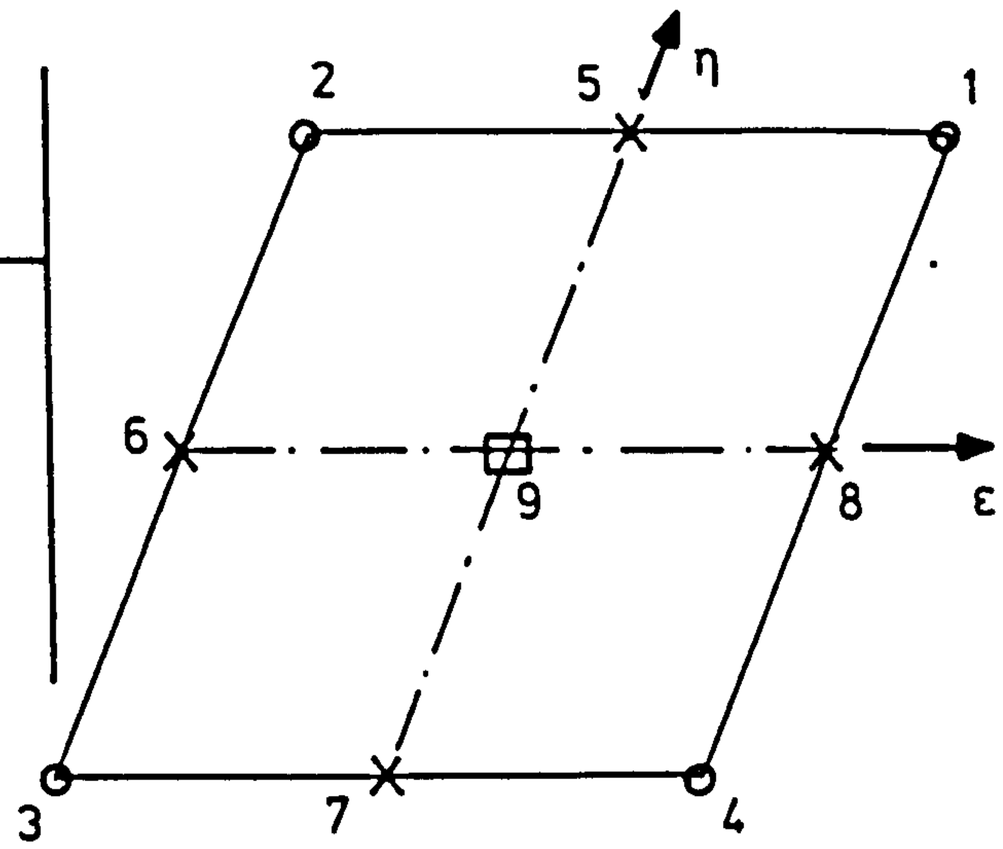

FIG. 10.1. CONSTRAINED DOF FOR DISCRETE-KIRCHOFF PLATE BENDING FINITE ELMENT

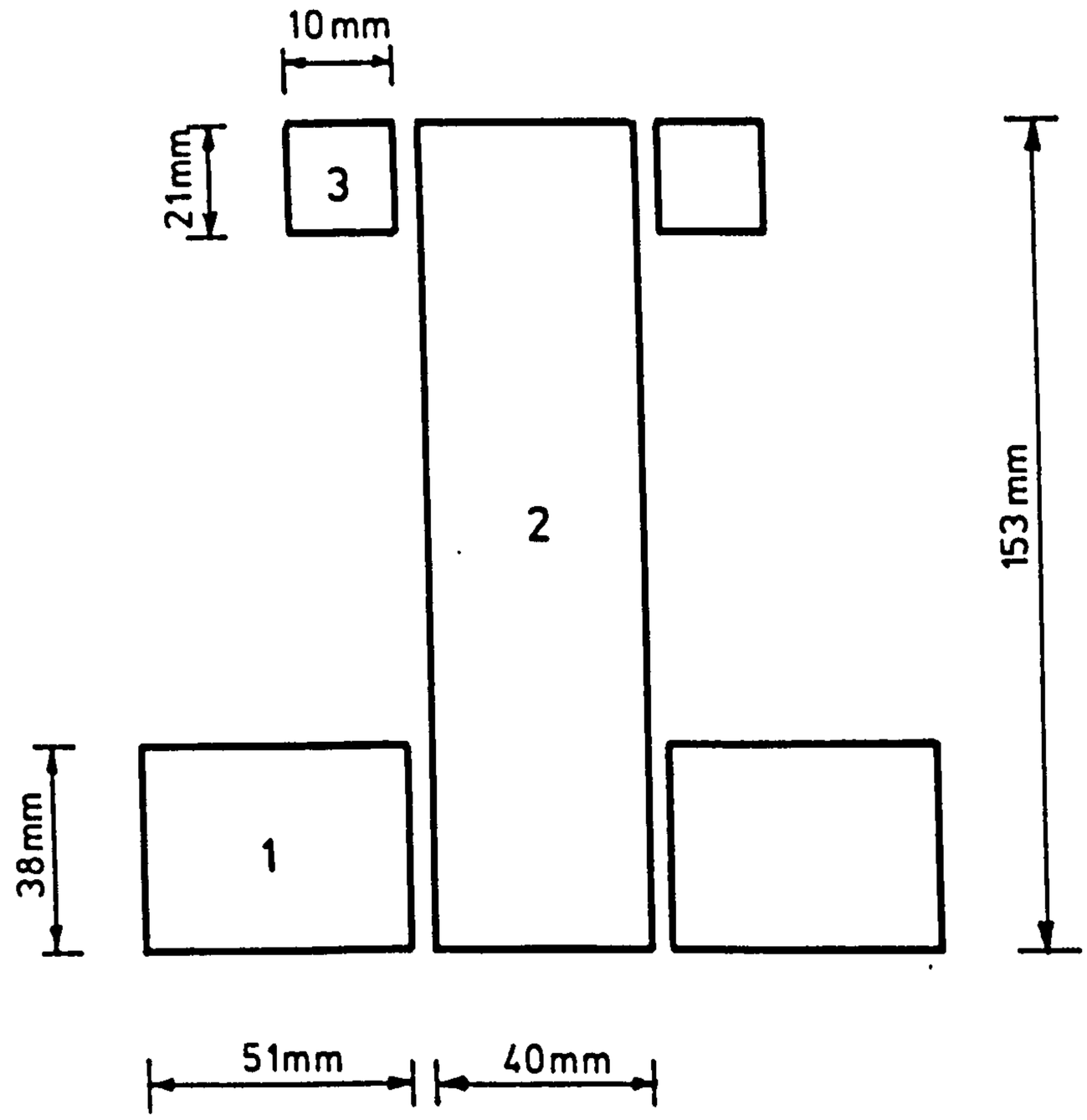

FIG. 10.2. IDEALISATION OF MODEL 1 PRECAST BEAMS FOR TORSIONAL STIFFNESS CALCULATION

feature in the bending strain energy and as the shear strain energy is assumed to be effectively zero for this element, then Δw_g can be set to zero.

10.1.2 Prestressed beam modelling

For the analysis of the composite model the Discrete-Kirchhoff element was used for in-situ concrete which was modelled as a plate. The prestressed beams were modelled as ribs attached to the plate. Even though each prestressed beam is a discrete unit the large number (22 in model 1) allowed the ribs to be smeared across the complete plan area of the plate mesh, similar in concept to the treatment of reinforcing steel in a normal reinforced concrete analysis. This approach is similar to that employed by the SNAP program, which is fully described in Chapter 8. Therefore, only the differences between the two approaches will be detailed here.

At each plan integration station, a through depth integration is carried out for the plate in the normal way. This yields stress resultant components for the direct and shear stresses in the plate. A second through depth integration is then carried out for the beam. In the beam integration only the direct stresses along the axis of the beams are evaluated.

The torsional stiffness of the beams is then considered. This is calculated as a linear quantity which is never degraded and its evaluation requires the twisting rotation along the beam axis.

The torsional stiffness is given by:-

$$T_n = \frac{GJ\ d\theta_t}{dn}$$, where n and t define the beam local coordinates

The twisting rotation is obtained from (using tensor notation):-

$$\begin{bmatrix} \frac{d\theta_n}{dn} & \frac{d\theta_n}{dt} \\ \frac{d\theta_t}{dn} & \frac{d\theta_t}{dt} \end{bmatrix} = \begin{bmatrix} \cos\theta & \sin\theta \\ -\sin\theta & \cos\theta \end{bmatrix} \begin{bmatrix} \frac{d\theta_x}{dx} & \frac{d\theta_x}{dy} \\ \frac{d\theta_y}{dx} & \frac{d\theta_y}{dy} \end{bmatrix} \begin{bmatrix} \cos\theta & -\sin\theta \\ \sin\theta & \cos\theta \end{bmatrix}$$

where the curvatures are given by:-

$$\kappa_x = \frac{d\theta_x}{dx} \; , \; \kappa_y = \frac{d\theta_y}{dy} \; , \; \kappa_{xy} = \frac{d\theta_x}{dy} + \frac{d\theta_y}{dx}$$

Multiplying out for $\frac{d\theta_t}{dn}$ and $\frac{d\theta_n}{dt}$ we obtain

$$\frac{d\theta_t}{dn} = - \frac{d\theta_x}{dx} \sin\theta \cos\theta - \frac{d\theta_x}{dy} \sin^2\theta + \frac{d\theta_y}{dx} \cos^2\theta + \frac{d\theta_y}{dy} \cos\theta \sin\theta$$

$$\frac{d\theta_n}{dt} = - \frac{d\theta_x}{dx} \sin\theta \cos\theta + \frac{d\theta_x}{dy} \cos^2\theta - \frac{d\theta_y}{dx} \sin^2\theta + \frac{d\theta_y}{dy} \sin\theta \cos\theta$$

now $\frac{d\theta_n}{dt} + \frac{d\theta_t}{dn} = 2\sin\theta \cos\theta \left(\frac{d\theta_y}{dy} - \frac{d\theta_x}{dx}\right) + \left(\frac{d\theta_x}{dy} + \frac{d\theta_y}{dx}\right)(\cos^2\theta - \sin^2\theta)$

and $\frac{d\theta_n}{dt} - \frac{d\theta_t}{dn} = \frac{d\theta_x}{dy} \cos^2\theta - \frac{d\theta_y}{dx} \sin^2\theta + \frac{d\theta_x}{dy} \sin^2\theta - \frac{d\theta_y}{dx} \cos^2\theta$

$$= \frac{d\theta_x}{dy} - \frac{d\theta_y}{dx}$$

Hence $\frac{d\theta_t}{dn} = \dfrac{\left[\frac{d\theta_n}{dt} + \frac{d\theta_t}{dn}\right] - \left[\frac{d\theta_n}{dt} - \frac{d\theta_t}{dn}\right]}{2}$

The strain displacement matrix [B] for the element is modified to include one extra term:-

$$[\epsilon] = [B] \; [u]$$

where [u] - vector of displacements (12 dof)

[B] - strain displacement matrix (4 x 12)

[ϵ] - strain vector

where $$[\epsilon] = \begin{bmatrix} \frac{d\theta_x}{dx} \\ \\ \frac{d\theta_y}{dy} \\ \\ \frac{d\theta_x}{dy} + \frac{d\theta_y}{dx} \\ \\ \frac{d\theta_x}{dy} - \frac{d\theta_y}{dx} \end{bmatrix}$$

10.1.3 Finite element mesh geometry

As mentioned earlier, during the 'wet' stage (i.e. during the initial prestressing and casting stages) the in-situ plate concrete was modelled as a material of very high strength and very low stiffness. However, this method led to severe problems with the boundary conditions. The Discrete-Kirchhoff element does not have a 'w' (vertical) degree of freedom at its midside nodes, therefore the analytical mesh could only be constrained at element corner nodes in the 'w' direction along a supported edge. This would not have been a problem if the plate had possessed realistic properties from the beginning of the analysis. Even though there is no explicit 'w' degree of freedom at the element mid-side nodes it is nevertheless still there, but is constrained to only move in modes dictated by the explicit degrees of freedom.

With the elemental corner nodes restrained and 'wet' plate concrete the analytical model sagged dramatically between the 'w' restraints. This was due to the very low transverse bending stiffness. This phenomenon can be overcome by restraining the tangential rotations

along a supported edge with preferably an elastic stiffness. However, only the less preferable method of restraining these rotations to zero was available. Due to the skewness of the deck, the supported edges did not lie in a Cartesian direction, as the preferred analytical model oriented the free edges in the Cartesian x direction. Therefore it was necessary to re-orientate the mesh with the supported edges aligned in the Cartesian x direction, this can be seen in Figure 10.3.

In reality, the model deck was supported on flexible 'elastomeric' type supports and hence it would have been desirable to also support the analytical model on flexible restraints. However, there was no simple method for doing this in the NFES program. Therefore, after considering the constraints of time, the anticipated errors arising from the use of fixed supports and the errors expected from other analytical modelling approximations it was decided to use fixed 'w' restraints for the NFES program analysis.

10.1.4 Material model

Of the material models that were available in the NFES program for the in-situ concrete of the plate, the one most suitable for our application treated the plate as multi-layered in the conventional manner. Each layer was assumed to be in plane-stress and was treated as a bi-axial material orientated in the Cartesian directions until after cracking when the orientation changed to the fixed crack directions. The stress-strain relationships were applied in an incremental fashion. For the compression-compression quadrant of the stress space the material behaviour was governed by the Von-Mises yield criterion combined with a multi-linear stress-strain curve, see Figure 10.4. For the tension-tension quadrant of the stress space the in-situ concrete was treated as either bi-linear or tri-linear. After cracking the incremental Poisson's ratio was set to zero also the

incremental in-plane shear modulus was reduced to 10% of its initial value. The effects of adopting an incremental approach to the stress-strain relationships is only really apparent with the Poisson's ratio effect. As the approach is incremental then even though Poisson's ratio is set to zero after cracking there will still be locked in Poisson strains from the increments before cracking. However, there will not be the same effect from the shear modulus since before cracking the material is isotropic and hence at the onset of cracking there will be no shear strain in the crack directions.

During the progress of the project a multi-layered rotating crack-model was also incorporated into the program. In a similar fashion to the fixed crack model above, each layer was assumed to be in plane-stress, however, for this model the material properties were assumed to rotate with the principal strain directions, also the stress-strain relationships were treated in a total and not incremental fashion.

The prestressing and reinforcing steels were modelled as elastic multi-linear uniaxial materials, the stress-strain curves for these can be seen in Figure 10.5.

The prestressed concrete in the beams or 'ribs' was modelled as a uniaxial version of the plate material model although the multi-linear stress-strain curves were of different shapes to account for the different strength and ductility of the two concretes. The adopted stress-strain curves can be seen in Figure 10.4.

10.1.5 Through depth integration

In a similar fashion to the SNAP program the effectively interlaced nature of the precast and insitu concretes was modelled by

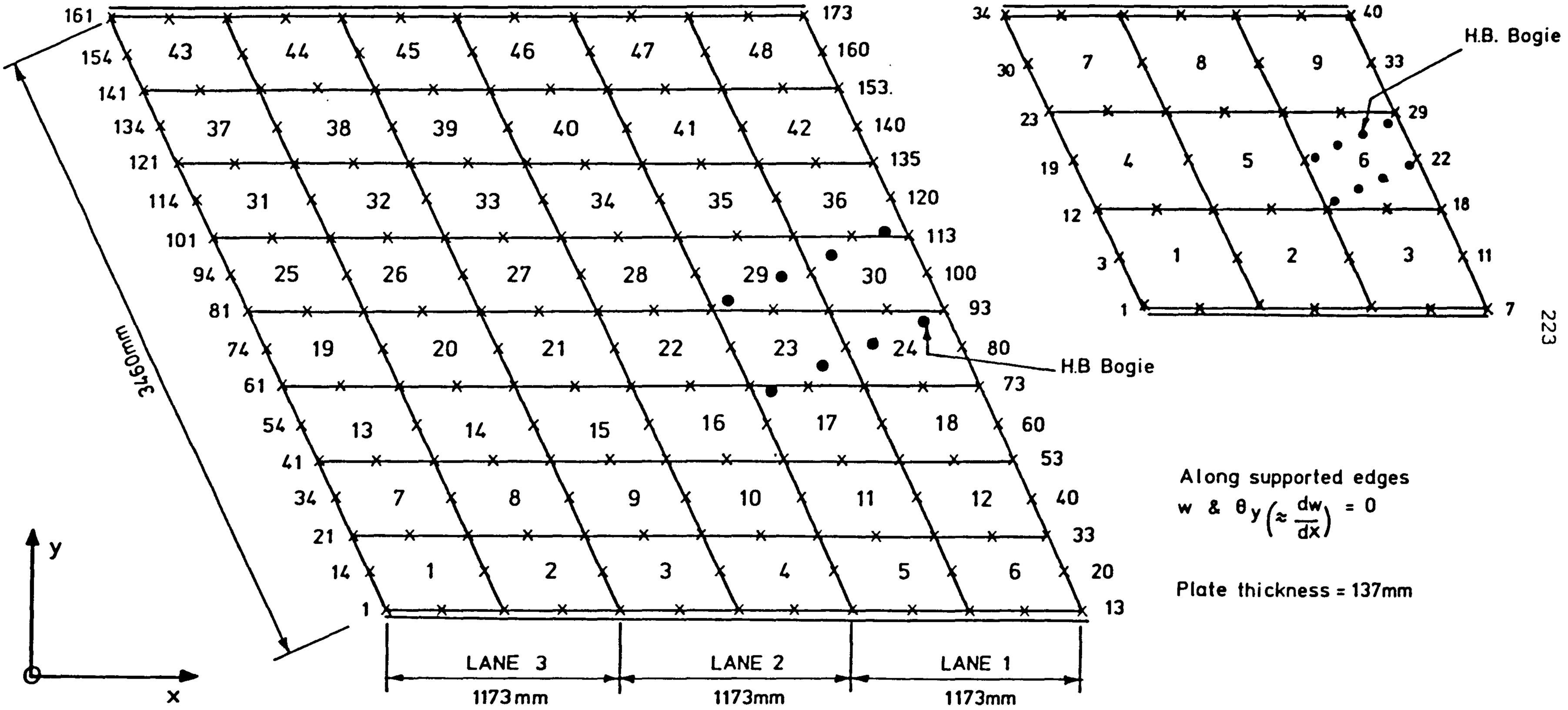

Along supported edges

w & $\theta_y \left(\approx \frac{dw}{dx}\right) = 0$

Plate thickness = 137mm

FIG. 10.3. THE TWO MESHES USED FOR THE NFES ANALYSIS OF MODEL 1

modification of the through depth integration scheme. Five integration stations were chosen for the plate (in-situ) concrete and 5 for the rib (precast) concrete making a total of 10 through depth integration stations. The integration schemes are shown in Figures 10.6 and 10.7 while the numerical details are the same as those given for the SNAP program in Chapter 9.

10.1.6 Beam torsional stiffness

In the NFES analysis the prestressed beams were modelled as uniaxial elements with only the strain in the direction of the beams being considered, however, as mentioned earlier there was also a linear rotary torsional stiffness associated with the beams. The value of the torsional rigidity was calculated on the basis of equivalent rectangles[2,3].

With reference to Figure 10.2:-

$$\frac{B_1}{D_1} = \frac{51}{38} = 1.342 \therefore K_1 = 0.1802$$

$$\therefore J_1 = 0.1802 \times 51 \times 38^3 = 504.29 \times 10^3 \text{ mm}^4$$

$$\frac{B_2}{D_2} = \frac{153}{40} = 3.825 \therefore K_2 = 0.279$$

$$J_2 = 0.279 \times 153 \times 40^3 = 2.73 \times 10^6 \text{ mm}^4$$

$$\frac{B_3}{D_3} = \frac{21}{10} = 2.1 \therefore K_3 = 0.234$$

$$J_3 = 0.234 \times 21 \times 10^3 = 4914 \text{ mm}^4$$

$$J_T = 2.73 \times 10^6 + (4914 + 504.29 \times 10^3)\ 2$$

$$= 3.748 \times 10^6 \text{ mm}^4$$

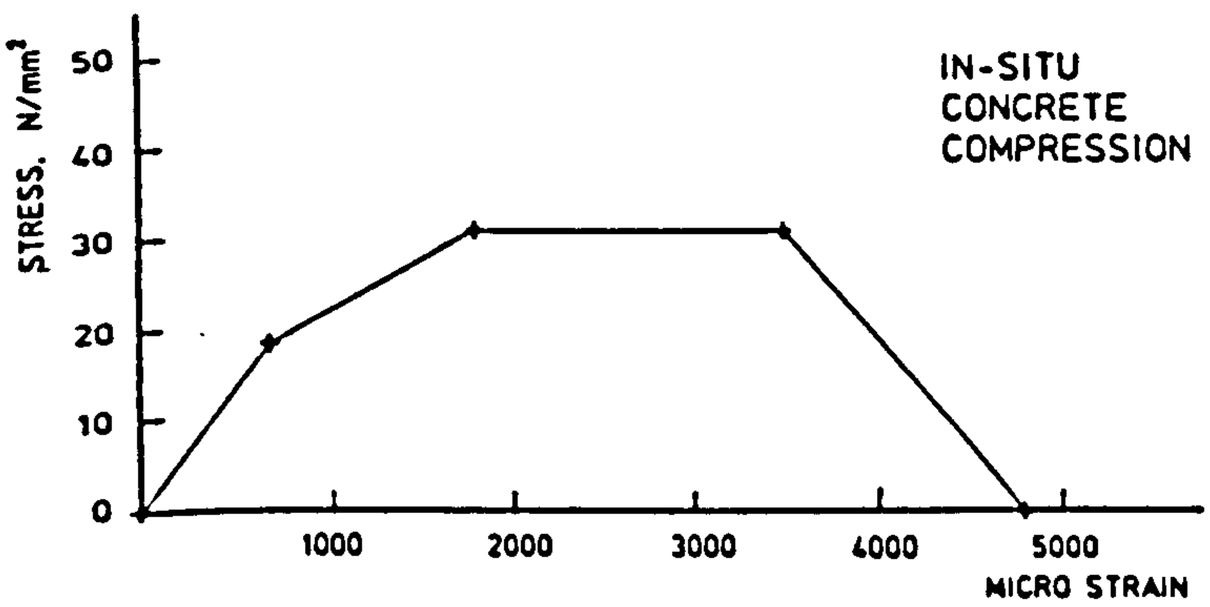

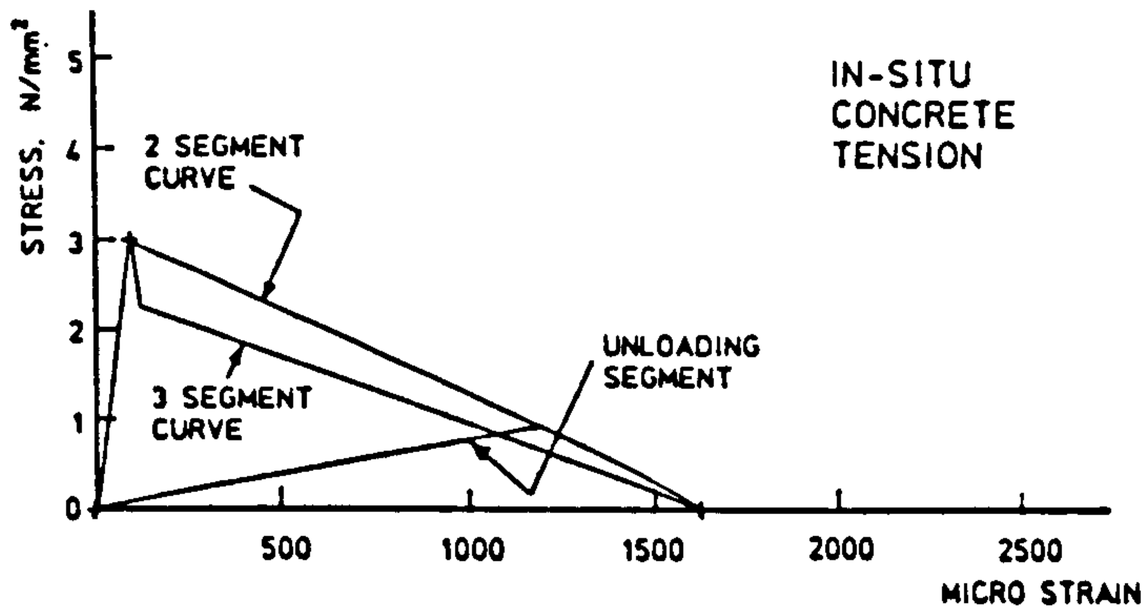

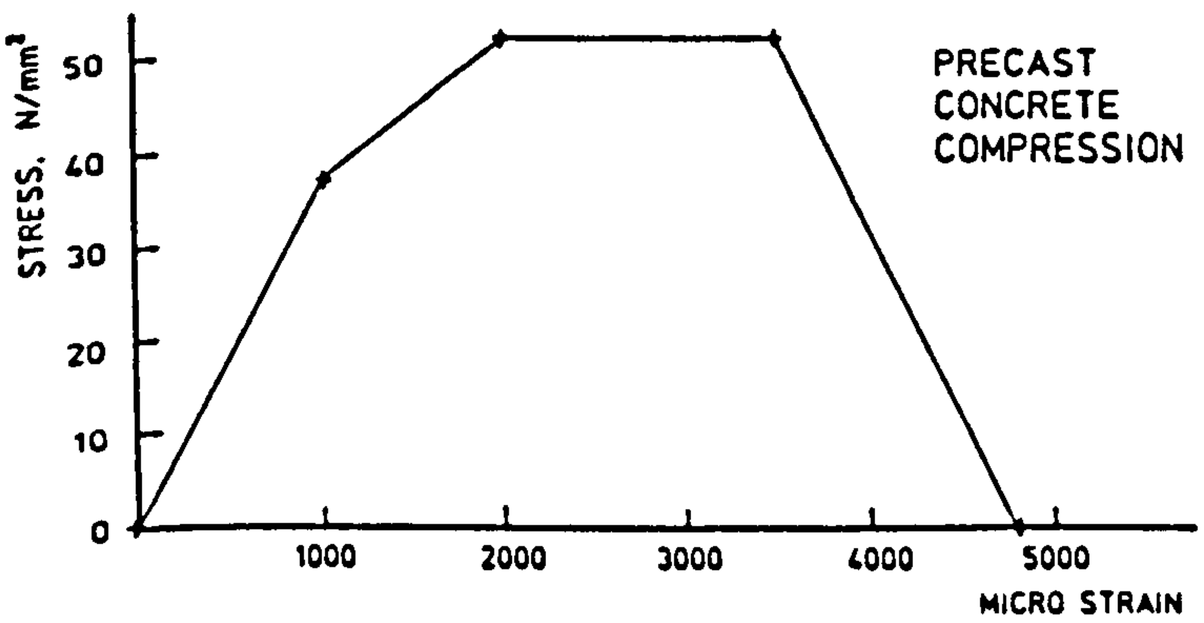

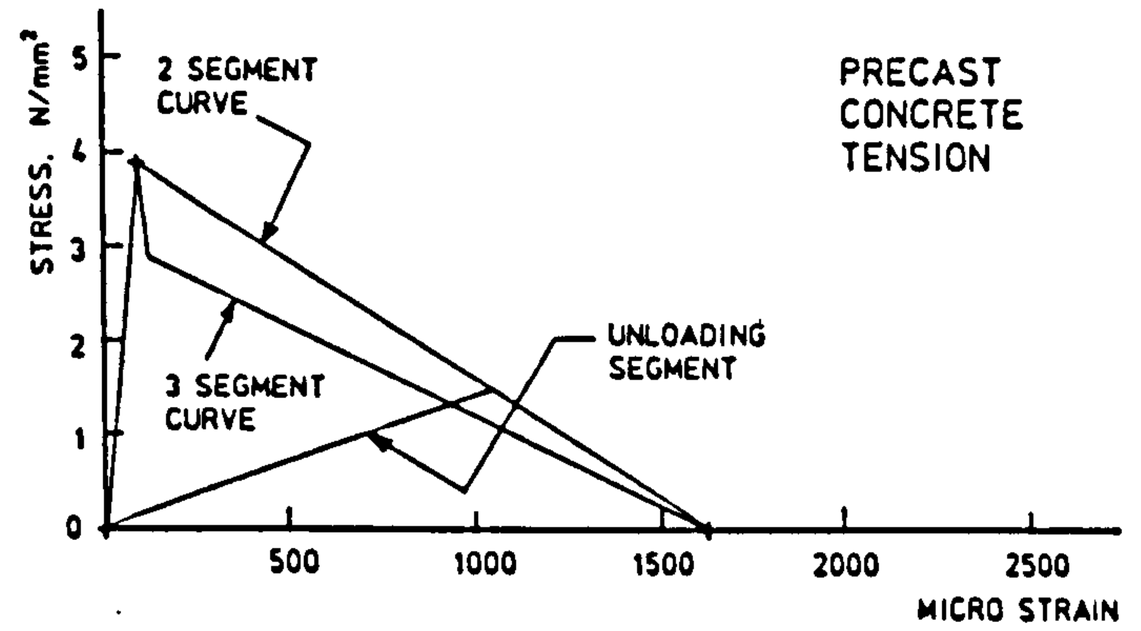

FIG. 10.4. CONCRETE STRESS-STRAIN CURVES USED IN THE NFES ANALYSIS OF MODEL 1

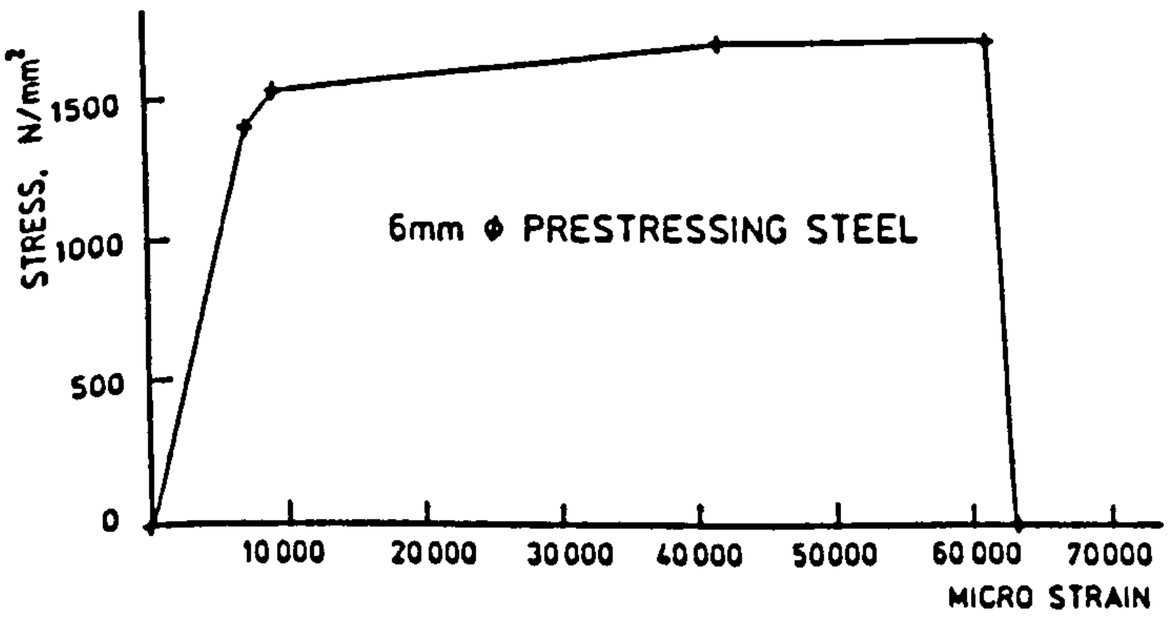

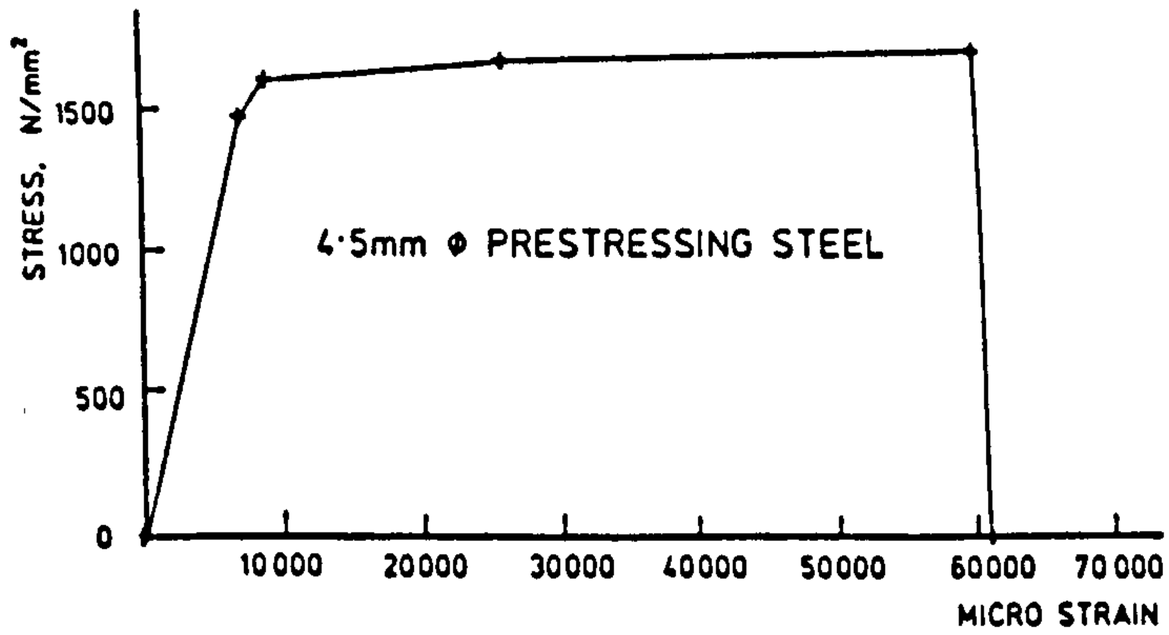

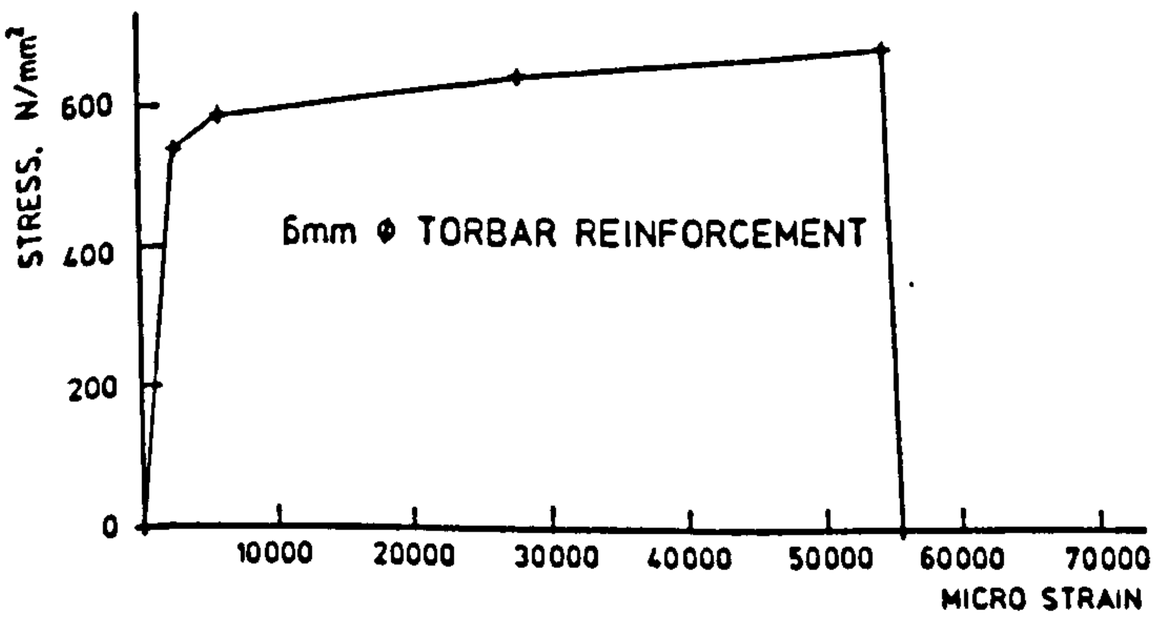

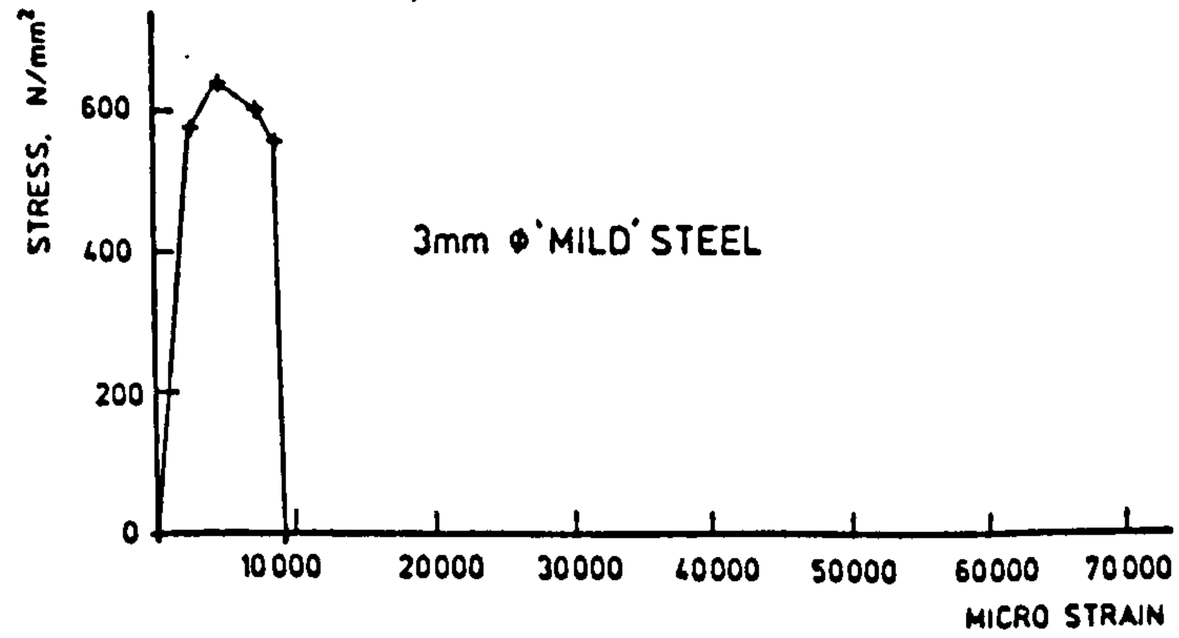

FIG. 10.5. STEEL STRESS-STRAIN CURVES USED IN THE NFES ANALYSIS OF MODEL 1

GJ is given by, assuming E = 35800 N/mm^2 and ν = 0.15:-

$$GJ = \frac{35800}{2(1+0.15)} \; 3.748 \times 10^6 = 58.34 \times 10^9 \text{ Nmm}^2$$

10.1.7 Finite element mesh

A finite element mesh with 3 elements in both the longitudinal and transverse directions was chosen for the initial analytical runs. Even though a mesh as coarse as 3 x 3 would not be expected to yield accurate results, it was useful for debugging the data and appraising different modelling strategies. Thus the increased resource requirements of the finer meshes would only be required for the final production runs. The limited amount of computing power that was available at the TRRL was also a constraint upon the fineness of mesh that could realistically be considered. A plot of the initial 3 x 3 mesh can be seen in Figure 10.3, the location of the HB bogie can also be seen on this Figure.

The constraint of time only allowed the most promising modelling strategy to be analysed with the finer 8 x 6 mesh although a number of modelling strategies were investigated with the coarse 3 x 3 mesh. It was desired to plot load-deflection graphs for the mid-point of the free edge nearest the HB Bogie to allow direct comparison with the experimental results. However, no vertical dof is present at the mid-point node with the Discrete-Kirchhoff element formulation for the 3 x 3 mesh. Therefore, a displacement combination incorporating all three plate bending dofs at the 2 adjacent nodes was formulated to predict the mid-span deflection. The free edge deflection profiles obtained from the 3 x 3 mesh using the prediction equation are compared against the free edge deflection profiles obtained from the 8 x 6 mesh in Figure 10.8.

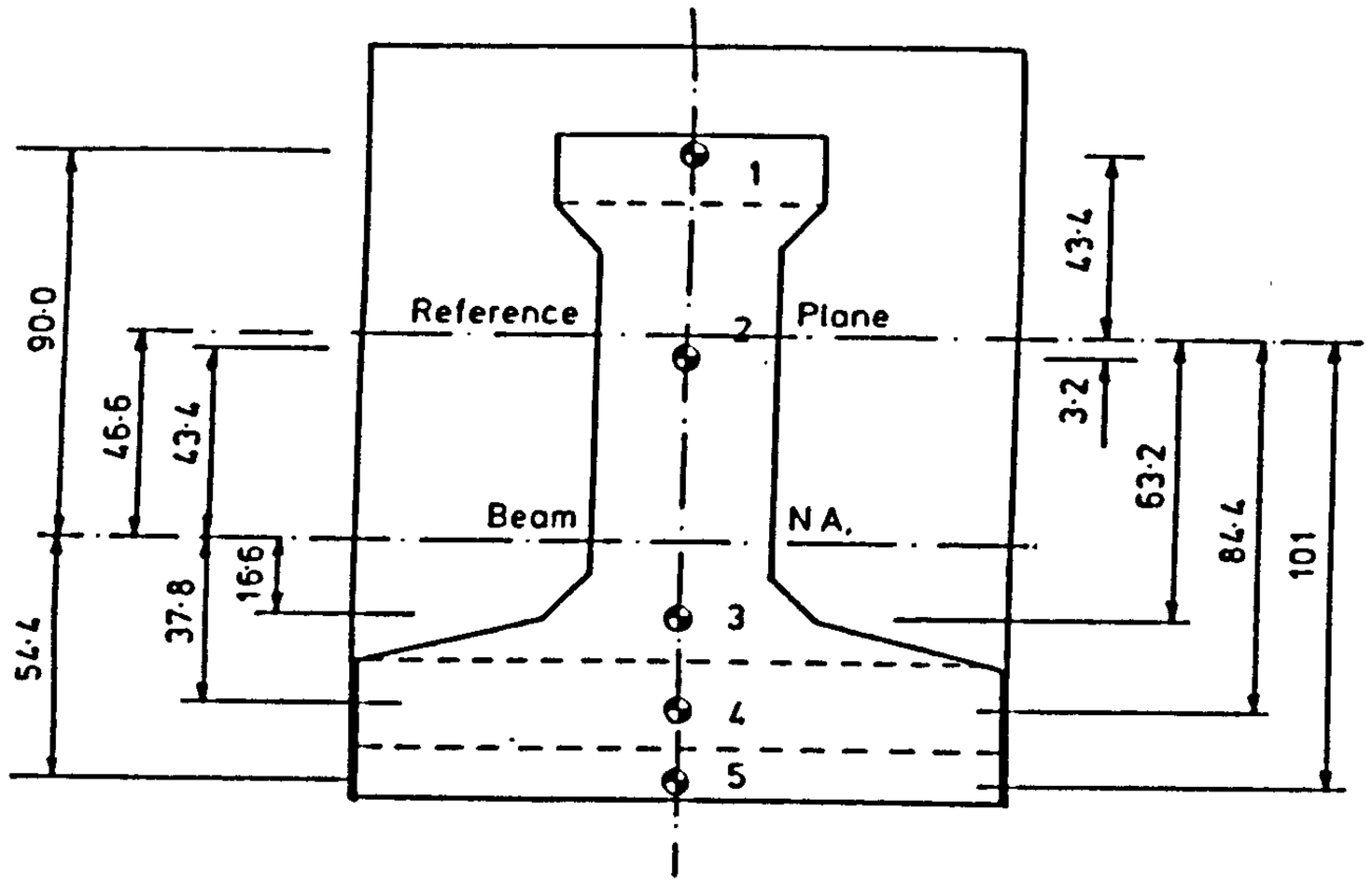

FIG. 10.6. BEAM INTEGRATION STATIONS FOR MODEL 1 NFES NON-LINEAR ANALYSIS

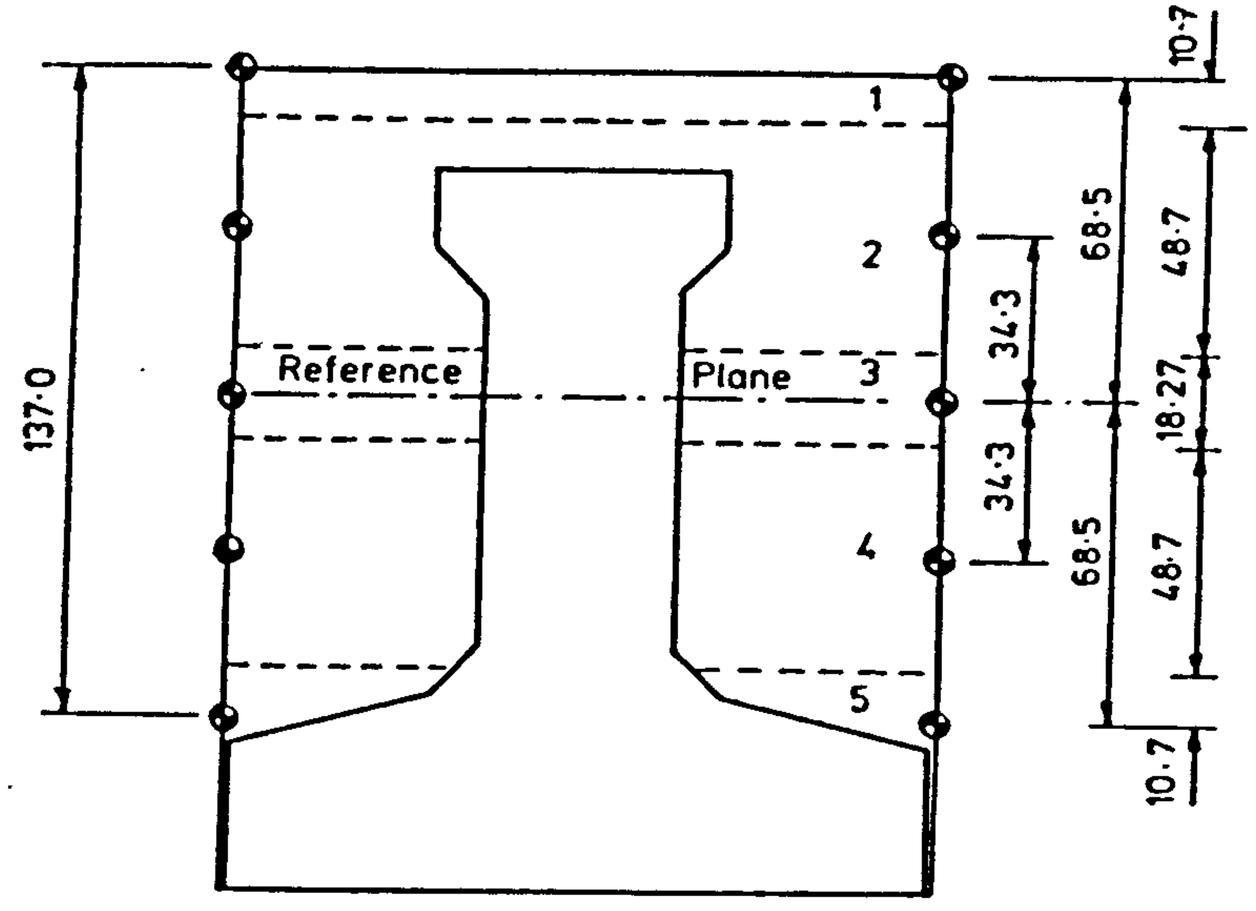

FIG. 10.7. IN-SITU INTEGRATION STATIONS FOR MODEL 1 NFES NON-LINEAR ANALYSIS

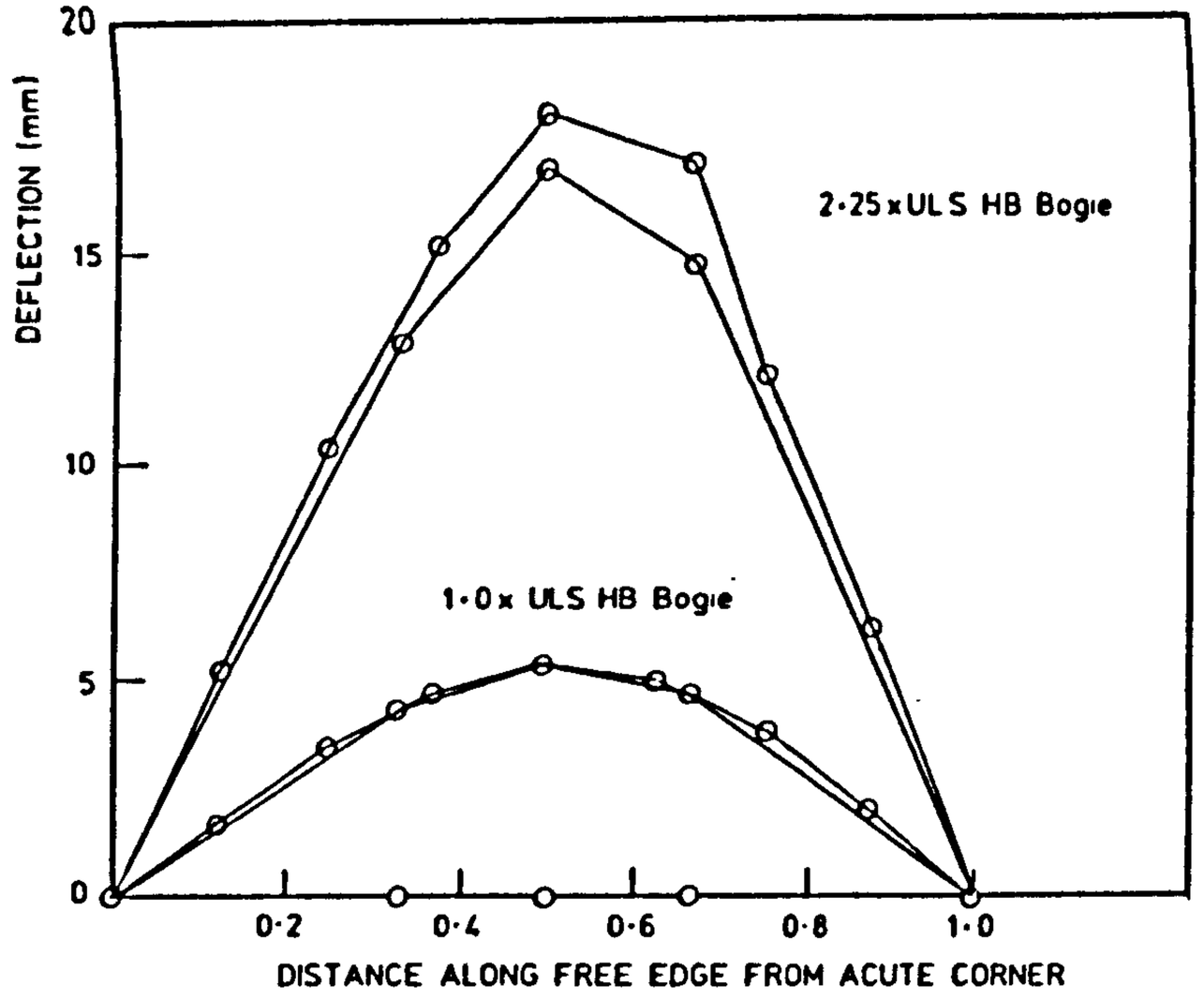

FIG. 10.8. COMPARISON OF FREE EDGE DEFLECTIONS FOR 3x3 MESH AND 8x6 MESH

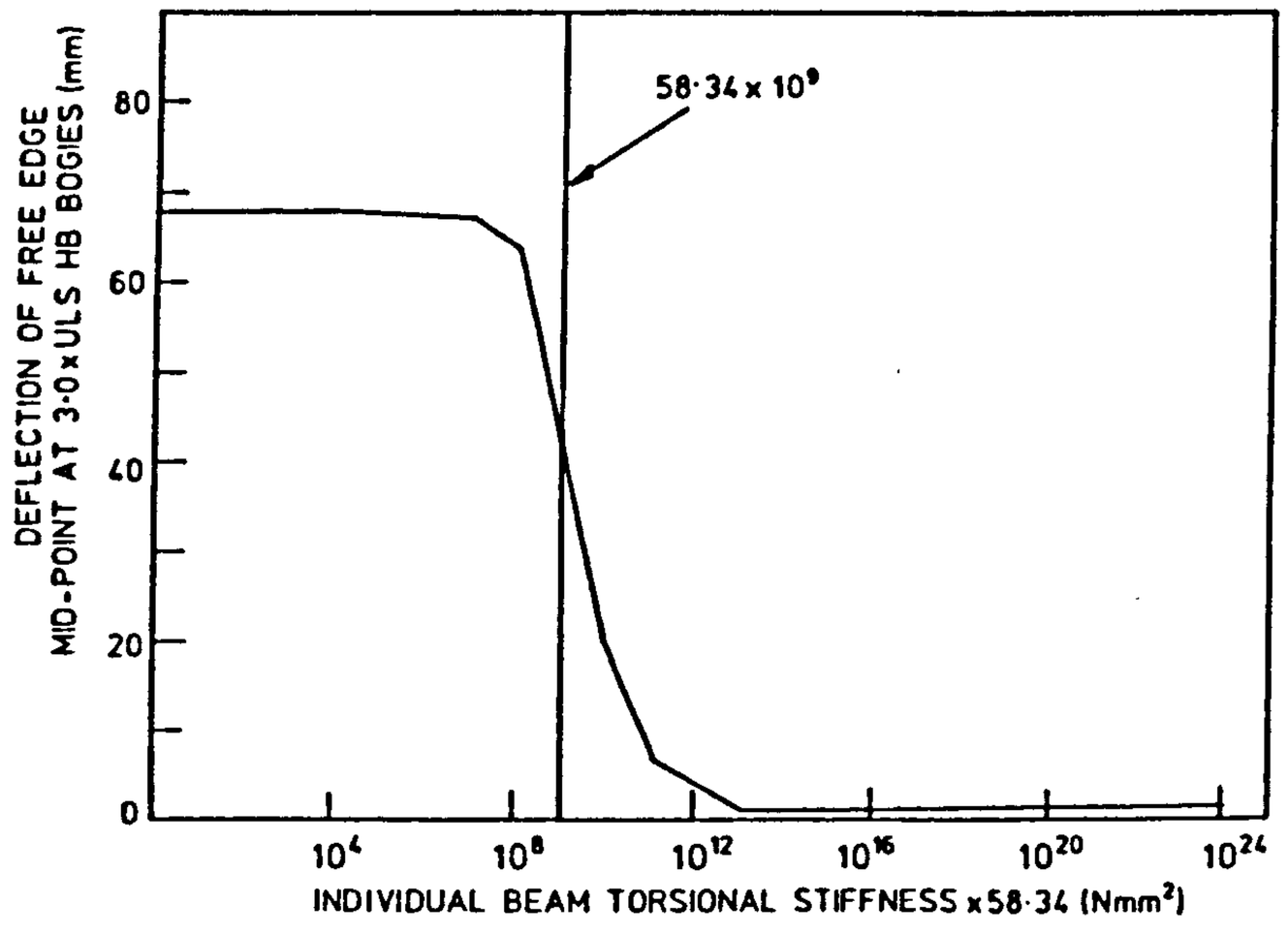

FIG. 10.9 EFFECT OF BEAM TORSIONAL STIFFNESS VARIATION AT A LOAD FACTOR OF 3·0 x ULS

10.1.8 Loading

The model decks had been constructed to a scale of 1:3.5 therefore the finite element analyses were carried out at 1:3.5, i.e. at model full size. Consequently, the load intensities given in BS5400 (1978) Part 2 had to be scaled before input to the finite element analysis, Table 10.1 lists the finite element load intensities and the appropriate partial safety factors, γ_{fL}, that were used.

The precast self weight and in-situ self-weight were applied at the 'wet' stage, i.e. with low stiffness, high strength plate concrete. The density correction loading was either applied at the 'wet' stage or at the cured 'hard' stage, i.e. normal stiffness and strength plate concrete. The super-imposed dead loading and the HA UDL loading was applied at the 'hard' stage and finally the HB load intensity was incrementally increased until failure. The location of each of the eight wheels of the HB bogie can be seen in the finite element mesh plot of Figure 10.3.

10.2 Finite element analyses

A number of different analyses were carried out upon the 9 element idealisation of model 1. Each of these analyses formed 'a series' of runs varying one or more of the factors in the finite element modelling of the problem, such as different loading, different stress-strain curves, etc. Each analytical series consisted of a number of individual runs and restarted runs so that the complete structural response could be traced for each 'series'. The base series of runs is known as the '∇ series' and examples of other series are the 'X series', 'Y series' and 'Z series'.

The load deflection plots for the 3 x 3 mesh finite element analyses can be seen in Figure 10.10. The traces refer to the HB bogie load

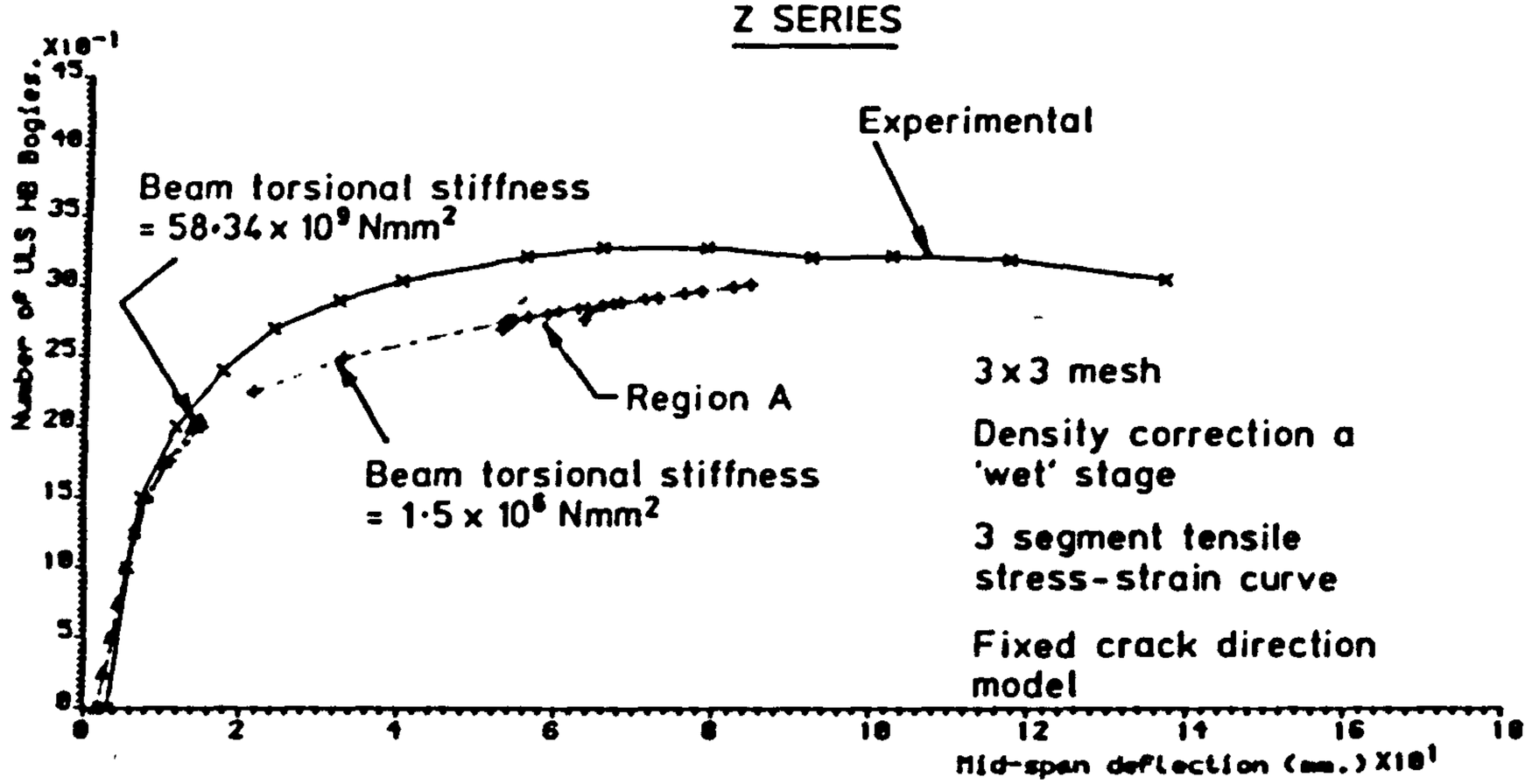

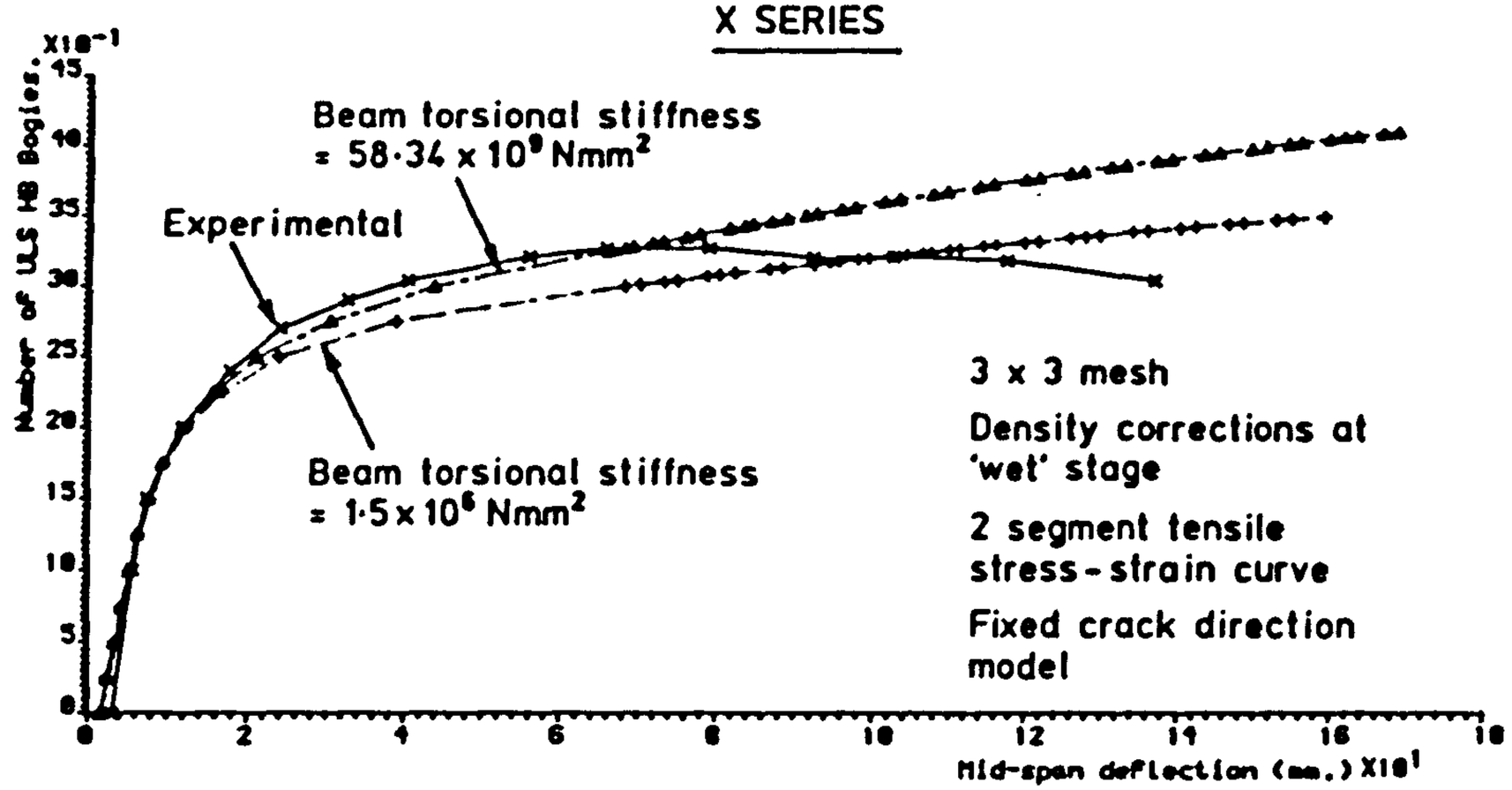

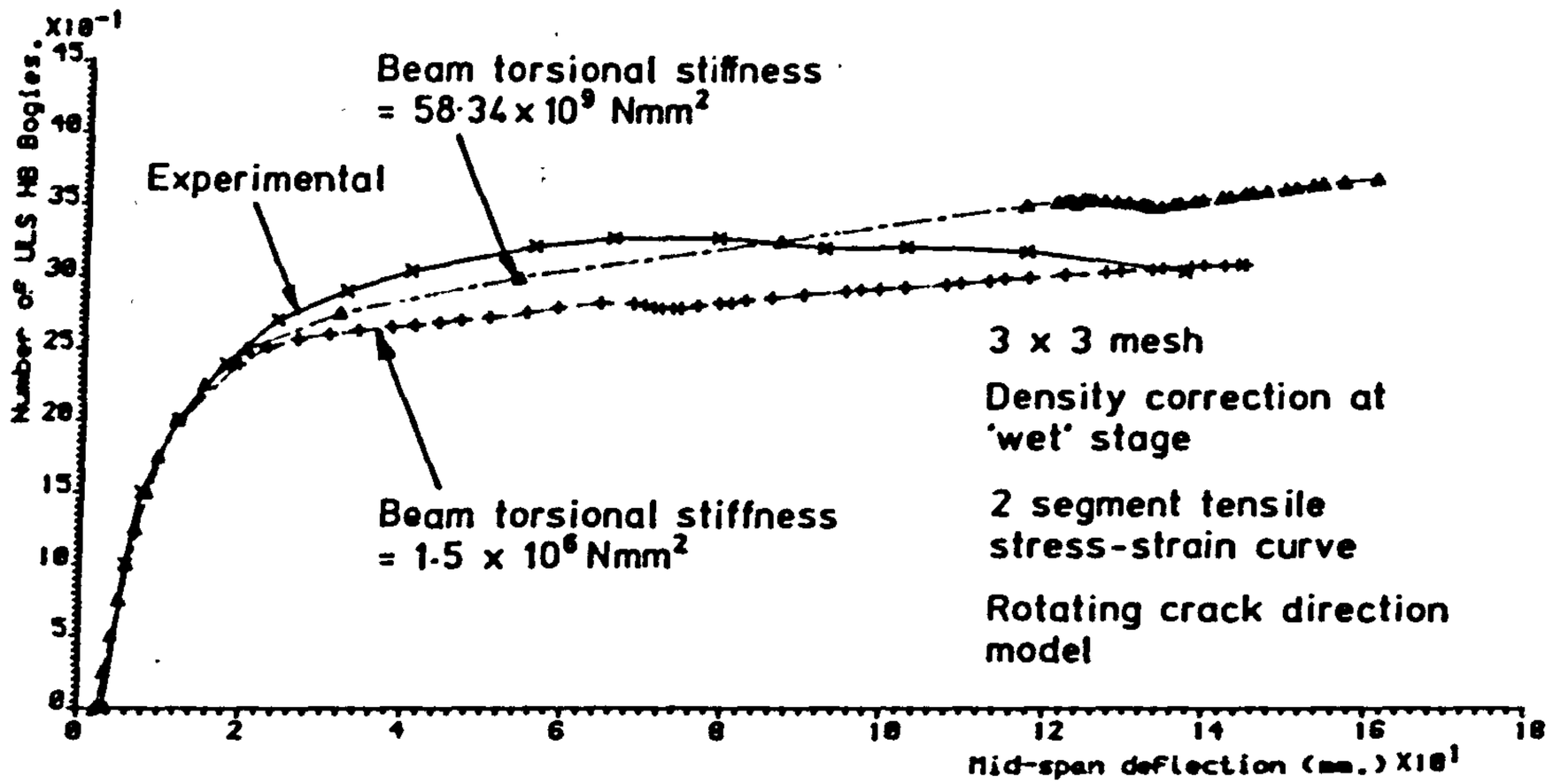

FIG. 10.10. PREDICTED LOAD-DEFLECTION RESPONSES FOR MODEL 1 OBTAINED FROM THE NFES NON-LINEAR FINITE ELEMENT PROGRAM USING DIFFERENT MODELLING PARAMETERS

and the deflection of the mid-point of the free edge adjacent to the HB bogie, node 22 in Figure 10.3. However, besides the HB bogie load there was also 257 x 10^3 N of fixed UDL loading representing the model self-weight density correction, super-imposed dead loading and HA UDL loading.

Initially, the analytical load application was arranged to follow that of the model test as closely as possible with the density correction UDL load being applied to the cured model structure. However, it was soon discovered that this philosophy led to severe difficulties with the material model. Under the density correction loading the cured in-situ concrete in the model analysis cracked with the fixed cracks predominantly aligned parallel to the supported edges, this can be seen in Figure 10.12. Although the plot shown in Figure 10.12 was obtained from the 8 x 6 mesh analysis. Subsequently, under the HB bogie loading the principal strain and stress directions rotated through angles of approximately 30° to 40° causing the fixed crack model such severe difficulties that it was not possible to continue with the analysis. This problem was overcome by applying the density correction at the 'wet' stage, that is with low stiffness plate concrete. Thus the whole density correction loading was carried by the prestressed beams alone and hence there was no cracking in the analytical model until the HB bogie load was applied. The crack pattern resulting from this modified load application can be seen in Figure 10.13, for which the load intensity is 1.0 x ULS HB (1.0 x ULS HB can be taken as 45 units of one BS5400 HB bogie at a scale factor of 1:3.5 with a partial safety factor, γ_{fL}, of 1.3). During the subsequent analysis to failure there was a change in the principal angle as the effects of the concentrated regime of the HB bogie load became more influential than the UDL loading regimes of the HA and

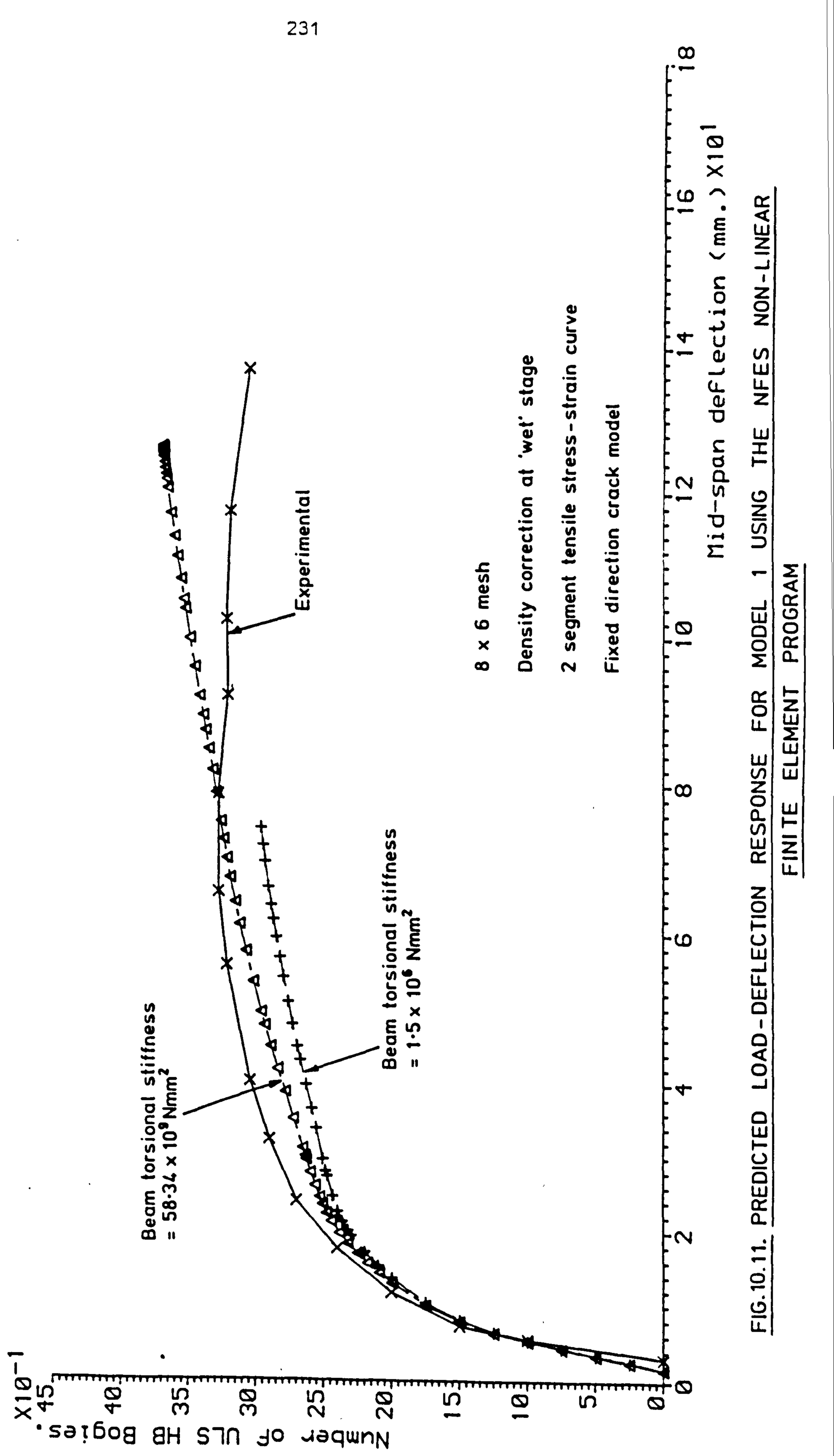

FIG.10.11. PREDICTED LOAD-DEFLECTION RESPONSE FOR MODEL 1 USING THE NFES NON-LINEAR FINITE ELEMENT PROGRAM

superimposed dead loadings. However these rotations were small and did not cause the fixed crack material model any serious problems.

The three segment stress-strain curve shown in Figure 10.4 was initially chosen to represent the tensile behaviour of the concrete. However severe numerical problems were encountered in region A of the load deflection curve in Figure 10.10 it was suspected that the steepness of the second segment in the tensile stress-strain curve was responsible. The numerical effects of different tensile stress-strain curves will be discussed later. To overcome these numerical difficulties the use of the 2 segment tensile stress-strain curve shown in Figure 10.4 was investigated. The various analyses can be identified from:-

∇ series - Density correction load applied to cured slab, 3 segment tensile stress-strain curve.

X series - Density correction load applied at 'wet' stage, 2 segment tensile stress-strain curve.

Y series - Density correction load applied to cured slab, 2 segment tensile stress-strain curve.

Z series - Density correction load applied at 'wet' stage, 3 segment tensile stress-strain curve.

From the general shape of the load-deflection curves of Figure 10.10 it can be seen that the stiffness of the analytical model is slightly less than that of the actual model stiffness at any load level, before the onset of significant non-linearities, at approximately 1.5 * the ULS HB load level. The reduced stiffness is apparent in the analytical response up until the maximum experimental load is attained. The stiffness of the experimental model then becomes

negative; whereas the analytical model maintains an approximately constant positive stiffness.

For an explanation of these observations, one must look at the finite element modelling in detail. The torsional stiffness of a homogeneous isotropic plate for a section width equal to one precast beam is given by:-

$$GJ = \frac{Ed^3}{6(1+\nu)}\, b = \frac{E}{2(1+\nu)}\, I \qquad \text{where b = width of 1 beam = 145 mm}$$

However because of the intertwined nature of the in-situ and precast concretes $GJ_t = GJ_i + GJ_p$; where t = total, i = in-situ, p = precast.

GJ_i is determined by the integration through depth and is a function of the position and volume of the insitu concrete. The volume of in-situ concrete is less than that of an isotropic plate and is also distributed through the depth in a non-uniform way. This is reflected in the special integration scheme that has been adopted, see Figure 10.7. The value of GJ_i given by this integration scheme for $E = 27750$ N/mm^2, $\nu = 0.15$, $I_i = 30.39 \times 10^6$ mm^4 is $GJ_i = 366.7 \times 10^9$ Nmm^2. The torsional stiffness of an isotropic plate of equivalent thickness for $E = 27750$ N/mm^2, $\nu = 0.15$, $I = 63.66 \times 10^6$ Nmm^2 is $GJ = 768.0 \times 10^9$ Nmm^2. The torsional stiffness adopted for the precast beams based upon the assumption that they act independently of the plate, see Section 10.1.6, is $GJ_p = 58.34 \times 10^9$ Nmm^2.

Therefore the ratio the composite plate torsional stiffness to the torsional stiffness of an isotropic plate of equivalent thickness is

$$= \frac{366.7 \times 10^9 + 58.3 \times 10^9}{768.0 \times 10^9} = 0.553$$

Therefore, it can be seen that there will be a 45% loss in torsional stiffness for the uncracked case. The ratio of the precast linear torsional stiffness to its equivalent 'fully composite' value is

$$= \frac{58.3 \times 10^9}{768.0 \times 10^9 - 366.7 \times 10^9} = \frac{58.3 \times 10^9}{401.3 \times 10^9} = 0.145$$

Figure 10.10 depicts the deflection response of the free edge mid-point, to increasing HB bogie load. The deflection at the free-edge mid-point will be influenced by the torsional stiffness of the slab, through the position of the HB bogie and its increasing dominance of the loading regime. Thus, for the free edge mid-point, one would expect the structure's analytical stiffness to be less than that of the experimental stiffness during the early stages, before the onset of significant cracking.

The inverted T beam with insitu fill form of construction is a composite of beams and in-fill concrete. Therefore, depending upon the linkage between the beams and the in-fill, the slab may act as one homogeneous unit, with the construction details having little effect upon the response. On the other hand the two components of the system may act as separate entities, so that the slab's response is akin to that of two sets of beams. One would expect the behaviour of the slab to change, within the limits of these two extremes, during loading to failure.

The linkage between the beams and the in-fill has two components, firstly there is a physical structural action due to the shape of the component parts and their interlinked nature. Secondly there is chemical bond between the two concretes. One would expect high displacement levels to be achieved before the physical linkage broke down completely. There was no evidence of complete physical linkage

breakdown during the tests. However, in critical areas during the later stages of the tests, the linkage between the structural components will, most probably, have depended upon their physical shape without the benefit of chemical bond.

If one examines the beam profile then it can be seen that the shape is better able to resist different force components with varying degrees of effectiveness. If we define a force system that is parallel and perpendicular to the beam axes, then the most seriously effected force components can be isolated. The presence of a top and bottom flange will facilitate a high resistance to vertical shears perpendicular to the beams. The compressive capacity of the interface and the continuous transverse reinforcement will enable effective resistance to perpendicular sagging and hogging moments. The transverse section test in Appendix 5.2 showed that perpendicular sagging moment-curvature response was not significantly effected by the form of construction. In the transverse section tests it was observed that all cracks began at the junction of two beams, subsequently some followed the beam profile whilst the majority continued vertically upwards.

The most severely effected aspect, will be the structural system's ability to resist torsional moments. With the loss of chemical bond and with little physical restraint there will be little resistance to in-plane shear stresses along the interfaces. Therefore, the structure may begin to act as a set of semi-independent beams for the resistance to torsion, and composite action, with strain compatibility, cannot be assured.

The torsional stiffness degradation, due to the reduction of in-plane shear resistance, will be in addition to the reduction in torsional

stiffness caused by cracks in the beams and in-situ fill. Therefore, the criteria for analytical torsional stiffness degradation should not be based solely on in-plane direct strains. The linear beam torsional stiffness facility in the NFES program allowed an investigation to be carried out, giving manual control of the magnitude of the beam torsional stiffness.

10.2.1 Effect of beam torsional stiffness variation

A series of problems were analysed in which the beam torsional stiffness was varied from 58.34 to 58.34 x 10^{24} Nmm^2 in ten steps. The results of this investigation are shown in Figure 10.9. The beam stiffness that was calculated earlier, using the method of equivalent rectangles, is shown as a vertical line on this figure. The beam torsional stiffness is given as the abscissa of this plot. While the deflection of the free edge mid-point at a load level of 3.0 x the ULS HB bogie load, is given on the ordinate. An HB Bogie load level factor of 3 was chosen to allow the non-linear effects of material degradation to have a significant effect.

For beam torsional stiffnesses between 58.34 and 58.34 x 10^7 Nmm^2 the displacement is virtually constant at 68 mm. For stiffnesses between 58.34 x 10^{13} and 58.34 x 10^{24} Nmm^2 the displacement is again relatively constant, however, this time the magnitude is extremely low at approximately 3 mm. For the region between those two states the displacement varies with changes in the torsional stiffness, however, it must be realised that in Figure 10.9 a log scale is used for the torsional stiffness axis. Figure 10.9 can be considered with the load deflection plots of Figures 10.10 and 10.11, where the analytical responses of slabs with beam torsional stiffnesses of 58.34 x 10^9 Nmm^2 and 1.5 x 10^6 Nmm^2 have been plotted with the experimental responses of the model deck. It can be deduced that for torsional stiffnesses

in excess of 58.34 x 10^{10} Nmm^2 an over stiff response will result. For torsional stiffnesses below 58.34 x 10^6 an under-stiff response will result, however, the effect is less pronounced. One torsional stiffness value will not be suitable for the complete analysis as the material degrades. Thus the presence of a constant linear torsional resistance fixed in a direction parallel to the beams is probably the cause of the positive, almost constant, structure stiffness towards the end of the load-deflection plot.

The effect upon structural failure, of prescribed material axes in the beams can be illustrated through the curvature and moment transformation equations. In the general case the principal curvatures will be at a finite angle to the beam axes. Transformation of these principal curvatures to the material directions will result in direct curvature and a twisting curvature. After application of the material model the resulting direct and twisting moments can be transformed back to the principal directions. The material stiffnesses in the principal directions will include a component from the torsional stiffness in the material direction. Therefore, with a linear beam stiffness, there will always be a positive stiffness component in the principal direction preventing total failure.

From the load-deflection plots of Figures 10.10 and 10.11 it can be seen that varying the linear beam torsional stiffness by a factor of 40000 has a moderate effect upon the analytical response of the structure. Therefore, while the NFES program produced useful and interesting results and allowed the effect of beam torsional stiffness variations to be investigated, its analytical philosophy was not totally satisfactory for this form of construction.

10.2.2 Effects of multilinear stress-strain curves for concrete in tension

Initially, stress-strain curves for concrete in tension involving three linear segments were employed for both the precast and in-situ concretes. These curves, which are shown in Figure 10.4 incorporated a second segment which has a gradient equal to the initial 'E' value before cracking negated. After cracking, when the stress had dropped to 75% of the cracking stress then the third segment took control. The tension stiffening in the third segment reduced linearly as the strain increased to its ultimate value. For all of those analyses an ultimate strain of 15 times the cracking strain was adopted. The analyses that used the three segment tension curve were denoted the Z series and the load-deflection responses obtained from these analyses can be seen in Figure 10.10. For the analysis with a beam torsional stiffness of 1.5×10^6 Nmm^2 the response progresses well until the displacement reaches approximately 54mm. After this level severe difficulties were encountered. These manifested themselves in the stiffness matrix having a positive determinant whilst also having a negative pivot. It has been suggested by Crisfield[4] that these two factors may indicate that a bifurcation point has been reached. At a limit point, with the structural load-deflection response subsequently falling one would expect both a negative determinant and negative pivots. However, a bifurcation point, after which there are multiple possible paths that the structure may follow, may be indicated by a negative pivot and positive determinant.

Crisfield has suggested, that to ensure the structure follows the state equilibrium path leading to the minimal failure load, a perturbation be applied to the structure. The eigenvector corresponding to the lowest eigenvalue defines the deflection mode in which the structure is most flexible. Therefore a component of this

eigenmode can be used to provide the perturbation, however, the direction in which it should be applied is unknown. Crisfield has suggested several methods for determining this direction and they have been incorporated into the NFES program.

Upon encountering the negative pivot during the model analysis, the program applied a positive component of the eigenmode. This caused the load deflection response to fall and subsequently to return up the same path. With a negative component of the eigenmode, the load-deflection response continued to rise. Moreover, with no perturbation, the structure followed the same path as the analysis with a negative component of the eigenmode had followed. The numerical problems intensified as the analysis progressed, eventually causing the analysis to be abandoned.

It was suspected that the steepness of the second segment of the concrete tension curve was the cause of the negative pivots and numerical difficulties. A two segment curve, which is also shown in Figure 10.4 was therefore introduced. Essentially, the curves are identical, except that the second and third segments of the three segment curve are combined into a single linear segment, in the two segment curve. The negative pivots and numerical difficulties did not occur with the two segment curve analysis, while the structure's response was almost identical to the response with the three segment curve. The similarity between the load-deflection curves can be seen in Figure 10.10.

It was concluded that the steepness of the second segment of the three segment curved was the primary cause of the negative pivots and numerical difficulties. It was not possible to exactly define what was happening to the structure when the negative pivot was

encountered. This may have been a bifurcation, however, the eigen-analysis was not successful in solving the problem.

10.2.3 Convergence

During the early stages of the analysis it was desired to remain under manual load control. This permitted the experimental load application to be modelled exactly, allowing direct comparison of results at different load levels. At the onset of significant non-linearity in the response, it was necessary to switch to Arc-length[5] control so that convergence could be achieved. While under Arc-length control, the magnitude of the increments were calculated automatically. It was found that the most successful approach incorporated small increments with few iterations, generally less than 5, rather than moderately sized increments with corresponding larger numbers of iterations during each increment. This was no doubt due, in part, to the recalculation of the stiffness matrix at the beginning of each increment while only a secant stiffness update was used during the iterations.

A stringent convergence criterion was applied to all of the analyses. The criterion involved the Euclidean norms of the residual force and total applied force vectors and was defined by:-

$$0.33 > \frac{100\ \sqrt{r^T r}}{\sqrt{p^T\ p}}$$

where r = Residual force vector

p = Total applied force vector.

However, it must be remembered that different element formulations will effect the stringency of criteria similar to this one. For example, if a vertical 'w' load is applied to the Discrete-Kirchhoff

element, then its formulation dictates that the consistent loading will include applied nodal moments, which have a significant effect upon the size of the total force norm. Conversely, for the Heterosis element, no nodal moments will be involved in the consistent loading and, therefore, relatively, the total force norm will be tighter.

A full range 8 x 6 mesh analysis, such as that shown in Figure 10.11, involved a large number of increments, typically 60. With 250 iterations and 40 line searches and using 5 hours and 41 minutes of central processor time on a Cyber 720 machine.

10.2.4 Fixed crack and rotating crack models

The majority of the analyses for this investigation were carried out using a fixed crack direction material model. A rotating crack model was used for two analyses and the load deflection response for these can be seen in Figure 10.10.

If a strain system ϵ_x, ϵ_y, γ_{xy} acts at a point and just causes cracking then provided the strain system is increased proportionally the fixed and rotating crack models will give similar results. However, if after cracking the proportions of the strain components change, then the fixed crack model will result in a stiffer response as the material model is no longer being applied in principal directions. This stiffer response is illustrated in the different load-deflection responses for the two material models which are shown in Figure 10.10. The non-proportionality of strain increments will be most pronounced in an analysis which involves a large fixed loading system in addition to a dissimilar loading system whose intensity is increased incrementally to induce failure. This is typical of bridge deck analyses, where the self-weight loading, superimposed dead

loading and HA loading constitutes the fixed loading system and the HB loading the incremental failure loading.

10.2.5 Crack patterns

Figures 10.12 to 10.18 show crack patterns that were obtained from the NFES analyses of model 1, the load-deflection response is shown in Figure 10.11. These plots show the crack states of different layers for different load levels. A layer refers to a particular through depth integration station of which there were 5 for the in-situ plate. It was not possible to obtain crack pattern plots for the beams at the time these analyses were carried out. Crack states are plotted for each of the 2 x 2 Gauss quadrature integration stations in the plan of each element. The presence of a crack at an integration station is shown by a line in the direction of the crack, There is no indication of the magnitude of the cracking strain at that point. Generally, at a particular load level either the top and bottom layers are shown or the top two and bottom two layers. If a crack is closing then it is shown as a dotted line.

The first crack pattern plot that is presented relates the design ultimate limit state with 45 units of one HB Bogie applied to the structure, see Figure 10.13. No cracking is indicated on the top surface and the soffit cracking is concentrated in the loaded obtuse corner region.

The second crack pattern under HB loading that is considered is at an HB Bogie load factor of 2 and can be seen in Figure 10.14. At this stage, the displacement level was approximately 13 mm. It can be seen that the top surface crack pattern is developing into a circular pattern around the HB bogie. The principal moment plot of Chapter 4 Figure 4.11 illustrates the results for a linear analysis at a load

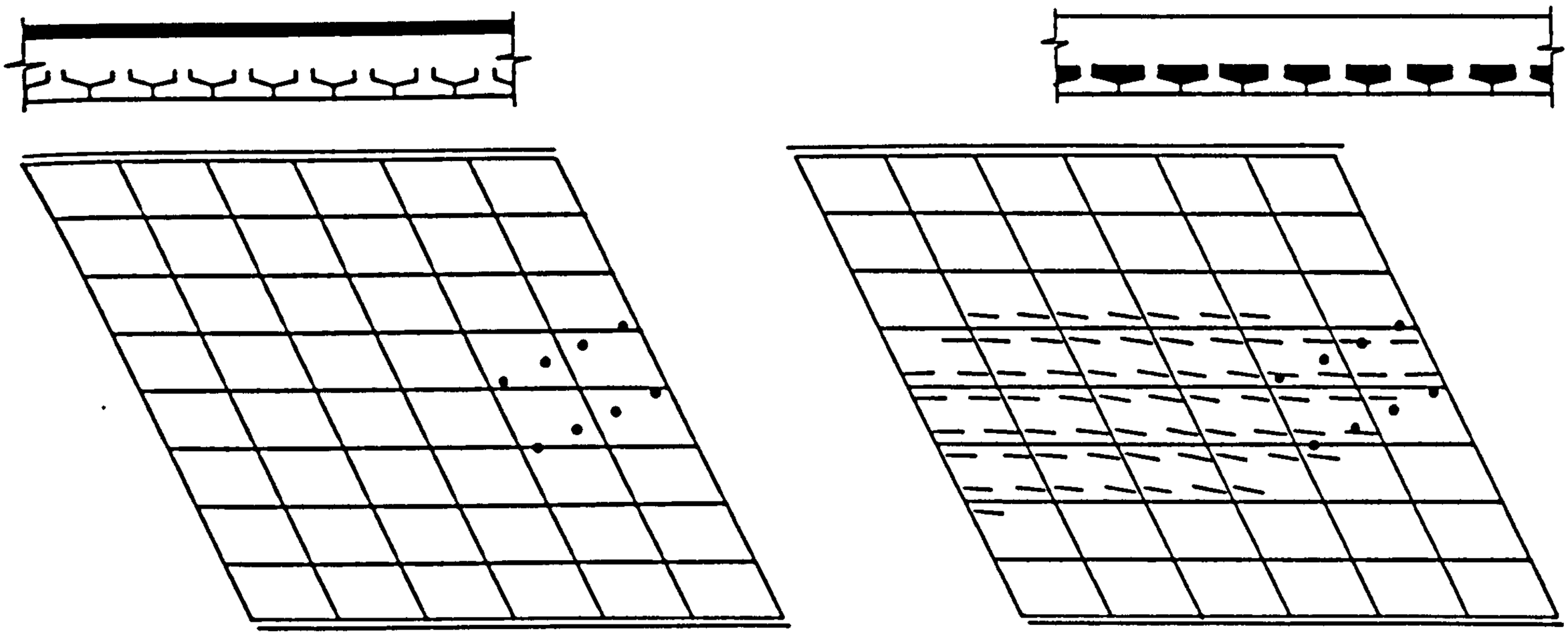

PLATE TOP LAYER

PLATE BOTTOM LAYER

KEY:-

LOADING TYPE: Density Correction loading applied to cured slab.

MATERIAL TYPE: 2 Segment concrete tension curve (see Fig. 10.4.)

LOAD LEVEL: Full HA etc. 0 x ULS HB Bogies

— crack opening

+ orthogonal cracks

--- crack closing

FIG. 10.12. CRACK PATTERNS OBTAINED FROM THE NFES ANALYSIS OF MODEL 1

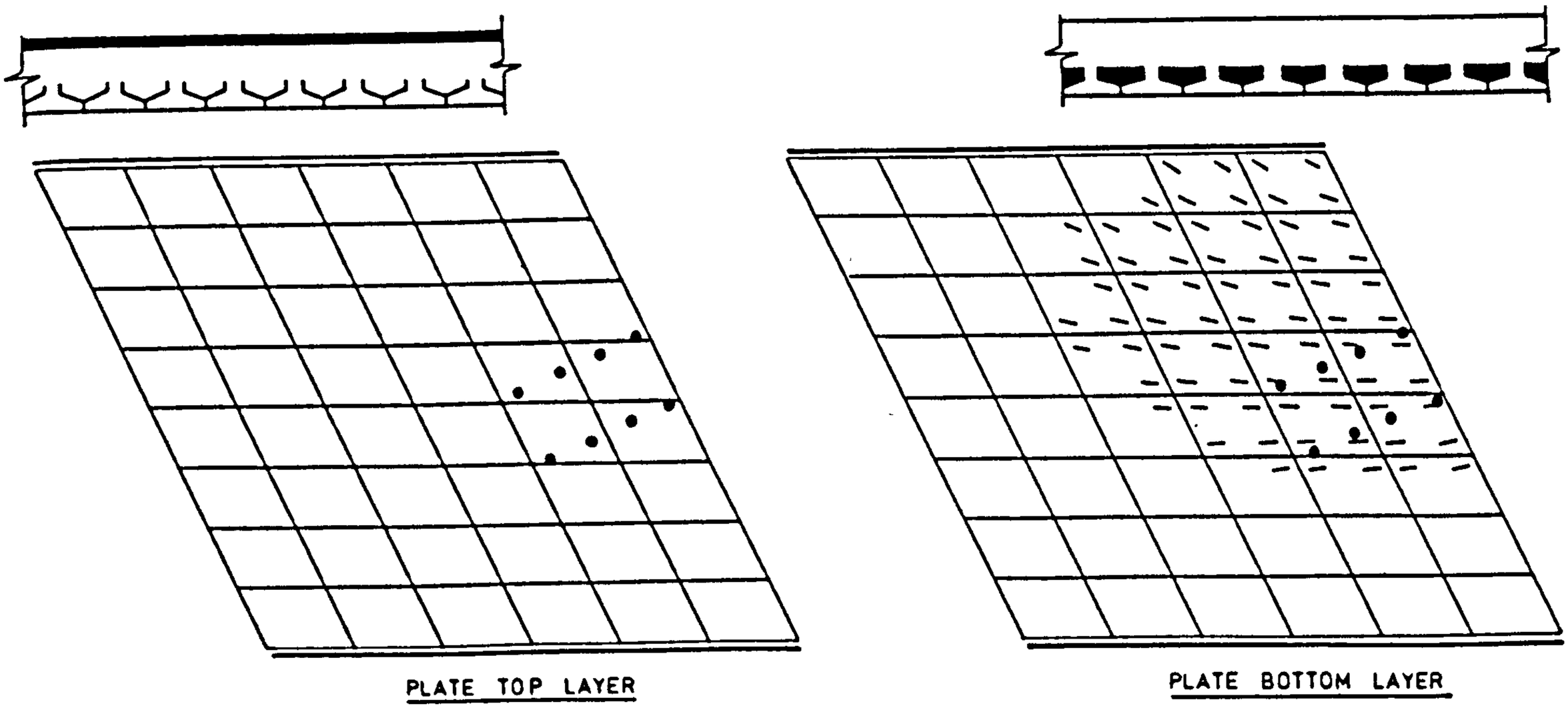

PLATE TOP LAYER

PLATE BOTTOM LAYER

KEY:-

LOADING TYPE : Density Correction loading applied at 'wet' stage.

MATERIAL TYPE: 2 Segment concrete tension curve. (Fig 10.4.)

LOAD LEVEL : Full HA etc. 1·0 x ULS HB Bogie.

— crack opening

+ orthogonal cracks

--- crack closing

FIG. 10.13. CRACK PATTERNS OBTAINED FROM THE NFES ANALYSIS OF MODEL 1

level of 1.0. Up until the onset of material non-linearity, one would expect the non-linear NFES analysis of Figure 10.14 to give similar results to the linear analysis of Chapter 4 Figure 4.11. Therefore, one would expect the initial top cracks to form approximately perpendicular to the maximum principal linear hogging moments. In general, if one compares Chapter 4 Figure 4.11 with Figure 10.14 this is seen to be the case. Although the linear analysis assumed an orthotropic plate, whereas the non-linear analysis included the prestressed beams as separate entities. The major differences in the principal crack directions for these two plots occurs in the bottom left hand corner of the slab of Figure 10.14. Figure 10.14 supports the experimental observation that top cracking began adjacent to the supports, especially the non-instrumented support line.

Besides the top layer, crack patterns are given for three other layers. These are the second layer down from the top, the fourth layer and the bottom layer. The bottom layer pattern, which is quite extensive can be seen in Figure 10.15. One set of orthogonal cracks are indicated under the HB bogie. The crack pattern plot for layer 4, which is also shown in Figure 10.15 shows extensive cracking in the obtuse corner region. However, the crack pattern plot of layer 2 shown in Figure 10.14 shows very limited cracking and this is centred around the non-instrumented support edge.

The next load factor at which crack pattern plots are given is 2.51. Plots for the top and bottom layers are shown in Figure 10.16. From the top layer crack pattern plot, it can be seen that the cracks cover about half the slab surface and surround the HB bogie in a continuous pattern between the supports. The similarity between this plot and the experimental top surface crack pattern plot of Chapter 5 Figure 5.9 can clearly be seen. The areas where crushing occurred in the

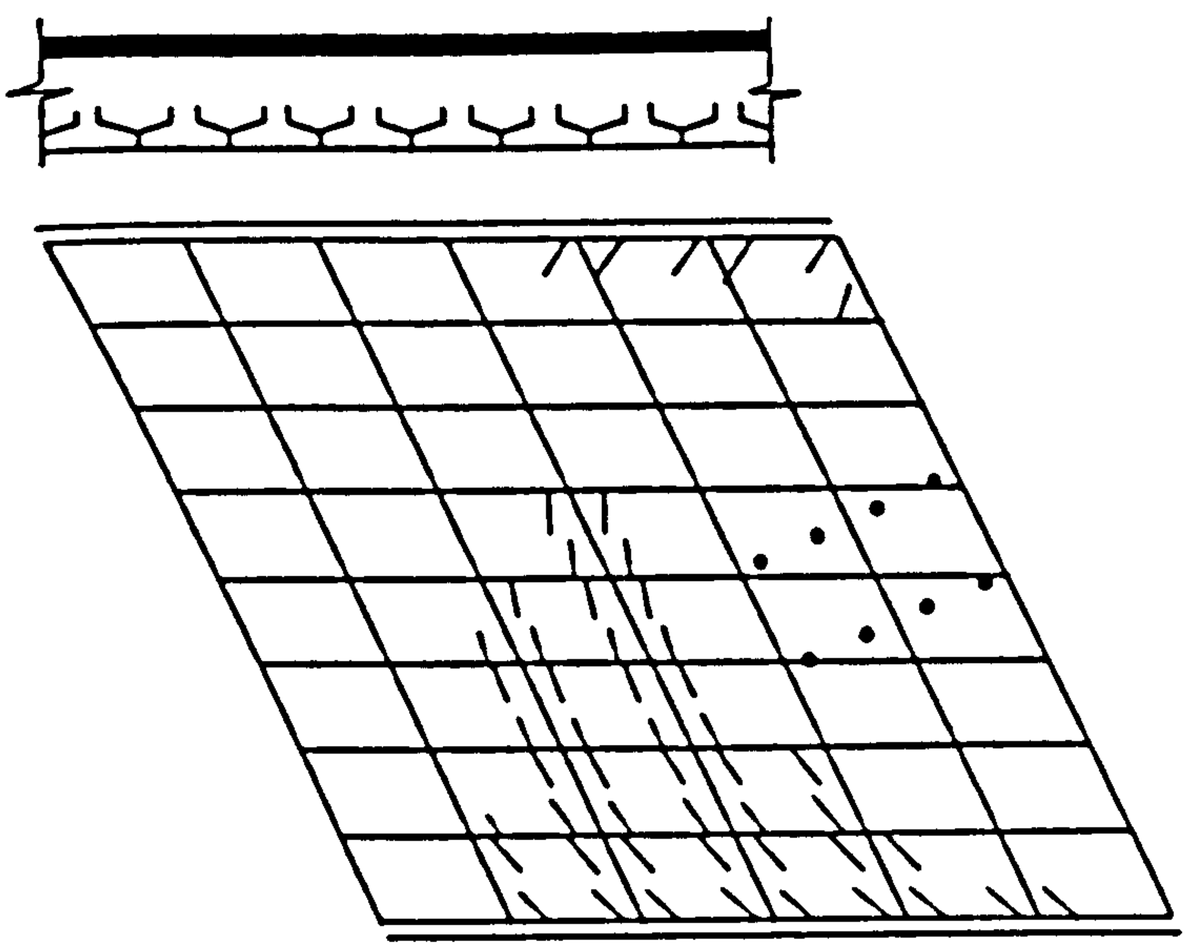

PLATE TOP LAYER

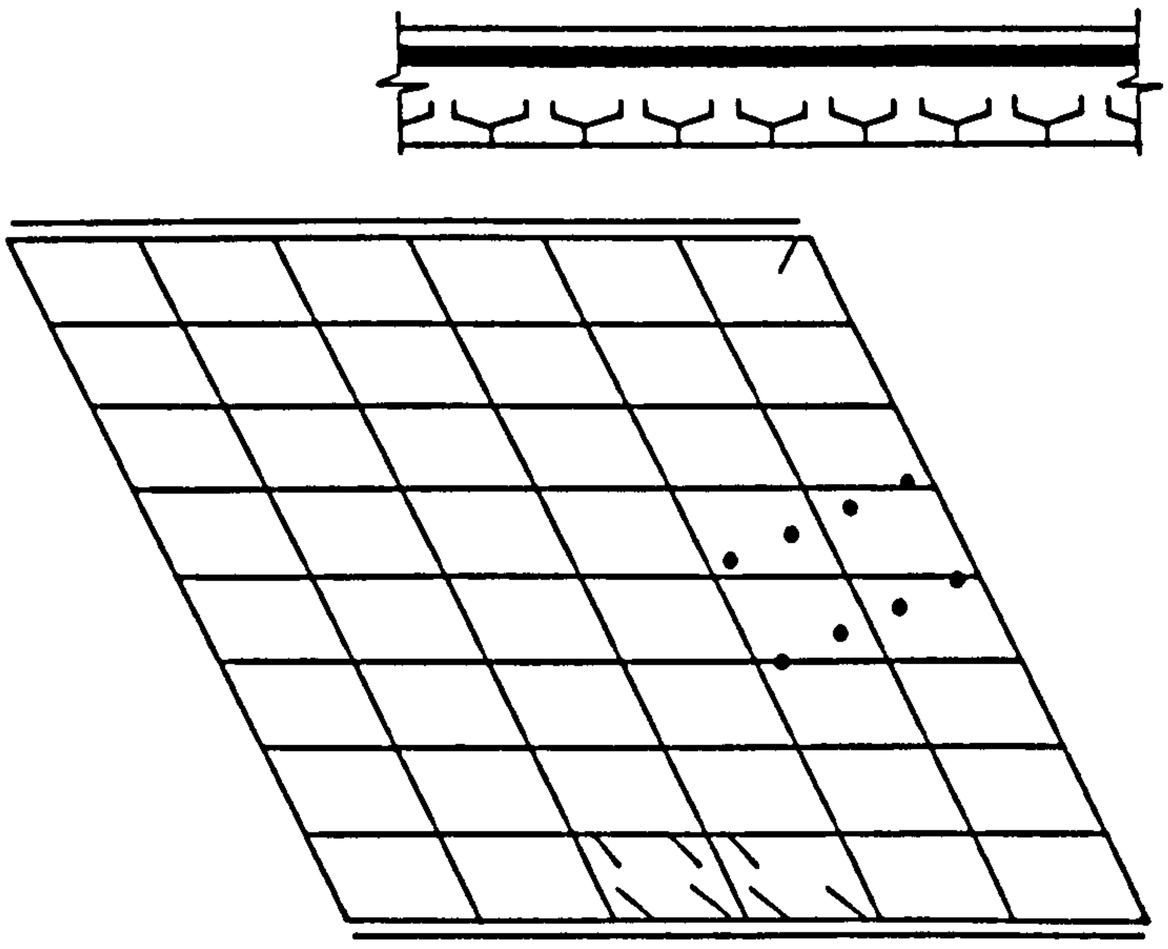

PLATE LAYER 2

KEY :-

LOADING TYPE. Density Correction loading applied at 'wet' stage

MATERIAL TYPE. 2 segment concrete tension curve (see Fig.10.4.)

LOAD LEVEL: Full HA etc. 2·0 x ULS HB Bogie.

—— crack opening

+ orthoganal crack

--- crack closing

FIG.10.14. CRACK PATTERNS OBTAINED FROM THE NFES ANALYSIS OF MODEL 1.

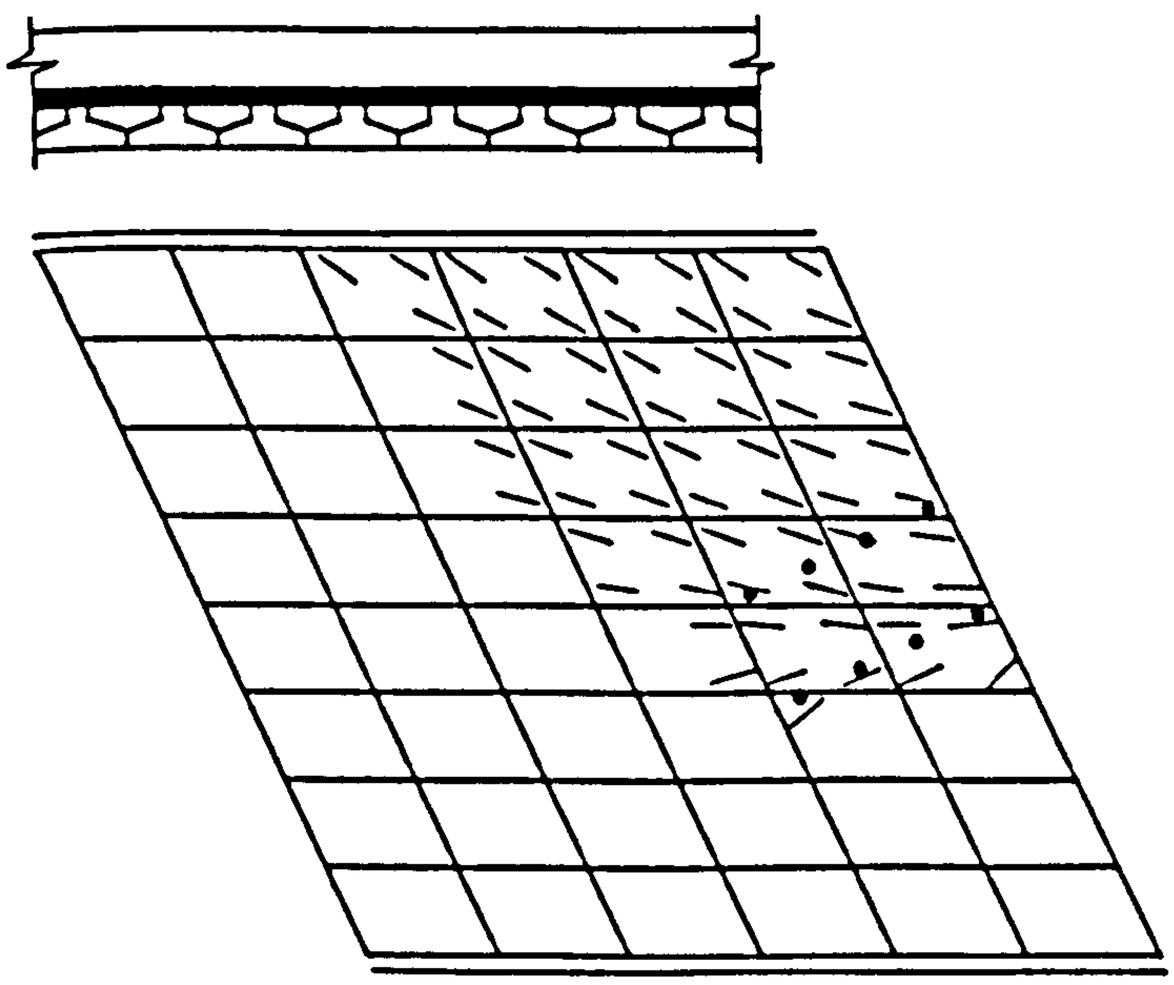

PLATE LAYER 4

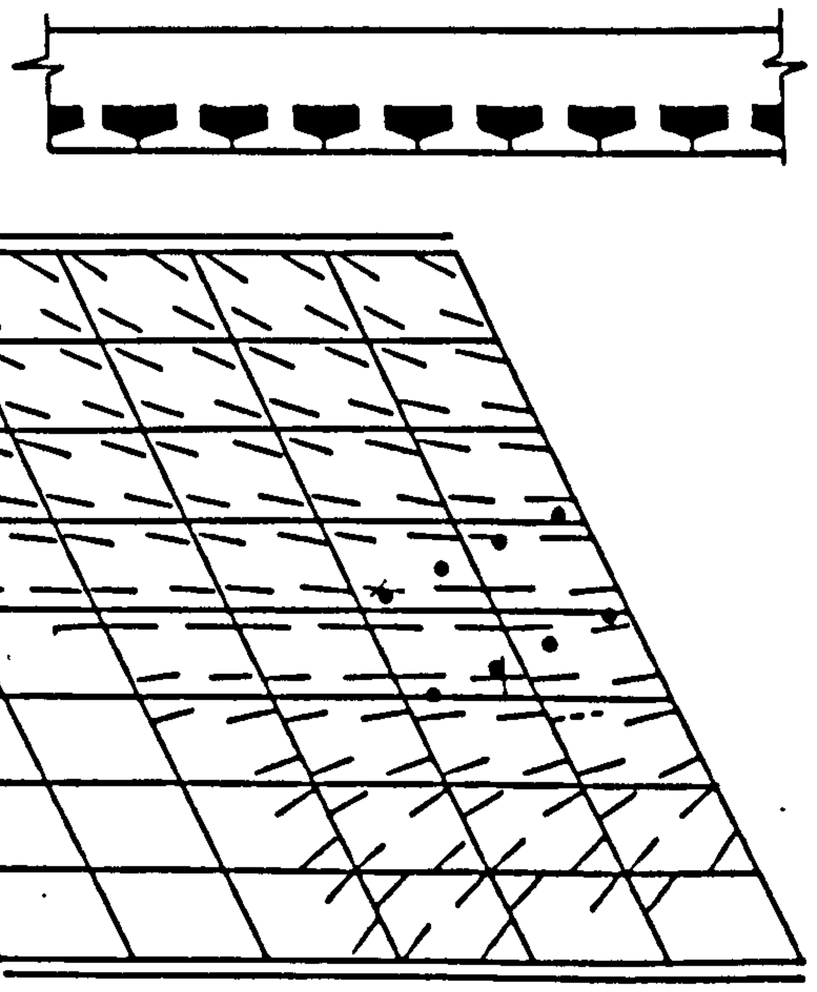

PLATE BOTTOM LAYER

FIG. 10.15. CRACK PATTERNS OBTAINED FROM THE NFES ANALYSIS OF MODEL 1

experiment are shown by cross hatching in the experimental plot of Figure 5.9. No indication is given on the analytical plots of the state of the concrete in compression.

The 'tearing' type cracking that was apparent on the top surface of both models during testing, and which has been more fully described in Chapter 7 Section 7.3, can be seen on the crack pattern plot of Chapter 5 Figure 5.9. The nature of this tearing cracking does not allow easy identification of the directions of the principal strains. Comparison of Figure 5.9 and Figure 10.16 reveals that where the experimental tearing cracks appear, the analytical cracks form at a small angle to the beam axis, generally between 10° and 40°. From Chapter 7 Section 7.3 and Figure 7.16 it can be seen that for a stress ratio (R) between -8 and -3 and for an angle of friction of between 40° and 60° then one would expect the tearing type cracking to become continuous again when the angle between the crack direction and the beam axis is in the range 35° to 55°. From the earlier comparison between the experimental and analytical crack pattern plots it was deduced that the tearing cracks became continuous again at a principal angle of approximately 40°.

The analytical soffit crack pattern that is shown in Figure 10.16 agrees closely with the experimental pattern of Chapter 5 Figure 5.8. This is surprising since the experimental plot refers to the soffits of the prestressed beams whereas the analysis refers to the bottom of the in-situ concrete. Therefore one would expect the prestress to bias the crack direction towards the beam axis. If one examines Appendix 5.3, then from the soffit strain gauge readings of Table 7, at load level 11, where all loading except HB has been applied, the soffit strains in the direction of the beams were approximately 100 $\mu\epsilon$. Foil strain gauges will almost certainly fail after concrete

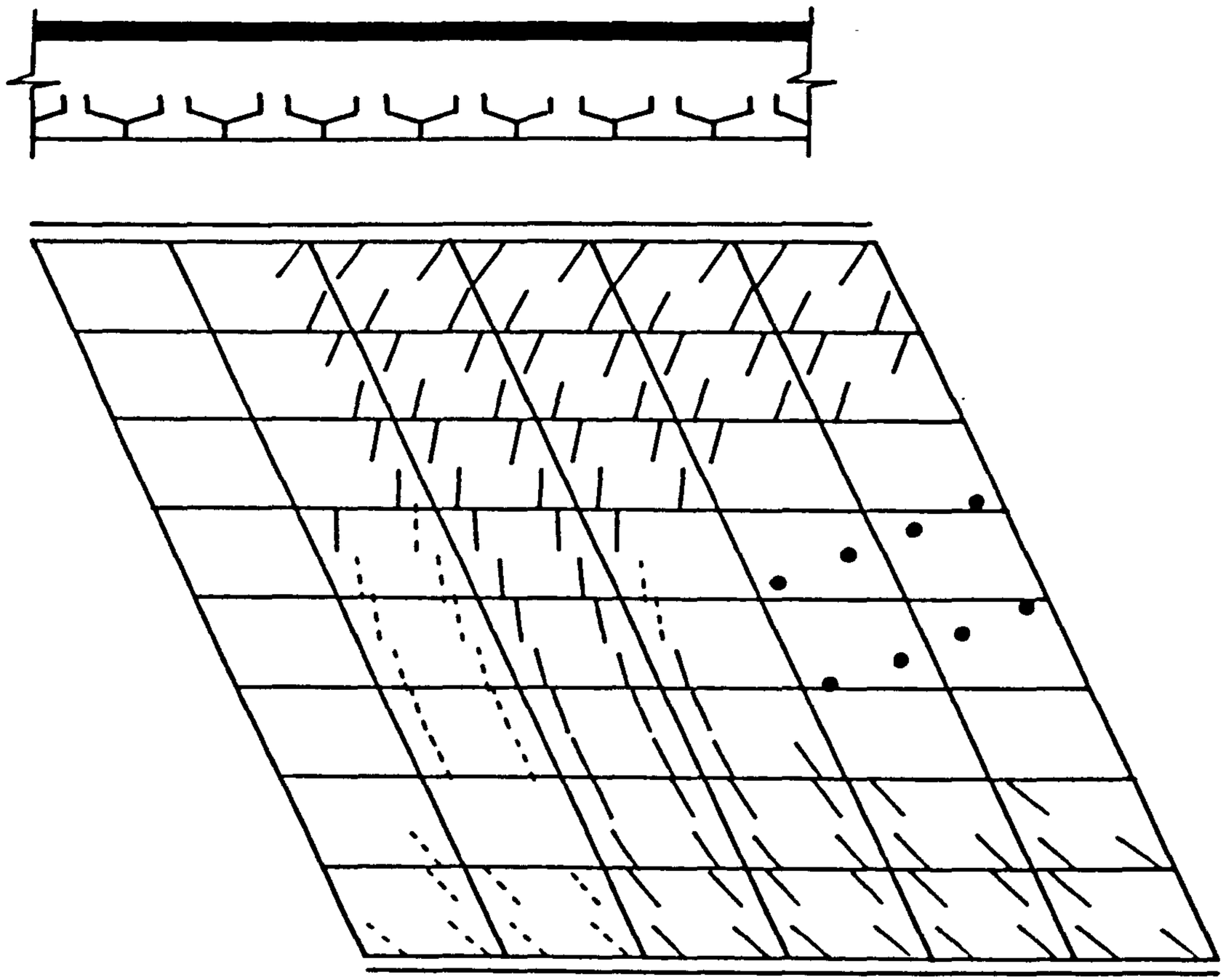

PLATE TOP LAYER

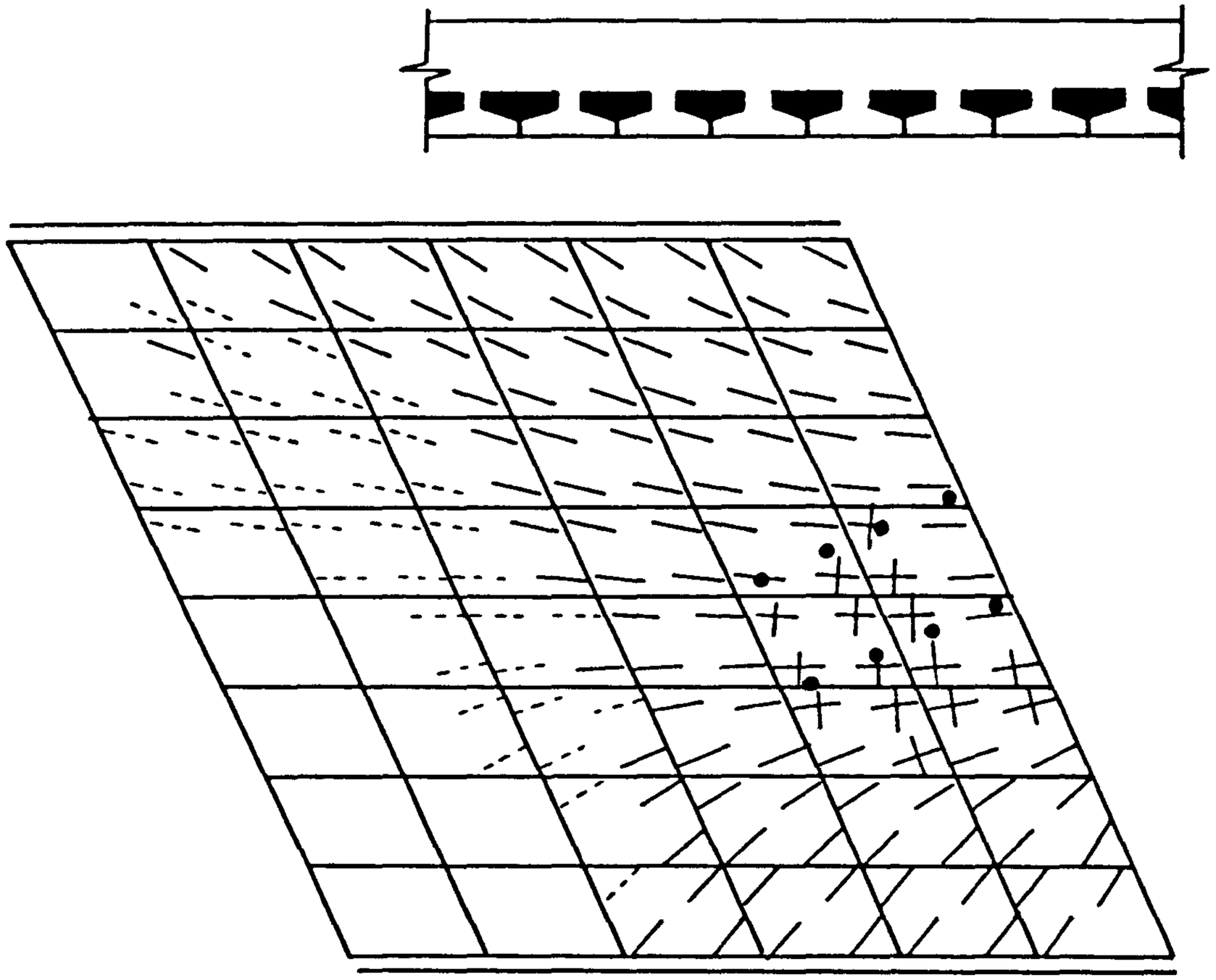

PLATE BOTTOM LAYER

KEY :-

LOADING TYPE: Density Correction loading applied at 'wet' stage

MATERIAL TYPE: 2 Segment concrete tension curve. (see Fig. 10. 4.)

LOAD LEVEL: Full HA etc. 2·51 x ULS HB Bogie

—— crack opening

+ orthogonal cracks

- - - crack closing

FIG.10.16. CRACK PATTERNS OBTAINED FROM THE NFES ANALYSIS OF MODEL 1

cracking and therefore from Appendix 5.3 Table 7 it can be deduced that cracks occurred at tensile strains of approximately 400 $\mu\epsilon$. This value is supported by the longitudinal section tests of Appendix 5.1 where, from the load deflection response and the de-mec strain reading it can be deduced that cracking occurred at beam soffit strains above 450 $\mu\epsilon$. For the physical test, assuming an 'E' value of 35800 N/mm^2 for the precast concrete and that the principal strain angles under the HB bogie at the time of precast concrete cracking were at a small angle to the beam axes, then the stress increment required above the load level 11 value to cause cracking was 35800 x 300 x 10^{-6} = 10.74 N/mm^2. With a tensile strength of 3.9 N/mm^2 (Chapter 5 Table 5.6), the stress increment required to place the beam soffit in a state of zero stress is 10.74 -3.9 = 6.84 N/mm^2.

The biasing effect of this prestress on the initial crack directions is severely reduced by the discontinuity in transverse stress between adjacent beam flanges. Moreover, the prestress delays cracking which results in the increased dominance of the HB Bogie in the loading regime. This will cause the initial crack directions to tend toward the principal directions of the stress increment resulting from the HB Bogie application.

In the majority of the NFES analyses the density correction was applied at the 'wet' stage. Thus, the analytical cracks form in the principal stress directions resulting from the load applied since the beginning of the 'hard' stage. With the exception of the small HA load, only HB Bogie loading is applied during the 'hard' stage and thus the analytical cracks will tend towards the principal directions of the HB Bogie load increment. These factors result in the similar analytical and experimental soffit crack patterns.

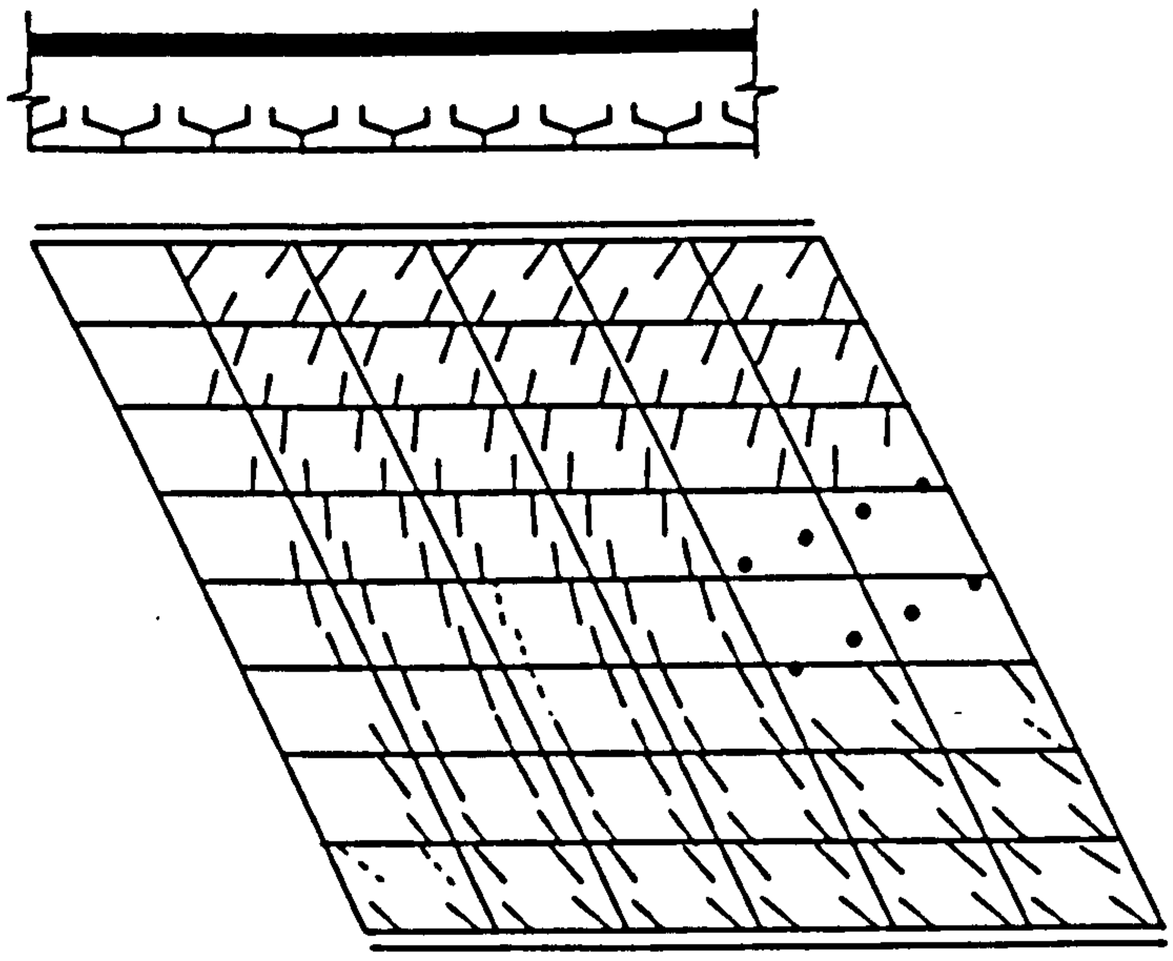

PLATE TOP LAYER

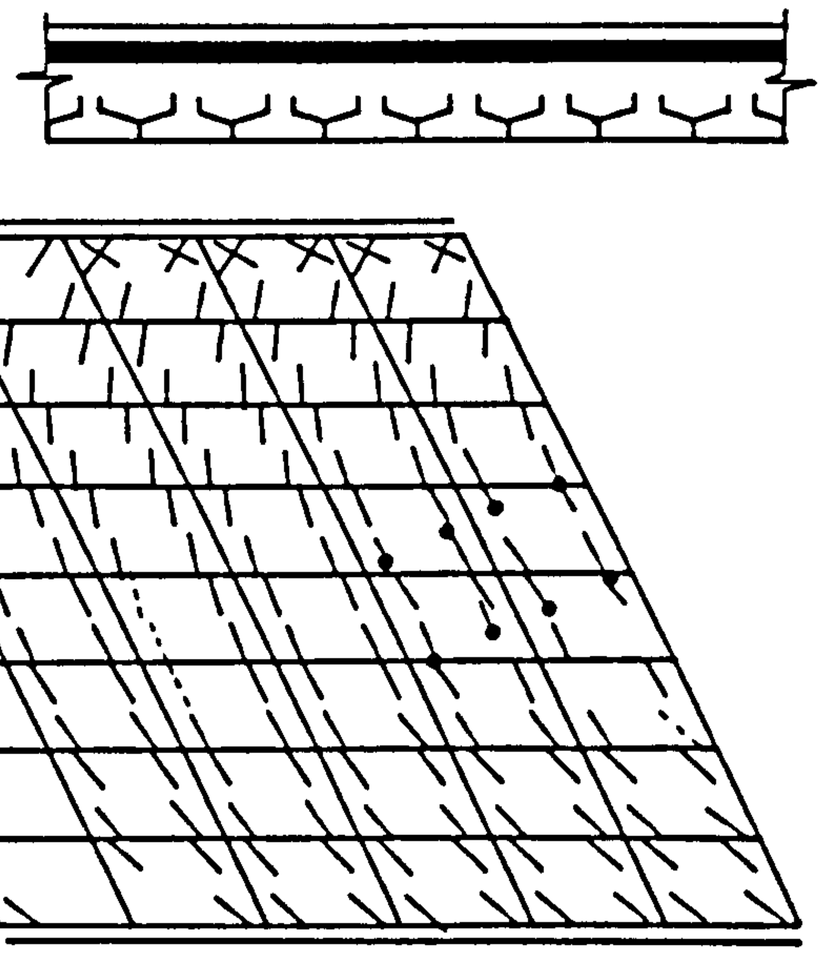

PLATE LAYER 2

KEY:-

LOADING TYPE: Density Correction loading applied at 'wet' stage

MATERIAL TYPE: 2 Segment concrete tension curve. (see Fig. 10.4)

LOAD LEVEL: Full HA etc. 2·95 x ULS HB Bogie

—— crack opening

+ orthogonal cracks

--- crack closing

FIG. 10. 17. CRACK PATTERNS OBTAINED FROM THE NFES ANALYSIS OF MODEL 1

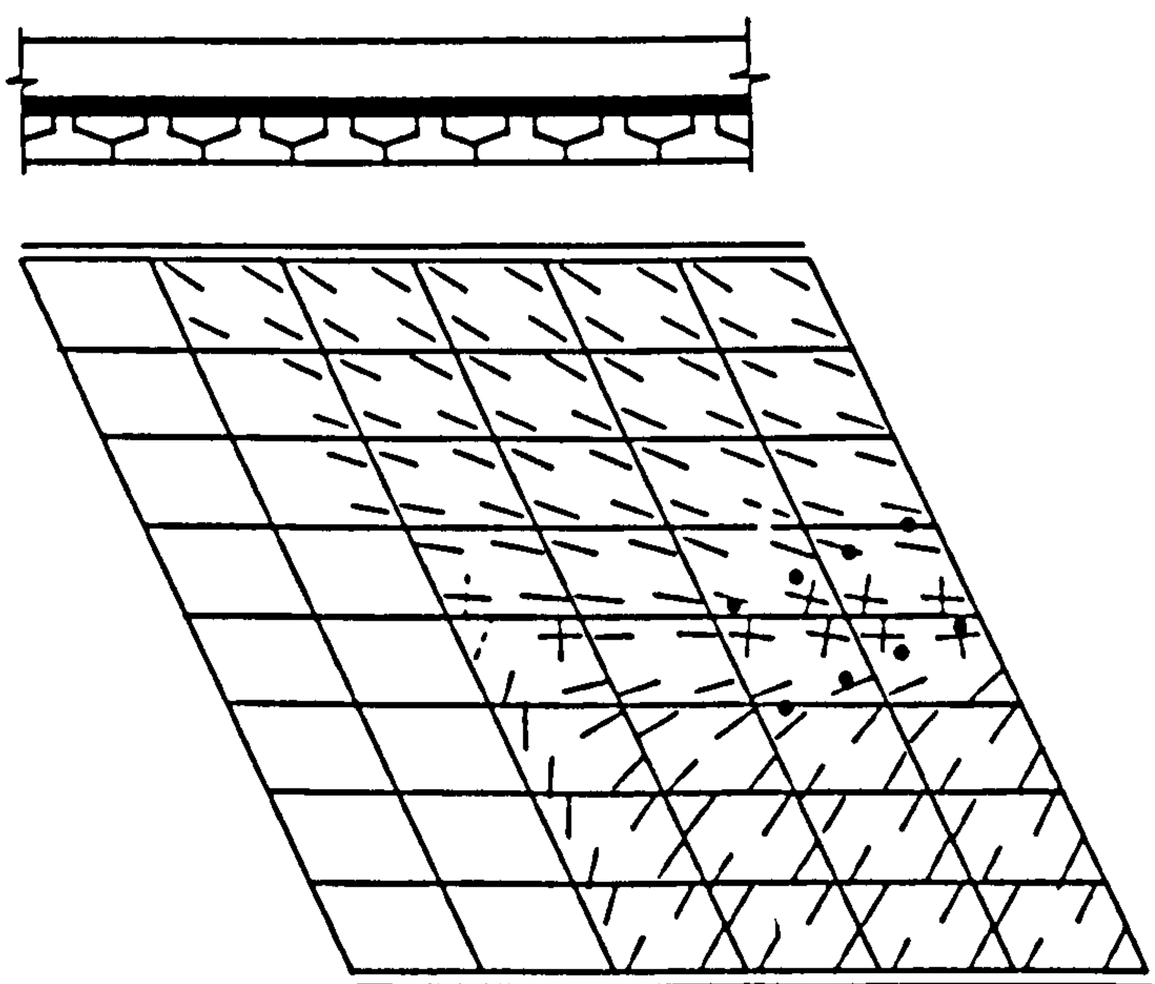

PLATE LAYER 4

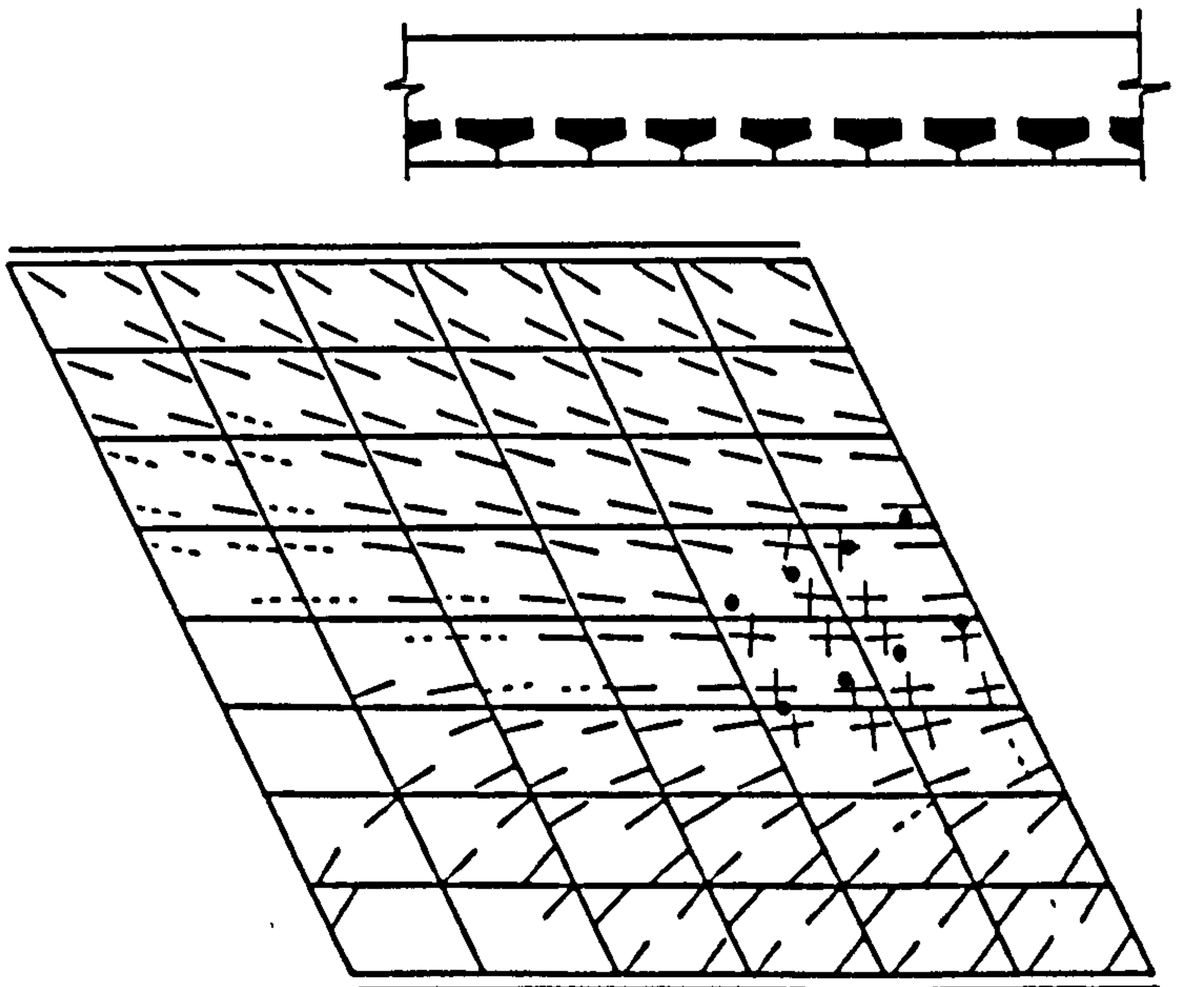

PLATE BOTTOM LAYER

FIG. 10. 18. CRACK PATTERNS OBTAINED FROM THE NFES ANALYSIS OF MODEL 1

It would appear that at the time of the model 1 test the prestress in the beam soffit was 35800 x 400 x 10^{-6} - 3.9 = 10.42 N/mm^2, this equates to a loss of approximately 53%. However, this calculation assumes an 'E' value of 35800 N/mm^2 and a tensile strength of 3.9 N/mm^2.

From the crack pattern plots of Figure 10.16. It can be seen that the analysis predicts significant double cracking under the HB bogie. It can be observed from the load deflection plot of Figure 10.11 at a load factor of 2.51 that the displacement level is relatively small while the crack pattern plots indicate a considerable number of closing cracks. This effect is most probably due to the redistribution of moments caused by the top cracking in a span wise band at mid-width. Thus the material activity is being polarised in the half of the deck that contains the HB bogie.

The final set of crack patterns, at a load factor of 2.95 are shown in Figures 10.17 and 10.18. By this time it can be seen that the cracking is very extensive on all of the plotted layers. The top layer pattern covers the complete model area except for a thin band along the unloaded free edge and the area around the HB bogie. It will be noticed that the NFES crack pattern is more extensive than the experimental one, however, many of the NFES cracks may correspond to experimental cracks that were not visible to the naked eye or that closed completely when the slab was unloaded to allow the crack pattern photographs to be taken and, therefore, did not appear on the experimental crack pattern plots. As far as crack direction is concerned, there is good agreement between the experimental and NFES patterns.

It will be noted that orthogonal cracking is predicted in the crack pattern plot of layer 2 along the instrumented support line. This would indicate that the analytical NA in this area is particularly high. It is interesting to note that the majority of cracks that were closing at the previous load level have become active again at this load level. Unusually the few closing cracks that were present appeared to be isolated amongst other active cracks and this phenomenon may be a function of the concrete tension stiffening and unloading curves.

The bottom layer pattern is similar to that at a load factor of 2.51, although the crack pattern has become more extensive in the less-loaded obtuse corner. The formation of a yield line pattern is not strongly suggested by the NFES analytical crack pattern plots, however there are indicators of a possible 'Y' shaped pattern.

10.3 REFERENCES

1. CRISFIELD, M.A., 'A Four-Noded Thin-Plate Bending Element Using Shear Constraints - A Modified Version of Lyons' Element', Comp. Meth. App. Mech. Eng. 38 (1983), pp 93-120.

2. TIMOSHENKO, S., 'Strength of Materials Part II Advanced', Van Nostrand, 1958.

3. 'Steel Designers Manual', Constructional Steel Research and Development Organisation, Granada Publishing, 1978.

4. CRISFIELD, M.A. and WILLS, J., 'Solution strategies of softening materials', Abstracts from the First World Congress on Computational Mechanics, Volume 1, University of Texas at Austin, September 1986.

5. CRISFIELD, M.A., 'A Fast Incremental/Iterative Solution Procedure that handles Snap-Through Computers and Structures', Vol. 13, No. 1-3, 1981, pp 55-62.

11. CONCLUSIONS AND RECOMMENDATIONS FOR FURTHER WORK

11.1 Conclusions

11.1.1 Composite construction

1. It is impossible to give firm guidance as to when concrete composite construction will be most economic. In 1973, a survey believed to be mainly of bridges with little skew, concluded that for spans of up to 18 m, composite construction often provided the cheapest solution. Optimization calculations based on material content or cost are not likely to be helpful in determining parameters, as the total cost is likely to be governed by particular site and construction conditions. By its nature, composite construction is particularly economical with falsework, and gaps can be spanned quickly.

2. Composite construction exposes high quality, factory made prestressed concrete on the soffit and is therefore likely to be durable.

3. Composite construction has been used for bridge decks with up to 15° of skew since at least the early 1950's. Some of the early structures were prestressed transversely, although many had little transverse reinforcement.

11.1.2 Analysis and design

4. With the introduction of the design abnormal load vehicle in the mid-1950's, analytical methods to predict the distribution of working loads in bridges were developed. Their suitability for use in predicting short term deflection distributions of

composite construction bridge decks were verified against data from full scale tests.

5. Tests to destruction on models of composite decks were first conducted at the C & C A in the late 1950's. Although scale models and loadings were not used, the results suggested that considerable transverse reinforcement would be required to mobilise the full, potential cross-sectional strength.

6. There are no directly relevant test data on interface shear behaviour of composite construction bridges. Although transverse bending stiffnesses may be calculated using the assumption of zero tensile concrete strength, the calculation of torsional parameters, and indeed the use of elastic analysis presuppose integral composite action.

7. Composite construction was, naturally, included in the range of Standard Bridges prepared by the Department of Transport. The reinforcement for these structures was specified to be parallel to the deck sides. An orthogonal arrangement is preferable for both stiffness and strength provision, but the loss of structural efficiency of non-orthogonal steel for plan shapes with a skew up to 25° is small and the arrangement simplifies construction.

8. The policy of treating reinforced and prestressed concrete as distinct structural systems for limit state design produces considerable conceptual difficulties for a designer considering a hybrid structural system such as composite construction.

For a reinforced structure, the ultimate limit state is generally considered for design. However, the current stress limit checks

effectively rule out consideration of moment redistribution. In effect, for new designs, linear elastic analyses are required for both the SLS and the ULS.

For prestressed concrete, design is governed by SLS criteria. For an ultimate load analysis; either the yield line method could be used, in which case the prestress would be ignored; or a lower bound plastic analysis would be used, with the prestress treated as an applied load.

From the limited study of current design methods conducted, it would appear that initial design would be based on linear analyses, using specified stress limits. A check would then be made on sections normal and parallel to the beam axes at the ULS. For the linear analyses at the ULS, it is advantageous to treat transverse sections as being cracked.

9. In reality reinforced, and fully prestressed concrete are not distinct, but are extremes at either end of a complete spectrum of concrete structures. Adoption of continuous criteria would be more logical and would lead to more rational design procedures, especially for shear and hogging over supports of continuous decks.

10. BS5400 does not cater for some structural features specific to composite construction. Interface shear is not checked. Transverse shear is treated in an empirical manner which presumes that the principal shear acts on sections orthogonal to the beam axes. As the prestress force is unidirectional and not in a principal direction, particularly when there is skew, the amount of prestress to limit inclined principal tensile stresses can be

prohibitive. If strictly applied, the code would limit the use of composite construction to decks with a very small angle of skew. The test results for the second model suggest that this is an unnecessary restriction on the freedom of a designer to provide the most economical solution.

11. Design of both the bridge decks studied was governed by SLS criteria for the outer-most prestressed beam. Once a beam and the prestressing details had been selected, the quantity of transverse reinforcement was determined using the Wood-Armer equations. Specifying cracked section properties in the transverse direction for the linear analysis required to predict moments reduced the amount of reinforcement significantly.

12. Design at the ULS can be based on yield line analyses. At failure, not all of the reinforcement crossing the theoretical yield lines of the models was in fact yielding. Because a relatively large number of bars cross a yield line, the theoretical factor of safety obtained on the basis of all steel having the characteristic strength is higher than that of a member with few bars crossing a yielding section. The use of a γ_{f3} factor greater than unity cannot be justified when a single yield line across a deck is considered, as the analysis can be based on statical principles.

11.1.3 Large scale model testing

13. The costs of testing increases logarithmically with scale. Ideally, tests should be conducted at full size. Compromises are inevitable when scaling is introduced. At the 1:3.5 scale used, specially strengthened and extended testing rigs had to be designed.

Although the major structural properties were represented, some doubt remains over the modelling of the prestressing, particularly with regard to bond after cracking and with regard to the behaviour of the precast - insitu concrete interfaces. On the whole, however, the data obtained provide the most reliable information currently available on this form of construction.

14. Subsidiary testing of: bearings; concrete and steel specimens; bond action; longitudinal and transverse slab slices and examination of concrete cores provided vital information needed to interpret the behaviour of the models. Such testing is time consuming and expensive, but contributed significantly to the success of the project.

11.1.4 Data collection

15. The specially designed automatic data collection system worked well and the procedures developed can be generally recommended.

16. The least satisfactory part of the data collection was the gathering of concrete tensile strains. Before cracking, strains due to loading are small. After cracking, they are dominated by the spacing and vagaries of local crack directions. Also, because of time constraints and the spasmodic nature of crack propagation, obtaining an accurate overall snapshot, at an instant of time and at a specified load level, was often very difficult. The only practical way in which cracked concrete tensile strains can be collected is through the use of a Demec gauge. From the experience gained on the present study it is recommended that Demec points are positioned in a systematic way and that they are continuous in orthogonal directions. In this

way it is unlikely that cracks will miss the Demec gauge lengths. If useful concrete tensile strain data are required, then a large proportion of the time available will have to be allocated to this aspect, since a large number of Demec points will be required. Copious amounts of data will be produced and this will require careful and detailed interpretation after completion of a test. It is recommended that for large scale tests an electronically readable Demec gauge is the most time efficient method for collecting the strain data. Despite the vast quantity of strain data gathered in this project, little of it was useful in assessing the structural response.

17. With hindsight, more stations would have been monitored for displacements. Values of displacements, after cracking, are difficult to interpret. This is due to the accumulated effects of different load positions, and sustained and cyclic load effects on material properties. However, the displacement readings gave a very clear picture of the curvatures in the slab and of the division into active and relatively 'rigid' regions as failure was approached.

18. Strain gauges attached to reinforcement and prestressing tendons gave useful information. However, precise interpretation of the stress distribution over a section is made difficult by the presence of cracks, which were inclined to the steel directions, and by the need to assess tension stiffening effects in the cracked concrete.

19. Reaction readings provided useful information on the changing load paths in the models. If useful reaction data are to be obtained then the model supports should be carefully designed and

verified before the initiation of a test. It is important to ensure that the model supports are representative of full size.

20. Visual inspection and recording of crack growth and separation provided essential, useful information which could be correlated with the numerical transducer readings during processing of the test results and the assessment of the structural response.

21. Visual inspection of cores provided vital information on the nature of cracking. Tearing cracks in the top layer of insitu concrete were not anticipated, but their relationship to separation of the insitu and precast concretes was clearly demonstrated. The cores also showed that shear cracking in adjacent insitu and prestressed concretes were at different inclinations, indicating that their formation was associated with separation. The relative rotations of parts of the slab were also clearly distinguishable in the cored specimens.

The cores showed that the concretes were well compacted and that the ducts for the transverse reinforcement were well filled. At sections where there was no separation, it was often impossible to distinguish between the insitu and precast concretes. The cores also allowed the final steel positions to be checked.

22. Loading was applied at first to prescribed load levels, but control was later switched to displacements. This was essential to examine the development of failure.

11.1.5 Model test results

11.1.5.1 Model 1

23. Application of SLS loadings produced no visible cracking and the structural response was essentially linear and elastic.

24. 45 units of HB loading, factored for the ULS, in an edge lane, with other loads also factored for the ULS produced no visible cracking.

25. A 50% increase in the HB loading produced narrow, well distributed cracking in the edge insitu concrete outside the edge beam nearest to the bogie.

26. A 100% increase in the HB bogie load produced well distributed cracking in the precast concrete of the soffit, in the centre of the outer lane. When the load on the bogie was removed, a permanent deflection of about only half a millimeter was recorded. Reloading produced an essentially linear response.

27. At higher bogie loads there were plastic strains and the load-displacement response became highly non-linear. The model sustained 3.27 times the ULS factored, 45 unit, bogie load.

28. This high value is due to the design of all precast beams to the SLS requirement of the most highly stressed edge beam, and the provision of lower bound transverse reinforcement to prevent section failure under any loading configuration. Although much higher than the design ultimate load, this factor is less than the value of 4.33 predicted by yield line theory. The main reason for this is that it is unlikely that all of the

reinforcement crossing the theoretical yield lines was in fact yielding.

29. When the bogie load was at about twice the ULS design value, the bearing reactions indicated a change in load path. The rate of increase of loading on the most heavily loaded obtuse corner bearing reduced, and load was shed from the next four bearings, to bearings in the centre of the support line. This behaviour is believed to be due to separation of the insitu and precast concretes. At higher load levels the slab lifted off the obtuse corner bearings.

30. Separation of the concretes was not anticipated and was first noticed on the end elevations when the bogie load had reached about 3.25 times its design ULS value. Because the top surface was covered with dead weights, the associated tearing cracks in the top layer of insitu concrete were not noticed until after completion of the testing programme. Although modelling was made as realistic as possible, it is not possible to say with certainty whether this type of action would occur with full sized construction.

31. Tests on models of transverse strips of the model deck indicated excellent bond between the insitu and precast concretes and between the insitu concrete and the reinforcement. In these tests, the vertical concrete interfaces were subjected primarily to tension. In the bridge decks, the state of stress on the interfaces would involve shear resulting from torsional moments and changes in the bending moment intensity, in addition to the tensile bending stresses, and no test data are known concerning strength criteria for these states.

32. Tests on models of longitudinal strips of the model deck indicated that those with insitu concrete confined by adjacent prestressed beams were stiffer than those with a single prestressed beam surrounded by insitu concrete. The tensile stiffness of concrete sandwiched between prestressed beams was largely restrained until cracking of the prestressed beams. Internal stresses in the insitu concrete before loading arise due to restraint of early thermal movement (tensile) and creep of the prestressed beams (compressive). They cannot, therefore, be calculated with any degree of certainty. There was no separation at the precast/insitu interfaces and visible cracks were continuous across the interfaces.

33. The tests on model 1 showed that, for decks with skews of up to 25°, current design procedures lead to well behaved structures with a considerable overload capacity. Failure is complicated by the nature of the composite construction and this is not addressed in the current code of practice (BS 5400).

34. Although the failure mechanism was complicated and involved a large shear crack, crushing of concrete and separation, it had a ductile nature.

35. The reasoning behind the code clauses to determine shear capacity is not readily discernible. Unlike the treatment of slabs, the length over which shear forces are to be averaged is set - at one beam flange width. On this basis, the maximum average shear stress on an equivalent reinforced concrete section was 2.65 N/mm^2. The calculated capacity of the shear reinforcement (which would have been ineffective according to BS8110 because of the

shallow depth) is equivalent to 0.31 N/mm^2. The net average shear stress on the composite section at failure was, therefore, far in excess of that allowed by the code.

36. Further studies to determine a rational method to predict the shear capacity and method of collapse in composite concrete bridges are needed.

11.1.5.2 Model 2

37. Application of SLS loadings produced minor cracking of the free edges, but the response was essentially linear and elastic.

38. Application of ULS loading, with 45 units of HB bogie loading centred in a design lane produced only minor cracking in the insitu concrete along both free edges. A few cracks were also noticed on the top surface above the support lines. The tangential structural response was essentially linear, but there were permanent deflections. These may have been due to inelasticity of the bearings or to transverse cracking.

39. Cracking of the outer prestressed beams was detected with twice the design ULS loading on the HB bogie. However, due to a power supply failure to the load control equipment, these may have formed at any load between 2 and 2.4 times the design load intensity. Structural response was still, essentially, linear.

40. Increasing the load on the HB bogie to 4 times its design value introduced further cracking and non-linear response. Due probably to variation in the level of prestress and concrete tensile strengths, the spread of soffit cracking was not uniform. However, at the higher load levels, the soffit crack pattern had

the appearance of continuous cracking across the flange gaps and it is reasonable to conclude that composite action was maintained at this stage.

41. As is to be expected with a slab having 40° of skew, much of the reaction was found to be concentrated on the obtuse corner bearings. At this stage, nearly a quarter of the total load was carried by the four bearings in the obtuse corner of the lane carrying the HB bogie.

42. For the test to failure, the HB bogie was moved closer to the free edge, and the lane configuration was different to that used for the design of the bridge. With the bogie load at 4.32 times the design intensity, the most heavily loaded obtuse corner bearing carried 15% of the total applied load. A shear crack was apparent in the insitu concrete of the free edge, but it did not pass through the beam flange.

A few new cracks formed on the beam flanges which intersected existing cracks. These suggest that good bond between the prestressing strand and the beam concrete existed and that the load path had changed.

43. Failure was progressive and ductile. When the bogie load reached five times its design intensity an acute corner lifted off its bearing.

44. Crushing of concrete in the vicinity of the HB bogie was observed at about five and a half times the design loading. At this stage tearing cracks were observed, along the beams, over the central

part of the deck and it was concluded that composite action was breaking down.

45. With the bogie load at about six times its design value, the shear crack in the insitu concrete of the edge beam had a vertical displacement of about 3 mm, and a horizontal relative displacement of about 2 mm at the soffit, with no relative horizontal displacement at the top. Later inspection of a core taken from the slab showed separation of the insitu and precast concretes and shear cracks at different inclinations in the two concretes. The load carrying mechanism in the obtuse corner region could not be deduced from the data. From visual observations, it was concluded that load was probably transferred transversely by the insitu concrete acting as struts between the upper and lower flanges of adjacent beams.

Although the obtuse corner bearing attracted a slightly increasing proportion of the total load up to failure, the adjacent bearings shed load after the HB bogie load reached four times its design value. It was concluded that this was due to the breakdown of composite action.

46. The maximum average shear stress on the edge beam, considered as a reinforced concrete section, was 4.03 N/mm^2. This is much higher than an isolated beam could have withstood and emphasises the need for a more rational approach to design against shear failure.

47. The deck was not capable of supporting any additional load as the displacement at the HB bogie was further increased. The load carrying capacity began to reduce and the test was eventually

stopped when at least two tendons were heard to rupture. The failure is very complicated and not anticipated in current codes of practice.

11.1.6 Analytical techniques

11.1.6.1 Non-linear finite element analysis

48. Non-linear analysis would appear to be a logical choice for the assessment of a structure at the actual ULS. Non-linear analysis takes into account the large redistribution of moments that occurs as failure is approached.

49. The models examined during the present study were over strong by load factors of 3.3 and 6.0 on the HB loading for models 1 and 2 respectively. Therefore, large non-linear effects were not apparent at the design ULS.

50. For realistic shear distributions to be obtained it is essential that the supports are modelled accurately. For the analysis of reinforced concrete slabs, the relatively few physical supports allow each physical support to be modelled by a discrete analytical support. This would be the preferred approach for composite slabs, however, this would require very fine meshes.

51. The element shape functions dictate how the support forces are distributed in the adjacent elements. For the finite element model to produce realistic stress predictions close to the supports this factor must be taken into account.

52. The supports in a composite slab are more akin to a line support than to discrete supports. Therefore, a method was developed for the finite element model to be supported on a line support and

not discrete supports. This approach gave encouraging results but requires further investigation.

53. The non-linear analysis of composite decks is complicated since the deck is constructed of two separate materials, one prestressed and one not. For most structural states these materials act compositely. A further complication is the gap that is generally present between adjacent beam flanges.

54. A numerical model for the analysis of composite bridge decks was developed during the present study. This model gave good agreement with the experimental response, however, further investigation and refinement is required.

55. It is difficult to justify the adoption of a complex bi-axial material model for concrete, since the behaviour of reinforced and prestressed concrete slabs is governed by concrete cracking and steel yielding. A simple and efficient uni-axial material model was selected for the present study. This philosophy allows the available computational resources to be reallocated so that finer meshes can be used. Since cracking is so fundamental to the behaviour of concrete slabs further development and refinement of this aspect of the material model is required.

56. In a physical slab the material properties will vary over the structural domain. To model this a method was developed in the present study to apply statistically varied material properties over the analytical structure. It was found that the adoption of this approach produced significantly different results for areas of constant stress. The adoption of variable properties resulted in better predictions of the displacement at failure.

57. Analyses of model 1 were carried out using an alternative non-linear program named NFES. These analyses allowed the effect of variations in torsional stiffness to be investigated. it was shown that the adoption of a torsional stiffness for the precast beams in the deck which was equivalent to the torsional stiffness of an isolated beam produced reasonable predictions.

58. The NFES program analyses allowed the implications of the fixed crack direction model to be evaluated. The investigations revealed that where the loading regime changes significantly as the structure moves towards failure, the failure state is unlikely to be modelled correctly by the fixed crack model and high failure load predictions will probably result. The loading regime changes significantly with 'real' bridge slabs where the loading regime which causes initial cracking is generally dominated by UDL loading. As the structure moves towards failure, the HB bogie load increases in dominance resulting in a significantly different overall loading regime.

59. During all the non-linear analyses conducted for the present study the power of restarting and program intelligence was clearly apparent. Restarting allows a complete analysis to be divided into a set of smaller runs. This results in lower costs for the analysis and also allows the solution method to be modified in the light of the developing structural behaviour. Programming limited intelligence into the analysis program allowed the solution method to be modified by the program as the structural response varied during a run. This resulted in lower costs since the program was able to achieve convergence when otherwise it would not.

60. During the present study new convergence criteria were developed for non-linear analyses. These criteria were shown to be effective for slab analyses where one attempts to compare residual moments to direct forces when checking for convergence.

61. Sophisticated solution procedures were adopted in the present study and these allowed the full structural response up to failure to be investigated.

11.1.6.2 Yield line analysis

62. A yield line failure mechanism was not apparent in either slab. Disintegration of integral action and failure of steel tendons and concrete occurred before a mechanism formed.

63. Resolving moments of resistance requires a constant lever arm in all directions. The depths of the longitudinal prestressing and transverse reinforcing steel are significantly different. The gaps between the beam soffit flange makes resolution of hogging moments of resistance conceptually difficult.

64. The yield line method cannot be recommended for concrete composite construction bridges with a significant skew.

11.1.7 Deflection profile predictions

11.1.7.1 Non-linear finite element analyses

65. The analytical deflection profiles for model 1 in the first non-linear comparison, at a load factor of 2.7, are good. The physical model does, however, appear to be more flexible. There is less agreement in the model 2 comparison and again the physical structure exhibits greater flexibility.

66. For the subsequent model 1 deflection profile comparisons, up to failure, there is excellent agreement. The only deviation is close to the unloaded free edge where the experimental profile 'kicks up' but the analytical one does not. This deviation probably results from the allowance of tensile support reactions in the analysis. The analytical boundary condition modelling requires refinement so that tensile reactions are not permitted.

There is poor agreement for the final model 2 deflection profile comparisons where the physical structure exhibits far greater flexibility. The flexibility of the analytical structure may be increased by correct modelling of gaps between beam flanges. The increased skew of model 2 increases the importance of torsional stiffness in the structural behaviour. The increased stiffness of the analytical profiles could be a result of incorrect modelling of this feature and requires further investigation.

67. Variations in fundamental material parameters produced little change in the shape of the deflection profiles.

11.1.8 Reaction profile predictions

11.1.8.1 Non-linear finite element analysis

68. For structural states up to the maximum load the model 1 analytical reaction profiles are in good agreement with the experimental profiles. There is little difference between the linear and non-linear profiles until high displacement levels are reached and the maximum load is approached.

69. For model 2, the magnitude of the obtuse corner reaction is poorly predicted by the analysis for all structural states. For

the comparisons at lower loads, this phenomenon is difficult to explain, but may be connected to the use of relatively few supports. At higher load levels the breakdown of composite action begins and this appears to reduce the magnitude of the obtuse corner reaction significantly in the physical model. This factor no doubt contributes to the poor analytical predictions.

70. In analysis, there are generally fewer supports, which are also at different locations, to those in the physical model. This makes the prediction of reactions and the shear force distribution in a structure difficult. With fewer supports, it is difficult to predict the magnitude of the obtuse corner reaction with any accuracy. For a composite concrete deck, which has many supports, it is probably reasonable to obtain shear forces by averaging over 2 or 3 supports adjacent to the obtuse corner.

71. It is considered that the location of the obtuse corner analytical support is of importance in the prediction of reactions. If possible, it is recommended that the analytical obtuse corner support be placed in the same location as the corresponding physical support. Most analytical obtuse corner supports are located at the corner of the structure which most probably contributes to the poor predictions.

11.1.9 Crack patterns

72. The plotting of crack patterns provides a valuable insight into the behaviour of a structure in a non-linear analysis. The power of this was clearly shown in the present study.

73. Non-linear analyses produce massive amounts of output which has to be interpreted by the engineer. The only practical way in which an overall picture of the structural behaviour can be obtained is through graphical presentation of the data.

11.2 Recommendations for further work

11.2.1 Experimental investigations

1. During the present work very useful data were obtained from subsidiary tests on longitudinal and transverse slices of the model decks. This data could be enhanced by further tests on similar slices but subjected to inverted loading. Thus, the response of composite construction to hogging moments could be investigated.

2. Torsion is fundamental to the behaviour of composite concrete structures. Extremely useful and interesting data could be acquired from tests on slices of the model decks which are subjected to torsional loadings. Comprehensive data could be obtained from a series of tests of both longitudinal and transverse sections of varying widths.

3. The behaviour of composite construction is complex and tests on apparently simple structures, such as slices, can yield complicated failure modes. Tests on typical concrete interface specimens would provide valuable data that could be used in the assimilation of the longitudinal and transverse section test data.

4. Composite construction has the potential to provide the optimum structure for many bridge problems. Further testing of model composite bridge structures is required to increase our knowledge

and understanding of their structural behaviour. The principal criteria in any model test should be the quality and reliability of the data obtained.

11.2.2 Analytical investigations

5. The 'biaxial' beam structural model requires further refinement, especially the treatment of the gaps between adjacent precast beam flanges, before it could be recommended for general use.

6. The behaviour of the concrete material models in the tensile region requires refinement. Cracking is fundamental to the behaviour of most concrete structures and therefore the development of this aspect of the material model should be productive.

7. Further comparisons with other published experimental and analytical investigations are required, before non-linear methods could be recommended for general use.

8. The development and refinement of non-linear solution procedures, such as those contained in the SNAP program, is required to reduce the high cost of a full range non-linear analysis. The viability and accuracy of newer finite elements, which have fewer degrees of freedom and require lower order integration, requires investigation.

9. Informative results could be obtained from analyses of model 2 with the NFES finite element program. These analyses would allow the effect of torsional stiffness variation on the behaviour of model 2 to be evaluated.

PAGE NUMBERING AS ORIGINAL

APPENDIX 9.1 YIELD LINE ANALYSES OF THE MODEL DECKS

Introduction

When assessing the capacity of a composite slab bridge deck, the yield line analytical method may be used. This technique is based on the theory of plasticity, and provides a theoretical upper bound to the load intensity that can be sustained.

There are a number of particular concerns when the method is used for prestressed composite construction. To perform a yield line analysis, it is necessary to derive the moment of resistance of sections on the yield line through resolution of the moments of resistance in the steel directions. To be able to perform this resolution, a constant lever arm is required in all directions. For sagging moments, the effective depths of the longitudinal (prestressed) reinforcement and the transverse reinforcement (which is threaded through web holes above the flanges) are significantly different and, therefore, so are the lever arms. For transverse hogging moments compression between the beam flange sides cannot be expected. The outermost fibres of the compression block are, therefore, at the level of the bottom of the in-situ concrete, whereas the compression block for longitudinal hogging moments is in the prestressed soffit flanges of the beams. The lever arms for the transverse and longitudinal hogging moments can be, therefore, considerably different.

Yield line analyses of Model 1

The purpose of these yield line analyses is to assess the ability of the method to provide an estimate of the ultimate load capacity, by comparing predictions with the test data of model 1. The loading

considered is self weight with density correction and superimposed dead load, factored for the ultimate limit state; one third of the uniformly distributed part of HA loading on lane 3 and the full uniformly distributed part of HA loading on lane 2, both factored for the ultimate limit state; and an HB bogie, with an unknown number of units, positioned in lane 1 as shown in Figure 1.

Loading for test to failure

1. Self weight plus density correction:

   0.0144 x 1.15 = 0.01656 N/mm^2 all over.

2. Superimposed dead load:

   0.00196 x 1.75 = 0.00343 N/mm^2 all over.

3. HA, udl component

   0.00812 x 1.3 = 0.01056 N/mm^2 lane 2, see Figure 1.

4. 1/3 HA, udl component = 0.00352 N/mm^2 lane 3, see Figure 1.

5. HB bogie, lane 1, see Figure 1, wheel load P kN

   Total udl in lane 1 = 0.020 N/mm^2

   Total udl in lane 2 = 0.0305 N/mm^2

   Total udl in lane 3 = 0.0235 N/mm^2

Best estimate of actual section resistances, see Appendices 5.1 and 5.2

M_1 = 132 kNmm/mm, M_2 = -43 kNmm/mm

μM_1 = 34.5 kNmm/mm, $\mu' M_2$ = -9.3 kNmm/mm

The sagging section resistances were obtained from tests while the hogging resistances were derived using actual material properties and partial safety factors equal to unity.

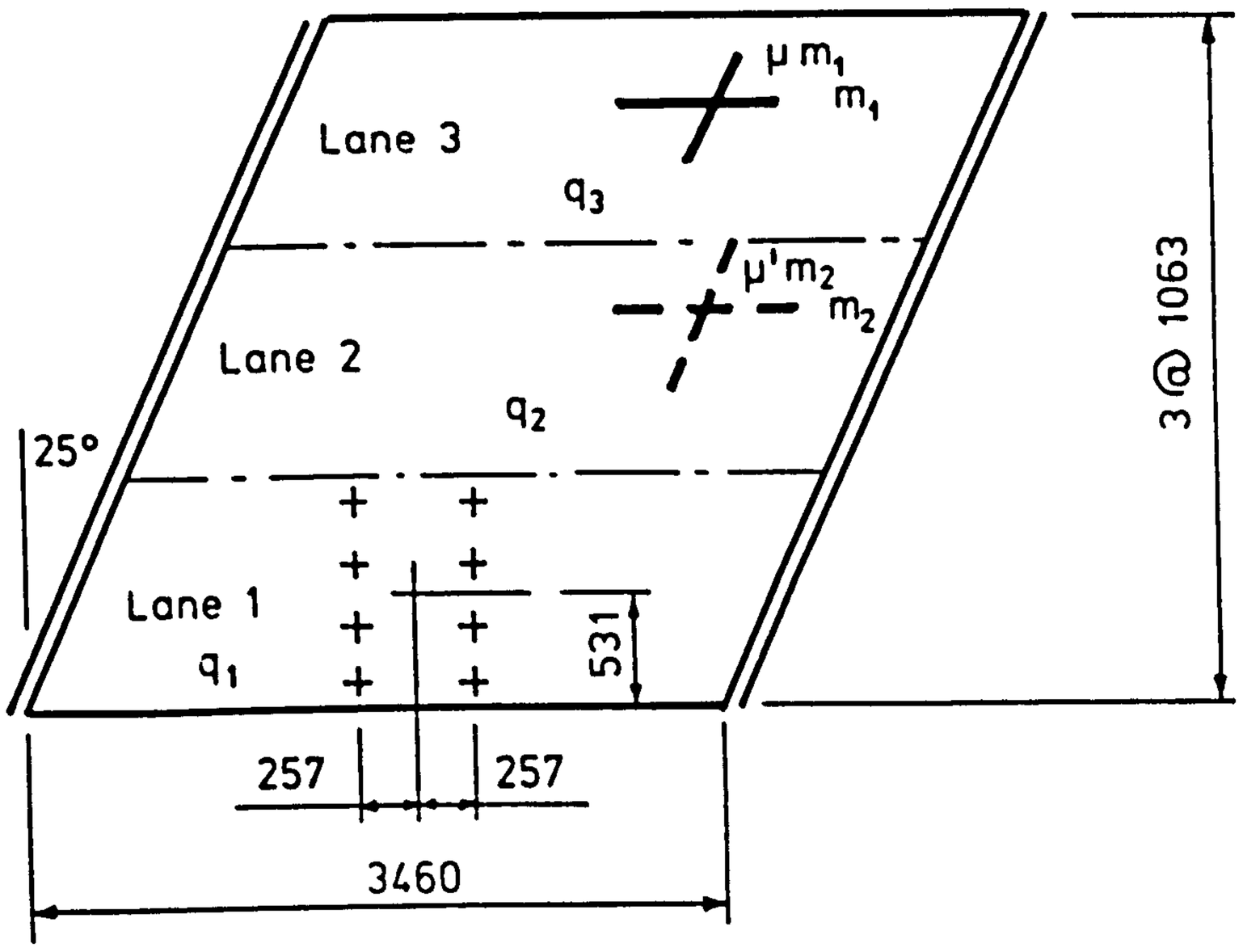

FIG 1. GENERAL ARRANGEMENT FOR THE MODEL DECK 1 YIELD LINE ANALYSIS

Mechanisms

Four different mechanisms were considered for this yield line analysis of model 1. This analysis was carried out to obtain the most realistic estimate of the strength of the model slab. Each of the mechanisms is described in detail below.

Mechanism 1: A sagging yield line following the mid-span section parallel to the supports.

Energy dissipated for a unit displacement of the centre line:

$2 \times M_1 \times \sin^2 65 \times (3190/\sin 65)\ (1/1568) = 486.8$ kN.mm

Work done by udls:

$(0.02 + 0.0305 + 0.0235)\ 3460 \times 1063 \times 0.5 = 136.0$ kNmm

Work done by HB bogie:

Deflection of the centroid of an axle $= \frac{1730 - 257}{1730} = 0.852$

Work done $= 8P \times 0.852 = 6.816P$

Equating: $6.816P = 486.8 - 136.0$

$P = 51.46$ kN

Bogie load: $8P = 411.7$ kN

Scale 45 units of HB bogie load (at $\gamma_{fl} = 1.30$) $= 95.51$ kN

No. of 45 units of HB bogie load $= 4.31$

Testing of model 1 was stopped before all of the tendons on the centre line were yielding. However, a plot of the HB bogie load against deflection, see Figure 5.1, suggested that the load capacity was almost exhausted. A number of yield line patterns involving hogging yielding were, therefore, investigated.

Mechanism 2: Mechanism 2 is illustrated in Figure 2. As the values of three parameters have to be determined, a computer program was written

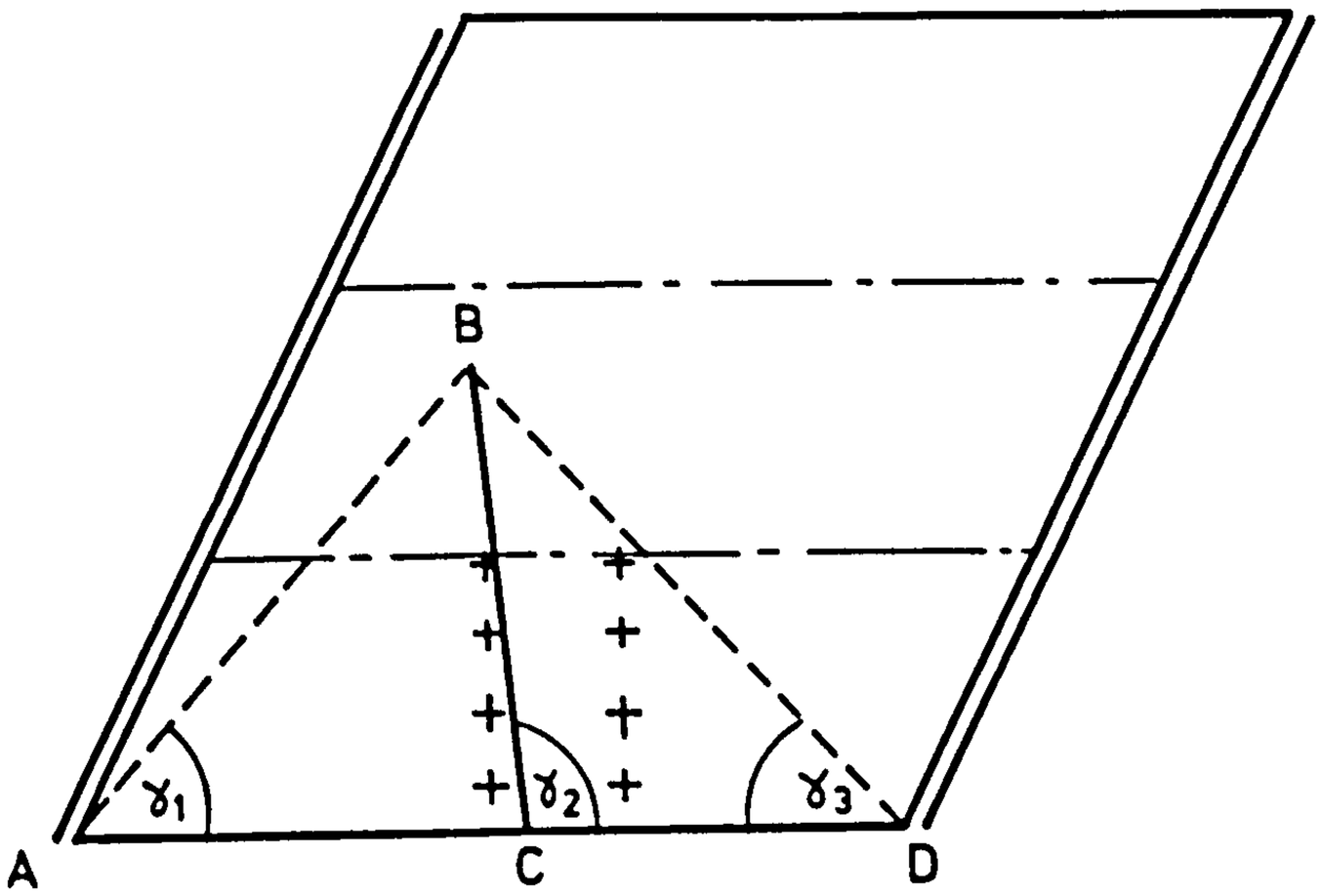

MECHANISM 2

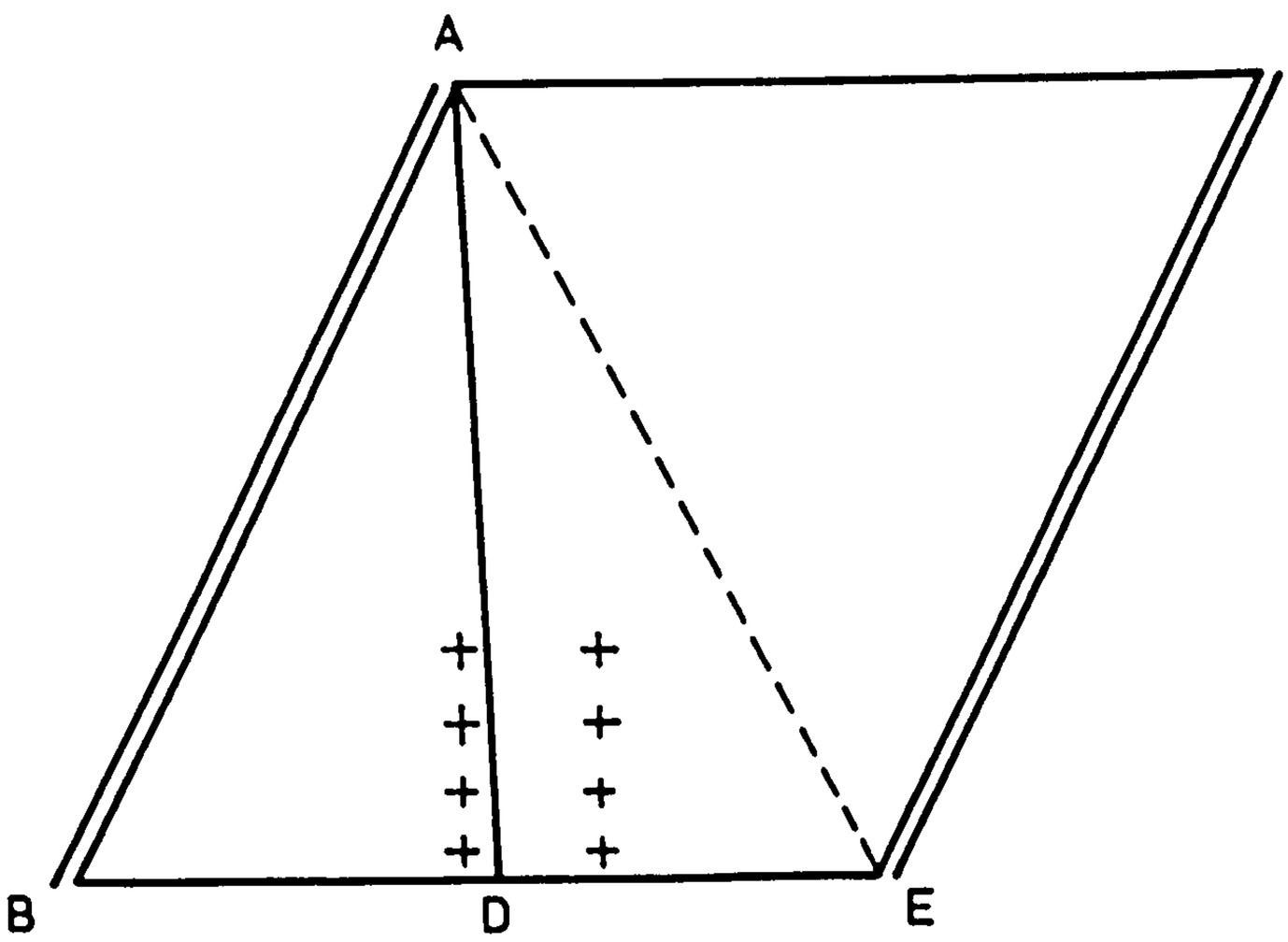

MECHANISM 3

FIG 2. MODEL DECK 1 TRIAL YIELD LINE PATTERNS

and used to obtain the critical yield line locations. The angles to the yield lines were found to be $\gamma_1 \approx 30°$, $\gamma_2 \approx 65°$, $\gamma_3 \approx 51°$. Therefore, BD ≈ 2495 mm, AB ≈ 2415 mm, BC ≈ 1832 mm and AC ≈ 1774 mm. As BC is parallel to the supported edge, only M_1 was considered effective in sagging. The critical value of the bogie load was 601 kN. (Equivalent to 6.3 no. of 45 units of HB bogie load at $\gamma_{f1} = 1.30$)

Mechanism 3: For mechanism 3, the sagging yield line is taken into the obtuse corner opposite the HB bogie (see Figure 2), and only one hogging yield line is considered. The critical value of the bogie load was found to be approximately 870 kN (equivalent to 9.1 no. of 45 unit HB Bogies at $\gamma_{f1} = 1.30$), and so this mechanism is unlikely to form.

Mechanism 4: For mechanism 4, see Figure 3, y was found to be 1032 mm and the critical value of the bogie load was 414 kN (equivalent to 4.33 no of 45 unit HB bogies at $\gamma_{f1} = 1.30$). Agreement of this mechanism with the soffit crack pattern shown on Figure 5.8 of Chapter 5 is not unreasonable, although it is clear that a well defined mechanism was not produced. The sagging yield line parallel to the free edge was not observed and would be above the visible soffit. Cracking on the top surface, as shown in Figure 5.9 of Chapter 5, is consistent with the incipient formation of this mechanism.

The maximum bogie load sustained by the model was 3.26 x 1.3 x 73.5 = 311 kN. Thus the total load on the model at failure was only 75% of the predicted total load. A number of reasons could be postulated for this. The method is an upper bound approach. However, realistic estimates of the plastic section strengths have been incorporated into the analysis, provided all of the reinforcement is yielding. Yield

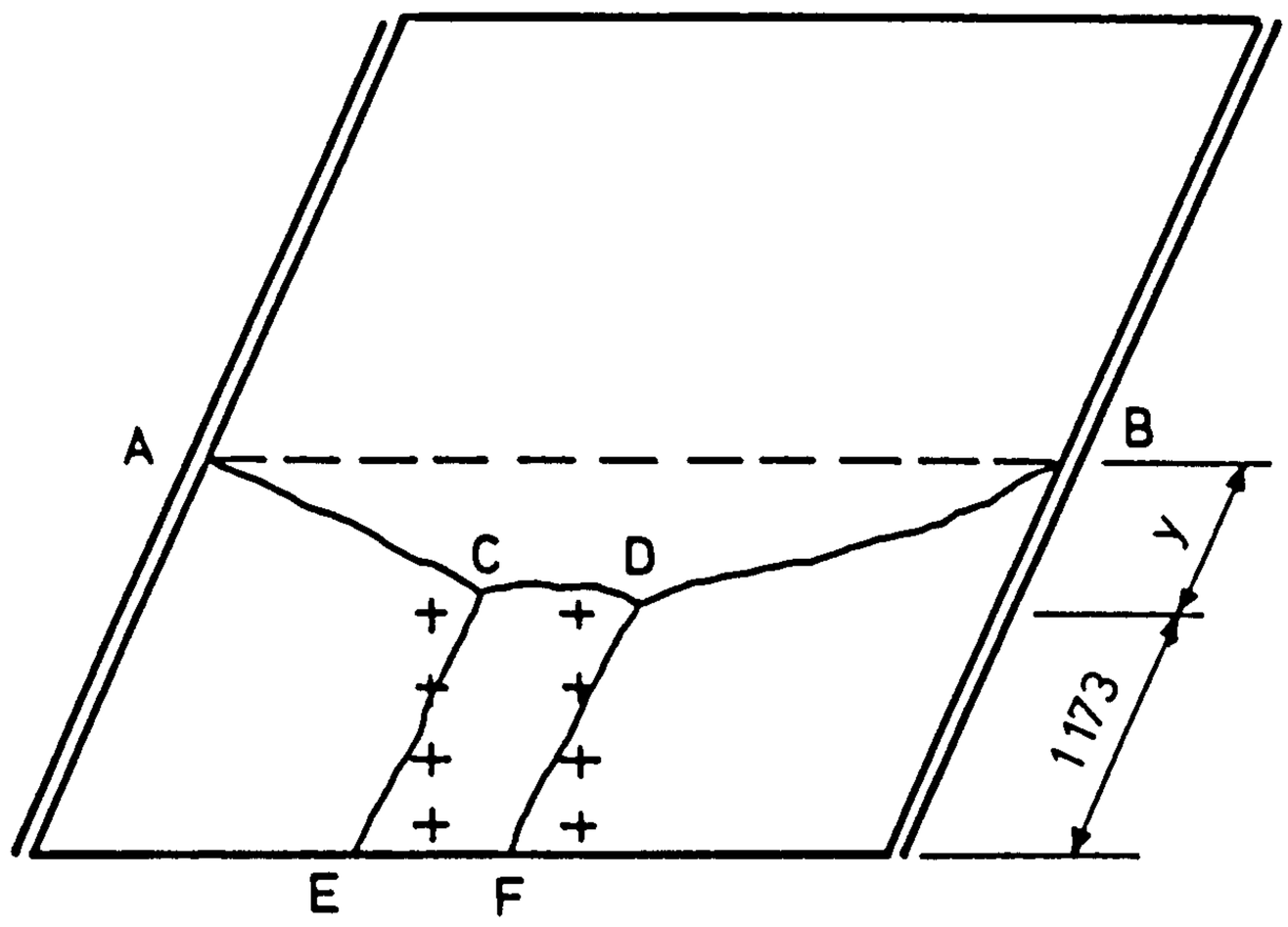

MECHANISM 4

FIG. 3. MODEL DECK 1 TRIAL YIELD LINE PATTERNS.

lines AC and BD are inclined at only about 28 degrees to the longitudinal tendon direction, and it is, therefore, unlikely that all of this steel was yielding. To test the effect of this hypothesis, the yield line analysis was repeated, but with the contributions of the moment of resistance of the sections perpendicular to the free edge on ACDB reduced by a third. The predicted value of the bogie load is reduced to 290 kN. This is similar to the maximum load sustained and it is thus reasonable to postulate that the test was stopped before full yielding of the longitudinal tendons crossing ACDB had occurred.

Discussion

Since yield line analysis involves reinforcement over a considerable portion of a structure, it seems reasonable to consider the flexural capacity per unit length to be based on higher steel strengths than would be used for an individual section check. Beeby[2] has calculated that, if the value of γ_m for two bars crossing a critical section is 1.15, then, for a uniform probability of failure for members with different numbers of bars, the values of γ_m for ten and fifty bars crossing a failing section would be 0.97 and 0.91, respectively. To determine these values, Beeby assumed a normal distribution for the strengths of individual bars and, based on test data, a standard deviation for the yield strengths of individual bars of 10% of the characteristic strength. For a simple mechanism consisting of a single yield line crossing the centre of a slab, it is difficult to justify any value for γ_{f3} other than unity, as the value of the work done can be determined accurately.

Yield Line Analysis of Model 2

As with the model 1 yield line analyses the purpose of the model 2

analyses was to obtain the most realistic estimate of the model's strength. The design load effects safety factor (γ_{f_3}) was taken as unity for all mechanisms.

The yield line analysis technique does not lend itself to computerisation in a way that other structural analysis techniques, such as the finite element method, do. However, the hand calculations required to assemble the energy equations can become tedious and prone to error for anything more complex than a basic mechanism with uniform loading on a right slab. A semi-automated analysis technique was, therefore, developed using an algebraic manipulation package called REDUCE[3]. This system allowed the input of the data describing the problem in the form of expressions including variables such as α, δ etc. After the energy equations had been assembled, partial derivatives with each of the variables could be obtained by the program. The resulting equations could be set to zero and solved simultaneously to obtain the critical configuration.

Loading

The loading that was considered for these analyses corresponds to that given in Chapter 7 section 7.1.3, for the test to failure of model 2, and can be seen in Figure 5. Three UDL intensities were applied to the complete slab area, namely density, density correction and superimposed dead load. In addition live load UDL's and KEL's consisting of footpath live load along both footpaths and full HA UDL and KEL in lane 2 were also considered. A factored HB bogie was placed at mid-span and as close to the free edge allowed by BS 5400 Pt 2 (1978) cl. 3.2.9.1. The 6 load components are described below:-

1. Self weight and density correction:

   (0.00598 + 0.01495) 1.15 = 0.0241 N/mm^2 all over

2. Superimposed dead load:

   0.0024 x 1.75 = 0.0042 N/mm^2 all over

3. Footpath live load:

   0.0025 x 1.50 = 0.0038 N/mm^2 along both footpaths

4. Full HA UDL:

   0.01091 x 1.30 = 0.01418 N/mm^2 in lane 2

5. Full HA KEL:

   9790 x 1.30 = 12730 N at mid-span in lane 2

6. HB bogie:

   73470 x 1.30 β = 95510 β N at midspan.

<u>Best estimate of actual section resistances, see Appendix 7.1</u>

Using the longitudinal section test ultimate sagging moment then:-

M_1 = 360 kNmm/mm

$M_2 = \alpha_2 M_1$ = -120 kNmm/mm $\therefore \alpha_2$ = -0.333

$M_3 = \alpha_3 M_1$ = 55 kNmm/mm $\therefore \alpha_3$ = 0.153

$M_4 = \alpha_4 M_1$ = -41 kNmm/mm $\therefore \alpha_4$ = -0.114

Section resistances other than the longitudinal sagging resistance were derived using actual material properties and partial safety factors equal to unity.

<u>Mechanisms</u>

Six mechanisms were considered and these can be seen in Figures 6 and 7. However, essentially, there are only two different basic patterns. Patterns 1 to 4 belong to one family, while patterns 5 and 6 belong to the second family.

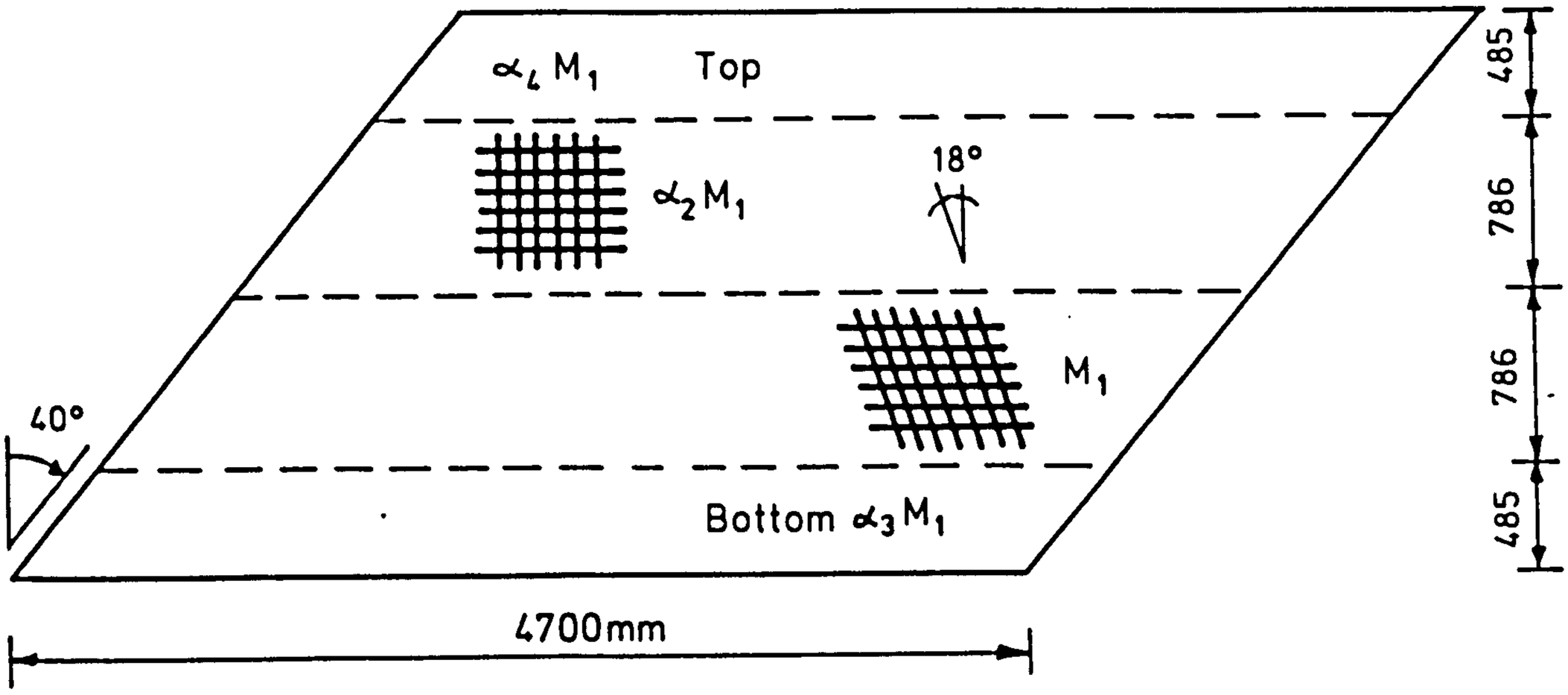

FIG. 4. GENERAL ARRANGEMENT FOR MODEL DECK 2 YIELD LINE ANALYSIS

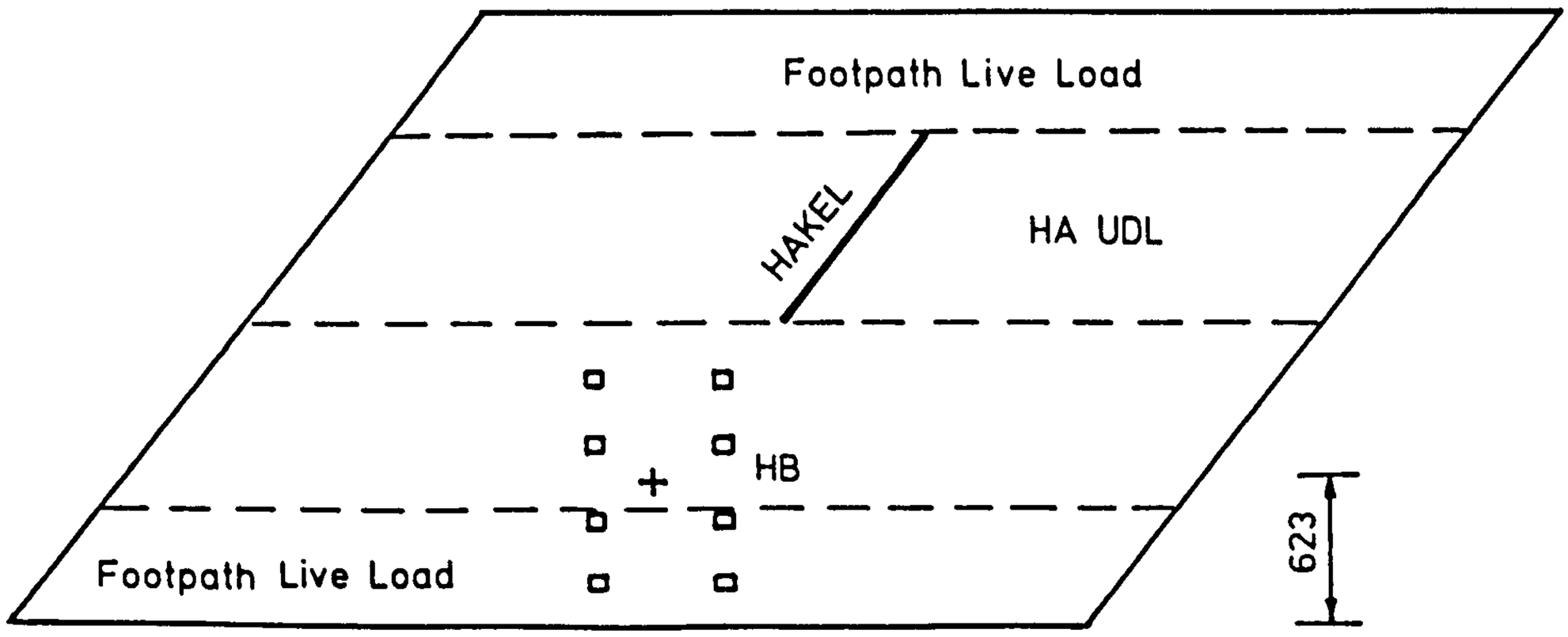

FIG. 5. LOADING REGIME ADOPTED FOR THE YIELD LINE ANALYSIS OF MODEL DECK 2

Mechanism 1: This is the simplest pattern, consisting of a single sagging yield line at midspan, see Figure 6. Energy dissipated by yield lines for a unit displacement of centre line:

$$\left[\left[2542 \quad \frac{1}{2350}\right] M_1 + \left[2814 \quad \frac{1}{2122}\right] \alpha_3 \, M_1\right] 2 = 924.9 \text{ kNmm}$$

Work done by all loads except HB bogie:-

$= 216.4$ kNmm

Work done by HB bogie:-

$$\text{deflection of axle} = \frac{2350 - 257}{2350} = 0.89$$

$\therefore$ work done $= 0.89 \times 95.51 \, \beta = 85 \, \beta$ kNmm

Equating: $216.4 + 85 \, \beta = 924.9$

$\therefore \beta = 8.3$

$\therefore$ No. of 45 units of HB bogie load (at $\gamma_{f1} = 1.30$) $= 8.3$

It will be noticed that this factor of 8.3 is considerably greater than the experimental failure factor of 6.02 given in Appendix 7.2, Table 1. In fact, the premium over the experimental factor, at 38% is similar to the premium calculated for model 1 in the previous section. If the calculated ultimate longitudinal section resistance is used instead of the longitudinal section test ultimate moment, then $\beta =$ 7.7. If the design section strengths were to be used, with $\gamma_{f3} = 1.0$, then the factor $\beta \approx 6.1$ which is within 2% of the actual failure factor for the experiment.

The positioning of the HB bogie significantly closer to the free edge than the design position, introduced the possibility of a 'Y' shaped mechanism forming, therefore, further mechanisms were investigated.

Mechanism 2: The details of mechanism 2 can be seen in Figure 6. The formation of a 'Y' shaped mechanism will depend upon the relative moment capacities in the transverse direction, compared to the longitudinal direction and with the width/span ratio of the structure. For an analysis of this type, where the failure load is applied through a factored HB bogie load, the relative importance of other load types, such as UDL's and KEL's is reduced. This is particularly true for the composite construction form, which possesses a high inherent factor of safety. Therefore, the problem reduces to minimising the energy dissipation in the yield lines, while maximising the displacement of the HB bogie. In order for the HB bogie displacement to be maximised the only remaining variable in mechanism 2 is the location of the longitudinal hogging line at 2542 δ from the free edge.

The details for this mechanism were fed into the REDUCE program, assuming a unit displacement of the HB bogie. This analysis gave the critical value for δ to be 0.53 with β = 9.7. The load energy dissipation equation was calculated as $45.64 + 112.6\ \delta + 95.51\ \beta$ kNmm. However, if a more accurate value had been used for the bogie deflection, then the factor β would have increased. Therefore, this path was not pursued. The crack patterns shown in Chapter 7 Figure 7.8 and 7.9 suggest that a hogging yield line was not forming.

Mechanism 3: The high span/width ratio of this model suggested that the yield line pattern shown in Figure 6 as mechanism 3 was possible. Essentially, this mechanism is the same as mechanism 2, except that the hogging yield line has been allowed to align itself along the free edge.

Examination of Figure 6 will reveal that it is impossible for mechanism 3 to yield a lower value of β than mechanism 1. While the energy dissipated by the longitudinal sagging steel is the same for both mechanisms, there is additional energy dissipation by the transverse sagging steel in mechanism 3, which also has a lower load energy dissipation than mechanism 1.

Mechanism 4: Mechanism 4, the configuration of which can be seen in Figure 7, is essentially the same as mechanism 3, except that the unit displacement now only occurs at one point, which is along the free edge. Mechanism 4 produces a similar yield line energy dissipation equation to that of mechanism 3. However, the load energy dissipation equation will be reduced due to the reduced deflection of the HB bogie. Therefore, a higher HB bogie load factor, β, will result.

Mechanism 5: Mechanisms 1 to 4 considered global forms of failure involving a large proportion of the slab. There is the possibility of a more local mode of failure, see Figure 7, occurring in the free edge zone of the slab. Mechanism 5, was utilised to investigate the possibility of this mode of failure occurring. The geometry of this mechanism is such that the sagging yield line bd can assume virtually any orientation. Thus the geometry of the pattern is defined by three variables α, γ and δ. The REDUCE program was used to obtain the critical values for these three variables which were 1.18, 0.299 and 0.70 respectively with $\beta = 16.8$. It will be seen that in the critical pattern the transverse sagging yield line is aligned along the transverse sagging steel, thus there is no energy dissipated by this steel.

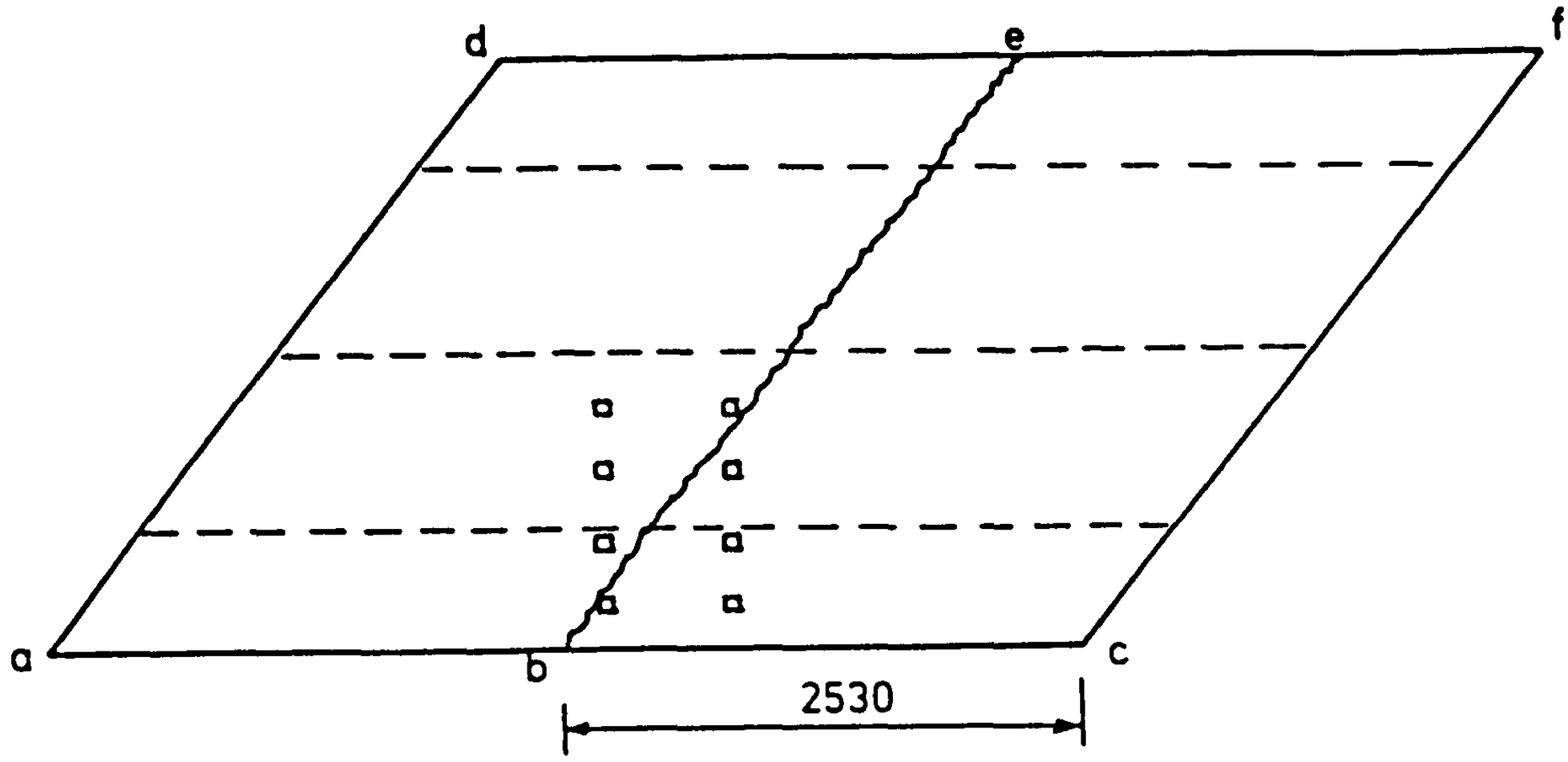

Mechanism 1

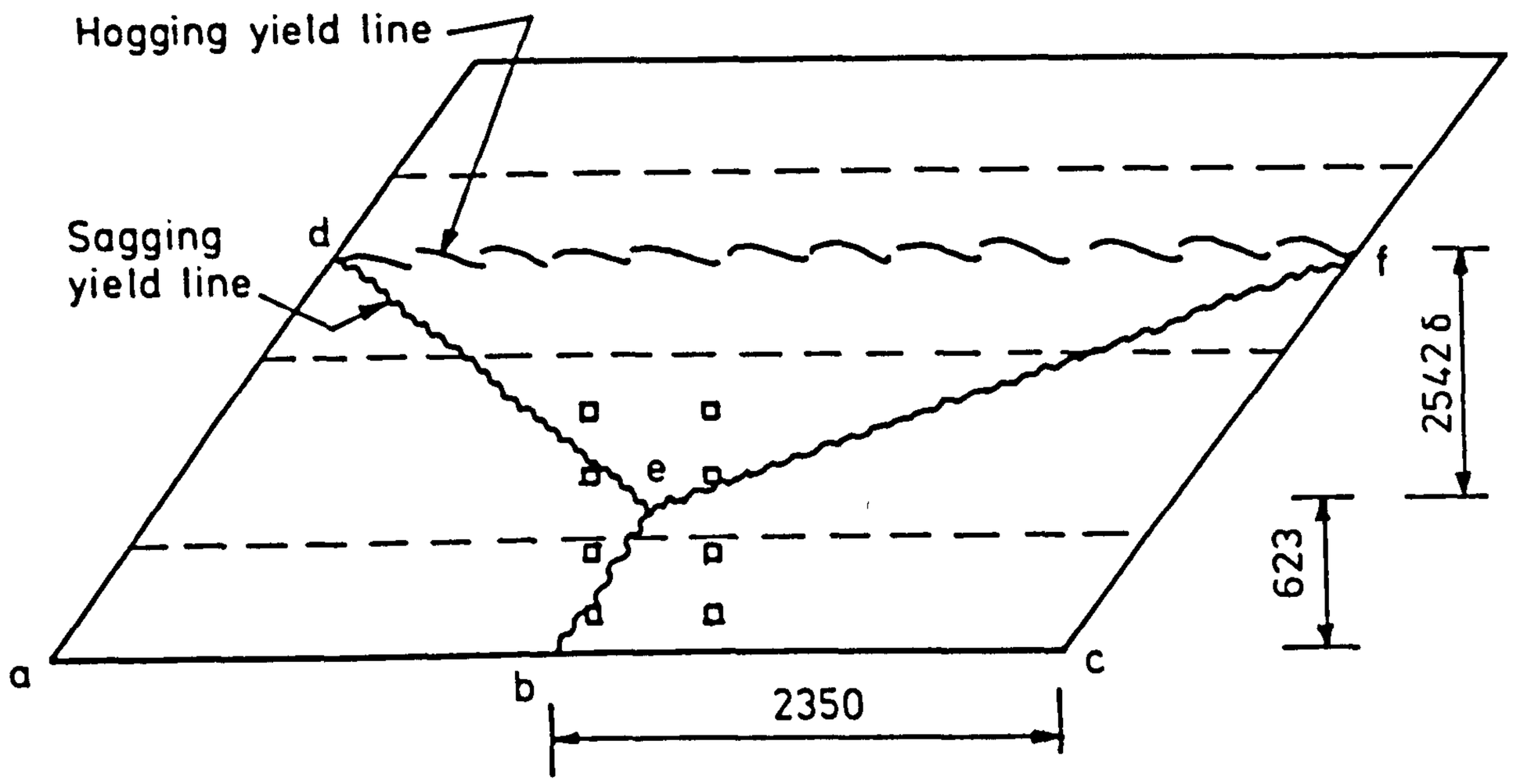

Mechanism 2

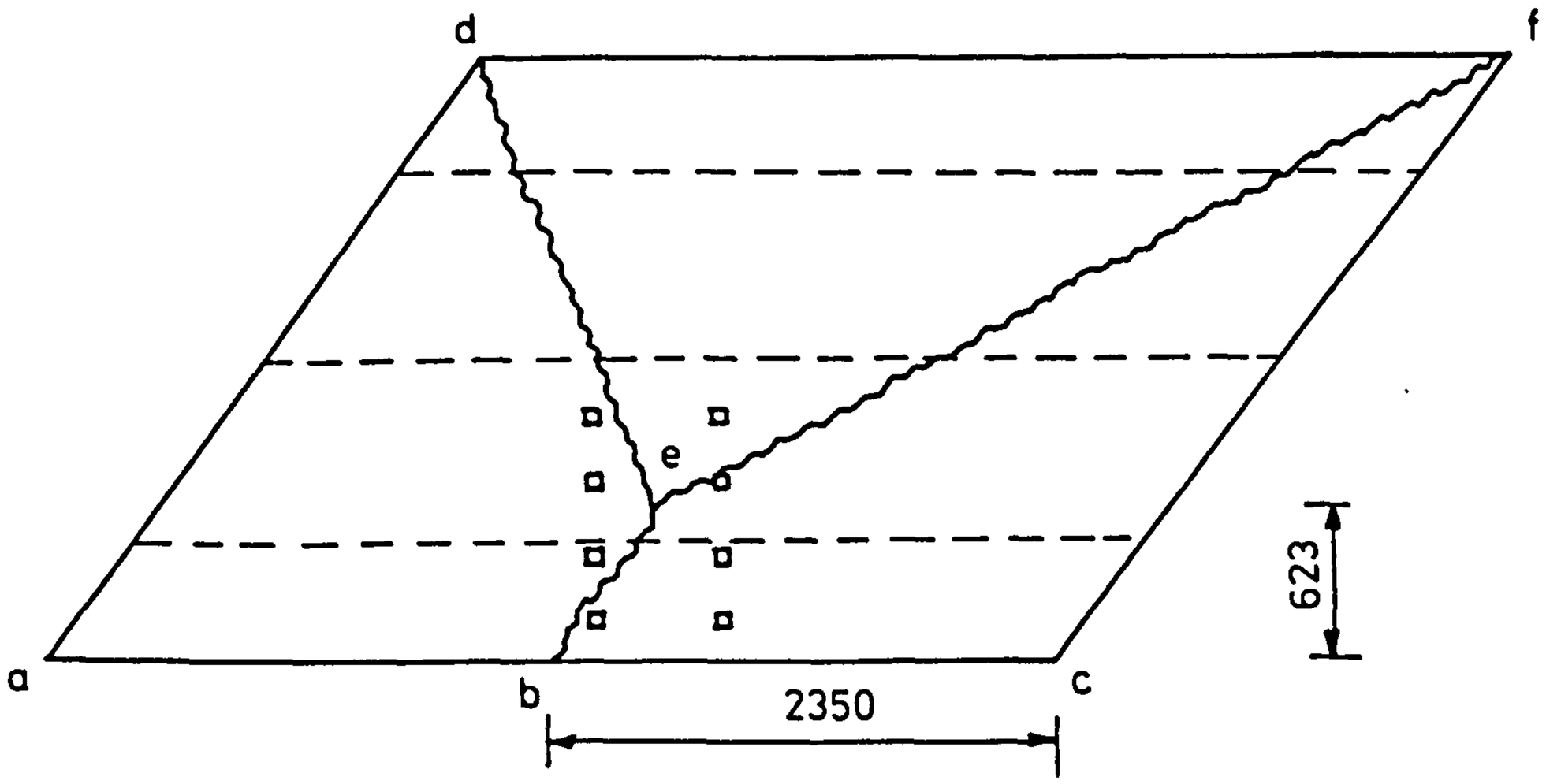

Mechanism 3

FIG. 6. MECHANISM ADOPTED FOR THE YIELD LINE ANALYSIS OF MODEL 2

One of the major influences upon the formation of this pattern is the geometry of the HB bogie. As the bogie becomes larger the deflection of each of the wheels reduces and hence the load energy also reduces. This can be illustrated by re-analysing the pattern assuming that the total HB bogie load is applied through its central point. In this case, the reduce program gives critical values of $\alpha = 1.27$, $\gamma = 0.48$ and $\delta = 0.625$ with $\beta = 13.7$. Thus, this apparently simple change has reduced the HB bogie factor by 18%.

Mechanism 6: Using the correct application points for the HB bogie load, the REDUCE program gave 0.70 as the critical value for δ for mechanism 5. The large value of this factor increases the likelyhood of a pattern similar to mechanism 5, but stretching across the complete model width, becoming critical. However, if the mechanism were to cover the whole width, then it is likely that the apex of the pattern, point d, would be located at the corner of the slab, see Figure 7. With this pattern, the sagging yield line would be closely aligned along the transverse sagging steel. Thus mechanism 6, which can be seen in Figure 7 was obtained. The geometry of this pattern is defined through one variable, α. Using the REDUCE program, the critical value for the HB bogie factor β was 16.4 at $\alpha = 1.20$. Thus, it can be seen that this value of β is less than that for mechanism 5, but is double that for mechanism 1.

Discussion

It can be seen that the energy dissipated by the longitudinal sagging steel dominates the failure mode for all of the selected mechanisms. Thus for the mechanisms with a failure mode involving the complete model width, the problem essentially simplifies to locating the

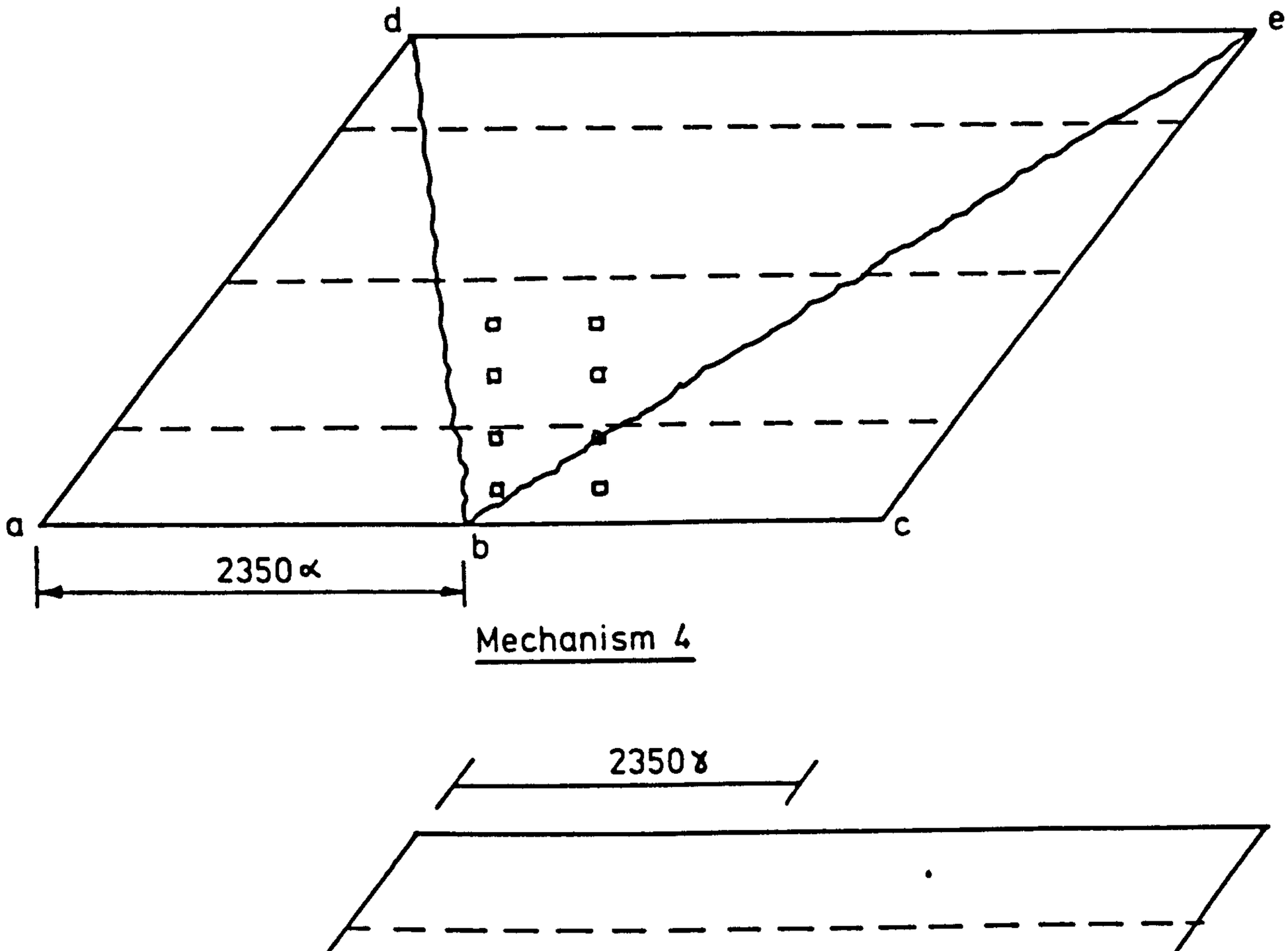

Mechanism 4

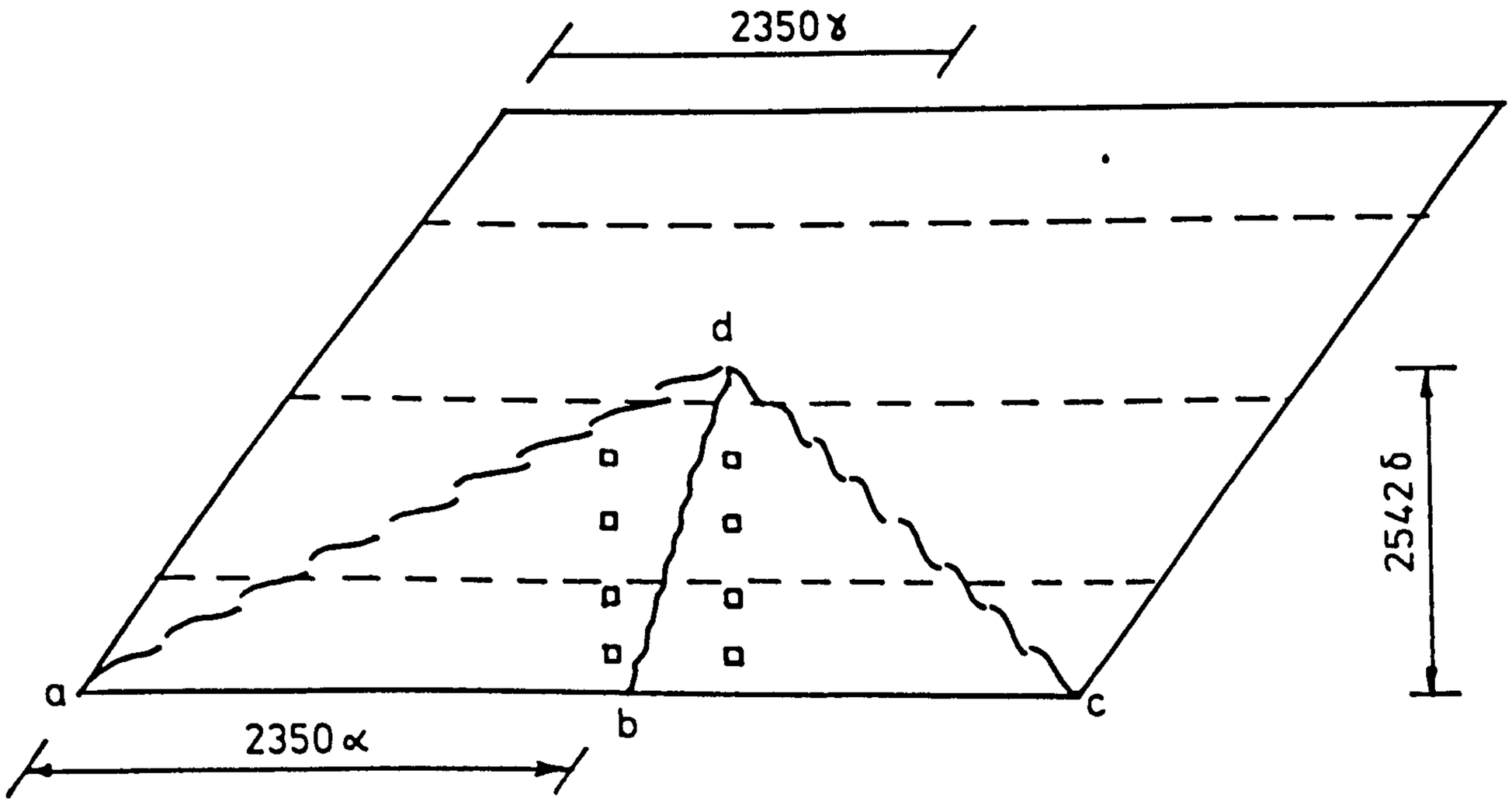

Mechanism 5

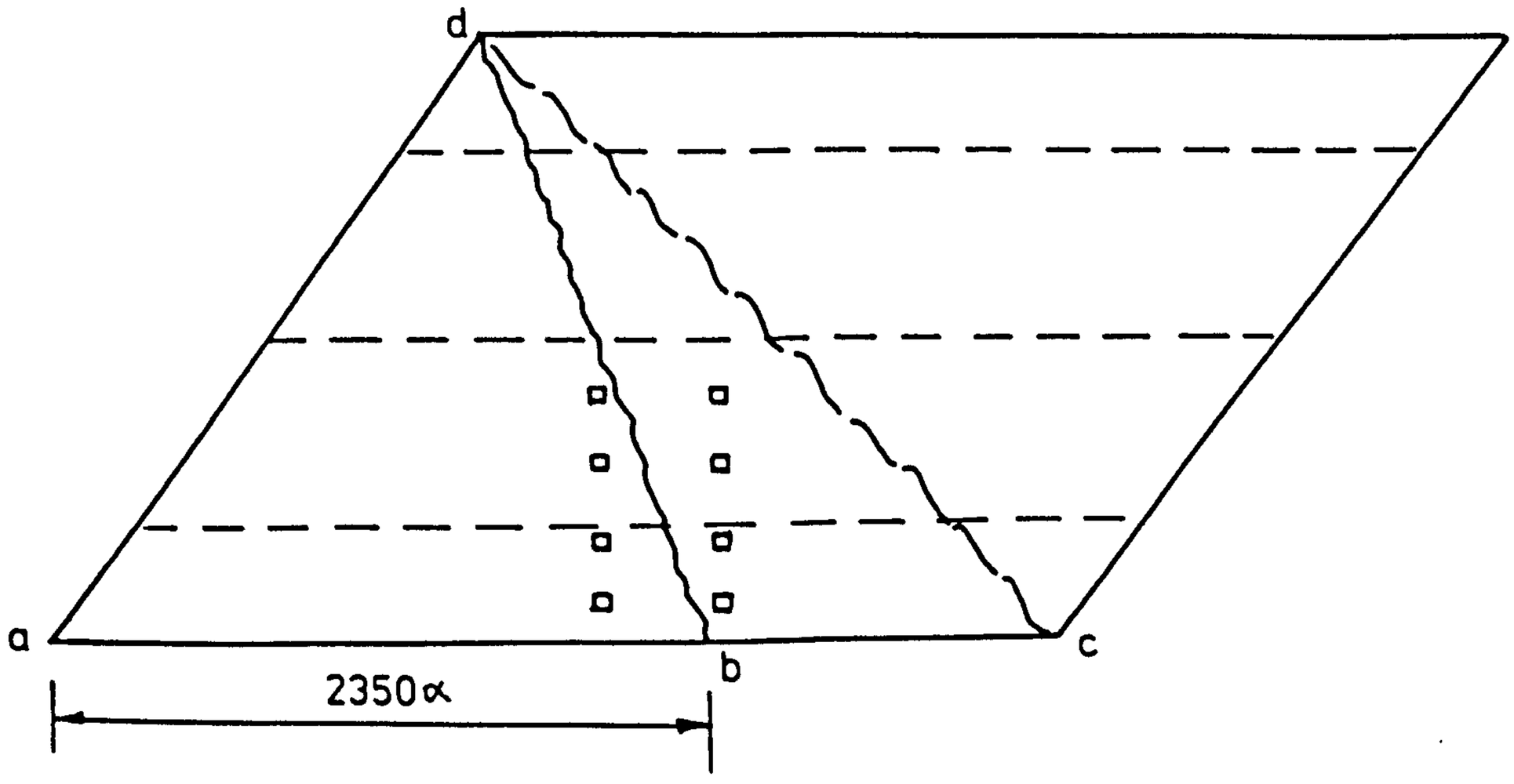

Mechanism 6

FIG. 7. MECHANISMS ADOPTED FOR THE YIELD LINE ANALYSIS OF MODEL 2

pattern that maximises the load energy dissipation. The factored HB bogie failure criteria of the current investigation significantly reduces the importance of loading types besides the HB bogie.

Theoretically, the yield line method is an upper-bound approach. However, through tests, it has been shown to give good predictions of a slab's load carrying capacity. The lowest value of β, for all the mechanisms considered here, was 8.3, for mechanism 1. However, this is 38% greater than the actual failure factor of 6.02 for the composite slab. The value of 8.3 was calculated using the actual loading and section resistances with γ_{f_3} set to unity. In the test, the load-deflection curve had reached its falling branch. However, inspection of the model and the steel strain readings indicated that a yield line mechanism had not fully formed. At least three tendons were heard to rupture and the composite action of the slab was breaking down. It is interesting to note, that if the yield line calculations are performed with the design section resistances, then β for the critical mechanism reduces to 6.1, which is within 2% of the actual failure factor. If one sets γ_{f_3} to the BS5400 Pt 4 (1978) value of 1.15, then β reduces to 5.30, which is approximately 12% below the experimentally obtained value.

References

1. BS 5400 (1978) Parts 2 and 4, British Standards Institution.

2. Beeby, A.W.
"A proposal for changes to the basis for the design of slabs", Technical Report 547, Cement & Concrete Association (1982).

3. Hearn, Anthony C
"REDUCE User's Manual", Version 3.2, Rand Publication CP78 (Rev 4/85), April 1985.